Dynamics of the unstable wake modes in automotive aerodynamics : from simplified models to real vehicles

Guillaume Bonnavion

To cite this version:

Guillaume Bonnavion. Dynamics of the unstable wake modes in automotive aerodynamics : from simplified models to real vehicles. Fluid mechanics [physics.class-ph]. Université Paris Saclay (COmUE), 2018. English. NNT : 2018SACLY010 . tel-01915961

HAL Id: tel-01915961
https://pastel.hal.science/tel-01915961

Submitted on 8 Nov 2018

HAL is a multi-disciplinary open access archive for the deposit and dissemination of scientific research documents, whether they are published or not. The documents may come from teaching and research institutions in France or abroad, or from public or private research centers.

L'archive ouverte pluridisciplinaire **HAL**, est destinée au dépôt et à la diffusion de documents scientifiques de niveau recherche, publiés ou non, émanant des établissements d'enseignement et de recherche français ou étrangers, des laboratoires publics ou privés.

NNT : 2018SACLY010

Thèse de doctorat

Dynamics of the unstable wake modes in automotive aerodynamics: from simplified models to real vehicles

Thèse de doctorat de l'Université Paris-Saclay
préparée à l'Ecole nationale supérieure de techniques avancées

Ecole doctorale n°579 Sciences mécaniques et énergétiques, matériaux et géosciences (SMEMAG)
Spécialité de doctorat : Mécanique des fluides

Thèse présentée et soutenue à Palaiseau, le 5 Octobre 2018, par

GUILLAUME BONNAVION

Composition du Jury :

Annie Leroy Maître de Conférences - HDR, Université d'Orléans (PRISME)	Rapporteur
Jonathan Morrison Professeur, Imperial College London (Department of Aeronautics)	Rapporteur
Jacques Borée Professeur, ISAE-ENSMA (Institut PPRIME)	Président
Thomas Castelain Maître de Conférences, Université Lyon 1 Claude Bernard (LMFA)	Examinateur
Lutz Lesshafft Chargé de Recherche, Ecole polytechnique (LadHyX)	Examinateur
Olivier Cadot Professeur, University of Liverpool (School of Engineering)	Directeur de thèse
Denis Sipp Maître de recherches, ONERA Meudon (DAAA)	Co-directeur de thèse
Jean Délery Président du Conseil Scientifique, CNRT R2A	Invité
François Richez Ingénieur de recherche, ONERA Meudon (DAAA)	Invité

Sciences mécaniques et énergétiques, matériaux et géosciences - ED 579
ENSTA ParisTech, Université Paris-Saclay

Thèse de doctorat

Soutenue par
Guillaume Bonnavion

Pour obtenir de titre de
Docteur de l'Université Paris-Saclay
Specialité : Mécanique des Fluides

Dynamics of the unstable wake modes in automotive aerodynamics: from simplified models to real vehicles

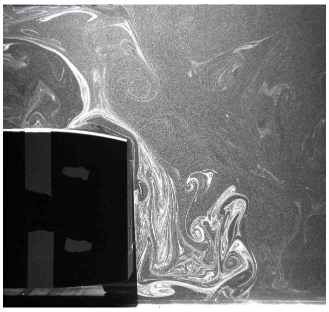

Manuscrit temporaire, soutenance le 5 octobre 2018

Jury

Rapporteurs :	Dr. Annie Leroy	Université d'Orléans (PRISME)
	Pr. Jonathan Morrison	Imperial College London
Examinateurs :	Pr. Jacques Borée	ISAE-ENSMA (PPRIME)
	Pr. Lutz Lesshafft	École polytechnique (LadHyX)
	Dr. Thomas Castelain	Université Lyon 1 (LMFA)
	Dr. Jean Délery	CNRT R2A - ONERA Meudon
	Dr. François Richez	ONERA Meudon (DAAA)
Encadrants :	Pr. Olivier Cadot	University of Liverpool
	Dr. Denis Sipp	ONERA Meudon (DAAA)

Abstract

Since the recent discovery of asymmetric modes in the wake of a simplified vehicle geometry, reminiscent from a bifurcation at low Reynolds numbers at first evidenced experimentally by Grandemange *et al.* (2012*a*) and recently confirmed numerically by Evstafyeva *et al.* (2017), some questions related to the aerodynamic development of ground vehicles such as the influence of lateral wind, pitch and afterbody boat-tail classically used during shape optimization in presence of these modes remain unanswered. Our work is devoted to assess those questions experimentally for simplified but also real geometries. The tests are conducted in an industrial wind-tunnel, at the 2/5-scale for the academic body – flat-backed Ahmed body – and at the full scale for the minivans – Renault Kangoo, Citroën Berlingo, Peugeot Partner and 5008. We show that the body's misalignment with respect to the incoming flow, *i.e.* yawing or pitching conditions, only modifies the asymmetric mode's orientation without affecting its intensity estimated with the base pressure gradient. We build a model predicting not only this orientation but also the consequences on the cross-flow aerodynamic loading. The contribution of the instability to the lift or side force coefficients is of the order of 0.02 independently of lateral wind or of the vehicle's pitch and the wake's fluctuations are identical to those of the cross-flow loading up to a factor of proportionality depending on the afterbody geometry. Usually used in view of drag reduction, afterbody boat-tails also impact the wake dynamics and its orientation but the instability is never suppressed. These results are retrieved for real vehicles such as minivans, whose wake is then subjected to the same asymmetric mode as well, revealed unambiguously during the bi-stable dynamics between the two wake states, observed during yaw or pitch sensitivity experiments; wake reversals corresponding to lock-in might also be triggered depending on the setup. Our results indicate that, for the four considered vehicles, the asymmetric wake mode is systematically present in the driving envelope, corresponding to the conditions encountered or likely to be in real-life. The control or the suppression of this mode should offer new optimization's perspectives since the wake would be symmetrized (Cadot *et al.*, 2015*b*); based on our results, this could be applied not only to simplified geometries but also to blunt based real vehicles such as minivans or SUVs.

Résumé

Depuis la découverte des modes asymétriques dans le sillage d'un corps simplifié d'automobile, réminiscents d'une bifurcation à bas nombre de Reynolds comme l'ont d'abord montré expérimentalement Grandemange *et al.* (2012*a*) puis récemment confirmé numériquement Evstafyeva *et al.* (2017), se posent des questions propres au développement aérodynamique des véhicules terrestres telles que l'influence du vent latéral, de l'assiette et du rétreint d'arrière-corps couramment utilisé en phase d'optimisation lorsque ces modes sont présents. Notre travail s'attache à répondre expérimentalement à ces questions pour des géométries simplifiées mais aussi réelles. Les essais sont réalisés en soufflerie industrielle à l'échelle 2/5 pour le corps académique – corps d'Ahmed à culot droit – et en pleine échelle pour les monospaces – Renault Kangoo, Citroën Berlingo, Peugeot Partner et 5008. Nous montrons que le désalignement du véhicule par rapport à l'écoulement incident, c'est-à-dire l'introduction d'un angle de dérapage ou d'assiette, n'a pour effet que de modifier l'orientation du mode asymétrique sans en changer l'intensité ; ces grandeurs sont estimées à l'aide du gradient de pression au culot. Nous construisons un modèle simple prédisant non seulement cette orientation mais aussi les conséquences sur les efforts aérodynamiques transverses. La contribution de l'instabilité sur les coefficients aérodynamiques de portance ou d'effort latéral est de l'ordre de $0,02$ indépendamment du vent de travers et de l'assiette du véhicule et les fluctuations du sillage sont égales à un facteur de proportionalité près à celles des efforts aérodynamiques transverses. Couramment utilisés pour réduire la traînée, les rétreints d'arrière-corps affectent également la dynamique du sillage et son orientation, mais l'instabilité n'est jamais supprimée. On retrouve ces résultats pour des véhicules réels de type monospace dont le sillage est donc également soumis au même mode asymétrique, révélé sans ambigüité par des expériences de sensibilité en assiette mettant en évidence une dynamique bistable entre deux états du sillage. Nos résultats indiquent que, pour tous les véhicules considérés, le mode asymétrique de sillage est systématiquement présent dans l'enveloppe de conduite qui correspond aux conditions rencontrées ou pouvant l'être en réalité. Le contrôle ou la suppression de ce mode devrait offrir de nouvelles perspectives d'optimisation en symétrisant le sillage (Cadot *et al.*, 2015*b*); d'après nos résultats, cette stratégie est applicable non seulement aux géométries simplifiées mais aussi aux véhicules réels à culot droit de type monospaces ou SUV.

À ma famille et à mes proches, pour tout ce qu'ils m'apportent.

« Le plus grand bonheur de l'étude consiste à trouver les raisons soi-même. »
René Descartes, *Les règles pour la direction de l'esprit* (1629)

Remerciements

Nombreux sont les lecteurs qui commenceront par jeter un œil, même furtif, à ces lignes. C'est pourquoi elles méritent une attention toute particulière bien que rédigées dans un autre état d'esprit que le reste du manuscrit… Pour autant, elles ne sont certainement pas les plus simples à écrire. Il est bien évidemment impossible de mentionner chacun mais, bien entendu, toutes les personnes ayant de près ou de loin, directement ou (très) indirectement participé à ce travail sont remerciées.

Sans originalité, je souhaite remercier mon directeur de thèse, Olivier Cadot. Lorsque, voici un peu plus de trois ans, tu m'as proposé de venir faire une thèse à l'UME, nous ne savions pas encore quel chemin nous allions parcourir. Tu as su partager tes talents d'expérimentateur hors pair, tu t'es beaucoup investi dans ce travail tout en me laissant l'autonomie nécessaire. Malgré l'éloignement géographique des deux dernières années, tu es toujours resté disponible et réactif. Ton enthousiasme aura aussi marqué cette thèse ! Pour ces raisons (et pour les autres !), je te remercie profondément.

La pertinence des remarques de mon co-directeur, Denis Sipp, sur ce travail principalement expérimental ainsi que la capacité à me faire rebondir dans les moments de creux m'ont été très précieuses et je t'en suis extrêment reconnaissant. Merci aussi d'avoir initié le volet numérique de ce travail grâce auquel j'ai énormément appris, même si le temps nous a quelque peu manqué…

La partie numérique de ce travail n'aurait pas pu voir le jour sans l'ONERA Meudon (et plus particulièrement le Département d'Aérodynamique, Aéroélasticité, Acoustique DAAA) où j'ai été chaleureusement accueilli et grâce auquel j'ai pu avoir accès aux *clusters* de calcul. Je dois principalement remercier François Richez qui m'a encadré, soutenu et surtout beaucoup appris sur la simulation numérique. Merci infiniment pour le temps que tu m'as consacré en plus de tes autres activités ! La CFD et elsA ont été moins obscurs grâce à ton concours, mais, malheureusement, un an et demi n'aura pas suffi à tout terminer. Je souhaite aussi mentionner ta relecture détaillée de ce manuscrit. Merci également à Patrick Gardarein, mailleur professionnel, pour les trucs et astuces de maillage sous IcemCFD !

Être rapporteur d'une thèse n'est pas tâche aisée, en particulier lorsque le mémoire est long. Je souhaite donc remercier chaleureusement Annie Leroy et Jonathan Morrison pour leur investissement, leurs commentaires détaillés et précis, ainsi que pour les nombreuses questions qu'ils ont soulevées et surtout pour l'intérêt qu'ils ont porté à ce travail. Merci également à Jacques Borée d'avoir accepté de présider mon jury de thèse, mais aussi pour les nombreuses discussions que nous avons eues au cours de ces trois années. La boucle est bouclée : tu m'as donné les bases de MécaFlu à l'ENSMA et tu présides aujourd'hui mon jury ; merci ! Je souhaite également remercier Thomas Castelain pour ses remarques très pointues ainsi que Lutz Lesshafft qui a permis d'ouvrir la soutenance vers de nouvelles perspectives liées à la stabilité et au contrôle pendant la discussion.

Je tiens également à remercier vivement le Centre National de Recherche Technologique Recherche en Aérodynamique et Aéroacoustique des véhicules terrestres (CNRT R2A) pour avoir co-financé cette thèse avec l'ENSTA ParisTech mais aussi avoir financé l'acquisition du scanner de pression, des platines de translation, du culot modulable, des rétreints et du matériel nécessaire aux essais (plancher plat...). Son Conseil Scientifique a supervisé et guidé ces travaux et ses membres en sont chaleureusement remerciés : Jean Délery, Président (qui m'a fait l'immense honneur de prendre part au jury de thèse), Vincent Herbert (Groupe PSA), Sylvain Parpais et Denis Ricot (Groupe Renault), Rémi Vigneron (GIE-S2A), Charles Pezerat (Laboratoire d'Acoustique de l'Université du Maine, Le Mans), Thomas Castelain (Université Lyon 1 Claude Bernard, LMFA) et Reynald Bur (ONERA DAAA). Les discussions que nous avons eues au cours de ces trois ans ont été remarquablement fructueuses et la liberté et l'autonomie que vous m'avez laissées un atout indéniable. Je n'oublie pas non plus que, sans le CNRT R2A, nous n'aurions pas pu disposer des moyens d'essais exceptionnels et du support technique et logistique dont nous avons bénéficié. Je remercie particulièrement le Groupe PSA et le Groupe Renault de nous avoir fourni les véhicules pour les essais pleine échelle, ainsi que le Groupe PSA de nous avoir permis d'utiliser le corps d'Ahmed. Je salue aussi les interactions que nous avons eu avec Marc Michard et sa participation aux essais.

Je remercie également l'ensemble du *staff* des souffleries du GIE-S2A et tout particulièrement Philippe Thébault, technicien responsable de la soufflerie 2/5ème. Ton grand professionnalisme, ton soin méticuleux apporté aux essais mais aussi tes connaissances techniques, ta grande vigilance et ta bonne humeur (oui, oui, c'est quand tu ne râles plus qu'il faut s'inquiéter !) ont été un atout majeur du succès de ces travaux. Tout ceci n'aurait pas non plus été possible sans le concours de David Pérez, technicien responsable de la PIV. Merci pour tout le travail que tu as réalisé, aussi bien en séances que lors du traitement des données (et il y en avait !). Il ne faut bien sûr pas oublier Eric Van Grevenynghe, ingénieur, dont la bonne humeur et l'aide apportée ont été précieuses. Bien sûr, je remercie aussi Rémi, Christian, Christophe ainsi que tout le personnel (notamment les techniciens S1) du GIE-S2A avec lesquels travailler a toujours été un plaisir, mais aussi pour ce que vous avez apporté à ces travaux et à ma réflexion. Je remercie aussi Antoine Évrard qui m'a mis le pied à l'étrier pour les essais (décidément, ils sont bien ces ensmatiques !).

Sans aide, impossible de réaliser des essais ; la contribution de Thierry Pichon, de Nicolas Baudet, de Lahcène Cherfa est telle que rien n'aurait été possible sans eux. Un immense merci à vous pour les discussions sur la conception des pièces, leur fabrication, leur installation et leur transport, ainsi qu'à Jean-Marc Besnier pour la conception et l'installation du plancher plat. Le culot modulable a été conçu en collaboration avec Aero Concept Engineering (Magny-Cours, France) et fabriqué par leurs soins. Je souhaite les remercier pour leur grand professionnalisme, en particulier Alexis Lapouille et Rémy Cavecchia, qui est désormais en thèse.

Je souhaite aussi remercier l'ensemble des collègues (actuels et passés) de l'Unité de Mécanique de l'ENSTA ParisTech et de l'IMSIA pour toutes les discussions scientifiques (ou pas !), le soutien, les conseils et la bonne ambiance du labo qui fait que, même par un pluvieux matin d'automne, travailler reste un plaisir ! Sans ordre de préférence, Corinne, Sabine, Marica, Caroline, Habibou, Jean-François, Benjamin, Olivier, Jean, Romain, Cyril, José, mes collègues stagiaires, doctorants, anciens doctorants et post-doctorants (Julie, Marie, Arnaud, Joosung, Rogers, Manuel, Ángels, Stefania, Jin-Jack, Tommy, David, Emil, Nicolas, Romain, Robin, Aurore et ceux que j'ai oubliés ici !). J'aurais voulu mettre une anecdote pour chacun, mais cela aurait été beaucoup trop long ; simplement, un immense merci. Aurélien Joly, mon co-bureau, a participé bien plus qu'il ne l'imagine au succès de ce travail ; pour toutes les raisons que tu sais, je te remercie et je te souhaite bon courage dans la dernière ligne droite. Je salue également les discussions riches que nous avons eues avec Pierre Moussou. Je remercie aussi l'ensemble des membres de la communauté des sillages 3D décollés et du contrôle (notamment les membres du GDR 2502 Contrôle des Décollements) avec lesquels nous avons eu des discussions enrichissantes, notamment Fabien Harambat, Christophe Sicot, Ruying Li, Diogo Barros, Yann Haffner, Eliott Varon, Stéphanie Pellerin, Bérangère Podvin et tous ceux (nombreux) que je n'ai pas cités mais qui, j'en suis sûr, se reconnaîtront. Luc Pastur a été le témoin privilégié du déroulement de cette thèse et je souhaite te remercier vivement pour tout ce que tu y as apporté mais aussi pour ta jovialité, ta bonne humeur et tes encouragements constants. Je remercie également l'ensemble des membres du DAAA, ainsi que les collègues doctorants / post-doctorants (Lucas et Johann qui furent mes premiers co-bureaux, Quentin qui fut le suivant, Léopold, Jean-Lou, Carlos, Luis, Denis, Jahnavi, Tobias, Ye-Bonne, Nicolas, Tristan, Colin, Nicolo, Simon. . .).

It is impossible for me not to mention Professor Hassan M. Nagib from Illinois Institute of Technology, Chicago, IL. Hassan, since the very first time you started tutoring me when I went to grad school, you taught me your passion for good and for hard work. I really appreciated my master's research with you there and the support you gave me throughout my Ph.D. as well as having you in the audience during two talks, at APS in Denver and during the BBVIV conference in Carry-le-Rouet. I want you to know that nothing would have been possible without your mentoring. Thank you!

Impossible également de ne pas mentionner tous mes amis pour leur soutien, en particulier Armande qui m'a fait le plaisir immense de venir assister à la soutenance et Perrine pour ses encouragements. Je souhaite également remercier (même si, à ce niveau-là, c'est plus que remercier !) Pierre Pradel (Merci Binôme ! ©ENSMA) ; être binômes, c'est quand même quelque chose (et on n'en dira pas plus ici !). Un petit coucou à toute la promo ENSMA 2014 (très bon esprit !), à cette école à laquelle je dois beaucoup et aussi à Alexandre Glad (eh oui, on va peut-être bien pouvoir continuer à faire des bétaillères. . . une hybride pour toi ?).

L'investissement demandé par une thèse est si important que la famille du doctorant joue également un rôle crucial. Papa, Maman, je souhaite vous remercier du fond du cœur pour tout ce que vous avez fait pour moi mais aussi et surtout pour votre soutien sans faille au cours de ces années, mais aussi au cours de celles qui m'ont conduit là où je suis aujourd'hui. Je souhaite également remercier mes grands-parents, mais également d'autres membres de ma famille. Papi, Mamie, vos attentions m'ont donné quotidiennement l'énergie pour toujours aller de l'avant. Michel, tu as été un exemple pour moi et les nombreuses discussions scientifiques (ou pas !) m'ont non seulement fourni de très nombreuses nouvelles pistes de réflexion mais aussi fait voir les choses différemment lorsque c'était nécessaire. Renée, thank you so much for your unconditional support. Je dois aussi signaler ma tante Antoinette et mes cousins Chloé et André. Je souhaite dédier ce travail aux membres de la famille qui nous ont quitté (mes grands-parents paternels, Lino et Perrine). Je salue également Florence, Sabri, Margot, Victor, Jean-Michel et Nathalie, la *jolie* famille qui m'aura permis de m'évader. Enfin, comment ne pas mentionner Sandra ? Même lorsque tu étais toi-même dans le *rush* de la rédaction et de la soutenance, tu as toujours été là lorsque j'en ai eu besoin. Ta relecture du manuscrit et tes commentaires m'ont été d'une grande aide et ton emménagement avec moi m'a apporté une bouffée d'oxygène très bénéfique lors de la fin de la rédaction et de la préparation de la soutenance. Pour tout ce que tu m'apportes et pour toutes les bonnes choses à venir, merci.

Ah, un dernier mot pour vous remercier, vous, qui lisez ce manuscrit.

Contents

Abstract v

Résumé vii

Remerciements xiii

Contents xvii

Nomenclature xxiii

List of figures xxvii

List of tables xxxv

1 Introduction 1
- 1.1 General context of the study 2
- 1.2 From simplified models to real vehicles 4
- 1.3 Turbulent wake of the Ahmed body 7
- 1.4 Motivations of this work 13
- 1.5 Outline of the thesis 14

2 Experimental setup 17
- 2.1 Wind tunnels 19
  - 2.1.1 Full-scale wind tunnel 19
  - 2.1.2 Model-scale wind tunnel 20
- 2.2 Measurement devices 22
  - 2.2.1 Pressure scanner for unsteady measurements 22
  - 2.2.2 Force balance for unsteady measurements 25
- 2.3 In-wake velocity measurements 26
  - 2.3.1 Tomographic system for in-wake velocity measurements 26
  - 2.3.2 Particle Image Velocimetry system 27
- 2.4 Flat-backed Ahmed body 27
- 2.5 Vehicles used for full-scale studies 29

2.6 Experimental procedure: acquisition of data 30
2.7 Data post-processing 30

I Simplified geometries: flat-backed Ahmed bodies 33

3 Experimental investigation of the mean flow around the squareback Ahmed body 35
3.1 Brief literature review 37
3.2 Setup 38
3.3 Results 39
  3.3.1 Mean velocity field 39
  3.3.2 Mean base pressure distribution 42
  3.3.3 Reynolds number effect 43
3.4 Discussion 44
3.5 Concluding remarks 46

4 Unstable wake dynamics with body inclination and ground proximity 47
4.1 Literature review 49
4.2 Setup 51
4.3 Results 54
  4.3.1 y-instability 54
    4.3.1.1 Baseline of the squareback configuration 54
    4.3.1.2 Wake sensitivity towards the ground clearance c^* 55
    4.3.1.3 Wake sensitivity towards the yaw angle β in the unstable regime $c^* > c^*_S$ 58
    4.3.1.4 Wake sensitivity towards the pitch angle α in the unstable regime $c^* > c^*_S$ 59
    4.3.1.5 Resulting wake orientations for the squareback geometry . 62
    4.3.1.6 Baseline with a rear cavity 63
    4.3.1.7 Wake sensitivity to the body orientation with the rear cavity 64
    4.3.1.8 Resulting wake orientations with the rear cavity 64
    4.3.1.9 Aerodynamic loading applied to the body varying its inclination and the ground proximity and contribution of the y-instability 64
  4.3.2 z-instability 70
    4.3.2.1 Baseline case with $W_b^* = 0.940$ 70
    4.3.2.2 Wake sensitivity towards the ground clearance c^* 71
    4.3.2.3 Wake sensitivity towards the yaw angle β in the unstable wake regime $c^* > c^*_S$ 73
    4.3.2.4 Wake sensitivity towards the pitch angle α in the unstable wake regime $c^* > c^*_S$ 77
    4.3.2.5 Wake orientations resulting from the z-instability 78
    4.3.2.6 Aerodynamic loading applied to the body varying its inclination and contribution of the z-instability 79
4.4 Discussion 82
  4.4.1 Role of the phase dynamics of the unstable wake 82
  4.4.2 Phase dynamics adaptation and consequences on cross-flow force . . 84
  4.4.3 A general model for the y- and the z-instabilities 87

4.4.4 Identification of a drag optimum during wake bistability 89
4.5 Concluding remarks 90

5 Boat-tailing effect on the unstable wake of the Ahmed body 91
5.1 Literature review 93
5.2 Preamble: two-dimensional potential flow approach 98
5.2.1 Computational setup 98
5.2.2 Wake estimation 99
5.2.3 Results 100
5.2.4 Short conclusion 104
5.3 Experimental setup 105
5.4 Results 107
5.4.1 Baseline: squareback afterbody 108
5.4.2 Shape optimization with boat-tails 109
5.4.3 Contribution to drag 112
5.4.4 Contribution the cross-flow loading 116
5.4.5 Effect on the wake dynamics 117
5.4.6 Influence of the boat-tails' geometry on the aerodynamic loading and on the wake dynamics 126
5.4.7 Three-dimensional boat-tail 131
5.5 Discussion 133
5.5.1 On the two-dimensional mechanism related to boat-tailing 133
5.5.2 Impact on the unstable wake modes 134
5.5.3 Strength and orientation of the wake mode 134
5.5.4 Importance of boat-tails locations 136
5.5.5 Control of the aerodynamic loading 138
5.6 Concluding remarks 138

6 Towards a stability analysis of the wake of flat-backed Ahmed bodies 141
Preliminary remarks: objectives of the simulations 143
6.1 Motivations and brief literature review 143
6.2 Numerical setup 144
6.2.1 Description of the computational case 144
6.2.2 RANS and URANS equations 148
6.3 Results 150
6.3.1 Steady simulation 150
6.3.2 Unsteady simulation 156
6.3.3 Yawing conditions 159
6.4 Discussion 160
6.4.1 Accuracy of steady and unsteady simulations 160
6.4.2 Stability analysis of the wake 161
6.5 Concluding remarks 162

II Industrial geometries: real road vehicles 163

7 Wake bi-stability created by static instabilities 165
7.1 Setup 167
7.2 Results 170

7.2.1 Baseline of the vehicles: wake symmetry-breaking 170
7.2.2 Wake reversal operated by the ground clearance 173
7.2.3 Identification of a reversed wake state with the pitch angle α 174
7.2.3.1 Successful identification of a reversed wake state 175
7.2.3.2 Stabilization operated by the cooling flow 177
7.2.4 Wake bistability under yawing conditions 178
7.2.5 Baseline with closed air-intake and wake state selection 183
7.2.6 Wake reversals triggered by the pitch angle α with closed front air-intake 186
7.2.7 Wake state selection operated by the yaw with closed front air-intake 190
7.2.8 Manipulations of the flow around the vehicles 193
7.2.8.1 Effect of rear tappers 193
7.2.8.2 Influence of the underbody roughness 196
7.2.8.3 Wake sensitivity to external disturbances 199
7.3 Discussion 203
7.4 Concluding remarks 205

8 Wake multi-stability created by boundary layer reattachment 207
8.1 Setup 209
8.2 Results 210
8.2.1 Baseline 211
8.2.2 Influence of the yaw angle 212
8.2.3 Multi-stable case 214
8.3 Discussion 216
8.3.1 Turbulent flow reattachment versus wake instability caused by symmetry-breaking modes 216
8.3.2 Impact of wake multi-stability on the aerodynamic loading of real vehicles 217
8.4 Concluding remarks 217

9 Conclusion and perspectives 219
9.1 General synthesis 221
9.2 Perspectives and possible future work 222

III Appendices 225

A Software for unsteady pressure measurements 227
A.1 Motivations 228
A.2 Description of the solution 228
A.3 Results, advantages and future developments 229

B Effect of a base cavity on the wake modes of the squareback Ahmed body at various ground clearances and application to drag reduction 231
B.1 Brief literature review 232
B.2 Experimental setup 232
B.3 Results 233
B.3.1 Bifurcations of the wake operated by the ground clearance 233
B.3.2 Mechanism for drag reduction 234
B.4 Concluding remarks 236

C Sensitivity analyses of the flow around boat-tailed flat-backed Ahmed bodies 237
C.1 Setup 239
C.2 Results 239
C.2.1 Sensitivity analyses with a y-unstable boat-tailed configuration ($\theta_T = 7.5°$, $\theta_B = 5°$) and three-different geometries 239
C.2.2 Sensitivity analyses with the 3D boat-tailed configuration 251
C.2.3 Sensitivity analyses on a boat-tailed configuration triggering the periodic wake mode 257
C.3 Discussion 260
C.4 Concluding remarks 264

D Mesh independence of the RANS simulations 265
D.1 Numerical setup 266
D.2 Mesh independence 266
D.2.1 Independence towards mesh density 266
D.2.2 Independence towards full or symmetrized space 266
D.3 Concluding remarks 268

List of references 269

Résumé étendu en Français 287
1 Contexte et revue bibliographique . . . . a
2 Dispositif expérimental et méthodes . . . . b
3 Écoulement moyen autour d'un corps d'Ahmed à culot droit . . . . d
4 Dynamique du sillage instable du corps incliné à proximité du sol . . . . . e
5 Effet de rétreint sur le sillage instable du corps d'Ahmed . . . . g
6 Vers une analyse de stabilité du sillage du corps d'Ahmed i
7 Multi-stabilité de sillage en présence de modes statiques . . . . k
8 Multi-stabilité de sillage lors d'un recollement de couche limite . . . . m
9 Conclusions . . . . o

Nomenclature

Latin

$\mathcal{W}^*$	Universal base aspect ratio based on major-minor axes	
ℓ_B	Boat-tail length (projected on the $\boldsymbol{e}_x$-axis)	m
ℓ_S	Length of the slant in 2D potential simulations	
ℓ_{rb}	Length of the recirculation length in 2D potential simulations	
$\hat{g}$	Complex base pressure gradient	$\mathrm{Pa} \cdot \mathrm{m}^{-1}$
$\mathbf{e}$	Strain rate tensor	s^{-1}
$\mathcal{C}$	Courant–Friedrichs–Lewy number	
σ_{c_p}	Inhomogeneity of the pressure distribution	Pa
c	Ground clearance	m
c_p	Instantaneous pressure coefficient	
c_S	Critical ground clearance for saturated instability	m
c_b	Base suction coefficient	
C_{f_x}	Streamwise skin-friction coefficient	
C_f	Skin-friction coefficient	
c_x	Drag coefficient	
c_y	Side force coefficient	
C_y^B	Side force coefficient of the stable *basic flow*	
c_z	Lift coefficient	
C_z^B	Lift coefficient of the stable *basic flow*	
d_{cav}	Base cavity depth	m
d_{S}	Diameter of the cylindrical supports of the Ahmed body	m
f^*	Strouhal number based on U_∞ and H	
f_b	Sampling frequency of the force balance	s^{-1}
f_e	Sampling frequency of the pressure scanner	s^{-1}
f_{p_x}	Pressure drag per dimensionless unit width	
f_{p_z}	Contribution of pressure to lift per dimensionless unit width	
g_y	Horizontal component of the base pressure gradient $\hat{g}$	$\mathrm{Pa} \cdot \mathrm{m}^{-1}$

g_z	Vertical component of the base pressure gradient $\hat{g}$	$\mathrm{Pa} \cdot \mathrm{m}^{-1}$
g_r	Modulus of the base pressure gradient $\hat{g}$	$\mathrm{Pa} \cdot \mathrm{m}^{-1}$
H	Height of the Ahmed body	m
H_b	Height of the base of the Ahmed body	m
k	Turbulence kinetic energy	J
L	Overall length of the Ahmed body	m
l_M	Length of the base's major axis	m
l_m	Length of the base's minor axis	m
N	Number of pressure sensors placed on the base and used for computation of the base suction coefficient c_b.	
n_{mesh}	Number of mesh points at a given ground clearance	
N_c	Number of channels of the pressure scanner	
p	Pressure	Pa
p_∞	Free-stream static pressure	Pa
Q	Second invariant of the velocity gradient ∇u	s^{-2}
Q_∞	Dynamic pressure	Pa
r_f	Radius of the upstream rounded edges of the Ahmed body	m
r_{s_b}	Radius of the lateral fillets of the Ahmed body (bottom part)	m
r_{s_t}	Radius of the lateral fillets of the Ahmed body (top part)	m
S	Model's projected frontal surface	m^2
S_{ij}	Dissipation rate	s^{-1}
t_C	Convective time scale $t_C = H/U_\infty$	s
T_∞	Regulated temperature inside the wind-tunnel test section	K
U_∞	Free-stream velocity	$\mathrm{m} \cdot \mathrm{s}^{-1}$
u_τ	Wall friction velocity	$\mathrm{m} \cdot \mathrm{s}^{-1}$
W	Width of the Ahmed body	m
W_b	Width of the base of the Ahmed body	m
x_i^+	Dimensionless distance to the nearest wall in simulations $x_i^+ \in \{x^+, y^+, z^+\}$	

Greek

α	Pitch angle	°
α_b	Vehicle's *natural* pitch angle in the baseline configuration	°
β	Yaw angle	°
δ^1	Boundary layer thickness	m
κ	Probability of exploration of the wake state P	
λ_f	Normal distance between the ground and the top of the vehicle's wheel-arch (front axle)	m
λ_r	Normal distance between the ground and the top of the vehicle's wheel-arch (rear axle)	m
Λ_{fr}	Wheelbase of the Ahmed body	m
Λ_r	Distance between the rear supports and the base of the Ahmed body	m
Λ_t	Track of the Ahmed body	m

μ_T	Eddy dynamic viscosity	$\mathrm{kg \cdot m^{-1} \cdot s^{-1}}$
ν	Air kinematic viscosity	$\mathrm{m^2 \cdot s^{-1}}$
ν_T	Eddy kinematic viscosity	$\mathrm{m^2 \cdot s^{-1}}$
ω	Specific rate of dissipation	$\mathrm{s^{-1}}$
Ω_{ij}	Enstrophy	$\mathrm{s^{-1}}$
Ψ	Streamfunction	
ρ	Air density	$\mathrm{kg \cdot m^{-3}}$
τ_w	Wall shear-stress	Pa
θ_B	Bottom boat-tail angle	$^\circ$
θ_S	Angle of side boat-tails	$^\circ$
θ_T	Top boat-tail angle	$^\circ$
φ	Phase of the base pressure gradient $\hat{g}$	rad
φ_M	Base pressure gradient's orientation counted the direct orientation from the major axis of the base	rad

Subscripts

M	Related to the major axis of the base of the Ahmed body
m	Related to the minor axis of the base of the Ahmed body

Superscripts

$*$	Dimensionless quantity based on the scaling length H and on the scaling velocity U_∞
$\mathcal{A}$	Wake of the axisymmetric bluff-body
B	Basic flow without the instability

Acronyms and abbreviations

AUSM	Advection Upstream Splitting Method
CFD	Computational Fluid Dynamics
CFL	Courant–Friedrichs–Lewy
DNS	Direct Numerical Simulation
PANS	Partially Averaged Navier-Stokes
PDF	Probability Density Functions
PIV	Particle Image Velocimetry
RANS	Reynolds Averaged Navier-Stokes
RSB	reflectionnal Symmetry-Breaking
SUV	Sport Utility Vehicle
ZDES	Zonal Detached Eddy Simulation

Notations

A	Mean value of the coefficient $a(t)$: $A = \overline{a\,(t)}$
a	Instantaneous value of the coefficient $a\,(t)$

A'	Mean value of the standard deviation of the coefficient $a\left(t\right)$: $A' = \overline{\mathrm{Std}\left(a\left(t\right)\right)}$
a'	Instantaneous value of the standard deviation of the coefficient $a\left(t\right)$: $a' = \mathrm{Std}\left(a\left(t\right)\right)$

List of Figures

1.1 Wake flow visualizations for various bluff bodies 5
1.2 Several models of simplified vehicles 7
1.3 Neutral curves of four global modes in the control parameters space (W^*,Re) for a flat plate facing the flow 9
1.4 Wake of the Ahmed body: static symmetry-breaking at high Reynolds numbers 11
1.5 Base pressure distributions of bluff bodies subject to static wake instabilities 13

2.1 Full-scale wind tunnel of the GIE-S2A 19
2.2 Model-scale wind tunnel of the GIE-S2A 21
2.3 Principle of the unsteady pressure measurement 22
2.4 Response to an impulse of the measurement systems 24
2.5 Experimental apparatus 29

3.1 Schematic view of body with the velocity planes investigated in chapter 3 . 39
3.2 Cross-sections of the mean velocity field alongside the body in the horizontal plane $z^* = 0$ at $U_\infty = 20$ m.s^{-1} 40
3.3 Cross-sections of the mean velocity field U^*_{xz} in the plane $y^* = 0$ 40
3.4 Cross-sections of the mean velocity field at the base the body 41
3.5 Mean base pressure distributions $C_p(y^*, z^*)$ for squareback Ahmed body . . 42
3.6 Cross-sections of the mean velocity field alongside the body varying the Reynolds number 43

4.1 Experimental apparatus 52
4.2 Baseline configuration of the squareback Ahmed body subject to the y-instability 55
4.3 Sensitivity maps of the base pressure gradient response to a variation of the ground clearance c^* 56
4.4 Modulus and phase time series of the base pressure gradient with corresponding PDF for the baseline 57
4.5 Stable flow for the squareback Ahmed body 58
4.6 Sensitivity maps of the base pressure gradient response to a variation of the yaw angle β 58

4.7 Modulus and phase time series of the base pressure gradient with corresponding PDF for $\beta = 1.0°$ 59
4.8 Sensitivity maps of the base pressure gradient response to a variation of the pitch angle α 60
4.9 Modulus and phase time series of the base pressure gradient with corresponding PDF for the unlocked case $\alpha = +1.0°$. 61
4.10 Base pressure distributions $c_p(y^*, z^*)$ under pitching conditions. 61
4.11 Cross-sections of the mean velocity field for three pitch angles 62
4.12 Baseline configuration of the Ahmed body with the base cavity 63
4.13 Sensitivity maps of the base pressure gradient response with the cavity in Cartesian description 65
4.14 Sensitivity maps of the base pressure gradient response with the cavity in polar description 65
4.15 Cross-sections of the mean velocity field with the rear cavity ($d^* = 0.285$) . 66
4.16 Aerodynamic loading applied on the body in the ground clearance sensitivity analysis 66
4.17 Mean and fluctuating drag force and base suction coefficients vs. yaw and pitch angles 68
4.18 Mean and fluctuating cross-flow force coefficients vs. yaw and pitch angles 68
4.19 Mean side force coefficient vs. yaw β without the cavity 69
4.20 Components of the fluctuating force coefficients compared to the fluctuating base pressure gradients vs. yaw and pitch angles 69
4.21 Baseline configuration of the Ahmed body subject to the z-instability . . . 71
4.22 Sensitivity maps of the base pressure gradient response to a variation of the ground clearance c^* for the z-instability 72
4.23 Conditionally averaged base pressure distributions at $c^* = 0.080$ and associated gradient dynamics 73
4.24 Sensitivity maps of the base pressure gradient response to variations of the yaw angle β for the z-instability 74
4.25 Modulus and phase time series of the base pressure gradient with corresponding PDF for wake bistability in yawing conditions 75
4.26 Most probable pressure gradients *vs.* yaw angle at different ground clearances 77
4.27 Sensitivity maps of the base pressure gradient response to variations of the pitch angle 78
4.28 Cross-sections of the mean velocity field and associated mean base pressure distributions 79
4.29 Mean and fluctuating drag force and base suction coefficients *vs.* yaw and pitch angles 81
4.30 Mean and fluctuating cross-flow force coefficients *vs.* yaw and pitch angles 81
4.31 Mean lift coefficient *vs.* inclination of the boat-tailed body 81
4.32 Components of the fluctuating force coefficients compared to the fluctuating base pressure gradient *vs.* yaw and pitch angles 82
4.33 Phase dynamics adaptation of the base pressure gradient of the unstable wake for the $y-$instability and z-instability 88

5.1 Definitions of the base and of the boat-tails 93
5.2 Variation of drag with base slant angle, Ahmed body and real vehicle . . . 95
5.3 Setup of the potential flow simulation 99
5.4 Wake and inviscid flow streamlines for the 2D simulation 100

5.5 Simulation based on the Free Streamline Theory with length of the recirculation bubble set to 2 H and slant length to $\ell_S = H$ 101
5.6 Wake simulation based on the Free Streamline Theory with length of the recirculation bubble set to 2 H and slant length to $\ell_S = 0.1\ H$ 101
5.7 Free Streamline Theory wake simulation with length of the recirculation bubble set to 2 H and variable slant length 102
5.8 Influence of the length of the recirculation bubble 102
5.9 Experimental apparatus for boat-tailing experiments 106
5.10 Three geometries investigated in § 5.4.6 107
5.11 Baseline configuration of the squareback Ahmed body ($\alpha = \beta = 0°$, $c^* = 0.168$) 109
5.12 Total aerodynamic loading as a function of the boat-tail angles and polar curves 110
5.13 Base suction and drag deviation of boat-tailed afterbodies with respect to the baseline and fluctuations 112
5.14 Mean pressure coefficient C_p plotted along a line of constant x_i^* 114
5.15 Aerodynamic pressure drag f_{p_x} on the rear afterbody 115
5.16 Cross-flow force coefficients of boat-tailed afterbodies with respect to the baseline and fluctuations 116
5.17 Aerodynamic lift f_{p_z} on the rear afterbody 117
5.18 Cartesian components of the base pressure gradient as a function of the top and bottom boat-tail angles 118
5.19 PDF of the base pressure gradient for one-sided boat-tailed geometries . . 119
5.20 PDF of the base pressure gradient for two-sided boat-tailed geometries . . 120
5.21 Cross-sections of the mean velocity field for boat-tailed geometries 122
5.22 Cross-sections of the mean vorticity field for boat-tailed geometries 123
5.23 Wake dynamics: space-time analysis and base pressure gradient's phase spectra of y-fluctuating cases 124
5.24 Wake dynamics: space-time analysis and base pressure gradient's phase spectra 125
5.25 Typical mean base pressure distributions resulting from the use of boat-tails 125
5.26 Mean pressure coefficient plotted for the three geometries 127
5.27 Cross-sections of the mean velocity field U_{xz}^* for the 3 boat-tail geometries . 129
5.28 Space-time diagram and associated phase spectra for the three considered boat-tail shapes 130
5.29 Spectra of the base pressure gradient's phase for the two boat-tail shapes at $\theta_T = 12.5°,\ \theta_B = 12.5°$ 131
5.30 Modulus and phase time series of the base pressure gradient with corresponding PDF for the 3D boat-tailed case 132
5.31 Conditionally averaged base pressure distribution for the 3D boat-tailed afterbody 132
5.32 Phase spectra for the two maximal boat-tail angles at different locations . 137
5.33 Mean pressure coefficient plotted for the the maximum angles with boat-tails at different location 137

6.1 Numerical apparatus 146
6.2 Schematic view of body with the velocity planes investigated numerically . 148
6.3 Cross-sections of the mean velocity field alongside the body in the horizontal plane $z^* = 0$ at $U_\infty = 20$ m.s^{-1} 151

6.4 Cross-sections of the mean velocity field U^*_{xz} in the plane $y^* = 0$ 151
6.5 Downstream component of the skin-friction coefficient on the body 152
6.6 Cross-sections of the mean velocity field at the base of the body 154
6.7 Mean base pressure distributions $C_p(y^*, z^*)$ for squareback Ahmed body . . 154
6.8 Coherent structures in the mean wake of the squareback Ahmed body . . . 155
6.9 Cross-sections of the mean velocity field U^*_{xz} in the plane $y^* = 0$ for the unsteady simulation 157
6.10 Cross-sections of the mean velocity field at the base the body 157
6.11 Time series of the side force coefficient 158
6.12 Instantaneous base pressure distributions $c_p(y^*, z^*)$ for squareback Ahmed body 159
6.13 Base pressure distributions and cross-sections of the mean velocity field at the base the body under yawing conditions 160

7.1 Experimental setup: pressure taps locations, definition of the distances λ_f and λ_r and of the pitch and yaw angles 167
7.2 Real vehicles in the full-scale wind-tunnel 169
7.3 Mean base pressure distributions in the baseline configuration 171
7.4 Probability density functions of the Cartesian components of the base pressure gradient in the baseline configuration 171
7.5 Wake reversal operated by the ground clearance for the Peugeot 5008 . . . 173
7.6 Sensitivity maps of the base pressure gradient response to variations of the pitch angle for the Peugeot 5008 175
7.7 Wake reversal operated by the pitch for the Peugeot 5008 and mean lift coefficient *vs.* pitch angle 176
7.8 Mean vertical base pressure gradient *vs.* pitch angle variation for the Peugeot Partner with open air-intake 177
7.9 Mean and fluctuating base pressure gradients for the Renault Kangoo at yaw179
7.10 Mean and fluctuating aerodynamic coefficients *vs.* yaw angle for the Renault Kangoo 179
7.11 Mean base pressure distributions for the Renault Kangoo at yaw 180
7.12 Modulus and phase time series of the base pressure gradient and of the lift force with corresponding PDF for the bi-stable configuration of the Kangoo at yaw. Time-series of the lift force. Space-time diagram. 181
7.13 Mean base pressure distributions for states P and N observed at yaw for the Kangoo 182
7.14 No-pitch yawing conditions for the Kangoo with state P selected 182
7.15 Vehicles with closed front air-intake 183
7.16 Mean base pressure distributions in the baseline configuration with closed front air-intake and probability density functions of the base pressure gradient184
7.17 Sensitivity maps of the base pressure gradient response to variations of the pitch angle of the Citroën Berlingo with closed front air-intake 186
7.18 Pitch experiment with the Citroën Berlingo: cross-sections of the mean velocity magnitude and corresponding mean base pressure in $y^* = 0$. 187
7.19 Modulus and phase time series of the base pressure gradient and of the lift force with corresponding PDF for the bi-stable configuration of the Berlingo at pitch 188
7.20 Pitch sensitivity analysis for the Citroën Berlingo 189

7.21 Time series of the lift coefficient for the Citroën Berlingo in the bi-stable case 190
7.22 Sensitivity maps of the base pressure gradient response to variations of the yaw angle of the Peugeot Partner with closed front air-intake 191
7.23 Conditionally averaged mean base pressure distributions for states P and N of the Partner 191
7.24 Yaw sensitivity analysis for the Peugeot Partner 192
7.25 Mean drag coefficient *vs.* pitch angle for the Citroën Berlingo and yaw angle for the Peugeot Partner 193
7.26 Control devices tested for the Peugeot Partner 194
7.27 Mean base pressure distribution for the Peugeot Partner at $\Delta\alpha = 2.3°$ and associated mean base suction and drag coefficients C_b and C_x 195
7.28 Baseline of the Citroën Berlingo with the smooth underbody 197
7.29 Ground clearance experiment for the Berlingo with the smooth underbody 198
7.30 Pitch experiment for the Berlingo with the smooth underbody 198
7.31 Geometrical modifications of the Citroën Berlingo with the smooth underbody 199
7.32 Citroën Berlingo with smooth underbody and roof cross-bar or with roof cross-bar and rear spoiler 200
7.33 Bi-stable wake dynamics of the Citroën Berlingo with roof crossbar, rear spoiler, smooth underbody and closed front air-intake 202

8.1 Experimental setup for the Renault Mégane 209
8.2 Baseline configuration of the Renault Mégane 211
8.3 Evolution of the mean and mean fluctuations of global coefficients 213
8.4 Mean base pressure distributions for the Renault Mégane under yawing conditions 213
8.5 Time series of the lift and PDF of the lift and drag coefficients for the bi-stable case 214
8.6 Space-time diagram of vertical base pressure during bistability and gradient's spectrum 214
8.7 Multi-stable case of the Renault Mégane 215

A.1 Screenshot of the LabVIEW user interface 230

B.1 Mean base pressure distributions of the squareback Ahmed body in stable and unstable flow regimes. 233
B.2 Mean base pressure distribution of the flat-backed Ahmed body with a base cavity 234
B.3 Drag reduction and base pressure recovery with the base cavity 235
B.4 Mean spatial standard deviation of the wake of the Ahmed body 235

C.1 Base pressure gradient response to a variation of the ground clearance for a y-unstable boat-tailed afterbody 240
C.2 Modulus and phase time series of the base pressure gradient with corresponding PDF for the baseline of the y-unstable case 241
C.3 Aerodynamic loading applied on the y-unstable body in the ground clearance sensitivity analysis 241
C.4 Base pressure gradient response to variations of the yaw angle for a y-unstable boat-tailed afterbody 242

C.5 Aerodynamic loading applied on the body *vs.* yaw angle 242
C.6 Base pressure gradient response to variations of the pitch angle for a y-unstable boat-tailed afterbody 244
C.7 Aerodynamic loading applied on the body *vs.* pitch angle 244
C.8 Sensitivity alignment experiments for the y-unstable case with boat-tailed body 246
C.9 Most probable pressure gradients *vs.* ground clearance for different boat-tails geometry with $\theta_T = 7.5°$ and $\theta_B = 5°$ 247
C.10 Most probable pressure gradients *vs.* yaw angle for different boat-tails geometry with $\theta_T = 7.5°$ and $\theta_B = 5°$ 247
C.11 Most probable pressure gradients *vs.* pitch angle for different boat-tails geometry with $\theta_T = 7.5°$ and $\theta_B = 5°$ 248
C.12 Mean lift coefficient *vs.* pitch angle for *T75B5-sl* and *T75B5-cs*. 249
C.13 Sensitivity alignment experiments for the y-unstable case with boat-tailed body: effect of the geometry 249
C.14 Fluctuations of the cross-flow forces and of the base pressure gradient *vs.* body alignment for the slanted and short boat-tails 250
C.15 Sensitivity maps of the base pressure gradient response to a variation of the ground clearance c^* for the *3D* configuration 252
C.16 Aerodynamic loading applied on the body in the ground clearance sensitivity analysis 252
C.17 Sensitivity maps of the base pressure gradient response to a variation of the yaw angle β for the *3D* configuration 253
C.18 Aerodynamic loading applied on the body *vs.* yaw angle 253
C.19 Sensitivity maps of the base pressure gradient response to a variation of the pitch angle α for the *3D* configuration 255
C.20 Aerodynamic loading applied on the body *vs.* pitch angle 255
C.21 Cross-flow forces sensitivity to the body's alignment for the *3D* geometry . 257
C.22 Base pressure gradient response to variations of the yaw angle for the periodic wake mode 258
C.23 Base pressure gradient response to variations of the pitch angle for the periodic wake mode 259
C.24 Mean cross-flow forces *vs.* body inclination for the configuration *T125B10* 259

D.1 Mean wakes in the $y^* = 0$ and $z^* = 0$ planes for the two computational setups and base pressure distribution 268
1 Sillage du corps d'Ahmed : instabilités à grand nombre de Reynolds . . . . b
2 Souffleries du GIE-S2A c
3 Champs moyens de vitesse au culot du corps . . . . d
4 Diagrammes de réponse du gradient de pression au culot à une variation de l'alignement du corps . . . . f
5 Coefficient d'effort transverse en fonction de l'angle du corps . . . . f
6 Fluctuations moyennes en fonction des angles de rétreint θ_T et θ_B pour les efforts transverses et les gradients de pression au culot . . . . h
7 Diagrammes spatio-temporels du coefficient de pression $c_p(y^*, z^*)$ au culot pour différents arrière-corps . . . . h
8 Champs de vitesse moyens au culot du corps . . . . j
9 Distributions de pression moyenne au culot $C_p(y^*, z^*)$ pour le corps d'Ahmed à culot droit . . . . j

10 Distributions de pression moyennes $C_p(y^*, z^*)$ au culot des véhicules alignés avec l'écoulement l
11 Distributions de pressions moyennes $C_p(y^*, z^*)$ au culot des véhicules après renversement du sillage (état N) et dynamique bi-stable l
12 Coefficients d'efforts en fonction du dérapage pour la Mégane . . . . n
13 Distributions moyennes de pression au culot de la Renault Mégane en dérapage . . . . n

List of Tables

2.1 Characteristics of the two pressure scanners 23
2.2 Measurement ranges, accuracy and repeatability of the force balance installed in the full-scale wind tunnel 25
2.3 Accuracy and repeatability of the force balance installed in the model-scale wind tunnel 25
2.4 Dimensions of the flat-backed Ahmed body 28

3.1 Dimensions of the base of the Ahmed body 38

4.1 Dimensions of the after-bodies 51
4.2 Investigated ranges of ground clearance c, yaw angle β and pitch angle α for the Ahmed bodies subject to the y- and the z-instabilities 52
4.3 Characteristic mean and fluctuation coefficients for baseline configurations 55
4.4 Yaw angles associated with regions l_1, b_1, b_2 and l_2 of figure 4.24 74

5.1 Characteristics of the afterbodies used for the sensitivity analyses and configuration's names 107
5.2 Characteristic mean and fluctuating coefficients for the baseline configuration with the new afterbody 108
5.3 Fit coefficients C_{x_0} and C_{z_0} for the polar curves 112
5.4 Mean and fluctuating aerodynamic coefficients for the study of the boat-tail geometry 126
5.5 Mean aerodynamic coefficients for $\theta_T = 12.5°,\ \theta_B = 12.5°$ 131
5.6 Mean and fluctuating aerodynamic coefficients for the *3D* boat-tailed afterbody 132

6.1 Dimensionless dimensions of the Coarse and Fine meshes 147
6.2 Characteristic mean force and base suction coefficients 153
6.3 Characteristic mean force and base suction coefficients for unsteady simulations 158

7.1 Dimensions of the vehicles and Reynolds numbers 170

7.2 Characteristic mean and fluctuating coefficients for baseline configurations of the four vehicles 172
7.3 Characteristic mean and fluctuating aerodynamic coefficients for baseline configurations of the four vehicles with closed air-intake 185
7.4 Characteristic mean and fluctuating aerodynamic coefficients for three baselines configurations of the Citroën Berlingo 196

8.1 Characteristic dimensions of the Renault Mégane 209
8.2 Mean and fluctuating aerodynamic coefficients of the Renault Mégane . . . 211

D.1 Characteristic mean force and base suction coefficients for the two meshes . 266
D.2 Characteristic mean force and base suction coefficients for the half-space and the full-space simulations 267

CHAPTER 1

Introduction

This chapter introduces the context of the study in § 1.1 and gives some motivations for the extended study of real vehicles' wakes dynamics. Due to multiple constraints, it appears necessary to conduct most of the studies on simplified reduced-scale models as detailed in § 1.2. The present study considers flat-backed Ahmed bodies and focuses on their wakes. Some literature background concerning laminar bifurcations in the laminar regime which are responsible for the observed turbulent wake dynamics is provided in § 1.3. Despite previous studies, numerous questions remain unanswered and a few more raised by our earlier results. § 1.4 therefore gives the motivations of this work. Finally, the outline is given in § 1.5.

Contents

1.1 General context of the study 2
1.2 From simplified models to real vehicles 4
1.3 Turbulent wake of the Ahmed body 7
1.4 Motivations of this work 13
1.5 Outline of the thesis 14

1.1 General context of the study

In a globalizing world, the exchanges between different regions or countries follow a constantly increasing trend. The role of transport has become so important that the worldwide society nowadays depends on it. As of now, road transportation represents more than 85% of the transportation solutions (Sarron *et al.*, 2018). Besides, there is a global increase of the number of registered personal vehicles in all European Union countries, with roughly a million new ones every two years (ICC, 2018). Over more than 16 millions sold in 2016, about 88% correspond to personal vehicles. In the current context of global warming, environmental considerations have received much attention in particular as regards the reduction of greenhouse gas emissions. The contribution of transportation to the total emissions is estimated to about $15-25\%$ depending on the studies (Palmer, 2007; Dekker *et al.*, 2012; Baude *et al.*, 2017). Anyway, an increase of more than 20% was observed over the last 25 years (La Notte *et al.*, 2018). Because ground transportation is one of the major contributors, the reduction of the related emissions appears as an effective driver of the action. Since the first EURO norms[1], always more stringent regulations are regularly imposed to the manufacturers to reduce the environmental impact of their vehicles. Targeted threshold were then introduced to encourage the development of more efficient cars against financial penalties. The averaged emission based on all car models sold by the manufacturers was namely of 130 grams of CO_2 per kilometer in 2015 with a target of 95 g CO_2/km by 2021. The current applicable norm on pollutants emissions in Europe is the EURO6c and will be replaced in September 2019 by the EURO6d-TEMP (2021 for EURO6d) for newly certified vehicles. Worldwide, different standards which are sometimes more stringent are in use. Local regulations[2] also sometimes restrain the access to vehicles with limited pollutant emissions levels.

The basic requirements of transportation, such as maximizing the inner volume of ground vehicles with respect to the outer one, impose general features to the vehicles, in particular concerning their shape which will directly impact the energy consumption of the ground vehicles. For instance, one of the constraints on minivans' shape design is that they must be able to carry a standard European pallet[3]. Similarly, the passengers versions are constrained by the need of a maximized cargo space. In addition, increasing safety requirements and higher comfort standards lead to more massive vehicles, which the recent customers' demand does not contradict. The drawback of such shapes is obviously an increased air resistance which highers the fuel consumption and therefore the pollutants emission.

Besides, the spreading of electric vehicles unveils new practical limitations such as the effective range of these cars, *i.e.* the distance the user can drive without loading the batteries. As a matter of fact, for commercially available personal vehicles and except for some specific models, the range obtained during approval cycles is rarely larger than

---

[1] These norms were first introduced by the European Union in the beginning of the 1990's and are updated regularly. The corresponding emission levels can be found online at `https://www.transportpolicy.net/standard/eu-light-duty-emissions/`.

[2] Related for instance to windshield markers such as *Crit'Air* in France, *Registry-Sticker* in Belgium, *Umweltplaketten* or *Diesel-Fahrverbot* – forbidden use of pre-EURO6 Diesel engines – in Germany, *Umwelt-Pickerl* in Austria which allow – or not – to drive in certain areas at certain times and are delivered depending on the EURO standard fulfillment of the vehicles. In some other countries as Norway, toll prices may be reduced for EURO6 vehicles.

[3] The standard European pallet, also referred to as EUR-pallet, Euro-pallet or EPAL-pallet is $1.2 \times 0.800 \times 0.144$ m. When loaded, the height of the ensemble is about 1.5 m. It usually constraints the rear shape of light commercial vehicles that must be able to carry one.

$250 - 300$ km[1] against usually more than $700 - 800$ km for thermal engines depending on the gas tank capacity. Added to the quite long required charging time (usually more than two hours), this constitutes a severe limitation of the large diffusion of such vehicles and thus enforces the need for a reduced energy consumption. It must also be emphasized that the operating range would be even more limited for trucks or for buses and that hybrid systems, spreading widely since the pioneering Toyota Prius commercially launched in Japan in 1997, are also subject to similar limitations. Besides, a new approval cycle called *Worldwide harmonized Light vehicles Test Procedure* (WLTP) progressively replaces the *New European Driving Cycle* (NDEC) last modified in 1997 since September 2017 and will be applicable to all newly approved vehicles in 2019. It corresponds to more realistic driving conditions than the previous cycle during which approval was conducted in a wind-tunnel with a simulated moving ground, the vehicle being kept aligned with the stream and therefore requires more advanced aerodynamic studies. In particular, the phase of real driving conditions forces to take the effect of sideslip conditions into account. The aim of this new approval cycle is to reduce the gap between standard and real-life consumption and emissions pointed out for instance by Khan & Frey (2018). As a matter of fact, a recent study by Baldino *et al.* (2017) reports that only 10% of EURO6-approved vehicles actually respect those emission standards in real driving conditions.

In order to reach the targeted pollutant emissions and the desired fuel consumption, three main optimization levers are identified: engine optimization by means of turbocharged engines associated with downsizing[2], mass reduction owing to new materials and aerodynamic drag reduction. The aerodynamic drag can be defined as the force acting on a vehicle by the surrounding air stream against its motion. Its contribution to the power consumption becomes predominant for driving speeds above $70 - 80$ km.h^{-1} (Hucho, 1998*a*), *i.e.* in typical countryside roads and highways conditions. To get an idea, this means that in average, roughly one third of the CO_2-emissions are directly related to the aerodynamic loading of the vehicle. Recently, huge efforts have been engaged to reduce the vehicles' mass despite high comfort and safety requirements with expected large reduction of the fuel consumption (Pagerit *et al.*, 2006).

The drag force is consequently directly related to the shape of the ground vehicles and in particular to the induced pressure difference between the front and rear parts. The aerodynamic performances of very different shaped vehicles can be compared using the drag coefficient C_x and the vehicle's frontal surface S, the product of which being directly proportional to the actual applied force. Over the last century, the drag coefficient C_x has been reduced by a factor of three in average (Hucho, 1998*a*). The most efficient series vehicles now reach drag coefficients around 0.19 (1996 General Motors EV1 and 2013 Volkswagen XL1) for specifically designed shapes while more conventional vehicles rank around 0.22 (2013 Mercedes-Benz CLA or 2017 BMW 5-Series). Among the most efficient vans, one may cite the 2000 Audi A2 (with $C_x \approx 0.28$) or the Ford C-Max ($C_x \approx 0.29$), anyway much more efficient than common vehicles of the mid-century such as the Citroën 2CV ($C_x \approx 0.51$) or the VW Beetle ($C_x \approx 0.48$) thus showing the breakthrough performed in seventy years. It is interesting to highlight that the overall drag of the vehicles have largely decreased thanks to the reduction of the drag coefficient despite an increasing front surface (Hucho, 1998*b*). If one considers that the general shape of the vehicles cannot be optimized much more, two additional levers of action can be discussed. Either the introduction of flow control – active or passive – aiming at reducing flow separation or low pressure areas responsible for pressure drag either the comprehension of some physical phenomena contributing to the vehicle's total drag. The present manuscript is focused on the later but we want to briefly discuss the possibility of flow control. For industrial applications, a global approach must be undergone. As a matter of fact, if passive control were applied for instance by means of diffusers or spoilers, their use has to be fulfill the shape design or the loading capacity requirements. Similarly, if one considers active control, a global energy-balance has to be considered. Active systems indeed require energy whose impact on consumption has to be taken into account. In addition, as mentioned by Le Good *et al.* (2011), the introduction of streamlined shapes encounters a customers' resistance. This paradoxical situation was already highlighted by Lay (1933) in the middle of the previous century. The main misunderstanding probably originates from the shape design which sometimes goes against aerodynamicists needs and requirements although the current trend is to introduce more and more efficient vehicles since low fuel consumption has become a marketing argument. Nonetheless, the current wake-up call on global warming and pollutant emissions as well as the need for increasing mobility with electric vehicles might counteract this statement soon, in particular since there is no formal opposition between efficiency and enjoyable shape design. From a marketing point of view, pollutant emissions and low fuel consumption are now used as advertising tools. The shape complexity of real cars suggests that investigations from a fundamental point of view are quite difficult to perform with such vehicles. The use of simplified geometries therefore appears as an interesting solution as described in the following sections.

---

[1] From the manufacturers' websites (consulted in June 2018), it can rank up to 539 km Tesla Model S, is about 400 km for a Nissan Leaf or a Renault Zoé, 300 km for a BMW i3 but is only 200 km for a Volkswagen e-Golf or $150 - 170$ km for the Peugeot Partner Electric/Citroën E-Berlingo, Peugeot iOn/Citroën C-Zero or Smart ForTwo Electric Drive. The actual range in real driving conditions with A/C, lights or the radio on and in the traffic is smaller.

[2] Smaller engine's cubic capacity

1.2 From simplified models to real vehicles

Not only the very complex shape of real ground vehicles but also the length scales involved lead to two additional problems. For experiments, in addition to financial limitations related to expansive test campaigns, real cars – and even more real lorries, train or buses – require large facilities. Only a few are spread all around the world[1]. There is a significant part of the overall development cost which is ascribed to testing and which can be lowered by the use of simplified models. In addition, there is more flexibility allowed by models as they are easier to manufacture and modifications can be handled quite easily either by the use of several interchangeable geometries as considered in this work or by the use of clay to change the general shape.

From a fundamental point of view, a car is a bluff body – *i.e.* not streamlined – whose shape, at least for squareback and hatchback vehicles, leads to a massive flow separation at the rear. This separated area, called the wake, is characterized by very small velocity magnitudes and flow moving in the upstream direction. The development of a wake with this characteristic is typical of bluff bodies (some geometries are shown in figure 1.1). However, their dynamics and mean topologies are quite different, in particular because of strong three-dimensional effects for three-dimensional bluff bodies. The specificity of those bodies is related to the high bluffness of the geometry (Roshko, 1993) which creates a significant pressure drag – because of suction generated by pressures lower than the free-

---

[1] Among these facilities, one may cite that of the GIE-S2A in France, the ACE Climatic Wind Tunnel in Canada, the Auto Research Center (ARC) in the United States, the MIRA Full Scale Aerodynamic Wind Tunnel in the United Kingdom or the German-Dutch Wind Tunnels DNW in the Netherlands.

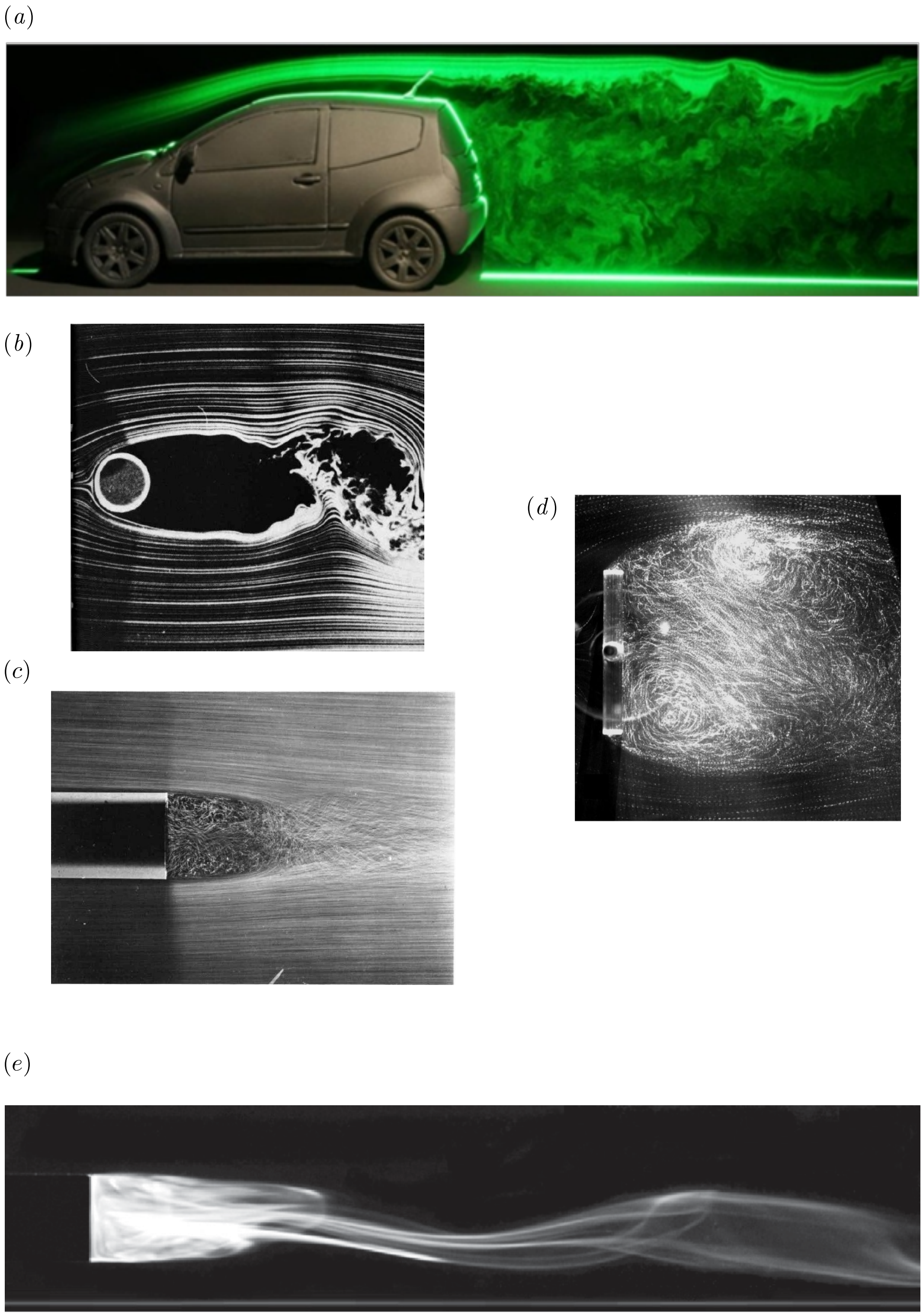

Figure 1.1 – Wake flow visualizations for various bluff bodies: (*a*) model-scale Citroën C2 (reproduced from Grandemange (2013)), (*b*) cylinder in cross-flow (T. Cork & H. M. Nagib reproduced from Van Dyke (1982)), (*c*) flat-based axisymmetric bodies of revolution (H. Werlé reproduced from Van Dyke (1982)), (*d*) flat plate facing the flow (reproduced from Cadot (2016)), (*e*) squareback Ahmed body (reproduced from Grandemange *et al.* (2012*a*)). Visualization techniques are smoke in air stream illuminated by a laser sheet (*a*), or captured by photograph (*b*), air bubbles in a water stream (c, d) and ink in a water stream (*e*).

stream's – but also wake unsteadiness. As an illustration, the wake is generally admitted to contribute to about one third of the total's vehicle drag (Hucho, 1998*a*). In an inviscid fluid, the d'Alembert paradox states that the resistance to the motion of any solid should be zero (d'Alembert, 1752). Kirchhoff (1869) and later Brillouin (1910) provide a first attempt modeling a wake with an infinite separation and a zero pressure coefficient. This corresponds to a Helmholtz wake and can be made more realistic imposing a wake of finite length. In the latter case, it is referred to as the Free Streamline Theory assessed in Roshko (1954*a*). Although this model constitutes the starting point of more recent approaches about recirculating bubbles (Roshko, 1954*b*, 1955; Wu, 1962; Roshko, 1993; Verhoff, 2010), it must face some severe limitations. The main one is that the length of the recirculating bubble is fixed arbitrarily in the theory so that any possible drag level can actually be obtained. In particular, for an infinite wake (Helmholtz flow), it will be underestimated. Even if the current knowledge of wakes may let the early studies a bit outdated, Sychev (1982) proposed that the Helmholtz flow could be one of the asymptotic solution to the extent of an infinite Reynolds number ($\mathrm{Re} \to \infty$). To date, it is the only available theoretical approach since the numerical resolution of Navier-Stokes equations does not provide any additional clue for solving this problem. One implication of these control volume analyses is that the pressure inside the bubble – responsible for the base drag – is closely related to its shape since large streamlines' curvature implies low pressure levels at the separating line. As a consequence, the general recirculating bubble shape and in particular its length appear as an important parameter in drag prediction.

A great effort has been recently made for axisymmetric bodies on the modeling and measurements of the characteristics of their wakes (Grandemange *et al.*, 2014*a*; Rigas *et al.*, 2014, 2015); reduced order models aiming at providing powerful tools for feedback control have been proposed by the authors and the general properties of the wake are quite well understood. However, these elongated cylinders poorly model road vehicles. In that aim, more representative geometries such as the Ahmed (Ahmed *et al.*, 1984), the Windsor (Le Good & Garry, 2004), the ASMO (Aljure *et al.*, 2014) or the GTS (McArthur *et al.*, 2016) models have been used over the years. They are represented in figure 1.2. They all have in common a three-dimensional bluff body shape with a vertical blunt base. Although most of them are of reduced scale, larger bodies such as the squareback declination of the Ahmed body has been investigated by Grandemange *et al.* (2015) at the industrial scale; similarly, generic but realistic vehicle's shapes are now introduced such as the full-scale DrivAer vehicle (Heft *et al.*, 2011, 2012*a*,*b*). The overall models' proportions are derived from mean values of actual road vehicles of the decade during which the models became in use. Even if much more simple than real vehicles, these models still leave numerous unresolved problems and open questions about the surrounding flow dynamics in particular about their wakes.

One of the most questionable points in the use of simplified models is their accuracy or, in other words, the possibility to transfer fundamental discoveries on industrial geometries. Although not always the case, we aim at showing that results obtained with Ahmed bodies can be recovered on real vehicles subject to a static instability as reported by Cadot *et al.* (2016) for a commercial Renault Kangoo. The Reynolds number of model-scale and full-scale tests being close – they only differ by about one order of magnitude and correspond to fully turbulent flows – there is a probability that the observations can be fully extended from one case to the other. As a matter of facts, some drag reduction devices successfully investigated on simplified geometries such as truck's base cavities (Mason & Beebe, 1978; Coon & Visser, 2004) are now implemented on full-scale vehicles and provide interesting energy savings. Even if full scale testing of real –

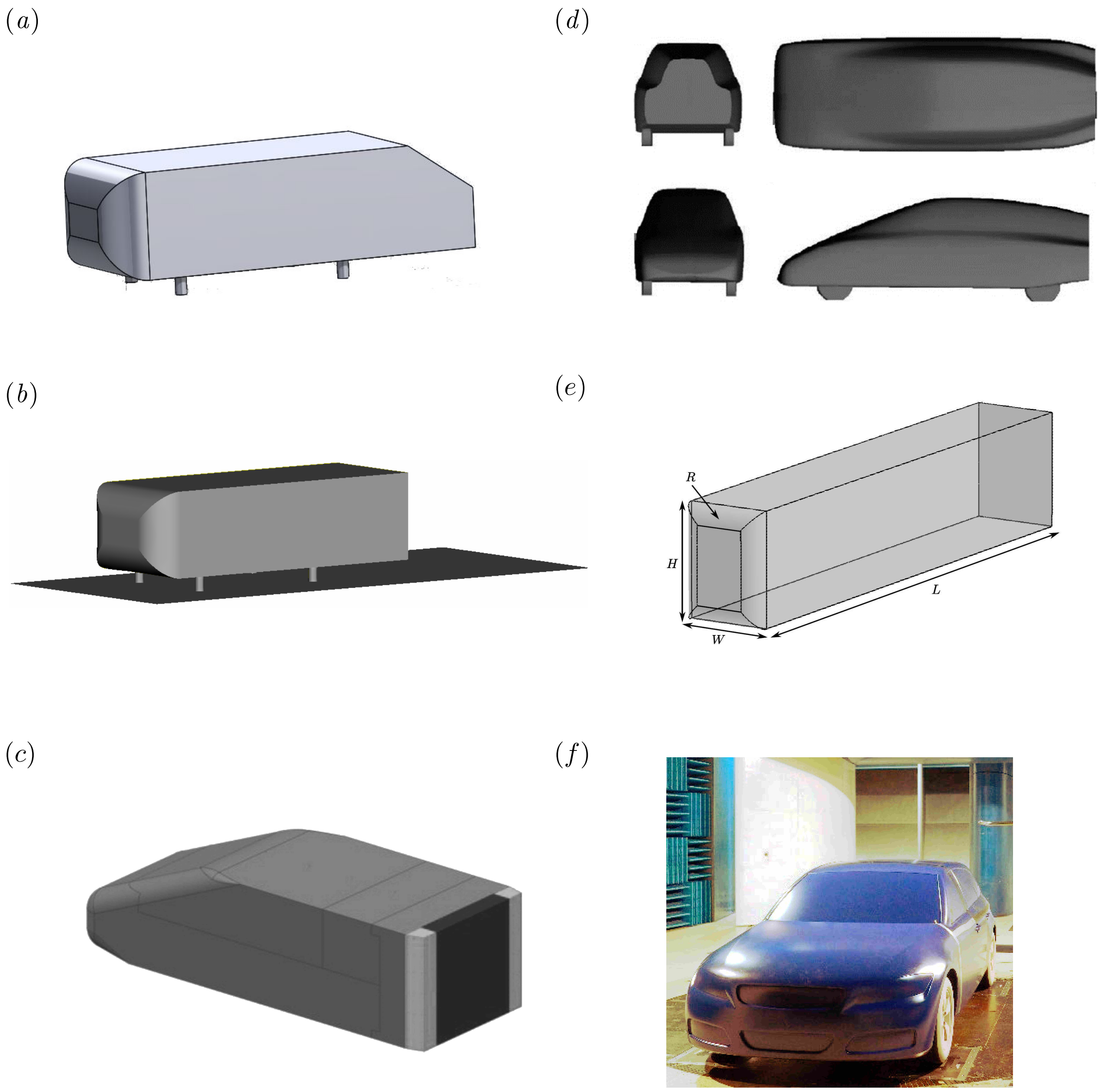

Figure 1.2 – Several models of simplified vehicles: (*a*) slanted Ahmed body (adapted from `https://grabcad.com/library/ahmed-body-4`), (*b*) squareback Ahmed body, (*c*) Windsor model (adapted from Pavia *et al.* (2016)), (*d*) ASMO model (reproduced from Aljure *et al.* (2014)), (*e*) GTS model (adapted from van Raemdonck *et al.* (2016)), (*f*) DrivAer model (adapted from Avadiar *et al.* (2018)). Flow direction is from left to right.

complex – vehicle's shapes seems unavoidable, fundamental research on models brings, in our opinion, a valuable hindsight on the observed phenomenon and allows broader possibilities for flow control since solutions are not limited – or much less – by industrial requirements.

1.3 Turbulent wake of the Ahmed body

The Ahmed body, since the early studies by Ahmed (1983); Ahmed *et al.* (1984) has become a reference geometry not only in the automotive industry but also for fundamental research. A particular region of interest is the turbulent wake, because it is the location of all the unsteadiness and of most of the drag generation around the body. This work deals with the squareback version of the body, corresponding to a slant angle of 90° in Ahmed (1983); Ahmed *et al.* (1984). Its shape is much more representative of SUV or vans than the 25°- or 35°-slanted variants rather modeling sedans. As first reported by Grandemange *et al.* (2013*b*, 2014*b*, 2013*c*) and then retrieved by other studies among whose Barros *et al.* (2014); Östh *et al.* (2014); Volpe *et al.* (2015); Cadot *et al.* (2015*b*); Mirzaei *et al.* (2015); Barros *et al.* (2016); Li *et al.* (2016); Evrard *et al.* (2016); Barros *et al.* (2017); Varon *et al.* (2017); Lucas *et al.* (2017); Brackston *et al.* (2018) the wake of the body exhibits a permanent asymmetry at Reynolds numbers of $\mathrm{Re} \sim 10^4 - 10^5$ based on the body's cross-flow dimensions – height or width depending on the papers without impact on the Reynolds number since the ratio of both is always close to one.

This asymmetry originates in a laminar Hopf bifurcation at very low Reynolds number as shown experimentally by Grandemange *et al.* (2012*a*) and then retrieved numerically by Evstafyeva *et al.* (2017). In the following, Reynolds numbers are based on the body's height. Experimentally, the wake is completely symmetric up to $\mathrm{Re} = 310$ ($\mathrm{Re} = 340$ numerically). It then becomes unsteady symmetric up to $\mathrm{Re} = 365$. A steady asymmetric wake state is afterwards observed and finally an unsteady one is reported for $\mathrm{Re} \geq 415$. This transition scenario is proposed by Ruelle & Takens (1971) to be a step on the route to turbulence and this statement is verified for the Ahmed body. Bifurcation scenarii are reported throughout the literature for simplified geometries such as two- and three-dimensional cylinders (Williamson, 1996; Zdravkovich, 1997; Jackson, 1987; Sreenivasan *et al.*, 1987; Provansal *et al.*, 1987), axisymmetric bodies (Fabre *et al.*, 2008; Bohorquez *et al.*, 2011; Bury & Jardin, 2012; Rigas *et al.*, 2016), spheres (Natarajan & Acrivos, 1993; Johnson & Patel, 1999; Ormières & Provansal, 1999; Tomboulides & Orszag, 2000; Thompson *et al.*, 2001; Pier, 2008; Fabre *et al.*, 2008; Szaltys *et al.*, 2012; Chrust *et al.*, 2013), spheroids (Khoury *et al.*, 2012) and disks (Meliga *et al.*, 2009; Szaltys *et al.*, 2012; Yang *et al.*, 2014).

Unfortunately, only few references were found in the literature for geometries in the scope of this study, *i.e.* three-dimensional bluff bodies among whose cubes (Raul *et al.*, 1990; Saha, 2004; Klotz *et al.*, 2014). In Klotz *et al.* (2014), the authors report longitudinal vorticity in the basic flow originating from a transverse gradient of pressure induced by the corners of the geometry, with periodically time-dependent oscillations of the recirculation region in agreement with Saha (2004). The only available stability analysis is provided by Marquet & Larsson (2014) in which the authors consider a 3D flat plate of constant thickness. The main results are summarized below with figure 1.3 adapted from the paper. For a large width-to-height aspect ratio, the most unstable mode is identified as an unsteady mode with an asymmetry along the smallest plate axis corresponding to vortex-shedding. When the aspect ratio, denoted L in the paper, is reduced in the range $1 < L < 1.5$, which is the case in our problem, a static asymmetry is identified in agreement with Grandemange *et al.* (2012*a*) and Evstafyeva *et al.* (2017). However, unlike experimental observations which result in an horizontal symmetry-breaking, Marquet & Larsson (2014)'s work with a flat plate indicates that it should take place vertically. Nonetheless, despite the apparent similarities of the plate (Marquet & Larsson, 2014) and of the Ahmed body problems (Grandemange *et al.*, 2012*a*; Evstafyeva *et al.*, 2017), several discrepancies must be highlighted. In the stability analysis for the plate, only the results for a height-to-width plate aspect ratio of $1 \leq H/W \leq \infty$ are presented but there is no reported information for $0 \leq H/W \leq 1$; the results of the latter case are deduced from those of $1 \leq H/W \leq \infty$[1]. The plate is considered in an infinite space; under this assumption, a given body can actually solve two problems depending on the chosen axis orientation. The aspect ratio can indeed be chosen as H/W or W/H – or equivalently, there exist two plates having a given aspect ratio H^*, the *minor* axis of the one being the *major* of the other. The critical Reynolds numbers are different for both plates – although related one each other by the aspect ratio – but the symmetry-breaking will take place along the *major* axis in both cases (Marquet & Larsson, 2014). However, some major differences between the bifurcations for the Ahmed body and the plate must be highlighted. First, the main one is related to the bluffness of the body. While the simplified vehicle produces a wake whose cross-flow dimension is about the same order of the body's, that of the plate diverges and is therefore much larger. The same kind of analysis performed with the three-dimensional Ahmed body would be undoubted helpful in deeply understanding the transition. Furthermore, there is a major geometrical difference between the body and the plate, which modifies the flow separation that can be either rather horizontal or rather vertical. It is related to the length of the body along the stream direction (noted e in figure 1.3). The longer the body, the more flow separating at the front is likely to reattached which would lead to an ultimate horizontal separation; this is the case for the Ahmed body for which, contrary to the plate, the separation at the blunt trailing edge is horizontal. It is vertical for the plate since the flow has no chance to reattached on the thickness e that is much smaller than the cross-flow dimensions. Besides, the investigations on the body are conducted with a ground; as a result, only a *minor* axis symmetry-breaking can occur – horizontal asymmetry – since the symmetry along the *major* axis is already broken by the floor.

---

[1] Private communications with O. Marquet

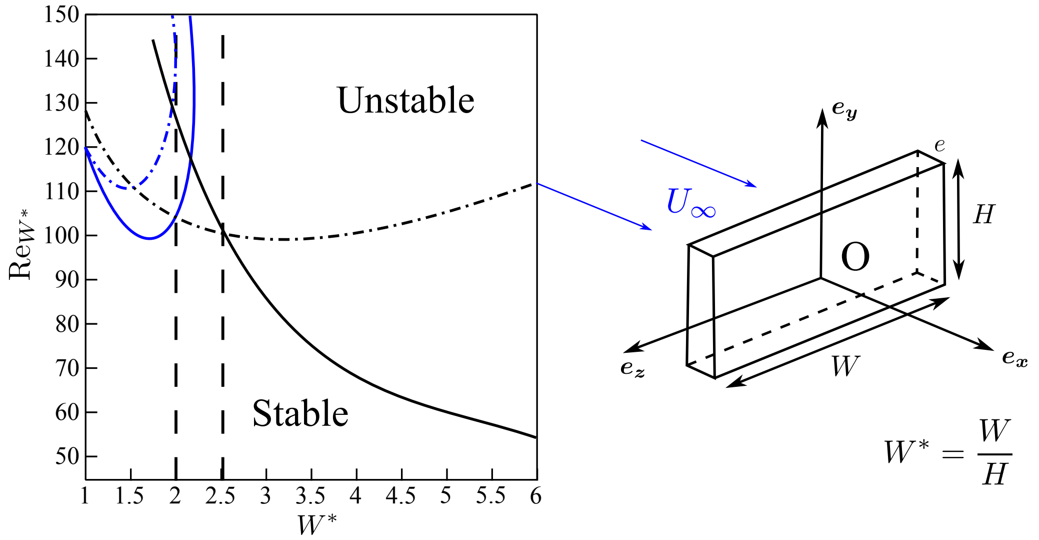

Figure 1.3 – Neutral curves of four global modes in the control parameters space (W^*,Re) for a flat plate facing the flow. The black lines stand for unsteady modes ($\omega \neq 0$) while the blue lines stand for steady modes ($\omega = 0$). Solid lines: (AS_y, S_z) modes; dashed-dotted lines: (S_y, AS_z) modes. Adapted from Marquet & Larsson (2014).

The dynamics of the wake of the Ahmed body at high Reynolds numbers, first reported in Grandemange *et al.* (2013*b*), is governed by static symmetry-breaking modes – also referred to as Reflectionnal Symmetry-Breaking modes (RSB) for instance in Evrard *et al.* (2016) that are the consequences of this laminar bifurcation. When the Reynolds number is increased up to the turbulent regime, the symmetry of the problem indeed has to be statistically satisfied which leads to the random exploration of two mirror wake modes (Grandemange *et al.*, 2013*b*; Cadot *et al.*, 2015*b*; Evrard *et al.*, 2016). These authors report that the wake persists in one state during a typical time scale of $500 - 1000$ times the characteristic convective time scale of the flow based on the body's height and on the free-stream velocity before a very quick switch of a few convective times only occurs and the wake goes in the mirror asymmetric configuration where it remains for another $500 - 1000$ times the characteristic convective time scale and so on. This slow dynamics[1] follows a stochastic behavior (Varon *et al.*, 2017) and, accordingly, no periodicity can be identified out of the switching motion. In a recent paper, Brackston *et al.* (2016) successfully apply a stochastic model derived from that of an axisymmetric bluff body (Rigas *et al.*, 2014, 2015) to the unstable wake of the Ahmed body. Both geometries are indeed subject to similar wake dynamics, the main difference being the phase of the rectangular body that is bounded by the corners ad the existence of a *minor* and a *major* base axes unlike axisymmetric bluff bodies. The authors successfully model the wake symmetry-breaking modes of the Ahmed body using a nonlinear Langevin equation[2], the deterministic part of which describing the large-scale flow structure while the stochastic forcing corresponds to the wake switches. It was shown that the presence of a permanent asymmetric wake state is also a general property of the turbulent wakes of bluff-bodies (Grandemange *et al.*, 2013*b*, 2014*b*; Rigas *et al.*, 2014, 2015, 2016; Gentile *et al.*, 2016, 2017; Mariotti *et al.*, 2017). Typical Reynolds numbers of the hereabove mentioned papers on the turbulent wake of the Ahmed model are of the order of $\mathrm{Re} \sim 10^4$ up to $\mathrm{Re} \sim 10^5$ based on the body's height but Grandemange *et al.* (2015) showed in a seminal work – which results are confirmed in Evrard *et al.* (2017) – that the phenomenon is still observable at the industrial scale corresponding to a Reynolds number of $\mathrm{Re} \simeq 2.5 \times 10^6$. In this manuscript, results are obtained for $\mathrm{Re} \simeq 4.0 \times 10^5$ and are consequently expected to be comparable to the hereabove mentioned studies.

In this turbulent range of Reynolds numbers, Grandemange *et al.* (2013*a*) report the existence of either an horizontal either a vertical wake instability originating from these modes mainly depending on the body's base width-to-height aspect ratio. For the sake of the simplicity, the wake subject to those symmetry-breaking static modes will be referred to as *unstable wake* or *wake subject to a static instability* throughout the manuscript. The corresponding figure is reproduced in 1.4(a). In the same paper, the authors also assess the influence of the ground clearance of the model. As a matter of fact, one can observe that, for ground clearances – normal distance from the body to the ground – higher than roughly 10% of the height of the body, a wake asymmetry related either to the major base axis is reported. Bodies wider than high are expected to be subject to an horizontal asymmetry (figure 1.4b, c) versus a vertical one for bodies higher than wide (figure 1.4d, e). As a result, either left/right or top/bottom asymmetric states of the wake, respectively called y- and z-instabilities, where y and z refer to the wake asymmetry directions can be observed. This notation is that of Grandemange *et al.* (2013*a*) and is used throughout. States N, associated with a **N**egative base pressure gradient (horizontal for the y-instability, vertical for the z-instability) are shown in figures 1.4(b, d) while states P, associated with a **P**ositive base pressure gradient (horizontal for the y-instability, vertical for the z-instability) are shown in figure 1.4(c, e). Bistability will refer to the alternate exploration of these wake states. The physics however is more complicated than simply based on the geometrical dimensions of the afterbody since the authors also report an overlapping region in which both kinds of instabilities could occur. In this case, they would not occur simultaneously. It is likely that the selection between both instabilities is operated by the surroundings of the body. In particular, it seems that the model's supports or the ground, which actually change the overall symmetry of the problem, can

---

[1] Compared to vortex shedding for which a frequency close to a Strouhal number of $\mathrm{St} \sim 0.2$ (Strouhal, 1878) is classically identified. This characteristic frequency can be identified in the wake (Grandemange *et al.*, 2014*b*) since vortex emission also occurs but is not related to that of the wake reversals.

[2] A Langevin equation is a stochastic differential equation. It aims at describing the time evolution of degrees of freedom of a system which are changing slowly compared to the other variables whose fast changes force the stochastic behavior in the equations. It was originally introduced in Langevin (1908).

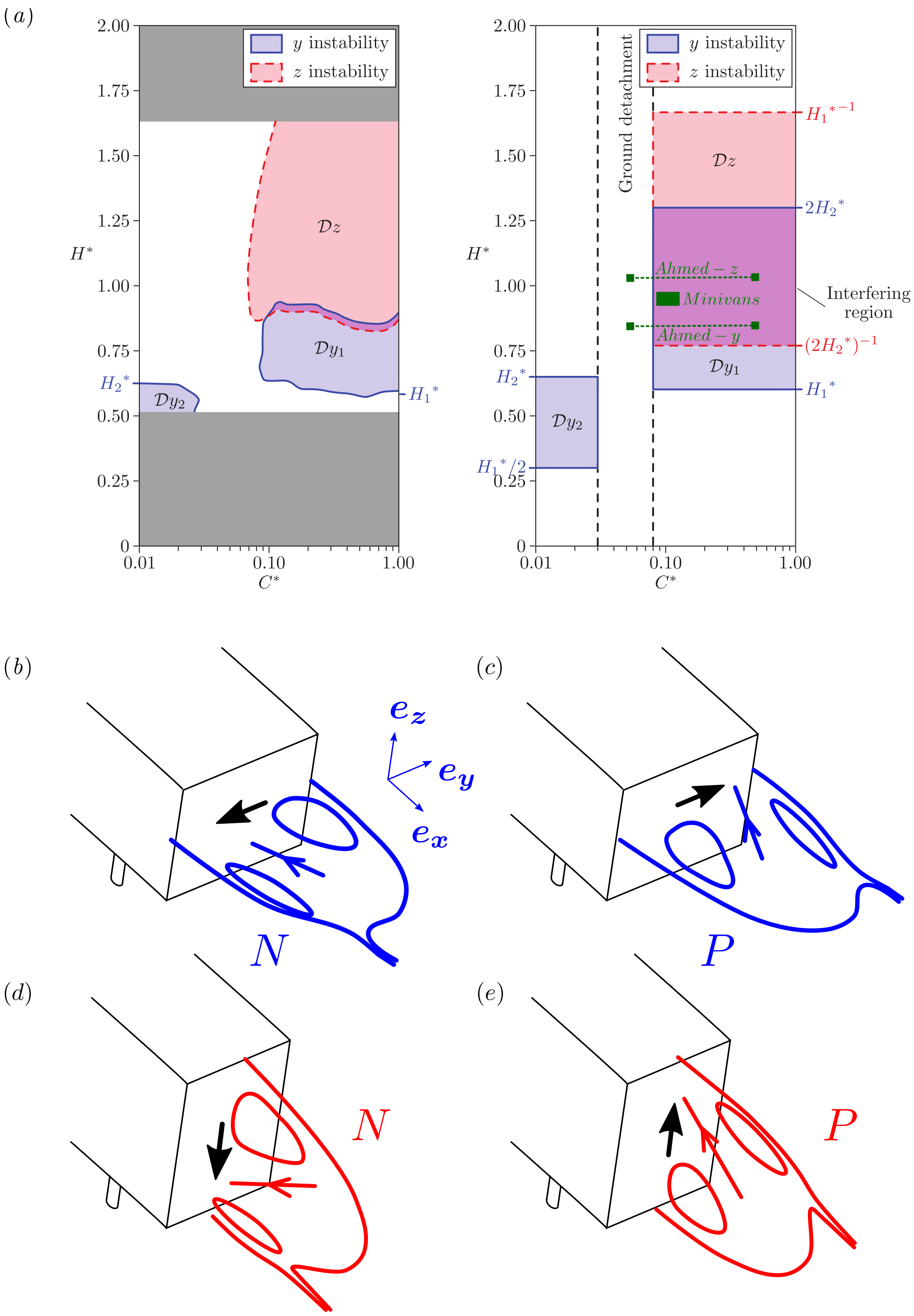

Figure 1.4 – Domains of development of the instabilities measured from the experiments (left) and predicted by the model of Grandemange *et al.* (2013*a*) (right). Figure adapted from Grandemange *et al.* (2013*a*) in which the body's width W is used as the scaling length. In green, investigated base aspect ratios: *Ahmed-y*, Ahmed body subject to the y-instability (§ 4.3.1); *Ahmed-z*, Ahmed body subject to the z-instability (§ 4.3.2); *Minivans*, Renault Kangoo, Peugeot 5008 and Partner and Citroën Berlingo investigated in chapter 7. Sketches of the recirculating bubbles for the y-instability $(b-c)$ and z-instability $(d-e)$ interpreted from mean wake measurements of Grandemange *et al.* (2013*a*). Thick arrows located on the base display the corresponding base pressure gradients and those in the wake the base impinging jet direction. (b, d) are associated with wake state N (**N**egative base pressure gradient) and (c, e) with wake state P (**P**ositive base pressure gradient) following the terminology of Grandemange *et al.* (2013*a*).

disturb the flow so much that they can ultimately lead to the selection of one or the other configuration.

The importance of the aspect ratio in determining the instability which actually takes place is confirmed by the work on the Global Transportation System – GTS – body, for which van Raemdonck *et al.* (2016) or Schmidt *et al.* (2018) identify a static vertical instability of the wake, with the existence of a bi-stable switching dynamics in the latter case. The criterion proposed by Grandemange *et al.* (2013*a*) seems also applicable on the Windsor body (Perry *et al.*, 2015, 2016*b*; Pavia *et al.*, 2018) as shown in figure 1.5(a, b). However, recent works highlight the importance of the underbody flow such as Barros *et al.* (2017) using perturbations or Pavia & Passmore (2018) using wheels; their authors report a change of the wake asymmetry since a vertical instability is observed. The resulting base pressure distributions (figures 1.5c, d) are very close to that obtained with the GTS model (figures 1.5e, f).

We add in figure 1.4(a) the base aspect ratios that we consider in this manuscript. It turns out that all investigated cases are in the *interfering region* of the model proposed in Grandemange *et al.* (2013*a*). Comparing to their experimental result (left), we expect the body *Ahmed-y* to be subject to a y-instability and *Ahmed-z* as well as the minivans to be subject to a z-instability. The wake sensitivity has to be assessed and the understanding of the preference of one or the other must be described.

Since the seeding works of Herry *et al.* (2011) and more importantly Grandemange *et al.* (2013*b*), many works have reported these asymmetric states with various geometries having in common vertical rectangular bases: flat plates (Cadot, 2016), square-back Windsor model (Perry *et al.*, 2016*a*,*b*; Pavia *et al.*, 2018; Pavia & Passmore, 2018), square-back Ahmed body both experimentally (Volpe *et al.*, 2015; Brackston *et al.*, 2016; Li *et al.*, 2016; Barros *et al.*, 2017; Evrard *et al.*, 2016) and numerically (Pasquetti & Peres, 2015; Evstafyeva *et al.*, 2017; Lucas *et al.*, 2017). To the author's knowledge, Grandemange *et al.* (2013*a*) apart, only the recent work of Schmidt *et al.* (2018) reports such bi-stable wake dynamics for a body taller than wide. However, there are unfortunately only few papers reporting experiments on real road passenger vehicles. Among them, Cadot *et al.* (2016) report the identification of static asymmetries of the wake leading to bi-stable wake dynamics of a Renault Kangoo at yaw. It seems that z-asymmetries of the wake of real vehicles are very common provided they have a blunt vertical afterbody (Grandemange, 2013; Evrard *et al.*, 2017; Avadiar *et al.*, 2018; Wang *et al.*, 2018). These asymmetry-related instabilities have a substantial impact on the aerodynamic loading of the body as demonstrated by the fluid-structure interaction experiment of Cadot (2016) and are therefore of big interest regarding industrial geometries.

Finally, the existence of such wake asymmetries opens a wide field for drag reduction, in particular based on strategies of symmetrization of the wake. As shown by Cadot *et al.* (2015*b*), the instability has a substantial contribution to drag, not only because it generally leads to low pressures increasing suction but also because it introduces an asymmetry in the wake. Several attempts have been performed on simplified geometries such as the Ahmed body by means of passive – control cylinder in the wake (Grandemange *et al.*, 2014*b*; Cadot *et al.*, 2015*b*), base cavity (Evrard *et al.*, 2016; Lucas *et al.*, 2017; Bonnavion *et al.*, 2017*b*) – or active flow control – flaps (Brackston *et al.*, 2016), unsteady blowing (Barros *et al.*, 2014, 2016; Li *et al.*, 2016; Evstafyeva *et al.*, 2017). Drag reductions up to 9% are obtained although it is not clear yet what the real part due the instability suppression alone is. Another strategy, though only briefly investigated on the Ahmed body by Grandemange *et al.* (2013*c*) but more in details for the Windsor body (Littlewood & Passmore, 2010; Perry *et al.*, 2015, 2016*b*; Pavia *et al.*, 2016) is the use of a boat-

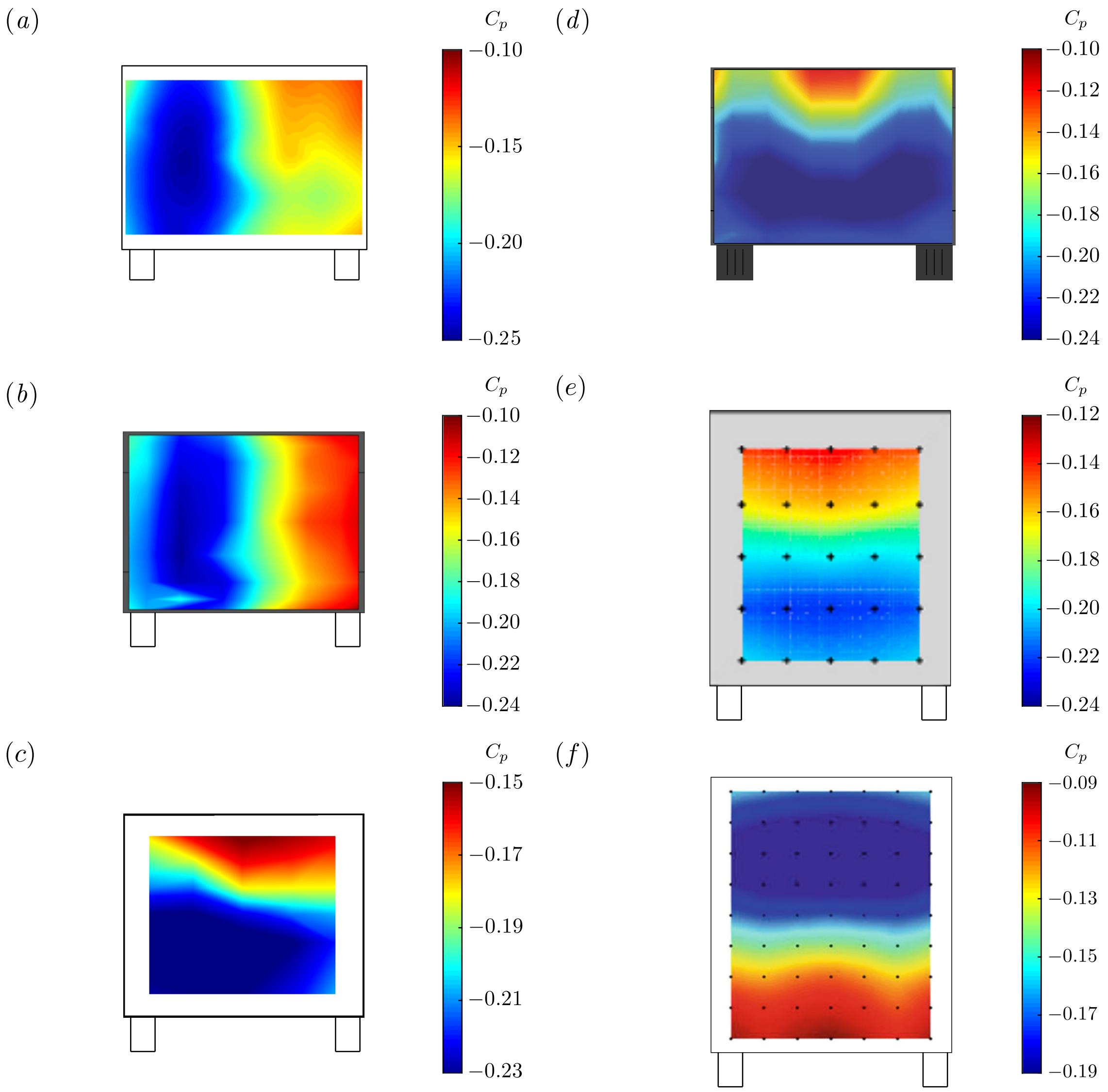

Figure 1.5 – Base pressure distributions of bluff bodies subject to static wake instabilities. y-wake asymmetry: (a) for the squareback Ahmed body at the industrial scale (adapted from Grandemange *et al.* (2015)) and (b) for a Windsor body (adapted from Perry *et al.* (2016b)). Only states P are shown. z-wake asymmetry: (c) for the squareback Ahmed body with underbody disturbances (adapted from Barros *et al.* (2017)) and (d) for a Windsor body with wheels (adapted from Pavia & Passmore (2018)). Only states P are shown. GTS model displaying (e) P state (adapted from Castelain *et al.* (2018)) and (f) N state (adapted from van Raemdonck *et al.* (2016)).

tailed afterbody, which yields promising drag reduction results with only basic shape modifications.

1.4 Motivations of this work

The short literature review provided in §§ 1.2 and 1.3 is mainly focused on simplified vehicles geometry and on the wake of the Ahmed body, in particular about its instabilities and their origin. It will be completed throughout the manuscript with the particular concerns of each chapter. Numerous questions remain unanswered despite the several conducted studies.

In the turbulent flow regime, previous studies by Grandemange *et al.* (2013a) and Cadot *et al.* (2015*b*) highlighted the importance of the ground clearance of the Ahmed squareback model in its wake dynamics. Other misalignment such as cross-wind – or equivalently yawing conditions – have been investigated by Volpe *et al.* (2015) or Evrard *et al.* (2016) but no work was conducted on pitching conditions applied to the body even if they are very likely to be encountered in real-life driving conditions (payload mass, throttle or breaking phase…). Besides, the literature crucially lacks studies about the impact of the reported wake dynamics on the instantaneous aerodynamic loading – not only drag, but also lift and side force. In short, no clear relationship is reported in previous works. These studies deal with bodies subject to the y-instability; for those subject to the z-instability, only Grandemange *et al.* (2013*a*) discusses the effects of the ground clearance. Castelain *et al.* (2018) modify the underbody flow by changing its porosity which is somehow related. As a matter of fact, Cadot *et al.* (2015*b*) show that the stream velocity exiting the underbody is influenced by the ground clearance. To our knowledge, the body's alignment is never considered and no relationship between the wake state and the instantaneous loading is found in previous studies. A more detailed understanding of the wake instability is needed before flow control strategies can be implemented.

In the present thesis, only basic flow control strategies based on shape modifications are considered. Results obtained with a base cavity are reproduced and we also investigate the boat-tailing effect. The aim of our work is not only to achieve drag reduction or to study the pressure distribution on the afterbody since these questions have already been assessed (Mair, 1969; Peterson, 1981; Littlewood & Passmore, 2010; Grandemange *et al.*, 2013*c*; Perry *et al.*, 2015, 2016*b*; Pavia *et al.*, 2016). None of these studies focuses on the wake dynamics and only a few report wake topologies and base pressure distributions. Similarly, none reports any attempt to symmetrize the wake. The boat-tail shape and length are investigated for simple bodies and the influence of the ground vicinity or of misalignments is not taken into account.

Finally, the possibility to extend results obtained with simplified geometries to real vehicles is often inferred but less usually verified. In particular, the bi-stable wake dynamics of the turbulent wake of the Ahmed body is only reported in two papers dealing with real vehicles and these are originating from our research group (Cadot *et al.*, 2016; Bonnavion *et al.*, 2017*a*). In particular, no other studies investigating unsteady wake dynamics or consequences on the aerodynamic loading applied to the vehicle were found. However, it is worth mentioning that the extension from model-scale to full-scale Ahmed bodies is successfully reported by Grandemange *et al.* (2015).

1.5 Outline of the thesis

This section details the organization of the present manuscript. It is divided in two main parts; each chapter provides a small reminder of the setup, the results, a discussion and concluding remarks.

General considerations about the experimental setup are given in chapter 2, with detailed descriptions of the wind-tunnels, of the measurement devices and of the considered vehicles: flat-backed Ahmed bodies and full-scale road vehicles. The measurement methodology is detailed as well as the post-process of the data.

Part I is dedicated to simplified geometries at the model-scale. The mean flow around the Ahmed body is first considered in chapter 3, in which we investigate the velocity fields but also the mean base pressure distribution. The effect of the Reynolds number on flow separation at the forebody is briefly investigated. The dynamics of the unstable turbulent wake of the Ahmed body is studied in chapter 4. Sensitivity analyses of the wake response to changes of the body's alignment or ground proximity are performed with focus on the base pressure gradients and on the related cross-flow aerodynamic loading. Two different blunt base aspect ratios are considered in order to study all possible cases (y- or z-instabilities) and a stable flow solution is also considered. A wake model based on phase adaptation is proposed and satisfactorily used to predict the cross-flow loading generated by the instability. Geometrical modifications of the afterbody are then considered in chapter 5. Boat-tailing is investigated through its consequences on drag, on the afterbody pressure distribution but also on the cross-flow forces. Both averaged and fluctuating values are considered and relationship with the wake dynamics are found. Different boat-tail geometries are studied. Chapter 6 gives some preliminary results of steady and unsteady simulations of the flow around a squareback Ahmed body in ground vicinity. They aim at being used for wake stability analyses after further developments.

Part II of this manuscript is dedicated to real road vehicles aerodynamics. Chapter 7 is focused on the asymmetries in real vehicles' wakes. In particular, we aim at showing that they are created by similar static asymmetric wake modes as for simplified geometries and that they obey similar dynamics, in particular regarding the vehicle's alignment or ground vicinity. We also aim at revealing a second wake state and hopefully obtain a wake bi-stable dynamics. Different modifications are performed such as closing the front air-intake system, modifying the underbody roughness or installing side tappers or a base cavity on the vehicles. Besides, a different case of wake multi-stability created by boundary layer reattachment is investigated in chapter 8 with the experimental study of a Renault Mégane under yawing conditions. The dynamics is compared to that created by static wake asymmetries and the impact on the aerodynamic loading is investigated.

Finally, chapter 9 summarizes the results and aims at providing a general synthesis of this work and provides perspectives on future works which could nicely complement the present one.

Some appendices are also proposed. Appendix A complements chapter 2 and gives details about the software dedicated to pressure data acquisition that was developed during this work. The cavity effect mentioned in chapter 4 is further investigated in Appendix B at various ground clearances. Appendix C complements the analysis of chapter 5 varying the body's inclination and ground proximity. The mesh independence of the numerical results presented in chapter 6 is briefly checked in Appendix D.

CHAPTER 2

Experimental setup

This chapter introduces the experimental setup of this work. The full-scale (§ 2.1.1) and then the model-scale (§ 2.1.2) industrial wind-tunnels of the GIE-S2A are presented. Afterwards, the focus is set on the measurements systems employed to characterize unsteady wall-pressure (§ 2.2.1) and aerodynamic loading (§ 2.2.2). In-wake measurements systems are then considered: the tomographic device of the full-scale facility (§ 2.3.1) and the Particle Image Velocimetry appliance (§ 2.3.2). Afterwards, we briefly describe the common features of the flat-backed Ahmed bodies of Part I (§ 2.4) and present the vehicles considered in Part II (§ 2.5). Finally, the experimental procedure and data post-treatment are presented in §§ 2.6 and 2.7.

Contents

2.1 Wind tunnels 19
  2.1.1 Full-scale wind tunnel 19
  2.1.2 Model-scale wind tunnel 20
2.2 Measurement devices 22
  2.2.1 Pressure scanner for unsteady measurements 22
  2.2.2 Force balance for unsteady measurements 25
2.3 In-wake velocity measurements 26
  2.3.1 Tomographic system for in-wake velocity measurements 26
  2.3.2 Particle Image Velocimetry system 27
2.4 Flat-backed Ahmed body 27
2.5 Vehicles used for full-scale studies 29
2.6 Experimental procedure: acquisition of data 30
2.7 Data post-processing 30

2.1 Wind tunnels

The experiments are carried out at the GIE-S2A in Montigny-le-Bretonneux (France)[1], in an industrial complex primarily dedicated to automotive aerodynamics founded in 2001 by PSA Peugeot Citroën, Renault SA and the CNAM (*Conservatoire National des Arts et Métiers*). The whole facility is composed by two wind-tunnels described in § 2.1.1 and in § 2.1.2.

2.1.1 Full-scale wind tunnel

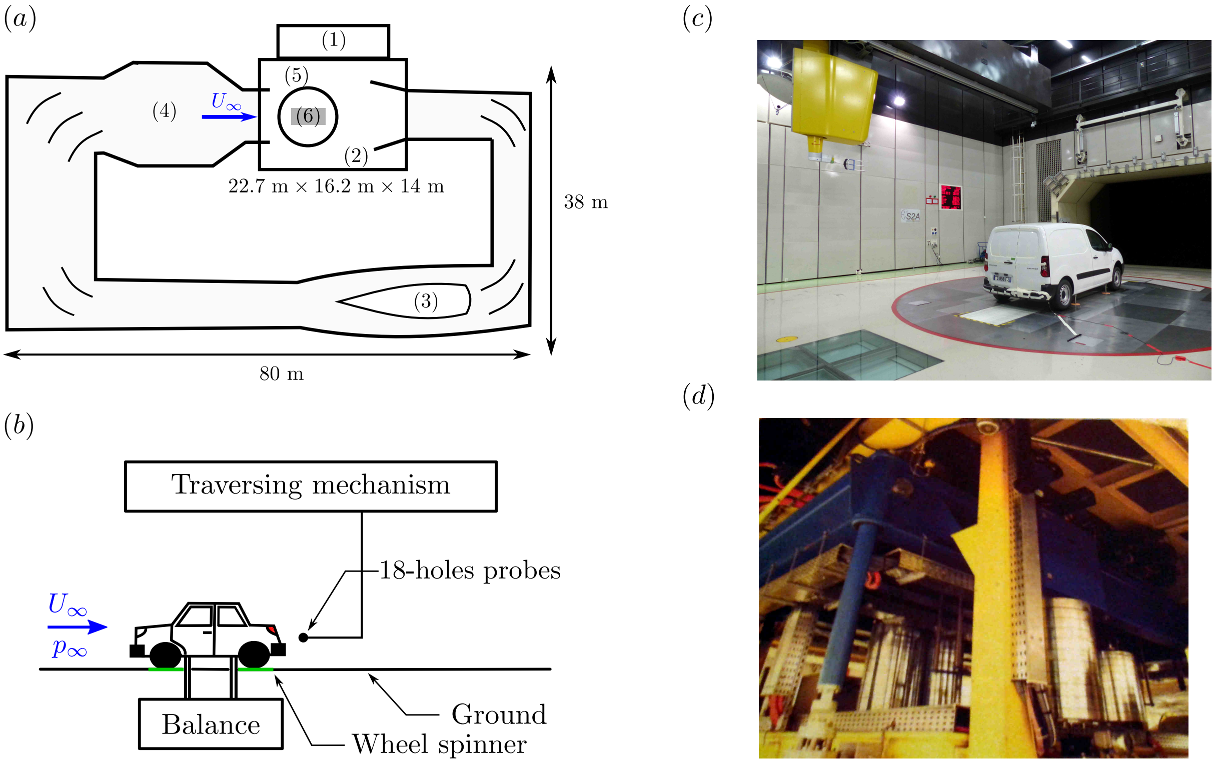

Figure 2.1 – Full-scale wind tunnel of the GIE-S2A: (*a*) schematic top view with characteristic dimensions. See text for numbers' description. (*b*) Schematic side view of the test section with a vehicle and the force balance. (*c*) Photograph of the plenum with a Peugeot Partner during a test session. (*d*) The force balance of the full-scale wind tunnel (reproduced from Délery *et al.* (2017)).

The full-scale wind tunnel, a detailed description of which can be found in Waudby-Smith *et al.* (2004), is used for real cars testing. A sketch of the whole facility is provided in figure 2.1(*a*) and a side view of the test section with the vehicle in figure 2.1(*b*). A photograph taken during a test session is available in figure 2.1(*c*), on which the yellow component is the traversing system used for tomographic measurements (see § 2.3.1). The facility is operated from the command room (1). It is a 3/4-open jet closed-loop tunnel, the test section (2) being a 24 m^2-nozzle expanding in a 22.7 m-long, 16.2 m-wide and 14 m-high plenum, with a contraction ratio of 6 : 1. The flow is driven by a 8.3 m-diameter fan (3) designed by Aiolos. It is composed of nine composite blades. Due to the geometry of the test section, the free-stream flow is guided by the ground only, motivating the characteristic *3/4 open jet*. The turbulence rate and the flow non-uniformity of the facility lie below 0.4% at a free-stream velocity of $U_\infty = 160$ km.h^{-1}.

---

[1] GIE-S2A: `https://www.soufflerie2a.com/en/`

The maximum allowable wind speed is around $U_\infty = 210$ km.h^{-1}; in this thesis, two free-stream velocities are considered: $U_\infty = 140$ km.h^{-1} and $U_\infty = 120$ km.h^{-1} when the tomographic system (§ 2.3.1) is in use. This wind-speed is obtained by means of the combination of a set of pressure sensors located at the contraction entrance and another tap at the nozzle exit.

For a better repeatability of the tests, the temperature inside the vein is regulated around $T_\infty = 293.2$ K with an uncertainty of less than 0.5 K in the tranquilizer and regulation chamber (4). This tunnel may also be used for acoustic testing but this characteristic is not used in this work.

The tunnel is equipped with a 8 m-diameter turntable (5) on which the car is placed to adjust its yaw angle β with a precision of $\pm 0.1°$, *i.e.* the angular deviation of the vehicle with respect to the incoming flow. This angle is counted following the direct orientation, the value $\beta = 0°$ corresponding to the body or the model aligned with the incoming flow. For convenience, this angle is expressed in degrees throughout.

The vehicle is attached with four struts controlled by hydraulic actuators which allow adjusting its ground clearance c, defined as the normal distance from the vehicle to the ground. Each axle is placed independently with a precision of ± 1 mm; the vehicle's pitch angle α can therefore be adjusted. The road effect is simulated by means of a 6 m-long and 1 m-wide rolling belt (6) located below the vehicle and moving at the simulated air-velocity. Wheels are rotating at the same speed in order to take the wheels-wake interaction into account owing to four wheel spinner units of exposed areas of 0.340×0.265 mm^2. The importance of the road simulation in the accurate estimation of the force coefficients and of the flow topology with respect to real driving conditions is discussed for instance in Fago *et al.* (1991).

The developing floor boundary layer is controlled by two floor-suction systems which can be used independently, one of them being located at the nozzle exit with the primary suction plate inclined upwards in the flow direction to avoid any pressure gradient at the front of the vehicle (Wickern *et al.*, 2003). The second system is located on the turntable upstream of the moving belt simulating the road. In our experiments, its displacement thickness equals $\delta^1 = 6$ mm at this last point. When the rolling road is activated as in the present work, the boundary layer displacement thickness at the center of the vehicle approaches zero ($\delta^1 \approx 0$ mm).

Two on-site measurements systems are available: a force balance located beneath the wind-tunnel floor described in § 2.2.2 and a tomographic system for in-wake velocity measurements detailed in § 2.3.1. In addition, unsteady pressure measurements are conducted with the pressure scanner described in § 2.2.1.

2.1.2 Model-scale wind tunnel

The model-scale wind-tunnel is a 2/5-th scale reduction of the full-scale facility described in § 2.1.1 and is shown in figure 2.2(a). This facility is used for instance in Evrard *et al.* (2016)'s work. The incoming flow is a 3/4 open-jet with a cross-section of $2.60 \text{ m} \times 1.47$ m and the plenum (2) dimensions are $9.30 \text{ m} \times 6.60 \text{ m} \times 4.15$ m; the contraction ratio is equal to 6 as for the full-scale facility. The thickness of the boundary layer is controlled by suction so that its displacement thickness equals $\delta_1 = 3$ mm at a distance $l_0 = 1.40$ m upstream of the nose of the model. The flow inhomogeneity is lower than 0.5% with an angular deviation smaller than 0.25° at the considered regime. The free-stream velocity is set to $U_\infty = 20.0$ m.s^{-1} and the temperature inside the vein is regulated with an uncertainty of less than 0.1 m.s^{-1} and 0.5 K respectively. A schematic side view of this facility with a flat-backed Ahmed body is given in figure 2.2(*b*) on which the setup for vertical Particle Image Velocimetry (PIV) planes (see § 2.3.2) is also depicted. In figure 2.2(*c*) showing the plenum, one can see the turntable on which the model is installed. A Pitot-static tube is mounted at the beginning of the test section to measure the static pressure p_∞ and the free-stream velocity U_∞. The wind exits the nozzle and then flows towards the photographer, driven by the fan pictured in figure 2.2(*d*).

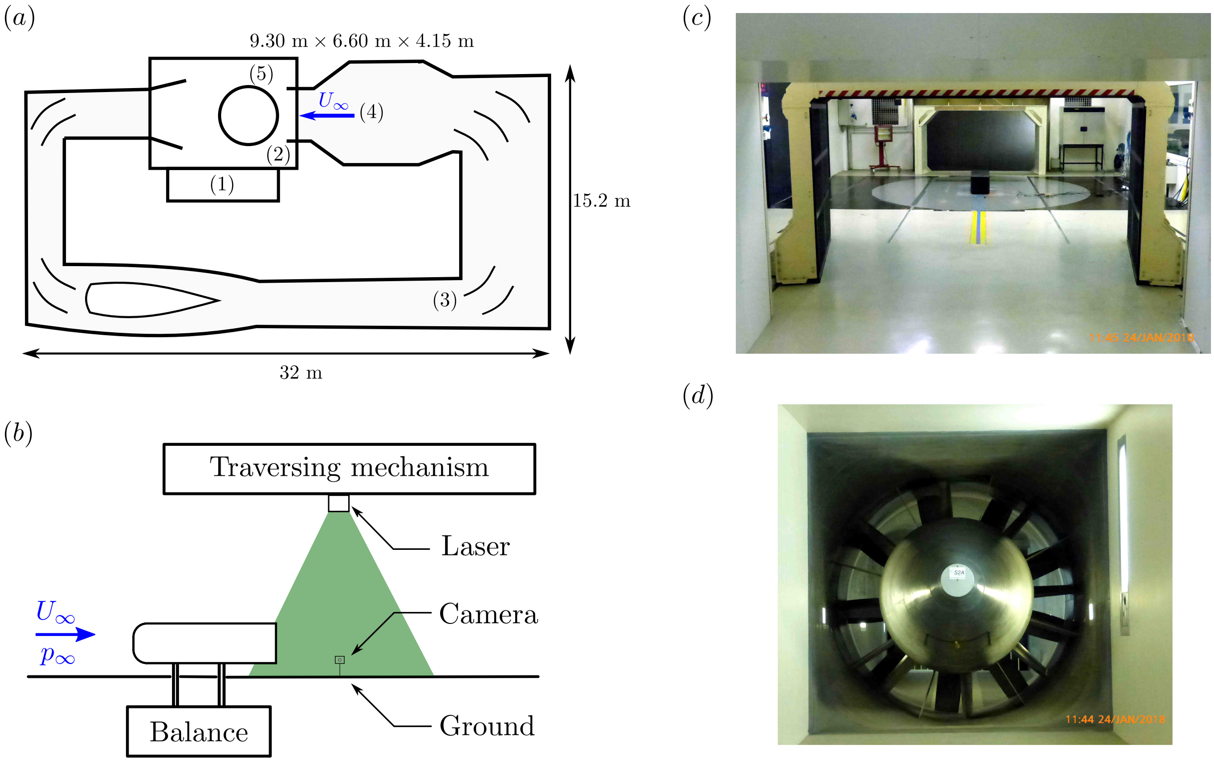

Figure 2.2 – Model-scale wind tunnel of the GIE-S2A: (*a*) schematic top view with characteristic dimensions. The numbers are the same than those used in figure 2.1. (*b*) Schematic side view of the test section with the Ahmed body and the force balance. The setup for vertical PIV measurements is also shown. (*c*) Photograph looking upstream of the test section with a flat-backed Ahmed body installed, (*d*) the driving fan of the model-scale wind tunnel.

The tunnel is equipped with a 2.1 m-diameter turntable (5) driven from the control room on which the model is placed to adjust its yaw angle β with a precision of $\pm 0.1°$. Unlike in the previous facility, tests are performed in fixed-ground conditions as no rolling-belt is available. The ground clearance c and the pitch angle α of the model cannot be adjusted directly from the facility but a control system was installed for this work; it is described in § 2.4.

Two on-site measurements systems are available: a force balance located beneath the wind-tunnel floor described in § 2.2.2 and a Particle Image Velocimetry system (see § 2.3.2). In addition, unsteady pressure measurements are conducted with the pressure scanner described in § 2.2.1; this last device is controlled by a customarily acquisition suite although the wind-tunnel offer to customers now include a 100 Hz pressure acquisition option that was not available at the beginning of this work.

2.2 Measurement devices

The devices used for pressure and aerodynamic loading measurements are presented in § 2.2.1 and § 2.2.2.

2.2.1 Pressure scanner for unsteady measurements

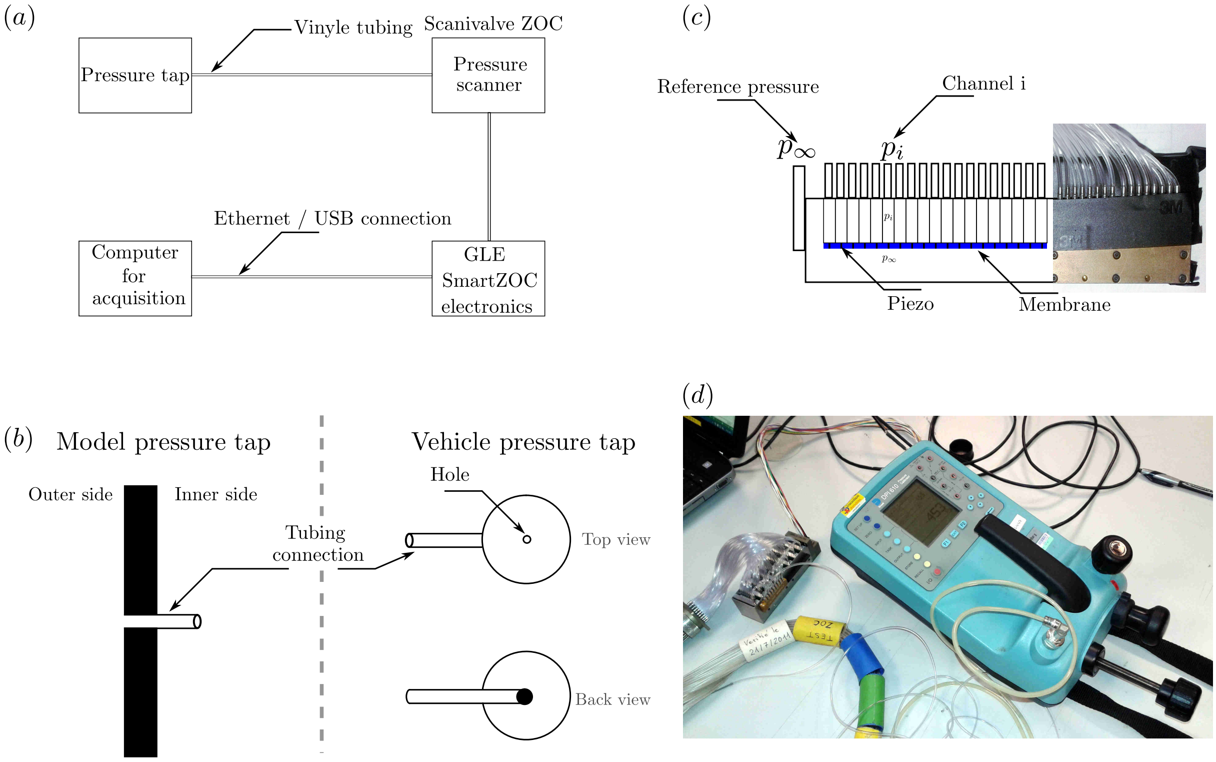
(a)
Vinyle tubing
Scanivalve ZOC
Pressure tap
Pressure scanner
Ethernet / USB connection
Computer for acquisition
GLE SmartZOC electronics
(c)
Reference pressure
Channel i
p_∞
p_i
p_i
p_∞
Piezo
Membrane
(b)
Model pressure tap
Outer side
Inner side
Tubing connection
Vehicle pressure tap
Hole
Top view
Back view
(d)

Figure 2.3 – Principle of the unsteady pressure measurement: (*a*) Whole acquisition chain, (*b*) schematic of a pressure tap: *(left)* cross-view through the model wall and *(right)* top and back views for vehicle's taps and (*c*) schematic close view of the pressure scanner showing the piezo-electric sensors placed on the membrane (in blue) as well as the cavity at the measured pressure p_i and that at the reference pressure p_∞. (*d*) Druck DPI 610 pressure calibrator while calibrating the ZOC33.

Wall-pressure is measured on the Ahmed body or on the vehicles by means of pressure taps connected with a vinyl tubing to a Scanivalve ZOC pressure scanner. A schematic of the measurement principle is given in figure 2.3(*a*) in which the whole acquisition chain is represented. Pressure taps (figure 2.3*b*) consist either in a hole through the model wall equipped with a hollow cylinder made of stainless steel (for the Ahmed body), either in a hole made on a hollow circular plate and equipped with a hollow cylinder glued on the vehicle. The hollow cylinder serves as the output and a vinyl tubing is connected to it to bring the pressure level back to the scanner.

Two types of pressure scanners are used in this work but both work the same way: a 32-channels Scanivalve ZOC22b and a 64-channels Scanivalve ZOC33. Each of the $N_c = 32$ (respectively $N_c = 64$) pneumatic input to which the vinyl tubing is connected corresponds to an internal membrane equipped with a piezo-electric sensor measuring its deformation as schematically shown in figure 2.3(*c*). On the other side of the membrane, the pressure level is regulated owing to a thirty-third input (respectively sixty-fifth) serving as the reference pressure. In our configuration, it is taken as the free-stream pressure p_∞ obtained directly from the facility thanks to a static pressure measurement at the nozzle exit.

Table 2.1 – Number of channels N_c, sampling frequencies f_e, measurement ranges and accuracy of the two pressure scanners used in this work and accuracy associated with the pressure coefficients c_p.

	N_c	f_e	Measurement range	Accuracy	Precision on c_p
ZOC 22b	32	200 Hz	10" H2O ($\approx$ 2491 Pa)	±3.75 Pa	$\sim 1 \times 10^{-3}$
ZOC 33	64	100 Hz	20" H2O ($\approx$ 4982 Pa)	±7.5 Pa	$\sim 2 \times 10^{-3}$

The piezo sensors convert the deformation into an electrical current which is sent to the electronics. All channels are measured one after the other but, in view of the trigger whose frequency is of the order of 65 kHz, the measurement can be estimated as synchronous for all channels with respect to the characteristic time scales of study. The main characteristic of both pressure scanners are given in table 2.1. The operating conditions of these scanners require a minimum temperature of 10°C, which may be bothering for full-scale testing as the vehicle is generally equipped one or two days ahead the tests. In such cases, proper storage conditions have to be ensured. A particular care is also provided as regards the derive of sensors with respect to time. In order to obtain the lowest possible, electronics are warmed up before testing. The maximum derive is observed to be around 0.2 Pa per minute. The other important parameter regarding these acquisition systems is their accuracy, which depends on the measurement range of the pressure scanners. A summary is given in table 2.1. The final output is a combination of 32 (respectively 64) relative pressure measurements, *i.e.* $p - p_\infty$. These pressures are then made non-dimensional into a pressure coefficient c_p defined in equation (2.1).

$$c_p = \frac{p - p_\infty}{\frac{1}{2}\,\rho\,U_\infty^2} \tag{2.1}$$

where ρ denotes the air density and U_∞ the free-stream velocity of the flow. The uncertainty on the pressure coefficient is given in table 2.1.

The analogical signal is converted by the electronics into a digital signal. Two electronics are used in combination with each pressure scanner: a GreenLake Engineering GLE/SmartZOC100-Ethernet with the ZOC22b and a GLE/SmartZOC200-USB from the same manufacturer with the ZOC33. The principle of operation is similar though, only the link to the computer differs (Ethernet *vs.* USB) and thus the conditioning of the data. The digital signal is read by a custom LabVIEW acquisition procedure developed specifically for each of the electronics as the conditioning of data is different. The strategy is to decompose the electronics output frame by frame and then to interpret each piece of information, *i.e.* the time stamp and each of the $N_c = 32$ (resp. $N_c = 64$) differential pressure measurements separately. The acquisition system is fully described in Appendix A (page 227) and in Bonnavion *et al.* (2018).

The output from the electronics being a voltage, a calibration is required to obtain an actual differential pressure in Pascals. This operation was performed at the GIE-S2A using the Druck DPI 610 pressure calibrator shown in figure 2.3(*d*). The device imposes a known pressure on all of the pneumatic sensors of the pressure scanner. An acquisition (with off-set correction) is performed during about 30 seconds and the averaged measured value is computed. Afterwards, a linear law of conversion can be derived for each channel independently. This procedure was performed on the ZOC33 scanner before its first use. Besides, the calibration data of the ZOC22b were verified imposing a known pressure and checking the output. All the setup used during calibration is similar to that used during the tests and the temperature in the calibration room is very close to that usually chosen for testing. The calibration of the strain gauges is not verified by this method; it is operated by the scanner's manufacturer at regular time intervals.

The pressure scanners are operated respectively at $f_e = 200$ Hz for the ZOC 22b and $f_e = 100$ Hz for the ZOC 33, the latter limitation being that of the GLE/SmartZOC200 electronics which is unable to transfer the right amount of data for the 64 pressure channels at a higher frequency because of the low baud rate of the link with the computer imposed by the electronics. Nonetheless, the main limitation is introduced on the system by the vinyl tubing whose natural cut-off frequency is a function of the tubes' length. In order to have comparable data, we ensure that all channels are tubed with similar material, in particular as to the length. For model-scale tests, the cut-off frequency ranks around 50 Hz while it is of the order of 20 Hz for full-scale geometries (see figure 2.4*a*). A simple experiment is conducted to ensure that the scanner's sensitivity and response frequency are adapted to our study. We consider the worst configuration of a full-scale vehicle and let a balloon explode in front of the sensors. The response to this impulse can be found in figure 2.4(*a*) in which only one channel is displayed but all have a similar behavior. Only the ZOC22b scanner is presented in this chapter but the response time of the ZOC33 is similar. From figure 2.4(*a*), the duration of the perturbation, for a tubing length of 2 m, *i.e.* longer than those usually obtained for full-scale tests (about $1 - 1.5$ m maximum) or for model-scale tests (of the order of 3.0×10^{-2} m) to an impulse – explosion of a balloon – is of the order of about 0.05 s. As a result, we retrieve a maximum operating frequency of about 20 Hz for this setup. The problem of filtering imposed by tubing has been detailed for instance in Yoshida *et al.* (1992) or Rofail *et al.* (2004). As a consequence, the time resolution is sufficient to capture the long-time dynamics investigated in the following chapters since it is rather of the order of 1 Hz.

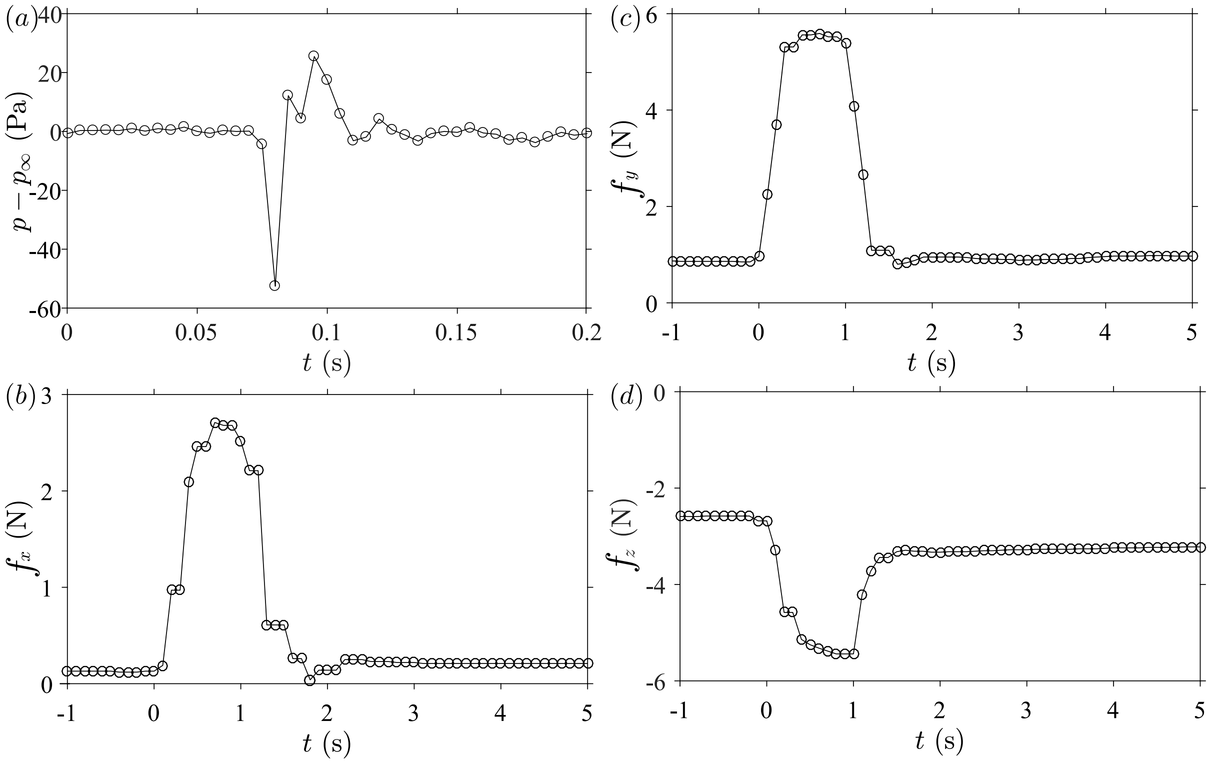

Figure 2.4 – Response to an impulse of the measurement systems: (*a*) Pressure scanner, (b, c, d) model-scale force balance. (*b*) Drag f_x, (*c*) side force f_y, (*d*) lift f_z.

The pressure sensors are typically placed at the base of the model and vehicles and at other additional locations mentioned in the associated chapters. N of them, located at the base, are used to assess a base suction coefficient c_b as shown in equation (2.2).

$$c_b\left(t^*\right) = -\iint_{H_b \times W_b} c_p \, ds \approx -\frac{1}{N}\sum_{i=1}^{N} c_p\left(y_i^*, z_i^*, t^*\right) \tag{2.2}$$

where H_b is the base height and W_b its width. The minus sign in the base suction coefficient definition ensures the same trend as the pressure and thus the total drag as shown for instance in chapter 4. This coefficient is always positive in separated flow areas (Roshko, 1993).

2.2.2 Force balance for unsteady measurements

The aerodynamic loading is measured owing to a six-components aerodynamics balance provided by Schencker GmbH and located out of the flow beneath the wind-tunnel floor as indicated on the sketches provided in figure 2.1(*b*) and in figure 2.2(*b*). A picture of the balance of the full-scale tunnel, reproduced from Délery *et al.* (2017), is shown in figure 2.1(*d*). The three components f_i, $i \in \{x, y, z\}$ of the total loading are measured at a sampling frequency of $f_b = 10$ Hz. These forces, measured in Newtons, are non-dimensionalized into the force coefficients c_i according to equation (2.3) where ρ is the air density, S the model's projected front surface area and U_∞ the free-stream velocity.

$$c_i = \frac{f_i}{\frac{1}{2}\,\rho\, S\, U_\infty^2}, \; i \in \{x, y, z\} \tag{2.3}$$

Table 2.2 – Measurement ranges, accuracy and repeatability of the force balance installed in the full-scale wind tunnel (§ 2.1.1) and precision associated with the force coefficients c_i.

	Range	Accuracy	Repeatability	Precision on c_i
f_x	0 – 6000 N	1 N	0.3 N	$\sim 1 \times 10^{-3}$
f_y	±6600 N	0.5 N	0.2 N	$\sim 1 \times 10^{-3}$
f_z	±9000 N	2 N	0.4 N	$\sim 2 \times 10^{-3}$

Table 2.3 – Accuracy and repeatability of the force balance installed in the model-scale wind tunnel (§ 2.1.2) and precision associated with the force coefficients c_i.

	Accuracy	Repeatability	Precision on c_i
f_x	0.3 N	0.1 N	$\sim 1 \times 10^{-3}$
f_y	0.3 N	0.1 N	$\sim 1 \times 10^{-3}$
f_z	0.5 N	0.2 N	$\sim 2 \times 10^{-3}$

The measurement accuracy and repeatability of the force balances installed in the full-scale (see § 2.1.1) and in the model-scale (see § 2.1.2) wind-tunnels are respectively given in table 2.2 and in table 2.3 in which the accuracy and repeatability associated with the force coefficients c_i are also given.

Measurements are performed owing to strain gauges installed on six bars visible in figure 2.1(*d*) – one for each component and for each axle. Each of those bars is loaded in traction-compression. The gauges transform the actual elastic deformation into an electrical current. This analogical signal is then converted digitally through an electronic system and then acquired with the in-house acquisition chain.

The response to an impulse[1] can be found in figure 2.4($b-d$) for each of the three components of the force balance installed in the model scale wind-tunnel. An impulse is given at $t = 0$ s with the body installed. The response of all three components is quite similar. The peak is reached after 0.75 s and the characteristic relaxation time is of about 1 s; this means that the force balance is able to capture fluctuations up to about 1 Hz, much higher the typical investigated frequencies in this work.

The static loading created by the body creates an offset to the measured value which might change depending on the ground clearance, pitch angle or yaw angle of the model. A reference (tare) is performed regularly. In that aim, a short acquisition is made in no-wind conditions and the averaged value is removed from the measurements in order to obtain the real aerodynamic loading. As the model or the vehicles are rotated owing to the turntable, the coordinate system of study is as well. Nevertheless, that associated with the balance does not. As the considered angles are small, both will be taken as coincident.

From the obtained time series of the force coefficients, it is possible to compute the mean value C_i and the standard deviation C_i'. Those values are used in the manuscript as the characteristic ones for the aerodynamic loading.

Since the balance is a six-components model, we could also have used the force moments to characterize the loading applied to the body. However, these components saturate earlier than forces and do not bring any additional information. Besides, because of the translation stages, the pitching moment would not be accurately estimated unless a tare is done before each experiment.

2.3 In-wake velocity measurements

Afterwards, two methods of wake velocity measurements are presented in § 2.3.1 and § 2.3.2.

2.3.1 Tomographic system for in-wake velocity measurements

The tomographic system installed in the full-scale tunnel aims at helping characterize the velocity and the pressure in the wake of the tested vehicle at any location that the system can reach. It is moved by means of a three-axis explorer designed and supplied by Aerotech ATE.

A 18-holes probe is used for in-wake measurements in all three space directions. The probe can be placed at any location in the wake of the vehicle. This probe measures static and dynamic pressures so that the three components U_x, U_y, U_z of the mean velocity can be obtained. A control program is implemented so that the measurements can be performed automatically in a constant x_i-plane ($x_i = x,\ y$ or z). Typically, planes parallel to the base of the vehicle (constant x-plane) or the centerline plane (constant y-plane) are investigated. Because of the size of the mast (visible in yellow in figure 2.2c) and the presence of the probe, this measurement system is highly intrusive and may affect the wake so much that it can change totally its topology (see chapter 7). Nevertheless,

---

[1] The impulse can be modeled as a Dirac delta function whose spectrum corresponds to that of a *white noise*, *i.e.* contains equally all frequencies. This allows a characterization of the response time without having to swipe all the frequency domain.

in case such changes occur, the fields are impacted and such situations can be identified easily.
The typical duration of such measurements is of about 20 minutes during which synchronous unsteady base pressure measurements are performed. They are used to identify the perturbations introduced by the measurement system.

2.3.2 Particle Image Velocimetry system

As a short reminder, Particle Image Velocimetry (PIV) is based on particle tracking. Two frames are captured with a small delay of a few microseconds (typically $25-50$ μs). The test section is sowed with smoke made of particles of about 1 μm of diameter which can be captured individually by the camera(s). The focus is adjusted on a laser sheet which defines a plane in the wind-tunnel. Each particle is identified twice: a first time in the first snapshot and again on the second one. Its displacement must be large enough to be able to derive the velocity field but small enough to ensure that particle tracking works without inverting them. The principle of PIV is fully described for instance in Raffel *et al.* (1998).
Unsteady velocity fields are measured using a two-dimensional PIV equipment. It is based on a dual pulse Nd:YAG laser (200 mJ, 4 ns) creating a laser sheet whose thickness is 5 mm combined with a Dantec FlowSense EO 4 MPx CCD (Charge Coupled Device) camera. Image pairs are shot at a rate of 4 Hz and 400 snapshots are recorded. The interrogation window size is set to 32 × 32 pixels, which corresponds to a maximal physical size $\Delta_y^* \times \Delta_z^* = 0.017 \times 0.017$ (or $\Delta_x^* \times \Delta_z^* = 0.017 \times 0.017$ for vertical planes) and with an overlap of 50%. Using conventional notations, the PIV gives access to the field $\boldsymbol{u}_{xz}^* = u^*\boldsymbol{e}_x + w^*\boldsymbol{e}_z$ in the $y^* = 0$ plane and to $\boldsymbol{u}_{xy}^* = u^*\boldsymbol{e}_x + v^*\boldsymbol{e}_y$ in the $z^* = 0$ plane. A schematic of the setup while installed for $y^* = 0$-PIV planes is represented in figure 2.2(*b*).
In addition, three-dimensional PIV is considered to obtain all three components of the velocity vector in a given plane. In this work, we investigate a constant x^* plane. The setup is similar to the previous one except for the two cameras that are now required. As a result, we obtain $u^*\vec{e}_x + v^*\vec{e}_y + w^*\vec{e}_z$ in the investigated plane. The principle of the 3D PIV, also called Stereo PIV, is detailed hereafter. In order to obtain the most accurate estimation of the downstream velocity component, the two cameras described above are placed with an angle of 90° between them. Both cameras are aligned with an angle of about 45° to the laser sheet. The main challenge is to keep the angle small enough so that defocusing remains acceptable without introducing a large perturbation in the flow and with the prescribed angle between the cameras. Focusing problem can be solved by means of optical Scheimpflug adapters to satisfy the so-called Scheimpflug condition (Prasad, 2000): the lens plane, the object plane and the image plane for each cameras have to intersect in a common line on the laser sheet. However, this method creates a strong perspective distortion, which is corrected by the software by means of a second order mapping function (Raffel *et al.*, 1998).

2.4 Flat-backed Ahmed body

The three-dimensional bluff body considered in Part I (chapters 3 through 5) is a flat-backed Ahmed body derived from the initial geometry introduced by Ahmed *et al.* (1984) which has become a reference for simplified road vehicles shapes. Two different models are studied and the details can be found in the associated chapters. Only the common features are presented here as only the afterbodies are different; details about the afterbodies can be found in the corresponding chapters.

The body is sketched in figure 2.5 and its characteristic dimensions are given in table 2.4. The length L refers to that of the whole body including the afterbody and the height H and the width W refer to those of the front part of the body only. The cross-dimensions of the base H_b and W_b are given in the corresponding chapters since different dimensions are used. For easier comparison between cases, the height H of the body is used as the characteristic length for non-dimensionalization and the corresponding values are indicated by the superscript *.

Table 2.4 – Dimensions of the flat-backed Ahmed body.

Dimension	Dimensional value	Dimensionless value based on H
Height of the body H:	0.298 m	1.000
Width of the body W:	0.350 m	1.174
Length of the body L:	0.994 m	3.336
Wheelbase Λ_{fr}:	0.477 m	1.601
Track Λ_t:	0.290 m	0.973
Location of rear supports Λ_r:	0.290 m	0.973
Projected surface area S:	0.104 m^2	1.174
Upstream edge radius r_f:	0.10 m	0.336
Lateral fillet radius (top) r_{s_t}:	1.0×10^{-2} m	0.034
Lateral fillet radius (bottom) r_{s_b}:	6.0×10^{-3} m	0.020
Support diameter d_{S}:	2.0×10^{-2} m	0.007

The body is basically a rectangular cuboid with the four upstream rounded edges (characteristic radius $r_f = 0.1$ m). The junction between the side panels of the model and its roof (respectively its underbody) are smoothed with fillets of characteristic radius $r_{s_t} = 1.0 \times 10^{-2}$ m (respectively $r_{s_b} = 6 \times 10^{-3}$ m). The body is equipped with four cylindrical supports made of aluminum of diameter $d_{\text{S}} = 2.0 \times 10^{-2}$ m located at a distance Λ_r upstream of the base. The wheelbase Λ_{fr} corresponds to the distance between the front and rear feet, the track Λ_t to the distance between left and right supports.

The yaw angle β (figure 2.5*d*) of the body is adjusted owing to the turntable described in § 2.1.2. As the adjustment of the ground clearance c, *i.e.* the normal distance from the body to the ground, and of the pitch angle α are not available in the model-scale facility, the body is equipped with two Standa 8MVT188-20 translation stages placed inside and driven by a 8SMC4-USB controller which allow adjusting the ground clearance on each axle independently. These stages were chosen because of the quite high payload mass as the body's ranks around $m \simeq 32$ kg with the equipment installed, and of the displacement range which was required to be at least 50 mm. The ground clearance c^* can thus be adjusted at the front within the range $c_f^* \in [0.050, 0.170]$ and independently at the rear, c_r^* within an identical range. The repeatability and the precision of the ground clearance is, in non-dimensional value with respect to H, $\delta c^* \sim 3.4 \times 10^{-3}$. The independence of each axis allows for a pitch angle α computed from equation (2.4):

$$\tan\alpha = \frac{c_f - c_r}{\Lambda_{fr}} \tag{2.4}$$

where the wheelbase Λ_{fr} is kept constant owing to a sliding system mounted inside the body. It is required because measurements of the loading are operated on the model's supports by the balance: creating a torque or an effort must consequently be avoided.

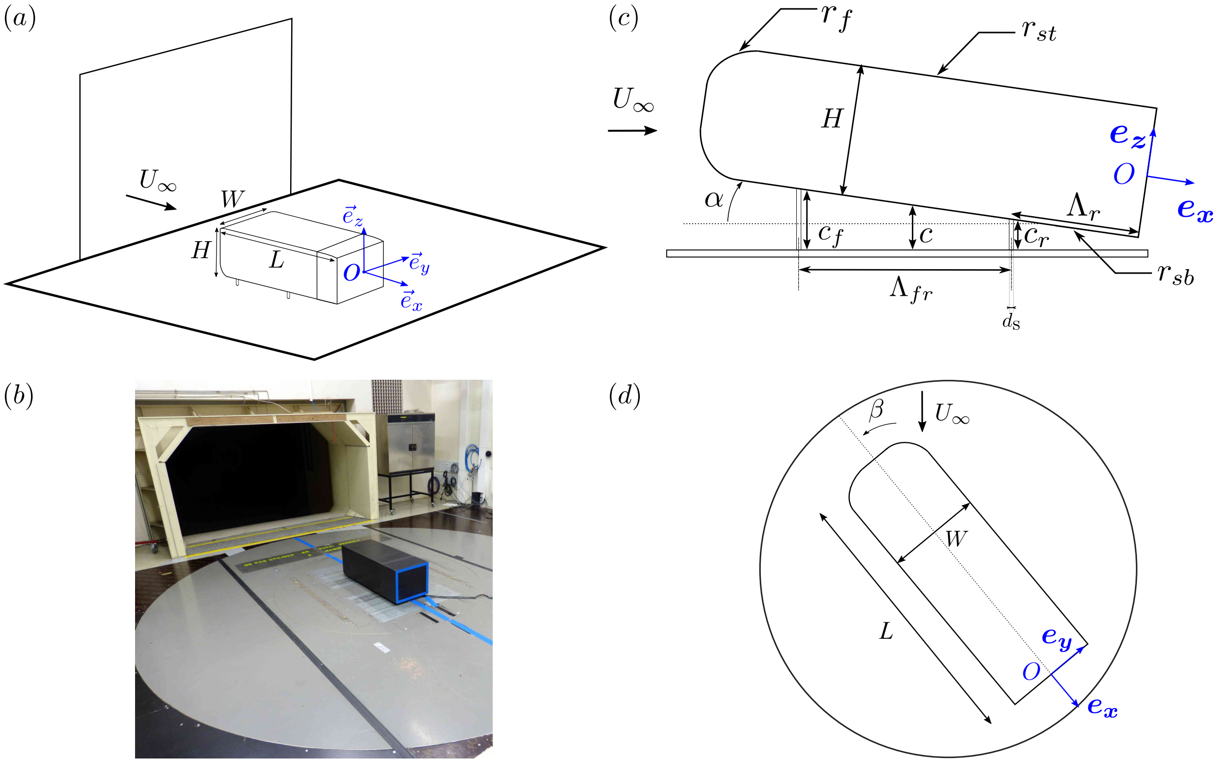

Figure 2.5 – Experimental apparatus: (*a*) schematic view of the Ahmed body in the model-scale wind tunnel of the GIE-S2A with the characteristic dimensions of the body and the coordinate system; (*b*) photograph of the body installed for a test campaign. (*c*) Schematic side view with definitions of the ground clearance, of the yaw angle and of the support locations and (*d*) top view of the model with definition of the yaw angle β.

Furthermore, a constraint would be applied to the body when creating a pitch angle without this system. The angle is counted positively in the clockwise orientation as shown in figure 2.5(*c*) and is varied in the range $\alpha \in [-1.5°, 1.5°]$. For convenience, α is only expressed in degrees throughout.

The coordinate system used throughout the manuscript (for Ahmed bodies) is defined as follows. Its origin is set at the center of the base of the model. The $\boldsymbol{e}_x$ axis is chosen pointing downstream, $\boldsymbol{e}_y$ axis is pointing to the right of the body (viewed from behind) and $\boldsymbol{e}_z$ is vertical as shown in figure 2.5. The same coordinate system is used for the vehicles.

2.5 Vehicles used for full-scale studies

Four vehicles with a blunt afterbody are considered in chapter 7: a Peugeot Partner, a Citroën Berlingo, a Peugeot 5008 and a Renault Kangoo. The details about the vehicles and in particular their dimensions can be found in § 7.1. Because of the limited availability of the vehicles, some tests are performed with a Citroën Berlingo, a sister-ship car of the Peugeot Partner. The impact on the results is discussed in the associated chapter 7.

These vehicles are characterized by an almost vertical base and can be modeled quite well, in first approximation, by a flat-backed Ahmed body. Actually, the Windsor geometry investigated for instance in Passmore *et al.* (2010); Littlewood & Passmore (2010); Littlewood *et al.* (2011); Littlewood & Passmore (2012); Pavia *et al.* (2016); Perry *et al.* (2016*b*) is much closer to a real vehicle's shape but the comparison of the results obtained with the Ahmed body by Grandemange *et al.* (2013*b*) and those on the latter one by

Passmore *et al.* (2010) yield the conclusion that the shape of the front of the body has a negligible influence on the wake dynamics investigated on the blunt based vehicles, *i.e.* that the results can be interpreted together with those presented on this manuscript for the flat-backed Ahmed body.

Only one hatchback vehicle is considered in this manuscript in chapter 8. It is a 2015-Renault Mégane whose shape differs from the flat-backed body presented in § 2.4 or the vans described hereabove. It is closer to the classical Ahmed body with a slant angle (Ahmed *et al.*, 1984). A full description of the vehicle including its characteristic dimensions can be found in § 8.1.

2.6 Experimental procedure: acquisition of data

We follow the same procedure for data acquisition during both model-scale and full-scale test campaigns. Once the model or the vehicle are installed in the vein and connected to the balance, the wind tunnel needs to be warmed up to reach its regulation temperature of T_∞. We take advantage of the installation time of about 1 hour to warm up the electronics of the pressure scanner. Notice that the GLE/SmartZOC200-201 electronics require the scanner to actually acquire data to properly reach their operating temperature.

Once ready, we start the acquisitions by a reference point ($c^* = 0.168$, $\alpha = 0°$, $\beta = 0°$). This point is always the same in order to compare different campaigns. Both the pressure and the aerodynamic loading measurement systems require an offset correction which is performed as follow. We acquire data for about 10 s in no-wind conditions, average them and then subtract the obtained quantity from the measurement. So that the derive does not influence the results, this procedure, also called a tare, has to be performed periodically. Regular acquisitions are synchronous for the pressure and the force balance – and contingently PIV – and last about 3 min. Although this is not enough to reach a statistical convergence of the data, it is more than enough to capture the typical dynamics of the problem.

Experiments are made changing one parameter at a time – ground clearance, alignment, geometry... Some points in particular before and after performing a tare are measured twice to ensure a good reproduction of the results. In addition, the absence of hysteretic behavior is ensured for critical points. The homemade acquisition software allows for a real-time post-processing as described in Appendix A. However, only raw results – relative pressure in Pascals – are recorded for post-processing for bigger flexibility.

2.7 Data post-processing

The acquired data are first made non-dimensional using equations (2.1) and (2.3) for the pressure and forces respectively. A low-pass filter is then applied using a Matlab procedure. It consists in a moving average over n points, n being calculated so that the filtered frequency equals to 2 Hz regardless of the considered time series. As a result, the width of the filtering window is 100 points for pressure acquisitions at 200 Hz, 50 at 200 Hz and 5 points for the force balance sampling at 10 Hz. For the filtering operation, an overlap of 50% is chosen between two consecutive windows. A Matlab routine was written to post-process all sets of experiments at once.

In addition to the time series and for the sake of brevity, we introduce a base pressure gradient computed. Out of the N pressure sensors located at the base of the vehicle or of the model, four called A, B, C and D – and indicated with their locations in each of the chapters – are used to compute a complex base pressure gradient which is representative of the instantaneous configuration of the wake. The procedure is described below. The Cartesian components g_y^* and g_z^* of the base pressure gradient are computed as:

$$g_y^*\,(t^*) = \frac{1}{2} \times \left[\frac{c_p(y_A^*, z_A^*, t^*) - c_p(y_B^*, z_B^*, t^*)}{y_A^* - y_B^*} + \frac{c_p(y_C^*, z_C^*, t^*) - c_p(y_D^*, z_D^*, t^*)}{y_C^* - y_D^*} \right] \tag{2.5}$$

and:

$$g_z^*\,(t^*) = \frac{1}{2} \times \left[\frac{c_p(y_A^*, z_A^*, t^*) - c_p(y_C^*, z_C^*, t^*)}{z_A^* - z_C^*} + \frac{c_p(y_B^*, z_B^*, t^*) - c_p(y_D^*, z_D^*, t^*)}{z_B^* - z_D^*} \right] \tag{2.6}$$

where y_i^* and z_i^* stand for the coordinates of sensor i. Afterwards, a complex base pressure gradient is formed as $\hat{g}^* = g_y^* + \mathrm{i}\ g_z^*$ (where $\mathrm{i}^2 = -1$). Equivalent to this expression is the polar form of the gradient given in equation (2.7) where the modulus $g_r^* = |\hat{g}^*|$ referred to as strength and the argument $\varphi = \arg(\hat{g}^*)$ called the phase appear.

$$\hat{g}^* = g_r^* \times \exp(\mathrm{i}\varphi) \tag{2.7}$$

The four components of the base pressure gradient – horizontal g_y^*, vertical g_z^*, strength g_r^* and phase φ – are used in the manuscript. They are considered not only with their time series but also through their histograms, normalized to yield Probability Density Functions (PDF). The histograms are plotted with 150 intervals. They are also used to create bifurcation diagrams; in this case, the normalization is done with the maximum of each.

We also consider spectra of some variables. The power spectral density estimate is found using Welch's overlapped segment averaging estimator (Welch, 1967). The signal is divided into longest possible segments with 50% overlapping. Each segment is windowed with a Hamming window and then averaged. The variable that we consider for computing the spectrum is always taken as a time series. For instance, phase spectra do not refer to a Fourier analysis but to spectra of the variable $\varphi\,(t^*)$ defined in equation (2.7), similarly to any other quantity $a\,(t^*)$.

Space-time diagrams may also be considered. In this case, data is acquired along a vertical or an horizontal line of pressure sensors. We mainly focus on the planes $y^* = 0$ (symmetry plane, mid-track) and $z^* = 0$ (mid-height of the base). Finally, when base pressure distributions are investigated, we use a cubic interpolation between the sensors to plot the continuous maps.

Part I

Simplified geometries: flat-backed Ahmed bodies

CHAPTER 3

Experimental investigation of the mean flow around the squareback Ahmed body

This chapter focuses on the mean flow around the squareback Ahmed body. It is characterized thanks to experimental PIV results yielding the mean velocity fields both in horizontal and vertical planes (§ 3.3.1). The flow alongside and above the body are considered as well as the mean wake properties. Afterwards, the mean base pressure distributions are presented in § 3.3.2. Finally, an experimental study shows that varying the Reynolds number influences the mean flow around the body and may lead to separation near the forebody; however, we confirm in § 3.3.3 that they are almost not present under the considered test conditions. A brief discussion follows (§ 3.4); it is focused on the symmetries of the problem and on the flow topology around the Ahmed body, whose main characteristics motivate the focus on the wake only without further study of the forebody in the following chapters.

Contents

3.1 Brief literature review **37**
3.2 Setup **38**
3.3 Results **39**
    3.3.1 Mean velocity field 39
    3.3.2 Mean base pressure distribution 42
    3.3.3 Reynolds number effect 43
3.4 Discussion **44**
3.5 Concluding remarks **46**

3.1 Brief literature review

The wake flow behind bluff bodies and downstream the separation point have been investigated for decades, since the pioneering work of Kirchhoff (1869) followed later by Brillouin (1910). The basic idea is to separate the wake from the outer flow which is expected to more or less follow a potential flow-like evolution. A separating line divides the two regions.

Since then, the increasing understanding of the problem together with the improving computing capabilities have allowed to target the problem of bluff bodies' wakes in a more detailed way, in particular regarding simplified vehicles geometries. Even though most of the studies deal with the high unsteadiness of the wake of the Ahmed body, some present instantaneous or averaged velocity fields around the model. A common feature of several experimental works including Beaudoin *et al.* (2004), Franck *et al.* (2009), Conan *et al.* (2011) and Grandemange (2013) but also numerical studies such as Peres & Pasquetti (2013); Pasquetti & Peres (2015) or Pellerin *et al.* (2016) is a separation of the flow after the rounded afterbody for Reynolds number of the order of $\mathrm{Re} \sim 10^4$ based on the body's height. However, reattachment occurs relatively quickly since the forebody curvature is carefully selected to avoid a massive separation (Ahmed *et al.*, 1984). At lower Reynolds numbers ($\mathrm{Re} \sim 10^3$), Spohn & Gilliéron (2002) report a consistent longer separation. A significant amount of flow moving upstream is accordingly reported by Bruneau *et al.* (2017) for a squareback Ahmed body at $\mathrm{Re} = 15000$ in a Direct Numerical Simulation (DNS). However, for a close geometrical setup, McArthur *et al.* (2016) did not identify a significant reverse flow. Out of all of the previous studies, that of Lucas *et al.* (2017) is expected to be the more relevant to compare with since the same geometry is simulated in the same range of Reynolds numbers. The author report large detachments at the front of the body – on all sides. More generic studies such as the Direct Numerical Simulations by Lamballais *et al.* (2008, 2010) show that the flow separation is intimately related to the surface's rounded curvature.

Although responsible for a destabilization of the flow through the y-instability in view of the base aspect ratio of the present body (Grandemange *et al.*, 2013*a*), the ground clearance is not expected to strongly modify the surrounding flow. As a matter of facts, the side and top flow are not impacted and only the underbody flow is accelerated as the body is raised away from the floor according to Cadot *et al.* (2015*b*). The topology of the mean flow around the body is consequently expected to be independent of this parameter. Additional work has been performed on close geometries such as a wall-mounted cube by means of a three-dimensional Large-Eddy Simulation by Krajnović & Davidson (2002) and allows conclusions regarding the effect of the underbody flow.

From the literature, the mean wake length is observed to be considerably shorter in three-dimensional cases (Grandemange, 2013; Evrard *et al.*, 2016; Li *et al.*, 2016; Barros *et al.*, 2017; Schmidt *et al.*, 2018; Castelain *et al.*, 2018) than for two-dimensional cases (low Reynolds number flow of Grandemange *et al.* (2012*a*) or Evstafyeva *et al.* (2017), two-dimensional backward facing step of Armaly *et al.* (1983)). In the first case, it corresponds to about $1.8 - 2.4$ times the body's height *versus* 3 up to 8 times that length in two-dimensional configurations. In fact, the reattachment length after the step is found to first increase linearly with the Reynolds number and then starts to plateau for $\mathrm{Re} \leq 500$ (Armaly *et al.*, 1983) or at least increases slower for 2D experiments and computations (references reported in Williams & Baker (1999)). Even 3D experiments and computations of the 2D geometry lead to significantly identical results (Armaly *et al.*, 1983; Jiang *et al.*, 1995; Williams & Baker, 1999), with a continuous increase of the bubble length unlike what is reported in the literature concerning the Ahmed or Windsor body, thus highlighting the predominant effect of three-dimensional phenomena in the wake closure.

3.2 Setup

We first describe the experimental setup used in this chapter. The experiments are conducted in the model-scale wind tunnel of the GIE-S2A with the boundary layer suction device on (see § 2.1.2 for details about the facility). The model is a squareback Ahmed body whose base height is $H_b = 0.298$ m and width is $W_b = 0.350$ m yielding a base aspect ratio of $W_b^* = W_b/H_b = 1.174$. For this analysis, the body is aligned with the incoming flow ($\beta = 0°$). The body is presented in § 2.4 and its characteristic dimensions are given in table 2.4. In this chapter, the base's dimensions, given in table 3.1, are identical to that of the body ($H_b = H$ and $W_b = W$). Schematic views of the model with the associated dimensions are provided in figure 2.5.

Table 3.1 – Dimensions of the base of the Ahmed body used in the chapter. The body's dimensions are given in table 2.4.

Dimension	Dimensional value	Dimensionless value based on H
Height of the base H_b:	0.298 m	1.000
Width of the base W_b:	0.350 m	1.174

The ground clearance of the model c – indicated in figure 3.1(b) – and defined as the normal distance from the body to the ground can be adjusted simultaneously on all supports in the range $c_f^* \in [0.050, 0.170]$. Details about the setup can be found in § 2.4. Doing so, we make sure that the body remains parallel to the ground so that no pitch angle is created ($\alpha = 0°$). Three different ground clearances $c^* = c/H$ are considered in this chapter: $c^* = 0.067$, $c^* = 0.101$, and $c^* = 0.168$. The flow around the body is characterized by Particle Image Velocimetry (setup described in § 2.3.2) and multiple planes are investigated. Several PIV investigations are conducted in both horizontal planes (at mid-height of the body, $z^* = 0$) shown in figure 3.1(a) and vertical ones located mid-width ($y^* = 0$) indicated in figure 3.1(b). Finally, the base pressure is estimated experimentally at the $N = 21$ locations shown in figure 3.1(c) which are also used to compute the base suction coefficient C_b defined in equation (2.2).

Only the mean flow is considered in this chapter. One of the main questionable points can be the experimental estimation of the *mean flow*. As a matter of fact, as described later on in chapter 4 with the same geometry, large unsteadiness of the flow field can be identified around the body, in particular in its wake. Besides, statistical convergence is quite hard to achieve because of the typical long-time dynamics of the problem of about $t \sim 20$ s (see chapter 4). For PIV measurements, it is even harder as the typical duration is of about 100 s, *i.e.* only five times longer than the characteristic time scale. Since PIV planes are only used for flow visualizations, we consider that the mean flow is correctly represented though as we ensure that the observed patterns are reproducible and respect the global symmetries of the problem. In addition, as one has access to all 400 snapshots, one can compare the instantaneous flow field to the mean result. On top of that, only the wake is known to be subject to highly unsteady phenomena (Grandemange *et al.*, 2013*b*, 2014*b*; Volpe *et al.*, 2015; Brackston *et al.*, 2016; Evrard *et al.*, 2016); special care has to be taken for these planes so that the presented fields match the symmetries of the setup.

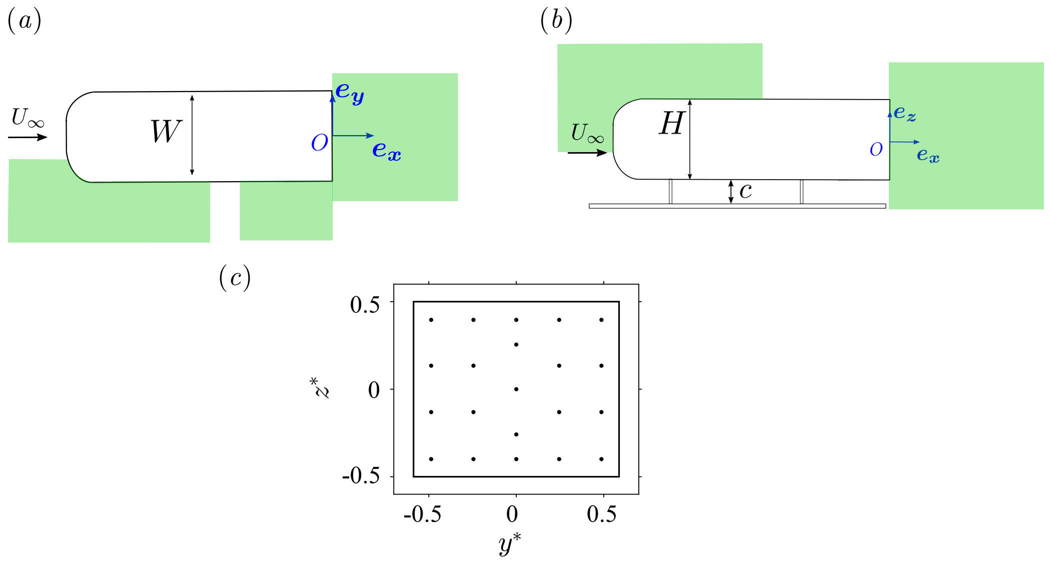

Figure 3.1 – Schematic view of body with the velocity planes investigated in chapter 3 and the coordinate system: (a) top view, (b) side view, (c) location of the $N = 21$ pressure sensors for base pressure measurements.

Finally, owing to synchronous base pressure measurements, we ensure that the obtained field is representative of the whole dynamics.
For all investigated cases but in § 3.3.3, the mean flow velocity is set to $U_\infty = 20$ m.s^{-1}, used as the scaling unit. This yields a Reynolds number based on the body's height of $\mathrm{Re}_H = U_\infty H/\nu \simeq 4.0 \times 10^5$, ν being the air kinematic viscosity.

3.3 Results

This section is organized as follows. We first discuss the mean velocity field around the body in § 3.3.1 with focus on the wake. Afterwards, the base pressure distribution is investigated in § 3.3.2. Finally, the influence of the Reynolds number on the velocity field is characterized in § 3.3.3. Numerical simulations of the mean flow around the body can be found in chapter 6 where they are compared to the present results.

3.3.1 Mean velocity field

In order to characterize the flow field surrounding the body, we study the mean data obtained experimentally with PIV (see § 2.3.2). The horizontal planes indicated in figure 3.1(a) are first considered. Only the case $c^* = 0.168$ identical to Ahmed *et al.* (1984); Barros *et al.* (2017) is presented but the results in the $z^* = 0$ plane are independent of the ground clearance and the analysis can be extended to all aligned configurations. The data are presented for $U_\infty = 20$ m.s^{-1}; a study at different Reynolds numbers is shown in § 3.3.3. Experimental data are given in figure 3.2(a, b).
At the front of the body, there is a stagnation point identified owing to the streamline normal to the body's surface and a zero velocity. It is located in $y^* = 0$ thus respecting the transverse symmetry of the problem. There is no observable flow separation after the rounded forebody. The radii of curvature r_f are indeed chosen to minimize the influence of the geometry on the wake flow (Ahmed *et al.*, 1984). We can observe that the flow is parallel to the body up to the massive separation point visible in figure 3.2(b) and located

at the blunt trailing edge. Its location is imposed by the sharp geometry of the blunt body and remains constant over time. To sum up, we can say that the flow in horizontal planes alongside the Ahmed body is equivalent to the inviscid one as long as one remains far enough from the edges on which we expect longitudinal vortices to be generated.

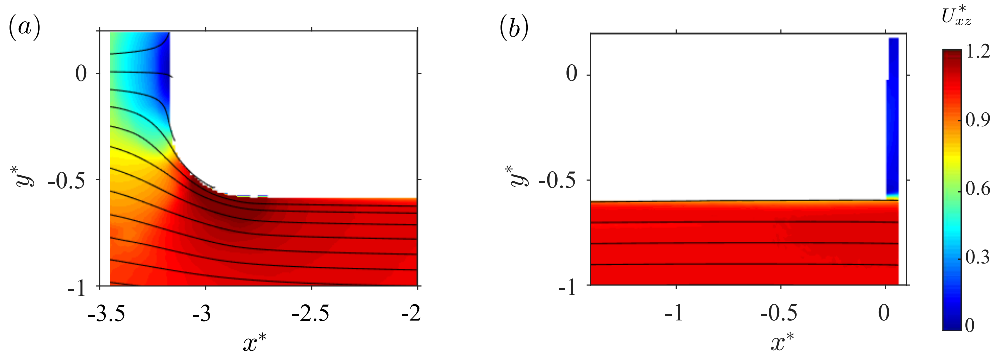

Figure 3.2 – Cross-sections of the mean velocity field alongside the body visualized using streamlines superimposed to the modulus of the velocity in the horizontal plane $z^* = 0$ at $U_\infty = 20$ m.s^{-1}. The body is aligned with the incoming flow ($\beta = 0°$) and in no-pitch conditions ($\alpha = 0°$) with $c^* = 0.168$.

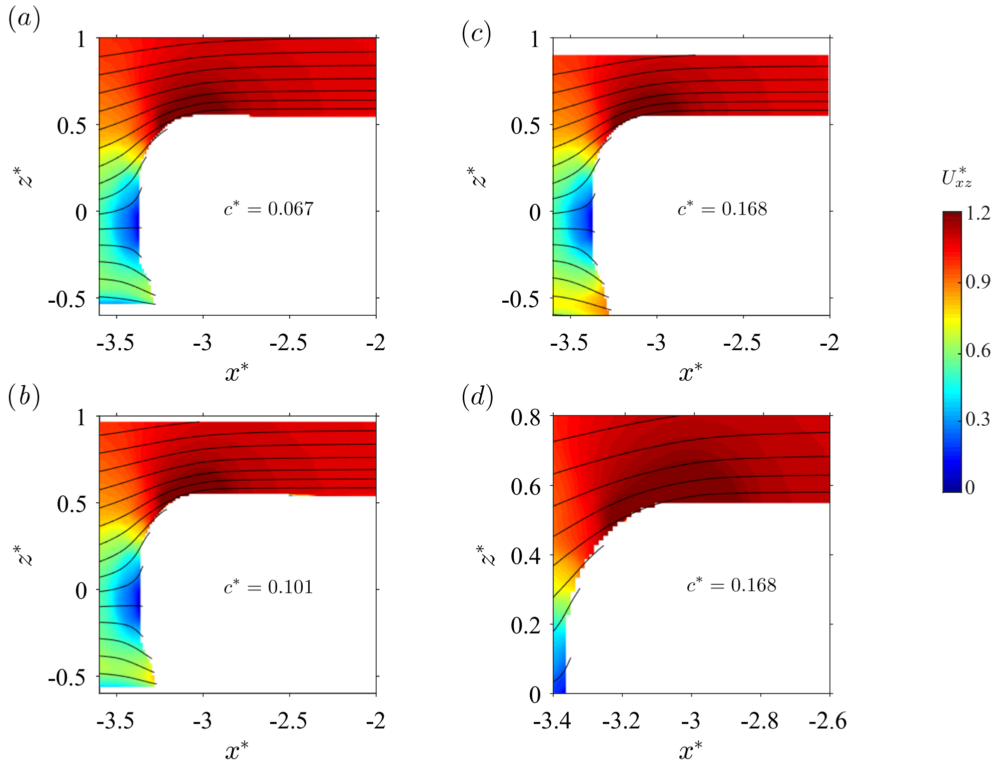

Figure 3.3 – Cross-sections of the mean velocity field U^*_{xz} in the plane $y^* = 0$ for the squareback Ahmed body aligned with the incoming flow ($\alpha = 0°$, $\beta = 0°$) obtained experimentally at various ground clearances: (a) $c^* = 0.067$, (b) $c^* = 0.101$, (c) $c^* = 0.168$ with close view in (d).

Afterwards, the vertical plane $y^* = 0$ is investigated in figure 3.3 near the front edge of the body in order to characterize the flow separation induced by the front curvature and the potential effect of the ground clearance. With our PIV data, we only have access to the top circle arc because of the body's shadow preventing from measurements elsewhere. Nonetheless, since the underbody flow velocity increases with the ground clearance as shown in the work of Cadot *et al.* (2015*b*), no significant separation reducing the flow rate is expected to take place below the body. In all investigated cases, a stagnation point at the front leading edge of the body is identified; in addition, high velocity magnitudes near the circle arcs of the forebody can be observed since the flow remains attached due to the curvature transfer from the geometry to the streamlines. It is interesting to highlight that the stagnation is not centered on the front surface but located slightly below the mid-height. This phenomenon, observed for all studied ground clearances, can be ascribed to a ground effect. This absence of symmetry is discussed in § 3.4.

Unlike the fields presented in Lucas *et al.* (2017) but in agreement with the rounded forebody of McArthur *et al.* (2016), no significant flow separation can be observed around the forebody, in particular at high ground clearances as shown in the close view of figure 3.3(d). Experimentally, due to the PIV uncertainty, it can only be ensured that if a separation were to occur, its size normal to the body's surface would be below the resolution of the PIV, *i.e.* a few millimeters only. Anyway, we do not retrieve the flow features obtained by Lucas *et al.* (2017) for the same body. For the lowest ground clearance (figure 3.3a), there could be a small flow separation around $-3.2 \lesssim x^* \lesssim 2.7$ although we are within the PIV uncertainty. Nonetheless, the outer flows or the wakes are not affected. Since the flow along the body is steady – the fields presented in figure 3.3($a-d$) are similar to the instantaneous snapshots –, it is excluded that any unsteadiness observed in the wake (see following chapters) originates from a flow separation at the front of the body (Grandemange, 2013). The flow in the present work is assumed to be representative of that of Evrard *et al.* (2016) as the same body – and the same afterbody in this chapter – is used. Last, in agreement with Cadot *et al.* (2015b), the magnitude of the underbody flow velocity increases with the ground clearance as can be observed for $-3.5 \lesssim x^* \lesssim -3.2$ and $z^* \simeq -0.5$ in the figures.

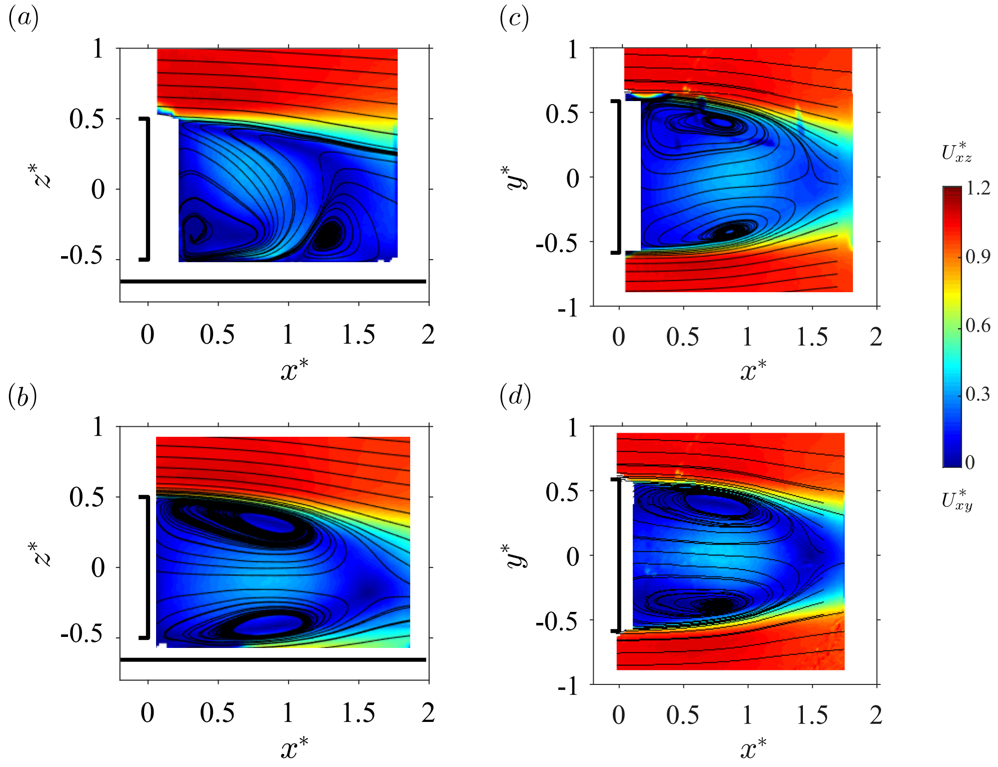

Figure 3.4 – Cross-sections of the mean velocity field at the base the body visualized using streamlines superimposed to the modulus of the velocity in the vertical plane $y^* = 0$ (left column) and horizontal plane $z^* = 0$ (right column). The body is aligned with the incoming flow ($\beta = 0°$) and in no-pitch conditions ($\alpha = 0°$). (a, c) $c^* = 0.067$, (b, d) $c^* = 0.168$.

Finally, the mean wake is briefly characterized owing to the two orthogonal planes y^* and z^* at the base of the body indicated in figure 3.1(a, b). In all cases, the mean wake appears to be symmetrical in the horizontal planes (figure 3.4b, d) thus respecting the symmetry of the problem. We recall that the mean experimental fields are obtained by averaging of the 400 PIV snapshots. The symmetry of the mean wake can be interpreted by the fact that, despite its unsteadiness, statistical symmetry is restored to match the symmetries of the geometry. The size of both recirculating structures is identical in average. The fields are colored by the velocity magnitude U^*_{xz} (respectively U^*_{yz}) and the wake is clearly identified by the very low velocities (with respect to the free-stream's) and characterized by reverse flow. The pattern is quite similar to that obtained before the onset of the instability at very low Reynolds numbers ($\mathrm{Re}_H = 310$) by Grandemange *et al.* (2012*a*). The wake is almost symmetric in the $y^* = 0$ plane at high ground clearance (figure 3.4*b*) as expected since the ground influence becomes negligible (see § 4.3.1.2). However, for the lowest ground clearance $c^* = 0.067$, the wake is stabilized and then displays a strong asymmetry since the ground now represents an anti-symmetry plane to the flow. This is clearly appearing in figure 3.4(a). The experimental wake length obtained at $\mathrm{Re}_H \simeq 4.0 \times 10^5$ – *i.e.* in the fully turbulent regime – is about 1.7 H. It is shorter than the separation length of more than 2 H around the steady bifurcation (Grandemange *et al.*, 2012*a*).

3.3.2 Mean base pressure distribution

The mean base pressure distributions $C_p(y^*, z^*)$ shown in figure 3.5 are obtained at the following ground clearances: $c^* = 0.067$, $c^* = 0.101$ and $c^* = 0.168$. At first glance, the results strongly depend on the model's ground clearance. The mean distribution shown in figure 3.5(a) for $c^* = 0.067$ is symmetric in the horizontal direction but shows a vertical gradient because of the vicinity of the ground and its stabilizing effect (see Grandemange *et al.* (2013*a*); Cadot *et al.* (2015*b*) and chapter 4, in particular § 4.3.1.2). In the unstable wake regime (§ 4.3.1.2), the distributions of figure 3.5(b) and figure 3.5(c) should be the same. However, they are slightly different because of the underlying convergence problem; both show an almost uniform mean base pressure distribution though. It will be shown in the next chapters that these distributions are not representative at all of the instantaneous wake topology because of the symmetry-breaking modes (Grandemange *et al.*, 2012*a*, 2013*b*; Evrard *et al.*, 2016; Evstafyeva *et al.*, 2017). It consequently appears questionable to investigate only half of the body or time-averaged data – first order statistics – only as it is sometimes done.

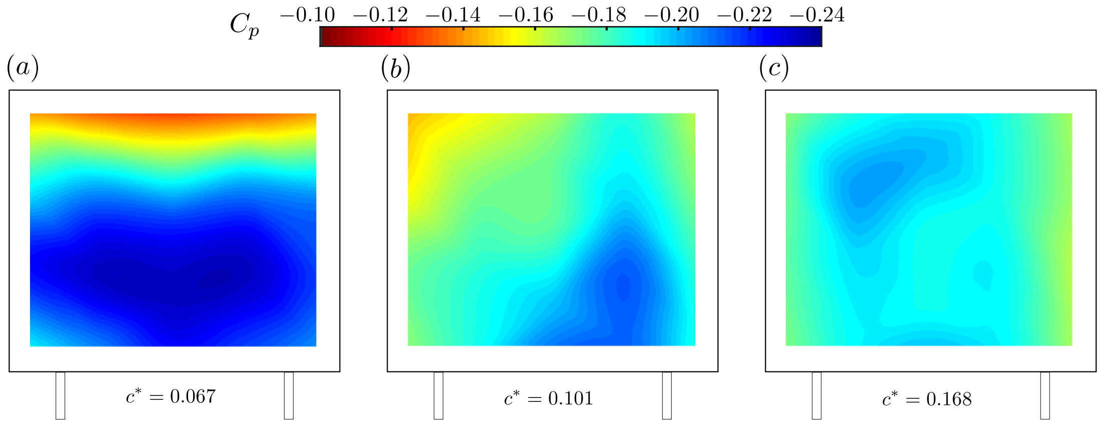

Figure 3.5 – Mean base pressure distributions $C_p(y^*, z^*)$ for squareback Ahmed body ($\alpha = \beta = 0°$) at various ground clearances: (a) $c^* = 0.067$ (b) $c^* = 0.101$ (c) $c^* = 0.168$.

It must be emphasized that the pressure distributions are not area-weighted, which might result in a small bias in the estimation of the base suction coefficients since the taps are not uniformly distributed. However, as previously shown by Evrard *et al.* (2016) with the same body, there is an excellent agreement between the base suction and the model's total drag. There is no further impact on the results with our definition of the base pressure gradients.

3.3.3 Reynolds number effect

In this section, the influence of the Reynolds number on the flow presented in § 3.3.1 is finally assessed through a modification of the mean free-stream velocity U_∞. Only the flow alongside the body shown in figure 3.2(*a*) is studied experimentally for U_∞ [m.s^{-1}] $\in \{5, 10, 15, 20, 25\}$, which corresponds to a range of Reynolds numbers of $1.0 \times 10^5 \lesssim \mathrm{Re}_H \lesssim 5.0 \times 10^5$[1]. The results are presented in figure 3.6. The flow past the body in the vertical plane $y^* = 0$ is expected to be similarly affected but this statement was not verified experimentally.

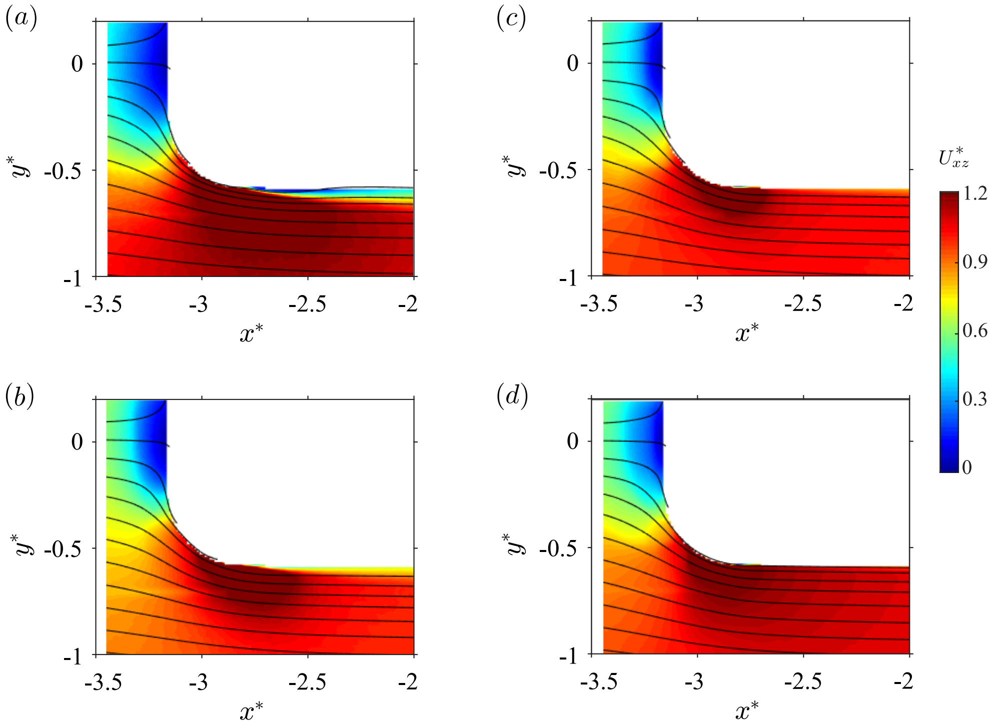

Figure 3.6 – Cross-sections of the mean velocity field alongside the body visualized using streamlines superimposed to the modulus of the velocity in the horizontal plane $z^* = 0$ varying the Reynolds number experimentally. The body is aligned with the incoming flow ($\beta = 0°$) and in no-pitch conditions ($\alpha = 0°$) with $c^* = 0.168$: (*a*) $\mathrm{Re}_H \simeq 1.0 \times 10^5$ ($U_\infty = 5$ m.s^{-1}), (*b*) $\mathrm{Re}_H \simeq 2.0 \times 10^5$ ($U_\infty = 10$ m.s^{-1}), (*c*) $\mathrm{Re}_H \simeq 3.0 \times 10^5$ ($U_\infty = 15$ m.s^{-1}), (*d*) $\mathrm{Re}_H \simeq 5.0 \times 10^5$ ($U_\infty = 25$ m.s^{-1}). The case $\mathrm{Re}_H \simeq 4.0 \times 10^5$ ($U_\infty = 20$ m.s^{-1}) is shown in figure 3.2(*a*).

---

[1] Increasing the Reynolds number more than this range would not trigger flow separation and decreasing it more would request the use of a smaller model since the considered free-stream velocity is already very small ($U_\infty = 5$ m.s^{-1}) compared to the maximum wind-tunnel velocity of $U_\infty \approx 59$ m.s^{-1}. Wind tunnels should not be used at very low regimes with respect to their nominal operating conditions since it introduces a lot of uncontrolled unsteadiness in the flow. Although the investigated range of study is quite narrow, we still observe some discrepancies as shown in figure 3.6.

For the minimum considered Reynolds number of $\mathrm{Re}_H \simeq 1.0 \times 10^5$, a large flow separation can be identified starting from the rounded edge of the forebody in figure 3.6(a). The flow fully separates from the body's side thus generating a recirculation zone characterized by very small velocity magnitudes and a reverse flow. Although not investigated here since it is not the main purpose of the work, it would have been interesting to check whether reattachment occurs upstream of the blunt afterbody or not. As a consequence of the separation, we expect the wake behavior to be potentially affected. A similar flow topology was identified by Spohn & Gilliéron (2002) at low Reynolds numbers ($\mathrm{Re} \sim 10^3$) and is also reported for $\mathrm{Re} \simeq 4.5 \times 10^4$ by Grandemange (2013). Flow separation is still observable at $\mathrm{Re}_H \simeq 2.0 \times 10^5$ in figure 3.6(b) but reattachment occurs more rapidly leading to a shorter recirculation bubble. The wake properties are not expected to be modified anymore in this configuration. In addition, one can observe that, compared to the previous case, the low velocity area in front of the body is drastically reduced. For Reynolds numbers bigger than $\mathrm{Re}_H \simeq 3.0 \times 10^5$ (figure 3.6c, figure 3.2a,figure 3.6d), the flow is almost similar: the separation disappears and the streamlines become parallel to the body's side. Besides, the front low-velocity area is insensitive to the change of Reynolds number. All experiments of the following chapters are conducted in this flow configuration, *i.e.* the wake separation point is prescribed by the geometry of the afterbody only.

The shortening of the separation region near the front curved area is also reported by Barros (2015). However, it turns out that this region is also highly dependent on the front curvature as the same work reports a separation at similar Reynolds numbers as our work ($\mathrm{Re} \simeq 4.0 \times 10^4$) unlike figure 3.2($a$). In addition, similar separations are also reported by other authors during numerical investigations (Peres & Pasquetti, 2013; Pellerin *et al.*, 2016), but also experimentally at $\mathrm{Re} \simeq 1.3 \times 10^6$ in water tunnel visualizations (Beaudoin *et al.*, 2004; Franck *et al.*, 2009).

3.4 Discussion

The mean flow around the Ahmed body presented in this chapter shows that streamlines are mainly parallel to the body's surface. Owing to well-chosen front radii of curvature, flow separation is very limited and, when it occurs, leads to a reattachment well upstream the blunt afterbody for the studied Reynolds number based on the model's height of about $\mathrm{Re}_H \simeq 4.0 \times 10^5$. These flow characteristics ensure that no wake unsteadiness (Grandemange *et al.*, 2013b) originates directly from the front of the model, in particular from massive flow separation. The symmetries of the problem are respected so that, for the mean variables, the transformation $y^* \to -y^*$ does not modify the flow properties. We highlight in the last section 3.3.3 that the Reynolds number strongly affects the flow separation on the sides of the model, even for small variations; however, this case is not considered in this work since we impose $U_\infty = 20$ m.s^{-1} regardless of the experiment. This point shows that the forebody design has to be carefully checked for different operating conditions though in order to avoid large flow separations.

Unlike for the previous $y^* \to -y^*$ transformation, that implying $z^* \to -z^*$ cannot be done without consequences on the flow. The ground indeed corresponds to an infinite anti-symmetric plane in the inviscid flow theory and the model is kept in a too-close vicinity for its influence to be negligible. This absence of symmetry is clearly observable in the mean velocity fields (figure 3.2) specifically with the location of the stagnation point, which is not located at $z^* = 0$ corresponding to the body's mid-height but slightly lower. Even though the model's supports cannot be neglected, this shift cannot be ascribed to them since they are absent from the numerical simulations in which the same asymmetry can be observed (see § 6.3.1).

The small separation and quick reattachment on the upstream sections of the body – if such separation were to occur – lead to a parallel flow subject to a massive detachment past the body's blunt base with given separation points imposed by the geometry only. As a consequence, the results obtained in this manuscript can be compared not only to those obtained with other flat-backed Ahmed bodies (among which Ahmed *et al.* (1984); Evrard *et al.* (2016); Barros *et al.* (2017); Lucas *et al.* (2017)) but also to other generic geometries such as the SAE (Cogotti, 1998), the ASMO (Aljure *et al.*, 2014), the GTS (McArthur *et al.*, 2016) or the Windsor (Littlewood & Passmore, 2010; Littlewood *et al.*, 2011; Littlewood & Passmore, 2012; Passmore *et al.*, 2010; Perry *et al.*, 2016*a*,*b*; Pavia *et al.*, 2016, 2018; Pavia & Passmore, 2018) models as done throughout.

All the unsteadiness is then concentrated in the bluff body's wake which nonetheless statistically – in average for a long observation period – respects the problem's symmetry for the $y^* \to -y^*$ transformation. When the instability is present as in figure 3.4(b, d), there is an almost vertical symmetry despite the presence of the ground. At least, the strong asymmetry of the stable flow regime (figure 3.4a, see also § 4.3.1.2) is suppressed.

We finally focus on the mean wake properties. Its length – corresponding to the recirculation length – appears as one of the most interesting parameters to consider. We suspect that it is prescribed by the outer free-stream conditions, in particular the turbulence level and three-dimensional effects. As a matter of fact, the three-dimensional turbulent wake observed in this chapter is much shorter – considering the distance between the separation and the closure points – than that of a two-dimensional backward facing step at $\mathrm{Re} \simeq 7000$ investigated by Armaly *et al.* (1983); in the latter case, the ratio of the reattachment length to the step height was experimentally measured to be about 8. This hypothesis is corroborated by the longer wake observed at low Reynolds number (about 2 H) by Grandemange *et al.* (2012*a*).

The influence of the underbody flow is confirmed by the quite different topology obtained with respect to the wall-mounted cube of Krajnović & Davidson (2002)). However, it is comparable in length with the average wake of a bus-shaped body, *i.e.* with a base higher than wide (Krajnović & Davidson, 2003); despite the different base aspect ratios, the mean wakes are similar in topology. From the two planes, a toroidal wake structure can be inferred, similar to that shown for the body with a cavity in Evrard *et al.* (2016) and redrawn in Lucas *et al.* (2017).

The wake actually corresponds to an envelope of very small or even negative longitudinal velocities with flow moving upstream in the recirculation bubble. Four shears layers can consequently be seen as the limit between the wake and the surrounding mean flow, similarly as a separating line in the sense of Kirchhoff (1869); Brillouin (1910). Its role is rather to the vortex sheets in which the high fluctuations clearly delimit the wake and the – inviscid – free-stream flow. About this separating line, one may say that it clearly separates the region in which unsteadiness occurs, *i.e.* the wake, from the outer conditions which are much more steady. Kirchhoff (1869)'s theory on the Helmholtz separating seems particularly adapted to the present problem: the length of the recirculation zone is prescribed by the outer turbulence and the pressure inside the bubble is – at the first order and in average – almost homogeneously imposed by the streamlines' curvature, this allowing a complete decoupling between the wake and the outer flow. In the following chapters, the work is focused on the wake unsteadiness and the mean flow left apart.

3.5 Concluding remarks

The mean flow around the squareback Ahmed body is characterized experimentally at $\mathrm{Re}_H \simeq 4.0 \times 10^5$ thanks to PIV and base pressure measurements. We found that the flow remains attached around the whole body at the considered Reynolds number except when the massive separation near the blunt trailing edge occurs. Since the surrounding flow is observed to be steady, this ensures that all fluctuations studied in the following chapters originate from the wake and not from the flow history. Should the Reynolds number be lowered, then this statement does not hold anymore since detachment-reattachment along and on top of the body occur. To summarize in one sentence, we can say that the flow around this bluff body respects the overall symmetries of the problem; the question of its unsteadiness is considered in the following chapters.

CHAPTER 4

Unstable wake dynamics with body inclination and ground proximity

The global wake dynamics of a three-dimensional bluff body at $Re \simeq 4.0 \times 10^5$ *is investigated experimentally in this chapter. It is focused on the squareback Ahmed body which has a blunt rectangular trailing edge leading to a massive flow separation and thus the formation of a wake. Two different aspect ratios of the rectangular base are considered: wider than it is tall (minor axis perpendicular to the ground) in § 4.3.1 and taller than it is wide (major axis perpendicular to the ground) in § 4.3.2. Measurements of the spatial distribution of the pressure at the base of the body and velocity fields are used as topological indicators of the wake flow. Sensitivity analyses of the base pressure gradient expressed in polar form (modulus and phase) varying ground clearance (§§ 4.3.1.2 and 4.3.2.2), yaw (§§ 4.3.1.3 and 4.3.2.3) and pitch (§§ 4.3.1.4 and 4.3.2.4) are performed. Above a critical ground clearance and regardless of the body's inclination, the modulus is always large due to the static symmetry-breaking instability, but slightly smaller when directed along the minor axis of the base rather than along the major axis. The wake instability can be characterized through a unique wake mode, quantified by this modulus (strength of the asymmetry) and a phase (orientation) identified as the key ingredient of the global wake dynamics (§ 4.4.1). Additional measurements with a rear cavity (§ 4.3.1.7) allow to characterize the response of a* basic flow *without the instability. It is found that the phase dynamics of the unstable wake is constrained in such way by the inclination and the ground clearance that the component of the pressure gradient parallel to the minor axis of the rectangular base equals that of the* basic flow *while the other component related to the major axis fully reveals the instability and adjusts to preserve the large modulus (§§ 4.4.2,4.4.3). In most cases, the dynamics explore only two possible opposite values of the component along the major axis. Their respective probability depends on the geometrical environment of the wake: base shape, body inclination, ground proximity and body supports. Finally, a drag optimum is find during these bi-stable dynamics regardless of the body's alignment (§ 4.4.4). The main results of this chapter are published in Bonnavion & Cadot (2018).*

Contents

4.1 Literature review . . . **49**

4.2 Setup . . . **51**

4.3 Results . . . **54**

- 4.3.1 y-instability . . . 54
  - 4.3.1.1 Baseline of the squareback configuration . . . 54
  - 4.3.1.2 Wake sensitivity towards the ground clearance c^* . . . 55
  - 4.3.1.3 Wake sensitivity towards the yaw angle β in the unstable regime $c^* > c^*_S$ . . . 58
  - 4.3.1.4 Wake sensitivity towards the pitch angle α in the unstable regime $c^* > c^*_S$ . . . 59
  - 4.3.1.5 Resulting wake orientations for the squareback geometry 62
  - 4.3.1.6 Baseline with a rear cavity . . . 63
  - 4.3.1.7 Wake sensitivity to the body orientation with the rear cavity 64
  - 4.3.1.8 Resulting wake orientations with the rear cavity . . . 64
  - 4.3.1.9 Aerodynamic loading applied to the body varying its inclination and the ground proximity and contribution of the y-instability . . . 64
- 4.3.2 z-instability . . . 70
  - 4.3.2.1 Baseline case with $W_b^* = 0.940$ . . . 70
  - 4.3.2.2 Wake sensitivity towards the ground clearance c^* . . . 71
  - 4.3.2.3 Wake sensitivity towards the yaw angle β in the unstable wake regime $c^* > c^*_S$ . . . 73
  - 4.3.2.4 Wake sensitivity towards the pitch angle α in the unstable wake regime $c^* > c^*_S$ . . . 77
  - 4.3.2.5 Wake orientations resulting from the z-instability . . . 78
  - 4.3.2.6 Aerodynamic loading applied to the body varying its inclination and contribution of the z-instability . . . 79

4.4 Discussion . . . **82**

- 4.4.1 Role of the phase dynamics of the unstable wake . . . 82
- 4.4.2 Phase dynamics adaptation and consequences on cross-flow force . 84
- 4.4.3 A general model for the y- and the z-instabilities . . . 87
- 4.4.4 Identification of a drag optimum during wake bistability . . . 89

4.5 Concluding remarks . . . **90**

4.1 Literature review

In addition to the general literature review made on static symmetry-breaking modes of the turbulent wake of the Ahmed body conducted in § 1.3, we here focus on the specific problem of the body alignment in the turbulent regime. In their paper, Grandemange *et al.* (2013*a*) made a thorough study of the impact of the base aspect ratio and body's distance to a wall on the static wake asymmetries. The impact of the aspect ratio has already been intensively discussed and is not addressed here. However, the body's normal distance to a wall appears as a crucial parameter in the study. In this paper, the authors indeed show that a wake stabilization is operated by the ground as the clearance drops below about 8% of the body's height; a pitchfork bifurcation of the base pressure gradient computed along the longest base axis is reported in this work. The threshold appears lower for the z-instability than for the y though. For small clearances ($c/H < 0.06$), viscous effects prevent the development of the underbody flow yielding a similar behavior as that of a backward facing step (Herry *et al.*, 2011). As the body is raised ($0.06 \leq c/H \leq 0.12$), a jet emanating from the underbody causes the base pressure to drop and thus drag to increase before the instability arises through a pitchfork bifurcation. The dynamics then appears to be almost independent of the ground clearance, although Cadot *et al.* (2015*b*) showed later that a full saturation of the instability is not instantaneously reached as the clearance is increased. As a matter of facts, the influence of the ground can still be observed in the unstable regime, for instance through a vertical base pressure gradient. A full description of the wake bi-modal dynamics can be found for instance in Grandemange *et al.* (2013*b*) and Evrard *et al.* (2016) and will also be characterized in this chapter.

Although much less extensive than the studies of Grandemange *et al.*, a previous attempt to characterize the effect of the ground clearance of a bluff body on its wake was made by Garry (1996) for bodies of different aspect ratio (width-to-height ratio $W/H = 0.857$). The *model B* considered in the paper is somehow similar to the Ahmed body in terms of shape with a reversed aspect ratio. Only the mean base pressure is reported. At very small clearances ($c/H < 0.08$), the base pressure is almost insensitive to the ground distance except for $c/H \simeq 0.038$ that corresponds to the apparition of the jet emanating from the underbody.

Only a few sensitivity experiments towards the Ahmed body alignment are reported in the literature; none of them is performed in the stable regime. One might mention Grandemange *et al.* (2015) Volpe *et al.* (2015), Cadot *et al.* (2015*b*) or Brackston *et al.* (2016) that report a yaw misalignment of the body subject to the y-instability. It turns out that the effect of the yaw is to permanently select a wake orientation and thus to remove the bi-modal switching dynamics. Angles of very small magnitude are sufficient to provide such results. Similar findings are reported with different geometries such as a generic car Willy model (Gohlke *et al.*, 2007; Guilmineau *et al.*, 2013) and a Windsor body (Windsor, 2014; Howell, 2014, 2015; Perry *et al.*, 2016*b*; Pavia *et al.*, 2016; Gaylard *et al.*, 2017; Pavia *et al.*, 2018). In our opinion, the numerous studies conducted on the Windsor body (Passmore *et al.*, 2010; Littlewood & Passmore, 2010; Littlewood *et al.*, 2011; Littlewood & Passmore, 2012; Perry & Passmore, 2013; Windsor, 2014; Howell, 2014, 2015; Perry *et al.*, 2015, 2016*a*,*b*; Pavia *et al.*, 2016; Gaylard *et al.*, 2017; Pavia *et al.*, 2018) show that its wake dynamics is similar to that of the Ahmed body (Grandemange *et al.*, 2013*b*, 2014*b*; Volpe *et al.*, 2015; Li *et al.*, 2016; Evrard *et al.*, 2016; Brackston *et al.*, 2016; Barros *et al.*, 2017; Varon *et al.*, 2017; Brackston *et al.*, 2018), proving therefore the less importance of the forebody geometry. Besides, the similarity provides additional comparisons while doing experimental studies.

To our knowledge, there are no reported studies about the effect of a pitch angle for the Ahmed body subject to horizontal wake fluctuations. However, some experiments have been conducted on cylindrical bluff bodies of revolution by Mariotti & Buresti (2013) and later on by Gentile *et al.* (2017). A similar wake orientation lock-in as that observed in yawing conditions for the simplified vehicles is reported; the necessary angular deviation is found to be as small as 0.2°. Similar selection of the wake orientation can be performed using disturbances in the vicinity of the body in areas of high sensitivity (Parezanović & Cadot, 2012) following the initial idea of Parezanović & Cadot (2009). A few works have been conducted on simple geometries such as spheres (Vilaplana *et al.*, 2013) but, in the context of our study, the most interesting consider Ahmed bodies with small cylinders (Grandemange *et al.*, 2013*b*, 2014*b*) or small bodies (Barros *et al.*, 2017). The authors report a wide range of wake dynamics, from bistability to wake lock-in. In Barros *et al.* (2017), the wake rotates so that it can present a static vertical asymmetry. In the latter paper, as well as in Gentile *et al.* (2017) – for an axisymmetric bluff body –, this selection is modeled as a pitchfork bifurcation, with either the disturbance size or the misalignment angle as the bifurcation parameter.

Regarding flow control performed on this geometry, one may cite the experimental work of Evrard *et al.* (2016) in which, following preliminary ideas of Morel (1979) and Dutton & Addy (1998), a base cavity is used to reduce drag. The case was then reproduced numerically by Lucas *et al.* (2017). Drag reduction by 9% is reported thanks to a 15% base pressure increase and a removal of the static wake asymmetry leading to its symmetrization. The effect is generalized at various ground clearances – even in the stable flow regime – by Bonnavion *et al.* (2017*b*), highlighting the additional geometrical contribution of the cavity (Dutton & Addy, 1998). Nevertheless, no sensitivity analyses of this stabilized and symmetrized wake towards the body's inclination were found in the literature.

Concerning the sensitivities of the higher than wide body, the literature is also very incomplete. For a body higher than wide ($W/H = 0.741$[1]), we can mention the recent study by Schmidt *et al.* (2018) in which the authors report, for the second time after the initial results of Grandemange *et al.* (2013*a*), a top/bottom wake bi-stability – ascribed to a z-instability following the notations introduced in § 1.3 and in figure 1.4(c) on page 11. According to the authors, the characteristic time scale of the wake switching identified in Grandemange *et al.* (2013*b*) and extensively studied afterwards is retrieved. In a previous paper, van Raemdonck & van Tooren (2008) also report the wake asymmetry for a similar model but not the bi-modal dynamics. This vertical asymmetry of the wake is a general feature of this kind of bodies – as explained in § 1.3 from Marquet & Larsson (2014) – and is also reported for instance by Castelain *et al.* (2018) for the aspect ratio $W/H = 0.893$ or Cabitza (2014) for $W/H = 0.859$. In the latter work, the baseline configuration shows very brief wake reversals but the flow is strongly influenced by the holding support (Barros *et al.*, 2017); in addition, the wake appears unbalanced which then prevents from a true bi-modal dynamics. As concern cross-wind conditions (yaw angle), the numerical simulations of Mu (2011) show that the wake asymmetry is impacted by the misalignment and can switch from a vertical asymmetry in the baseline to an horizontal one in sideslip conditions. The effect of the body misalignment in pitching conditions has to our knowledge not been studied although, for real geometries presenting the same kind of base pressure distributions and wake dynamics, Cadot *et al.* (2016) and Bonnavion *et al.* (2017*a*) were able to identify a bi-stable dynamics by combining pitching and yawing conditions.

---

[1] The model is a GETS (General European Transport System) geometry (van Raemdonck & van Tooren, 2008) representing a simplified European long-haul heavy-duty vehicle. The height-to-width base aspect ratio, $H/W = 1.35$, is the inverse of the original Ahmed model (Ahmed, 1983; Ahmed *et al.*, 1984).

In their extensive study, Grandemange *et al.* (2013*a*) identified an *interfering region* in which rectangular blunt based bluff bodies are either subject to an horizontal wake asymmetry referred to as y-instability or a vertical one – z-instability. In their work with a body wider than high, Barros *et al.* (2017) explore the phenomenon of *symmetry exchange* and are able to select either one or the other of the hereabove mentioned instabilities. In particular, the presence of wheels seems to trigger a z-instability either for width-to-high aspect ratios as shown by the *configuration 2* of Kabanovs *et al.* (2017*a*) with $W/H = 1.302$ or by the Windsor body of Forbes *et al.* (2017) ($W/H = 1.346$) and Pavia & Passmore (2018) with $W/H = 1.346$. The influence of the wheels is also reported for an ASME body by Wang *et al.* (2018).

4.2 Setup

In this chapter, we consider two different flat-backed Ahmed bodies (Ahmed *et al.*, 1984). From a fundamental point of view, they correspond to three-dimensional bluff bodies with a blunt vertical after-body. Different schematic views are provided in figure 4.1. The front of both bodies is identical and the overall dimensions are given in table 2.4. Two distinct after-bodies characterized by two different aspect ratios of $W_b^* = W_b/H_b = 1.174$ for the square-back after-body and $W_b^* = W_b/H_b = 0.940$ for the boat-tailed after-body and depicted in figure 4.1(*d*) are considered in this chapter. The dimensions of the after-bodies are indicated in table 4.1. We chose the body's height − equal to the base's − $H_b = H = 0.298$ m as the scaling unit. The boat-tail shape is a circle arc tangential to the main body, characterized by two parameters, its length $\ell_B = 0.160$ m (*i.e.* $\ell_B^* = 0.537$) and the angle $\theta_S = 12.5°$. The main characteristic dimensions of the bodies considered in this chapter are given in table 2.4.

Table 4.1 – Dimensions of the after-bodies indicated in figure 4.1. The body's overall dimensions are given in table 2.4.

Dimension	Dimensional value	Dimensionless value based on H
Height of the base H_b:	0.298 m	1.000
Width of the base W_b:	0.350 m / 0.280 m	1.174 / 0.940
Length of the boat tail ℓ_B:	0.160 m	0.537
Angle of the boat tail θ_S:	12.5°	–

For the squareback afterbody ($W > H$), a cavity can be created at the base by pushing inward the body a rectangular sliding board whose dimensions are $(H_b^* - 0.067) \times (W_b^* - 0.067)$. The cavity depth considered here is $d^*_{\text{cav}} = d_{\text{cav}}/H_b = 0.285$ for the entire study. Further details regarding this cavity can be found in Evrard *et al.* (2016) in which the same model was used with different cylindrical supports and at a fixed ground clearance though. The cavity depth of $d^*_{\text{cav}} = 0.285$ was sufficient in Evrard *et al.* (2016); Lucas *et al.* (2017) to suppress the static wake instability of the squareback configuration (see § 4.3.1.1) and has therefore be chosen. The boat-tailed geometry ($H > W$) is not equipped with such device.

The ground clearance c, *i.e.* the normal distance from the body to the ground, and the pitch angle α of the models – indicated in figure 4.1(*a*) – are adjusted owing to the two translation stages mounted inside the body and described in § 2.4. The ground clearance c^* can thus be adjusted at the front within the range $c_f^* \in [0.050, 0.170]$ and independently at the rear, c_r^* within an identical range. The pitch angle α computed after equation (2.4), is varied in $\alpha \in [-1.5°, 1.5°]$. The yaw angle β of the model – indicated in figure 4.1(b) – is varied in $\beta \in [-2.0°, 2.0°]$ for the squareback afterbody and $\beta \in [-6.0°, 6.0°]$ for the boat-tailed one owing to the rotating table described in § 2.1.2. A summary of the geometric changes for the Ahmed bodies subject to the y- and the z-instabilities is provided in table 4.2.

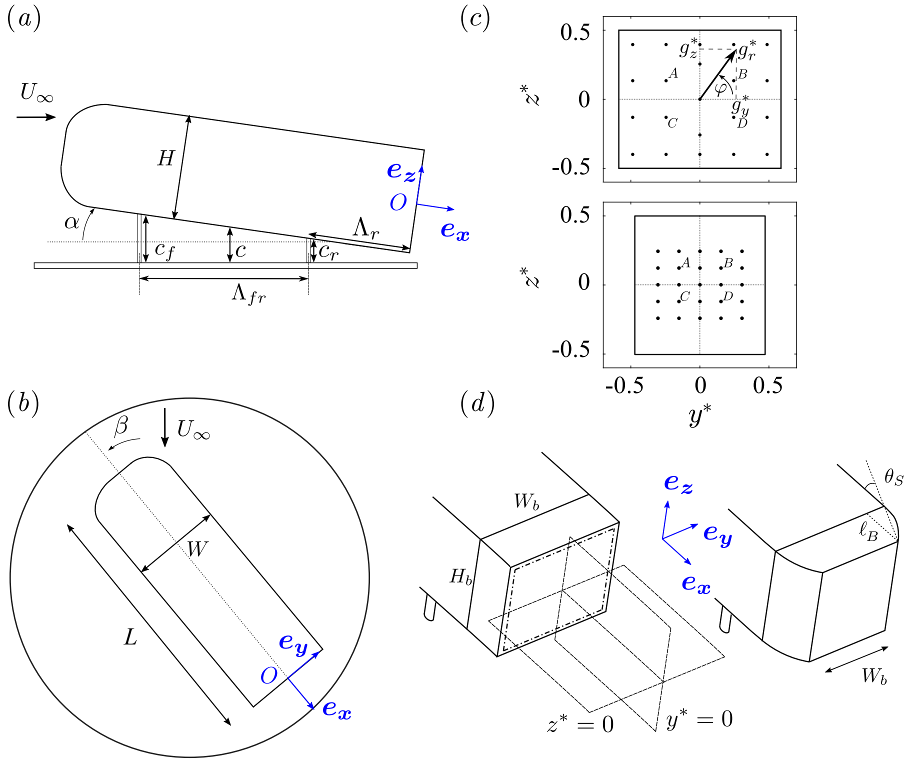

Figure 4.1 – Experimental apparatus: schematic side view (a), top view (b) of the main body and rear views (c) of the square-back (top) and boat-tailed (bottom) body bases. In (c), the bases of the models are equipped with pressure sensors (black dots); the four points A, B, C, D are used for calculation of the base pressure gradient $\hat{\boldsymbol{g}}^*$ (see text). Schematic view (d) of the square-back (left) and boat-tailed (right) after-bodies and representation of the fixed horizontal and vertical laser planes used for Particle Image Velocimetry. They correspond to $y^* = 0$ and $z^* = 0$ for the aligned body case. The rectangular board that creates the cavity of the square-back after-body (when pushed inwards the body) is shown by the dashed rectangle in (d).

Table 4.2 – Investigated ranges of ground clearance c, yaw angle β and pitch angle α for the Ahmed bodies subject to the y- and the z-instabilities and baseline configurations.

Parameter	$W^* = 1.174$ (y-instability)	$W^* = 0.940$ (z-instability)
Ground clearance c^*	$[0.050, 0.170]$	$[0.060, 0.200]$
Yaw angle β	$[-2.0°, 2.0°]$	$[-6.0°, 6.0°]$
Pitch angle α	$[-1.5°, 1.5°]$	$[-1.2°, 0°]$
Baseline	$c^* = 0.168,\ \alpha = \beta = 0°$	$c^* = 0.168,\ \alpha = \beta = 0°$

The experiments are carried out at the GIE-S2A in the model-scale wind-tunnel dedicated to automotive aerodynamics presented in § 2.1.2. The free-stream velocity, also used as a scaling unit, is set to $U_\infty = 20.0 \pm 0.1$ m.s^{-1} and the static temperature inside the vein is regulated at $T_\infty = 293.2 \pm 0.5$ K. Under those conditions, the corresponding Reynolds number is $\mathrm{Re} = U_\infty H/\nu \simeq 3.5 \times 10^5$, ν being the air kinematic viscosity.

For the squareback afterbody, unsteady pressure is measured at the $N = 21$ locations (y_i^*, z_i^*) indicated by the black dots at the base of the body in figure 4.1(c) owing to the ZOC22b pressure scanner presented in § 2.2.1 operated at the sampling frequency of 200 Hz while the aerodynamic loading is estimated by means of the pressure balance described in § 2.2.2 at the sampling frequency of 10 Hz. The pressure taps are the *Model pressure taps* presented in figure 2.3(b). The instantaneous pressure coefficient c_p, base suction coefficient c_b and the drag, side force and lift coefficients c_x, c_y, c_z are computed as detailed in equations (2.1), (2.2), and (2.3) respectively.

Out of the $N = 21$ pressure sensors, four marked A, B, C and D in figure 4.1(c) are used to compute the complex base pressure gradient $\hat{g}$ following the procedure described in § 2.7[1]. The Cartesian components of the gradient g_y^* and g_z^* derived from equations (2.5) and (2.6) then yield the complex gradient from equation (2.7), whose modulus g_r^* and phase φ are considered in the chapter. For the boat-tailed afterbody, the unsteady pressure measurements are operated at the $N = 25$ locations (y_i^*, z_i^*) indicated by the black dots at the base of the body in figure 4.1(c). The pressure scanner used for this geometry is the Scanivalve ZOC33 presented in § 2.2.1 operated at the sampling frequency of $f_e = 100$ Hz. Since the actual cut-off frequency is about 50 Hz and since an additional low-pass filtering is operated, the results are actually comparable to those of the squareback geometry obtained with the ZOC22b. The complex base pressure gradient $\hat{g}^*$ from equation (2.7) is computed from the data collected at the four sensors marked A, B, C and D in figure 4.1(c). The procedure is the same as in equations (2.5) and (2.6) with the updated sensors' locations.

The PIV system described in § 2.3.2 is used in the two orthogonal planes located at the base of the body and drawn in figure 4.1(d): a vertical one at mid-width ($y^* = 0$-plane) and an horizontal one at mid-base height ($z^* = 0$-plane). We recall that the corresponding physical sizes, expressed with H_b as the scaling unit, are $\Delta_y^* \times \Delta_z^* = 0.017 \times 0.017$ for the $z^* = 0$-plane or $\Delta_x^* \times \Delta_z^* = 0.017 \times 0.017$ for the $y^* = 0$-plane. The coordinate system used throughout the chapter is defined as follows. Its origin is set at the center of the base of the model. The $\boldsymbol{e}_x$ axis is chosen pointing downstream, $\boldsymbol{e}_y$ axis is pointing to the right of the body (viewed from behind or, in other words, looking upstream) and $\boldsymbol{e}_z$ is vertical as shown in figure 4.1. Actually, when either a pitch or a yaw angle is applied to the body, the local coordinate system $(\boldsymbol{e}_x, \boldsymbol{e}_y, \boldsymbol{e}_z)$ associated with the base in figure 4.1(d) will not coincide with the PIV (Particle Image Velocimetry) measurements fields anymore. Details about PIV measurements can be found in § 2.3.2. Since the considered angles are small (less than 2°), we decided for the sake of simplicity to keep the same name for the space coordinates of the velocity fields. Using conventional notations, the PIV gives access to the field $\boldsymbol{u}_{xz}^* = u^*\boldsymbol{e}_x + w^*\boldsymbol{e}_z$ in the $y^* = 0$ plane and to $\boldsymbol{u}_{xy}^* = u^*\boldsymbol{e}_x + v^*\boldsymbol{e}_y$ in the $z^* = 0$ plane.

---

[1] There is not a unique way to define these Cartesian components of the gradients. More important than their actual values is the fact that their sign accurately represents the wake orientation as this is the case in the present work.

4.3 Results

This section is divided into two main parts. The first one is focused on the squareback geometry with the aim to investigate the y-instability thanks to base pressure gradient's sensitivity analyses (§ 4.3.1). The second part of the results will consider the boat-tailed geometry in order to investigate sensitivity analyses of the z-instability (§ 4.3.2).

4.3.1 y-instability

Starting from the baseline investigated in § 4.3.1.1, we perform sensitivity analyses changing the ground clearance c, the yaw β and the pitch angle α of the model in §§ 4.3.1.2, 4.3.1.3, 4.3.1.4. The resulting wake orientations are given in § 4.3.1.5. The same analyses are then reproduced with the rear cavity, with a description of the baseline in § 4.3.1.6 and the analyses in § 4.3.1.7. The wake topology is given in § 4.3.1.8. Finally, the aerodynamic loading related to the instability is deduced from the wake measurements in § 4.3.1.9.

4.3.1.1 Baseline of the squareback configuration

We chose the baseline as the case where the body is aligned with the incoming flow, *i.e.* $\beta = 0°$ and $\alpha = 0°$ with a ground clearance $c^* = c/H_b = 0.168$. The ground clearance is higher than the critical one of Cadot *et al.* (2015*b*). As a consequence, in view of the base's aspect ratio, we expect the wake to be driven by a static y-instability as defined in Grandemange *et al.* (2013*a*). The main characteristics are expected to be an horizontal symmetry-breaking of the wake (Grandemange *et al.*, 2013*b*) with random switches between the two mirror wake states following a stochastic dynamics (Grandemange *et al.*, 2013*b*,*a*; Cadot *et al.*, 2015*b*; Volpe *et al.*, 2015; Rigas *et al.*, 2015; Evrard *et al.*, 2016; Brackston *et al.*, 2016).

The results are presented in figure 4.2. The mean base pressure distributions $C_p(y^*, z^*)$ given in figure 4.2($a-b$) are obtained using conditional averaging on g_y^*. All events with $g_y^* < 0$ correspond to state N (as Negative) of the wake and yield the mean distribution of figure 4.2(a) while those with $g_y^* > 0$ are associated with state P (as Positive) and correspond to figure 4.2(b). The denomination N and P was first introduced by Grandemange *et al.* (2013*b*) and used in other works such as Evrard *et al.* (2016). These two distributions are skew-symmetric one with respect to the other. The threshold on the horizontal pressure gradient at $g_y^* = 0$ comes naturally from the PDF given in figure 4.2(c) which presents two peaks at $g_y^* \simeq -0.2$ and $g_y^* \simeq 0.2$ (in blue). That of the vertical gradient g_z^* (in red) shows that its mean value is close to zero while negative values occurring with a low probability correspond to rotations of the wake while switching from one state to the other. From the space-time analysis provided in figure 4.2(d) at the base's mid-height ($z^* = 0$), the wake remains in one state for about $500 - 1000 \times t^*$ before a switch of a few t^* only occurs. Similar results were obtained in Evrard *et al.* (2016).

The characteristic mean and mean standard coefficients for the baseline configuration are given in the first row of table 4.3. The mean drag coefficient C_x lies within the range $0.25 \leq C_x \leq 0.35$ reported in the literature (Ahmed *et al.*, 1984; Barros *et al.*, 2014; Evrard *et al.*, 2016; Volpe *et al.*, 2015) and the base suction as well as the other forces are similar to that measured by Evrard *et al.* (2016) at $c^* = 0.111$ when the body was equipped with NACA-profiled supports. Unfortunately, side force and lift coefficients are rarely reported in other studies. The large magnitude of the side force fluctuation C_y' (compared to those of the other components) is associated with the y-instability (Grandemange *et al.*, 2013*b*;

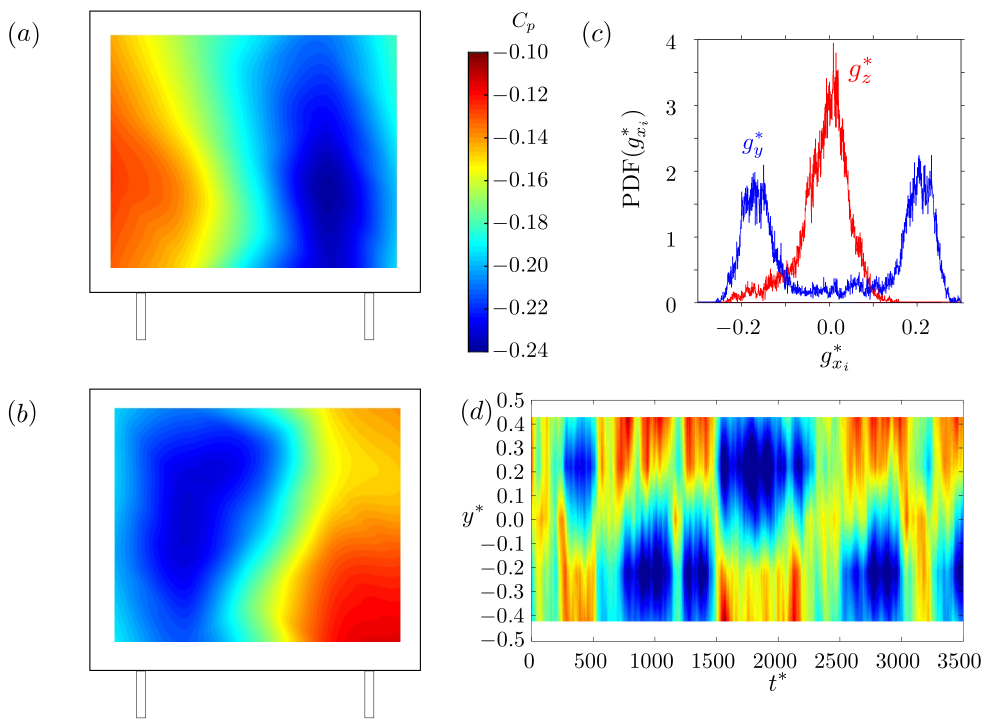

Figure 4.2 – Baseline configuration of the squareback Ahmed body ($\alpha = \beta = 0°$, $c^* = 0.168$). Conditionally averaged base pressure distributions $C_p(y^*, z^*)$ for state N of the wake (*a*) and for state P of the wake (*b*); (*c*) Probability Density Functions of the vertical base pressure gradient g^*_y (in blue) and of the horizontal base pressure gradient g^*_z (in red); (*d*) space-time diagram of $c_p(y^*, z^* = 0, t^*)$ along the line $z^* = 0$.

Evrard *et al.*, 2016). Comparing this baseline with the case investigated by Evrard *et al.* (2016), it can be concluded that the influence of the supports is negligible on the wake dynamics and on the aerodynamic properties.

Table 4.3 – Characteristic mean and fluctuation coefficients for baseline configurations defined as $c^* = 0.168$, $\alpha = 0°$, $\beta = 0°$ without ($d^*_{\text{cav}} = 0$) and with ($d^*_{\text{cav}} = 0.285$) the rear cavity for the squareback geometry ($W^*_b = 1.174$). The boat-tailed geometry ($W^*_b = 0.940$) investigated in § 4.3.2 is also given.

	W^*_b	C_b	C'_b	C_x	C'_x	C_y	C'_y	C_z	C'_z
$d^*_{\text{cav}} = 0$	1.174	0.183	0.006	0.287	0.004	−0.003	0.020	−0.118	0.005
$d^*_{\text{cav}} = 0.285$	1.174	0.137	0.006	0.259	0.004	−0.003	0.005	−0.122	0.004
$d^*_{\text{cav}} = 0$	0.940	0.124	0.002	0.279	0.002	−0.001	0.000	−0.158	0.002

It is interesting to notice that, if the baseline's results are in agreement with the experimental observations of Grandemange *et al.* (2013*a*), phase lock-in at $\varphi \simeq -\pi/2$ is not observed unlike in other works both experimentally (Barros *et al.*, 2014; Li *et al.*, 2016; Barros *et al.*, 2017) and numerically (Krajnović & Davidson, 2005*a*,*b*; Mirzaei *et al.*, 2015).

4.3.1.2 Wake sensitivity towards the ground clearance c^*

The sensitivity of the wake and of its dynamics with respect to the ground clearance c^* are investigated first. As a reminder, the ground clearance $c^* = c/H$ corresponds to the normal distance from the body to the ground. This experiment is conducted in no-yaw and no-pitch conditions ($\alpha = 0°, \beta = 0°$). A similar experiment was published by Grandemange *et al.* (2013*a*) for a width-to-height aspect ratio of $W^* = 1.351$. The response to the geometrical modifications is assessed through the statistics of the base

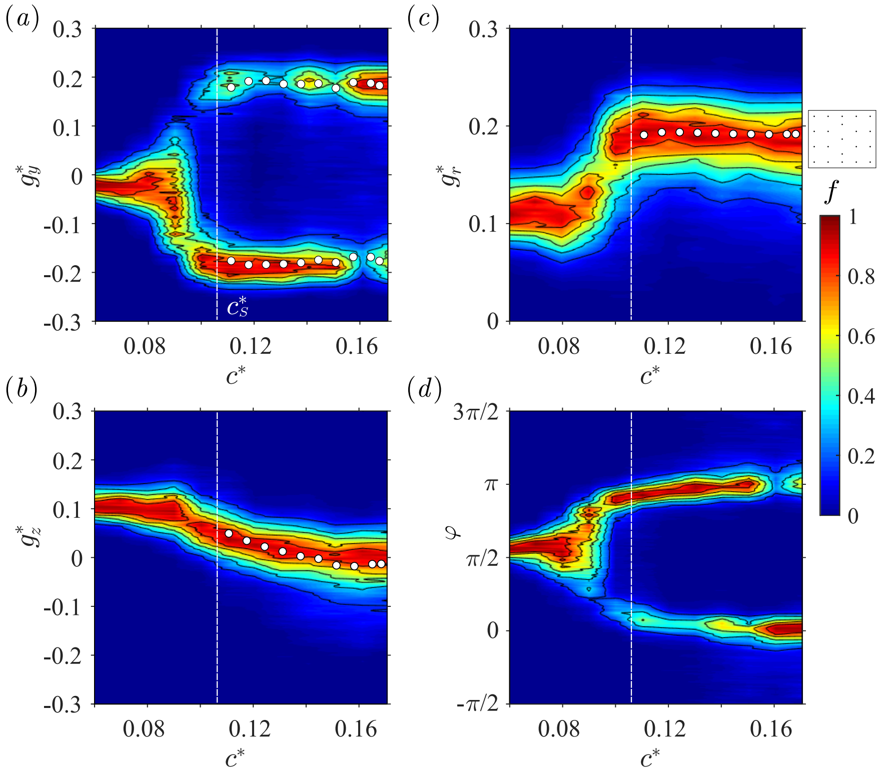

Figure 4.3 – Base pressure gradient response to a variation of the ground clearance c^*. Sensitivity maps (a) $f(c^*, g_y^*)$, (b) $f(c^*, g_z^*)$, (c) $f(c^*, g_r^*)$ and (d) $f(c^*, \varphi)$. The clearance $c_S^* \simeq 0.105$ is defined as the threshold from which the instability is saturated. White symbols are predictions using the model discussed in § 4.4.1.

pressure gradient $\hat{g}^*$ considering each of its components both in Cartesian (g_y^*, g_z^*) and in polar (g_r^*, φ) form by representing its probability density function f normalized by its most probable value. As a result, we obtain four two-dimensional sensitivity maps for each study, that in terms of the ground clearance c being given in figure 4.3.

When the body is gradually lifted-up in figure 4.3(a), the most probable branch for $g_y^* \sim 0$ observed for $c^* < 0.080$ bifurcates into two symmetrical branches resulting from a y-instability as fully described by Grandemange *et al.* (2013a); Cadot *et al.* (2015b). Reversely, this means that this instability is suppressed in the vicinity of the ground and replaced by a symmetric wake through a pitchfork bifurcation. To be more precise, it corresponds to a super-critical pitchfork bifurcation (Cadot *et al.*, 2015b), the symmetrical branch of which in the unstable regime being the target of most control strategies as its drag is expected to be lower (Evrard *et al.*, 2016). The bifurcation corresponds to a non-hysteretic phenomenon, *i.e.* the threshold is identical regardless whether the body is lifted up or pulled down. The vertical pressure gradient component g_z^* shown in figure 4.3(b) initially ranking around $g_z^* \sim 0.1$ in the floor vicinity, suddenly decreases during the transition $0.080 \lesssim c^* \lesssim 0.105$. Afterwards, a significant decrease towards zero can still be identified as the body is moved away from the ground. Independently of the sign of g_y^*, *i.e.* of the random switching dynamics, the permanent wake asymmetry introduced by the symmetry-breaking (SB) modes can be seen in the modulus g_r^* displayed in figure 4.3(c). The modulus saturates to a constant value when $c^* \simeq 0.105$ as shown in the figures, *i.e.* when the decrease of the horizontal component of the gradient g_z^* stops decreasing. It is consequently associated with the continuous change of the gradient orientation φ shown in figure 4.3(d): from initial locking at $\varphi = \pi/2$ at low ground clearances, two preferred orientations saturating towards $\varphi = 0$ and $\varphi = \pi$ are identified. The most important

result is that, in the unstable regime, the wall proximity affects the gradient orientation by producing a vertical gradient component but keeping the gradient modulus constant.
From this analysis, two main regions are clearly defined: the stable region corresponding to $c^* \lesssim 0.080$ and the fully saturated unstable region for $0.105 \lesssim c^*$ whose lower bound $c_S^* = 0.105$ can be defined as the critical ground clearance following the idea of Cadot *et al.* (2015*b*). The unstable region has already been characterized in the case of the baseline whose ground clearance of $c^* = 0.168 > c_S^*$ ensures the full saturation in § 4.3.1.1. The base pressure distribution and wake dynamics are similar to that of the baseline discussed in figure 4.2.

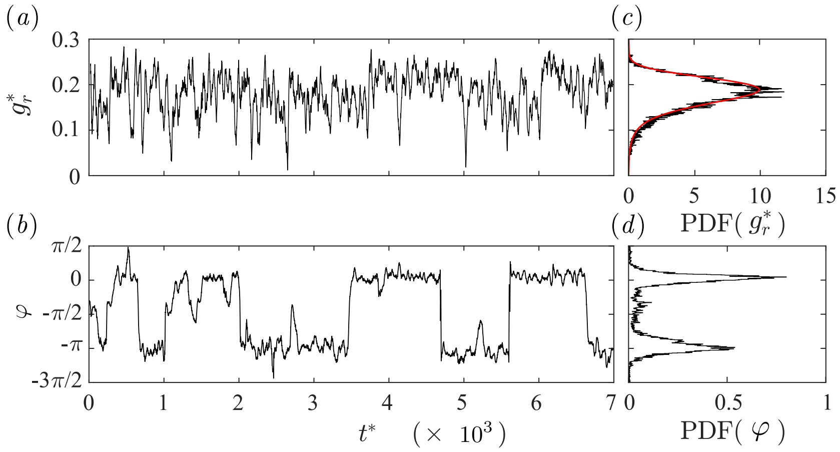

Figure 4.4 – Modulus $g_r^*(t^*)$ (a) and phase $\varphi(t^*)$ (b) time series of the base pressure gradient with corresponding probability density functions $(c-d)$ for the baseline. The smooth red line superimposed to PDF(g_r^*) is a best fit of Rigas *et al.* (2015)'s PDF model.

The dynamics can also be characterized owing to the polar form of the base pressure gradient in figure 4.4. The modulus fluctuates around its mean value following a high-frequency dynamics as shown in the time-series of figure 4.4(a). The fluctuations follow a stochastic dynamics as shown by the good agreement of the PDF (figure 4.4c) with the model of Rigas *et al.* (2015), a best fit of which is given by the smooth superimposed red line. The phase dynamics shown in figure 4.4(b) consists in two main characteristics: long-time duration of typically $t^* \sim 500 - 1000$ during which the phase is locked around $\varphi = 0$ or $\varphi = \pi$ and random π-jumps. This long-time bi-stable dynamics was fully described in Grandemange *et al.* (2013*b*) using a Cartesian description of the gradient. The two values of $\varphi = 0$ and $\varphi = \pi$ correspond to the two peaks of the PDF given in figure 4.4(d). The dynamics is not only made of phase jumps since the probability of the phase to reach $\varphi = -\pi/2$ is not null. This corresponds to a long-time evolution related to phase drift or wake rotation. Compared to the time-scale during which a wake state is selected, the dynamics of the reversals is very quick; this work is mainly focused on the low-frequency dynamics of the wake and the latter one will not be extensively discussed.
The stable case in the vicinity of the ground is presented in figure 4.5. The mean base pressure distribution $C_p(y^*, z^*)$ shown in figure 4.5(a) is nearly symmetric in the horizontal direction consistently with PDF of the horizontal pressure gradient g_y^* centered in $g_y^* \simeq 0$ (blue curve in figure 4.5b). A vertical pressure gradient is easily identifiable but its strength is about the half of that of the unstable case. This low pressure area at the bottom of the base is likely to be created by the recirculation of the underbody flow. This case is not investigated in details as the manuscript is focused on the static asymmetric wake states which are not present here.

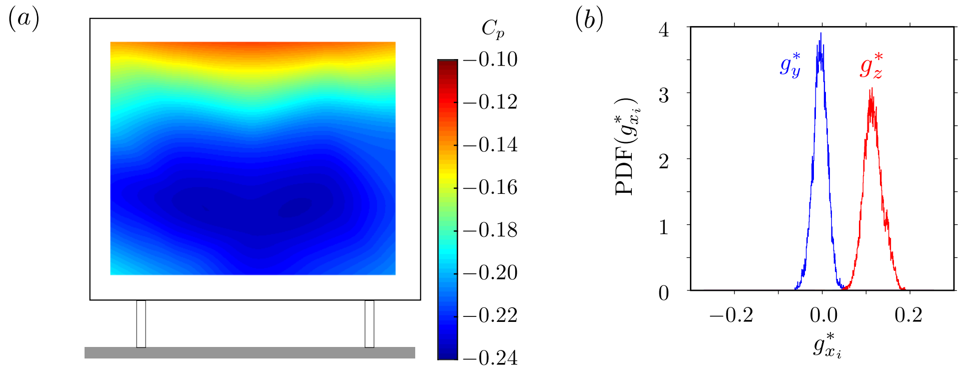

Figure 4.5 – Stable flow for the squareback Ahmed body ($\alpha = \beta = 0°$, $c^* = 0.060$). Mean base pressure distribution $C_p(y^*, z^*)$ (*a*) and (*b*) Probability Density Functions of the vertical base pressure gradient g_y^* (in blue) and of the horizontal base pressure gradient g_z^* (in red).

4.3.1.3 Wake sensitivity towards the yaw angle β in the unstable regime $c^* > c_S^*$

The sensitivity of the wake towards the yaw angle β in the unstable regime $c^* > c_S^*$ is considered in this section. The starting point is the baseline configuration (see § 4.3.1.1). Cross-wind conditions are simulated owing to the turntable described in § 2.1.2 and only small angles ($|\beta| \leq 2.0°$) are considered. The results are presented in figure 4.6. A similar analysis was already reported in several studies whose results are in agreement with the present ones (Volpe *et al.*, 2015; Cadot *et al.*, 2015*b*; Evrard *et al.*, 2016).

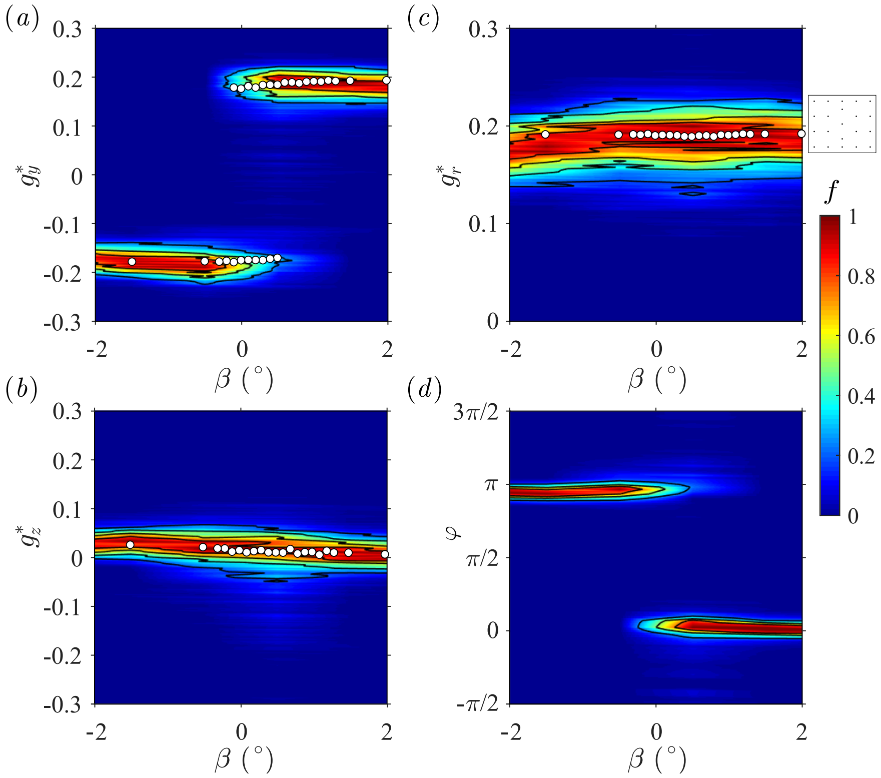

Figure 4.6 – Sensitivity maps (*a*) $f(\beta, g_y^*)$, (*b*) $f(\beta, g_z^*)$, (*c*) $f(\beta, g_r^*)$ and (*d*) $f(\beta, \varphi)$. White symbols are predictions using the model discussed in § 4.4.1.

There is a discontinuous transition between the two opposite branches of g_y^* in figure 4.6(*a*) resulting from a phase jump (figure 4.6*d*) between values close to 0 and π. The vertical component g_z^* (figure 4.6*b*) is nearly zero but presents a slight unexpected affine variation with the yaw angle β. This perturbation comes most likely from the imperfections and the asymmetries of the setup, among which one can cite wind inhomogeneity, non-zero roll angle and cable passage behind the rear right-hand side cylindrical support only. The transition between the two branches of g_y^* occurs with a fairly constant modulus g_r^* as shown in figure 4.6(c). Because of the constant modulus, the setup imperfection affects slightly the phase φ (figure 4.6d) which deviates from $\varphi_0 = 0$ or $\varphi_0 = \pi$. As a conclusion, the yaw does not modify the gradient modulus but drives the phase jumps statistics.

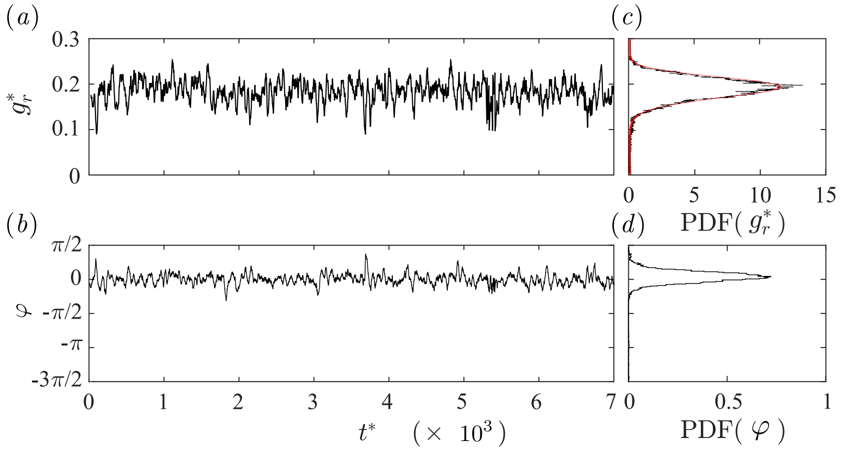

Figure 4.7 – Modulus $g_r^*(t^*)$ (a) and phase $\varphi(t^*)$ (b) time series of the base pressure gradient with corresponding probability density functions ($c - d$) for $\beta = 1.0°$. The smooth red line superimposed to PDF(g_r^*) is a best fit of Rigas *et al.* (2015)'s PDF model.

Time series of the modulus $g_r^*(t^*)$ and of the phase $\varphi(t^*)$ of the base pressure gradient are given with the corresponding probability density functions for $\beta = 1.0°$ and $\alpha = 0°$ in figure 4.7. The behavior of the modulus g_r^* (figure 4.7a) is very similar to that of the baseline described in figure 4.4(a) but the very small values associated with phase jumps which are absent in yawing conditions. The fluctuations follow the same stochastic dynamics as before; the agreement of the PDF (figure 4.7c) with the model of Rigas *et al.* (2015) is still excellent. The phase dynamics shown in figure 4.7(b) only presents high-frequency fluctuations associated with turbulence while the long-time dynamics identified in figure 4.4(b) has disappeared as a consequence of the wake state selection seen in figure 4.6(d). The associated PDF (figure 4.7d) is now single-peaked. Only state P of the wake related to $\varphi = 0$ is presented here. State N ($\varphi = \pi$) shows similar features except for the value of the phase.

As regards the mean base pressure distributions $C_p(y^*, z^*)$ obtained under yawing conditions, one can say that they are almost steady as no wake reversal occurs from the single-branch solution of figure 4.6. The modulus being independent of the yaw angle (figure 4.6c), the two possible mirror base pressure distributions are those observed alternately during wake bistability for the baseline and shown in figure 4.2($a - b$). Negative horizontal gradients related to state N correspond to figure 4.2(a) and positive gradient, *i.e.* state P of the wake, to figure 4.2(b).

4.3.1.4 ***Wake sensitivity towards the pitch angle α in the unstable regime $c^* > c_S^*$***

The sensitivity of the wake towards the pitch angle α in the unstable regime $c^* > c_S^*$ is considered in this section. The starting point is once again the baseline configuration (see § 4.3.1.1) and the yaw angle is set to $\beta = 0°$. The front and rear ground clearances are adjusted for a given pitch but keeping $\bar{c}^* = \frac{1}{2}(c_f^* + c_r^*) = 0.168$ in order to recover the baseline when $c_f^* = c_r^*$ by means of the translation stages described in §§ 3.2 and 4.2. Only small angles ($|\alpha| \leq 1.5°$) are considered. The results are presented in figure 4.8.

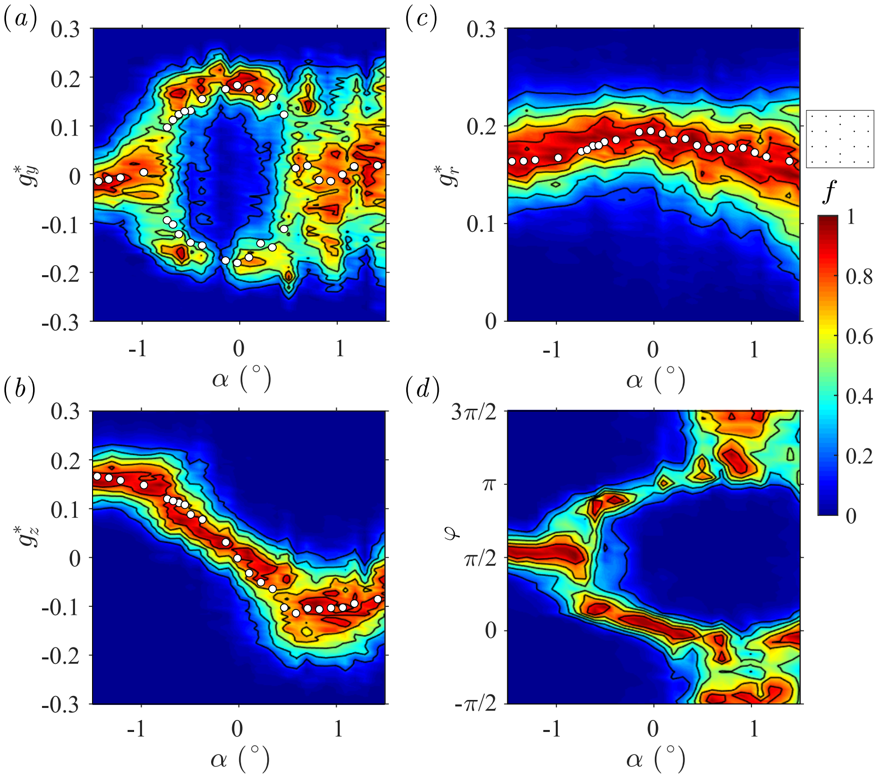

Figure 4.8 – Base pressure gradient response to variations of the pitch angle α. Sensitivity maps (*a*) $f(\alpha, g_y^*)$, (*b*) $f(\alpha, g_z^*)$, (*c*) $f(\alpha, g_r^*)$ and (*d*) $f(\alpha, \varphi)$. White symbols are predictions using the model discussed in § 4.4.1.

In figure 4.8(*a*) corresponding to the sensibility map of the horizontal gradient component g_y^*, three main regions can be identified. For large nose-down angles, *i.e.* $\alpha \lesssim -0.75°$, a single-branch solution around $g_y^* \simeq 0$ is identified. When the angle is reduced in magnitude, it bifurcates into two branches which appear to be symmetric with respect to the gradient orientation (same absolute value). This holds in the whole range $-0.75° \lesssim \alpha \lesssim 0.5°$. For larger nose-up angles, *i.e.* when $\alpha \gtrsim 0.5°$, the horizontal component varies almost uniformly in the range $|g_y^*| \lesssim 0.2$. The effect of the pitch angle variations on the vertical gradient component g_z^* is shown in figure 4.8(*b*) which displays an almost linear evolution with the pitch angle α in the range $-0.75° \lesssim \alpha \lesssim 0.5°$. Outside of this central range, there seems to be a saturation to extreme values. Despite the large discrepancies between these three regimes described hereabove, the modulus g_r^* (figure 4.8*c*) shows a smooth evolution with the pitch angle α. It is almost symmetric evolution, with a maximum reached around $\alpha \simeq -0.25°$. The phase φ shown in figure 4.8(*d*) has a very similar behavior to that of the horizontal gradient g_y^* (figure 4.8*a*). The single branch at $\varphi = \pi/2$ for $\alpha \lesssim -0.75°$ bifurcates into two branches in the range $-0.75° \lesssim \alpha \lesssim 0.5°$. Nevertheless, unlike the horizontal gradient, these branches are not constant but almost linear functions of the pitch angle α due to the constraint created by the vertical gradient g_z^* (see figure 4.8*b*). In the unlocked regime ($\alpha \gtrsim 0.5°$), the phase explores the $[-\pi, 0]$ interval almost uniformly, unlike to nose-down cases. This different behavior is attributed to the wall proximity at the trailing edge which has a major effect on the underbody flow in nose-up configurations. This means that without the wall influence, *i.e.* far enough from the wall, the nose-up configuration should be the anti-symmetric of the nose-down configuration unlike what is observed here. There is indeed no phase lock-in at $\varphi = -\pi/2$ for $\alpha \gtrsim 0.5°$ but a global unlocking in the $[-\pi, 0]$ interval. In fact, despite the imposed averaged ground clearance $c^* = \frac{1}{2}(c_f^* + c_r^*) = 0.168$, the rear part of the body is much closer to the ground. Most importantly, a similar conclusion as for the ground clearance and the yaw experiments can be drawn. The small pitch angle variation produces a component g_z^* of the vertical pressure gradient but keeping the modulus g_r^* slightly modulated, maximum for horizontal alignment and minimum for vertical alignment.

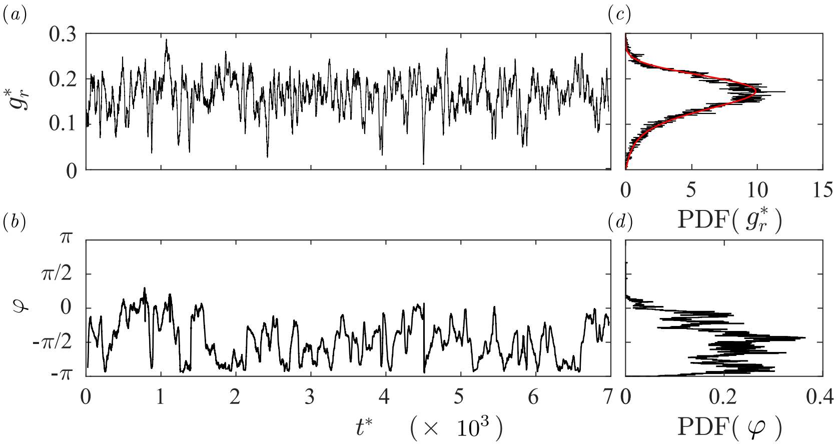

Figure 4.9 – Modulus $g_r^*(t^*)$ (*a*) and phase $\varphi(t^*)$ (*b*) time series of the base pressure gradient with corresponding probability density functions ($c - d$) for the unlocked case $\alpha = +1.0°$. The smooth red lines superimposed to PDF(g_r^*) is a best fit of Rigas *et al.* (2015)'s PDF model.

While the locked case is very similar to that obtained with a yaw angle (figure 4.7) except for the phase value ($\varphi \simeq \pi/2$ in this case), the unlocked case (corresponding to nose-up configurations) shown in figure 4.9 is quite different. There is no phase lock-in but large phase fluctuations associated with random wake rotations in the range $[-\pi, 0]$ with some phase jumps as the one observed at $t^* = 4.5 \times 10^3$ in figure 4.9(*c*). Some similarities with the diffusive dynamics of the turbulent axisymmetric wake presented in Rigas *et al.* (2014, 2015) can be identified. However, the main (and important) difference is that the random walk of the phase is bounded for the Ahmed body.

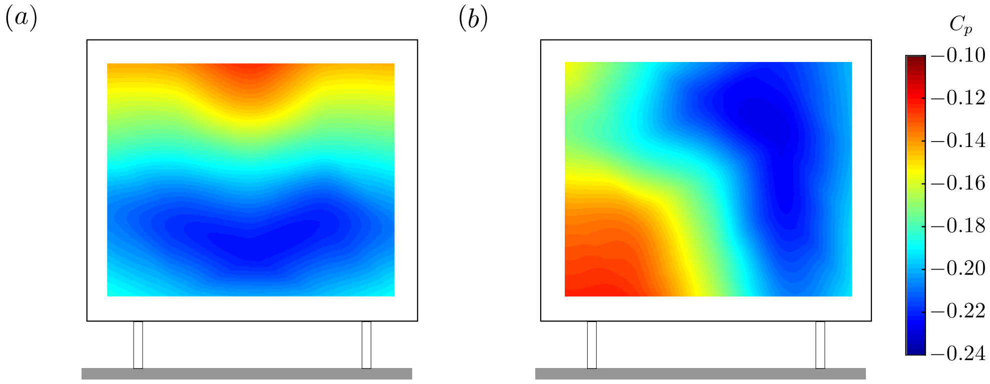

Figure 4.10 – Base pressure distributions $c_p(y^*, z^*)$ under pitching conditions. (*a*) Mean distribution associated with lock-in at $\varphi = \pi/2$, (*b*) instantaneous distribution observed during wake un-locking.

Similarly to the three regions of the horizontal base pressure gradient highlighted in figure 4.8(*a*), typical base pressure distributions can be identified. In the bi-stable region ($-0.75° \lesssim \alpha \lesssim 0.5°$), the alternately explored base pressure distributions $C_p(y^*, z^*)$ are

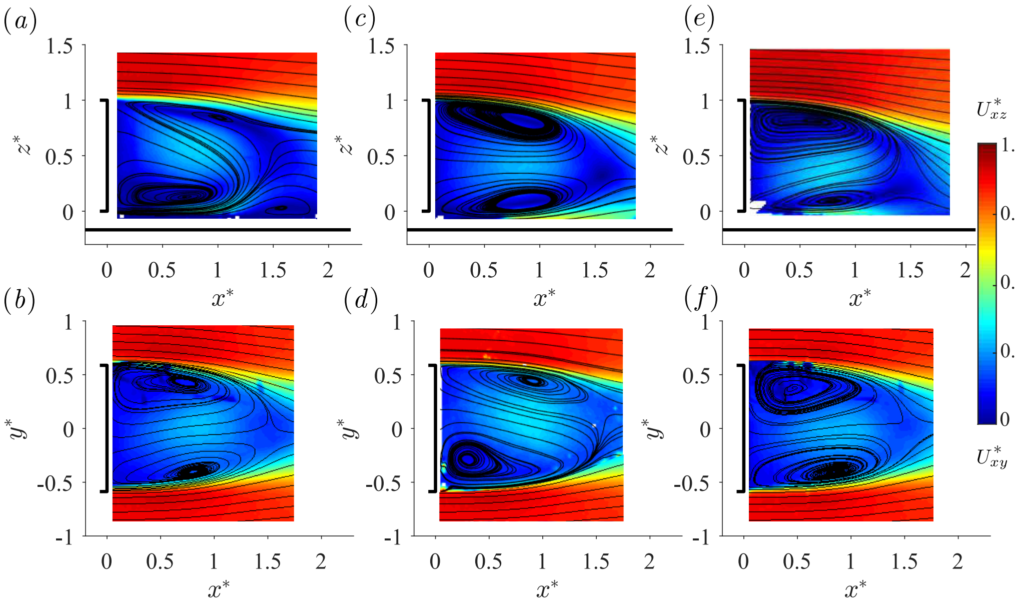

Figure 4.11 – Cross-sections of the mean velocity field visualized using streamlines superimposed to the modulus of the components in the vertical plane (x^*, z^*) (top row) and horizontal plane (x^*, y^*) (bottom row) for (a, b) nose-down $\alpha = -1°$, (c, d) baseline $\alpha = 0°$ (P state, see text) and (e, f) nose-up $\alpha = +1°$.

similar of those of the baseline (figure 4.2a, b). As the vertical base pressure gradient g^*_z increases (in magnitude) and the phase deviates from $\varphi = 0$ or $\varphi = \pi$ (figure 4.8b, d), the high pressure area simply moves towards the top or the bottom of the base but the general features remain identical. However, as lock-in around $\varphi \simeq \pi/2$ occurs, the wake undergoes a rotation by a quarter of revolution and the pressure stratification is now oriented upwards, with a maximum pressure at the top of the base. The associated distribution is given in figure 4.10(a). As to nose-up configurations for which phase unlocking occurs ($\alpha \geq 0.5°$), the mean distribution would not be meaningful. As a consequence, we show an instantaneous map in figure 4.10(b). The spatial distribution persist but it rotated as the phase explores the interval $\varphi \in [-\pi, 0]$.

4.3.1.5 Resulting wake orientations for the squareback geometry

The mean flows of the wake measured in the two perpendicular planes confirm the four different wake orientations discussed in the previous sections according to the base pressure gradient alignments. For the baseline case, the mean flow has been conditioned by $-\frac{\pi}{2} < \varphi_{0°} < \frac{\pi}{2}$ in order to capture the P state only ($i.e.$ phase lock-in $\varphi_{0°}(t*) \simeq 0$) in figures 4.11($c, d$). The N state ($i.e.$ phase lock-in $\varphi_{0°}(t*) \simeq \pi$) is not shown. It corresponds to the mirror state of the P one and can be deduced by the transformation $(y^*, z^*) \rightarrow (-y^*, z^*)$. These states are fully described in Grandemange *et al.* (2013b) and we use the same terminology in this work. We can see in figure 4.11 that the strong wake asymmetry is successively detected in the $y^* = 0$ plane in figure 4.11(a), in the $z^* = 0$ plane in figure 4.11(d) and in the $y^* = 0$ plane in figure 4.11(e) while the wake in the other perpendicular plane is always more symmetric. They respectively correspond to the phase lock-in $\varphi_{-1°} \simeq \pi/2$ (figure 4.11a, b), $\varphi_{0°} \simeq 0$ (state P in figure 4.11c, d) or equivalently $\varphi_{0°} \simeq \pi$ (state N, not shown) and finally to the mean orientation (with $-\pi < \varphi_{1°}(t^*) < 0$) towards a negative vertical pressure gradient (figure 4.11e, f).

As a summary of the wake sensitivity to the body orientation in the saturated regime of the instability, it is found that independently to the phase dynamics, the modulus of the base pressure gradient depends upon the vector orientation, maximum for an horizontal alignment with ${g^*_{r0}}^y \simeq 0.187$ and minimum for a vertical alignment with ${g^*_{r0}}^z \simeq 0.159$. Ground clearance, yaw and pitch variations produce a vertical component g^*_z of the pressure gradient that constrains the phase dynamics because of the modulus properties. Different phase dynamics scenarios have been identified: phase lock-ins, phase jumps and bounded drifts. As depicted in the mean PIV fields, the phase of the base pressure gradient is confirmed to be an accurate indicator of the global wake orientation.

4.3.1.6 Baseline with a rear cavity

The same experiments are reproduced with the base cavity described in § 4.2 and shown in figure 4.1(d). Its depth is chosen as $d^*_{\text{cav}} = 0.285$. With respect to the squareback case, the instability is removed (Evrard *et al.*, 2016; Lucas *et al.*, 2017). The base pressure distribution (figure 4.12a) is now almost uniform and, more importantly, almost steady. The two Cartesian base pressure gradients g^*_y and g^*_z are almost null and their PDFs are narrow (figure 4.12b) because of the very small fluctuations. A space-time diagram is reproduced in figure 4.12(c) and shows that no instantaneous wake asymmetry can be identified. These results are in total agreement with those of Evrard *et al.* (2016); Lucas *et al.* (2017).

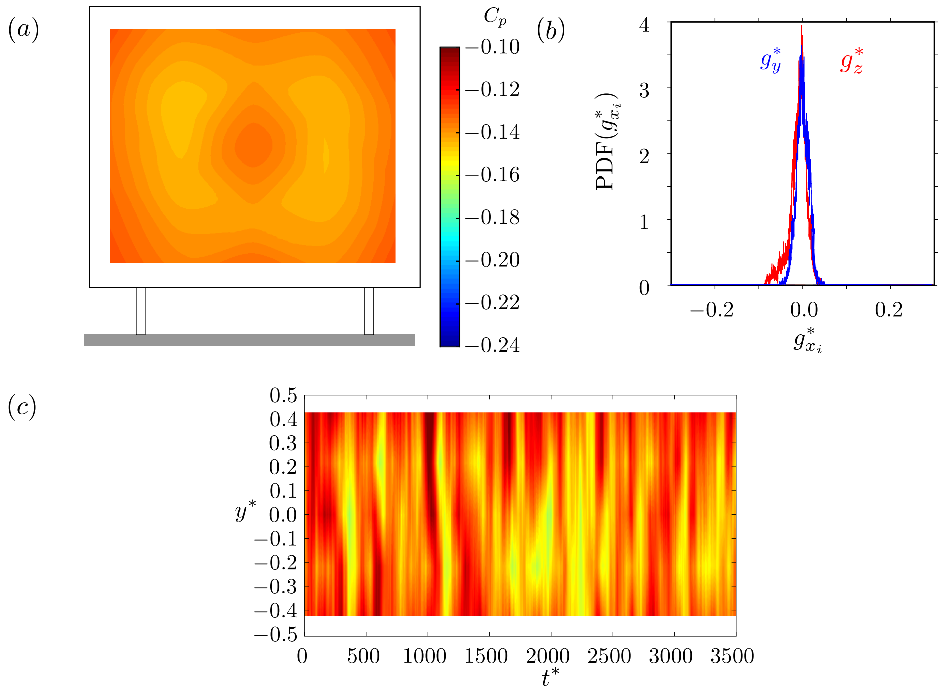

Figure 4.12 – Baseline configuration of the squareback Ahmed body ($\alpha = \beta = 0°$, $c^* = 0.168$) with the base cavity ($d^*_{\text{cav}} = 0.285$): mean base pressure distribution $C_p(y^*, z^*)$ (a), Probability Density Functions of the vertical base pressure gradient g^*_y in blue and of the horizontal base pressure gradient g^*_z in red (b) and space-time diagram of $c_p(y^*, z^* = 0, t^*)$ along the line $z^* = 0$ (c).

The mean and standard coefficients of the baseline with the cavity are given in table 4.3. All standard coefficients C'_i are of the order of 10^{-3} in agreement with the suppression of the wake fluctuations while the mean base suction C_b and drag C_x are reduced by 25.1% and 9.6% with respect to the baseline without the cavity. Drag reduction is discussed later in appendix B.

4.3.1.7 Wake sensitivity to the body orientation with the rear cavity

The three sensibility analyses of figures 4.3, 4.6, 4.8 are reproduced in this section with the base cavity. The results are presented together in Cartesian coordinates (figure 4.13) and then in the polar form (figure 4.14). For the baseline configuration with the rear cavity, both Cartesian components of the base gradient are ranking about zero as already highlighted in figure 4.12.

The bifurcation operated by the ground clearance around $c^* \simeq 0.08$ (figure 4.3) has been completely suppressed in agreement with the flow stabilization observed by Evrard *et al.* (2016); Lucas *et al.* (2017) and the Cartesian base pressure gradients are now fluctuating around zero regardless of the ground clearance (figure 4.13a, b) resulting in a very small modulus g_r^* (figure 4.14a) and a poorly defined phase φ (figure 4.14b). The phase dynamics observed in the squareback case is now replaced by trivial permanent lock-in except when the phase is poorly defined for small moduli. The loss of phase dynamics is the consequence of the suppression of the wake instability. From figures 4.13(c, d, e, f), a slight change of the body inclination, *i.e.* of the yaw angle β or of the pitch angle α shifts almost linearly the horizontal component g_y^* for the yaw or the vertical component g_z^* for the pitch. Meanwhile, the other component g_z^* (respectively g_y^*) remains constant. The modulus (figure 4.14a, c, e) is reduced by more than a factor of two with respect to the squareback case. Nonetheless, it is now a function of the yaw and pitch angles and reaches a minimum around the baseline when the horizontal (respectively vertical) base pressure gradient changes sign.

4.3.1.8 Resulting wake orientations with the rear cavity

The three mean wake configurations with the cavity are displayed in figure 4.15. They should be compared to the same planes in the squareback case (figure 4.11). The mean wake observed for the nose-down configuration at $\alpha = -1°$ in figure 4.11(a, b) is similar to that of the figure 4.15(a, b) with the cavity. The main difference is that the separation from the floor is prevented in the latter case. In addition, the wake reflectional symmetry is better. For the baseline configuration (figure 4.15c, d) the wake is fully symmetrized as in Evrard *et al.* (2016); Lucas *et al.* (2017). The wake for the nose-up configuration at $\alpha = +1°$ in figure 4.15(e, f) is also similar to that without the cavity (figure 4.15e, f). The pitch angle α applied to the body hence orientates the wake in a similar manner regardless of the afterbody geometry.

4.3.1.9 Aerodynamic loading applied to the body varying its inclination and the ground proximity and contribution of the y-instability

The aerodynamic loading applied on the body is compared in the stable and unstable wake regimes for the squareback case and the body with the cavity through the ground clearance sensitivity analysis. The mean base suction in figure 4.16(a) and the mean drag in figure 4.16(b) follow the same evolution and decrease when the instability arises around $c^* \sim 0.08$. Afterwards, the base suction is almost independent of the ground clearance while the drag linearly increases as the body is gradually raised because of the increasing cylindrical supports frontal surface. The mean side force C_y presented in figure 4.16(c) is almost zero but, because statistical convergence is very hard (if not impossible) to reach because of the long-time dynamics of the wake reversals (see figure 4.2b). The magnitude of the lift C_z given in figure 4.16(d) increases with the instability and is then independent of the ground clearance. The lift is negative for this model. It must be emphasized that,

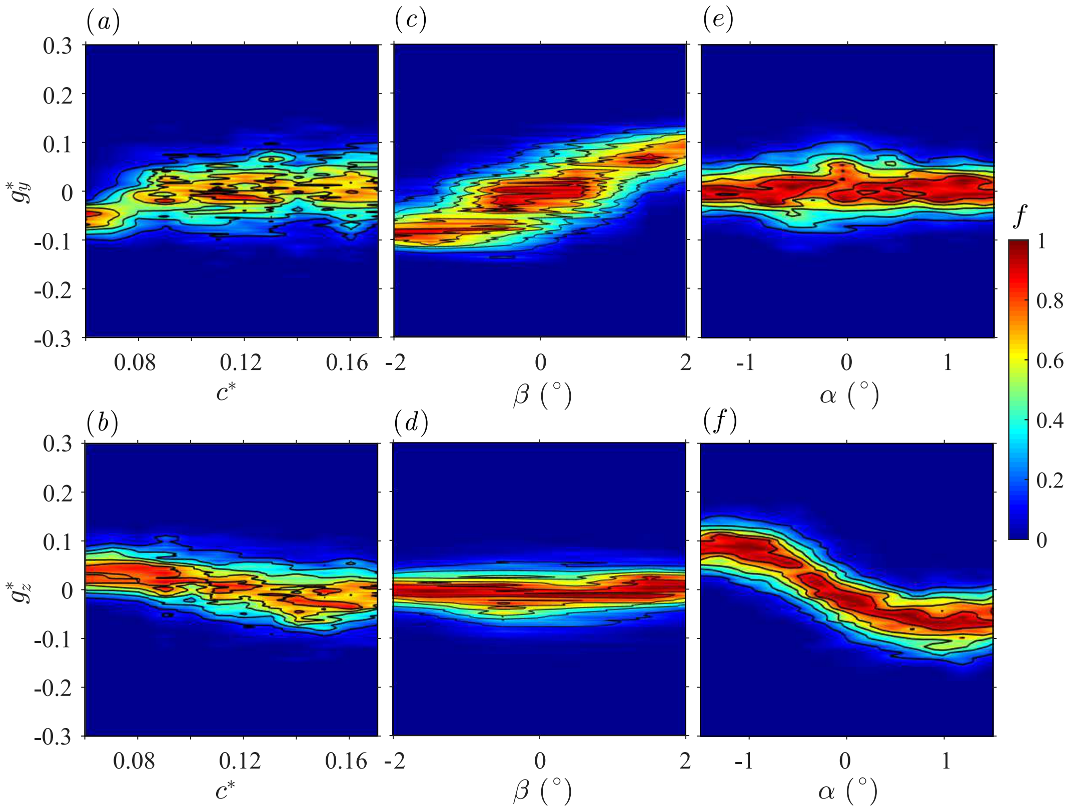

Figure 4.13 – Rear cavity $d^* = 0.285$. Base pressure gradient response to ground clearance c^* (a, b), yaw β (c, d) and pitch angle α (e, f). Sensitivity maps of the horizontal component g_y^* (a, c, e) and vertical component g_z^* (b, d, f).

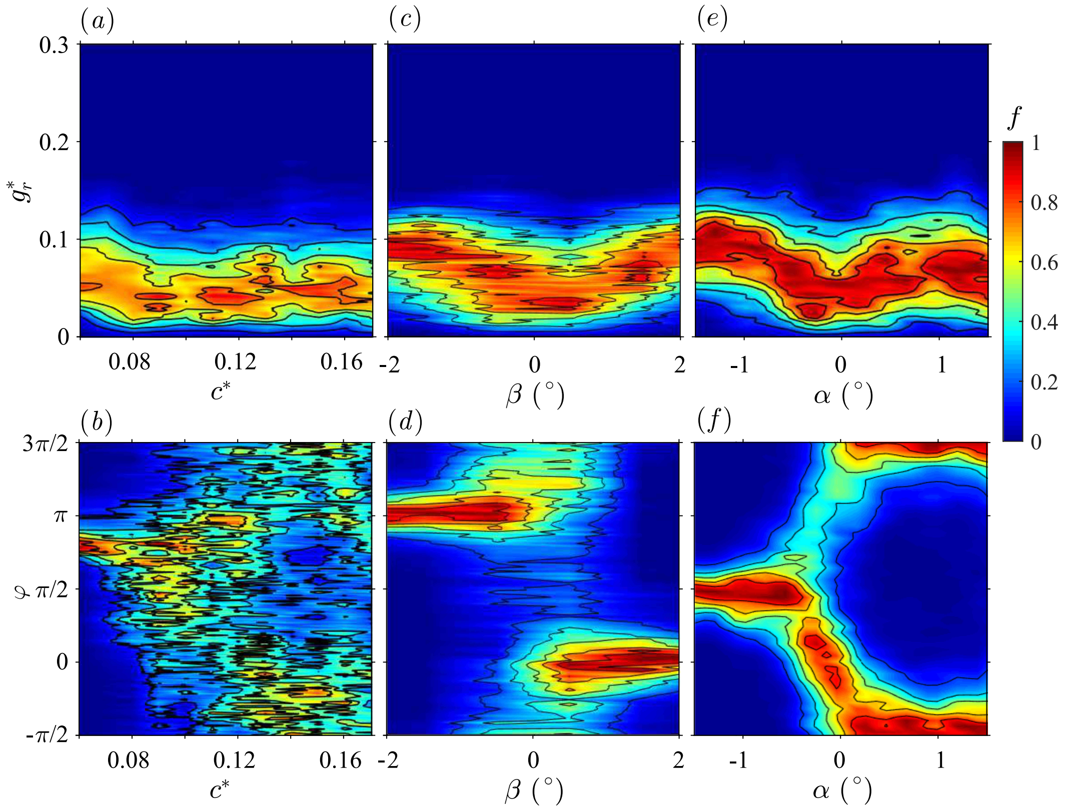

Figure 4.14 – Rear cavity $d^* = 0.285$. Base pressure gradient response to ground clearance (a, b) $f(c^*, \hat{g}^*)$, yaw (c, d) $f(\beta, \hat{g}^*)$ and pitch angle (e, f) $f(\alpha, \hat{g}^*)$. Sensitivity maps of the gradient modulus g_r^* (a, c, e) and phase φ (b, d, f).

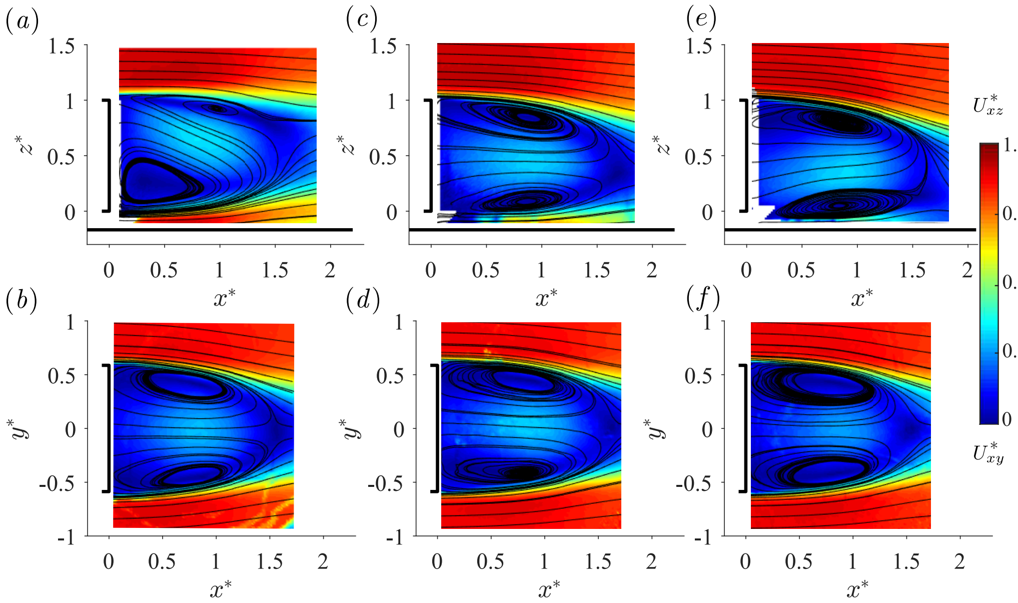

Figure 4.15 – Cross-sections of the mean velocity field visualized using streamlines superimposed to the modulus of the components in the vertical plane (x^*, z^*) (top row) and horizontal plane (x^*, y^*) (bottom row) for (a, b) nose-down $\alpha = -1°$, (c, d) baseline $\alpha = 0°$ and (e, f) nose-up $\alpha = +1°$ with the rear cavity $(d^* = 0.285)$.

based on these analyses (figure 4.16$a-d$), the contribution of the instability to the loading cannot be identified as the behaviors with and without the cavity are the same except for the base suction and the drag as discussed in appendix B. Similarly, we present the fluctuations in figure 4.16($e-h$). It is clear that the instability triggers lateral fluctuations of the wake as the side force fluctuations C'_y burst by one order of magnitude while all three other coefficients remain unchanged. The same trends for the mean drag C_x and the mean lift coefficient C_z are reported for a fixed ground experiment with a rectangular prism model by Fago *et al.* (1991).

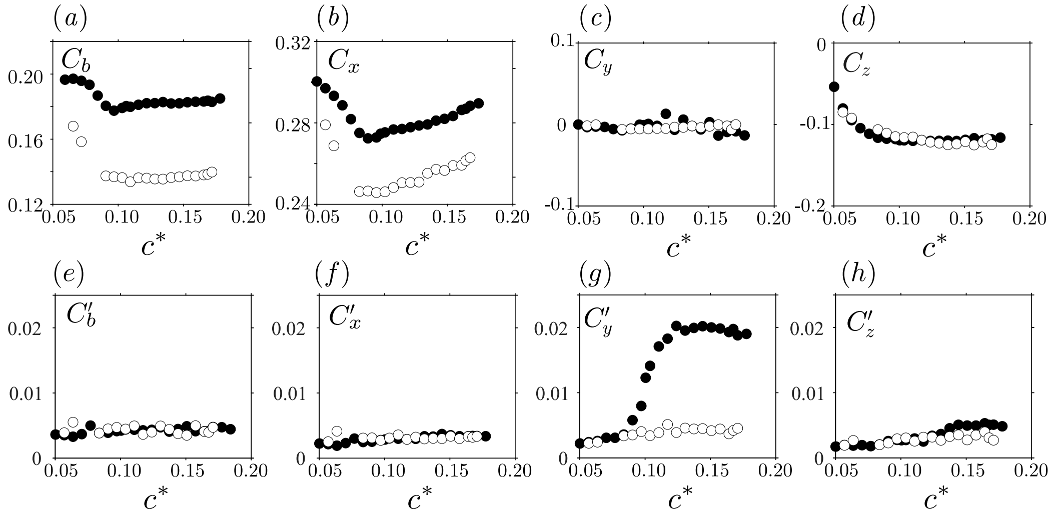

Figure 4.16 – Aerodynamic loading applied on the body in the ground clearance sensitivity analysis: mean (top row) and fluctuating (bottom row) base suction (a, e), drag force (b, f), side force (c, g) and lift coefficients (d, h) vs. ground clearance without (black filled circles) and with (empty circles) the rear cavity.

The aerodynamic loading applied on the body in the unstable wake regime is now compared for the squareback case and the body with the cavity for the yaw and the pitch sensitivity experiments in order to estimate the contribution of the y-instability to the resulting loading in such configurations. The four mean coefficients are plotted against the yaw angle β and the pitch angle α in figure 4.17($a-d$). The mean base suction in figure 4.17(a) and the drag in figure 4.17(b) are commented together as they present the same evolution. As expected, the drag is minimal when the body is aligned with the flow (or equivalently said in the bi-stable configuration) and its increase is symmetric with respect to the yaw angle. A similar behavior can be observed for the pitch experiment (figure 4.17c, d). Comparing the two sets of experiments with and without the cavity, the stabilization of the wake operated by the cavity is really hard to identify on the mean values of the base suction C_b and of the drag C_x as the behaviors are very similar for both the yaw and the pitch experiments (figure 4.17$a-d$) in spite of very different mean levels (see appendix B).

The y- and z-components of the mean force coefficients obtained for the yaw and pitch sensitivity experiments are shown in figure 4.18($a-d$) with and without the rear cavity (filled and empty circles respectively). A clear stabilization of the unstable wake can be seen in the mean horizontal y-component in figure 4.18(a) obtained with the yaw variations. For the body subject to the y-instability, the evolution can be described as two linear parts for $|\beta| \geq 1.5°$ with a non-linear shift for small values of the yaw angle corresponding to the imprint of the instability. On the contrary, with the cavity, *i.e.* for the stable flow, $C_y(\beta)$ becomes a truly linear function of the yaw angle without any shift around $\beta \pm 0.5°$. As a result, the mean side force coefficient C_y^B obtained for the *basic flow* without the instability changes linearly with β as for the cavity experiment for which the instability is removed (Evrard *et al.*, 2016; Lucas *et al.*, 2017). We recall that the superscript ^{B} refers to the *basic flow* without the instability throughout. A model is proposed below. For the other mean coefficients, we can hardly distinguish any effect induced by the rear cavity. The force coefficient fluctuations shown in figure 4.18($e-h$), fluctuations crisis, *i.e.* strong increase of the fluctuations, are associated with phase unlocking and fluctuations are drastically reduced otherwise.

The mean side force coefficient C_y^B for the *basic flow* without the instability introduced in the previous paragraph is believed to be a linear function of the yaw angle β. One can indeed derive the following equation from a linear fit of the cavity experiment:

$$C_y^B = -0.055 \times \beta \tag{4.1}$$

where β is expressed in degrees. Equation (4.1) is displayed as the red solid line in figure 4.19(a). Because the instability creates an asymmetry of the wake and because this asymmetry is identified with the base pressure gradient (or more precisely in this case with its horizontal component g_y^*), we compare the strength of the instability $C_y - C_y^B$ to the mean horizontal base pressure gradient G_y^* in figure 4.19(b). The two curves turn out to be proportional such that the mean side force coefficient can be directly related to the mean base gradient as:

$$C_y(\beta) = C_y^B(\beta) - \frac{G_y^*(\beta)}{10} \tag{4.2}$$

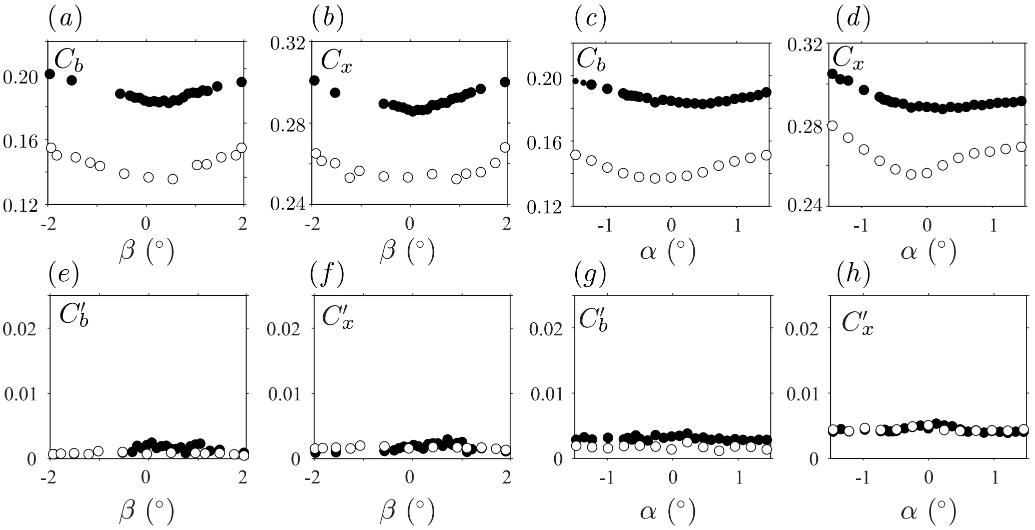

Figure 4.17 – Mean (top row) and fluctuating (bottom row) drag force and base suction coefficients vs. yaw (a, b, e, f) and pitch angles (c, d, g, h) without (black filled circles) and with (empty circles) the rear cavity.

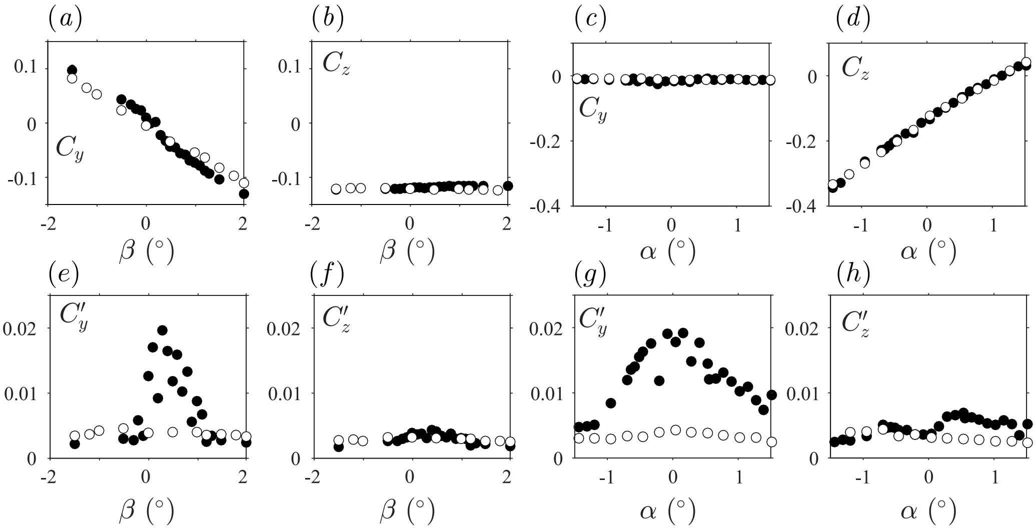

Figure 4.18 – Mean (top row) and fluctuating (bottom row) cross-flow force coefficients vs. yaw (a, b, e, f) and pitch angles (c, d, g, h) without (black filled circles) and with (empty circles) the rear cavity.

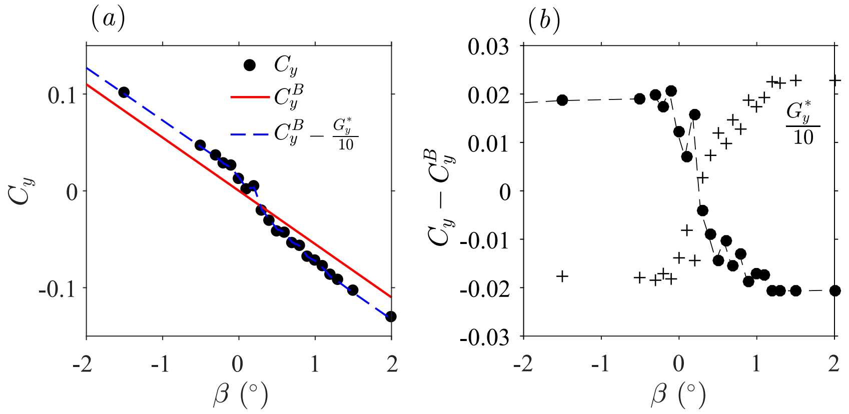

Figure 4.19 – Mean side force coefficient vs. yaw β without the cavity. In (a), measured force coefficient (symbols), basic flow coefficient (red line) and coefficient computed from equation (4.2) (blue dashed line, see text). In (b), mean contribution of the instability $C_y - C_y^B$ (filled circles) and mean horizontal base pressure gradient G_y^* (crosses).

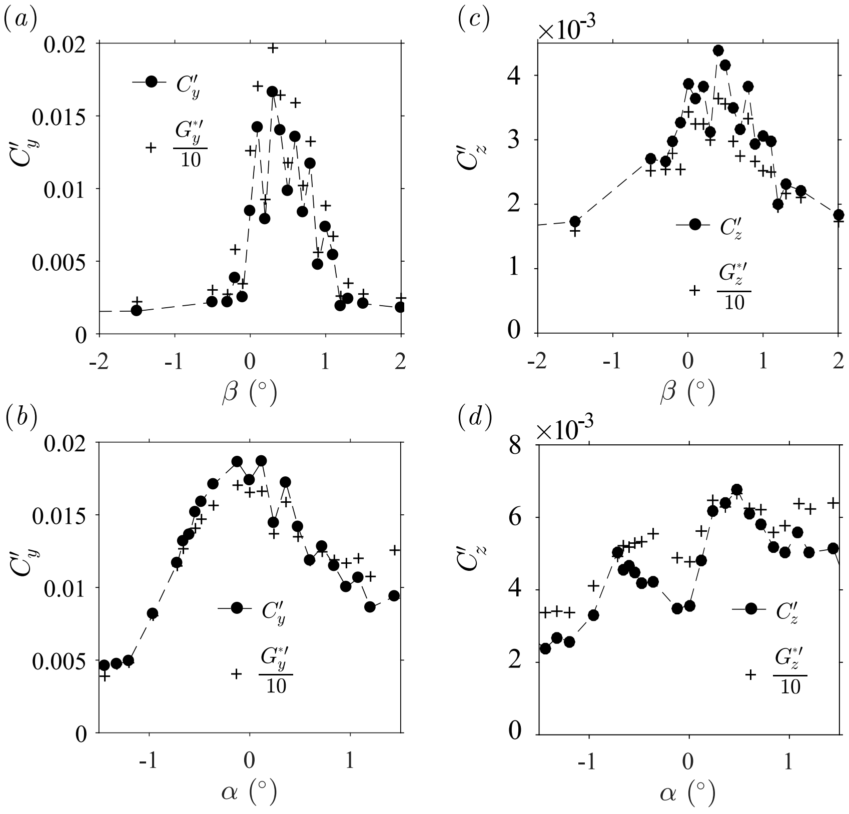

Figure 4.20 – Components of the fluctuating force coefficients C_y' and C_z' (filled circles) compared to the fluctuating base pressure gradients $G_y^{*\prime}$ and $G_z^{*\prime}$ (crosses) vs. yaw β (top row) and pitch angle α (bottom row).

Equation (4.2) is plotted with an excellent agreement with the experimental data as the blue dashed line in figure 4.19(a). As the loading without the instability C_y^B is constant, the following equation (4.3) is easily deduced as the instantaneous expression equivalent to (4.2):

$$c_y(t^*) = C_y^B - \frac{g_y^*(t^*)}{10} \tag{4.3}$$

implying that:

$$C_y' = \frac{G_y^{*\prime}}{10} \tag{4.4}$$

The standard deviation of the side force coefficient C_y' is plotted in figure 4.20(a) for yaw variation and figure 4.20(b) for pitch variation and matches satisfactorily with $G^{*\prime}_y/10$.
The mean lift coefficient C_z does not seem to be affected by the instability from figure 4.18(b) for the yaw experiment or figure 4.18(d) for pitch variations as the values without or with the rear cavity are identical. As a consequence, one can state, regardless of the base pressure gradient orientation φ:

$$C_z = C_z^B \tag{4.5}$$

Similarly to (4.3), the instantaneous relationship (4.6) can be deduced from (4.5):

$$c_z(t^*) = C_z^B + \frac{g^{*\prime}_z(t^*)}{10} \tag{4.6}$$

implying that:

$$C_z{}' = \frac{G_z^{*\prime}}{10} \tag{4.7}$$

Although the fluctuations are about one order of magnitude smaller vertically than horizontally, we still see good agreements in figures 4.20(c, d) between the two sets of data.

4.3.2 z-instability

Starting from the baseline investigated in § 4.3.2.1, we perform sensitivity analyses changing the ground clearance c, the yaw β and the pitch angle α of the model in §§ 4.3.2.2, 4.3.2.3, 4.3.2.4. The resulting wake orientations are given in § 4.3.2.5, similarly to the previous part. Finally, the aerodynamic loading related to the instability is deduced from the wake measurements in § 4.3.2.6.

4.3.2.1 Baseline case with $W_b^* = 0.940$

The baseline is chosen for the body aligned with the incoming flow, *i.e.* in no-yaw and no-pitch conditions ($\alpha = \beta = 0°$), with a ground clearance $c = 5.00 \times 10^{-2}$ m, *i.e.* $c^* = 0.168$. The configuration is similar to that of § 4.3.1.1 but with a base higher than wide. From Grandemange *et al.* (2013a), in view of the base aspect ratio ($W_b^* < 1$), we expect the body to be subject to a static z-instability of the wake.
The results are presented in figure 4.21. The mean base pressure distribution $C_p(y^*, z^*)$ is given in figure 4.21(a). It clearly shows that the symmetry-breaking occurs in the vertical direction, *i.e.* the distribution is nearly symmetric along the $\boldsymbol{e_y}$-axis while a vertical gradient is easily identifiable. This is confirmed by the two PDFs of the Cartesian base pressure gradients in figure 4.21(b). Following the terminology of Grandemange *et al.*

(2013*a*), the wake is permanently locked in the N state since there is only one peak on the histogram. We consequently expect the phase to be locked around $\varphi \simeq -\pi/2$.

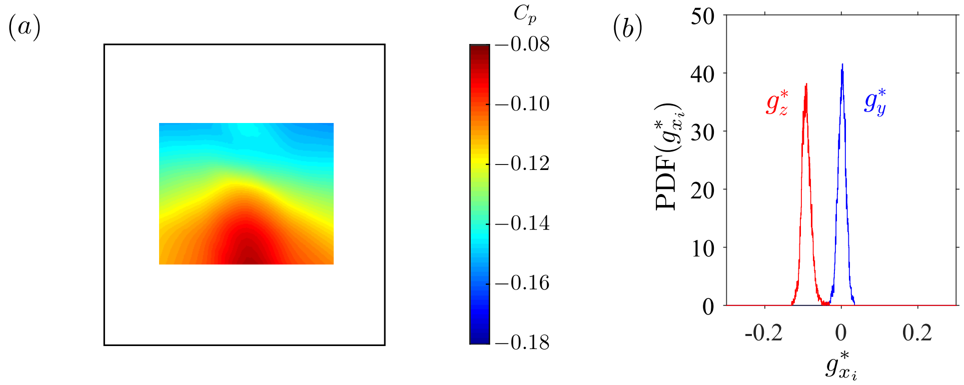

Figure 4.21 – Baseline configuration of the boat-tailed Ahmed body ($\alpha = \beta = 0°$, $c^* = 0.168$) with $W^*_b = 0.940$: mean base pressure distribution $C_p(y^*, z^*)$ (*a*), Probability Density Functions of the vertical base pressure gradient g^*_y in blue and of the horizontal base pressure gradient g^*_z in red (*b*).

The characteristic mean and fluctuating coefficients for the baseline configuration are given in table 4.3. The mean drag coefficient C_x is within the usual interval $0.25 \leq C_x \leq 0.35$ reported in the literature (Ahmed *et al.*, 1984; Barros *et al.*, 2014; Evrard *et al.*, 2016; Volpe *et al.*, 2015) but lower than that of the squareback configuration of § 4.3.1.1 since the body is equipped with boat-tails leading to base pressure recovery and drag reduction (see chapter 5 for a detailed study of the boat-tail effect on the wake of the Ahmed body). The mean base suction coefficient C_b is also smaller for the same reasons. None of the fluctuating coefficients is bigger than 2×10^{-3} or way larger than the others thus confirming unambiguously that the baseline is not subject to wake multi-stability. In the light of the results reported in § 4.3.1, it must be emphasized that this does not mean that the wake is stabilized but rather that a static asymmetric state has been permanently selected (phase lock-in), in agreement with the observations made on figure 4.21($a - b$).

4.3.2.2 Wake sensitivity towards the ground clearance c^*

The sensitivity response of the base pressure gradient due to variations of the ground clearance c^* within the range $c^* \in [0.060, 0.200]$ is investigated through the four sensitivity maps presented in figure 4.22 in Cartesian and polar descriptions. Increasing the ground clearance has almost no impact on the horizontal pressure gradient g^*_y which remains close to zero (figure 4.22*a*). The biggest impact is now on the vertical component g^*_z shown in figure 4.22(*b*) which very quickly changes sign around $c^* \simeq 0.08$, from a positive branch ($g^*_z \simeq 0.1$) to a negative one ($g^*_z \simeq -0.1$). During this transition, a bi-stable dynamics characterized in the following is obtained. This result is similar to that of Grandemange *et al.* (2013*a*) for which saturation of the gradient on a positive branch is identified at $c^* \simeq 0.133$ (with a base aspect ratio of $W^*_b = 0.746$). In figure 4.22(*b*), this result is satisfactorily reproduced but for the switch ground clearance identified at $c^* \simeq 0.08$. The difference might be ascribed to a Reynolds number effect. In our experiment, it is almost ten times larger than in Grandemange *et al.* (2013*a*)'s work ($\mathrm{Re}_H \simeq 4.0 \times 10^5$ *vs.* $\mathrm{Re}_H \simeq 4.5 \times 10^4$). The decrease of the critical ground clearance c^*_S with the increasing Reynolds number has been reported by Cadot *et al.* (2015*b*) in the case of the y-instability discussed in § 4.3.1. c^*_S was indeed observed to be about

30% larger at a Reynolds number of $\mathrm{Re}_H = 1.6 \times 10^5$ than at $\mathrm{Re}_H = 1.7 \times 10^4$. This critical value related to the the z-instability is not reached in the present experiment at the considered Reynolds number since is value is smaller than the minimum ground clearance $c^* = 0.060$ permitted by the set-up. However, that associated with the y-instability was found as $c_S^* = 0.105$ (§ 4.3.1). We can then conclude that the critical ground clearance for the y-instability is bigger than the one for the z-instability, in agreement with the reported results of Grandemange *et al.* (2013*a*). The modulus g_r^* is almost insensitive to the ground clearance change (figure 4.22*c*). The larger fluctuations observed for $c^* \simeq 0.08$ are a consequence of the bi-stable phase dynamics identified owing to the branches switch in figure 4.22(*d*). The modulus is about twice smaller in magnitude with respect to the squareback geometry (§ 4.3.1) because of the different afterbody shapes. The phase φ plotted in figure 4.22(*d*) switches from $\varphi \simeq \pi/2$ to $\varphi \simeq -\pi/2$ during the wake reversal. A small adaptation can be observed in the region $c^* \in [0.07, 0.08]$ because of a slight change of the horizontal component of the gradient g_y^* (figure 4.22*a*).

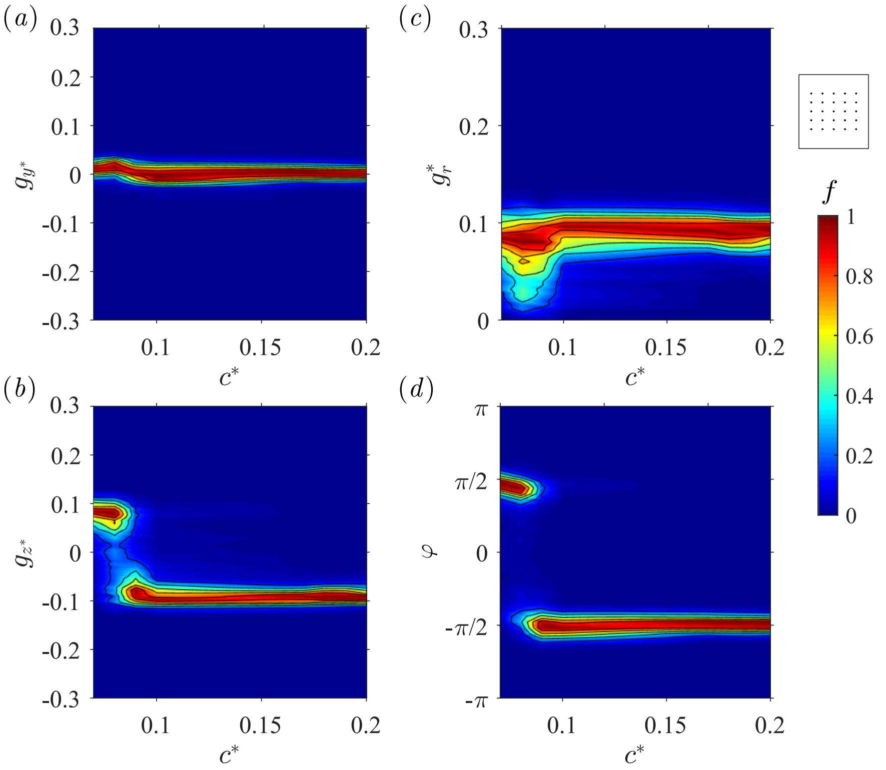

Figure 4.22 – Base pressure gradient response to a variation of the ground clearance c^* for the boat-tailed body $W_b^* = 0.940$. Sensitivity maps (*a*) $f(c^*, g_y^*)$, (*b*) $f(c^*, g_z^*)$, (*c*) $f(c^*, g_r^*)$ and (*d*) $f(c^*, \varphi)$.

This part brings an additional information with respect to the paper of Grandemange *et al.* (2013*a*) about the y- and z-instabilities. In the previous work, the body's and the base aspect ratio were identical so that no conclusions could be drawn about which one dominates for the selection of the instability. Thanks to the present analysis, we are able to state that the base aspect ratio is the relevant parameter since that of the body W/H is unchanged with respect to the previous § 4.3.1.

We focus back on the bi-stable case at $c^* = 0.080$. It is identified as a transition between two wake orientations: $\varphi \simeq \pi/2$ below and $\varphi \simeq -\pi/2$ above (as for the baseline). The corresponding base pressure distributions are given in figure 4.23 with the bi-stable dynamics of the base pressure gradient. The two distributions are almost anti-symmetric despite the presence of the ground similarly to the observations made for the y-instability (see § 4.3.1.1). The dynamics of the modulus is not affected by the bi-stable behavior except during phase jumps which are associated with low magnitude events (such around $t^* \simeq 1000$). The phase varies between $\varphi \simeq \pi/2$ and $\varphi \simeq -\pi/2$ following a stochastic dynamics with a typical time-scale of about 500 t^*, *i.e.* shorter than for the y-instability. Wake reversals occur either with phase jumps, either with a global rotating motion.

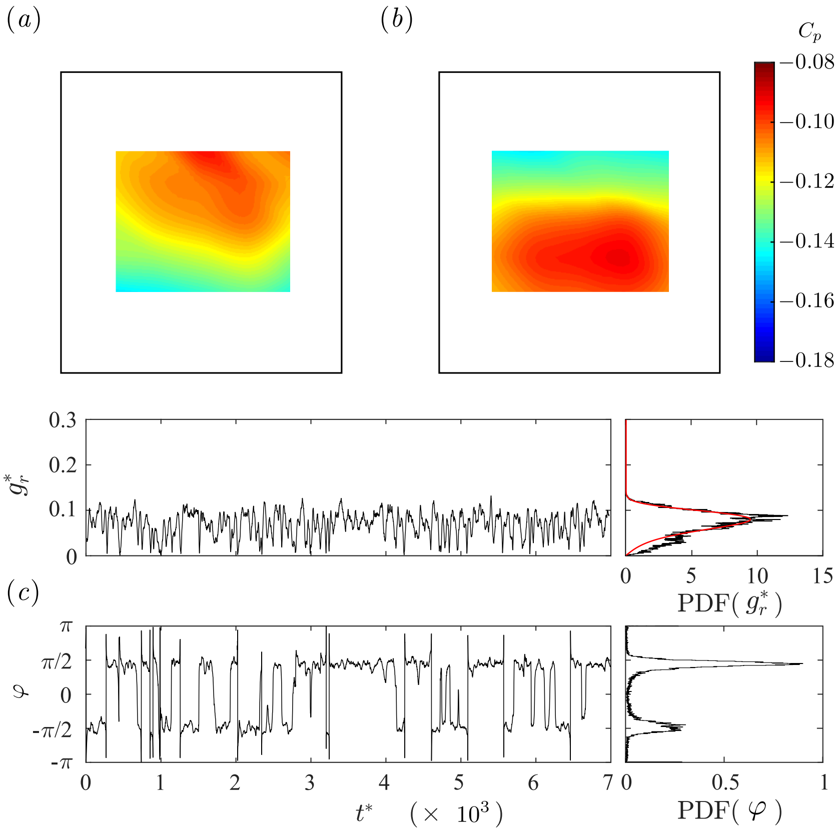

Figure 4.23 – Base pressure distributions $C_p(y^*, z^*)$ obtained by conditional averaging on the vertical base pressure gradient at $c^* = 0.080$: (a) state P of the wake, (b) state N. (c) Modulus $g_r^*(t^*)$ and phase $\varphi(t^*)$ time series (left) of the base pressure gradient with corresponding probability density functions (right) for $c^* = 0.080$. The smooth red line superimposed to PDF(g_r^*) is a best fit of Rigas *et al.* (2015)'s PDF model.

In the following sections § 4.3.2.3 and § 4.3.2.4, the effects of the yaw and of the pitch angle on the unstable wake are investigated.

4.3.2.3 Wake sensitivity towards the yaw angle β in the unstable wake regime $c^* > c_S^*$

The sensitivity analysis to the yaw angle β with a fixed pitch $\alpha = 0°$ is shown in figure 4.24. The ground clearance is that of the baseline ($c^* = 0.168 > c_S^*$). The results being reasonably symmetric with respect to β (as expected in view of the geometrical configuration), we only comment them for $\beta \leq 0°$ but the analysis can be extended to positive angles.

We first consider the horizontal base pressure gradient g_y^* in figure 4.24(a). Four distinctive regions successively named l_1, b_1, b_2 and l_2 are identified and then reported in all four sensitivity maps by vertical dashed lines. The corresponding yaw angle values are summarized in table 4.4 and detailed hereafter. In region l_1, for $|\beta| \leq 2.5°$, the base pressure gradient remains almost identical to that of the baseline: it is locked with a vertical direction oriented towards the ground ($g_z^* \simeq -0.1$ in figure 4.24*b*) with a corresponding modulus close to $g_r^* \sim 0.1$ and a phase of $\varphi \sim -\pi/2$ (figure 4.24*c*, *d*). When the magnitude of yaw angle β is further increased up to the range $2.5° \leq |\beta| \leq 4.5°$, the wake becomes bi-stable in the region b_1. The horizontal gradient alternately explores the two branches (figure 4.24*a*) with small phase jumps of amplitude $\delta\varphi_1 \sim \pi/7$ ($\sim 26°$) (figure 4.24*d*). The horizontal component g_z^* (figure 4.24*b*) nor the modulus g_r^* (figure 4.24*c*) are not affected. Should the magnitude of the yaw be further increased, then another bi-stable regime is observed in region b_2. The horizontal gradient component g_y^* starts decreasing gently while the vertical component g_z^* explores alternately the negative and the positive branches. This results in larger fluctuations of the modulus and in phase jumps of $\delta\varphi_2 \sim 3\pi/4$ in figure 4.24(*d*). In the last region l_2 for $|\beta| > 5.5°$, the gradient orientation is locked with a vertical direction oriented towards the top ($\varphi \simeq +\pi/2$) and a modulus close to $g_r^* \simeq 0.15$.

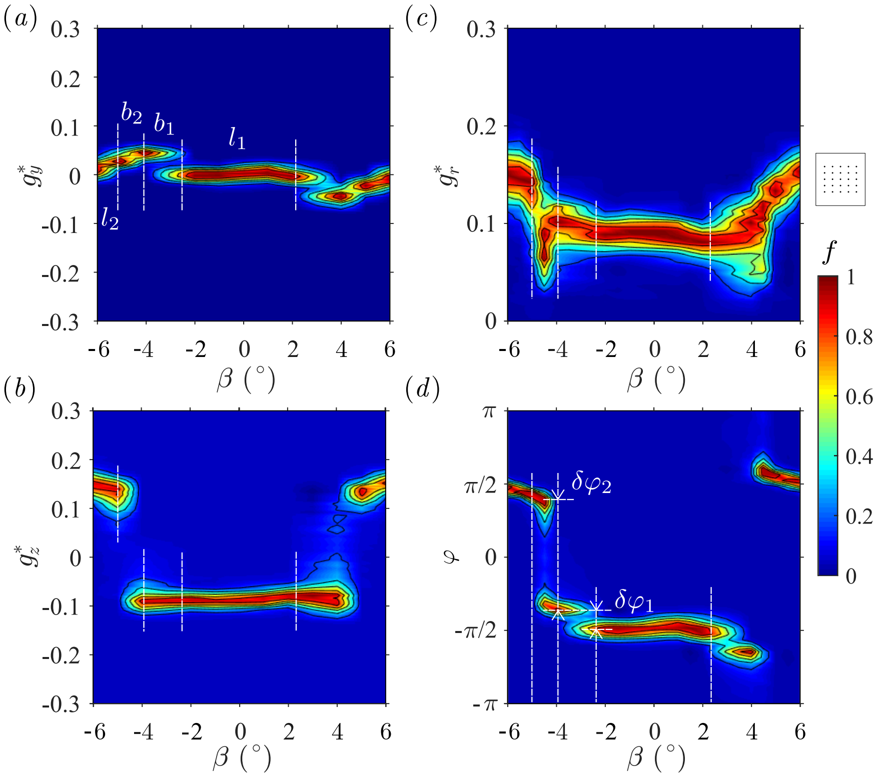

Figure 4.24 – Base pressure gradient response to variations of the yaw angle β for the z-instability. Sensitivity maps (*a*) $f(\beta, g_y^*)$, (*b*) $f(\beta, g_z^*)$, (*c*) $f(\beta, g_r^*)$ and (*d*) $f(\beta, \varphi)$.

Table 4.4 – Yaw angles associated with regions l_1, b_1, b_2 and l_2 of figure 4.24 for the Ahmed body subject to the z-instability with $c^* = 0.168$.

Region	Yaw angle	Wake dynamics
l_1	$\lvert\beta\rvert \leq 2.5°$	State N
l_2	$\lvert\beta\rvert > 5.5°$	State P
b_1	$2.5° \leq \lvert\beta\rvert \leq 4.5°$	Intermittent separation on boat-tail
b_2	$4.5° \leq \lvert\beta\rvert \leq 5.5°$	Bi-stability between states N and P

From this analysis, we can observe that the yaw around $|\beta| = \pm 4°$ triggers the switch of the negative vertical pressure gradient component of the baseline observed in l_1 to a positive vertical component in l_2. This sensitivity to the yaw angle has also been identified on industrial geometries (see chapter 7 and Cadot *et al.* (2016) or Bonnavion *et al.* (2017*a*)).

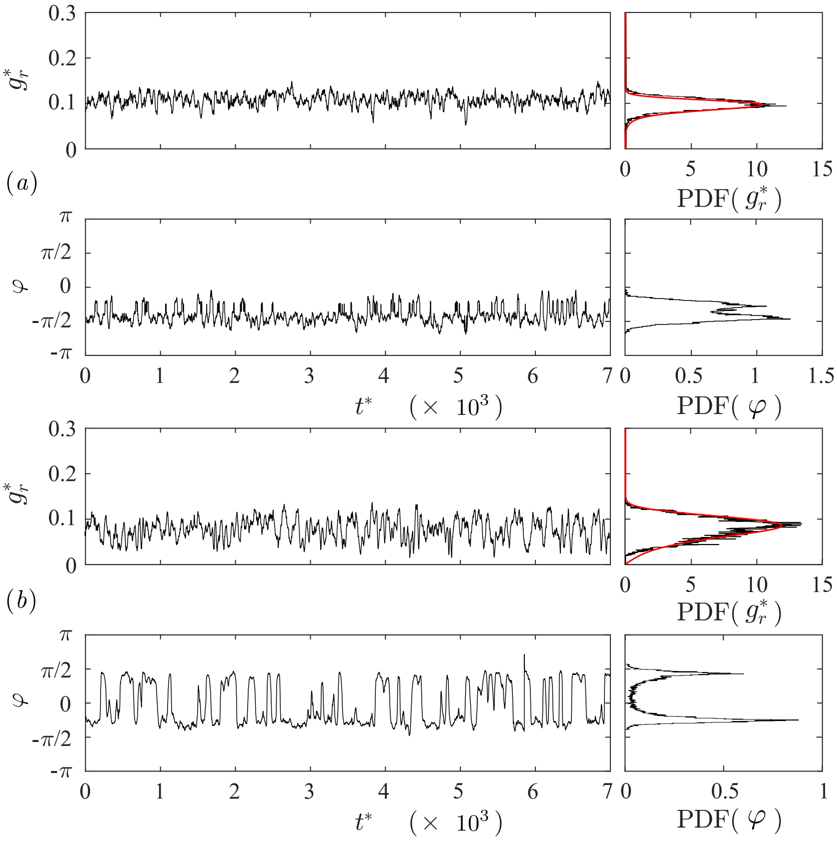

Figure 4.25 – Modulus $g_r^*(t^*)$ and phase $\varphi(t^*)$ time series (left) of the base pressure gradient with corresponding probability density functions (right) for (a) $\beta = -3°$, (b) $\beta = -5°$ at $c^* = 0.168$. The smooth red lines superimposed to PDF(g_r^*) in (a) and (b) are best fits of Rigas *et al.* (2015)'s PDF model.

The dynamics of the two bi-stable cases b_1 and b_2 evidenced during the yaw sensitivity analysis in figure 4.24 are investigated in detail. Time series of the modulus ${g_r}^*$ and of the phase φ of the base pressure gradient are given in figure 4.25(a) for $\beta = -3°$ and in figure 4.25(a) for $\beta = -5°$ with the associated PDFs. The bi-stable dynamics b_1 (figure 4.25a) shows very little sensitivity of the modulus g_r^* whose PDF is very well fitted by Rigas *et al.* (2015)'s model. The phase φ is characterized by high-frequency switching between the two most probable values. This bistability is most likely related to the boat-tails[1] and is quite different to that created by the wake reversals identified in b_2. This bi-stable region would consequently not be observed with a squareback afterbody.

The latter one is similar to that obtained in ground clearance sensitivity (figure 4.22d and figure 4.25). Classically, the modulus fluctuates about its most probable values with a standard deviation slightly bigger than for locked wakes due to phase jumps (see the analysis of figure 4.4). With respect to wake bistability related to the y-instability described in § 4.3.1 (see in particular figure 4.4), the rate of random switching between the two most probable phases is substantially larger. For an identical duration of 7000 t^*, about 42 switches are observed in figure 4.25(b) for only 8 in figure 4.4 for horizontal wake reversals. The typical persistence in a state for this kind of wake bistability ranks consequently about $100 - 200$ t^* (*vs.* $500 - 1000$ t^* for the y-instability).

The sensitivity towards the yaw angle β and the existence of the two branches of solutions was highlighted at the baseline's ground clearance $c^* = 0.168$ in the previous paragraphs.

---

[1] In particular, we suspect that it is related to an intermittent flow separation on the leeward boat-tail. As a matter of fact, the yaw angle of $2.5 - 4.5°$ the boat-tail angle of 12.5° which leads to a total apparent angle of $15 - 17°$, *i.e.* close to the critical value for separation.

The same analysis is reproduced at three other ground clearances in order to quantify the effect of the ground clearance on the critical yaw angle β_c at which the second kind of bistability (type b_2) occurs. The values are chosen depending on the wake behavior in no-yaw conditions ($\beta = 0°$): $c^* = 0.060$ that corresponds to a locked positive vertical gradient ($\varphi \simeq +\pi/2$), $c^* = 0.080$ associated with a bi-stable dynamics (between $\varphi \simeq +\pi/2$ and $\varphi \simeq -\pi/2$) and $c^* = 0.124$, similar to $c^* = 0.168$ with a locked negative vertical gradient ($\varphi \simeq -\pi/2$). These points can be retrieved in figure 4.26 where the results are presented. The results are limited to $\beta \in [-6°, 0°]$ in view of the symmetry of the problem. We recall that all points belong to the unstable wake regime, *i.e.* $c^* > c^*_S$.

The branches of most probable gradients (in Cartesian description) are extracted in figure 4.26(a) with the following procedure. The location of the maxima of the two branches of the sensitivity maps, *e.g.* figure 4.24 for $c^* = 0.168$, are identified for each value of the yaw angle β. As the maps are normalized, the first maximum is 1. For the same angle, a second maximum might be present. It is plotted only if the peak exceeds 0.10, *i.e.* 10% of the observation time which is about identical for each test. These peaks are plotted in figure 4.26(a) for the four investigated ground clearances. The most probable horizontal base pressure gradient g^*_y of the gradient remains close to zero with a significant evolution for yaw angles around $\beta \sim -4°$ for the two largest ground clearances. As for the vertical gradient g^*_z, each of the branches is associated with one state of the wake: state P for positive gradients and state N for negative ones. The terminology is the same as in Grandemange *et al.* (2013a). The general behavior is that for large yaw angles, state P is selected regardless of the ground clearance. As the body is realigned, switching to state N may occur, either during bistability either through a permanent selection. The closer the body to the ground, the smaller the critical angle β_c at which this transition occurs. As a consequence, this may eventually lead to bistability in the aligned configuration for $c^* = 0.080$ or even persistence in state P for $c^* = 0.060$. Otherwise, state N is selected as for the baseline.

The modulus and the phase of all four configurations are then plotted together in figure 4.26(b) and figure 4.26(c). All four cases collapse reasonably well. The modulus g^*_r and the phase φ are discussed in detail. The ground clearance has very little effect on the gradient modulus (figure 4.26c). As a consequence, as two branches are identified for the vertical gradient in figure 4.26(a), this means that the wall only changes the gradient orientation (see the phase in figure 4.26d) even in the unstable regime (in which ground clearance becomes an irrelevant parameter of study for the y-instability).

For yaw angles $|\beta| < 3°$, and whatever the ground clearance is, the modulus shown in figure 4.26(b) is found to be almost constant and the gradient has only two opposite phase orientations $+\pi/2$ and $-\pi/2$ as can be seen in figure 4.26(c). For larger yaw $|\beta| > 3°$ the N state becomes yaw-dependent and the modulus not as well defined. At large ground clearances, one would indeed have expected the recovery of the top/down symmetry of the flow which would lead to a bi-stable dynamics independently of the ground proximity. Hence the bi-stable transition is likely to result from a competitive effect between ground clearance and supports. This effect is investigated in the following paragraph.

A small disturbance (dimensionless size $0.134 \times 0.067 \times 0.067$ in the $\boldsymbol{e_x}$, $\boldsymbol{e_y}$, $\boldsymbol{e_z}$ coordinate system) is placed between the two front cylindrical supports of the model in the baseline configuration ($c^* = 0.168$, $\alpha = 0°, \beta = 0°$). This disturbance models a fifth cylindrical support identical to the four others. This experimental point is indicated by the black triangle in figure 4.26 that clearly shows a permanent wake reversal from branch N to branch P. The horizontal gradient component g^*_y is indeed almost unaffected (figure 4.26a) as the differences are within those created by the defects of the setup while the positive gradient changes to $g_z^* \simeq +0.12$. The modulus (figure 4.26*b*) is very similar to the baseline configuration while the phase is associated to that of state P (figure 4.26*c*). On the basis of this simple experiment, one can draw a plausible mechanism for the change of branch as yaw increases. It is likely that in yaw conditions, the wake of the front leeward support that develops under the body gets closer to the mid-track as the yaw increases. Such wake state selection due to a model's supports or wheels is also reported by Pavia & Passmore (2018) for the squareback Windsor geometry.

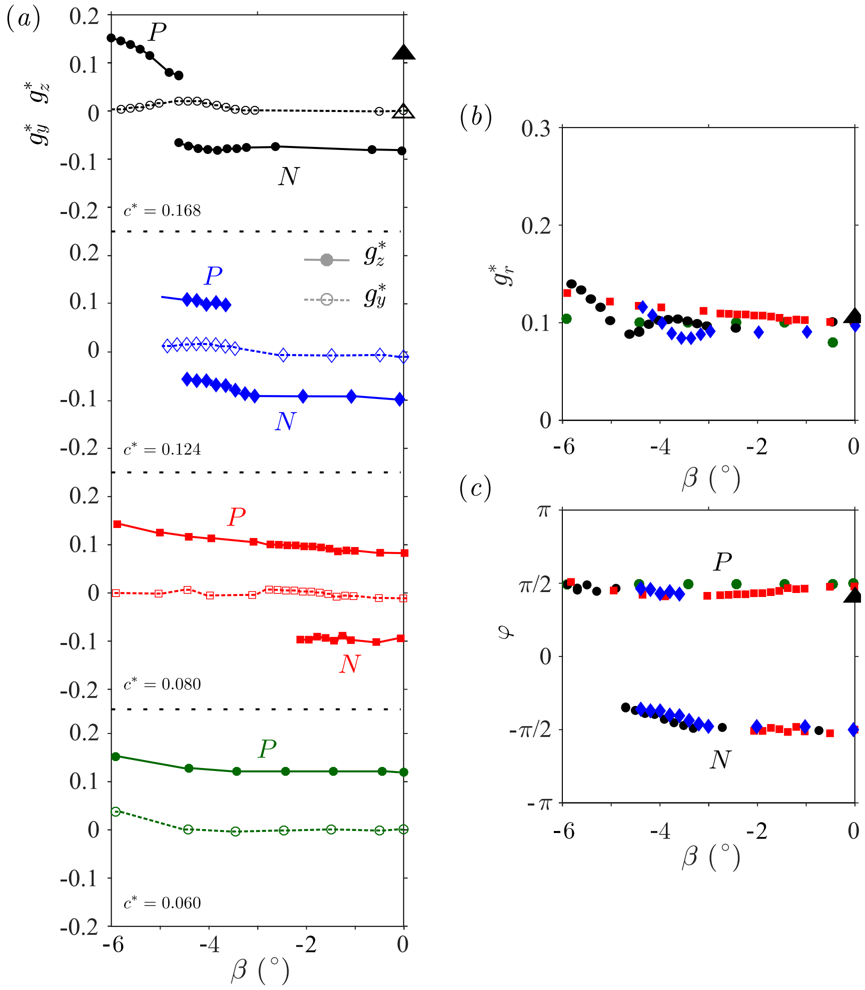

Figure 4.26 – Most probable pressure gradients g_y^* and g_z^* (*a*), g_r^* (*b*) and φ (*c*) versus the yaw angle at different ground clearances (with descending value from top to bottom in *a*). The triangle corresponds to the experiment with the disturbance placed under the body.

4.3.2.4 Wake sensitivity towards the pitch angle α in the unstable wake regime $c^* > c_S^*$

Finally, the sensitivity toward the pitch angle α is investigated. For this experiment, the yaw angle is set to $\beta = 0°$ and the front and rear ground clearances are adjusted for a given pitch but keeping $c^* = \frac{1}{2}(c_f^* + c_r^*) = 0.168$. We restricted the range of pitch angle to nose-down configurations since the aim is to highlight wake reversals which, from § 4.3.1, need more negative pitch angles as the baseline corresponds to the bottom state N. The goal is to let the top state P appear. The four sensitivity maps are presented in figure 4.27. The pitch angle has almost no effect on the horizontal component (figure 4.27*a*) except for a disturbance around $\alpha = -0.4°$ that corresponds to the switching region with a bi-stable dynamic in figure 4.27(*b*) of the vertical component of the gradient. The modulus

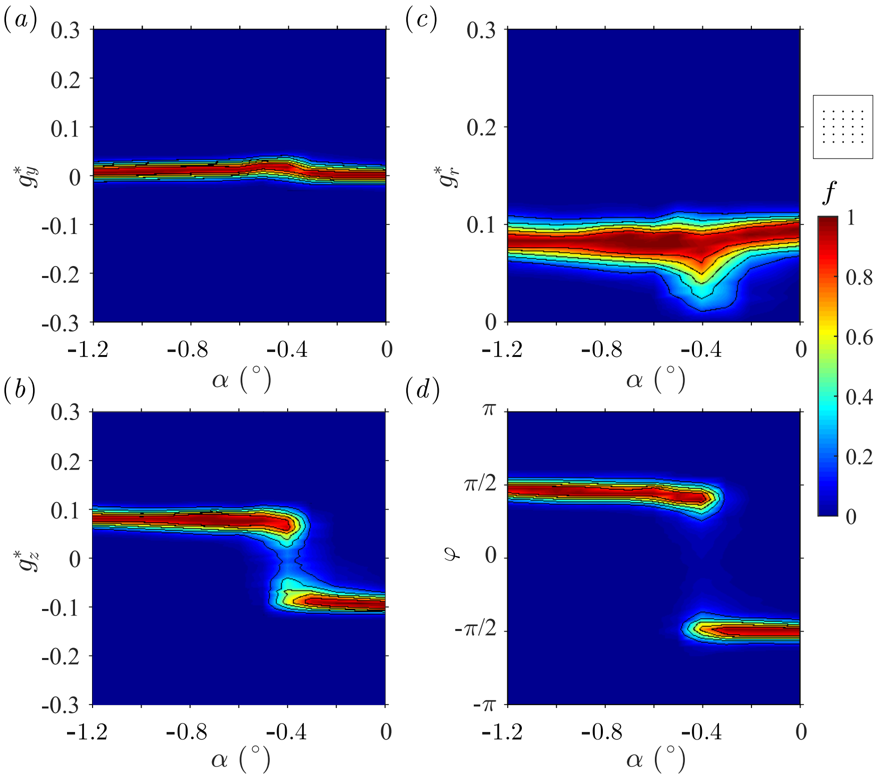

Figure 4.27 – Base pressure gradient response to variations of the pitch angle α for the z-instability. Sensitivity maps (a) $f(\alpha, g_y^*)$, (b) $f(\alpha, g_z^*)$, (c) $f(\alpha, g_r^*)$ and (d) $f(\alpha, \varphi)$.

(figure 4.27c) is again not affected; at most one may note larger fluctuations for the critical yaw angle. We recover the two expected phase values of $\varphi \simeq \pi/2$ for state P ($\beta \leq -0.6°$) and $\varphi \simeq -\pi/2$ for state N ($\beta \geq -0.4°$). As a result of the constraint imposed by the horizontal gradient around $-0.5° \leq \beta \leq -0.4°$, the phase slightly adapts in this range as shown in figure 4.27(d).

One may wonder what typical base pressure distributions are associated with the yaw and the pitch experiments. If we compare the sensitivity maps for each of the experiments in figure 4.22, figure 4.24, figure 4.27 and figure 4.26, we can observe that the two branches of solutions for the vertical gradient g_z^* (and consequently for the phase φ) are identical. As a result, the base pressure distributions are similar to those explored during the bi-stable dynamics identified during the ground clearance sensitivity experiment and shown in figure 4.23(a, b).

4.3.2.5 Wake orientations resulting from the z-instability

The different wake configurations are illustrated by their mean flow in the vertical plane in figure 4.28 together with their corresponding mean base pressure distribution. The baseline, in (a), lets appear the bottom orientation of the wake (state N): the negative vertical pressure gradient observed in the pressure distribution is associated with a skewed feedback flow oriented towards the bottom edge of the base. The fields are harder to interpret than for the squareback geometry. In fact, because of the boat-tailed shape, the afterbody develops four strong longitudinal vortices (one at each corner of the base). They are responsible for the two saddle points in the figures 4.28($a-d$) while only one was observed for the squareback geometry in figures 4.11(a, c, e).

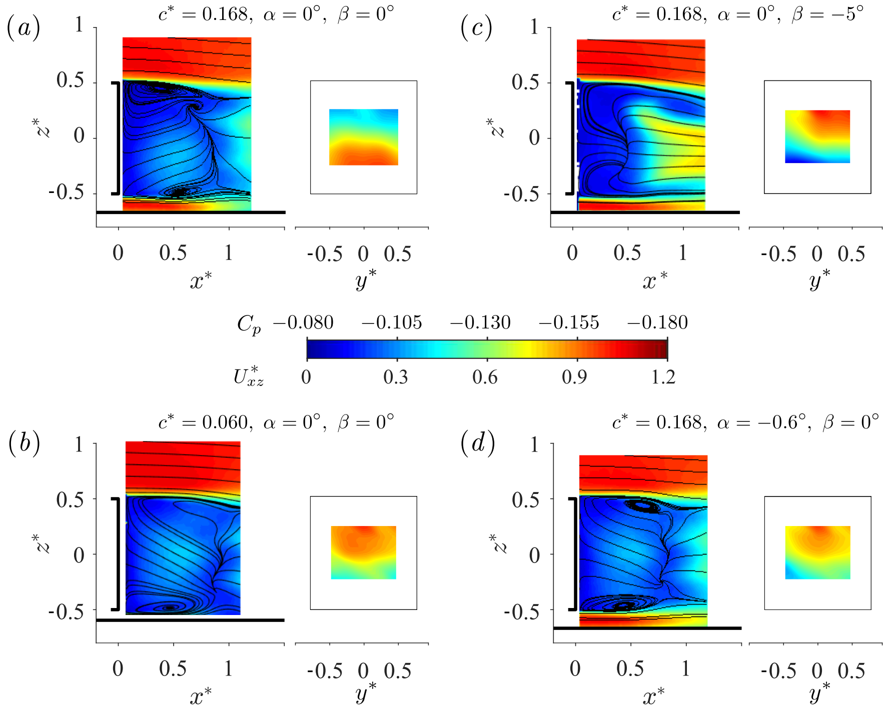

Figure 4.28 – Cross-sections of the mean velocity field visualized using streamlines superimposed to the modulus of the components in the vertical plane (x^*, z^*) for (a) baseline configuration ($\alpha = \beta = 0°$, $c^* = 0.168$), (b) $\alpha = \beta = 0°$, $c^* = 0.060$, (c) $\alpha = 0°$, $\beta = -5°$, $c^* = 0.168$, (d) nose-down configuration $\alpha = -0.6°$ ($\beta = 0°$). The associated mean base pressure distributions $C_p(y^*, z^*)$ are also provided.

For each of the three sensitivity analyses, wake reversals were identified and the associated fields are provided in figure 4.28. In figure 4.28(b), low ground clearances select state P of the wake characterized by a skewed feedback flow oriented to the top edge of the base and a reversed mean base pressure distribution. Wake reversals operated by the yaw angle shown in (c) can be clearly seen in the pressure distribution, which is similar although tilted to that obtained at $c^* = 0.060$ (figure 4.28b). As the PIV plane is fixed, figure 4.28(c) shows rather the longitudinal vortices originating from the body's edges than the wake orientation. However, the selection operated by the (negative) pitch angle is clearly visible in figure 4.28(d) with the same characteristic base pressure distribution.

4.3.2.6 Aerodynamic loading applied to the body varying its inclination and contribution of the z-instability

Figure 4.29 shows the mean base suction C_b and the mean drag coefficient C_x and their fluctuations as a function of the yaw and pitch angles. Both parameters have the same evolution with respect to the investigated parameters both in terms of mean value and fluctuations and are consequently commented together. For the yaw experiment (figure 4.29a, b, e, f), the drag and the base suction show a plateau for $|\beta| \leq 4°$. Both are consequently independent of the geometrical setup, similarly to what has been observed for the Renault Kangoo at yaw (see chapter 7 and Bonnavion *et al.* (2017a)). During the bistability ($|\beta| \simeq 4°$), both reach a minimum. This result puts a new insight on some control strategies aiming at suppressing the wake bistability whilst it might, in some cases as here, be the less detrimental configuration! After the transition, an almost linear increase can be observed. For the pitch experiment (figure 4.29c, d, g, h), the drag and the base suction are almost insensitive to the body's orientation, with again a slight reduction during bistability ($\alpha \simeq -0.4°$) though. Similarly to the y-instability investigated in § 4.3.1, the contribution of the z-instability to the mean drag C_x (if any) cannot be extracted from these results.

The mean side force and lift coefficients obtained for small yaw and pitch inclinations around the baseline, *i.e.* small misalignments of the body, are shown in figure 4.30($a-d$). The mean side force C_y appears to be a linear function of the yaw angle β (figure 4.30a) suggesting therefore that it is not modified by the z-instability. Its fluctuations are correspondingly small regardless of the angle (figure 4.30b). However, the mean lift coefficient C_z (figure 4.30c) shows a strong dependence to the yaw as two levels corresponding each to one wake orientation, either at $C_z^P \simeq -0.14$ for the P state or at $C_z^N \simeq -0.18$ for the N state, can be identified. The contribution of the z-instability to the lift can then be extracted straightforwardly. It is given by $C_z^P - C_z^B$ in the P state and $C_z^B - C_z^N$ in the N state and is found to be about 0.02 for all angles. As expected, there is a fluctuation crisis during the bi-stable dynamics at the transition as shown in figure 4.30(f). For the pitch sensitivity analysis, neither the mean side force coefficient C_y nor its fluctuations C_y' (see figure 4.30c and figure 4.30g respectively) are affected by the instability: no dependence of the mean value and no fluctuation crisis are identified. On the contrary, the mean lift coefficient C_z (figure 4.30d) and its fluctuations C_z' (figure 4.30h) reveal the z-instability. They indeed behave in a similar manner as the side force c_y for the yaw experiment in presence of the y-instability (figure 4.18a and figure 4.18e) as it is impossible that the observed behavior simply lies on the small geometrical changes applied to the setup when imposing a pitch angle to the body.

In absence of the z-instability and due to the geometrical modifications induced by a change of the pitch angle, the mean lift coefficient C_z^B of the stable *basic flow* should be a linear function of the pitch angle α following the same deduction as for the y-instability in § 4.3.1. Since the instability simply swifts the branches away from the stable solution, we can deduce the linear relationship $C_z^B(\alpha) = 0.11\alpha - 0.177$ (where α is expressed in degrees). This expression is plotted in figure 4.31(a) as the red continuous line. The estimated strength of the instability $C_z - C_z^B$ is compared to the mean vertical base pressure gradient G_z^* and an intensity of about 0.02 is retrieved similarly to the y-instability for the yaw experiment (§ 4.3.1.3). This relationship is plotted as the blue dashed line in figure 4.31(a); an excellent agreement with the experimental data (black circles) is found. As a result, the actual mean lift coefficient C_z can be directly related to the mean base pressure gradient:

$$C_z(\alpha) = C_z^B(\alpha) - \frac{G_z^*(\beta)}{5} \tag{4.8}$$

Afterwards, an instantaneous lift coefficient can be derived for the z-instability:

$$c_z(t^*) = C_z^B - \frac{g_z^*(t^*)}{5} \tag{4.9}$$

As a consequence, equation (4.9) yields $C_z' = G_z^{*\prime}/5$ in the case of the z-instability with the boat-tailed body. The two quantities are compared in figure 4.32($c-d$) and show an excellent agreement.

Since the mean side force coefficient C_y is not affected by the instability (figure 4.30$c-g$), it is equal to that of the *basic flow* C_y^B:

$$C_y = C_y^B \tag{4.10}$$

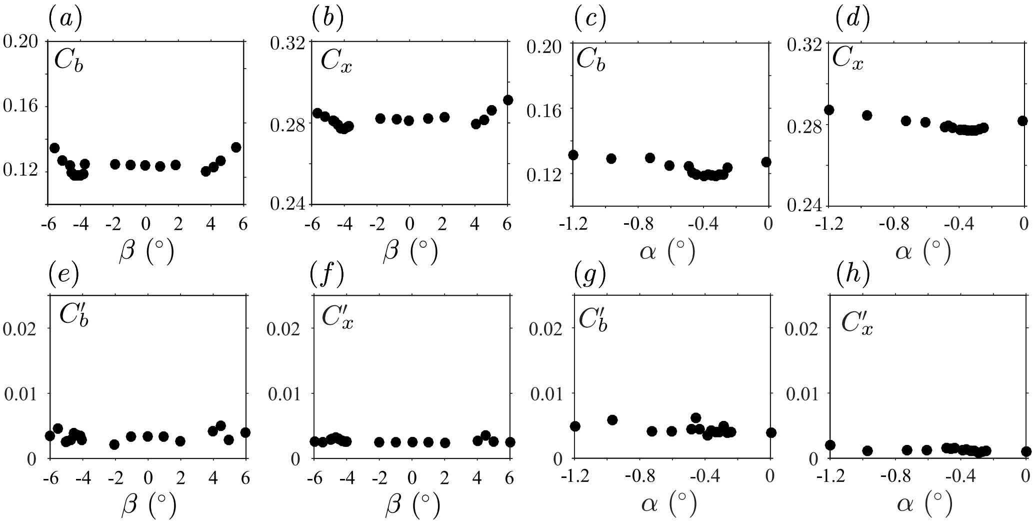

Figure 4.29 – Mean (top row) and fluctuating (bottom row) drag force and base suction coefficients *vs.* yaw (a, b, e, f) and pitch angle (c, d, g, h) for the boat-tailed geometry.

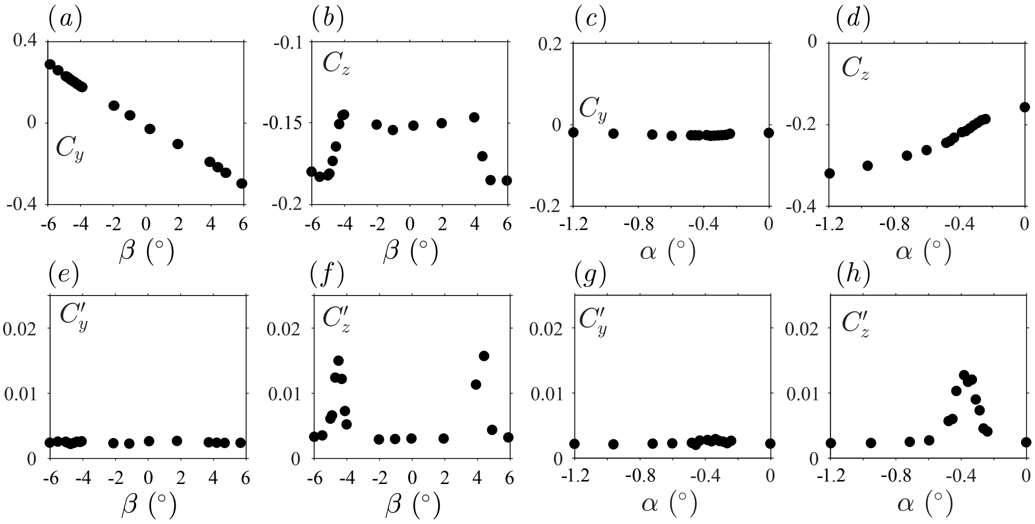

Figure 4.30 – Mean (top row) and fluctuating (bottom row) cross-flow force coefficients *vs.* yaw (a, b, e, f) and pitch angle (c, d, g, h) for the boat-tailed body.

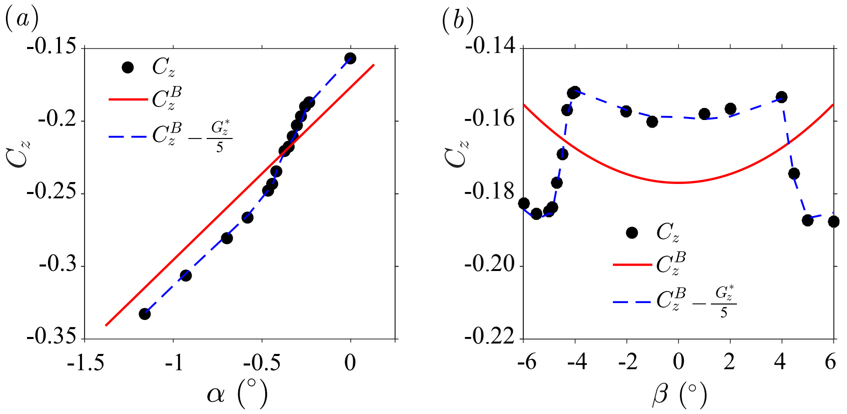

Figure 4.31 – Mean lift coefficient *vs.* inclination of the boat-tailed body. The measured force coefficient (symbols) are compared to the *basic flow* coefficient (red line) and coefficient computed from equations (4.8) (blue dashed line, see text). (a) Pitch angle sensitivity, (b) yaw angle sensitivity.

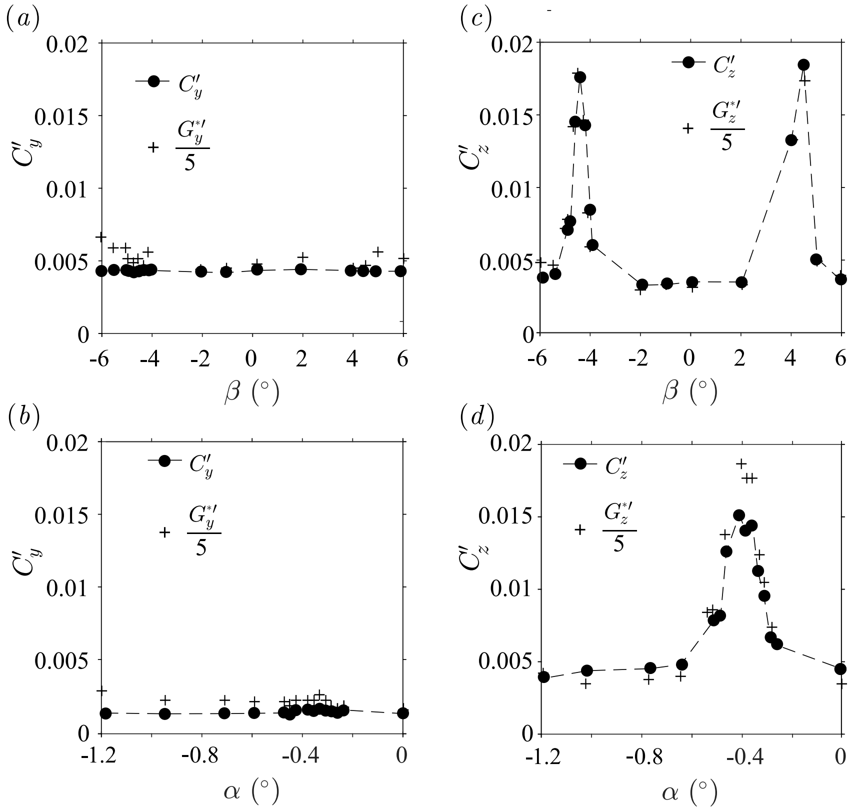

Figure 4.32 – Components of the fluctuating force coefficients C'_y and C'_z (filled circles) compared to the fluctuating base pressure gradient $G^{*\prime}_y$ and $G^{*\prime}_z$ (crosses) *vs.* yaw β (top row) and pitch angle α (bottom row) for the boat-tailed geometry.

The instantaneous side force coefficient c_y can then be obtained:

$$c_y(t^*) = C_y^B - \frac{g_y^{*\prime}(t^*)}{5} \tag{4.11}$$

where the relationship $C'_y = G^{*\prime}_y/5$ for the fluctuations is reasonably recovered in figure 4.32(a, b). The factor 5 instead of 10 identified for the y-instability lies in the different afterbody geometries, in particular since one is a squareback while the other is boat-tailed.

4.4 Discussion

4.4.1 Role of the phase dynamics of the unstable wake

The crucial role of the phase dynamics of the unstable wake is investigated in this section based on the polar form (g_r^*, φ) of the base pressure gradient $\hat{g}$. Once the instability is saturated, *i.e.* for $c^* \geq c_S^*$, the modulus g_r^* is found to be within the range $0.15 \lesssim g_r^* \lesssim 0.20$ regardless of the alignment of the body (ground clearance in figure 4.3c, yaw angle in figure 4.6c and pitch angle in figure 4.8c). Such values are *large* with respect to those related to the flow with the base cavity for which the modulus is rather about $g_r^* \simeq 0.10$ regardless of the experiment (figure 4.14a, c, e) that is of the same order of magnitude as the stable flow (figure 4.3c for $c^* < c_S^*$). These two results indicate unambiguously that the increase of the modulus magnitude results directly from the natural instantaneous asymmetry related to the symmetry-breaking modes of the wake.

The strength of the gradient appears to be larger when horizontally oriented than vertically: $g_r^*(\varphi = 0 \text{ or } \varphi = \pi) \simeq 0.187$ *vs.* $g_r^*(\varphi = \pi/2) \simeq 0.159$. This can be clearly observed in figure 4.8(c). Similar dynamics features as those of our yaw experiments (§ 4.3.1.3) are obtained by Grandemange *et al.* (2014b) as a vertical control cylinder is used to disturb the wake. Besides, Barros *et al.* (2017) report similar observations since the authors obtain the wake dynamics as in our pitch experiments (§ 4.3.1.4) while disturbing the underbody flow (and thus modifying the apparent ground clearance) with small bodies[1].

Since the ratio between the two oriented gradient's modulus is very close to the rectangular base aspect ratio W_b^* (1.176 *vs.* 1.174), we propose a simple interpretation based on geometrical arguments. The idea is to introduce the non-axisymmetry of the afterbody using different metrics in g_y and g_z directions. We first do the transformation (4.12):

$$g_y = W_b^* g_y^{\mathcal{A}} \tag{4.12a}$$

$$g_z = g_z^{\mathcal{A}} \tag{4.12b}$$

The superscript $\mathcal{A}$ is standing for the axisymmetric wake subject to a pressure gradient of constant modulus $g_r^{\mathcal{A}}$ independently to its orientation. The base pressure gradient $\hat{g}^{\mathcal{A}}$ can then be written in the complex form based on equation (4.12):

$$\hat{g}^{\mathcal{A}} = \frac{g_y}{W_b^*} + \mathrm{i} g_z \tag{4.13}$$

Finally, transforming the Cartesian components into their polar form, equation (4.13) yields:

$$\left(g_r^{\mathcal{A}}\right)^2 = g_r(\varphi)^2 \left(\frac{\cos^2\varphi}{W_b^{*2}} + \sin^2\varphi\right) \tag{4.14}$$

As a result of the transformation (4.12), we have $g_r\left(\pi/2\right) = g_r^{\mathcal{A}}$. As a consequence, the dimensionless modulus of the base pressure gradient of the non-axisymmetric wake is finally written as:

$$g_r^*\left(\varphi\right) = \frac{g_r^*\left(\frac{\pi}{2}\right)}{\sqrt{\left(1 - (1 - \frac{1}{W_b^{*2}})\cos^2\varphi\right)}} \tag{4.15}$$

Equation (4.15) will be referred to as the *wake model* in the following. It can be noticed that we indeed retrieve the guessed relation between the modulus in the two orthogonal orientations: $g_r^*\left(0\right)/g_r^*\left(\pi/2\right) = W_b^*$. The latter relation is in good agreement with the experimental measurements of the pitch sensitivity analysis given in figure 4.8(c) in which the white dots are the time averaged modulus $\overline{g_r^*}$ computed from equation (4.15) using the phase time-series $\varphi(t^*)$ and $g_r^*(\pi/2) = 0.159$. The most probable values of the two Cartesian components g_y^* and g_z^* are also accurately predicted (figure 4.8a, b) as $\overline{g_y^*} = \left(\overline{g_r^* \ \cos\varphi}|_{\varphi>\pi/2}, \overline{g_r^* \ \cos\varphi}|_{\varphi\leq\pi/2}\right)$ and $\overline{g_z^*} = \overline{g_r^* \ \sin\varphi}$.

Equivalently, the same procedure is successfully repeated for the two other sensitivity experiments in figure 4.3 and figure 4.6. The ground clearance analysis is restrained to the unsteady wake ($c^* \leq c_S^*$) as the model does not make sense in case of a stable flow. Since a good agreement with the data is found, this indicates that, regardless of the body's inclination and ground clearance, the unstable wake obeys the wake model of equation (4.15). Based on this fact, a simplification for the wake modeling is proposed:

---

[1] We were able to retrieve similar wake orientations with perturbations placed on top or below the body although these results are not included in the manuscript.

$$g_y^*(t^*) = g_r^*(\varphi) \cos \varphi(t^*) \tag{4.16a}$$
$$g_z^*(t^*) = g_r^*(\varphi) \sin \varphi(t^*) \tag{4.16b}$$

Consequently, the key ingredient is actually the comprehension of the phase dynamics of a unique turbulent symmetry-breaking mode of a known intensity. It must be understood how the phase dynamics adapts to the geometrical constraints imposed to the wake flow by the ground proximity, the body's supports or its inclination (pitch and yaw angles). This constraint is discussed in the following § 4.4.2.

The reader might object that the transformation (4.12) does not lead to a rectangular base as in the experiments but to an elliptical one instead. Since the elliptical modulation yields results in good agreement with experimental data, on can conclude that the right angles of the rectangular base do not introduce any singularities in the base pressure gradient modulus, which means that the previous observations hold.

The model derived in this section is satisfactorily verified for small angular deviations around the baseline ($|\beta| \leq 2°$ and $|\alpha| \leq 1.5°$). Limitations appear for larger values but, in such cases, it is questionable whether the instability only is involved since the symmetry of the setup is lost. For instance, the increase of the modulus g_r^* observed during the yaw experiment for the body subject to the z-instability (figure 4.24*c*) for angles larger than $|\beta| = 5.5°$ is not predicted by the current model.

4.4.2 Phase dynamics adaptation and consequences on cross-flow force

In the squareback case subject to the y-instability (§ 4.3.1.2), one of the most important results of this chapter is that, for all sensitivity experiments, only the horizontal component of the base gradient g_y^* may be subject to large discontinuous transitions regardless of the orientation while the vertical component g_z^* varies continuously. This statement justifies the terminology of y-instability introduced by Grandemange *et al.* (2013*a*) and used in this work.

The mean vertical gradient component G_z^* and the mean lift coefficient C_z deserve a specific attention when compared to the *basic flow* obtained with a rear cavity. This device has indeed almost no effect on the mean lift while the wake instability is suppressed and this statement is verified for all three sensitivity analyses (figure 4.16*d* and figure 4.18*b*, *d*). As a result, $C_z = C_z^B$. Besides, the asymmetry of the mean velocity in the vertical plane is also very similar without (figure 4.11*a*, *c*, *e*) and with (figure 4.15*a*, *c*, *e*) the cavity. Only the recirculation bubble elongates in agreement with Evrard *et al.* (2016) and Lucas *et al.* (2017) in relation with the higher base pressure (see appendix B). As a consequence of the similarity between the unstable and the *basic* flows, the wake asymmetries resulting from pitching conditions are not related to the wake instability but simply to the inclination of the body. During the ground clearance sensitivity analysis (figure 4.3), the ground and most importantly the model's cylindrical supports are responsible for the vertical gradient G_z^* which does not vanish even at large clearances.

In average, the unstable wake orientation adapts the vertical component of the base pressure gradient G_z^* to that of the – stable – *basic flow*:

$$G_z^* = \overline{g_r^*(\varphi) \sin \varphi} = G_z^{*B} \tag{4.17}$$

Equation (4.17) is crucial as the matching of the mean vertical component of the pressure gradient with that of the *basic flow* directly determines the allowed phase values.

The matching of the vertical component with that of the *basic flow* when associated with the gradient's modulus property derived in equation (4.15) directly affects the other component (here the horizontal one g_y^*) which consequently reveals the instability. Each discontinuous transition between the two branches of g_y^* observed in all three sensitivity analyses (figure 4.3*a*, figure 4.6*a*, figure 4.8*a*) is associated with a bi-stable wake dynamics during which two values of the gradient's phase are alternately explored (figure 4.3*d*, figure 4.6*d*, figure 4.8*d*). In this chapter, we have $\varphi = 0$ for state P and $\varphi = \pi$ for state N in no-yaw and no-pitch conditions. Equivalently, for the pitch experiment, the preferred phase value become φ and $\pi - \varphi$. The two wake states are explored with a probability of κ (respectively $1 - \kappa$). For the ground clearance and pitch sensitivity experiments (§§ 4.3.1.2, 4.3.1.4), since the vertical $\boldsymbol{e_z}$ axis corresponds to a reflectional symmetry, we theoretically obtain $\kappa = 1/2$. This value is almost never reached though because of unavoidable symmetry defects coming from multiple sources (cable passage, wind deviation, geometrical asymmetries...), and thus equal exploration is not always observed for ground clearance and pitch angle variations.

From this point of view, the base pressure gradient lock-in of the unstable wake at $\varphi \simeq +\frac{\pi}{2}$ for large nose-down configurations ($\alpha \lesssim -0.75°$) results from a matching with the vertical component of the *basic flow*'s gradient. When the pitch is increased such that the vertical component becomes smaller than the imposed geometrical constraint ${G_z^*}^B(\alpha)$ computed from equation (4.17), a bi-stable dynamics takes place between the two phase values φ_P and $\pi - \varphi_P$ to match the condition $G_r^* = {G_z^*}^B(\alpha)$ thus leading to the creation of an horizontal gradient. As a result, the phase φ continuously rotates from $\pi/2$ to a value slightly larger than π (see figure 4.8*d*). On the other hand, for nose-up configurations such that $0.5° \lesssim \alpha$, one would have expected a similar behavior with eventually phase lock-in around $\varphi \simeq -\pi/2$ if the setup were symmetric. Nevertheless, due to the floor proximity, the wake reaches a state of uniform phase distribution within the range $[-\pi, 0]$ instead. The dynamics then turns into a random wake rotation similar to that described in Rigas *et al.* (2014, 2015) for an axisymmetric bluff body. Still, the constraint on the gradient is satisfied as $G_z^*(\alpha) = {G_z^*}^B(\alpha) = G_r^*(\varphi)\,\overline{\sin(\varphi)}$. To summarize, as illustrated by the PIV measurements (figure 4.11), this reversal is equivalent to a global wake rotation of π with bi-stable regimes around the baseline. The same global rotation of the wake was observed by Barros *et al.* (2017) who qualified it as a *symmetry exchange*. The adaptation mechanism also provides a satisfactorily explanation for the wake reorientation observed for $0.105 \lesssim c^* \lesssim 0.16$ during the ground clearance sensitivity experiment (figure 4.3*d*).

Last, the constant modulus observed during the yaw experiment (figure 4.6*c*) is also justified by this approach since the vertical constraint remains identical for all yaw angles $\beta \in [-2°, 2°]$. In this case, the base pressure gradient undergoes a random dynamics of π phase jumps during the transition from phase lock-in at $\varphi \simeq \pi$ for negative yaw angles to phase lock-in at $\varphi \simeq 0$. These phase jumps are equivalent to a wake bistability between the P state (shown in figure 4.11*d*) and the N state of the wake (Grandemange *et al.*, 2013*b*). While the hereabove described adaptation of the unstable wake to the *basic flow* constraints in the vertical direction completely hides the instability in the mean vertical gradient and lift coefficient, the horizontal components are strongly affected. In fact,the instability vigorously manifests itself in the horizontal components.

Based on our experimental observations (see in particular § 4.3.1.9), we propose the following relationship for the instantaneous aerodynamics loading of the body based on a simple decomposition of a steady *basic flow* and the wake instability of strength g_{0r}^*

computed from equation (4.15):

$$c_y(t^*) = C_y^B - \frac{1}{10} g^*_{0r}(\varphi)\cos\varphi \tag{4.18a}$$

$$c_z(t^*) = C_z^B - \frac{1}{10} (g^*_{0r}(\varphi)\sin\varphi)' \tag{4.18b}$$

For the lift (z-component) given in equation (4.18b), only the wake fluctuations appear as a result of the adaptation mechanism described above. Equations (4.18) are similar to equations (4.6) and (4.3) in polar form. The contribution of the instability to the side force estimated as $|C_y - C_y^B| \simeq 0.02$ is clearly identifiable in figure 4.19(b).

Equations (4.18) summarize the observations made in this chapter in the saturated regime of the instability $c^* > c^*_S$. Physically, it indicates that the unstable wake is oriented to match the pressure difference produced by the body obstruction to the flow in the z-direction. It consequently imposes a pressure difference in the other y-direction related to the strength of the instability that mainly depends on the body geometry.

In equations 4.18, there is a factor 1/10 between the force and the pressure gradient contribution. In fact, it corresponds to the ability of the base pressure gradient induced by the wake dynamics to produce a lateral force on the body. Since the base is vertical and normal to the mean flow, there must be other surfaces impacted in order for the pressure loading to produce an actual force. Therefore, we introduce an effective distance ℓ on the lateral walls depicted in figure 4.1(d) on which the base pressure gradient is able to produce a pressure difference Δp_i contributing to the side force f_i $(i = y, z)$:

$$c_y(t^*) = C_y^B - \frac{\Delta p_y H_b \ell}{Q_\infty S} = C_y^B - g^*_y \frac{\ell}{H} \tag{4.19a}$$

$$c_z(t^*) = C_z^B - (\frac{\Delta p_z W_b \ell}{Q_\infty S})' = C_z^B - g^{*\prime}_z \frac{\ell}{H} \tag{4.19b}$$

In equations (4.19), the pressure gradients are expressed respectively as $\Delta p_y/Q_\infty = g^*_y W_b/H$, $\Delta p_z/Q_\infty = g^*_z$, where $Q_\infty = \frac{1}{2}\rho U_\infty^2$ is the dynamic pressure. Besides, the surface scaling unit is taken as $S = W_b \times H_b$, given in table 4.1. Based on the two systems (4.18) and (4.19), the effective distance corresponds to $\ell = H/10$. As a consequence, the base pressure gradient affects the lateral surfaces of the body on a characteristic length of about 10% of its height.

If we now focus on the boat-tailed afterbody presented in § 4.3.2, only the vertical component of the base pressure gradient g^*_z may be subject to large discontinuous transitions while the horizontal component g^*_y varies continuously except for the small discontinuities of g^*_y in figure 4.24(a). The body equipped with the afterbody of this study is therefore subject to a z-instability in the sense of Grandemange *et al.* (2013a).

In this configuration, the mean side force coefficient C_y is not affected by the instability and varies linearly with the yaw angle β (figure 4.30a) and is almost null for all other sensibility analyses (figure 4.30c); no fluctuation crises can be identified either. As a result, $C_y = C_y^B$. The horizontal gradient consequently adapts to that of the basic flow according to equation (4.20) which determines the allowed phase values.

$$G^*_y = \overline{g^*_r(\varphi)\cos\varphi} = G^{*B}_y \tag{4.20}$$

This matching affects the vertical gradient's component which, since the modulus is prescribed, reveals the instability. Each of the discontinuous transitions identified in the sensitivity maps of the gradient's response to alignment modifications (figure 4.22b, figure 4.24*b*, figure 4.27*b*) leads to a bi-stable wake dynamics characterized by the two phase values of $\varphi = \pi/2$ for state P and $\varphi = -\pi/2$ for state N. The notations φ and $\pi - \varphi$ are still adapted to the current study. The state exploration's probability κ is now different from 1/2 which is expected since the $\boldsymbol{e_z}$-axis does not correspond to a Reflectional symmetry axis because of the presence of the ground and of the model's support. Two cases are identified; either $0 \leq \kappa \leq 1$ for bi-stable cases, either simply $\kappa = 1$ or $\kappa = 0$ with a total absence of state switching (permanent phase lock-in).

Based on our experimental observations (see in particular § 4.3.2.6), the side force and the lift coefficients can be derived from a simple decomposition of a steady *basic flow* and the wake instability of strength g^*_{0r} computed from equation (4.15).

$$c_y(t^*) = C_y^B - \frac{1}{5} g^*_{0r} \left((\varphi) \cos\varphi\right)' \tag{4.21a}$$

$$c_z(t^*) = C_z^B - \frac{1}{5} (g^*_{0r}(\varphi) \sin\varphi) \tag{4.21b}$$

For the side force (equation 4.21a), only the wake fluctuations appear as a result of the adaptation mechanism described above. The contribution of the instability to the side force estimated as $|C_z - C_z^B| \simeq 0.02$. Interestingly and despite the different afterbody geometries, this contribution is equal to that of the y-instability.

4.4.3 A general model for the *y*- and the *z*-instabilities

Summing up the previous results, a unique model can be introduced for both situations. First of all, we need to introduce a common framework for the two base geometries. To do so, we introduce the two subscripts M and m respectively related to the *major* and the *minor* components of the rectangular base axes system displayed in figure 4.33. As a consequence, for the y-instability $M = y$ and $m = z$ while for the z-instability $M = z$ and $m = y$. In this new coordinate system, the base pressure gradient can be written as follows:

$$g^*_M(t) = g^*_r(\varphi_M) \cos\varphi_M \tag{4.22a}$$

$$g^*_m(t) = g^*_r(\varphi_M) \sin\varphi_M \tag{4.22b}$$

where the phase φ_M is counted following the direct orientation from the major axis.

The generalized wake model requires a universal definition of the base aspect ratio $\mathcal{W}^*$:

$$\mathcal{W}^* = \frac{l_M}{l_m} > 1 \tag{4.23}$$

where l_M is the length of largest side of the rectangular base and l_m that of the smallest. As a result, for the y-instability, $\mathcal{W}^* = W^*_b$, for the z-instability, $\mathcal{W}^* = (W^*_b)^{-1}$. The wake model can consequently be written with the general expression of equation (4.24) where $g^*_r\text{min}$ stands for the minimum pressure gradient's modulus obtained along the base's minor axis.

$$g^*_r\,(\varphi_M) = \frac{g^*_r\text{min}}{\sqrt{\left(1 - (1 - \frac{1}{\mathcal{W}^{*2}}) \cos^2\varphi_M\right)}} \tag{4.24}$$

With this new formalism, the observed unstable wake orientations match in average the minor component of the base pressure gradient that would be obtained without the

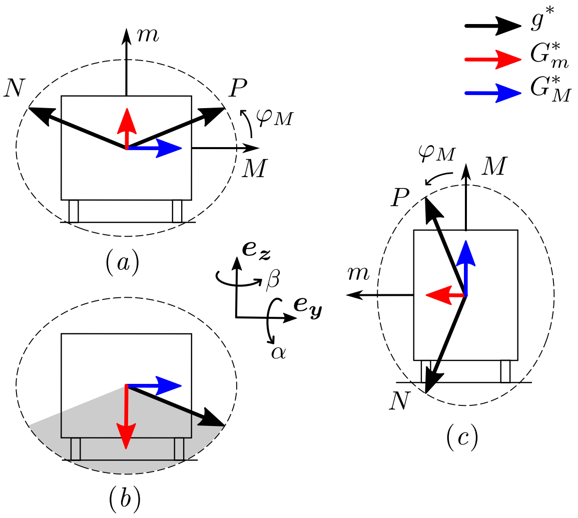

Figure 4.33 – Phase dynamics adaptation of the base pressure gradient of the unstable wake for the $y-$instability (a, b) and z-instability (c). The ellipse plotted with the dashed line corresponds to the modulus of the pressure gradient g_r^* computed from equation (4.24). The mean minor-component G_m^* (in red) adapts from that of the *basic flow*, thus restricting the possible phase dynamics. The bi-stable distribution with the two possible orientations P and N is shown in (a) for nose-down configurations while the grey area in (b) corresponds to the explored phase values for nose-up configuration. The mean major component G_M^* (in blue) depends on the phase probability distribution following equation (4.26b).

instability, *i.e.* that of the *basic flow*. This implies:

$$G_m^* = \overline{g_r^*(\varphi_M)\sin\varphi_M} = {G_m^*}^B \tag{4.25}$$

During wake bistability, the two phases φ_M for state P and $\pi - \varphi_M$ for state N are explored with respective probability κ and $1-\kappa$. The mean minor component G_m^* given in equation (4.26a) determines the value of the phase φ_M. In order to satisfy the modulus value imposed by the model, the mean major component is given in equation (4.26b); the fluctuations are computed in equation (4.26c)

$$G_m^* = g_r^*(\varphi_M)\sin\varphi_M = {G_m^*}^B \tag{4.26a}$$
$$G_M^* = g_r^*(\varphi_M)(2\kappa - 1)\cos\varphi_M \tag{4.26b}$$
$${G_M^*}' = 2\sqrt{\kappa(1-\kappa)}g_r^*(\varphi_M)\cos\varphi_M \tag{4.26c}$$

Two different cases are considered depending on whether the minor axis corresponds to a Reflectional symmetry (y-instability) or not (z-instability). The value of κ is impacted as explained in the associated chapters. An interesting consequence of the adaptation condition is that wake bistability occurs only if the intensity of the minor component is smaller than the modulus $g_r^*(\varphi_M)$. The matching of the minor component with that of the *basic flow*, together with its modulus property, affects consequently the major component that reveals the instability.

Assuming a steady *basic flow*, the instantaneous base pressure gradient $\hat{g}$ of the unstable wake can be written using a Reynolds-like decomposition based on a mean value and on fluctuations:

$$g_m^*(t^*) = {G_m^*}^B + g_m'^*(t^*) \tag{4.27a}$$
$$g_M^*(t^*) = G_M^* + g_M'^*(t^*) \tag{4.27b}$$

Similarly to what was done in §§ 4.3.1.9 and 4.3.2.6, the instantaneous cross-flow force coefficients can be computed from equations (4.27). Similarly, the force coefficients can be decomposed into two parts: a steady one from the *basic flow* and the unstable wake contribution into the fluctuations. It should be highlighted that the basic flow coefficients show a continuous evolution with the body's inclination and ground clearance. We obtain the following system of equations:

$$c_m\left(t^*\right) = {C_m^*}^B + \xi {g^*}'_m\left(t^*\right) \tag{4.28a}$$

$$c_M\left(t^*\right) = {C_M^*}^B + \xi g^*_M\left(t^*\right) \tag{4.28b}$$

where $\xi \in \mathbb{R}$ is a coefficient determined experimentally. It turns out to be $\xi = 1/10$ for the squareback body subject to the y-instability (§ 4.3.1) and $\xi = 1/5$ for the boat-tailed afterbody (§ 4.3.2). Different values of ξ are most probably obtained because the afterbody's geometries are different. Finally, it must be noticed that the mean minor gradient g_m^* is absent in equation 4.28a and replaced by its fluctuations; this is a consequence of the unstable wake adaptation along the minor axis represented by equation (4.26a). The model given in equations (4.28) is confirmed experimentally in § 4.3.1.9 for the y-instability and in § 4.3.2.6 for the z-instability.

To conclude this part, we give an estimation of the contribution of the wake instability to the side force coefficients. We experimentally obtain $\xi|G_M^*(\varphi_M = 0, \pi)| \simeq 0.02$ for this contribution, regardless whether the body is subject to the y-instability ($M = y$) or the z-instability ($M = z$). It is a substantial contribution to the total aerodynamics loading of the bodies since it represents about 7% of the drag coefficient (estimated owing to the cavity, see appendix B) and about 12 to 16% (depending on the geometry) of the lift coefficient of the baselines.

4.4.4 Identification of a drag optimum during wake bistability

This section is focused on the drag of the Ahmed body subject to the z-instability. Its mean value is plotted against the body's inclination in figure 4.29(b, d). Although no big changes nor fluctuation crises (figure 4.29f, h) are observed, the mean value shows an interesting property: it appears to be minimal when a wake bi-stable dynamics takes place as for $\beta \simeq \pm 4°$ or $\alpha \simeq -0.4°$. These cases also correspond to the highest (even if moderate!) fluctuations.

We recall that the wake asymmetry results from a steady bifurcation at low Reynolds numbers (Grandemange *et al.*, 2012*a*; Evstafyeva *et al.*, 2017) and then from the supercritical Hopf bifurcation operated by the ground clearance presented in Grandemange *et al.* (2013*a*); Cadot *et al.* (2015*b*) and discussed for the y-instability in § 4.3.1.2. The stable branches of this bifurcation correspond to the two phases φ and $\pi - \varphi$ of the base pressure gradient explored by the wake during the bi-stable dynamics. Following the idea of Cadot *et al.* (2015*b*), there must exist an unstable branch corresponding to a symmetric flow for which the drag of the Ahmed body should be minimal. This statement is the common motivation of flow control aiming at obtaining a symmetrical wake behind the body corresponding to the *basic flow* considered in this chapter. A few papers on the topic include Grandemange *et al.* (2014*b*); Evrard *et al.* (2016); Li *et al.* (2016); Evstafyeva *et al.* (2017); Lucas *et al.* (2017). These control strategies generally lead to beneficial results in terms of drag since the wake asymmetry is drastically reduced (see appendix B for the effect of a base cavity also considered in Evrard *et al.* (2016) and Lucas *et al.* (2017)). However, in our opinion, the *basic flow* is never obtained. In other terms, the hereabove mentioned strategies do not yield the drag optimum for a given geometrical configuration but only approach it. In addition, a side effect – if not a goal – is the suppression of the bi-stable dynamics which may seem contradictory with respect to the previous statement. From our results, bistability would be rather beneficial to drag. The same apparent contradiction is reported in Bonnavion *et al.* (2017*a*) for a Renault Kangoo at yaw; this case is investigated in details in chapter 7. In the light of Cadot *et al.* (2015*b*)'s results, we can provide the following explanation. The optimum unstable *basic flow* is explored during wake reversals which occur only during bistability; the shorter the characteristic time of the fluctuations, the bigger the drag reduction. As soon as a phase is permanently selected, the unstable state is not explored anymore and drag increases. This statement is in agreement with the observations on the body subject to the y-instability (figure 4.17b, d) although the drag optimum could also be explained by simple geometrical configurations as bi-stable dynamics are obtained when the body is aligned – or almost aligned – with the incoming flow. To summarize, we would like to emphasize that wake bistability does not imply higher drag. However, it is clear that better results would be obtained with the *basic flow* if the instability were to be removed (Cadot *et al.*, 2015*b*; Evrard *et al.*, 2016).

4.5 Concluding remarks

The turbulent wakes of flat-backed Ahmed bodies subject to a saturated y-instability or z-instability have been characterized through sensibility studies against three geometrical parameters: the model's ground clearance and its pitch and yaw angles. The base pressure gradient is used as a topological indicator of the instantaneous wake topology and is described classically using its Cartesian form but also using its polar form which gives a new insight on the results. Its response to the three parameters' changes is assessed in this chapter.

Above the critical ground clearance of c_S^* and for any pitch and yaw angles explored, a large permanent modulus indicates the existence of the static symmetry-breaking instability reported in Grandemange *et al.* (2012*a*). The base gradient modulus is found to be larger when directed horizontally than vertically and, the ratio being close to the base aspect ratio, a basic model derived from that of an axisymmetric wake is proposed to take into account of the rectangular base geometry. It basically aims at predicting the modulus for a given phase, *i.e.* wake orientation.

Three typical dynamics – locks-in, drifts and jumps – are identified for the phase φ of the base pressure gradient. Their exploration depends on the alignment of the body. Results suggest that the phase dynamics is the only key ingredient for the unstable wake when changing the body inclination or ground clearance as the base pressure gradient can be deduced from it thanks to our model. Furthermore, we show in this chapter that the phase dynamics is always constrained in order for the vertical component of the base pressure gradient to equal that of the gradient when the instability is suppressed or equivalently that of the *basic flow*. In addition to the gradient's dynamics, a relationship with the lateral aerodynamic loading (side force and lift force) of the body with and without the instability is proposed with the introduction of an effective length of influence of the base pressure.

In the following chapters, the adaptation mechanism evidenced here is generalized to industrial geometries which might explain the results evidenced in Bonnavion *et al.* (2017*a*) about vertical wake bistability under specific yaw and pitch conditions for a real minivan.

CHAPTER 5

Boat-tailing effect on the unstable wake of the Ahmed body

This chapter aims at identifying the role played by the introduction of a boat-tailed afterbody on the unstable wake dynamics of a flat-backed Ahmed body. As a preliminary study, we conduct some simple potential flow two-dimensional simulations in § 5.2 to check whether some simple mechanisms can be identified. A tunable afterbody (§ 5.3) is installed on the model. It can be used in a squareback configuration (§ 5.4.1) or with one or two boat-tails. First, a global optimization is conducted in § 5.4.2 in order to recover the results presented in the literature. We then investigate separately the consequences on drag (§ 5.4.3) and on the cross-flow forces (§ 5.4.4), considering the mean and fluctuating values. The wake dynamics explaining those findings and its dependency towards the boat-tail angles is studied in details in § 5.4.5. Afterwards, the impact of the bot-tail geometry on the aerodynamic loading and on the wake dynamics is presented in § 5.4.6. Finally, a 3D boat-tailed afterbody further reducing drag is studied in § 5.4.7. A discussion follows in § 5.5. The main result of the chapter is that boat-tails control the wake orientation without suppressing the instability which consequently impacts the cross-flow loading in a similar manner as for squareback afterbodies. The key results of this chapter are under consideration for publication in Journal of Fluids and Structures.

Contents

5.1 Literature review 93

5.2 Preamble: two-dimensional potential flow approach 98

5.2.1 Computational setup 98

5.2.2 Wake estimation 99

5.2.3 Results 100

5.2.4 Short conclusion 104

5.3 Experimental setup 105

5.4 Results 107

5.4.1 Baseline: squareback afterbody 108

5.4.2 Shape optimization with boat-tails 109

5.4.3 Contribution to drag 112

5.4.4 Contribution the cross-flow loading 116

5.4.5 Effect on the wake dynamics 117

5.4.6 Influence of the boat-tails' geometry on the aerodynamic loading and on the wake dynamics 126

5.4.7 Three-dimensional boat-tail 131

5.5 Discussion 133

5.5.1 On the two-dimensional mechanism related to boat-tailing 133

5.5.2 Impact on the unstable wake modes 134

5.5.3 Strength and orientation of the wake mode 134

5.5.4 Importance of boat-tails locations 136

5.5.5 Control of the aerodynamic loading 138

5.6 Concluding remarks 138

5.1 Literature review

We first define the terminology that will be used throughout the chapter; different afterbodies are schematically represented in figure 5.1, for a top/bottom boat-tailed geometry (figure 5.1*a*) and a three-dimensional one (figure 5.1*b*). The vertical blunt afterbody – corresponding to a separated flow area – is referred to as the *base* while the inclined parts, regardless of their geometries or locations – top, bottom or sides of the afterbody – are designed as *boat-tails* (BT in figure 5.1). Throughout the literature, diffusers, slants or spoilers are equivalently used. Our formalism is equivalent to that used in Han *et al.* (1992) and, as a consequence, *afterbody* refers to the ensemble {base + boat-tail}.

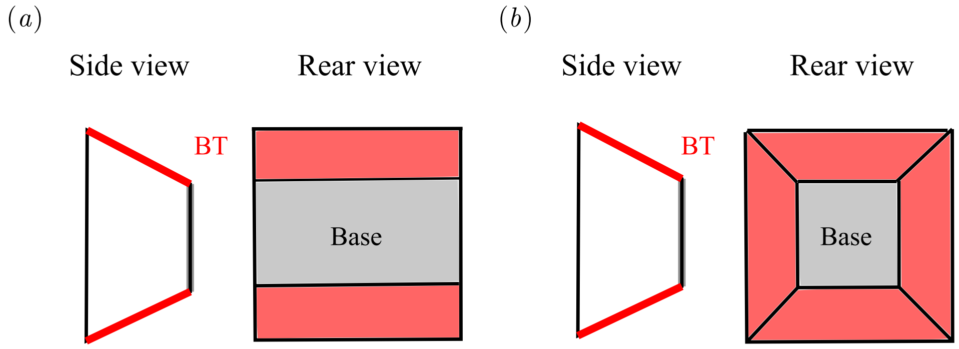

Figure 5.1 – Definitions of the base (vertical blunt geometry in grey) and of the boat-tails (in red) for two afterbodies in Side and Rear views: (*a*) top/bottom boat-tailed geometry, (*b*) three-dimensional boat-tailed geometry

One of the first studies regarding boat-tailing was conducted by Nash *et al.* (1963), who performed some two-dimensional computations around a symmetrical body equipped with boat-tails and studied their effect on the base pressure. They found that a reduction of the trailing edge section – corresponding to the base section in three-dimensional cases – leads to lower drag values because of base pressure recovery; the base pressure coefficient can even become positive yielding a zero or even negative base suction. However, it is not possible to cancel the total drag since negative pressure coefficients are still observed around the afterbody. With a streamlined geometry and without a blunt base, *i.e.* introducing a trailing edge as for an airfoil, a rear stagnation point can be created; however, the authors do not confirm whether this corresponds to a minimal drag or not. Under the simplifying hypothesis of a two dimensional potential flow up to separation[1] – corresponding to an infinite Reynolds number since no boundary layer develops –, a quick base pressure increase leading to a reduction of the total afterbody drag is identified with the increase of the boat-tail angle.

In the late 1960's, Mair (1969) stated that *"it has been known for many years that in low-speed flow the drag of a blunt-based body of revolution (...) may be reduced by the addition of a boat-tailed afterbody"*. In his pioneering work, an analysis is provided changing the boat-tail shapes. The Reynolds number is of the order of $\mathrm{Re} \simeq 4.6 \times 10^5$ based on cross-flow dimensions. Only the base drag is assessed and the total length of the body is modified. The authors report that small changes of the body's incidence (below 2°) were considered without significant changes on the results. Changing the afterbody geometry towards more streamlined cases with a long afterbody (more than 2.6 times the diameter) in order to mimic a water drop leads to a reduction of base drag by 72%, which can be related to the reduction of the body's bluffness as stated by Roshko (1954*b*, 1955, 1993). Despite the encouraging results, these geometries do not comply with the industrial constraints, *inter alia* regarding the vehicle's length or payload. Besides, these studies only concern axisymmetric bodies; we mentioned earlier that they are poorly representative of automotive shapes.

---

[1] As previously defined by Kirchhoff (1869) and Brillouin (1910), the flow can be modeled in the scope of the Free Streamline Theory with a potential region and a viscous recirculating bubble delimited by a separating streamline. This representation is considered in § 5.2 for a simple two-dimensional model. A theoretical approach can be found in Roshko (1954*a*).

Mair (1969) reports that excessive boat-tail length (above one radius of the body) does not provide additional drag reduction regardless of its geometry; an efficiency drop can even be observed for complex shapes such as quartic boat-tails[1]. It also appears that even-ordered polynomial functions giving the shape of the afterbody (second or fourth order) yield significantly better results than third order ones. In view of the large considered angles, the author report a possibly moving upstream separation point with the creation of a recirculating bubble degrading the aerodynamic performance of the model. Reducing the length of the boat-tails and their radius of curvature yields to an important result: the author states that the most important drag reduction is to be achieved, for a short afterbody, by using the largest possible angle without causing flow separation on the boat-tail. Considering elliptical afterbodies with different semi-apex angles, the author study the pressure distribution on the boat-tail that, again, depends on its length. It turns out that a low-pressure area appears on the circle arc for large angles before pressure increases because of the diffuser effect.

Similar conclusions as those of Mair (1969) are reported by Mariotti *et al.* (2017) on axisymmetric geometries. A relationship is found between the boat-tail angle and its drag reduction effectiveness, in particular as regards base suction. However, the authors note that the contribution of the slanted surface to the total drag is not to be neglected. They also report that separation and reverse flow might occur for large angles. In addition, the authors provide the base pressure distribution along the boat-tailed surfaces. They observe a pressure drop at the beginning of the curved shape and then a continuous pressure recovery, similarly to a diffuser. An interesting mention of the streamlines' curvature is made in the paper. The authors notice that a convex curvature of the streamlines and an acceleration of the flow outside the boundary layer over the lateral surface is created by the boat-tails, which decreases the pressure but is counterbalanced by a concave curvature of the streamlines in the wake with an appreciable base pressure recovery. The effectiveness of boat-tailing regarding drag reduction is also reported by Maull & Hoole (1967) for cylinders. The authors report that for angles as small as 2°, they were able to achieve a 20% pressure drag reduction. They also highlight that the wake vortices forming nearer the body (Bearman, 1965) and thus increasing the base suction are compensated by a base pressure recovery on the body. In addition, this paper provides a validation of theoretical results on boat-tails developed by Nash (1964).

Since the pioneering works on axisymmetric bodies, other researchers such as Hucho (1978); Garry (1981) have shown that reductions of the drag coefficients of vehicles and lorries by about 30% could be obtained by means of rounded afterbody trailers geometries. In a complete study, Wong & Mair (1983) consider a long body of square cross-section at a Reynolds number of $\mathrm{Re} \simeq 4.6 \times 10^5$ based on cross-flow dimensions. The authors first consider four-sided slanted afterbodies (referred to as *type A* afterbody) of length 0.49 times the diameter of the model. For limited angles of less than 30° with respect to the tangential line to the body, their results agree with those of Mair (1969) on axisymmetric bodies and drag reduction up to 100 counts[1] is observed. However, an increase is observed and ascribed to flow separation is the angle is further increased. Regarding the length, they find that the maximum reduction is reached around one diameter without additional gain for longer boat-tails. It is also reported that a sharp corner increases drag unlike fairings for a given geometry. Reduction is related to a pressure recovery on the boat-tail as long as the flow remains attached, also assessed in Payne *et al.* (1980). Afterwards, a two-sided slanted afterbody (referred to as *type B* afterbody) is studied. Unlike for the previous geometry, only angles smaller than 20° provide a reduction of drag, the force being significantly increased otherwise, in agreement with Morel (1978). The longer the boat-tail, the larger the loss of efficiency. It is ascribed to longitudinal vortices developing on the inclined geometries and opens new perspective for drag reduction in presence of such longitudinal vortices.

---

[1] Quartic refers to a function of the fourth polynomial order.

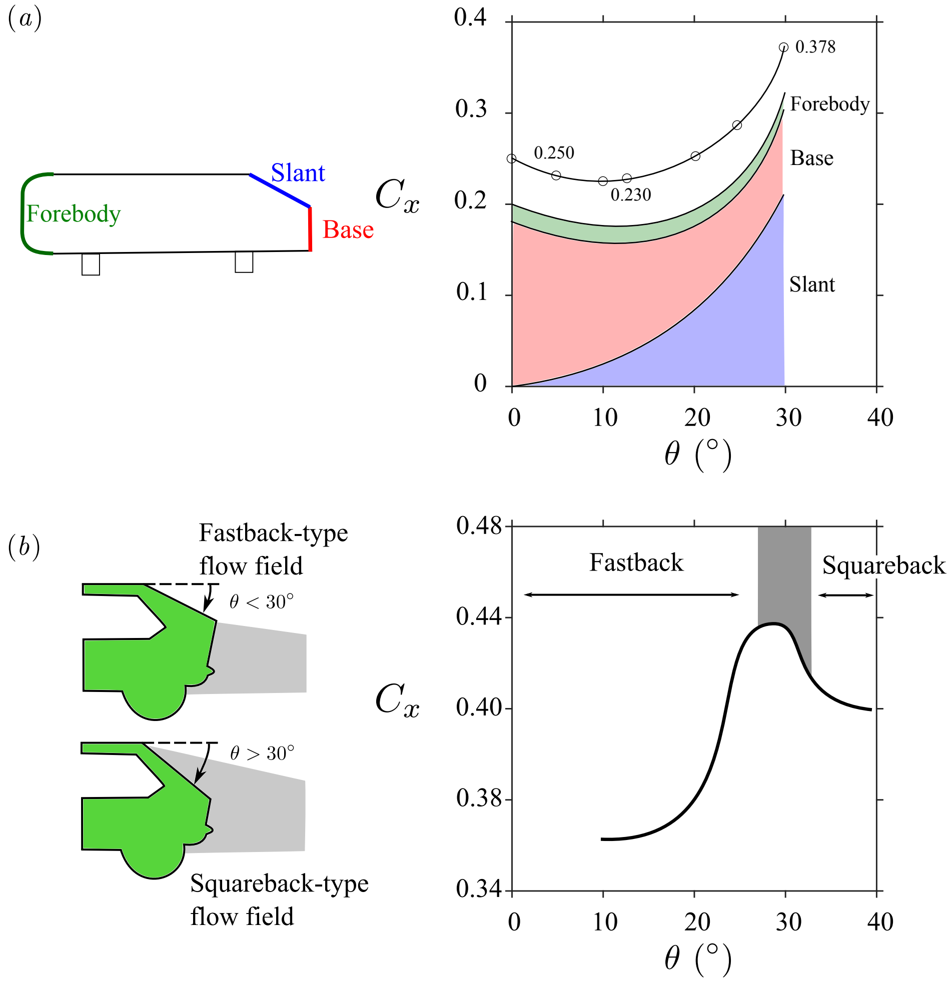

Figure 5.2 – (*a*) Variation of drag coefficient C_x of the Ahmed body with base slant angle θ. Figure adapted from Ahmed *et al.* (1984). The colors correspond to the different parts of the body: green - forebody, blue - slant, red - vertical blunt base. (*b*) Influence of rear-end inclination angle on drag coefficient C_x, separation line and wake formation, adapted from Hucho (1978).

Following the work of Wong & Mair (1983), further analyses were performed by Ahmed (1983); Ahmed *et al.* (1984) on the so-called Ahmed body. In this paper, the authors report that, increasing the body's slant angle, the contribution of the front part and of the rest of the body to drag is left unchanged while that of the base decreases significantly. However, the contribution of the slant is continuously increasing with its angle which yields an optimum for the total afterbody drag, found around 12° (figure 5.2*a* in which θ is the base slant angle and C_x the drag coefficient, adapted from Ahmed *et al.* (1984)). The perspective of drag reduction for real vehicles by means of boat-tailing is also emphasized by Hucho (1978) who reports a drag optimum for rear slant angles just after the transition from *fastback* to *hatchback* flow configurations, *i.e.* around 30° (figure 5.2*b*, reproduced from Hucho (1978)). The author also shows that drag may actually increase if the angles are not well chosen.

---

[1] A drag count is defined as a contribution of 10^{-3} to the drag coefficient c_x.

The Ahmed model's geometry is also considered by Han *et al.* (1992) in a numerical study. They show that, regardless of the angles and location of the boat-tails (side, spoiler or diffuser), base pressure increase up to the point where it sometimes overwhelms that of the free-stream ($C_p > 0$). Base suction consequently follows the reverse trend and even becomes negative in the latter case. Besides, the effect is enforced by the reduction of the base surface; the contribution of the detached flow area to drag is consequently strongly lower than for a squareback afterbody. Each of the boat-tails drag coefficient is found to increase with the angle. The striking result of this paper is that, in some cases, the drag of the boat-tailed body is larger than for the squareback. The optimum of drag is found for a backlight angle of 17.8°, a boat-tail angle of 18.9° and a ramp angle of 9.2°, with a decrease of 47.3% with respect to the squareback. In addition, a sensitive impact on lift is reported by the authors. The aerodynamic loading modifications are ascribed to the longitudinal vortices developing on the boat-tails which are strengthened. The effect however seems to match with the potential theory of vortices in ground proximity (Prandtl & Tietjens, 1934) as they generate a strong upwash / downwash disturbing the wake and responsible for drag increase. Consistently with the results reported by Bearman (1984) for a cylinder, weakening them reduces their contribution to the loading.

Recently, Grandemange *et al.* (2013*c*) derived a quadratic expression for the drag force – and a linear relationship for the lift – between the boat-tail angles and the mean loading applied on a flat-backed Ahmed body. For the first time, the contribution of the wake asymmetric state can be observed since wake reversals resulting from the use of different angles are identifiable thanks to velocity fields. A drag optimum is identified but for smaller angles than in previous papers: 10° at the top and 7.5° at the bottom. In particular, it appears that the optimum is reached for much smaller angles in three-dimensional than in two-dimensional cases which shows that the spanwise dimension has an important role in drag contribution. The contribution of the base to drag is reduced but counterbalanced by that of the slant, which results in a parabolic dependency between the angle and the drag as shown by several studies (Ahmed, 1983; Grandemange *et al.*, 2013*a*, 2015). In Grandemange *et al.* (2013*a*, 2015), the contribution of the boat-tails is separated in two parts. One corresponds to the pressure distribution which generates pressure drag, the other is ascribed to induced drag and therefore related to lift. Recently, Kim *et al.* (2016) presented a bio-inspired device for drag reduction changing the wake of the slanted Ahmed body; it consists in a movable rear spoiler whose angle can be adapted to reattach the flow. This technique provides quite good results (up to 17% drag reduction, thus retrieving the configuration of Ahmed (1983)) and highlights the importance of controlling the flow around a boat-tailed geometry.

Similar investigations were performed on the simplified Windsor model, starting with the work of Howell & Le Good (2008). Later on, Littlewood & Passmore (2010) tested the effect of a rear slant varying its angle from 0° to 20°. A drag optimum is found for 12° (2.7% drag reduction) in agreement with Ahmed (1983) or Howell & Le Good (2008), while the lift linearly increases with the chamfer angle. Perry *et al.* (2015, 2016*b*) further investigates this geometry with oriented base tappers located at the bottom and at the top of the blunt afterbody. The authors report that for angles smaller than 16°, the flow remains fully attached on the slants and full separation is observed above 20°. In the attached regime, three main results are reported. First, if only a bottom tapper is installed (top geometry similar to the squareback), drag increases regardless of the angle; in other configurations (top only or combined), the authors first report a decrease and then an increase of drag, with a minimum for 12° in agreement with Littlewood & Passmore (2010). The lift is obtained as a linear function of the angle. Second, the wake static asymmetry is not removed and, if a bi-stable wake dynamics is observed, Perry *et al.* (2016*b*) report that the switching frequency increases with the tapper's angle. Finally, base pressure distributions and PIV fields show that the wake is symmetrized in the horizontal plane with tappers – while it was initially asymmetric for the squareback. However, the asymmetry is transferred in the vertical plane; the velocity fields are almost similar but shifted by 90°. The same wake reorganization (velocity fields and base pressure), shift frequencies and relationships between tappers angles and the aerodynamic loading are retrieved in Pavia *et al.* (2016). However, despite an asymmetric wake, these paper do not bring any insight on the influence of the boat-tails on the asymmetric wake state.

The experiments with Ahmed bodies were extended to the industrial scale in Grandemange *et al.* (2015) in which the authors recover identical trends as in the model scale experiments for the drag and lift applied to the body. Besides, very similar base pressure distributions and wake topologies as those of simplified geometries are retrieved in the numerical study of Kabanovs *et al.* (2017*b*) dealing with a more realistic SUV geometry with wheels. Varney *et al.* (2017) report identical results and, interestingly, a similar effect is obtained when boat-tailing the sides of the base in the upper part only. Afterbody's boat-tailing is widely spread in transportation engineering with ground vehicles equipped with spoiler, diffusers… In optimal configurations, the flow remains attached along the boat tail with a developing boundary layer that grows substantially due to the adverse pressure gradient. While the initial curvature of the boat tail produces a low pressure detrimental for drag, the slant introduces a pressure recovery able to reduce the base suction in the separated region. The boundary layer growth limits the pressure recovery that will saturate once the potential flow does not decelerate any more (Mair, 1969).

A review of drag reduction capabilities offered by boat-tails on trailers is given in Landman *et al.* (2009) with reported reductions up to 20%. The focus is also set on the practical limits of such geometries. With a simplified geometry equipped with wheels, Peterson (1981) achieves up to 30% drag reduction with boat-tails at a speed of 100 km.h^{-1}. Applications on model-scale trailers equipped with inflatable boat-tails are reported in Leuschen & Cooper (2006). Besides, Lanser *et al.* (1991) obtained 10% drag reduction by a well-chosen combination of boat-tail angles on a trailer when aligned with the incoming flow and the impact of the afterbody rounding was confirmed by Buresti *et al.* (1997). More generally, almost all series vehicles have been optimized with diffuser and spoiler angles during their development; general know-how methods spread out during the last decades. As a result, the boat-tail effect on drag or lift is quite well-known but apart from few observations made by Perry *et al.* (2016*a*,*b*) and Pavia *et al.* (2016), there have not been thorough study on the asymmetric (and unstable) wake state and the literature consequently lacks references about the consequences of boat-tailing. This chapter therefore aims at retrieving the previously reported results and at assessing the impact on the wake dynamics from a fundamental point of view.

5.2 Preamble: two-dimensional potential flow approach

The aim of this section is to provide an approach of the boat-tailing effect based on a two-dimensional potential flow with a wake developing behind the body. It is modeled using Kirchhoff (1869) and Brillouin (1910)'s approaches on Helmholtz separated flows and Free Streamline Theory[1] with a recirculation bubble of prescribed constant pressure separated from the main potential flow by a separation streamline. As a matter of facts, early works by Nash *et al.* (1963) and more importantly Mair (1969) mention the wall-pressure distribution; three-dimensional effects such as vortices are not considered in these works. Besides, Maull & Hoole (1967)'s results on two-dimensional bodies are comparable suggesting that a simple approach can be performed.

The potential flow problem is defined using the streamfunction Ψ given in equations (5.1), whose derivatives may be related with the x-component of the velocity field u and the z-component of the velocity field w. The coordinate system is identical as that considered so far; the problem is thus solved in the $y^* = 0$ plane.

$$u = \frac{\partial \Psi}{\partial z} \tag{5.1a}$$

$$w = -\frac{\partial \Psi}{\partial x} \tag{5.1b}$$

The streamfunction Ψ is defined by integration and therefore obtained up to a constant. We arbitrarily impose $\Psi_{body} = 0$ on to the body, considered as a solid line. Under the previous assumptions, one must solve a Laplace problem whose governing equation is:

$$\nabla^2 \Psi = 0 \tag{5.2}$$

The associated boundary conditions for the streamfunction are $\Psi_{body} = 0$ considering the body as a solid line and $\Psi_\infty = U_\infty \times z$ corresponding to a uniform parallel flow at infinity. The upper limit of the domain is given an impermeability condition $\Psi_\infty = 10\ U_\infty \times H$ and the only outlet condition is imposed by the weak formulation since $\frac{\partial \Psi}{\partial n}|_{outlet} = 0$.

We first present briefly the computational setup (§ 5.2.1) and turn to the definition of the wake model based on the separating streamline (§ 5.2.2). The results are presented in § 5.2.3.

5.2.1 Computational setup

The computations are performed in a two-dimensional space using the FreeFem++ software (Hecht, 2012). It is a partial differential equations solver using a $C++$ idiom as language. FreeFem++ uses the finite elements method and the weak formulation of any variational problem. The Laplace equation solved in our example has therefore to be expressed in its variational form given in equation (5.3) where f is arbitrarily chosen (test function). The weak formulation of the problem implies that quantities' normal derivatives are null unless specified by the mean of a line integral (on the domain boundary). For this specific case, it makes sense as the flow returns to its undisturbed state at the downstream-infinity in the potential approximation.

---

[1] The difference between the Helmholtz flow and the Free Streamline Theory is that the Helmholtz wake is for a zero pressure coefficient in the separated region, *i.e.* an infinite bubble, *vs.* a finite wake in length in the second case.

$$\int_{\Omega} \nabla\Psi \cdot \nabla f = 0 \tag{5.3}$$

We use FreeFem++'s automated mesh tool which creates a Delaunay triangulation of the convex hull of the set of points. It is a triangulation where none of the points of the domain is included inside the circumscribed circle of any of the triangles of the plane. It consequently avoids to obtain elongated and skinny triangles as the smallest angle of all the triangles is maximized.

The two-dimensional body used in this simulation is shown in figure 5.3(a) with its characteristic dimensions. The forebody is a quarter of a circle; it is followed by a flat part corresponding to the model's roof and a slanted rear part. The slant angle is denoted θ_T. Finally, the body is terminated by a vertical base. The horizontal dimension of the slant, denoted ℓ_S, varies. The computational domain, sketched in figure 5.3(b), starts 3 H ahead of the body and terminates 8 H downstream. Its height is 10 H to avoid any blockage related effect.

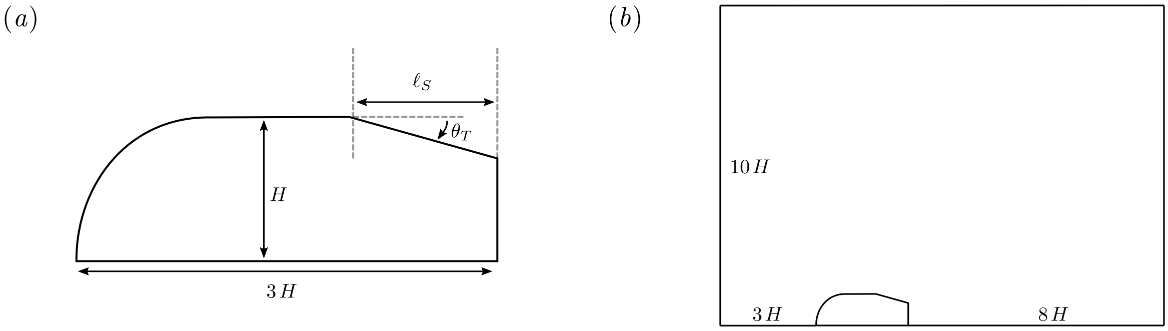

Figure 5.3 – Setup of the potential flow simulation: (a) schematic side view of the body with characteristic dimensions and (b) computational domain.

The two investigated parameters are the slant angle and its length. First, we change the slant angle for a given length. The angle is chosen in $\theta_T \in \{0°, 5°, 10°, 15°\}$; this case is reproduce three times with $\ell_S = 0.1\ H$, $\ell_S = 0.33\ H$ and $\ell_S = H$. Second, for a given geometry, we can investigate the effect of the slant's length. Such simulations also allow to change the recirculation length even if it is not the case in the experiments unless control is performed but investigating the consequences of such flow topology modifications might be full of insight. We estimate drag based on the wall-pressure distribution on the body. The contribution of several parts is estimated: the forebody consisting in the circle-arc and of the rectangular shape, the slant and the vertical part.

5.2.2 Wake estimation

This simulation is based on the Free Streamline Theory described in Brillouin (1910). The outer wake is a potential flow and the wake is separated from the mean stream by a separating streamline of constant pressure or equivalently[1] of constant velocity magnitude. In this simulation, we impose the recirculation length and we iterate to form the actual separating streamline. The velocity is computed at each node of this streamline, initialized as a straight line between the blunt afterbody – where separation actually occurs as mentioned earlier in chapter 3 – and the ground. We move the points up and down in order to reach the most constant velocity in the limit of 2% between each points. We assume that no flow separation will occur on the slant of the body and therefore keep the angle reasonably small. With this model, the pressure is constant in the recirculation bubble and equal to that of the separating streamline. In terms of streamfunction, it is described by $\Psi = 0$ similarly to the body's surface. As a consequence of the free streamline theory model, the pressure on this separating line in the wake area is constant.

---

[1] Simply applying Bernoulli's equation in this potential flow problem.

5.2.3 Results

We first set the length of the recirculation bubble to 2 H; this is much shorter than that behind a two-dimensional backward-facing step (Armaly *et al.*, 1983; Dahan *et al.*, 2012) but is more realistic for a three-dimensional bluff body (see chapter 3). The slant length is fixed to $\ell_S = H$ and the angle is varied. The flow streamlines are shown in figure 5.4. The streamlines are parallel upstream of the body (notice that not the whole domain is represented in figure 5.4 so that the size remains acceptable) and deviate at the forebody section. The blockage is quite low since the streamlines located at the top of the domain are not impacted and remain parallel. In the forebody region, they become closer which corresponds to higher velocity magnitudes and thus lower pressures. Just upstream of the massive separation modeled using the Free Streamline theory, the flow is parallel so that the influence of the upstream geometry of the body can be neglected. The separating streamline (in green) divides the wake and the inviscid flow region. It is curved with increasing concavity moving downstream and becomes nearly vertical in the bubble closure vicinity. This generates an inverted curvature to the other flow streamlines with a stagnation point at reattachment. At the end of the domain, they are nearly parallel so that the conditions are identical to the inlet's. The same flow topology can be observed for the squareback (figure 5.4*a*) and the slanted (figure 5.4*b*) configurations; the only difference is related to the afterbody shape and thus that of the wake since the separating streamline is tangent to the body's rear end (normal flow separation). This particular streamline $\Psi = 0$ corresponds to the free streamline and appears in green in figure 5.4.

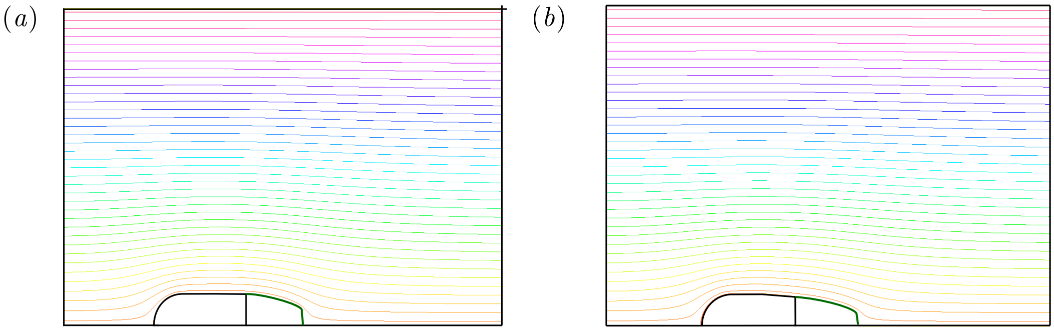

Figure 5.4 – Wake and inviscid flow streamlines for the 2D simulation with $\ell_S = H$ and $\ell_{rb} = 2\ H$: (*a*) squareback configuration $\theta_T = 0°$ and (*b*) slanted case $\theta_T = 5°$. The streamlines are colored by the value of the streamfunction Ψ imposed at $\Psi = 0$ on the body. The free streamline appears as the thick green one in the figures.

The pressure distribution along the body and the separating streamline is shown in figure 5.5(*a*). A stagnation point is identified at the front of the body where $C_p = 1$ and the pressure distribution on the circle-arc ($-3 \leq x^* \leq -2$), identical for all cases, shows a continuous drop with a minimum at the junction between the circle and the roof where flow separation could occur in real cases (see chapter 3). For the squareback model ($\theta_T = 0°$), the pressure increases and then slightly drops ahead of the flow separation and is then

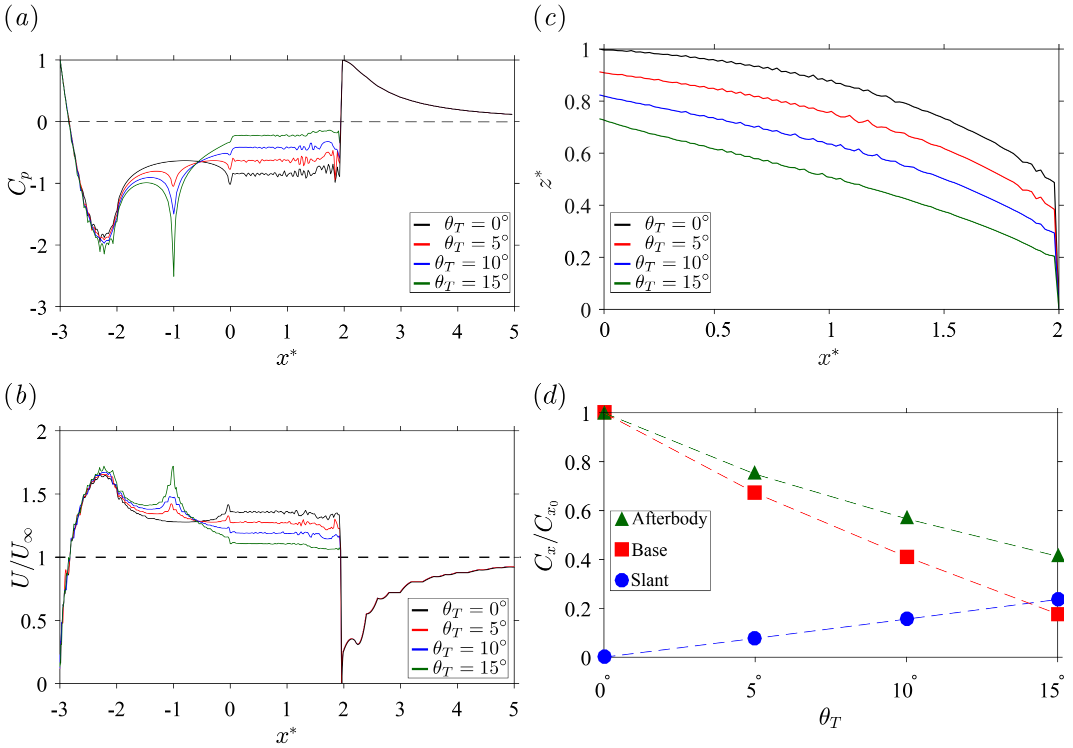

Figure 5.5 – Wake simulation based on the Free Streamline Theory with length of the recirculation bubble set to 2 H and slant length to $\ell_S = H$. (a) Pressure distribution and (b) velocity magnitude along the body and the separating streamline; the dashed line stands for free-stream conditions. (c) Geometry of the separating streamline for $\theta_T \in \{0°, 5°, 10°, 15°\}$ after the iterative process is terminated. (d) Contribution to the drag coefficient of the whole afterbody (green triangles), of the slant (blue dots) and of the vertical base (red squares) compared to the total drag of the squareback geometry C_{x_0}.

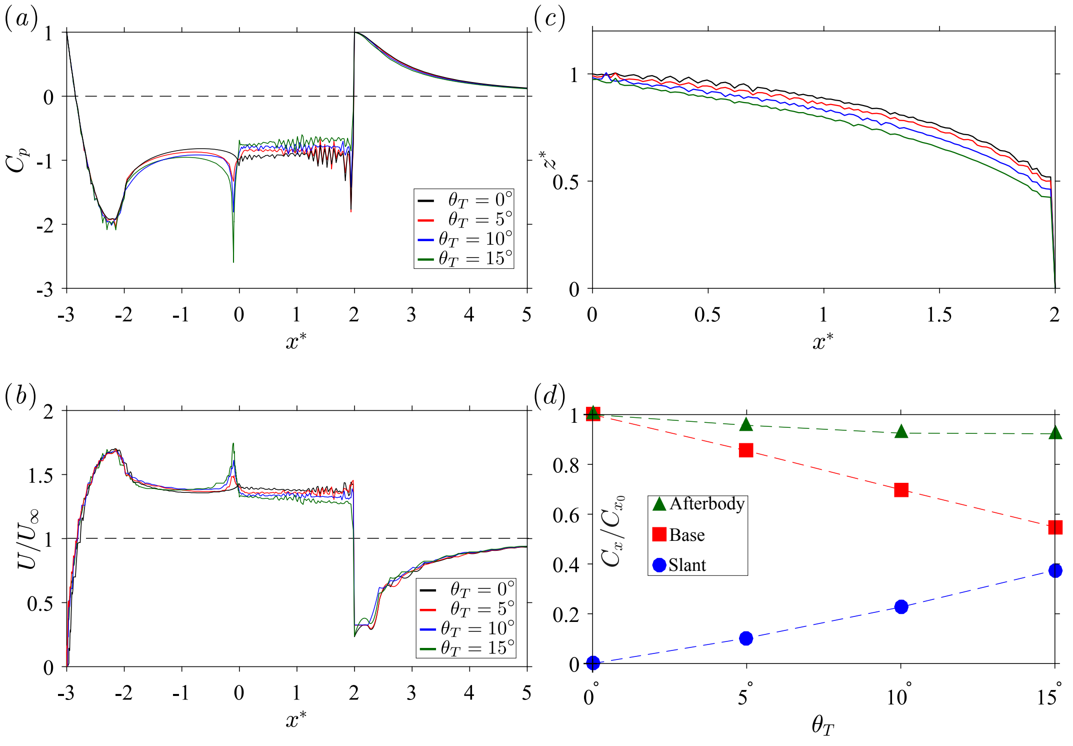

Figure 5.6 – Wake simulation based on the Free Streamline Theory with length of the recirculation bubble set to 2 H and slant length to $\ell_S = 0.1\ H$. (a) Pressure distribution and (b) velocity magnitude along the body and the separating streamline; the dashed line stands for free-stream conditions. (c) Geometry of the separating streamline for $\theta_T \in \{0°, 5°, 10°, 15°\}$ after the iterative process is terminated. (d) Contribution to the drag coefficient of the whole afterbody (green triangles), of the slant (blue dots) and of the vertical base (red squares) compared to the total drag of the squareback geometry C_{x_0}.

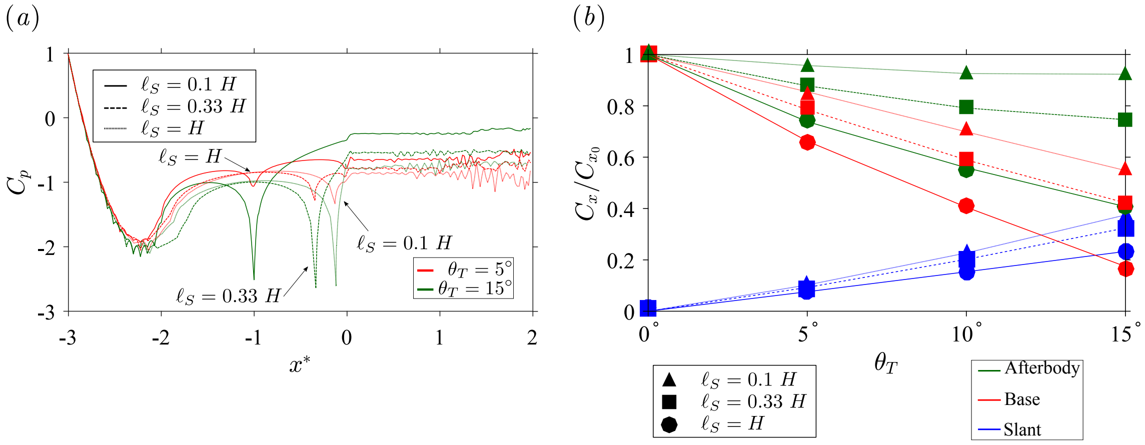

Figure 5.7 – Free Streamline Theory wake simulation with length of the recirculation bubble set to 2 H variable slant length. (a) Pressure distribution along the body and the separating streamline $\Psi = 0$. (b) Contribution to the drag coefficient of the whole afterbody (green curves), of the slant (blue curves) and of the vertical base (red curves) compared to the total drag of the squareback geometry C_{x_0}. Continuous line and circles for $\ell_S = H$, dashed line and squares for $\ell_S = 0.33\ H$ and dotted line and triangles for $\ell_S = 0.1\ H$.

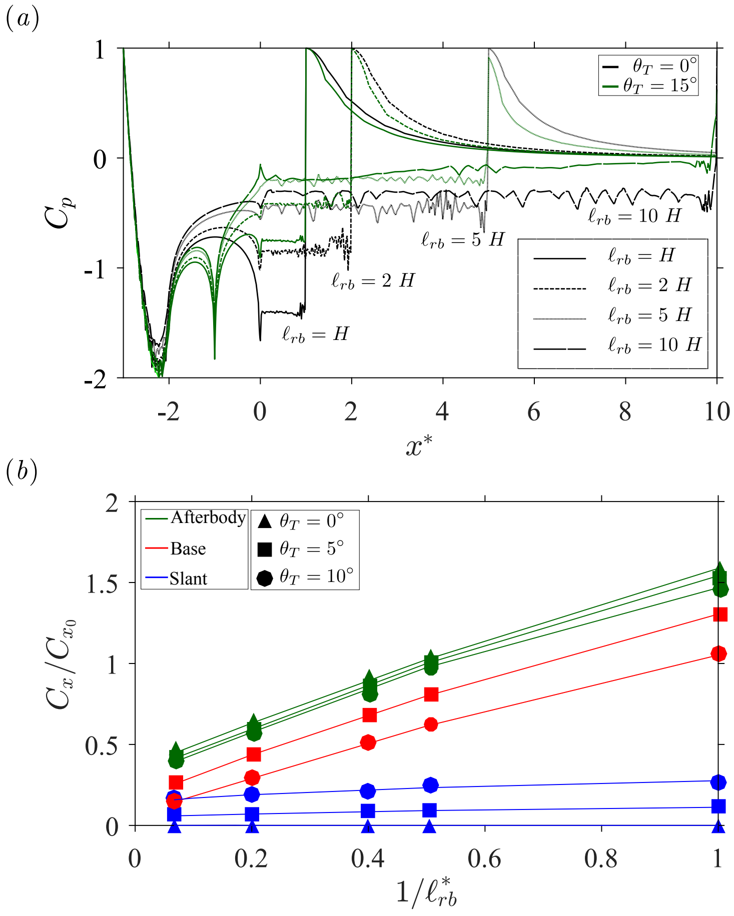

Figure 5.8 – Influence of the length of the recirculation bubble for a slant length of $\ell_S = H$ at various angles. (a) Pressure along the $\Psi = 0$ streamline: squareback configuration $\theta_T = 0°$ in black and $\theta_T = 15°$ in green. The various line styles are defined in the figure and associated with a bubble length. (b) Contribution of the base (red), of the slant (blue) and of the whole afterbody (green) to pressure drag *vs.* inverse of the recirculation length (made dimensionless using H) $1/\ell^*_{rb}$ for the slant angles $\theta_T = 0°$ (triangles), $\theta_T = 5°$ (squares) and $\theta_T = 10°$ (circles). The drag is expressed compared to the total afterbody drag C_{x_0} for a reference length arbitrarily chosen as $\ell_{rb} = 2\ H$.

constant due to the Free Streamline model. The same kind of distribution is observed on the roof of the model ($-2 \leq x^* \leq -1$) except that the singularity introduced by the change of curvature between the horizontal roof and the inclined slant – without fairings – leads to a strong but localized low pressure that consequently modifies the distribution both upstream and downstream by continuity. There is then a pressure recovery on the slant ($-1 \leq x^* \leq 0$) in order to match the level imposed at the separation point by the bubble length (see below). The pressure along the bubble separating streamline ($0 \leq x^* \leq 2$) is constant up to the convergence of the iterative process; there is again a stagnation point at $x^* = 2$ that can be explained by the sharp geometry of the bubble in the closing region (figure 5.5*c*) since no closure model is imposed. Afterwards, there is a smooth pressure decrease until free-stream conditions are reached asymptotically. It is noticeable that the flow properties in this region do not depend at all on the considered boat-tail angle. The velocity on the line $\Psi = 0$ can be deduced from Bernoulli's equation and is plotted in figure 5.5(*b*). The singularity at $x^* = -1$ provokes large velocity magnitudes while increased slant angles reduce the separating streamline's velocity as a proof of the reduction of the body's bluffness. The two upstream and downstream stagnation points are identified and the velocity is progressively increased downstream of the body to recover the inviscid free-stream conditions. Comparing the geometry of the free-streamline for all considered angles (figure 5.5*c*), it turns out that the only noticeable difference is that, when the angle is increased, its curvature is reduced since its end points – separation point and bubble closure – are prescribed. There is consequently a transfer of curvature from the recirculation bubble to the flow streamlines which is responsible for low pressure levels. Finally, the contribution of each part of the body to the pressure drag is estimated by integration of the pressure distribution at various slant angles (figure 5.5*d*). The drag of the whole afterbody (green triangles), *i.e.* the vertical base and the slant, is found to decrease; however, it does not follow a linear sink since its rate reduces for larger angles. An explanation can be found if one have a look at the separate contribution of the vertical base (red squares) and of the slant (blue circles). The base suction – integrated over the vertical part only – decreases almost linearly with the angle which can be explained by two distinct phenomena. First, as mentioned in figure 5.5(*a*), the mean base pressure increases with the boat-tail angle. Second, the base surface reduces. On the contrary, the contribution of the slant to drag increases linearly with the angle because of the low pressure introduced by the singularity that the diffuser effect is unable to compensate (figure 5.5*a*). The slant drag is not negligible for large angles and even overwhelms that of the base. Notice that unlike in the experiments reported in the papers of Ahmed (1983) or Wong & Mair (1983), the Free Streamline Theory flow solution does not lead to a pressure optimum in the tested configuration. The difference between the cases is that experiment are conducted with three-dimensional bodies while we are here addressing a two-dimensional problem. The physics associated with the third dimension is consequently responsible for the optimum.

For a shorter slant of length 0.1 H, the results presented in figure 5.6 are very similar. From the front stagnation point, the pressure drops continuously on the circular forebody and then increases on the roof until it starts to strongly decrease until the beginning of the slant; the bigger the slant angle the lower the pressure at the singular point and the stronger the recovery up to separation. The presence of the singularity is well identified on the velocity field with a sudden increase and decrease (figure 5.6*b*). Since the slant is small, the geometry of the separating streamline is almost identical for all cases (figure 5.6*c*). The total afterbody drag decreases slightly as shown in figure 5.6(*d*). The beneficial effect on the base suction – surface reduction and pressure increase – being almost overwhelmed by the contribution of the slant to drag. Similar results are obtained with the other recirculation lengths although not presented in the manuscript. The important point is that slants lead to higher base pressure – and thus lower base suction – thanks to a recovery but that the pressure at the singularity drops with the angle and therefore largely contributes to drag, showing that a compromise between both phenomena must be found in view of drag reduction.

The second study is conducted for a given slant angle while its length is varied. For the sake of clarity, only the angles $\theta_T = 5°$ and $\theta_T = 15°$ are presented in figure 5.7(a) for the three considered slant lengths $\ell_S = 0.1\ H$, $\ell_S = 0.33\ H$ and $\ell_S = H$. It can be observed that the length of the boat-tail does not modify the upstream base pressure distribution but changes the wake pressure for which the recovery is more important for longer slants. Besides, the singularity produces a slightly lower pressure for short slants but the overall behavior is unchanged. As concerns the drag, the results are summarized in figure 5.7(b). As expected, the contribution of the vertical base to drag is larger for shorter angles since its section is less reduced and the pressure in the wake lower. The contribution of the slant (blue circles) is more surprising since shorter slants produce more drag. As a matter of fact, the pressure is slightly lower near the singularity (see figure 5.7a) and the pressure recovery related to the diffuser effect is much less important. As a consequence, the overall drag of the afterbody (green triangles) is less reduced with short slants and starts to plateau very quickly; one may even expect an increase for larger angles.

Finally, we modify the length of the recirculation bubble and investigated the cases $\ell_{rb} = H$, $\ell_{rb} = 2\ H$, $\ell_{rb} = 5\ H$ and $\ell_{rb} = 10\ H$. The slant's length is set to the maximum value of $\ell_S = H$; only two angles are presented: $\theta_T = 0°$ (squareback configuration) and $\theta_T = 15°$ for the sake of clarity but the results are similar for all tested geometries. One can observe in figure 5.8(a) that only the pressure in the wake is modified by the recirculation length ℓ_{rb} regardless of the angle. As expected in view of the pressure distribution of figure 5.8(a), the length of the recirculation bubble has clearly no impact on the contribution of the slant to drag (figure 5.8b). On the contrary, since the pressure in the wake is modified – increased for longer bubbles –, the contribution of the base is modified regardless of the slant angle. As a direct consequence, the total afterbody drag is changed as well. Elongating the wake could therefore be beneficial. This drag reduction mechanism should be put in parallel to a remark of Appendix B about the cavity effect and brings a justification to the fact that increasing the wake's length, by reducing the streamlines' curvature, reduces drag.

5.2.4 Short conclusion

As a summary of this section, we recall the main results. For a two dimensional potential wake flow simulation with the Free Streamline Theory, we confirm that the pressure in the recirculation bubble – or equivalently that at the vertical base of the body – is prescribed by the wake length. The base pressure appears to increase with the boat-tail. On the contrary, larger angles – or equivalently decreased slant length – lead to the formation of very low pressure near the model thus contributing to drag; two competitive phenomena are then highlighted thanks to these simulations.

5.3 Experimental setup

Experiments are carried out in the model-scale wind tunnel of the GIE-S2A presented in § 2.1.2 with the flat-backed Ahmed body described in § 2.4; with respect to chapters 3 and 4, the afterbody is different. A photograph of the body placed in the wind-tunnel is provided in figure 5.9(a). The afterbody is specific and has been designed for this study with the computer-aided design software FreeCAD. It consists in a tunable rear part – colored in yellow in figure 5.9(b) – with four interchangeable components similar to the one presented in figure 5.9(c). The rear shape of the body can be modified up to a distance $\ell_B^* = \ell_B/H = 0.537$ upstream from the base. The overall dimensions of the Ahmed body presented in §§ 3.2 and 4.2 are not modified; in particular, the length is similar since the afterbody itself is modified unlike some other works reporting an additional geometry mounted on the model.

Two different boat-tails geometries are used in this study: circle-arcs and slants. Two lengths are considered in this work: $\ell_B^* = \ell_L^* = 0.537$ and $\ell_B^* = \ell_S^* = 0.168$. For the circular geometries, each part is designed following these rules: the junction between the rear part and the model's roof has an horizontal tangency. The boat-tail consists in a circle-arc and the characteristic angle θ_i is defined by the chord angle as shown in figure 5.9(c) while the subscript i stands either for the top ($i = T$) or the bottom ($i = B$) part. In this chapter, the considered chord angles are $\theta_i \in \{0^\circ, 5^\circ, 7.5^\circ, 10^\circ, 12.5^\circ\}$. Slanted geometries are obtained as the dashed line in figure 5.9(c), *i.e.* they are equivalent to the chord of circle-arcs. A fairing is present between the body and the slant to avoid excessive sharp edges. We also consider side boat-tails of angles $\theta_S = 12.5^\circ$ associated with square top and bottom parts ($\theta_T = 0^\circ$, $\theta_B = 0^\circ$) and with a three-dimensional configuration ($\theta_T = 7.5^\circ$, $\theta_B = 5^\circ$, $\theta_S = 5^\circ$). As a design prerequisite, the four components had to be easily interchangeable, robust enough for multiple tests and as light as possible – since the translation stages used for ground clearance and pitch adjustment had limited loading capacities. The whole afterbody including the interchangeable components was manufactured by Aero Concept Engineering[1] after a final step of common design.

The baseline is chosen for a the model's ground clearance of $c^* = 0.168$ and the body considered in no-yaw and no-pitch conditions, *i.e.* aligned with the incoming flow[2]. For the sensitivity analyses, the ground clearance c^* is varied in the range $0.060 \leq c^* \leq 0.200$. The free-stream velocity is set to $U_\infty = 20$ m.s^{-1}, yielding a Reynolds number based on the model's height H of $\mathrm{Re}_H = (U_\infty H)/\nu \simeq 4.0 \times 10^5$ as in chapter 4. It should be emphasized that, due to boat-tailing, the base height H_b changes and is therefore not taken as the scaling length but the body's height $H = 0.298$ m.

The model is instrumented with 49 pressure taps identified by the dots in figure 5.9(d) connected to the Scanivalve ZOC33b (20" H2O) pressure scanner controlled by a Green-Lake Engineering SmartZOC200 electronics and a custom LabVIEW acquisition suite for pressure measurements (see Appendix A for details about the conception of the acquisition chain). The pressure measurement system is fully described in § 2.2.1. We just recall that the sampling frequency is set to $f_e = 100$ Hz. $N = 25$ taps are located at the base and 6 on each exchangeable parts, defining two pressure lines at $y^* = 0$ and $z^* = 0$. The location of the sensors and of the pressure lines is indicated in figure 5.9(d). Synchronous force measurements are performed at $f_b = 10$ Hz (§ 2.2.2). Data are then low-pass filtered with a moving average over $t = 0.5$ s, *i.e.* $t^* = (tU_\infty)/H \simeq 33.6$. In this chapter, we must precise what the *base suction* refers to. We chose the same reference area as Han *et al.* (1992), namely only the vertical blunt afterbody corresponding to the separated flow region. The base suction coefficient c_b is then integrated over the surface depicted in grey in figure 5.1. Pressure and aerodynamic loading measurements are made dimensionless following equations (2.1), (2.2), and (2.3). The complex base pressure gradient is computed from the data collected at the four sensors marked A, B, C and D in figure 5.9.

---

[1] Aero Concept Engineering (ACE), Magny-Cours, France: `http://www.aero-ce.com/en/pages/accueil.html`

[2] The definitions of the ground clearance c and of the pitch and yaw angles respectively denoted by α and β are identical to those of the previous chapters and can be seen for instance in figure 4.1 on page 52.

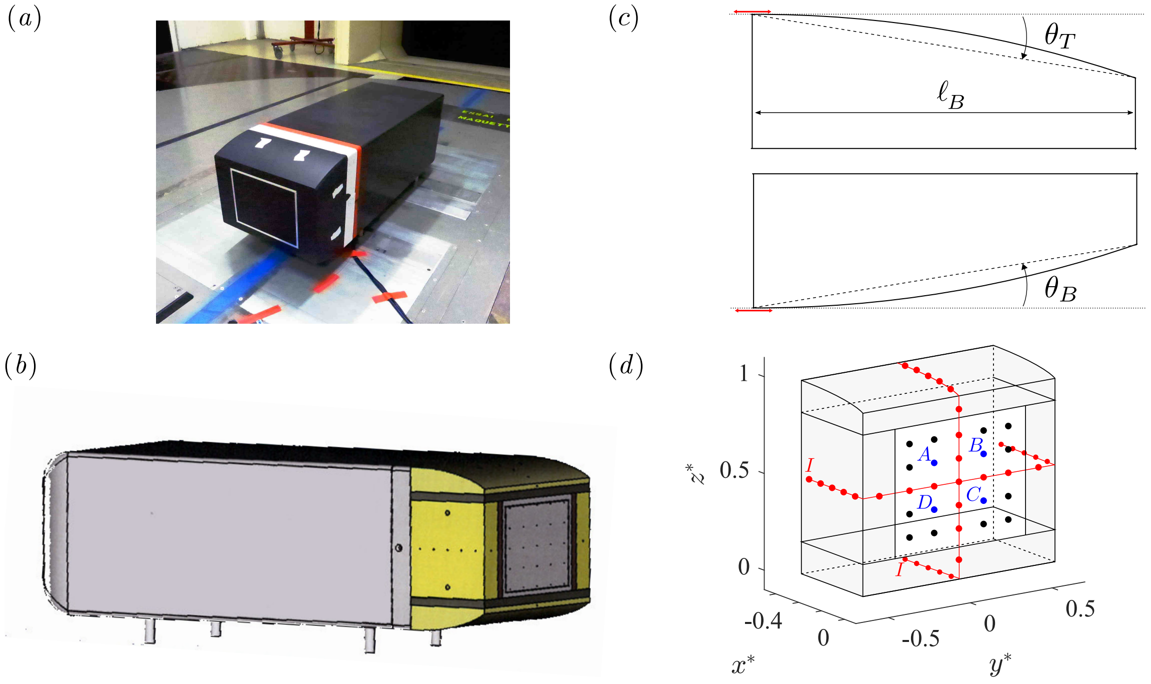

Figure 5.9 – Experimental apparatus: (a) view of the boat-tailed body mounted on the model in the GIE-S2A model-scale wind tunnel, (b) installed tunable rear afterbody modeled with FreeCAD (in yellow), (c) side view of the top and bottom removable boat-tail parts with definition of the chord angles θ_T and θ_B and of the length ℓ_B, (d) schematic view of the base of the body and of the boat-tails viewed from downstream and locations (x^*, y^*, z^*) of the pressure sensors. The sensors A, B, C, D are used for base pressure gradients calculations. The two red lines show the rows of sensors used for figures 5.11 and 5.14 and described in § 5.3. The top geometry is boat-tailed while the bottom one is squared, corresponding to a one-sided modified shape. The boat-tails are colored in grey.

The PIV system described in § 2.3.2 is used in the vertical plane $y^* = 0$ located mid-width at the base of the body. This plane is indicated in figure 5.9. The plane is chosen so that the top boat-tail is visible. The bottom one is not because of the shadow in the laser sheet created by the body. In addition, three-dimensional PIV yields $(u^*\vec{e}_x,\ v^*\vec{e}_y,\ w^*\vec{e}_z)$ in the $x^* = 0.45$ plane (transverse plane parallel to the base); the vorticity field can also be computed.

In § 5.4.6, several configurations are studied. They are presented in figure 5.10. The length and angles of the boat-tails are given in table 5.1 as well as the geometry – slant or circle-arc. The fluctuations correspond to those identified in § 5.4 for the body aligned with the incoming flow at $c^* = 0.168$.

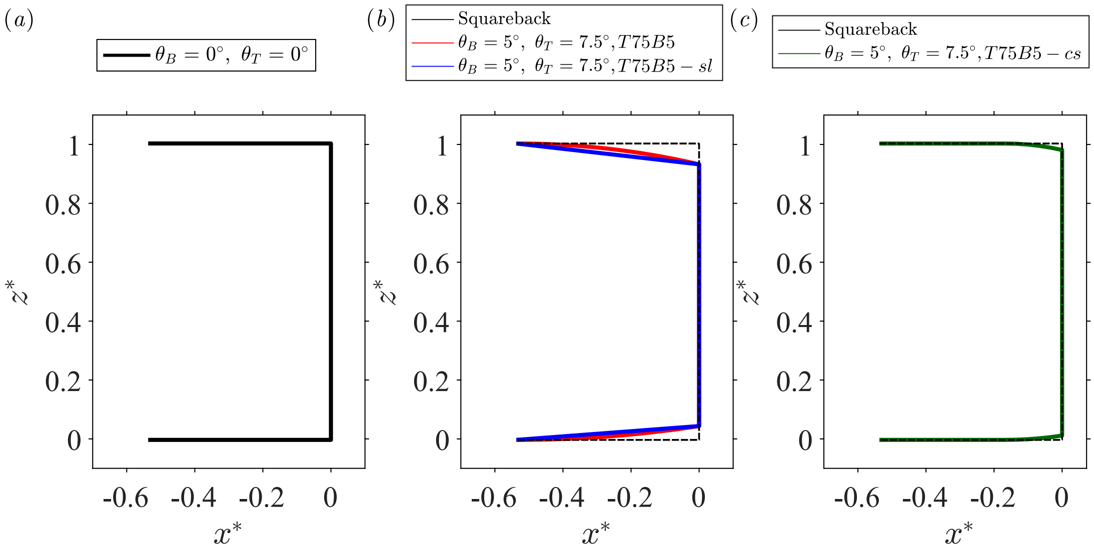
(a)
$\theta_B = 0°,\ \theta_T = 0°$
(b)
Squareback
$\theta_B = 5°,\ \theta_T = 7.5°, T75B5$
$\theta_B = 5°,\ \theta_T = 7.5°, T75B5-sl$
(c)
Squareback
$\theta_B = 5°,\ \theta_T = 7.5°, T75B5-cs$
z^*
x^*
1
0.8
0.6
0.4
0.2
0
-0.6
-0.4
-0.2
0

Figure 5.10 – Side view of the three geometries investigated in § 5.4.6: (*a*) Squareback geometry (baseline), (*b*) T75B5 (in red) and T75B5-sl (in blue), (*c*) T75B5-cs. The baseline appears as the dashed line. The terminology refers to table 5.1.

Table 5.1 – Characteristics of the afterbodies used for the sensitivity analyses (boat-tail angles, boat-tail length and shape), identified wake fluctuations (see § 5.4) and configuration's names.

Name	θ_T	θ_B	θ_S	ℓ_B^*	Shape	Wake fluctuations
T75B5	7.5°	5°	0°	0.537	Circle-arc	y-instability
T75B5-sl	7.5°	5°	0°	0.537	Slant	y-instability
T75B5-cs	7.5°	5°	0°	0.168	Circle-arc	y-instability
T125B125	12.5°	12.5°	0°	0.537	Circle-arc	periodic mode
T125B125-cs	12.5°	12.5°	0°	0.168	Circle-arc	y-instability
3D	7.5°	5°	5°	0.537	Circle-arc	y-instability

5.4 Results

This part is organized as follows. The baseline, identical to that of § 4.3.1 but with the modifiable afterbody in its squareback configuration, is first studied to confirm that previous results are not affected by the change of afterbody (§ 5.4.1). A global analysis with the lift and the drag forces is conducted with the aim of reproducing the linear and quadratic relationships first shown by Grandemange *et al.* (2013*c*) and confirmed by Grandemange *et al.* (2015) and Perry *et al.* (2016*a*,*b*). The effect of boat-tailing on mean and fluctuating drag related quantities (base suction and drag coefficient) are investigated in § 5.4.3. The analysis is reproduced for the side force and lift in § 5.4.4. We investigate the modifications of the wake dynamics created by boat-tailing in § 5.4.5; the impact of the boat-tail shape is then investigated in § 5.4.6. Finally, further drag reduction is achieved with a three-dimensional boat-tailed afterbody characterized in § 5.4.7.

5.4.1 Baseline: squareback afterbody

The baseline is chosen as the squareback case with the body aligned with the flow (yaw angle $\beta = 0°$), in no-pitch conditions ($\alpha = 0°$) and whose ground clearance is set to $c^* = 0.168$. The afterbody is different as the one considered here is the tunable described in § 5.3. This subsection ensures no noticeable change of the wake dynamics with respect to that investigated in § 4.3.1 can be ascribed to the new afterbody in its squareback configuration. The results for the baseline are presented in figure 5.11. Conditional averaging based on the sign of the horizontal base pressure gradient g_y^* leads to the two base pressure distributions shown in figure 5.11(a, b). As usual, negative gradients are associated with state N of the wake and positive with state P (Grandemange *et al.*, 2013*b*). These two distributions are linked by a vertical reflectional symmetry. The chosen threshold is a consequence of the PDF given in figure 5.11(c) which has the classical features of the y-instability (Grandemange *et al.*, 2013*b*). There is almost no vertical pressure gradient in the baseline configuration. The space-time analysis provided in figure 5.11(d) at the base's mid-height ($z^* = 0$) shows that the wake remains in one state for about $500 - 1000\ t^*$ before a switch of only a few t^* of duration occurs. The large ground clearance $c^* = c/H \geq c_S^* \simeq 0.105$[1] ensures that the body is in the unstable wake mode regime and that the instability is saturated. From the results presented in Grandemange *et al.* (2013*a*), the base aspect ratio of the studied body is in the *interference zone* in which either the y- or the z-instability can be triggered. For instance, Evrard *et al.* (2016) reports a y-instability versus a z one for Barros *et al.* (2017) with phase lock-in observed around $\varphi \simeq -\pi/2$ for almost similar base dimensions. Besides, the y-instability is retrieved in Barros *et al.* (2017) when the underbody flow is disturbed.

Table 5.2 – Characteristic mean and fluctuating coefficients for the baseline configuration defined as $c^* = 0.168,\ \alpha = 0°,\ \beta = 0°$ with the new afterbody.

C_b	C_b'	C_x	C_x'	C_y	C_y'	C_z	C_z'
0.174	0.008	0.281	0.004	−0.002	0.018	−0.118	0.006

The mean aerodynamic coefficients and their standard deviation are given in table 5.2. The imprint of the y-bistability can be identified on the fluctuations of the side force C_y' which are one order of magnitude higher than those of other coefficients. These aerodynamic quantities are similar to those given in table 4.3 except for the base pressure which is slightly higher (and thus the drag lower); it remains in the range reported in the literature though (Grandemange *et al.*, 2013*b*; Volpe *et al.*, 2015; Evrard *et al.*, 2016).

According to the results presented in this part, the wake dynamics fully characterized in § 4.3.1 is consequently preserved with the modifiable afterbody while it is in its squareback configuration. In our point of view, it consequently becomes unnecessary to indicate which afterbody was used for the squareback configuration and both will be referred to as the *squareback geometry* in the following. However, every change in the loading is computed from the present configuration.

---

[1] See Cadot *et al.* (2015*b*) for the definition of the critical ground clearance c_S^*. This value is experimentally determined in § 4.3.1.2 for a squareback afterbody with a wake subject to the y-instability.

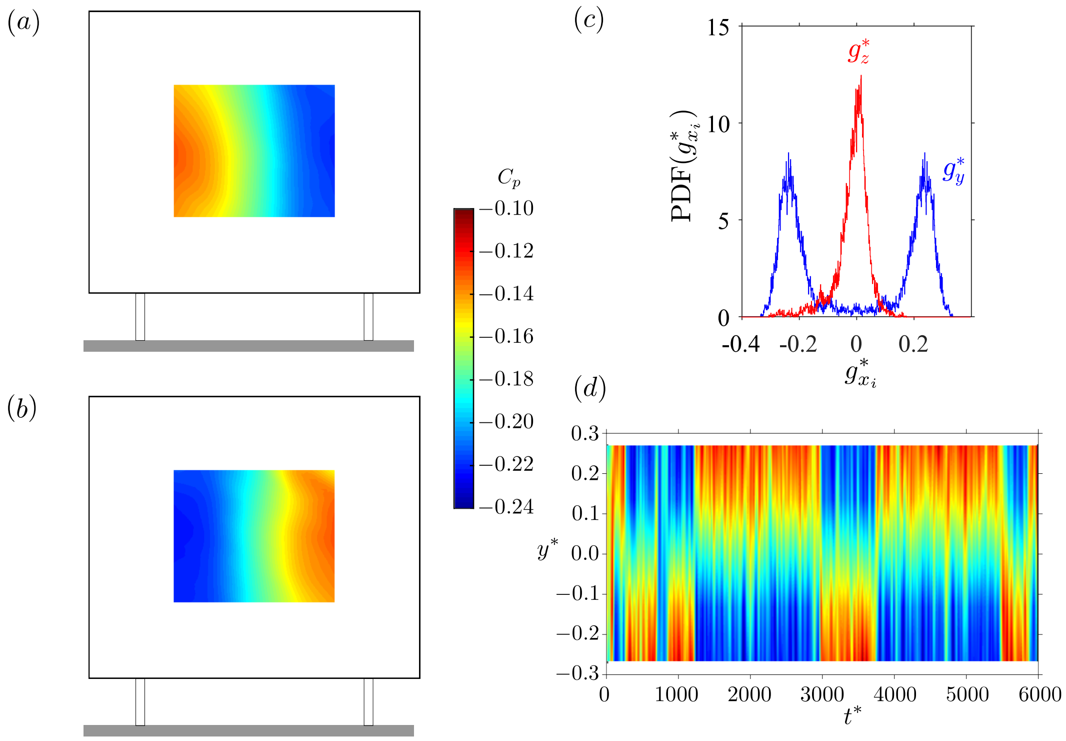

Figure 5.11 – Baseline configuration of the squareback Ahmed body with the new afterbody ($\alpha = \beta = 0°$, $c^* = 0.168$). Conditionally averaged base pressure distributions $C_p(y^*, z^*)$ for state N of the wake (*a*) and for state P of the wake (*b*). (*c*) Probability Density Functions of the vertical base pressure gradient g^*_y (in blue) and of the horizontal base pressure gradient g^*_z (in red); (*d*) space-time diagram $c_p(y^*, z^* = 0, t^*)$ along the vertical line of sensors $z^* = 0$ shown in figure 5.9(*d*).

5.4.2 Shape optimization with boat-tails

We first start with a shape optimization in order to identify optimal angles for minimum drag and lift compatible with industrial applications. In particular, Grandemange *et al.* (2013*c*) derived a bi-linear relationship between the drag, the lift and the top and bottom boat-tail angles. A similar trend was also observed later by Perry *et al.* (2016*b*) for a Windsor body. In these works, the authors also show that the lift-drag polar curves can collapse into a single parabola. From the results reported in the literature, it is obvious that the pressure distribution on the afterbody is responsible for the aerodynamic loading applied to the body. As a consequence, it is impossible to optimize one coefficient without taking into account the effect on the other.

The global evolution of the drag and lift forces with respect to the boat-tails is given in figure 5.12. Figures 5.12(*a*) and 5.12(*b*) are respectively plotted for a given top angle θ_T or a prescribed bottom angle θ_B while the other is modified; the mean drag coefficient C_x is represented. The black dots correspond to $\theta_T = 0°$ (resp. $\theta_B = 0°$), *i.e.* one-sided geometries, the blue to $\theta_T = 5°$ (resp. $\theta_B = 5°$), the red to $\theta_T = 7.5°$ (resp. $\theta_B = 7.5°$), the green to $\theta_T = 10°$ (resp. $\theta_B = 10°$), and finally the magenta to $\theta_T = 12.5°$ (resp. $\theta_B = 12.5°$). The behavior in both figures is similar and thus we comment them together. Regardless of the configuration, a quadratic dependency between the drag and the angle can be identified, in agreement with the results of Grandemange *et al.* (2013*c*). There is first a reduction as the angle is increased before the low pressure on the circle-arc counterbalances it and the global balance is affected with a drag increase. The optimal results are obtained for $\theta_B = 5°$ regardless of θ_T and $\theta_T = 7.5°$ for all θ_B. For one-sided geometries, the increase seems to be almost linear and those cases do not seem to obey

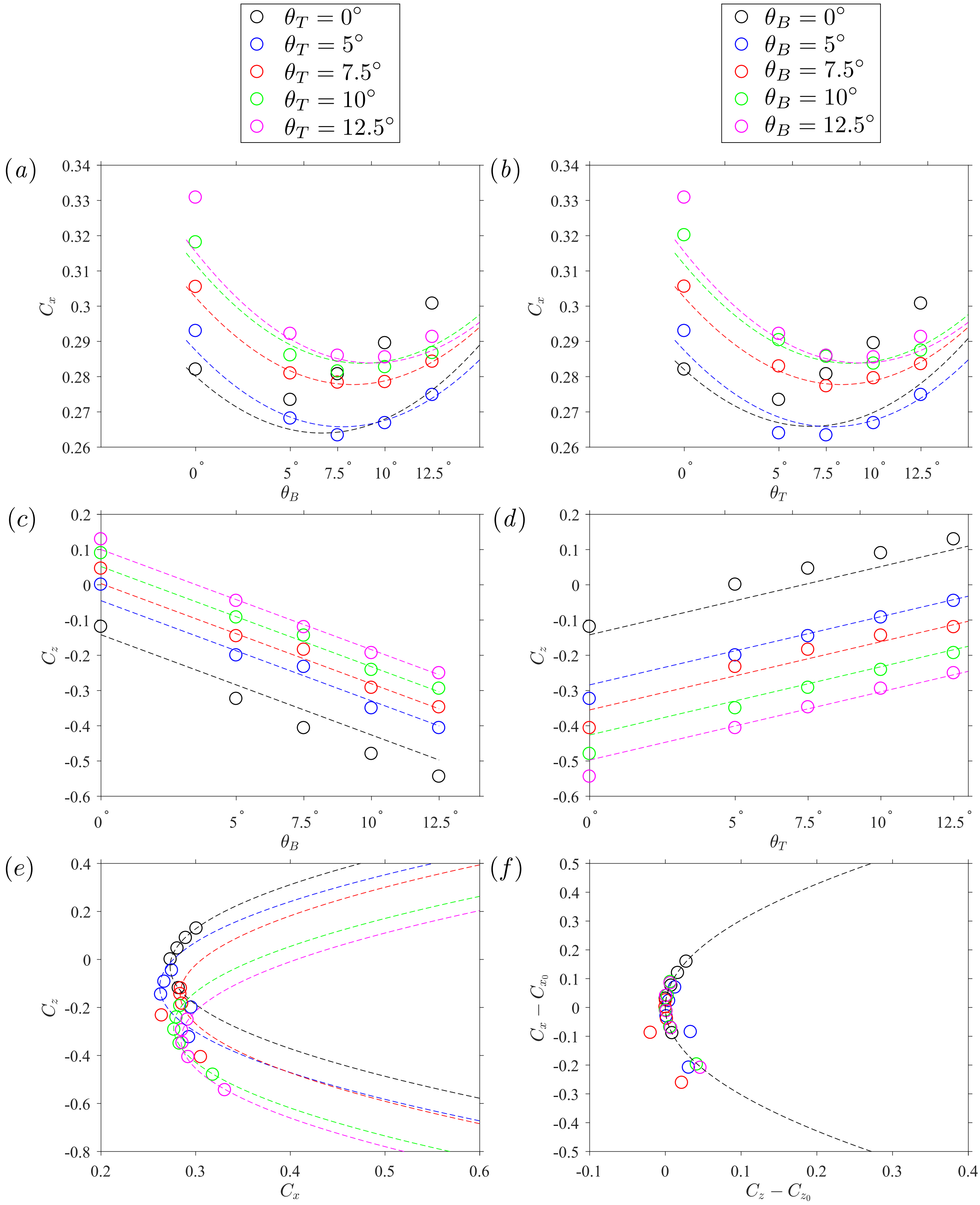

Figure 5.12 – Total aerodynamic loading as a function of the boat-tail angles θ_T and θ_B: mean drag coefficient C_x as a function of the bottom (a) and of the top (b) angles while the other is kept constant; mean lift coefficient C_z as a function of the bottom (c) and of the top (d) angles while the other is kept constant. The dashed lines are the fits given in the text. Polar curves: (e) C_z *vs.* C_x, (f) $C_z - C_{z_0}$ *vs.* $C_x - C_{x_0}$ (Grandemange *et al.*, 2013*c*; Perry *et al.*, 2015).

the same trend. Following the same idea as Grandemange *et al.* (2013*c*), we perform a quadratic fit of the data, considering all 20 cases two-sided at once and we obtain the following relationship (5.4) for the drag force:

$$C_x(\theta_T, \theta_B) = 0.2401 - 0.2763\ \theta_T + 0.6739\ \theta_B + 1.185\ \theta_T^2 - 0.5052\ \theta_B\theta_T - 1.507\ \theta_B^2 \quad (5.4)$$

where the angles are expressed in *radians*. Equation (5.4) is plotted as the dashed line in figures 5.12(*a*) and 5.12(*b*). A quite good agreement is found except for the single-sided boat-tails that we did not consider in the fit. Their behavior is indeed different for several reasons. First, in order to recover the baseline, the constant in equation (5.4) is rather 0.2820 instead of 0.2401. Second, it turns out that the points measured with one boat-tail never collapse with the predictions which means that some differences as those highlighted in the following of the chapter exist.

It must also be noted from equation (5.4) that optimization cannot be performed independently for both angles because of the presence of the bi-linear term $\theta_B\theta_T$ in the equation. Afterwards, the mean lift coefficient C_z is considered in figures 5.12(*c*) and 5.12(*d*) following the same plotting convention as in the two previous ones. There is an obvious linear relationship between the total lift and the boat-tail angles. Fitting all 15 two-sided cases at once yields equation (5.5).

$$C_z(\theta_T, \theta_B) = -0.1418 + 1.1090\ \theta_T - 1.6291\ \theta_B \quad (5.5)$$

with the boat-tail angles taken in *radians*. A similar relationship was derived in Grandemange *et al.* (2013*c*). A quite good agreement with the data is found even for one-sided cases even if none of these points are on the linear laws plotted with the dashed lines in figures 5.12(*c*) and 5.12(*d*). From equation (5.5), optimization could potentially be conducted independently for both angles; however, because of the drag (equation 5.4) such a method could potentially lead to very detrimental results in terms of the global performance of road vehicles. Our results match satisfactorily those of Grandemange *et al.* (2013*c*) for the flat-backed Ahmed body at a close Reynolds number but also those of obtained by Littlewood & Passmore (2010); Perry *et al.* (2016*a*); Pavia *et al.* (2016) with a Windsor model in the range of Reynolds numbers $10^5 \lesssim \mathrm{Re} \lesssim 10^7$.

In aerospace engineering, a common representation is to combine the data from figure 5.12(*a*−*d*) into a single curve $C_z = f(C_x)$ called the polar curve. A similar representation is reported in Grandemange *et al.* (2013*c*) and in Perry *et al.* (2016*a*) for instance. Data are presented in figure 5.12(*e*) in which the function f turns out to be of quadratic form. Only the results with a fixed bottom angle θ_B are presented as this curve contains all the needed information. The colors correspond to that of figure 5.12(a, c) and are indicated above the plots in the left column. It must first be noticed that all points align on a parabola for a given bottom angle θ_B. Interestingly, all have the same parameters and only differ by shifting constants. Using the formalism introduced in Grandemange *et al.* (2013*c*) given in equation (5.6), the parabolas are plotted as the dashed line in figure 5.12(*e*).

$$C_x = C_{x_0} + \gamma(C_z - C_{z_0})^2 \quad (5.6)$$

The parameter $\gamma \in \mathbb{R}$ in equation (5.6) should be common to all equations. The values of C_{x_0} and C_{z_0} are reported for all cases in table 5.3. From the experiments, a common factor γ is found as $\gamma = 0.263$. $C_x - C_{x_0}$ is plotted against $C_z - C_{z_0}$ in figure 5.12(f). Data collapse remarkably well on the curve $C_x - C_{x_0} = \gamma(C_z - C_{z_0})^2$ obtained from equation (5.6) for both one-sided and two-sided cases, substantiating the results reported in Grandemange *et al.* (2013*c*) and later on retrieved in Perry *et al.* (2016*a*).

Table 5.3 – Fit coefficients C_{x_0} and C_{z_0} for the polar curves of figure 5.12(e) and reused in figure 5.12(f)

θ	C_{x0}	C_{z0}
0°	0.282	0.111
5°	0.267	0.112
7.5°	0.273	0.124
10°	0.276	0.115
12.5°	0.282	0.105

5.4.3 Contribution to drag

The contribution of boat-tailing in terms of mean base suction C_b – computed over the blunt vertical surface shown in figure 5.1 only – and mean drag coefficient C_x and of their fluctuations denoted by the superscript "′" is investigated in this section. All 25 combinations of the top and bottom boat-tail angles (θ_T and θ_B defined in § 5.9) chosen in $\theta_i \in \{0°, 5°, 7.5°, 10°, 12.5°\}$ are considered. This study yields the two curves for the mean values and the two maps for the fluctuations given in figure 5.13. The sides of the base are not modified with respect to the squareback geometry.

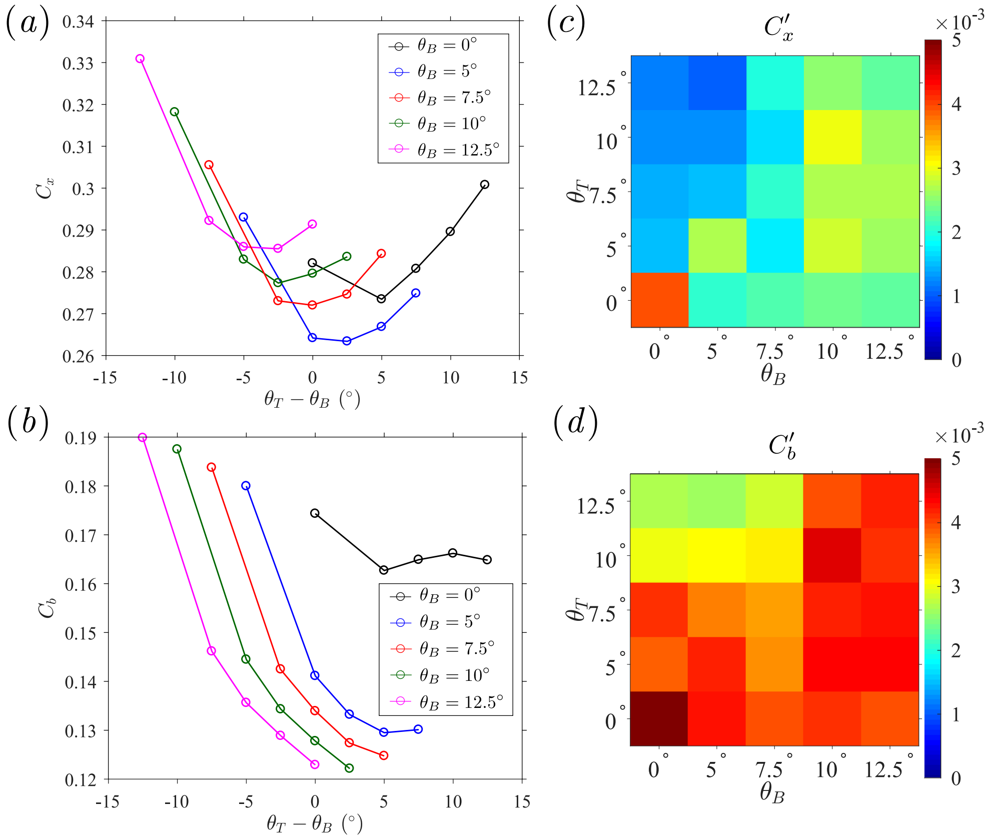

Figure 5.13 – Mean value of drag-related aerodynamic coefficients C_i as a function of the difference between the top and bottom boat-tail angles $\theta_T - \theta_B$ (a, b) for a given bottom boat-tail angle θ_B and standard deviation C'_i (c, d) as a function of the top and bottom boat-tail angles θ_T and θ_B: (a, c) drag coefficient c_x, (b, d) base suction coefficient c_b.

There seems to be an almost symmetric effect between the two boat-tails for most of the configurations as the curves all show a minimum for $|\theta_T - \theta_B| < 5°$. Some general trends can be highlighted for the mean values in figures 5.13(a, b). Large boat-tail angles and largely asymmetric configurations, *i.e.* one angle much larger than the other, result in drag increase compared to the squareback as shown in figure 5.13(a) or, in the best cases, in very small reduction. This is in agreement with previous findings by Mair (1969), Han *et al.* (1992) or Perry *et al.* (2016*b*). As a consequence, such strongly asymmetric geometries should be avoided in view of minimum drag seeking. On the contrary, it seems that the use of a small bottom angle $\theta_B = 5°$ leads to reduction as long as the top angle θ_T remains moderate. A particular focus is set on this configuration. Similarly, $\theta_T = 7.5°$ seems to yield more efficient results than the squareback case. The mean base suction coefficient C_b shown in figure 5.13(b) is globally reduced, the more for larger boat-tail angles in agreement with previous studies (see § 5.1). At most, one may notice a slight increase of the base suction for one-sided geometries not reported in previous papers. The main result is that the base suction computed from the separated flow area and the drag present different evolutions, showing unambiguously the contribution of the boat-tails to the total loading (Mair, 1969; Han *et al.*, 1992; Grandemange *et al.*, 2013*c*; Perry *et al.*, 2016*b*).

The standard deviations of the previously studied quantities are presented in a similar way in figure 5.13(c, d). Fluctuations of the drag coefficient C'_x (figure 5.13c) are reduced by at least a factor of two by boat-tailing. The simulatenous use of two large boat-tail angles leads to higher fluctuations even if they remain quite smaller than for the baseline case. In the case of large bottom angles, the damping seems to be smaller thus suggesting that unsteadiness is introduced in the wake owing to the interaction with the road. There is an interesting correlation with the fluctuations of the base suction coefficient C'_b given in figure 5.13(d) showing that the wake is responsible for the unsteadiness observed on the aerodynamic loading. However, they are always smaller than for the baseline.

It is largely emphasized in the literature review provided in § 5.1 that the boat-tails have a considerable contribution to the afterbody drag and therefore to the total drag force applied on the body, and this is certainly highlighted by figures 5.13(a, b). In order to understand this contribution, we plot the mean pressure distribution along two sensors lines at $y^* = 0$ and $z^* = 0$ in figure 5.14. Taking advantage of the overall symmetry of figures 5.13(a, b), we only consider two scenarii: one-sided boat-tailed geometries with $\theta_B = 0°$ and varying θ_T and two-sided boat-tailed geometries with $\theta_B = 5°$ and varying θ_T. We recall that the sides are not modified with respect to the squareback so that $\theta_S = 0°$).

We first comment figures 5.14(a, c) corresponding to one boat-tail mounted only. The pressure on the base (5 sensors located in the middle of the given pressure lines) is only slightly modified as could be inferred from figure 5.13(b), although a small increase can be observed. Despite the modification of the base wetted section, this does not provide a satisfactorily explanation for the drag changes reported in figure 5.13(a). However, it is remarkable that, if the pressure at the top of the base is almost not affected by the increasing angle, a sudden increase at the bottom exists. By continuity of the pressure, the distribution below the body is slightly modified but, once the afterbody is reshaped, no further modifications are measured. On the boat-tail however, the pressure level is directly related to the angle θ_T: the bigger the angle, the lower the pressure and the flow remains attached. Similar observations have been previously made (§ 5.1). This very low pressure on the circle-arc is consequently expected to contribute to the total pressure drag. A pressure recovery towards the base and its imposed pressure at the top is observed. One must also mention that, unlike for the squareback for which the pressure drops towards separation (favorable pressure gradient), it increases when a boat-tail is installed (adverse pressure gradient). More surprisingly, the exact same observation can be made on the opposite side whose geometry is unchanged. The same conclusions apply when only the bottom angle is varied although the results are not shown. In agreement with the unmodified shape, no noticeable modifications of the pressure along the horizontal sensor lines is reported in figure 5.14(c). The asymmetry of the distribution for the baseline is related to a not converged observation (see chapter 4).

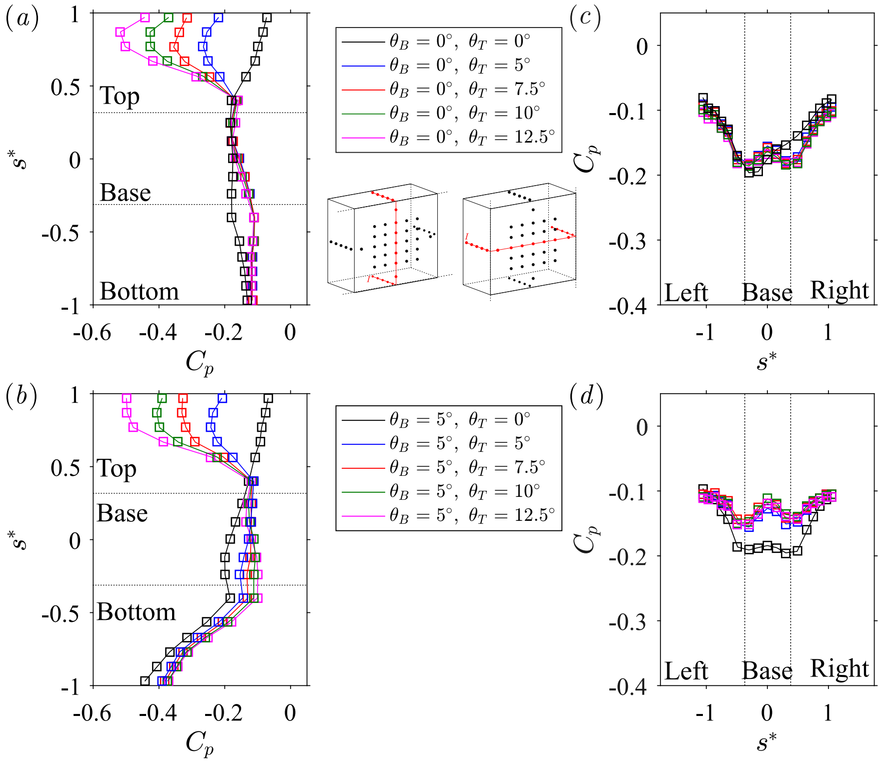

Figure 5.14 – Mean pressure coefficient C_p plotted along a line of constant x_i^*: (a, c) $x_i^* = y^* = 0$, (b, d) $x_i^* = z^* = 0.5$. Two investigated scenarii: (a, b) one-sided boat-tailed geometries with $\theta_B = 0°$ and varying θ_T, (c, d) two-sided boat-tailed geometries with $\theta_B = 5°$ and varying θ_T.

If the same analysis is reproduced with a combination of two boat-tails as in figures 5.14(b, d), the same remarks more or less apply. Only one typical scenario is presented, varying θ_T and with a prescribed $\theta_B = 5°$. The main differences with respect to the previous case are that the base pressure is further increased in agreement with the mean base suction (figure 5.13b) and that the pressure at the separation at the bottom of the base and accordingly on the lower boat-tail is now a function of the angle θ_T. The horizontal pressure distribution (figure 5.14d) is again unaffected by boat-tailing except for the base pressure which increases. Similar pressure distributions are reported in Grandemange *et al.* (2013c).

If we integrate the previous pressure distributions and take the projection along the $\boldsymbol{e_x}$ axis of the coordinate system following equation (5.7), we can obtain the pressure drag per unit width f_{p_x}:

$$f_{p_x} = \boldsymbol{e_x} \cdot \int_{-1}^{1} c_p(s^*) \boldsymbol{n} \, \mathrm{d}s^* \tag{5.7}$$

where $\boldsymbol{n}$ is the unit vector locally normal to the afterbody surface. The results are given in figure 5.15(a) for the one-sided scenario.

The contribution of the boat-tails to drag estimated owing to the downstream component of the pressure force $f_{p_{x_r}}$ is displayed with the blue empty circles in figure 5.15(a). It increases linearly with the boat-tail angle. However, the contribution of whole afterbody, *i.e.* the base and the boat-tails, f_{p_x} shown as the black curve with empty circles in figure 5.15 is not linearly increasing. Due to the slight base pressure recovery, base suction decreases. There is consequently a competitive mechanism between the beneficial effect of boat-tailing on the base contribution and the detrimental boat-tails generated drag. Considering the whole rear afterbody, a minimum of the pressure drag f_{p_x} is found around $\theta_T = 5°$ for the one-sided case. For angles larger than the optimal one, drag increase is related to the contribution of the boat-tails only overwhelming the beneficial effect originating from the reduction of the base section. Although the optimal angle is smaller in our case, similar results were presented in § 5.1; the closest configuration is that of Littlewood & Passmore (2010) who reports almost identical results. The total drag C_x measured with the force balance and displayed as the blue filled squares compares well with the total afterbody pressure drag (empty black circles). In particular, the same minima are obtained. We thus confirm that the contribution of the rest of the body to pressure drag – and less importantly to viscous drag[1] –, is insensitive to boat-tailing.

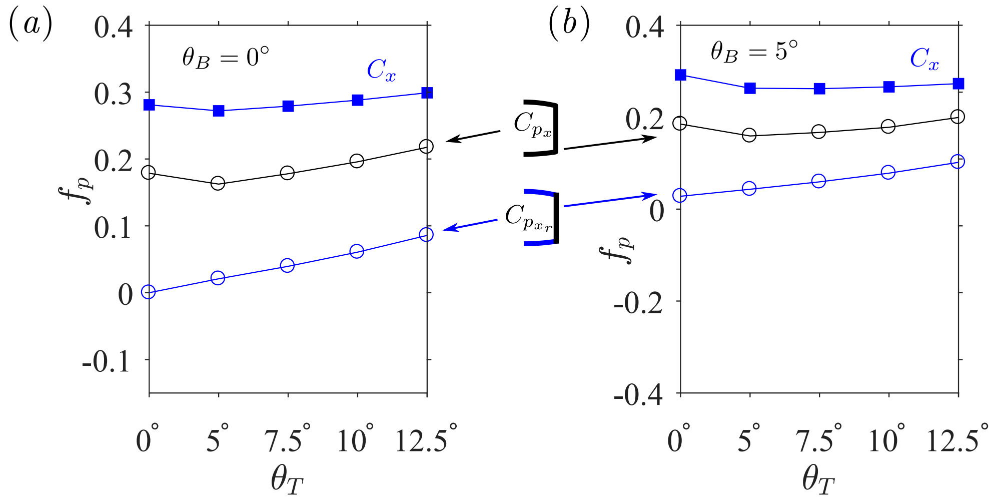

Figure 5.15 – Aerodynamic pressure drag f_{p_x} on the rear afterbody with one (a) or two (b) boat-tail(s) in place. In blue, the net drag force created on both boat-tails; in black the total drag force created on both boat-tails and on the base. (a) $\theta_B = 0°$ and varying θ_T, (b) $\theta_B = 5°$ and varying θ_T. In blue filled squares, total mean value of C_x measured with the force balance.

For the two-sided scenario ($\theta_B = 5°$ and varying θ_T) presented in figure 5.15(b), the only noticeable difference appears to be that the optimum is now found for $\theta_T = 7.5°$. It turns out that it also corresponds to the more efficient out of the 25 tested configurations in terms of total drag C_x. From the distributions shown in figures 5.14(c, d), the impact on the mean side force C_y is expected to negligible and related only to small asymmetries of the setup.

To summarize, we confirmed previous studies showing that, despite the base pressure recovery and the reduction of the blunt vertical base section, the contribution of the boat-tails to the total drag is not negligible because of the low pressure generated by the flow remaining attached. Optimal configurations are identified and should be considered when seeking for the minimal drag. However, in an engineering context, the cross-flow loading must also be taken into account. The effects on lift are sometimes reported (Han

---

[1] Viscous drag can be estimated to be about $10 - 15\%$ of the total drag (Barth, 1956).

et al., 1992; Littlewood & Passmore, 2010; Grandemange *et al.*, 2013*c*, 2015; Perry *et al.*, 2016*b*) but not on its fluctuations nor on the side force ones.

5.4.4 Contribution the cross-flow loading

The cross-flow forces, *i.e.* side force c_y and lift c_z, are considered in this section. The results are presented in figure 5.16 with the same formalism as in § 5.4.3, with the 25 configurations.

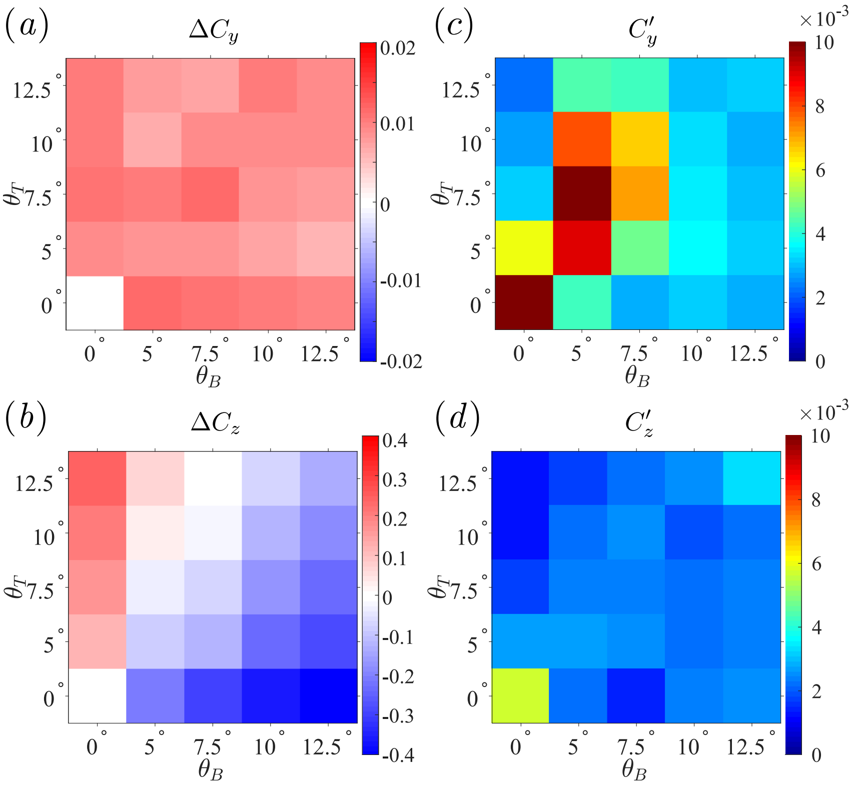

Figure 5.16 – Difference ΔC_i of the mean value of cross-flow aerodynamic coefficients C_i with respect to the squareback geometry ($\theta_T = \theta_B = 0°$) as a function of the top and bottom boat-tail angles θ_T and θ_B (a, b) and standard deviation C'_i (c, d): (a, c) side force coefficient C_y, (b, d) lift coefficient C_z.

The mean side force C_y (figure 5.16*a*) which shows little sensitivity to the boat-tail angle. It is slightly different than for the baseline though but, since all angles lead to similar values and because of the overall left-right symmetry of the problem, this suggests a symmetry-defect in the setup. The shift is very small though, by more than one order of magnitude with respect to the variations of the mean lift coefficient C_z (figure 5.16*b*). The latter shows that each of the boat-tails seems to contribute to the total loading proportionally to its chord angle. This effect is identical for both boat-tails and yields an almost exactly antisymmetric map. The fluctuating coefficients (figures 5.16*c*, *d*) however provide much more information. Depending on the component, two clear regions of intense fluctuations can be identified. Concerning the side force (figure 5.16*c*), it turns out that the simultaneous use of two boat-tails of moderate angles ($\theta_T \leq 10°$ and $\theta_B \leq 7.5°$), corresponding to the near diagonal squares, leads to nearly the same standard deviation as the baseline. On the contrary, larger angles and even more asymmetric configurations – located off-diagonal – are related to steadier side force loading. As regards the lift (figure 5.16*d*), one can observe that the fluctuations are considerably reduced by the use of

boat-tails but that an anomaly can be identified for $\theta_T = 12.5°$ and $\theta_B = 12.5°$ for which the standard deviation is more than twice that of the other investigated cases.
The integration of the pressure distributions of figure 5.14 and the projection along the $\boldsymbol{e_z}$ axis of the coordinate system yields equation (5.8) and one obtains the contribution of pressure to lift per unit width f_{p_z}:

$$f_{p_z} = \boldsymbol{e_z} \cdot \int_{-1}^{1} c_p(s^*) \boldsymbol{n} \, \mathrm{d}s^* \tag{5.8}$$

where $\boldsymbol{n}$ is the unit vector locally normal to the afterbody surface. The results are given in figure 5.17(a) for the one-sided scenario.

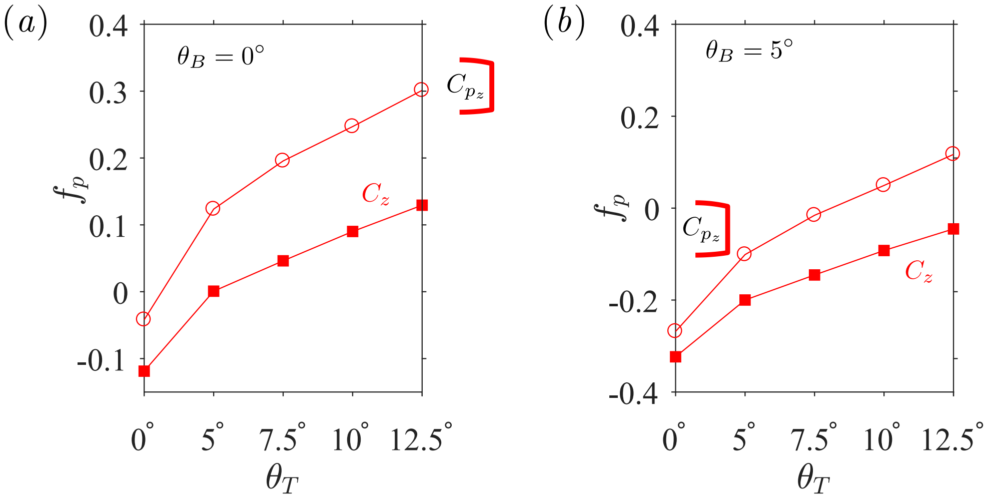

Figure 5.17 – Aerodynamic lift f_{p_z} on the rear afterbody with one (a) or two (b) boat-tail(s) in place. In red, the net lift created on both boat-tails. (a) $\theta_B = 0°$ and varying θ_T, (b) $\theta_B = 5°$ and varying θ_T. In red filled squares, total mean value of C_z measured with the force balance.

The lift force f_{p_z} created on the boat-tails is shown by the red empty circles. After a discontinuous transition when a boat-tail is installed, it grows linearly with the angle. This can be explained by the suction caused by the low-pressure on the circle-arc (figure 5.14). As a consequence, top boat-tails generate positive lift and bottom ones a negative contribution. The boat-tailed geometry is the only source of additional lift as the total lift of the model C_z measured with the force balance and displayed with the filled red squares displays a similar evolution reflecting that the contribution of the rest of the body is nearly constant. A similar observation is made for two-sided geometries in figure 5.17(b), the curve being only affected by an offset related to the bottom angle of $\theta_B = 5°$. This lift evolution is fully consistent with the results of Han *et al.* (1992), Grandemange *et al.* (2013c) or Perry *et al.* (2016b).

5.4.5 Effect on the wake dynamics

A mechanism has to be found to explain the drag and cross-flow loading sensitivity towards boat-tailing presented in §§ 5.4.3 and 5.4.4 and summarized in § 5.4.2. In that aim, we propose to study the base pressure gradients, found in chapter 4 to be an excellent topological indicators of the wake. Besides, we found in the same chapter a relationship between the instantaneous wake state and the body's cross-flow loading. A similar sensitivity analysis as that conducted in the previous sections with the forces is reproduced with the two Cartesian components g_y^* and g_z^* and the modulus g_r^* of the base pressure gradient $\hat{g}^*$. Their mean values and standard deviations are given together in figure 5.18.

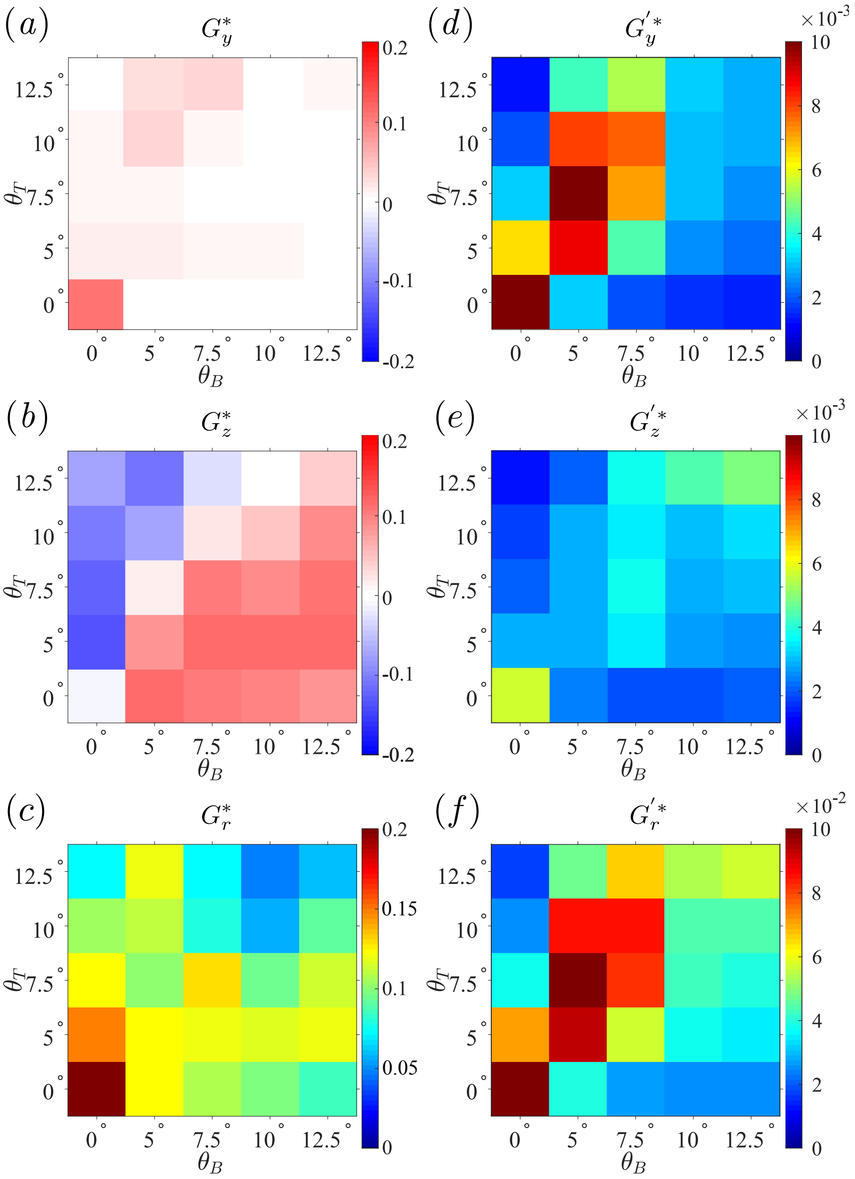

Figure 5.18 – Cartesian components g_y^* and g_z^* of the base pressure gradient $\hat{g}^*$ as a function of the top and bottom boat-tail angles θ_T and θ_B: (*a*) mean horizontal gradient G_y^*, (*b*) mean vertical gradient G_z^*, (*c*) modulus of the base pressure gradient G_r^*. Standard deviation of the base pressure gradients: (*d*) horizontal gradient $G_y^{'*}$, (*e*) vertical gradient $G_z^{'*}$, (*f*) modulus $G_r^{'*}$.

Figure 5.18(*a*) clearly shows the independence of the mean horizontal base pressure gradient G_y^* with respect to boat-tailing. Its main value is constantly close to zero. The vertical gradient G_z^* (figure 5.18*b*) has a quite different behavior though. The boat-tails impose a vertical gradient depending on their angle and location. This leads to a mean base pressure gradient oriented towards the smallest boat-tail angle. As a result, points below the diagonal of the matrix, *i.e.* $\theta_B > \theta_T$, are associated with positive values of G_z^* while those above, *i.e.* $\theta_B < \theta_T$, with rather negative values. When $\theta_B \simeq \theta_T$ – close to the diagonal terms of the matrix –, the vertical gradient is almost null similarly to the baseline. The geometrical constraint of the boat-tails applied to the vertical component of the base pressure gradient consequently depends directly on the angle and both angles have an opposite effect on the wake orientation. We notice that these two plots are similar to those of the side force and of the lift shown in figure 5.16(a, b), thus showing a clear correlation between these quantities. Finally, the mean modulus G_r^* is compared for all 25

configurations in figure 5.18(c). There is a clear reduction of the gradient when boat-tails are mounted, and the effect is fairly proportional to the angles. However, if $\theta_B = 5°$ or $\theta_T = 7.5°$, the modulus remains almost constant for all geometries.
The fluctuations are then studied in detail. In figure 5.18(d), those of the horizontal gradient are triggered when both boat-tail angles are comparable (diagonal terms) and smaller than $\theta_i \simeq 10°$. The fluctuations' intensity is comparable to the baseline. For larger angles, the fluctuations of the horizontal base pressure gradient are damped and replaced by those of the vertical one, in particular for $\theta_T = \theta_B = 12.5°$, as one can observe in figure 5.18(e). However, their magnitude is almost twice smaller.
Both gradients never show simultaneously large fluctuations. Off-diagonal terms correspond to a very low fluctuation level in all cases. Comparing figure 5.16 to figure 5.18 shows again an excellent agreement between the horizontal gradient and loading and similarly for the vertical ones. Two different behaviors can also be identified in the modulus' fluctuations in figure 5.18(f). While y-fluctuations correspond to large standard deviations of the strength, the z-fluctuations impact the modulus much less. The dynamics of the wake during the different fluctuation crises are studied in details in § 5.4.5: horizontal fluctuations, vertical fluctuations and more steady cases.

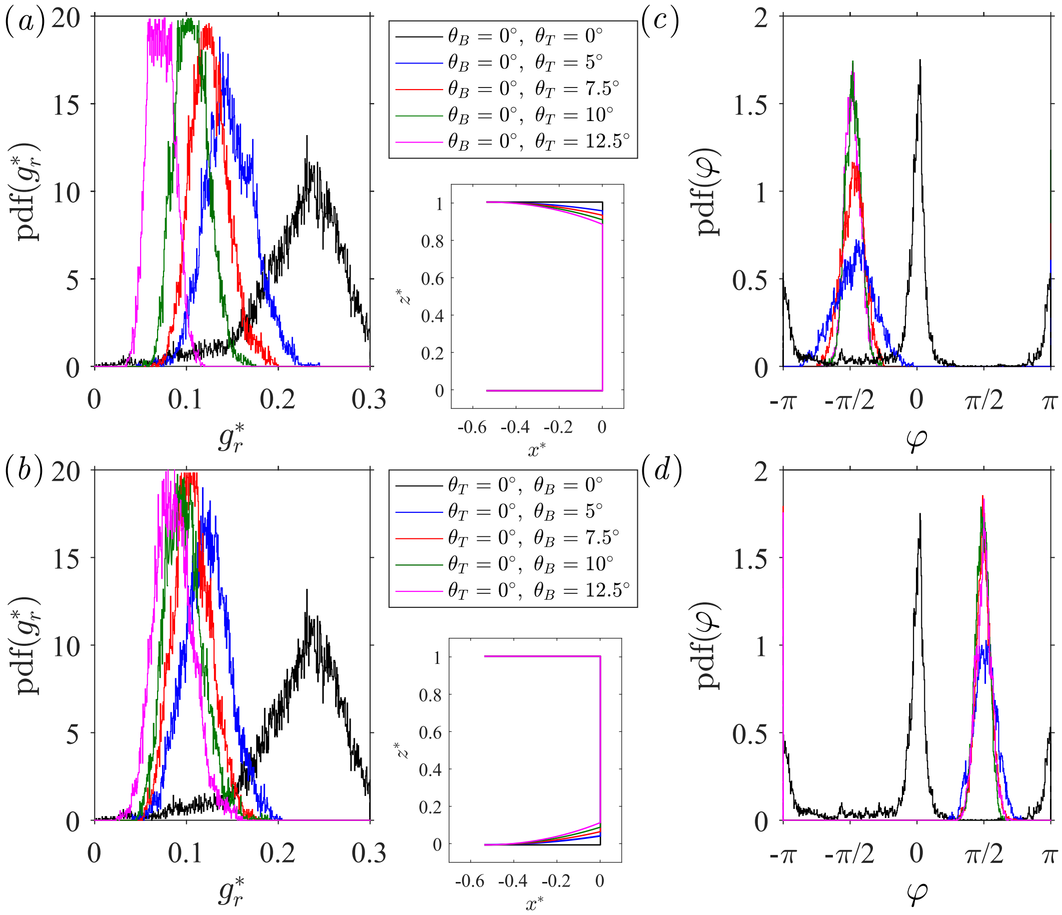

Figure 5.19 – Probability Density Functions of the base pressure gradient for one-sided boat-tailed geometries: $(a-c)$ Modulus g_r^*, $(b-d)$ phase φ.

This section deals with the effects of boat-tailing on the wake, in particular on its dynamics, namely the static orientation or the time scale associated with reversals if any. At first, the scenarii with one boat-tail only mounted either at the top (figure 5.19a, c) or the bottom (figure 5.19b, d) of the base. The modulus g_r^* and the phase φ are used as the topological wake indicator and their PDF are studied. Figures 5.19(a, b) shows that, with respect to the baseline (§ 5.4.1), the use of a boat-tail of length $\ell_B = \ell_L$ – regardless of its location either at the top or at the bottom of the base – leads to a reduction of the modulus of the gradient g_r^* by almost a factor of 2. As the boat-tail angle θ_i increases, a linear decrease of the modulus can be observed. Simultaneously, all probability density functions become narrower therefore indicating smaller fluctuations. The strength reduction is accompanied by an immediate rotation of the wake corresponding to phase lock-in (figure 5.19*c*). The same results but with lock-in at $\varphi = \pi/2$ instead of $\varphi = -\pi/2$ are obtained if only the bottom angle is modified (figure 5.19*d*). The similar behavior for the two boat-tails explains the anti-symmetry in the sensitivity maps in §§ 5.4.3, 5.4.4. Since there seems to be a competitive effect between the boat-tails, we investigate in the following the simultaneous use of two pieces.

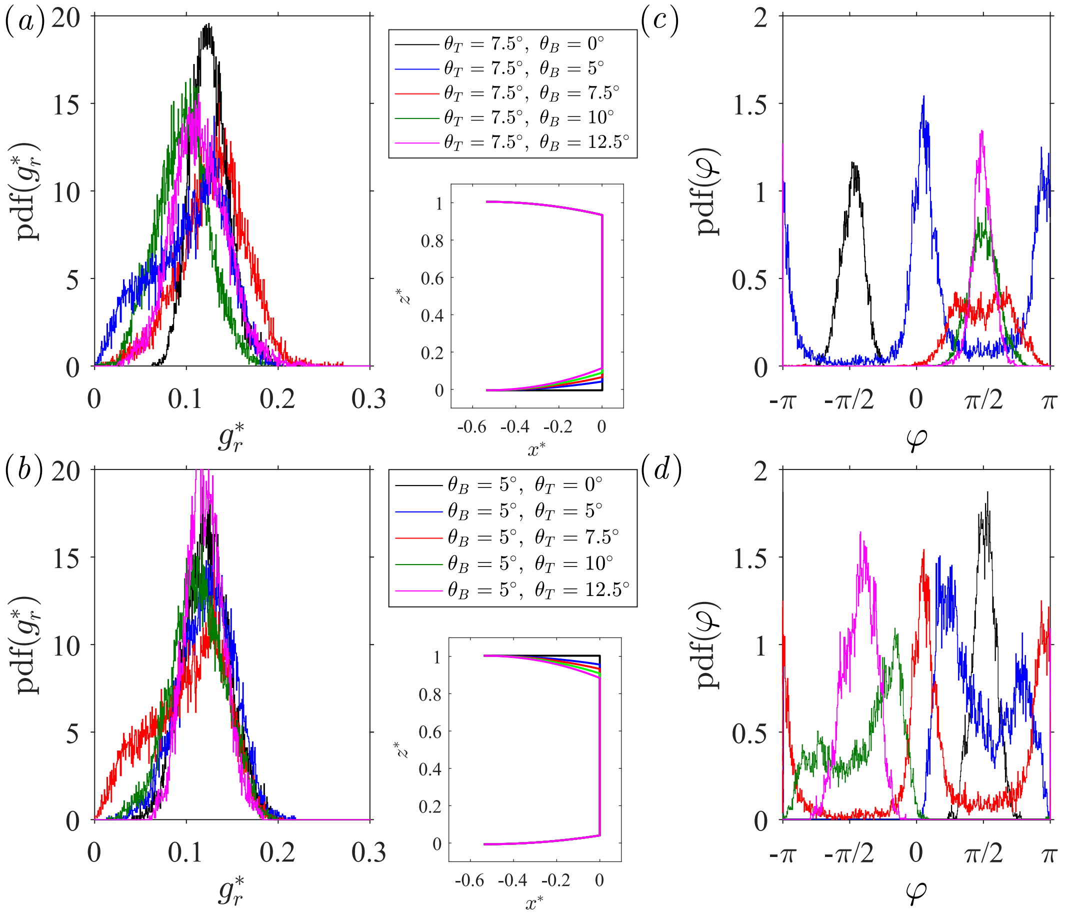

Figure 5.20 – Probability Density Functions of the base pressure gradient for two-sided boat-tailed geometries: $(a - c)$ Modulus g_r^*, $(b - d)$ phase φ.

All angles were combined together in previous sections. We chose to only investigate two cases; first, we set the top angle to $\theta_T = 7.5°$ while the bottom one is varied in $\theta_B \in \{0°, 5°, 7.5°, 10°, 12.5°\}$ and second, we set $\theta_B = 5°$ and vary θ_T. The results are summarized in figures 5.20(a, c) and 5.20(b, d) respectively. Since the results are similar, they are commented together. Only the latter case is considered in the following as it is easier to consider for PIV measurements. The influence of the boat-tail angle on the modulus g_r^* is very small (figure 5.20*c*). The initial value (in black) was already reduced with respect to the baseline by a factor of 2 as evidenced in figure 5.19(a, c). The behavior of the phase must be described in details as, in our opinion, it contains all the needed information to explain the different wake orientations reported in Perry *et al.* (2016*b*) as well as the fluctuations identified in the previous sections. We only comment figure 5.20(*d*) – bottom boat-tail varied – but the mechanisms and the conclusions are identical for figure 5.20(*c*) – top boat-tail varied – except that the other part of the base is explored.

When only the bottom boat-tail is installed, the wake is locked around $\varphi = +\pi/2$ in agreement with figure 5.19, corresponding to a vertical base pressure gradient only (null horizontal component) and shown by the black curve. When a 5°-bottom angle is installed at the top, a phase unlocking occurs and a bi-stable dynamics can be identified owing to the two peaks of the PDF of the phase shown in blue. The two most probable values correspond to φ and $\pi - \varphi$. As the angle is further increased to $\theta_T = 7.5°$, the red curve shows that the bi-stable dynamics now explores $\varphi = 0$ and $\varphi = \pi$, similarly to the square-back geometry (§ 5.4.1). The green ($\theta\ _T = 10°$) and magenta curves ($\theta_T = 12.5°$) show that a similar evolution is then observed: first a bi-stable dynamics with most probable orientations at φ and $\pi - \varphi$ (where $\varphi < 0$) until a permanent wake lock-in at $\varphi = -\pi/2$. Although only some angles are investigated, the transition seems to be continuous. These two figures explain the different wake orientations observed in Littlewood & Passmore (2010), Grandemange *et al.* (2013*c*) or Perry *et al.* (2016*b*). The other scenario presents the same features. In our opinion, this solves some of the questions raised by the fluctuations: bi-stable dynamics lead to large horizontal wake fluctuations and lock-in to lower levels. However, the question of vertical fluctuations persists. Besides, the wake reversals and lock-in explain the different base pressure distributions that one can observe in figures 5.19 and 5.20.

The wake orientations identified hereabove are confirmed by the velocity fields in the centerline plane ($y^* = 0$). Both one-sided and two-sided configurations are presented. The baseline configuration, characterized by left-right bistability associated with an almost null vertical pressure gradient since the instability is saturated (chapter 4.3.1.2), has a symmetric wake in the $y^* = 0$ plane with both recirculations of about the same size (figure 5.21*a*). The length of the recirculation area is about 1.7 in dimensionless units as shown in chapter 3. As one boat-tail is installed, *e.g.* $\theta_T = 5°$ and $\theta_B = 0°$ as shown in figure 5.21(*b*), phase lock-in (here at $\varphi = -\pi/2$) is easily identifiable. The upper recirculation grows and dominates the lower one. In addition to this rotation, the wake is slightly shortened with a length now ranking around 1.4 of the body's height H (not of the base's height H_b). As the angle is further increased up to $\theta_T = 12.5°$ (figure 5.21*c*), the global topology of the wake is not modified. However, the recirculation area becomes even shorter, now around 1.2. It can also be seen in figure 5.21(b, c) that the flow does not separate from the boat-tail; this is in agreement with Perry *et al.* (2015, 2016*b*) who report detachment for angles larger than 16°. As a consequence, the flow streamlines' curvature increases which partly explains the low pressures observed on curved geometries in figure 5.14.

The possible wake orientations in presence of two boat-tails are given in figures 5.21($d-f$). The case subject to horizontal fluctuations presented in figure 5.21(*d*) is very similar to the baseline, with two recirculating cores of about the same size, showing that the wake asymmetry is concentrated in the $z^* = 0$ horizontal plane. The same wake orientations as with one-sided boat-tails can also be obtained with two as in figure 5.21(*e*). However, the shortening of the recirculation area is more important than in the previous case for geometrical reasons. The topology of the case subject to vertical wake oscillations (figure 5.21*f*) is quite similar but the wake is way shorter than in other configurations and very similar to that of a cylinder in a turbulent flow. Similarly to one-sided geometries, no flow separation is identified on the boat-tails regardless of the considered angles. Similar modifications of the topology of the wake – shortening, orientation controlled by the flow orientation – are reported for the Windsor model by Perry *et al.* (2016*b*).

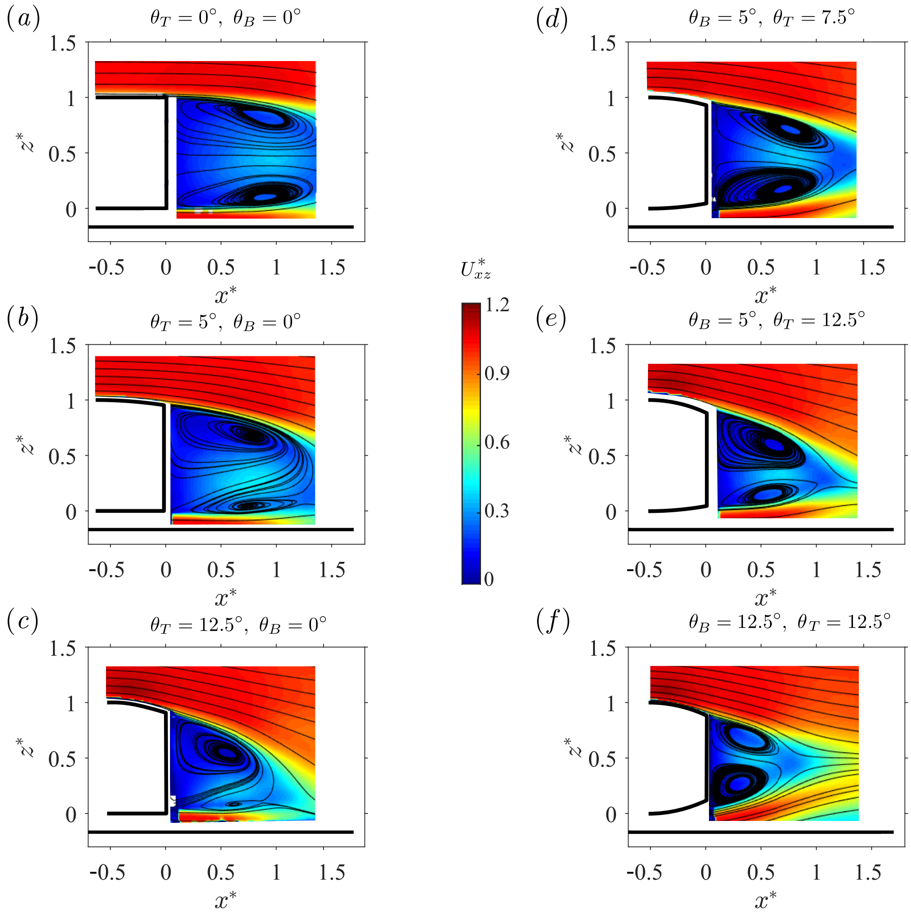

Figure 5.21 – Cross-sections of the mean velocity field U^*_{xz} visualized using streamlines superimposed to the modulus of the components in the vertical plane (x^*, z^*). One-sided configurations: (*a*) baseline, (*b*) small angle ($\theta_T = 5°$), (*c*) large angle ($\theta_T = 12.5°$). Two-sided configurations: (*d*) balanced small angles ($\theta_T = 7.5°,\ \theta_B = 5°$) leading to y-fluctuations of the wake, (*e*) lock-in at $\varphi = \pi/2$ ($\theta_B > \theta_T$), (*f*) large angles ($\theta_T = \theta_B = 12.5°$) leading to z-fluctuations of the wake.

Wong & Mair (1983) and Han *et al.* (1992) mention the creation of a pair of counter-rotating vortices contributing to drag on the boat-tails. In order to identify them, we plot the downstream component ω of the mean vorticity field in the plane $x^* = 0.45$. Compared to the baseline (figure 5.22*a*), figure 5.22(*b*) and figure 5.22(*c*) respectively related to the top and the bottom boat-tail show an important increase of the vorticity magnitude responsible for the drag but also the lift force on the circle-arcs. Interestingly, the sign of the vorticity is inverted with respect to the baseline, *i.e.* the vortices are rotating in the opposite direction. These two vortices are responsible for the lift generated on the boat-tails but also create induced drag. The presence of two boat-tails does not modify the general features of the longitudinal vorticity field with respect to one-sided geometries – comparing figures 5.22($d-f$) to figures 5.22($a-c$).

Since the question of lock-in is solved, we want to investigate further the dynamics of the fluctuations of the wake along the horizontal axis of the base when the boat-tail angle is increased – region of high fluctuations of g^*_y in figure 5.18(*d*). In that aim, we compare three specific cases: *(i)* baseline ($\theta_T = 0°, \theta_B = 0°$), *(ii)* $\theta_T = 7.5°, \theta_B = 5°$, *(iii)* $\theta_T = 10°, \theta_B = 7.5°$. We present results using a space-time diagram along the $z^* = 0$ pressure line and spectra of the phase φ of the base pressure gradient in figure 5.23.

The wake reversals for the squareback geometry, typical of the y-instability (§ 4.3.1.1),

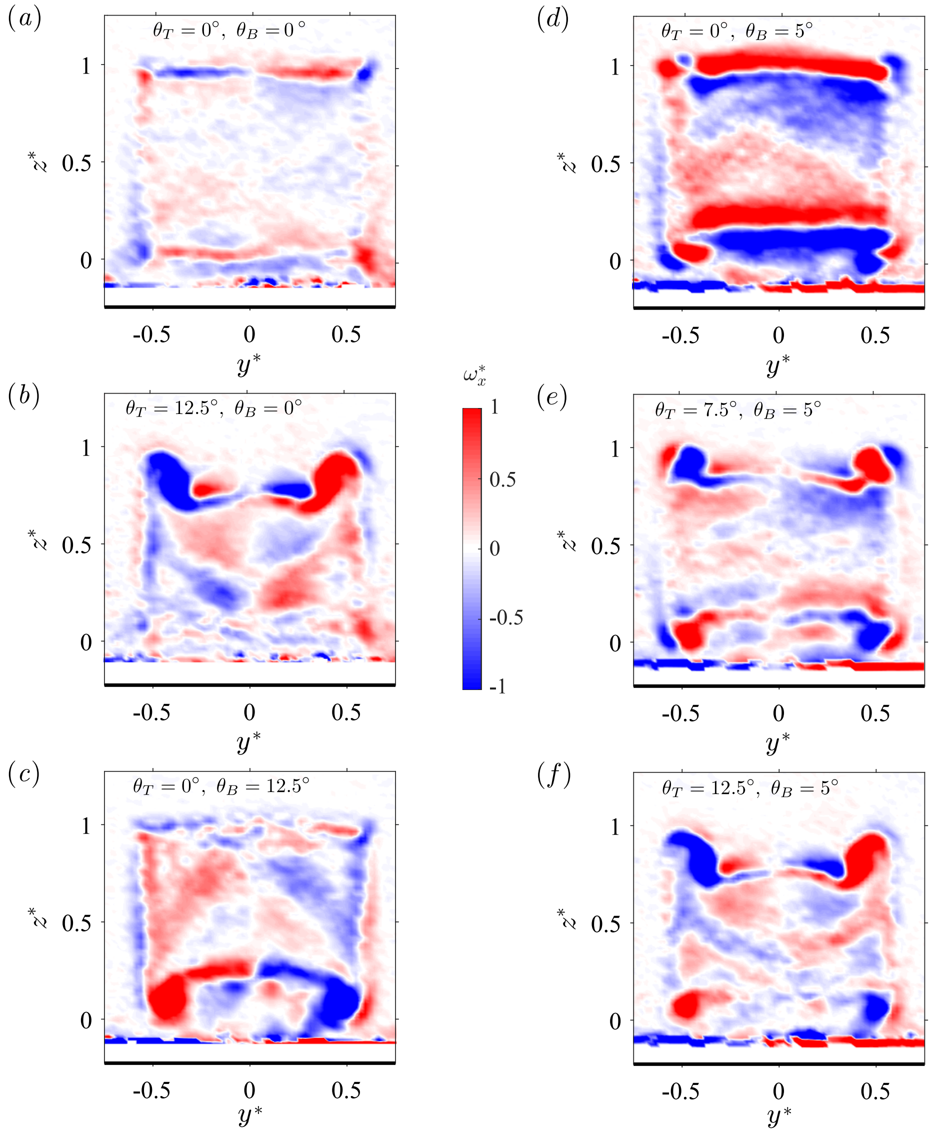

Figure 5.22 – Cross-sections of the mean vorticity field ω^* colored by the magnitude of the downstream component of the vorticity ω_x^*: (*a*) squareback case ($\theta_T = \theta_B = 0°$), (*b*) top boat-tail only ($\theta_T = 12.5°, \theta_B = 0°$), (*c*) bottom boat-tail only ($\theta_T = 0°, \theta_B = 12.5°$). Scenario with the top boat-tail angle fixed to $\theta_B = 5°$: (*d*) lock-in at $\varphi = \pi/2$ ($\theta_T = 0°$), (*e*) bistability between $\varphi = -\pi$ and $\varphi = 0$ ($\theta_T = 7.5°$), (*f*) lock-in at $\varphi = -\pi/2$ ($\theta_T = 12.5°$).

are easily identifiable in figure 5.23(*a*) and can be compared with those presented in figure 4.2(*c*) on page 55 or on the space-time diagrams of the y-unstable case of Evrard *et al.* (2016). The wake's orientation remains locked in one state for $500 - 1000\ t^*$ before a very quick reversal occurs. The associated spectrum does not exhibit a single peak but rather high energy in a wide range of low frequencies, accordingly to the stochastic motion (Rigas *et al.*, 2015; Brackston *et al.*, 2016). The first y-unstable case with boat-tails ($\theta_T = 7.5°, \theta_B = 5°$) is considered in figure 5.23(*b*). Wake reversals can still be identified but with respect to the baseline, their probability increases drastically, with a typical lock-in time now ranking around $250 - 500\ t^*$. Accordingly, the energy density increases in the high frequencies range ($f^* > 0.1$). This dynamics can be retrieved for all y-fluctuating cases identified in figures 5.16 and 5.18. we show another configuration in figure 5.23(*c*) with $\theta_T = 10°, \theta_B = 7.5°$. According to figure 5.18, it is still subject to y-fluctuations of the wake. The same features are retrieved for the wake orientation except that, yet, the typical lock-in type scale is rather around 100 t^*, resulting in a higher frequency dynamics. However, despite the different time scale, the wake reversal mechanisms remains almost identical for the three considered configurations. The increase of the typical switch frequencies with the boat-tail angles is already reported by Perry *et al.* (2016*b*). There is still no periodicity identifiable in the wake motion, which is consequently still ascribed to the static asymmetric wake states resulting from a laminar bifurcation (Grandemange *et al.*, 2012*a*).

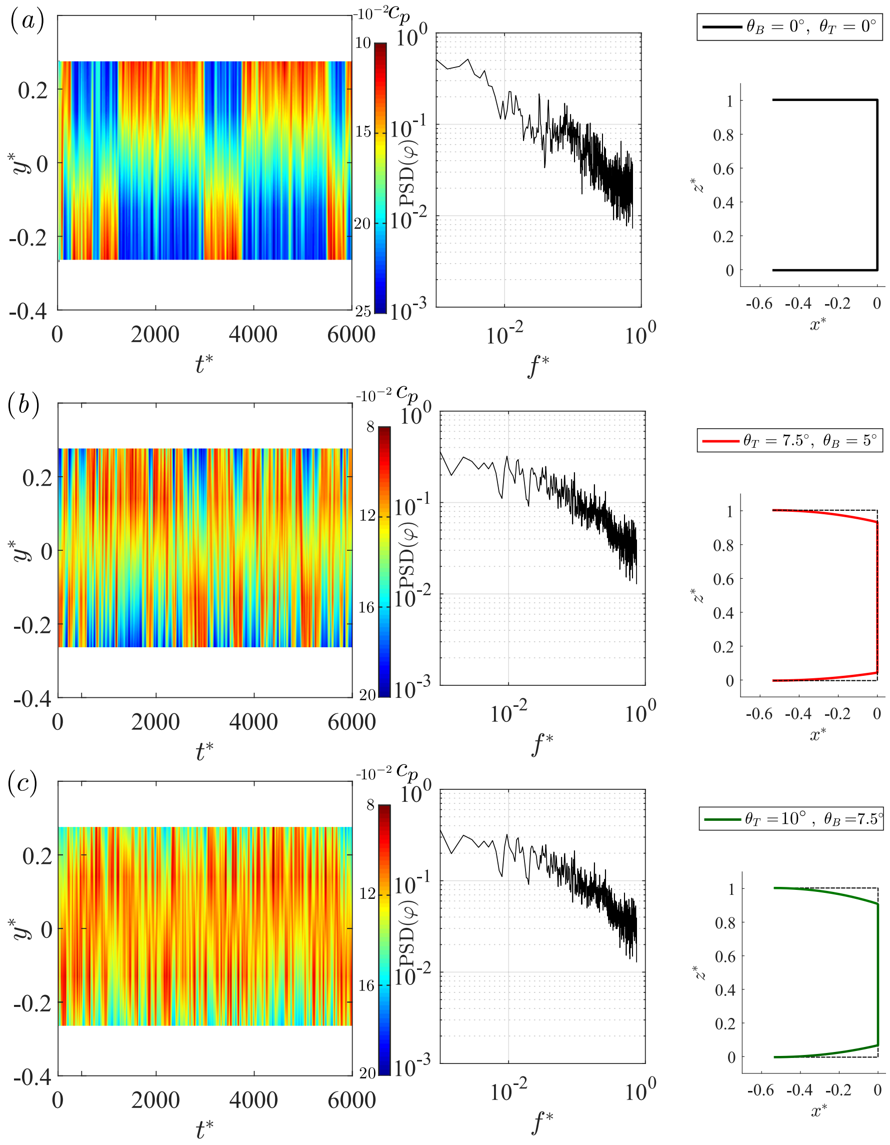

Figure 5.23 – Wake dynamics of y-fluctuating cases: space-time analysis along $y^* = 0$ and base pressure gradient's phase φ spectra: (*a*) baseline, (*b*) $\theta_T = 7.5°, \theta_B = 5°$, (*c*) $\theta_T = 10°, \theta_B = 7.5°$.

Finally, we turn to the last fluctuating case identified in figure 5.18, with z-fluctuations of the wake. The typical boat-tail angles yielding such configuration are large, for instance $\theta_T = 12.5°, \theta_B = 12.5°$. Results are presented in a similar way in figure 5.24. The second kind of fluctuations (z-fluctuations) is characterized by a very different time-scale for the wake reversals (figure 5.24*b*) since it is now of only about 5 t^*, resulting in a high-frequency dynamics. In addition, a clear periodicity can be identified owing to the peak in the φ-spectrum around $f^* = 0.2$, the characteristic frequency of vortex-shedding for such geometries (Grandemange *et al.*, 2013*b*). These two arguments, added to the fact that, due to boat-tailing, the aspect ratio becomes very unpropitious for vertical wake switch-

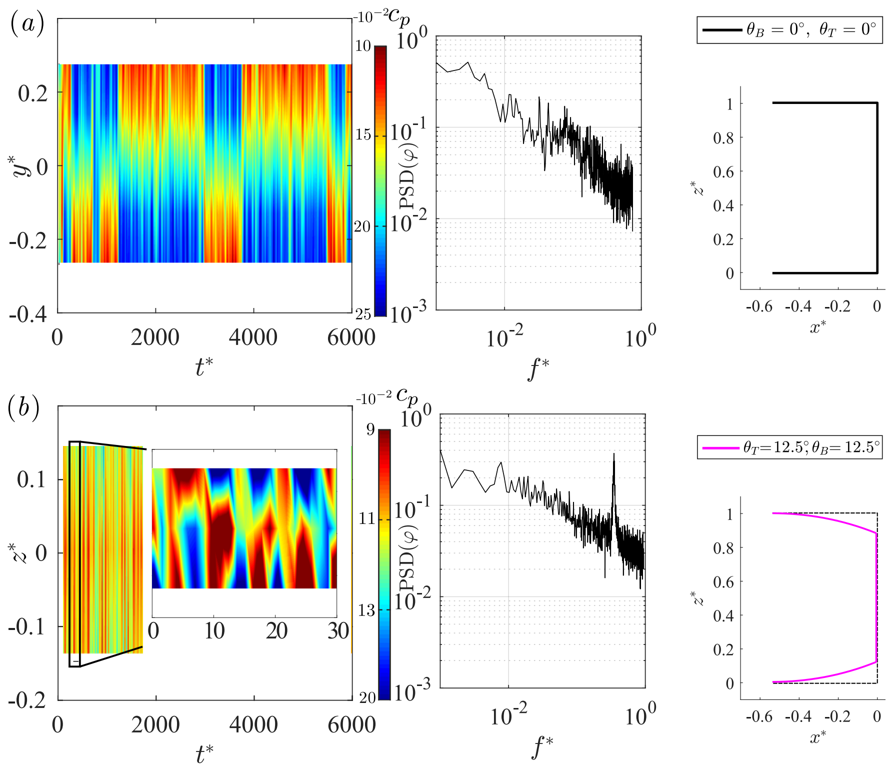

Figure 5.24 – Wake dynamics: space-time analysis and base pressure gradient's phase φ spectra: (*a*) baseline and analysis along $y^* = 0$, (*b*) periodic mode ($\theta_T = \theta_B = 12.5°$) and analysis along $z^* = 0$.

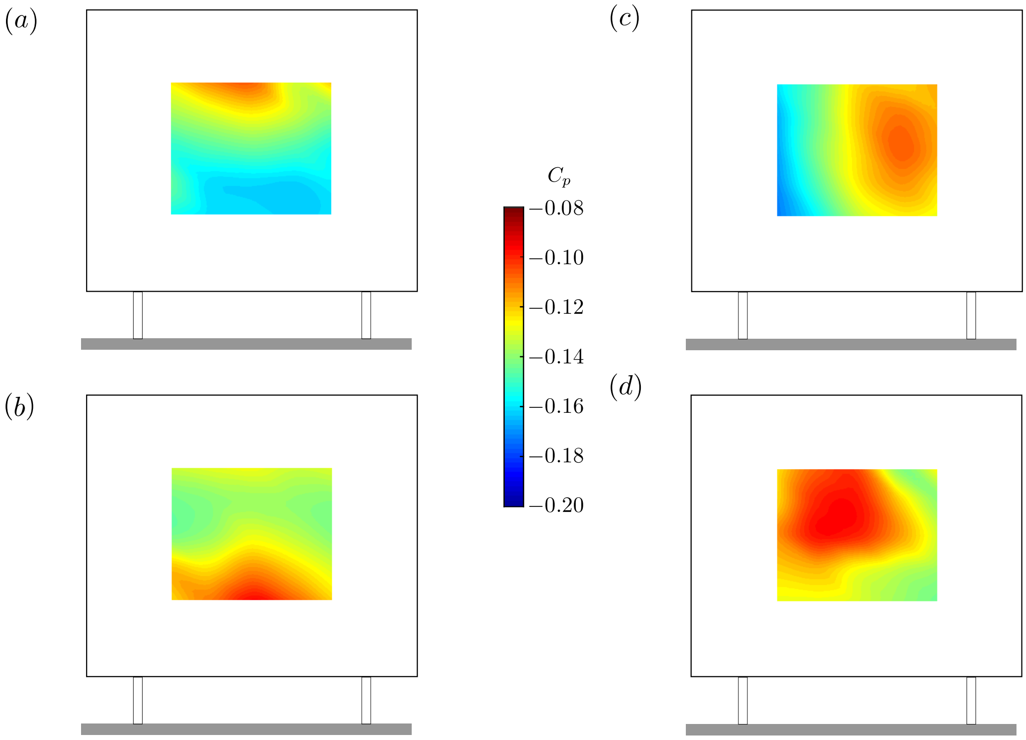

Figure 5.25 – Typical mean base pressure distributions $C_p(y^*, z^*)$ resulting from the use of boat-tails: (*a*) phase lock-in at $\varphi = \pi/2$, (*b*) phase lock-in at $\varphi = -\pi/2$, (*c*) conditionally averaged distribution for the y-instability with boat-tails (state P), (*d*) periodic mode (positive gradient).

ing according to Grandemange *et al.* (2013*a*), suggest that the wake is not expected to be driven by static asymmetric modes anymore. We assume that the symmetry-breaking modes of the wake are consequently removed and yield to a periodic motion. A proof is brought with the sensitivity analyses given in Appendix C. This observation is also in agreement with the linear stability scenario of Marquet & Larsson (2014), for which the increase of the width-to-height aspect ratio leads to the removal of the static instability yielding to the periodic one (vortex-shedding) as can be observed in figure 1.3 on page 9. We finally show the typical mean base pressure distributions resulting from the use of boat-tails in figure 5.25. Four cases must basically be presented: phase lock-in at $\varphi = \pi/2$, y-wake bistability, phase lock-in at $\varphi = -\pi/2$ and the periodic mode. The pressure levels are quite different because these configurations are obtained with different boat-tail angles. Nonetheless, figures 5.25($a-c$) clearly show the global rotation of a unique wake mode (as described in chapter 4); the periodic case (figure 5.25d) is a bit different since the structure of the mode is lost. Similar base pressure imprints as those related to global wake rotations and given in figure 5.25 are reported for the Windsor model with rear tappers in Littlewood & Passmore (2010); Perry *et al.* (2016*b*); Pavia *et al.* (2016). In these papers, a global wake rotation controlled by the tappers angles can indeed be identified as well.

5.4.6 Influence of the boat-tails' geometry on the aerodynamic loading and on the wake dynamics

In this section, the influence of the boat-tail geometry is studied for the two typical wake fluctuations previously identified: y-instability with $\theta_T = 7.5°, \theta_B = 5°$ ($T75B5$ in table 5.1) and z-periodic wake shifts with $\theta_T = 12.5°, \theta_B = 12.5°$ ($T125B125$ in table 5.1). Out of the 25 tested configurations, the optimal drag with the circular long boat-tails was identified as $\theta_T = 7.5°$ and $\theta_B = 5°$. This case is subject to the y-instability related to static asymmetric modes and wake bistability is present since the two mirror wake states P and N, similar to those of the baseline, are alternately explored. Three geometries with the same angles are compared: the circle-arcs of length $\ell_B = \ell_L$ investigated so far (referred to as $T75B5$ in table 5.1), slants of length $\ell_B = \ell_L$ ($T75B5-sl$ in table 5.1) and circle-arcs of length $\ell_B = \ell_S$ ($T75B5-cs$ in table 5.1).

Table 5.4 – Mean and fluctuating aerodynamic coefficients: mean base suction C_b, mean drag C_x, mean side force C_y, mean lift force C_z and associated standard deviations denoted by the superscript "′". The first column corresponds to the configuration: baseline, $T75B5$ with $\ell_B = \ell_L$ and circular boat-tail, $T75B5-sl$ with $\ell_B = \ell_L$ and slanted boat-tail, $T75B5-cs$ with $\ell_B = \ell_S$ and circular boat-tail. All angles (except for the baseline) are $\theta_T = 7.5°$ and $\theta_B = 5°$.

	C_b	C_b'	C_x	C_x'	C_y	C_y'	C_z	C_z'
Baseline	0.174	0.008	0.281	0.004	−0.002	0.018	−0.118	0.006
$T75B5$	0.133	0.004	0.262	0.002	−0.002	0.011	−0.145	0.003
$T75B5-sl$	0.109	0.004	0.236	0.002	−0.002	0.009	−0.146	0.006
$T75B5-cs$	0.169	0.005	0.278	0.002	−0.001	0.020	−0.133	0.003

The mean and the standard deviation of the force coefficients and of the base suction coefficient are given in table 5.4. With respect to the baseline (squareback geometry), long circular boat-tails of length $\ell_B = \ell_L$ (case $T75B5$) lead to base suction and thus drag reduction and lift increase (in terms of magnitude), still acting as a downforce. Though slightly reduced, the fluctuations of the lateral force C_y' remain quite large with respect

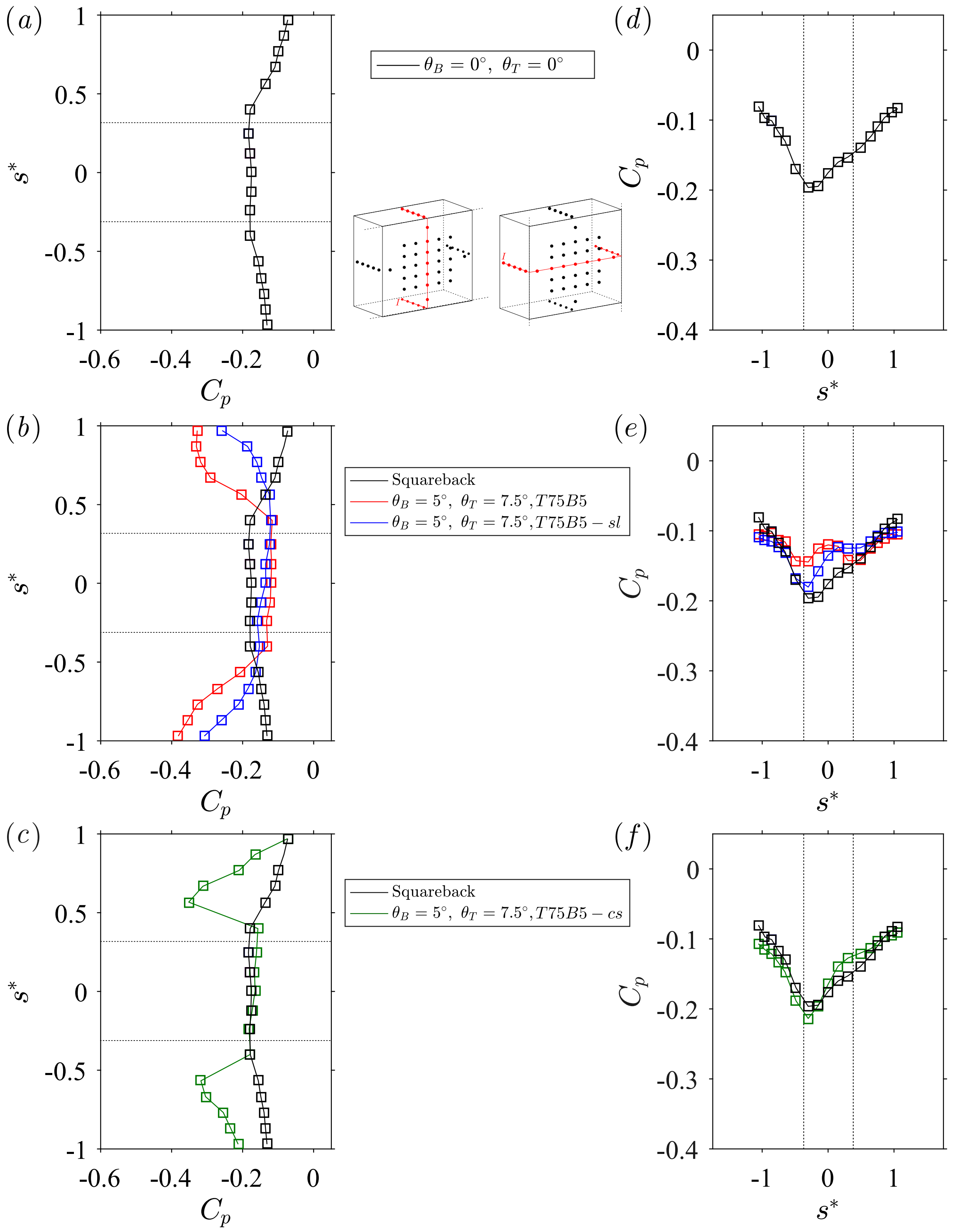

Figure 5.26 – Mean pressure coefficient C_p plotted along a line of constant x_i^* for the three geometries (long circle-arc, short circle-arc and slant) with $\theta_T = 7.5°$, $\theta_B = 5°$: (a, b, c) $x_i^* = y^* = 0$,(d, e, f) $x_i^* = z^* = 0$.

to other components', which are almost unaffected by boat-tailing, in agreement with the wake dynamics described in figure 5.23. For the case $T75B5 - sl$, the circle-arcs are replaced by slants. The drag C_x is further reduced – 16% compared to the baseline – but its fluctuations are unaffected. Compared to the circle-arcs, no clear influence can be observed on the side force C_y, on the mean lift C_z or on its fluctuations C_z'. The side force fluctuations C_y' are still one order of magnitude higher than those of other components thus showing that the horizontal fluctuations of the wake persist. As in the previous case, the fluctuations of the mean base pressure C_b' are divided by nearly two. To summarize, slants are more efficient than circle-arcs to reduce drag but the other components of the aerodynamic loading or their fluctuations are almost unaffected.

Back to circular boat-tails, we change the length and chose $\ell_B = \ell_L$ for the last configuration $T75B5 - cs$. Compared to the baseline, drag reduction is of $\Delta C_x = -0.003$ only, too close to the balance uncertainty (see § 2.2.2) to conclude about a real beneficial effect. C_x' is very close to the other measurements similarly to the mean side force coefficient C_y. Surprisingly, the effect on the mean lift coefficient C_z is much more important with a sensitive difference following the same trend as the other modified geometries. The main difference regarding this geometry lies in the side force fluctuations. Even though the mean value is comparable, the fluctuations C_y' are higher than in any other cases including the baseline. This suggests that the fluctuations of the wake in the horizontal direction are stronger than in the baseline or that the wake asymmetry is.

The wall pressure distribution for the three boat-tailed geometries is compared and the results are presented for the constant y- and z-pressure lines defined in § 5.3 in figure 5.26($a - b$). From figure 5.26(b, c) and as already spotted out with the base suction C_b in table 5.4, the base pressure recovery is more important with longer boat-tails; this observation is consistent with the *diffuser effect* of such geometries. The pressure distribution on both boat-tails depends much less on their length than on their shape since the red and the green curves almost present the same features. However, short boat-tails lead to much lower pressure levels than longer ones. Since the mean base pressure also appears to be lower, this explains the poorly efficient drag reduction. Compared to the squareback, the case $T75B5 - cs$ only benefits of the reduction of the base surface, which appears to be a very efficient drag reduction mean since it even overwhelms the contribution of the two boat-tails. Comparing the circle-arcs and the slants, the different curvatures of the pressure distributions must be highlighted. While circle-arcs lead to a concave shape with a minimum around the middle of the boat-tail, the distribution associated with slants is convex. The lowest pressure is reached at the upstream part of the boat-tail, *i.e.* just after the beginning of the slant, and it then continuously increases. This explains the better efficiency of this geometry. The role of fairing and of the singularities on boat-tail shapes is already assessed in Mair (1969). As expected due to the top/bottom orientation of the wake, there is almost no impact on the $z^* = 0$-pressure line of the geometry.

The wake topology of the three investigated configurations is studied owing to the mean velocity fields in the centerline plane ($y^* = 0$) in figure 5.27. The case with long boat-tails is reproduced from figure 5.21. With respect to the long circular boat-tails, the use of a slant (figure 5.27b) does not modify the global wake topology. Nonetheless, the curvature imposed to the streamlines by the geometry is drastically reduced, thus explaining the lower drag induced on the boat-tails for this configuration. As a consequence, the recirculation zone elongates. The wake obtained with the short circular boat-tails (figure 5.27c) is much closer to the baseline's (figure 5.21a) than the two others, even if a deviation is introduced by the afterbody geometry. There seems to be no flow separation on the boat-tail even if the poor resolution in this area does not allow a firm conclusion.

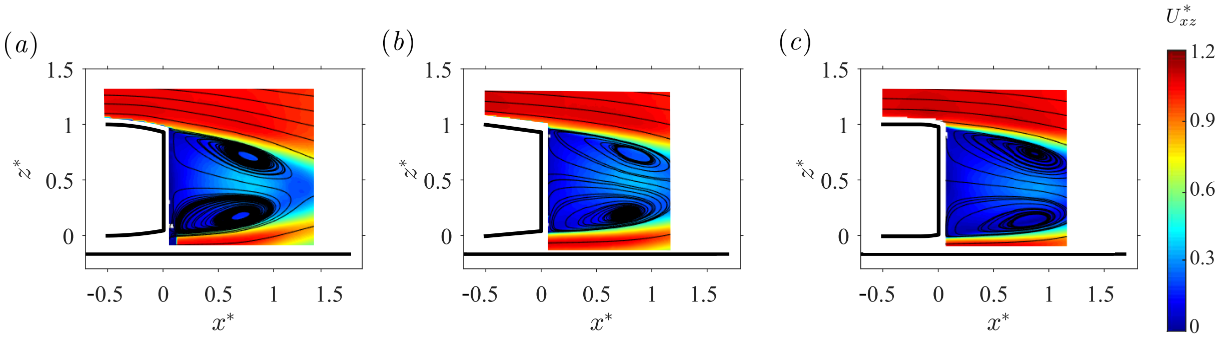

Figure 5.27 – Cross-sections of the mean velocity field U^*_{xz} visualized using streamlines superimposed to the modulus of the components in the vertical plane (x^*, z^*) for three geometries with $\theta_T = 7.5°$, $\theta_B = 5°$: (a) circular long boat-tails ($\ell_B = \ell_L$), (b) slanted long boat-tails ($\ell_B = \ell_L$), (c) circular short boat-tails ($\ell_B = \ell_S$).

All three cases being subject to left-right wake fluctuations, we want to assess whether the shape of the boat-tail or its length has an influence on its dynamics, *i.e.* on the characteristic time-scale. Space-time diagrams along the line z^* are presented in figure 5.28 together with the associated phase φ-spectra. The dynamics of the case with long circular boat-tails displayed in figure 5.28(a) was already discussed in figure 5.23; in short, the characteristic time scale of the fluctuations is about $250 - 500\ t^*$, *i.e.* half that of the baseline, and no periodicity is found in the motion. When a slanted geometry with the same angles is installed (figure 5.28b), the time-scale is slightly larger though not as much as the baseline's (about $400 - 800\ t^*$). There seems to be a global stabilization of the wake as the energy density of the high-frequencies is reduced by more than a decade (in log scale) and transferred to slower dynamics. Finally, the length of the boat-tail is studied in figure 5.28(c). There are only few discrepancies with the baseline (figure 5.23a) as the time scale and thus the spectrum are nearly identical. To summarize, the length of the boat-tail is a crucial parameter to modify the wake dynamics since it strongly impacts the frequency of the wake switches. However, the y-instability persists for all tested configurations.

We reproduce a similar analysis with a different pair of boat-tail angles; we consider $\theta_T = 12.5°$ and $\theta_B = 12.5°$, referred to as the $T125B125$ configuration in table 5.1, for which periodic vertical fluctuations of the wake were previously identified. As stated in table 5.1, only the configuration with short boat-tails referred to as $T125B125 - cs$ was available for comparison.

The aim is to determine whether the periodic wake mode is retrieved or if, in view of the base aspect ratio, the wake is subject to a y-instability. We first give the mean and fluctuating aerodynamic coefficients in table 5.5. With respect to the baseline, both the mean base pressure coefficient C_b and its fluctuations C'_b decrease while the drag C_x is increased in both cases. Similarly to the other configurations, a larger base pressure increase is obtained with the longer boat-tails. Drag and base suction fluctuations remain quite similar in terms of order of magnitude, with damping proportional to ℓ_B. However, even if the mean side force C_y is not impacted as expected because of the symmetry of the afterbody, its fluctuations strongly depend on the boat-tail length. With the shorter boat-tail, their order of magnitude compares to that of the baseline and suggest the presence of the y-instability. This is enforced by the fluctuations of the lift C'_z whose level is close to the squareback geometry while they burst in presence of the periodic mode for the $T125B125$-case. The suppression of the wake periodicity and thus of the periodic wake

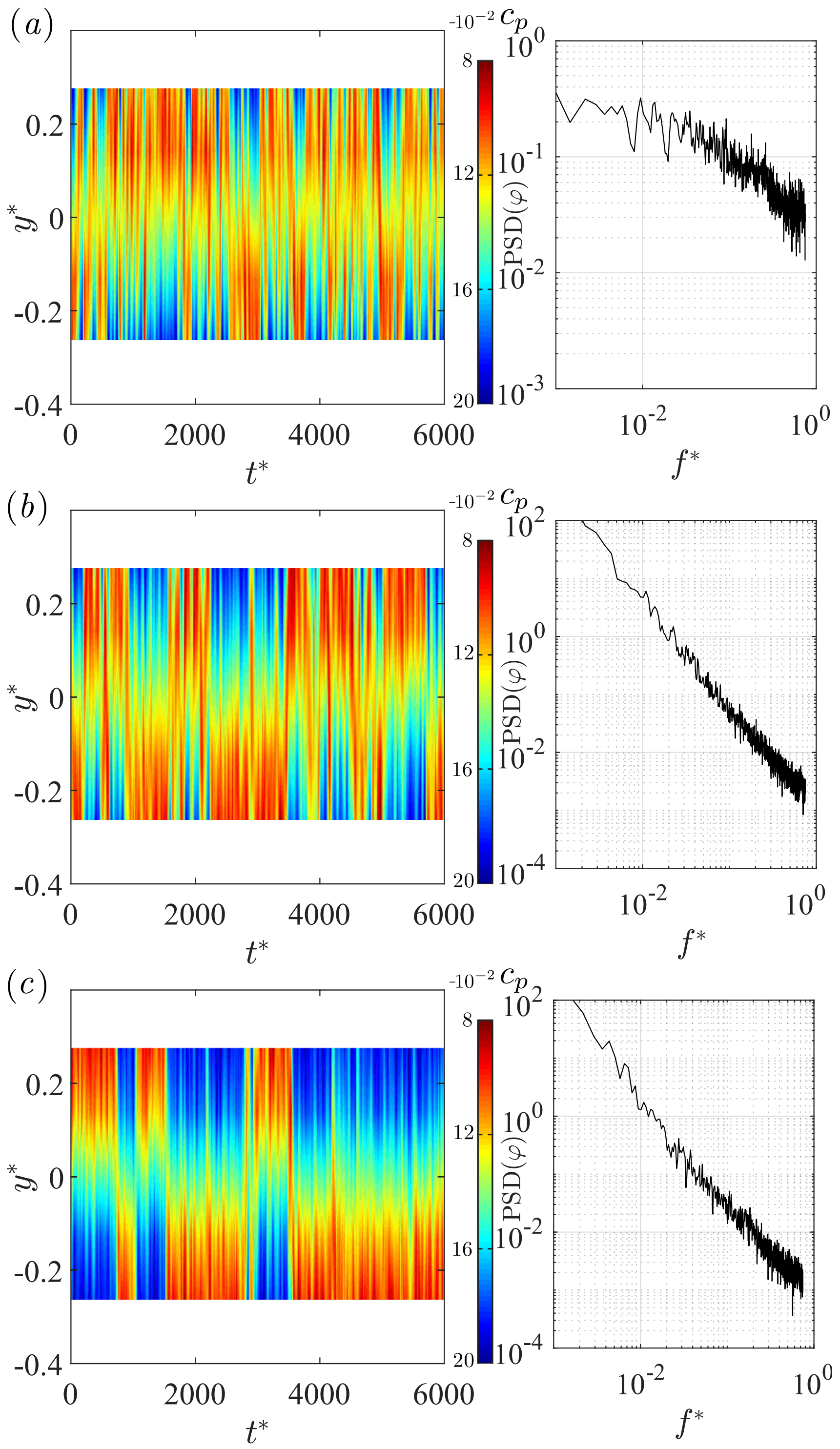

Figure 5.28 – Space-time diagram showing the pressure coefficient c_p along a line $z^* = 0$ and associated phase φ spectra for the three considered boat-tail shapes at $\theta_T = 7.5°$, $\theta_B = 5°$: (a) circular long boat-tails ($\ell_B = \ell_L$), (b) slanted long boat-tails ($\ell_B = \ell_L$), (c) circular short boat-tails ($\ell_B = \ell_S$).

mode is unambiguously shown by the two spectra of the gradient's phase φ presented in figure 5.29, in which the peak is absent for the shorter boat-tails thus indicating a random wake switching dynamics. As a consequence, we conclude that large flow deviations are not sufficient to replace the y-instability by a periodic mode but that the aspect ratio is the driving parameter since the proximity of both detached shear layers emanating from the top and from the bottom of the base and thus their interaction is necessary.

Table 5.5 – Mean aerodynamic coefficients: mean base suction C_b, mean drag C_x, mean side force C_y, mean lift force C_z and associated standard deviations denoted by the superscript "′". The first column corresponds to the configuration: baseline, $\ell_B = \ell_L$ and circular boat-tails ($T125B125$), $\ell_B = \ell_S$ and circular boat-tails ($T125B125 - cs$). All angles (except for the baseline) are $\theta_T = 12.5°$ and $\theta_B = 12.5°$.

	C_b	C'_b	C_x	C'_x	C_y	C'_y	C_z	C'_z
Baseline	0.174	0.008	0.281	0.004	−0.002	0.018	−0.118	0.006
$T125B125$	0.123	0.004	0.291	0.002	−0.002	0.003	−0.250	0.010
$T125B125 - cs$	0.158	0.006	0.292	0.002	−0.002	0.012	−0.178	0.005

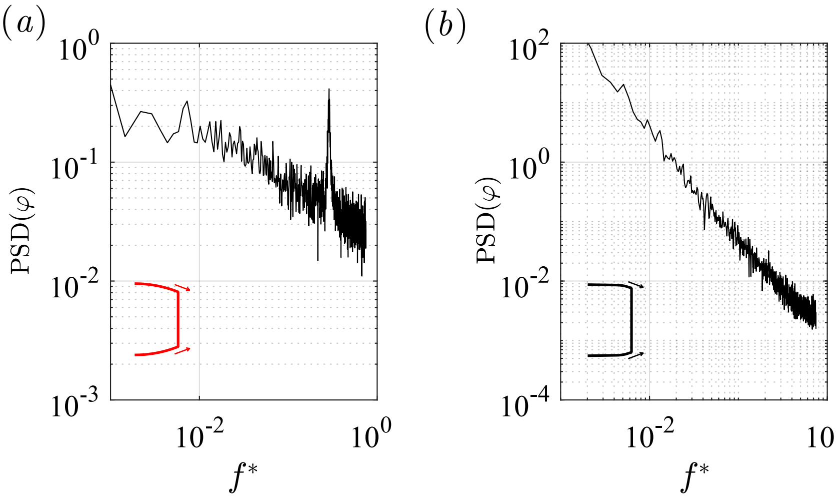

Figure 5.29 – Spectra of the base pressure gradient's phase φ for the two considered boat-tail shapes at $\theta_T = 12.5°$, $\theta_B = 12.5°$: (a) circular long boat-tails ($\ell_B = \ell_L$) subject to vortex-shedding, (b) circular short boat-tails ($\ell_B = \ell_S$) subject to the static instability.

5.4.7 Three-dimensional boat-tail

A three-dimensional boat-tail configuration is now investigated. All four base sides are modified. This configuration is chosen in view of obtaining the maximum drag reduction. Therefore, the top and bottom angles are chosen as the most efficient ones ($\theta_T = 7.5°$, $\theta_B = 5°$). We have seen in previous paragraphs that relatively small angles only lead to drag reduction since the low pressure generated on the boat-tails has a significant contribution to drag. Besides, side boat-tail angles should preserve the overall symmetry of the afterbody and are therefore identical on both sides of the base. That's why we chose $\theta_S = 5°$ for both side boat-tails of the considered afterbody. For this study, all boat-tails are circle-arcs.

The mean and fluctuating aerodynamic loading are given in table 5.6. Compared to the baseline, drag reduction by 20.3% is achieved thanks to the reduction of the base surface and of the base pressure recovery of nearly 50.6%. The wake is still subject to lateral fluctuations as proved by the large value of C'_y (almost that of the baseline) with respect to the other coefficients. This proves that nor the y-instability of the wake nor its fluctuations are removed. With respect to the two-dimensional boat-tailed cases with the same angles ($\theta_T = 7.5°,\ \theta_B = 5°$), the drag is further reduced showing the interest of 3D boat-tailed bodies in view of fuel efficiency. However, the impact on the lift or on the side force fluctuations is small.

Table 5.6 – Mean and fluctuating aerodynamic coefficients for the *3D* boat-tailed afterbody (see table 5.1): mean base suction C_b, mean drag C_x, mean side force C_y, mean lift force C_z and associated standard deviations denoted by the superscript "′".

C_b	C_b'	C_x	C_x'	C_y	C_y'	C_z	C_z'
0.086	0.001	0.224	0.002	−0.001	0.016	−0.155	0.004

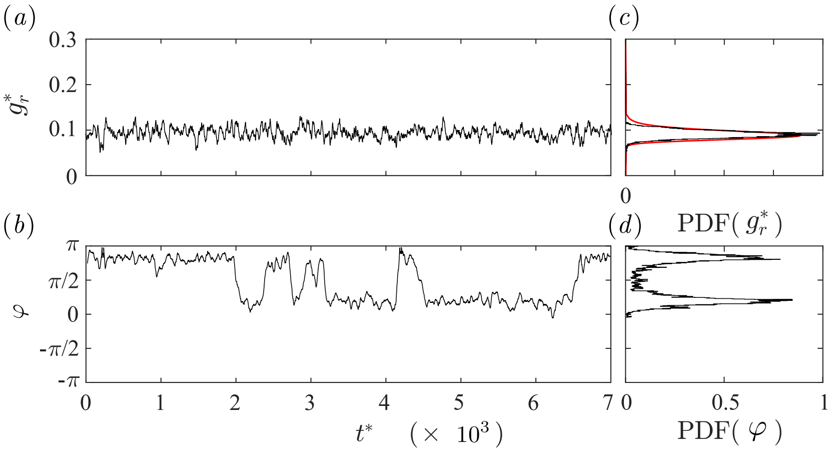

Figure 5.30 – Modulus $g_r^*(t^*)$ (a) and phase $\varphi(t^*)$ (b) time series of the base pressure gradient with corresponding probability density functions $(c-d)$ for the 3D boat-tailed case. The red curve in (c) is a best fit from Rigas *et al.* (2015).

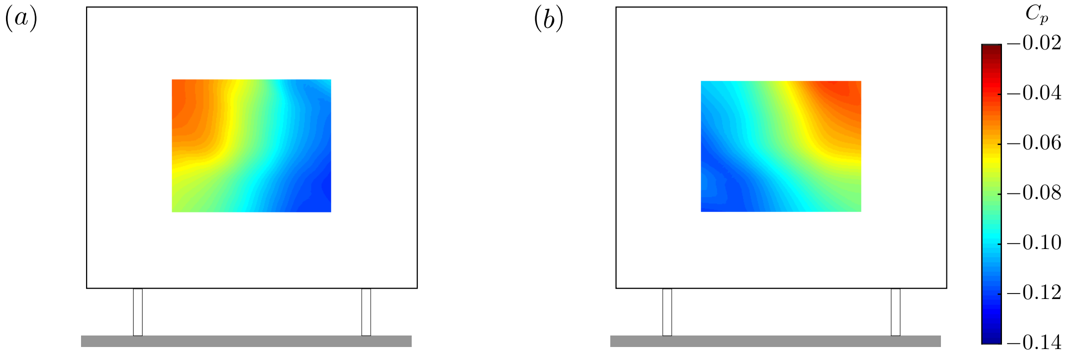

Figure 5.31 – Conditionally averaged base pressure distribution $C_p(y^*, z^*)$ for the three-dimensional boat-tailed afterbody: state N of the wake (a) and state P of the wake (b).

The wake dynamics is investigated through the base pressure gradient in the polar description (time series and PDF) given in figure 5.30. The modulus (figure 5.30a, c) is centered about 0.1 and experiences only high frequency small fluctuations related to the outer turbulence. In this case, very small values are never reached thus suggesting that phase jumps may not occur. The phase follows a very slow bi-stable dynamics between two values $\varphi = 0 + \epsilon$ and $\varphi = \pi - \epsilon$ where ϵ is a small deviation resulting from the adaptation mechanism presented in § 4.4.2 because of the vertical base pressure gradient imposed by the different boat-tail angles (figure 5.18*b*). The phase dynamics shown in figure 5.30(*b*) is very slow as only 8 reversals are observed in 7000 t^* thus yielding a characteristic time longer than 1000 t^*. Unlike the baseline configuration (similar to figure 4.4 in page 57), absolutely no phase jumps are observed; the wake reversals consist in continuous phase drift with constant modulus instead.

The associated base pressure distributions are given in figure 5.31(a, b). They are similar to those associated with state P and state N of the baseline (figure 5.11) but, as the two boat-tail angles are not equal, a (geometrical) vertical base pressure gradient is imposed. Compared to the previous pressure distributions, the colorbar has been re-scaled because of the large base pressure recovery. This is consistent with Han *et al.* (1992) in which the authors are able to obtain positive base pressure coefficients.

To sum up, the three-dimensional boat-tail does not strongly modify the wake's behavior except for the frequency of switch which becomes very small compared to the squareback geometry. The strength of the gradient is strongly reduced but the wake asymmetry not suppressed. Appendix C shows that the same y-instability as for the baseline still exists. The interesting drag reduction is the consequence of the base pressure recovery and of the limited angles which prevent excessive low pressure. Besides, the vertical blunt afterbody's surface corresponding to the detached flow area is also reduced by the geometry. Since there is no major drawback in terms of lift, such shapes appear as a promising design.

5.5 Discussion

After a summary of the two-dimensional phenomenon related with boat-tailing (§ 5.5.1), we discuss the impact on the wake modes (§ 5.5.2) and then more specifically on its strength and orientation (§ 5.5.3). The importance of boat-tail locations is highlighted in § 5.5.4 and a strategy of control of the aerodynamic loading is finally presented (§ 5.5.4).

5.5.1 On the two-dimensional mechanism related to boat-tailing

The two-dimensional potential flow simulation presented in § 5.2 already provides the essential mechanisms of boat-tailing to which some three-dimensional effects are added. Nonetheless, it is sufficient to explain the balance that needs to be found between the reduction of the contribution of the base to drag and the increasing one of the boat-tails that can simply be explained by the low pressure generated on this part of the afterbody. The general trends identified in § 5.2 are recovered throughout the rest of the chapter during the wind-tunnel testing campaigns. One of the major differences is that the real case leads to a drag optimum that is absent from the simulations. However, the transfer of curvature from the wake to the surrounding flow and its consequences on pressure is accurately modeled.

In addition, the Free Streamline model causes an underestimation of the drag as reported by Sychev (1982). In our opinion, it is mainly related to two reasons. First, the asymmetric wake modes (§ 5.5.2) are not taken into account. As a results, nor its contribution to drag nor the low pressure area resulting from the wake topology are represented. Second, the two-dimensional property of the flow and its inviscid property prevents from the formation of longitudinal vortices contributing not only to lift but also to drag (Wong & Mair, 1983; Han *et al.*, 1992).

5.5.2 Impact on the unstable wake modes

The first conducted analysis varying the boat-tail angles shows that the static asymmetric mode of the wake, responsible either for wake lock-in when the angles are strongly different either for a bi-stable dynamics for a balanced wake and associated with a y-instability in the sense of Grandemange *et al.* (2013*a*) is extremely robust. The wake behavior is very close to that studied in § 4.3.1 for the squareback geometry, except for the characteristic time scale which, as previously reported by Perry *et al.* (2016*b*), depends on the boat-tail angles. It appears indeed impossible to remove the instantaneous wake asymmetry for almost all tested boat-tailed configurations. The presence of the mode is unambiguously proved by its contribution to the cross-flow loading revealed clearly by the yaw sensitivity experiments presented in Appendix C. The symmetric wake resulting from the removal of the static asymmetric modes is not obtained in this work nor by other research teams on the Windsor geometry (Pavia *et al.*, 2016, 2018; Perry *et al.*, 2016*b*,*a*).
If the angles are largely increased, the two top and bottom shear layers eventually interact, the static asymmetric mode being then replaced by a periodic mode. This is consistent with the stability analysis of Marquet & Larsson (2014) for a flat plate for which the authors show that the static mode disappears for large aspect ratio, and only the periodic mode remains. However, this configuration is even more detrimental to drag in particular because of the boat-tailed induced drag contributing to the afterbody's suction. As shown in figure 5.18, z-fluctuations will eventually appear instead of y-fluctuations as for the baseline. A proof of the modes removal is brought in Appendix C considering the aerodynamic loading applied to the body varying its inclination. However, as can be seen in figure 5.13, the mean drag C_x does not benefit from this removal. It is said in Evrard *et al.* (2016) that the removal of the static asymmetric wake modes should be beneficial to drag. The present example shows that this must be done carefully. As a matter of fact, even if the wake asymmetry is actually removed, this mode is replaced by a periodic one that is more detrimental in terms of drag. Besides, the contribution of the vortex-shedding to the model's drag is enhanced (Mendona Bimbato *et al.*, 2013).
If side boat-tails are used so that the base aspect ratio gets reversed, the z-instability studied in § 4.3.2 will replace the y-one but the overall drag performance is identical as the implied mechanisms are the same (see § 4.4.3). This extreme robustness suggests that drag optimization could be performed taking advantage of the mode rather than trying to unconditionally remove it regardless of the effort[1]. As a matter of fact, we showed in § 4.3.2 that wake bistability can actually lower the overall drag coefficient because the symmetric unstable wake solution is explored; this seems again to hold for boat-tailed afterbodies and, in our opinion, bi-stable dynamics should not appear as a *no-go* despite the fluctuating side force loading. We finally would like to recall that phase lock-in – resulting from strong geometric asymmetries principally – does not correspond to a wake stabilization nor a mode removal (see §§ 4.3.1 and 4.3.2).

5.5.3 Strength and orientation of the wake mode

Afterwards, we want to understand whether the wake adaptation mechanism presented in §§ 4.3.1 and 4.3.2 still exists for the boat-tailed afterbody. In short, we recall that the strength of the wake asymmetry, assessed thanks to the modulus of the base pressure gradient, is imposed by the instability and almost independent of the body's alignment or ground clearance, with at most a correction in magnitude of a factor equal to the width-to-height aspect ratio of the base of the model. The wake adapts to the component of the pressure gradient along the base's minor axis, *i.e.* the smallest, which gives some allowed values for the phase φ. The key point is that the geometrical component has to be satisfied in average as discussed in § 4.4.3 on page 87. Following this rule, the wake orientation should be determined from the boat-tail angles only.

---

[1] This approach is successfully experimented in § 7.2.8.1 for real vehicles.

In view of the pressure lines shown in § 5.4, boat-tails lead to the formation of a low-pressure area whose strength is directly proportional to the angle. As a consequence, from a purely geometrical point of view, we have the following rule for top-bottom boat-tails. The case with side boat-tails is discussed in § 5.5.4 and is therefore not considered in this section. The minor axis of the base thus refers to the vertical one. If $\theta_B > \theta_T$, then the low-pressure is larger at the base and the vertical pressure gradient is oriented towards the top of the base, *i.e.* positive, and *vice-versa*. We consequently expect $\theta_B > \theta_T$ to lead to phase lock-in at $\varphi = +\pi/2$ and $\theta_B < \theta_T$ to $\varphi = -\pi/2$ or to a global wake unlocking where, in average $\overline{\varphi} = -\pi/2$. Besides, the wake model of equation (4.15) on page 83 predicts that the intensity of the gradient, *i.e.* its modulus, varies as the ratio of the *minor* to the *major* axes of the base, height-to-width in our case dealing with the y-instability.

From figures 5.18(c) and 5.19($a-b$), it can be observed that the modulus g_r^* of the base pressure gradient decreases linearly with the increasing boat-tail angle for one-sided modified geometries. This is consistent with the wake model (equation 4.15) since increasing the boat-tail angle reduces the base's height H_b while its width W_b remains unchanged. As can be observed in figure 5.18(b), it is the consequence of the gradual reduction of the mean vertical component G_z^* in agreement with the model. The phase behaves as expected with lock-in at $\varphi = -\pi/2$ for top boat-tails and at $\varphi = +\pi/2$ for bottom ones (figure 5.19c, d). As a consequence, we can say that afterbodies equipped with a single boat-tail follow the wake model presented in §§ 4.3.1 and 4.3.2 which is then more general than simply adapted to squareback geometries.

However, it seems that two-sided boat-tailed afterbodies behave differently. There are a few hints that suggest this difference as detailed below. First, we mentioned while commenting figure 5.12 that the fits of equations (5.4) and (5.5) were obtained by excluding the one-sided configurations whose points are indeed located out of the trend curves. One of the main reasons was said to be the constant value which was adapted to fit the baseline's results (§ 5.4.1). Second, the base pressure gradient's modulus g_r^* is now independent of the angles, *i.e.* of the actual aspect ratio of the base (figure 5.20a, b). Last, the vertical base pressure gradient rather increases with the boat-tail angle (figure 5.18b). In spite of these differences, the phase behavior is similar as expected with lock-in towards the smallest boat-tail angle or bi-stable behavior when both are of the same order. All two-sided configurations have similar behavior and we propose the following explanation.

Even if not removed, the static asymmetric wake mode is strongly attenuated (to the point that it can eventually be replaced by a periodic mode if the top and bottom shear layers get close enough) as shown by the rather small value of the modulus of the gradient g_r^* (figure 5.20a, b). The strength of the instability then becomes smaller than the purely geometrical constraint imposed by boat-tailing which becomes the important parameter and imposes the gradient's intensity. Since the modulus is constant (because the instability remains, it cannot drop below a given value), there is an adaptation phenomenon with an instantaneous non-zero horizontal base pressure gradient g_y^* resulting in wake bistability. If the angles are too large, thus leading to an important decrease of the gradient's modulus, the periodic mode may be triggered if the shear layers are close enough. Since the phase φ of the gradient still obeys the wake model, we can say that only the adaptation phenomenon is modified, the driving parameter being then the geometrical constraint rather than the base's aspect ratio. The attenuation must be estimated as a global parameter since one-sided geometries are not concerned regardless of the angle but two-sided do for all tested configurations. This can be ascribed to a reduction of the bluffness of the body (Roshko, 1993). As concerns the phase dynamics, we showed in figure 5.23 that the characteristic time scale of the wake fluctuations is drastically reduced with the modified afterbody. In fact, the change is rather related to the boat-tail length (figure 5.28a, c) than to its geometry (figure 5.28a, b). Since only the curvature of the boat-tails is different, the dynamics is related to this geometrical parameter.

The impact of the pressure gradient imposed by the boat-tails is very similar to a pitch angle applied to the body (§ 4.3.1.4) or to the use of small perturbations under the body. For the latter point, results reported in Barros *et al.* (2017) indeed show that both lock-ins at $\varphi \simeq \pi/2$ and $\varphi \simeq -\pi/2$ but also wake bistability between $\varphi \simeq 0$ and $\varphi \simeq \pi$ can be selected depending on the perturbation.

Finally, three-dimensional geometries lead to a very slow dynamics – the slowest of all of this manuscript, in fact – but the time-averaged wake orientation still respects the adaptation-orientation rule. In fact, boat-tails create a vertical base pressure gradient $g^b_{z^*}$ that the instability has to adapt with so that g^*_r matches the imposed value, leading to wake rotations. It must also be emphasized that phase jumps are also suppressed. Nonetheless, this case might not actually correspond to a stabilization of the wake since it is generally more related to a quicker dynamics.

5.5.4 Importance of boat-tails locations

This chapter is mainly focused on top-bottom boat-tailing – except in § 5.4.7 but side boat-tails only have not been considered[1]. It seems important to compare this configuration with $\theta_S = 12.5°$ ($\theta_T = \theta_B = 0°$) to that obtained with the same angles placed at the bottom and the top of the base ($\theta_T = 12.5°$, $\theta_B = 12.5°$, $\theta_S = 0°$) for both the short and the long circular boat-tails.

In chapter 4, the wake was found to be subject to a z-instability with phase lock-in at $\varphi = -\pi/2$ for the baseline configuration (§ 4.3.2.1). Modifying for instance the ground clearance as in § 4.3.2.2 leads to wake bi-stability for $c^* \simeq 0.080$ between two vertical wake modes. The associated phase dynamics appears to be very similar to that of y-instability, unlike that of the top-bottom boat-tails with the same angles for which, if it were to occur, one would rather have expected lateral fluctuations of the wake. Besides, the characteristic time scale of the motion remains about a hundred times bigger than that associated with vortex-shedding. Furthermore, the spectra of the wake orientation φ given for the side boat-tails in figure 5.32a and figure 5.32b for a bi-stable and wake locked case respectively are strongly different to that of the periodic case previously shown in figure 5.24(b). There is indeed no periodicity in the wake shifts. The mechanisms driving the wake are consequently different; the explanation provided in chapter 4 is that, in this case, the body's base aspect ratio becomes sufficiently small ($W^*_b < 1$) so that the wake becomes subject to a z-instability in the sense of Grandemange *et al.* (2013a) which originates from static asymmetric wake modes (Grandemange *et al.*, 2013b). It seems that the flow deviation is not enough to trigger periodicity but that a geometrical vicinity of the two shear layers is also necessary.

In spite of these differences, some similarities with the case $\theta_T = \theta_B = 12.5°$ must be highlighted. The mean pressure coefficient C_p plotted along a line of sensors is given in figure 5.33; $y^* = 0$ and $z^* = 0$ for the top-bottom boat-tails in figure 5.33(a, c) and

---

[1] A full study however is to be found in chapter 4, § 4.3.2 on page 70.

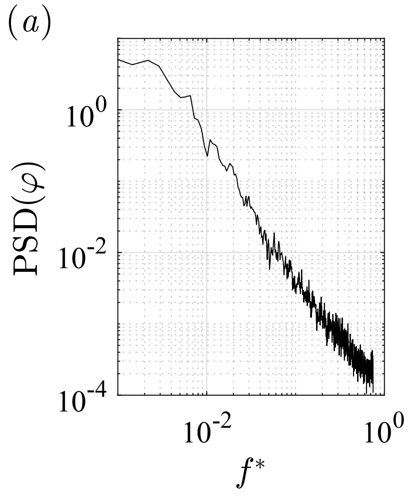

Figure 5.32 – Phase φ spectra for the two maximal boat-tail angles of $\theta_i = 12.5°$: (a) lateral boat-tailing at $c^* = 0.080$ (bi-stable case), (b) lateral boat-tailing at $c^* = 0.168$.

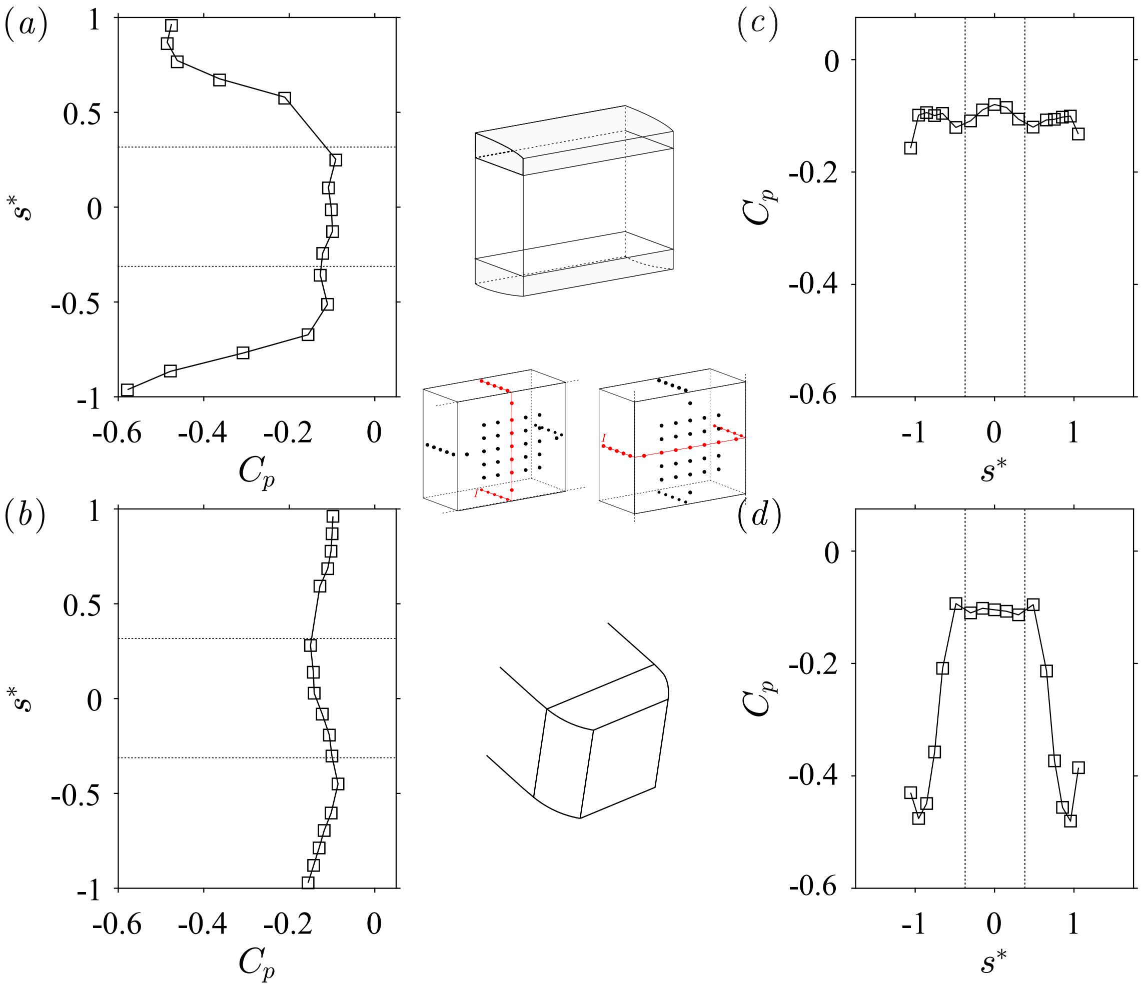

Figure 5.33 – Mean pressure coefficient C_p plotted along a line of constant x_i^* for the maximum boat-tail angles ($\theta = 12.5°$) with (a, c) top-bottom boat-tailing and (b, d) side boat-tailing. (a, b) $x_i^* = y^* = 0$ and (c, d) $x_i^* = z^* = 0$.

for the lateral ones in figure 5.33(b, d). No clear wake orientation can be observed at the base in the first configuration (figure 5.33a). As a consequence, the pressure is also almost constant horizontally (figure 5.33b). A large low-pressure zone can be identified symmetrically on each of the boat-tails. Almost the same comments can be made when the boat-tails are placed on each side of the base: two low-pressure areas develop on their curvature (figure 5.33d) with a recovery near the base; however, because of the presence of the instability and of its wake state N (see § 4.3.2.1), a vertical wake orientation with a negative gradient can be observed in figure 5.33(b).

5.5.5 Control of the aerodynamic loading

The aerodynamic loading applied on the model can be controlled when using different angles for the top and the bottom boat-tails as shown by equations (5.4) and (5.5). The quadratic relationship between lift and drag (equation 5.6) recalls that optimization must be performed globally. In addition, this chapter clearly highlights that base suction is only slightly impacted by boat-tailing but the beneficial effect on the base contribution to drag is enforced by the reduction of the base surface. However, one must ensure that the boat-tail's induced drag, originating from the low-pressure area related to the streamlines' curvature and from longitudinal vortices clearly visible in wake velocity fields (figure 5.22) and identified earlier in Wong & Mair (1983) or Han *et al.* (1992), remains limited compared to the gains at the vertical afterbody. Even if the impact of boat-tails on drag is directly correlated with their length, short geometries of about 16.8% of the model's height still have a considerable contribution. In first approximation, one may even say that the aerodynamic loading on the boat-tail is significant for the total one. In addition, the drag mechanism attributed to boat-tails seems quite easy to understand. As the flow remains attached, there is a transfer of curvature from the geometry to the flow. In the case of a circle-arc, the curvature is transferred along the whole boat-tailed while it is localized in presence of a slant. It consequently creates a low-pressure area in the mean flow which contributes to drag and lift (positively or negatively depending on the normal vector). The slant has a better efficiency because of the pressure recovery allowed by the diffuser effect without any additional curvature transfer. The effect of the curvature was already pointed out by Mariotti *et al.* (2017) and our results are in agreement with this paper.

The contribution of this work compared to previous papers is that we assess the existence of the wake static asymmetric modes and thus of the subsequent wake reversals. In our opinion, they should not be neglected in the estimation of the total aerodynamic loading with boat-tailed afterbodies. In particular, the contribution of these reversals to lift is crucial regarding the vehicle's stability.

5.6 Concluding remarks

In this chapter, the effects of boat-tailing on the wake of the flat-backed Ahmed body and on the aerodynamic loading are studied. A global sensitivity of the wake and of its properties towards the boat-tail geometry (size, shape, angle) is identified, resulting in different wake dynamics, from phase lock-in to wake bistability. An attenuation of the wake symmetry-breaking modes is identified without their complete removal which may lead to a symmetric wake. For large angles, a periodic mode can be identified though but its efficiency does not bring any interesting insight for drag reduction. The global loading being directly estimated from the geometry and the pressure forces on the body, optimization can be performed. One of the key results of this chapter is that the reduction of the base surface rather than the base pressure increase is responsible for drag reduction which may be counterbalanced or overwhelmed by boat-tail's drag originating in large low-pressure areas though. The strength of the mode being attenuated, we also show that the phase dynamics is strongly modified, in particular as the characteristic time scale changes with the geometry. An adapted wake model is finally presented which takes into account the hereabove mentioned attenuation and the resulting importance of the geometrically imposed pressure gradient. This chapter constitutes the baseline of the boat-tail effect with consequences on the loading and on the wake; its natural continuation is to change the body's alignment or ground clearance to study the wake sensitivity to these external disturbances as done in Appendix C. Besides, there might still exist a possibility to symmetrize the wake without detrimental effect on pressure drag with boat-tails that has not been found so far.

CHAPTER 6

Towards a stability analysis of the wake of flat-backed Ahmed bodies

This chapter presents some ongoing work whose final aim is to provide a stability analysis of the flow around the squareback Ahmed body in ground proximity. Reynolds Averaged Navier-Stokes simulations using a $k-\omega$ SST turbulence model are used to investigate the flow (§ 6.2). Both steady (§ 6.3.1) and unsteady (§ 6.3.2) calculations are performed; the first one provides an accurate representation of the basic flow *without the instability. In the unsteady case, vortex-shedding is accurately represented but not the static wake asymmetry. The relevance of the simulation is discussed in § 6.4.1. A stability analysis on these two flows should be able to provide the necessary information regarding whether they do or do not contain the wake static instability as indicated in § 6.4.2.*

Contents

Preliminary remarks: objectives of the simulations 143

6.1 Motivations and brief literature review 143

6.2 Numerical setup 144

6.2.1 Description of the computational case 144

6.2.2 RANS and URANS equations 148

6.3 Results 150

6.3.1 Steady simulation 150

6.3.2 Unsteady simulation 156

6.3.3 Yawing conditions 159

6.4 Discussion 160

6.4.1 Accuracy of steady and unsteady simulations 160

6.4.2 Stability analysis of the wake 161

6.5 Concluding remarks 162

Preliminary remarks: objectives of the simulations

In this chapter, we provide steady and unsteady Reynolds Averaged Navier-Stokes (RANS) simulations of the flow around a squareback Ahmed body. The aim is not to obtain an accurate representation of the physics; otherwise, we would rather have used Large Eddy Simulation (LES) or Zonal Detached Eddy Simulation (ZDES) for which the results are expected to be much more representative of the actual flow. Instead, we wish to understand whether the low-frequency wake dynamics corresponding to bi-stability (Grandemange *et al.*, 2013*b*) could be observed in the framework of unsteady RANS simulations and whether they could persist with those models. The justification for such approach is that the time scales related to turbulence effects are much longer than those determining the instabilities of the flow. The results presented this chapter are preliminary ones but are not given in order to accurately model the flow field nor to supplement the experiments.

6.1 Motivations and brief literature review

The wake of the flat-backed Ahmed body is, as demonstrated in chapter 4, highly unstable and subject to a long-time dynamics much slower than the typical time scale of vortex-shedding (Grandemange *et al.*, 2013*b*). This dynamics therefore requires large computational capabilities in order to accurately simulate the wake switching, in particular at high Reynolds numbers. Only a few works report the wake asymmetry (Pellerin *et al.*, 2016; Lucas *et al.*, 2017; Dalla Longa *et al.*, 2017; Evstafyeva *et al.*, 2017; Abikan *et al.*, 2018) and, as of now, only Dalla Longa *et al.* (2017) observed a wake switching without modifying the body's alignment – usually the yaw angle as done experimentally in § 4.3.1.3. There is a crucial need for understanding the underlying mechanism of the wake asymmetry of the body since the Hopf bifurcation operated at low Reynolds numbers (Grandemange *et al.*, 2012*a*; Evstafyeva *et al.*, 2017) persists in the turbulent regime and drives the wake dynamics but also because the symmetry-breaking modes contribution to drag is not negligible and is therefore one of the lever for minimum drag seeking (Cadot *et al.*, 2015*b*).

The wake flow behind the Ahmed body appears to be highly unsteady (Grandemange *et al.*, 2013*b*; Volpe *et al.*, 2015; Evrard *et al.*, 2016; Brackston *et al.*, 2016; Varon *et al.*, 2017), mainly non linear and three-dimensional. This consequently requires a consequent number of mesh points. In addition, the existence of two very distinct time scales of the problem (Grandemange *et al.*, 2014*b*) complicates the simulation, in particular since the low frequency dynamics has a relationship with the high frequency one (Pavia *et al.*, 2018). The computational time step must be small enough to ensure the numerical stability of the calculation but, since the longest time scale is actually quite large, this requires big computational resources if the aim is to simulate long physical times.

The literature lacks of stability analyses on the considered geometry. In addition, despite the numerous studies on the slanted Ahmed body, only a few numerical works were conducted on the squareback geometry (Khalighi *et al.*, 2001, 2012; Peres & Pasquetti, 2013; Pasquetti & Peres, 2015; Pellerin *et al.*, 2016; Evstafyeva *et al.*, 2017; Lucas *et al.*, 2017). Besides, some investigations were conducted by van Raemdonck *et al.* (2016) for the Ground Transportation System, a similar body with inverted aspect ratio. In this latter work, the effect of a slight body misalignment (yaw angle) is also considered. In addition, results from RANS and URANS simulations regarding the squareback geometry are now rarely reported, unlike those with the original slanted body. There are only few

stability analyses performed on the wake of the squareback geometry; for instance, one may cite that of Stankiewicz *et al.* (2005) but considering a two-dimensional setup for which the flow is different. In addition, Wee *et al.* (2004) did a linear stability analysis on the backward-facing step for a Reynolds of $\mathrm{Re} = 3400$. The problem is made even more complex by the presence of the ground that He *et al.* (2018) assess for an airfoil at low Reynolds number ($\mathrm{Re} \in [300, 1000]$). In their unsteady simulations, Khalighi *et al.* (2012) capture the vortex-shedding but not the low-frequency dynamics related to the symmetry-breaking modes of the wake (Grandemange *et al.*, 2013*b*).
Our approach is the following: we aim at showing that URANS simulations are sufficient to obtain the static wake asymmetry in order to perform sensitivity analyses and identify the disturbances. In other words, the aim would be to prove that the instability is contained in the unsteady *averaged* Navier-Stokes equations in spite of the apparent inconsistency with the permanently asymmetric wake state. Following works would consist in performing a linear stability analysis following for instance the method detailed in Beneddine *et al.* (2016, 2017), based on stability analyses performed on the mean flow – for unsteady simulations – or on the base flow obtained by steady simulations. Similar procedures were considered earlier for instance in Meliga *et al.* (2012) or Mettot *et al.* (2014).

6.2 Numerical setup

6.2.1 Description of the computational case

This section introduces the numerical setup and the flow solver *elsA*, and the supercomputing facilities. The problem is then characterized. The simulations are performed with *elsA – Ensemble Logiciel de Simulation en Aérodynamique* –, a multi-purpose software for applied Computational Fluid Dynamics (CFD) which has been developed at ONERA for about 20 years in collaboration with Airbus and Safran (Cambier *et al.*, 2013). This CFD suite is used for both internal and external aerodynamics from very low to high Mach numbers, *i.e.* from low subsonic to supersonic flows. It is based on the numerical resolution of the compressible three-dimensional Navier-Stokes equations. *elsA* is based on an Object-Oriented structure in which three programming languages are used (C++, Fortran, Python). The user interface is coded in Python and jobs are run on a distant supercomputer described below that the user interacts with by means of command lines in a terminal.
A cell-centered finite-volume method is used for the resolution of partial differential equations in the form of algebraic equations (Toro, 1999). Flow properties are calculated at discrete locations on a meshed space; in our case at the center of the cells. The divergence terms in volume integrals in partial differential equations are converted to surface integrals with the divergence theorem and these terms are computed as fluxes at the surfaces of each finite volume. The advantage of this method is to be conservative. Second-order schemes are used for space discretization and the chosen resolution scheme for ordinary differential equations consists in a backward Euler method, also called implicit Euler method, – used here to obtain exact steady solutions of the governing equations – with implicit schemes solved by *LU* relaxation methods (Butcher, 2016). No acceleration procedures such as multi-grid techniques are used in this work. The fluxes are computed with an AUSM plus (Advection Upstream Splitting Method) scheme well adapted for low Mach computations (Liou & Steffen, 1993). The convective and pressure fluxes are expressed using the eigenvalues of the flux Jacobian matrices. The method was originally proposed by Liou & Steffen (1993) and later improved by Chang & Liou (2003); Liou (2006) into

the AUSM plus method used here. Matrices are pre-conditioned with this kind of scheme. AUSM is an upwind scheme which consequently does not need any artificial viscosity unlike downwind or centered schemes. However, limiters are necessary and third order ones are used in our simulations. Besides, viscous fluxes are correlated over five mesh points.

The computational problems are build locally (geometry, mesh, parameters) and then run on a super-computing facility located at ONERA in Châtillon (France). Two different supercomputers are used because the operation of the first one was suspended during the thesis. Their main characteristics are given below. The first calculations were handled on the supercomputer called *Stelvio* that was first used in 2009 and upgraded in 2011 and again in 2013. It is an SGI ICE 8200 / ICE-X with 704 computing nodes and 8000 cores. It delivers 115 TFlop.s^{-1} of peak power. Batch jobs are handled with a LSF task manager. The second and current computer, *Sator*, is a NEC facility with 17360 CPU cores for a peak power of 667 TFlops/s (566 TFlops/s in average). 620 nodes are devoted to calculation with Intel Weon Broadwell E5-2680 processors with 14 cores. The system runs with a CentOS 7 operating system with Intel MPI for parallelism. The task manager is a SLURM job launcher. As of now, this computer is within the 500 most powerful in the world (rank 342 in June 2017, rank 473 in November 2017)[1]. In both cases, the files needed for computation are a case file with the number of iterations and the inlet boundary conditions, an *elsA* script with the computation parameters and a job file for the interface with the computing facility. All of these files are coded in Python language. The supercomputer used for the simulations only impacts the computation time and not the results.

The computational domain simulates the plenum of the model-scale wind-tunnel of the GIE-S2A described in § 2.1.2 in which the experiments are conducted. It is approached as a rectangular cuboid of size 9.30m×6.60m×4.15m (length×width×height). The boundary conditions are set as follows. The inlet and outlet sections as well as the sides of the simulated plenum are associated with a far-field boundary condition, *i.e.* the free-stream velocity U_∞, the static free-stream temperature T_∞ and the air density are prescribed. The values are chosen in agreement with the experiments that is $U_\infty = 20$ m.s^{-1} and $T_\infty = 293$ K. A wall boundary condition, *i.e.* impermeability and no-slip conditions, is applied to the body and to the floor. As regards the boundary layers, they are initialized with a zero thickness at the most upstream point of the domain. The distance to the body is identical to that of the experiments (see chapters 2 to 5) in which the boundary layer thickness is controlled by suction.

The coordinate system is the same as that introduced in experiments: the origin is set at the center of the base of the model. The $\boldsymbol{e}_x$ axis is chosen pointing downstream, $\boldsymbol{e}_y$ axis is pointing to the right of the body (viewed from behind) and $\boldsymbol{e}_z$ is vertical. The body and the floor (associated with a wall boundary condition) are shown in figure 6.1(*a*).

The model is similar to the squareback Ahmed body used for the experiments. All radii of curvature are the same and are represented. The only difference is the absence of the feet of the body which are not modeled for simplicity. Besides, we just consider its squareback configuration. The model is studied in no-yaw and no-pitch conditions ($\alpha = \beta = 0°$). Its ground clearance, defined as the normal distance from the underbody to the ground, is adjustable and three levels are considered in simulations: $c^* = 0.067,\ 0.101,\ 0.168$. They respectively represent setups before, during and after the pitchfork bifurcation operated by the ground clearance and described in § 4.3.1.2 in figure 4.3 (Grandemange *et al.*, 2013*a*; Cadot *et al.*, 2015*b*).

---

[1] Top 500, Sator: `https://www.top500.org/system/179090`

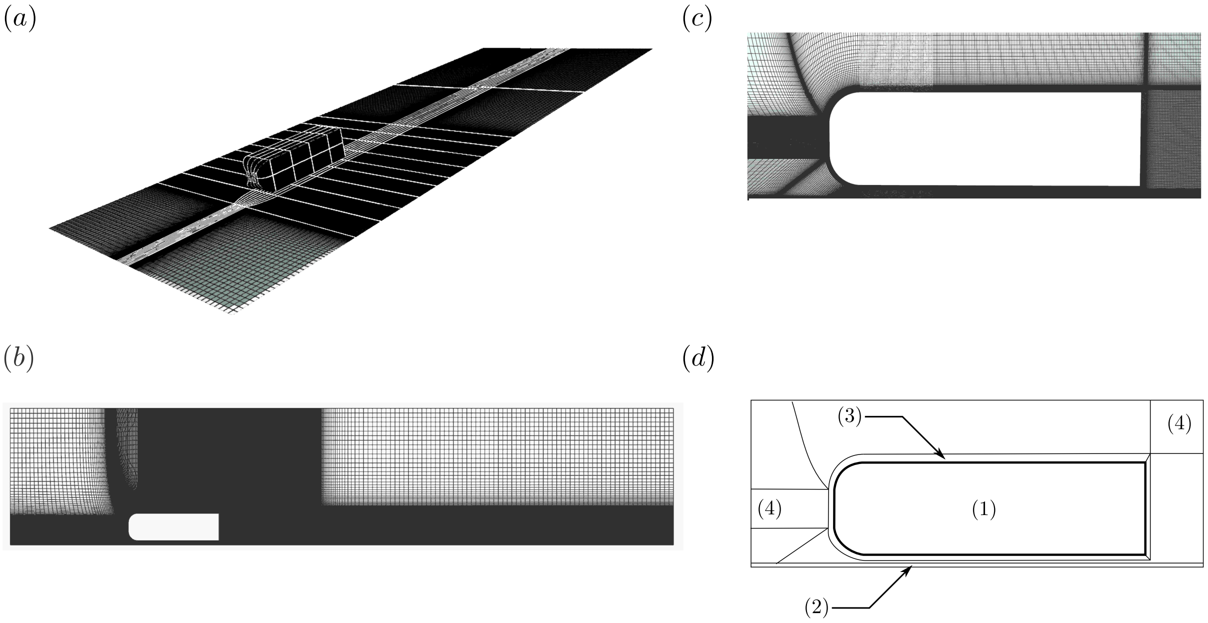

Figure 6.1 – Numerical apparatus: (a) view of the body and of the ground (wall boundary conditions) looking downstream and mesh trace on the floor and on the body; (b) side view of the mesh in the whole domain in the plane $y^* = 0$ with (c) close view on the body. (d) Schematic of the mesh structure in the plane $y^* = 0$ – see text for numbers.

We first build the body (shown in figure 6.1a, b, c) using an open-source Computer-Aided Design software, FreeCAD. Afterwards, the geometry is imported together with the computational domain representing the plenum into the meshing software. Under the here-above described conditions, the corresponding Reynolds number based on the body's height is $\mathrm{Re} = U_\infty H/\nu \simeq 4.0 \times 10^5$, ν being the air kinematic viscosity.

The structured mesh of this numerical study is generated thanks to the ANSYS IcemCFD meshing tool. The geometry described above is considered and we work on the half space $y < 0$, *i.e.* only a half space is meshed initially. As the ground clearance of the model is varying, the mesh is constructed so that it can be modified without re-meshing the whole domain just by changing the z-coordinate of all points corresponding to the ground.

The computational domain is divided into blocks. The mesh is created in each of them and then projected on the surfaces of the geometry. The parameters of the mesh such as its density are set on each of the block edges. The mesh is shown in figure 6.1(b, c) and modeled in figure 6.1(d) that we comment in the following. A fine O-grid mesh (3) is wrapped around the body (1) in order to capture the developing boundary layer. It is surrounded by a regular H-grid (4). A mesh refinement (2) is imposed near the ground for an accurate boundary layer representation. The mesh generation must obey some rules including but not limited to those presented hereafter.

Each cell must be as regular as possible, *i.e.* excessive stretching must be avoided. Similarly, very different cell sizes in a given neighborhood lead to poor mesh qualities. To do so, we generate a mesh with almost squared cells with a growth ratio between neighbors smaller than 1.1. Regularity is ensured as all parallel edges are assigned similar properties. The spacing between the points at both ends of edges as well as the maximum spacing on each edge are imposed to match the requested densities (see table 6.1). The bunching law are chosen as the default *Bi-geometric*, *i.e.* the two end heights and ratios define parabolas that are truncated where their tangent lines are identical. As a consequence, the spacing is linear between these points. To avoid the use of a hyperbolic distribution law, we ensure that there are enough nodal points to form the mentioned linear segment. In the case of computations in the whole space, the symmetrization of the mesh is performed using a mirroring tool included in the meshing suite; the symmetry plane is chosen as $y = 0$ and the local coordinate system is recomputed in the symmetric mesh to avoid negative cell volumes.

Two mesh densities are considered in this work: a Coarse mesh C and a Fine mesh F. Mesh-independence of the mean quantities such as drag, lift and base suction are checked. The dimensionless wall-distances associated with the mesh size in each directions are given in table 6.1 together with the resulting number of nodes for each ground clearance $n_{\text{mesh}}(c^*)$. Half-space computations are performed with F mesh only and result in about half the number of mesh points. The dimensionless wall-distances x_i^+ (where $x_i \in \{x, y, z\}$) are defined as:

$$x_i^+ = \frac{u_\tau \times x_i}{\nu}, \quad x_i \in \{x, y, z\} \tag{6.1}$$

where x_i is the distance to the nearest wall, u_τ the friction velocity at this nearest wall, and ν is the kinematic viscosity of the fluid. The distance from the wall is computed as the minimum orthogonal distance between the wall and the considered point in the fluid. The wall-friction velocity is defined in equation (6.2) as a function of the fluid density ρ and of the wall-shear stress τ_w:

$$u_\tau \equiv \sqrt{\frac{\tau_w}{\rho}} \tag{6.2}$$

Table 6.1 – Dimensionless dimensions of the Coarse and Fine meshes (C and F) in terms of x^+, y^+, z^+ and corresponding number of nodes $n_{\text{mesh}}(c^*)$ for the three considered ground clearances $c^* = c/H$ for the full space.

Parameter	Coarse mesh C	Fine mesh F
x^+	~ 300	~ 200
y^+	~ 1	~ 0.1
z^+	~ 500	~ 100
$n_{\text{mesh}}(0.067)$	$\sim$ 9.1 M	$\sim$ 35.0 M
$n_{\text{mesh}}(0.101)$	$\sim$ 9.5 M	$\sim$ 40.0 M
$n_{\text{mesh}}(0.168)$	$\sim$ 8.5 M	$\sim$ 44.4 M

Several turbulence models are implemented in *elsA*, ranking from *simple* one-equation models to more complex ones. Two models were tested in this work: a Spalart-Allmaras and a Kok $k - \omega$ model with Shear Stress Transport correction referred to as $k - \omega$ *SST*. The $k - \omega$ is a two-equation turbulence model. It brings two partial differential equations for the turbulence kinetic energy k and the specific rate of dissipation ω. The eddy-turbulent kinematic viscosity ν_T is consequently modeled by a function of k and ω. The Kok $k - \omega$ model is thoroughly described in Kok (2000). A Shear Stress Transport correction (Menter, 1993, 1994) is then applied. It basically consists in a limitation of the turbulent dynamic viscosity μ_T. This avoids the problem that the $k - \omega$ model is too sensitive to the inlet free-stream turbulence properties. The second model is a Spalart-Allmaras turbulence model introduced in Spalart & Allmaras (1992). It seems to perform poorly in our case because of the fully detached recirculating bubble downstream of the body and results are not reported in the manuscript.

We introduce a new tool for structures' visualizations: the Q-criterion. The second invariant of the velocity gradient ∇u, called Q, is defined in equation (6.3) below is classically used for flow visualization of coherent structures (Hunt *et al.*, 1988); for instance, positive values correspond to vortices.

$$Q = \frac{1}{2}\left(\Omega_{ij}^2 - S_{ij}^2\right) \tag{6.3}$$

It is calculated from the strain rate $\mathbf{e}$ and rotation $\boldsymbol{\omega}$ tensors, *i.e.* the symmetric and antisymmetric parts of the velocity gradient tensor $\nabla\mathbf{u}$, respectively given in equations (6.4a) and (6.4b).

$$\mathbf{e} = \frac{1}{2}\left(\nabla\mathbf{u} + \nabla\mathbf{u}^{\mathbf{T}}\right) \tag{6.4a}$$

$$\boldsymbol{\omega} = \frac{1}{2}\left(\nabla\mathbf{u} - \nabla\mathbf{u}^{\mathbf{T}}\right) \tag{6.4b}$$

The norm of each of the tensors can be computed and correspond respectively to the dissipation rate S_{ij} and to the enstrophy (or vorticity modulus) Ω_{ij} defined in equations (6.5a) and (6.5b) written with the Einstein summation convention:

$$S^2 = S_{ij}^2 = 2\ e_{ij} \cdot e_{ij} \tag{6.5a}$$

$$\Omega^2 = \Omega_{ij}^2 = 2\ \omega_{ij} \cdot \omega_{ij} \tag{6.5b}$$

The difference between these two norms finally yields equation (6.3).

The flow around the body is characterized at multiple locations in both horizontal planes (at mid-height of the body, $z^* = 0$) shown in figure 6.2(a) and vertical ones located mid-width ($y^* = 0$) indicated in figure 6.2(b). Finally, the base pressure is estimated experimentally at the base and we compute the base suction coefficient C_b defined in equation (2.2).

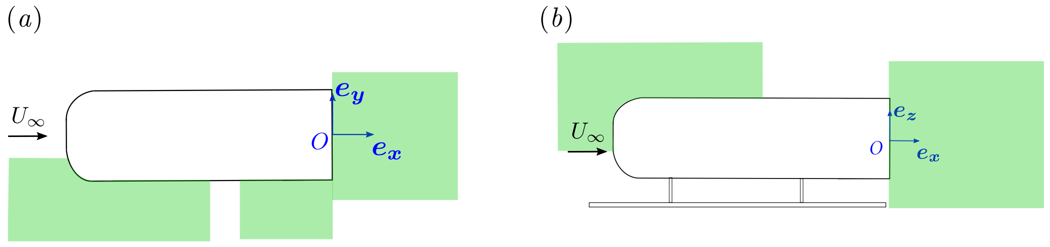

Figure 6.2 – Schematic view of body with the velocity planes investigated numerically and the coordinate system: (a) top view, (b) side view.

6.2.2 RANS and URANS equations

The equations that are being solved numerically are given in this section. If we perform steady RANS (Reynolds Averaged Navier-Stokes) simulations, the time-averaged equations of the fluid flow are considered. These equations are based on the Reynolds decomposition into the time-averaged and fluctuating quantities given in equations (6.6) derived from Reynolds (1895). For the sake of the brevity, we use the Einstein notation, $\overline{a}$ for time-averaging of any quantity a and δ_{ij} as the Kronecker symbol. The Reynolds stress $\left(-\rho\overline{u_i' u_j'}\right)$ is modeled owing to a turbulence model. The steady RANS incompressible equations write:

$$\frac{\partial \bar{u}_i}{\partial x_i} = 0 \tag{6.6a}$$

$$\rho \bar{u}_j \frac{\partial \bar{u}_i}{\partial x_j} = \rho \bar{f}_i + \frac{\partial}{\partial x_j}\left[-\bar{p}\delta_{ij} + \mu\left(\frac{\partial \bar{u}_i}{\partial x_j} + \frac{\partial \bar{u}_j}{\partial x_i}\right) - \rho\overline{u_i' u_j'}\right] \tag{6.6b}$$

If an unsteady simulation is considered, equation (6.6) becomes time dependent as stated in (6.7).

$$\frac{\partial \bar{u}_i}{\partial x_i} = 0 \tag{6.7a}$$

$$\rho\left(\frac{\partial \bar{u}_i}{\partial t} + \bar{u}_j \frac{\partial \bar{u}_i}{\partial x_j}\right) = \rho \bar{f}_i + \frac{\partial}{\partial x_j}\left[-\bar{p}\delta_{ij} + \mu\left(\frac{\partial \bar{u}_i}{\partial x_j} + \frac{\partial \bar{u}_j}{\partial x_i}\right) - \rho\overline{u_i' u_j'}\right] \tag{6.7b}$$

In fact, regardless of the type of simulation, unsteady equations are solved in elsA. For the RANS case, the time-integration scheme is chosen to be a backward Euler scheme adapted for a steady computation. The implicit Euler scheme, given in equation (6.8), is at the first order in time where R is the residual.

$$\frac{u_j^{n+1} - u_j^n}{\Delta t} - R(u^{n+1}) = 0 \tag{6.8}$$

The local pseudo time-step is controlled owing to the dimensionless Courant–Friedrichs–Lewy (CFL) number defined as (Courant *et al.*, 1928):

$$\mathcal{C} = \frac{(||U_i|| + c) \times \Delta t}{\Delta x_i} \tag{6.9}$$

where $||U_i||$ is the norm of the local velocity, c the speed of sound and Δt and Δx_i refer to (pseudo-)time and grid spacing respectively. As the resolution method is implicit, we can chose $\mathcal{C} > 1$ and we take $\mathcal{C} = 10$ for $c^* = 0.101$ and $c^* = 0.168$ and $\mathcal{C} = 5$ for $c^* = 0.067$. The CFL number is used as a numerical stability criterion in the simulations; it is ensured for $\mathcal{C} > 1$.

As for URANS simulations, the ordinary differential equations are marched in time following a Gear scheme given in equation (6.10), which is of second order in time. This scheme is an implicit iterative time integration scheme.

$$\frac{3u_j^{n+1} - 4u_j^n + u_j^{n-1}}{2\Delta t} - R(u^{n+1}) = 0 \tag{6.10}$$

Sub-iterations are performed using a Newton method. Newton's iterative algorithm equivalently known as Newton–Raphson methods are iterative methods for finding successively better approximations to the roots of a real-valued function. This method has a quadratic convergence rate. A more detailed description can be found for instance in Atkinson (1978). In order to avoid an excessive computation time, a maximum number of sub-iterations and a convergence criterion for the Newton method are given for sub-iterations in *elsA*.

The CFL number defined in equation (6.9) is not compatible with the Gear scheme of equation (6.10). Unlike for the steady simulation, the time step is not local anymore but global an imposed by the user. We chose $\Delta t = 1 \times 10^{-4}$ s for our simulations[1], *i.e.* on dimensionless units based on the free-stream velocity and the body's height, $\Delta t = 6.7 \times 10^{-3}$. The corresponding cut-off frequency then turns out to be $f^* \simeq 149$. It must be noticed that the steady simulation is not used as the initial condition of the unsteady one that is run from scratch instead.

6.3 Results

This section is divided into two parts; the steady simulations are considered in § 6.3.1 and the unsteady cases in § 6.3.2. The results presented in this section were obtained with the full-space configuration (symmetrized mesh). For comparison, the same experimental study is provided in chapter 3.

6.3.1 Steady simulation

This section is organized as follows. We first discuss the mean velocity field around the body and also consider the mean wake. Afterwards, the base pressure distributions and the mean aerodynamic loading are investigated. Some wake's coherent structures are then identified. The mesh independence of the results is shown in Appendix D. We recall that a full-space mesh is considered in this section.

The horizontal planes indicated in figure 6.2(a) are first considered to represent the velocity fields. Only the case $c^* = 0.168$ identical to Ahmed *et al.* (1984); Barros *et al.* (2017) is presented but the results in the $z^* = 0$ plane are independent of the ground clearance so that the analysis can be extended to all aligned configurations. The data are obtained with a free-stream velocity of $U_\infty = 20$ m.s^{-1}, corresponding to a Reynolds number based on the body's height of approximately $\mathrm{Re}_H \simeq 4.0 \times 10^5$. A stagnation point is clearly identified in the front of the body in figure 6.3(a) since the streamlines hit the wall perpendicularly. In agreement with the symmetries of the problem, it is located on the body's centerline ($y^* = 0$). There is no significant flow separation downstream of the rounded forebody in agreement with experimental observations (see chapter 3, figure 3.2 on page 40). The stream is then parallel to the body down to the separation point which can be observed in figure 6.3(b); it is located at the blunt trailing edge.

Similarly, the vertical plane $y^* = 0$ is investigated near the front edge of the body in order to characterize the flow separation induced by the front curvature and the potential effect of the ground clearance. Numerical mean fields are shown in figure 6.4 and are very similar to experimental observations of chapter 3 (figure 3.3 on page 40). For all cases, a stagnation point is identified at the front leading edge of the body; in addition, high velocity magnitudes near the circle arcs of the forebody can be observed since the flow remains attached due to the curvature transfer from the geometry to the streamlines. It is interesting to highlight that the stagnation point is not centered on the front surface but located slightly below the mid-height. This phenomenon, observed for all studied ground clearances, can be ascribed to a ground effect and is also observable experimentally. It is quite difficult to compare underbody velocities with experimental data but the order of magnitude of roughly 1 for the reduced velocity U/U_∞ for $c^* = 0.168$ is in excellent agreement with that reported in Cadot *et al.* (2015*b*) – in particular, in figure 6 of the previously mentioned paper, the authors report a velocity at the underbody exit of 1.15

---

[1] This is about two orders of magnitude smaller than the typical time for vortex-shedding estimated around 7×10^{-2} s.

that of the free-stream. However, there seems to be an overestimation of the underbody velocity for the lowest ground clearance compared to the data of Cadot *et al.* (2015*b*). At the upstream section of the body, the floor boundary layer is about 10 mm-thick which represents 20 − 50% of the body's ground clearance (depending on the configuration) and is slightly bigger than in experimental observations although of the same order of magnitude and similar to Lucas *et al.* (2017). At the underbody exit, the boundary layer height is of a few millimeters, within the experimental uncertainty of previous works as well experimental (Cadot *et al.*, 2015*b*; Barros *et al.*, 2016; Castelain *et al.*, 2018) as numerical ones (Lucas *et al.*, 2017).

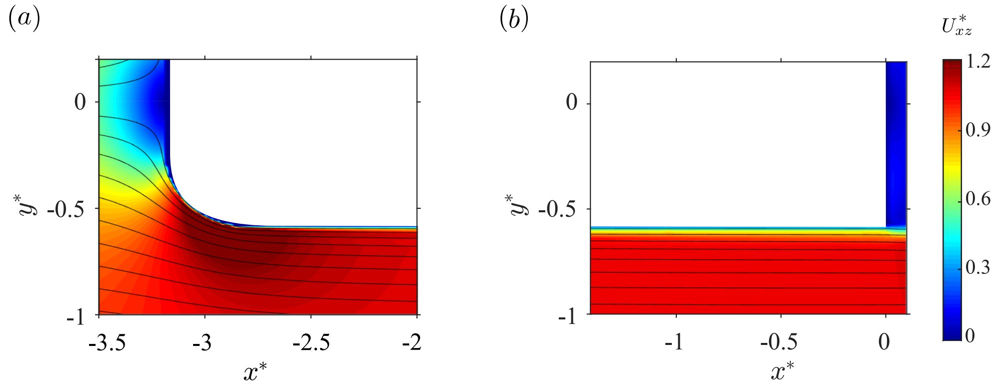

Figure 6.3 – Cross-sections of the mean velocity field alongside the body visualized using streamlines superimposed to the modulus of the velocity in the horizontal plane $z^* = 0$ at $U_\infty = 20$ m.s^{-1}. The body is aligned with the incoming flow ($\beta = 0°$) and in no-pitch conditions ($\alpha = 0°$) with $c^* = 0.168$.

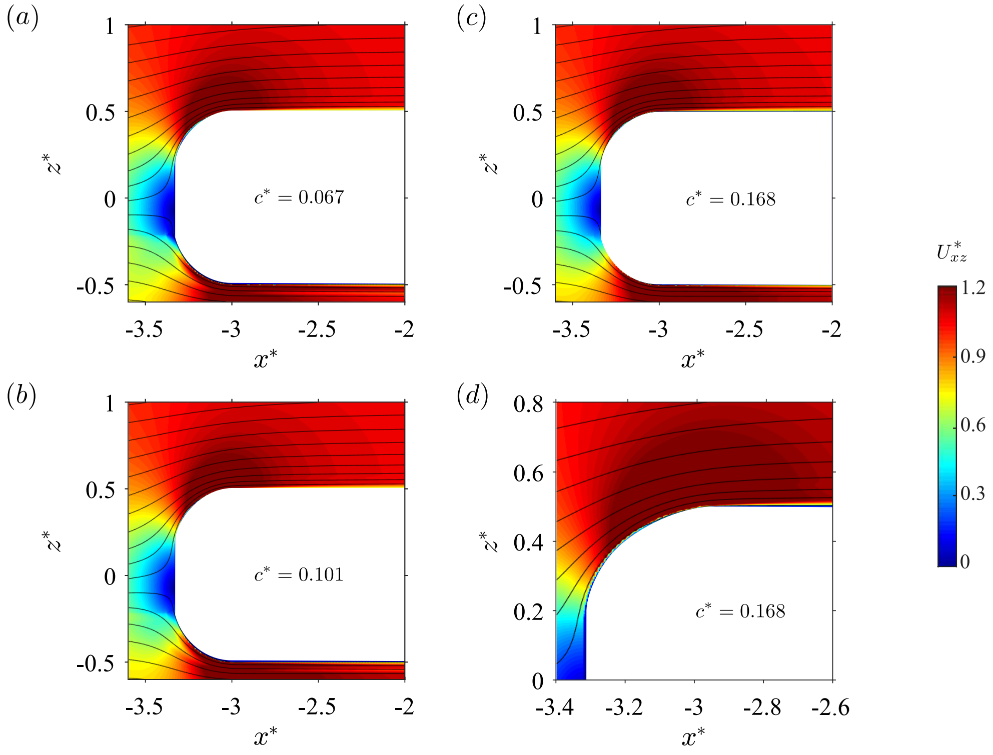

Figure 6.4 – Cross-sections of the mean velocity field U^*_{xz} in the plane $y^* = 0$ for the squareback Ahmed body aligned with the incoming flow ($\alpha = 0°$, $\beta = 0°$) obtained numerically at various ground clearances: (*a*) $c^* = 0.067$, (*b*) $c^* = 0.101$, (*c*) $c^* = 0.168$ with close view in (*d*).

The absence of flow separation at the front of the body inferred thanks to the mean velocity fields is unambiguously proved numerically owing to the skin-friction measured with the coefficient C_f defined in equation (6.11) where τ_w stands for the wall shear-stress and Q_∞ for the free-stream dynamic pressure.

$$C_f = \frac{\tau_w}{Q_\infty} = \frac{\tau_w}{\frac{1}{2}\rho U_\infty^2} \tag{6.11}$$

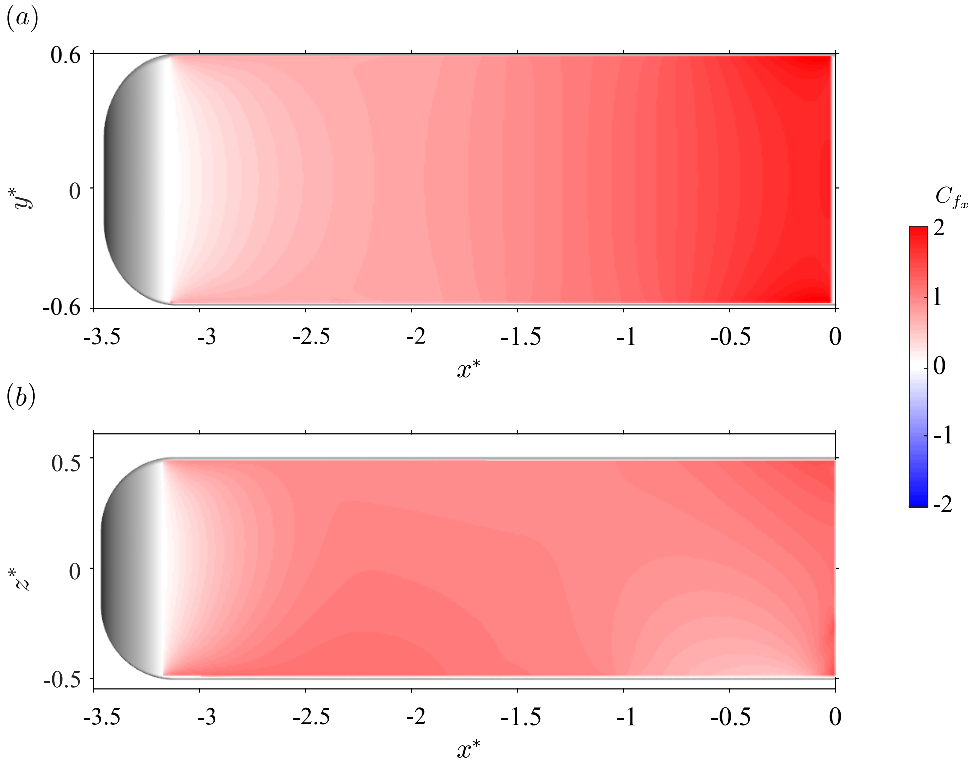

Figure 6.5 – Downstream component of the skin-friction coefficient C_{f_x} on the body for $c^* = 0.168$: (a, c) $z^* = 0.5$-plane, (b, d) $y^* = 0.59$.

In presence of a reverse flow induced by a separation on the sides of the body, the x-component of coefficient – aligned with the free-stream – would become negative and, in this case, appear in blueish in figure 6.5. It turns out that the streamwise skin friction coefficient C_{f_x} is always positive: the flow remains consequently attached to the body despite the front curvature at the considered Reynolds number of $\mathrm{Re}_H \approx 4.0 \times 10^5$. Its magnitude is lower near this area, showing that a separation could be triggered for instance by reducing the Reynolds number as done in chapter 3. It is interesting to notice in figure 6.5(b) that a perturbation on the side friction is created by the underbody flow near the base related to the exit section of the underbody. We recall that the model's supports are absent in the simulation.

Finally, the mean wake is briefly characterized owing to the two orthogonal planes y^* and z^* at the base of the body indicated in figure 6.2(a, b). Results are given in figure 6.6. The wake is almost symmetric in the $y^* = 0$ plane at high ground clearance but also for the lowest one, which is inconsistent with the results of chapters 3 and 4. In fact, the wake stabilization operated by the ground clearance (§ 4.3.1.2) is not captured at all by the RANS simulation shown in figure 6.6(b). In this latter case, the configuration is quite similar to that at high ground clearance (figure 6.6a). Compared to experimental results (see figure 3.4 on page 41), there is a clear underbody velocity overestimation at low ground clearance which is consistent with Cadot *et al.* (2015*b*); however, it seems much more accurate for $c^* = 0.168$.

For all simulations, the mean wake appears to be symmetrical in the horizontal plane (figure 6.6*c*, *d*) thus respecting the symmetry of the problem. The fields are colored by the velocity magnitude U^*_{xz} (respectively U^*_{yz}) and the wake is clearly identified by the very low velocities (with respect to the free-stream's) and characterized by reverse flow similarly to the experiments. However, compared to figure 3.4, the wake is longer with a length of about 2.3 H of the recirculation area against about 1.8 H for experimental planes. Similar fields are reported for by Khalighi *et al.* (2001) but also for the GTS model in van Raemdonck *et al.* (2016).

The mean base pressure distributions $C_p(y^*, z^*)$ shown in figure 6.7 for the steady case are obtained at the following ground clearances: $c^* = 0.067$, $c^* = 0.101$ and $c^* = 0.168$. At first glance, the numerical results do not largely depend on the distance towards the floor. We observe a pressure maximum at the center of the base with an almost circular shape surrounded by a uniform pressure distribution. The only influence of the ground clearance seems to be the shape of this area which becomes less circular as the floor becomes closer and switches to an ellipsoidal form (loss of symmetry in the vertical direction). The numerical results and in particular the base pressure distributions are comparable to those of Khalighi *et al.* (2001) for the squareback case (averaged unsteady RANS simulations) but also to those obtained in van Raemdonck *et al.* (2016) for a body whose base is higher than wide. The associated mean base suction coefficients C_b (defined in equation 2.2) are reported for all ground clearances in table 6.2.

Table 6.2 – Characteristic mean force and base suction coefficients for the squareback Ahmed body with $\alpha = 0°$, $\beta = 0°$ obtained numerically at various ground clearances for the fine mesh F and comparison to experimental data for the squareback geometry and the afterbody with a $d = 0.285$ H deep cavity (Appendix B).

Configuration	c^*	C_b	C_x	C_y	C_z
Simulations (F)	0.067	0.179	0.259	0.000	−0.146
	0.101	0.178	0.254	0.000	−0.149
	0.168	0.181	0.250	0.000	−0.160
Experiments (squareback)	0.067	0.198	0.285	−0.002	−0.060
	0.101	0.184	0.262	−0.003	−0.117
	0.168	0.185	0.278	−0.003	−0.118
Experiments (cavity)	0.067	0.161	0.265	−0.001	−0.092
	0.101	0.139	0.242	−0.003	−0.111
	0.168	0.137	0.259	−0.003	−0.122

The mean force coefficients applied to the squareback Ahmed body are given in table 6.2 in which experimental and numerical data for the fine mesh F are reported. The mean base suction coefficient C_b is also indicated. The configuration with a base cavity is discussed in § 6.4.1 and added for comparison. Despite the very different base pressure distributions displayed in figure 6.7 compared to experimental results discussed so far, the simulation yields the right order of magnitude for the base suction coefficient C_b, in particular at high ground clearances. The underestimation of drag is partly related to the absence of the model's supports but also to the general topology of the wake: the recirculation zone is indeed longer than in the experiments consistently with the underestimation of drag. Besides, the experimental trends are not recovered since the minimum drag is reached for

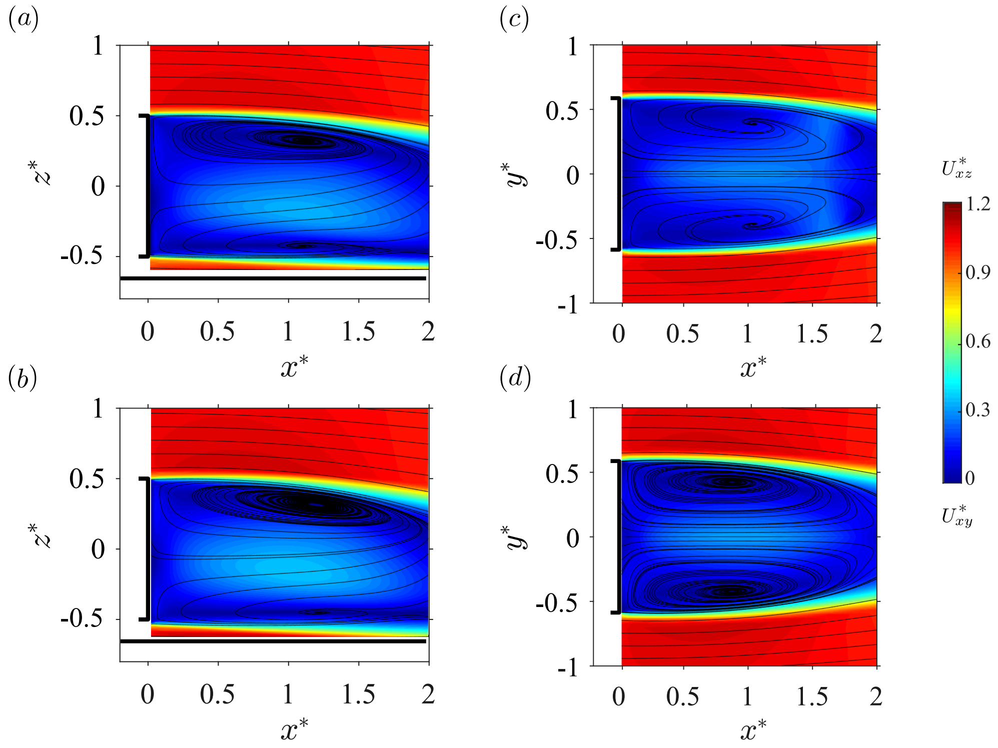

Figure 6.6 – Cross-sections of the mean velocity field at the base of the body visualized using streamlines superimposed to the modulus of the velocity in the vertical plane $y^* = 0$ (left column) and horizontal plane $z^* = 0$ (right column). The body is aligned with the incoming flow ($\beta = 0°$) and in no-pitch conditions ($\alpha = 0°$). (a, c) $c^* = 0.067$, (b, d) $c^* = 0.168$. Same plot dimensions as figure 3.4 chosen on purpose.

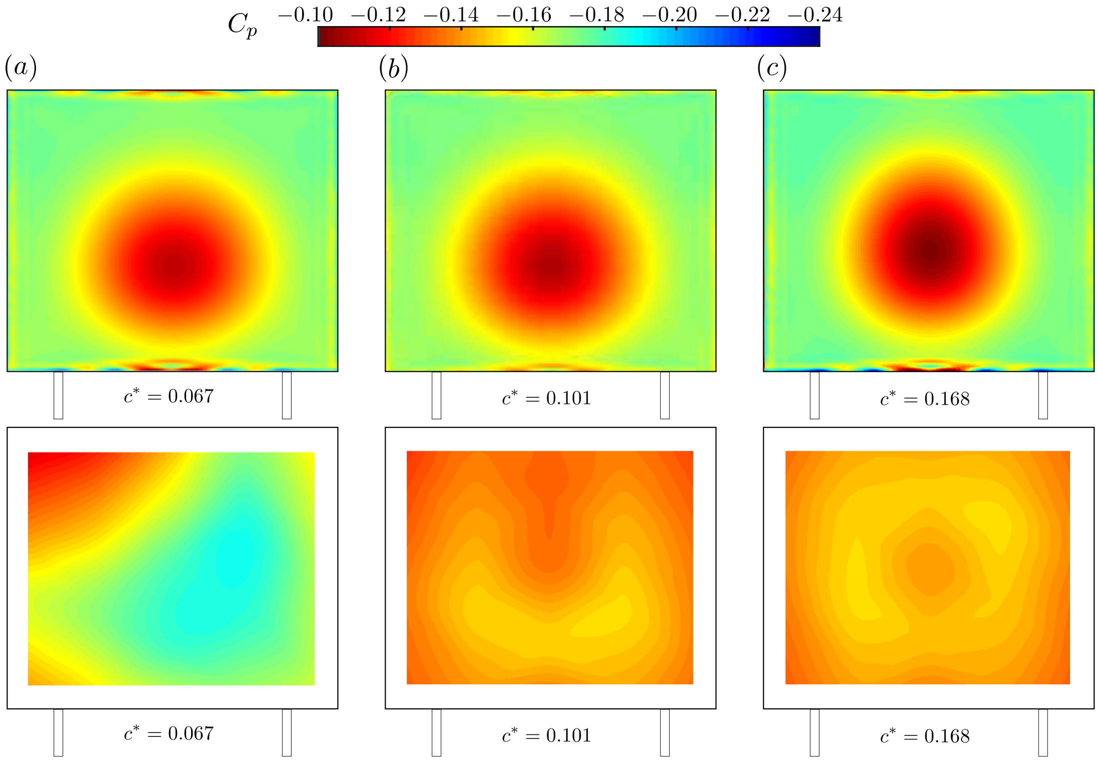

Figure 6.7 – Top row, mean base pressure distributions $C_p(y^*, z^*)$ for squareback Ahmed body ($\alpha = \beta = 0°$) at various ground clearances: (a) $c^* = 0.067$ (b) $c^* = 0.101$ (c) $c^* = 0.168$. Corresponding experimental distributions for the squareback Ahmed body with a base cavity of depth $d = 0.285\ H$ (see Appendix B) in the bottom row.

$c^* = 0.168$ *vs.* $c^* = 0.101$ which may be ascribed to the absence of the body's supports. Nonetheless, the numerical coefficients are of the same order of magnitude as those found in the literature on the same body (Grandemange *et al.*, 2013*b*; Evrard *et al.*, 2016; Lucas *et al.*, 2017).

We finally comment some of the coherent structures in the mean wake of the squareback Ahmed body owing to numerical flow visualizations provided in figure 6.8. A toroidal structure similar to a ring in the wake can be identified on the iso-pressure surfaces presented in figure 6.8(*a*) for $c^* = 0.067$ and figure 6.8(*b*) for $c^* = 0.168$. A similar wake structure is also reported by Krajnović & Davidson (2003), Rouméas *et al.* (2009), Lucas *et al.* (2017) and Dalla Longa *et al.* (2017).

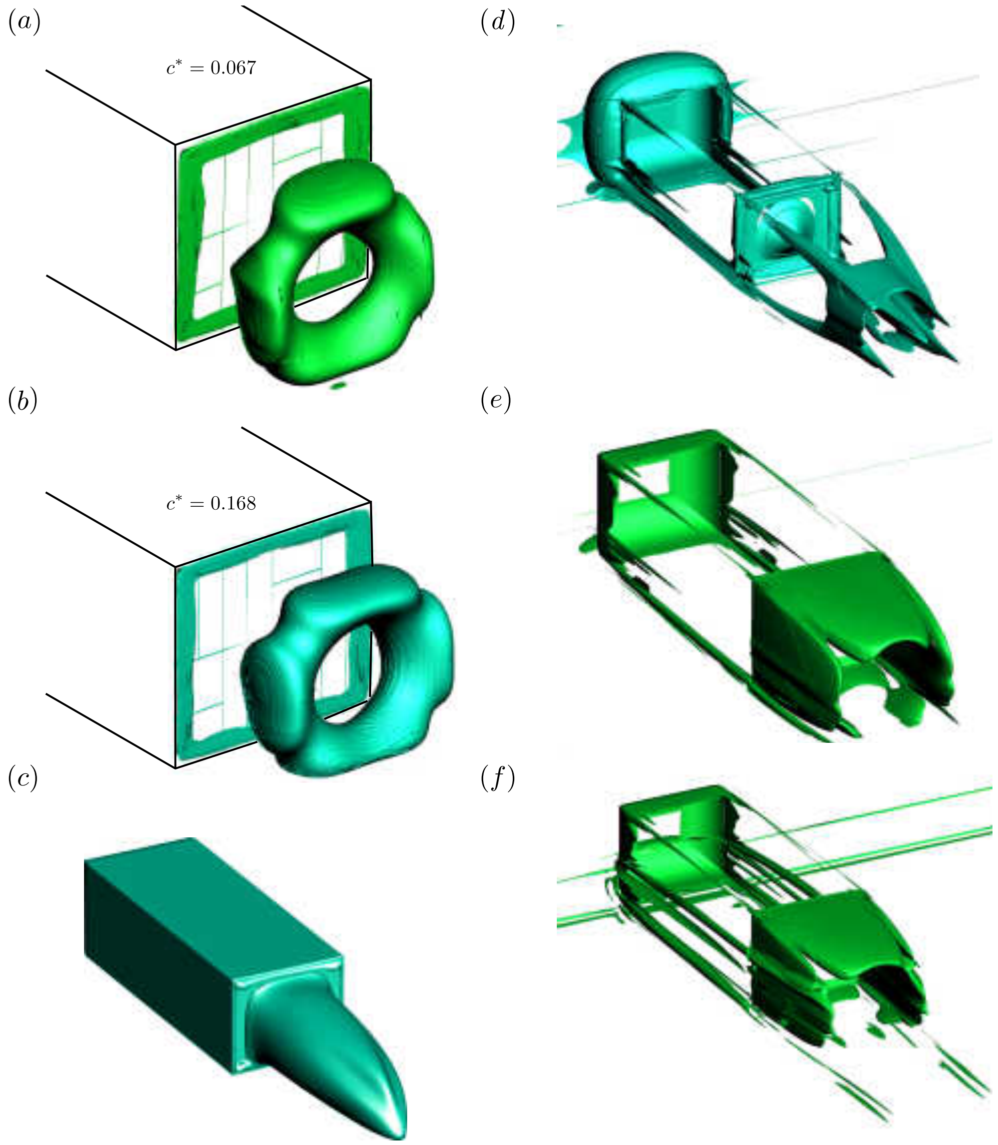

Figure 6.8 – Coherent structures in the mean wake of the squareback Ahmed body (simulations): iso-contours (*a*) $C_p = -0.186$ at $c^* = 0.067$ and (*b*) $C_p = -0.194$ at $c^* = 0.168$. (*c*) Iso-contour of zero velocity ($c^* = 0.168$). Q-criterion with (*d*) $Q < 0$ and (*e*) $Q > 0$ for $c^* = 0.168$; (*f*) $Q > 0$ for $c^* = 0.067$.

A zero-velocity cone is represented in figure 6.8(*c*) for the highest ground clearance ($c^* = 0.168$). It clearly defines the inner wake of the body inside which a reverse flow can be identified, *i.e.* an upstream flow motion. This cone corresponds more or less to the inner part of the toroidal wake structure identified hereabove, thus showing that recirculation occurs in the wake. The elongation of the recirculation area in presence of a cavity at the base of the body (see chapter 4 and associated appendix B) is a direct consequence of the negative longitudinal velocities inside the wake as the motion is stopped by the body's base only – or the bottom of the cavity. This reverse flow is also responsible for the oblique streamlines observed in the wake velocity fields.

Finally, we use the Q-criterion introduced in equation (6.3) to visualize some flow structures. Setting $Q < 0$ as in figure 6.8(d) unveils the vortices. The four longitudinal counter-rotating vortices created at the flow separation at the base are clearly visible. They converge and finally interact at the wake's closure. In addition, vorticity is generated along the body's rounded edge similarly to a vehicle's A-pillar vortex; the same observations are made in Lucas *et al.* (2017). Although no flow separation occurs at the body's front edge (see figure 6.3 and figure 6.4), there is a considerable vorticity generation. Finally, the wake torus creates a vortex-like behavior near the base of the body. We finally set $Q > 0$ and we observe the vortex sheets in figure 6.8(e) which delimit the wake region. While the top and the right ones are clearly symmetric because of the symmetries of the problem, there is a large difference between the top and bottom ones, the latter being much smaller than the other. This can be related to the presence of the ground as proved by figure 6.8(f) plotted at $c^* = 0.067$: the bottom sheet is strongly attenuated. Similar flow features are presented for a slanted Ahmed body in Corallo *et al.* (2015).

6.3.2 Unsteady simulation

The results of the unsteady simulations with the fine mesh are presented in this section. They should be addressed as preliminary results since the fields are not fully converged and since mesh-independence may not be satisfied. These simulations are initialized from scratch since it was not possible to destabilize the solution of the steady RANS equations presented in § 6.3.1 for which not even vortex-shedding is identified. The results of this section are challenged based on experimental observations and commented throughout.

The flow alongside the body is first considered in the two planes $y^* = 0$ and $z^* = 0$ in figure 6.9. The velocity fields are identical to those of the steady runs (figures 6.3 and 6.4); the flow separations at the front and on the sides of the body are consequently not dumped by the steady simulations which still provide an accurate diagnosis of such flow features at a lower computational cost. Besides, this shows that well-chosen curvatures (Ahmed *et al.*, 1984) avoid the flow unsteadiness at the forebody. The stagnation point still respects the horizontal symmetry of the setup in the plane $z^* = 0$, showing unambiguously that the mean flow around the body – wake excluded – is expected to be symmetric. However, similarly to the steady cases, it is slightly shifted below the body's mid-height by the ground. Finally, the flow around the body is mainly independent of the ground clearance for the considered locations. As a result, we expect the main impact to be concentrated on the wake.

In effect, the wake appears to be quite different compared to the steady simulations. First, even if its general organization in the mid-track symmetry plane $y^* = 0$ (figure 6.10a, b) is not drastically changed, one may notice that it is way shorter (about 1.8 H at $c^* = 0.067$ and 1.5 H at $c^* = 0.168$). However, it still presents a large downwash and seems to interact with the ground regardless of the considered ground clearance. Out of the two vortex cores (figure 6.10a, b), the top one is much larger than the other which almost disappears at high clearance. The wake consequently presents an asymmetry in the vertical mid-plane. In the horizontal plane $z^* = 0$ located at the body's mid-height, the wake is perfectly symmetric as shown in figures 6.10(c, d), unlike what would be expected with the y-instability. These fields are very far from those reported in other numerical papers (Peres

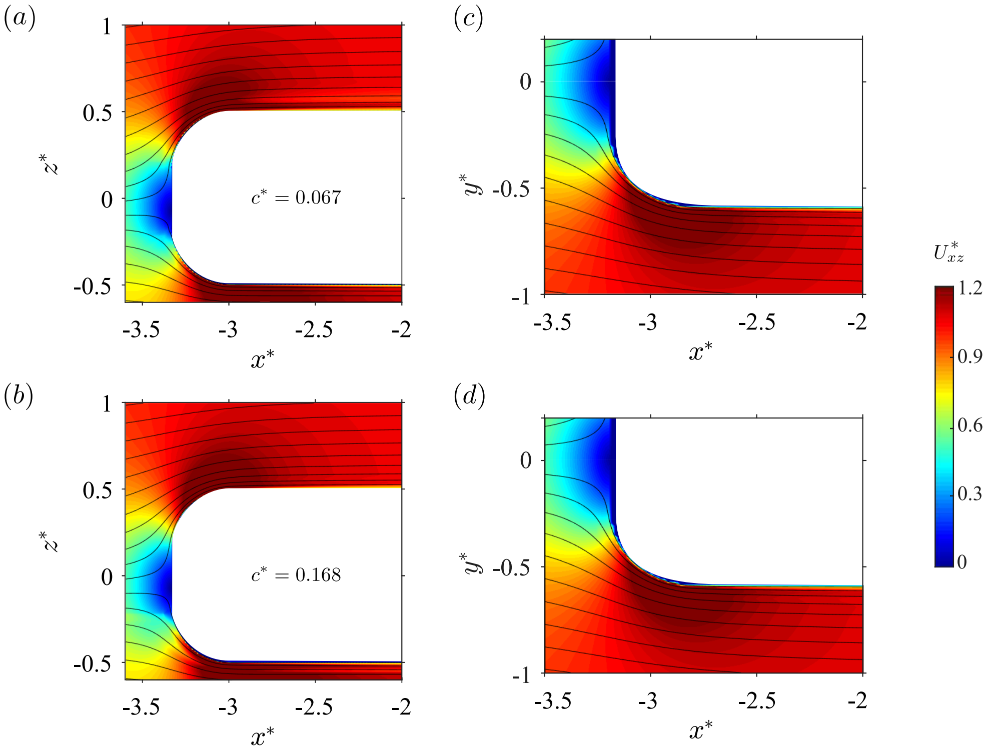

Figure 6.9 – Cross-sections of the mean velocity field U^*_{xz} in the plane $y^* = 0$ (a, b) and in the plane $z^* = 0$ (c, d) for the squareback Ahmed body aligned with the incoming flow ($\alpha = 0°$, $\beta = 0°$) obtained numerically at various ground clearances for the unsteady simulation: (a, c) $c^* = 0.067$, (b, d) $c^* = 0.168$. Instantaneous flow fields ($t^* = 100$).

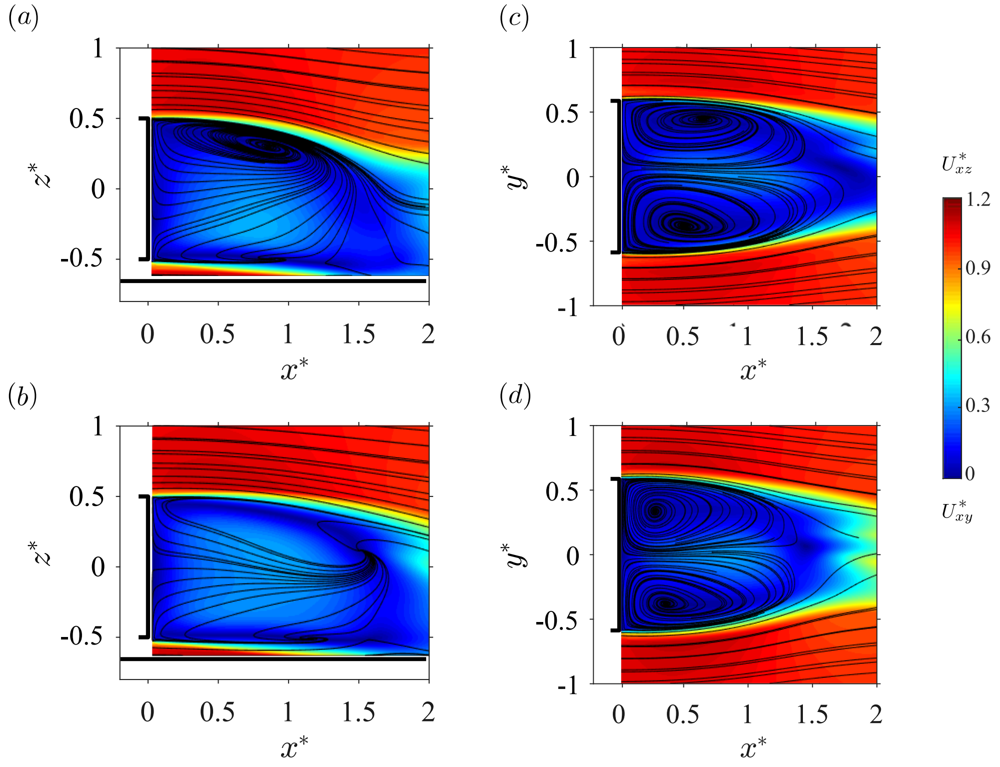

Figure 6.10 – Cross-sections of the mean velocity field at the base the body visualized using streamlines superimposed to the modulus of the velocity in the vertical plane $y^* = 0$ (left column) and horizontal plane $z^* = 0$ (right column). The body is aligned with the incoming flow ($\beta = 0°$) and in no-pitch conditions ($\alpha = 0°$). (a, c) $c^* = 0.067$, (b, d) $c^* = 0.168$. Instantaneous flow fields ($t^* = 100$).

& Pasquetti, 2013; Pasquetti & Peres, 2015; Dalla Longa *et al.*, 2017; Lucas *et al.*, 2017) and seem quite unreasonable compared to our experimental observations.
The mean aerodynamic loading is reported in table 6.3 for the two studied ground clearances and compared to the experimental data. The simulations reach a periodic regime after the transient is over; only the periodic regime is considered in this work. Aerodynamic coefficients are averaged over $t^* = 100$. As a consequence, the fluctuations are not presented since the simulated time is much too short compared to the dynamics' typical time scale. We are able to provide a quite accurate estimation of the drag and of the base suction despite the quite different pressure distributions. The side force is null for all configurations. Compared to the experiments, the lift force is overestimated. This might be related to a blockage effect or an inaccurately predicted ground boundary layer.

Table 6.3 – Characteristic mean force and base suction coefficients for the squareback Ahmed body with $\alpha = 0°$, $\beta = 0°$ obtained numerically unsteady simulations at various ground clearances for the fine mesh F and comparison with experimental data.

Configuration	c^*	C_b	C_x	C_y	C_z
Unsteady simulations (F)	0.067	0.200	0.290	0.000	−0.115
	0.101	0.188	0.273	0.000	−0.153
	0.168	0.187	0.280	0.000	−0.169
Experiments	0.067	0.198	0.285	−0.002	−0.060
	0.101	0.184	0.262	−0.003	−0.117
	0.168	0.185	0.278	−0.003	−0.118

A high frequency periodicity can be observed on the time series of the side force coefficient c_y, plotted in figure 6.11 for $c^* = 0.067$. The period is measured to be $t^* \simeq 5.58$, which corresponds to a dimensionless frequency of $f^* \simeq 0.179$. Grandemange *et al.* (2014*b*) and Pavia *et al.* (2018) show that it is characteristic of the vortex-shedding but not related to the wake static asymmetry associated with symmetry-breaking modes. As a consequence, the cross-flow loading applied to the body is periodically affected.

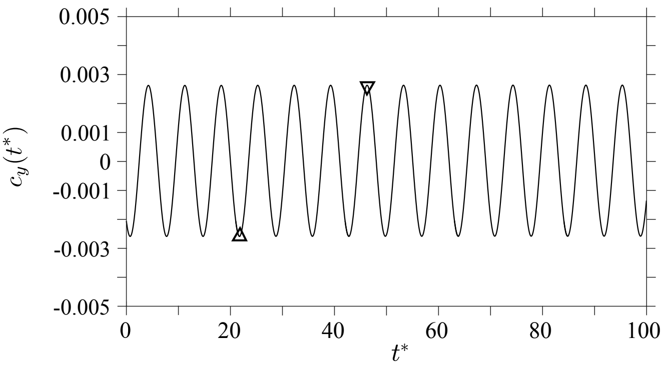

Figure 6.11 – Time series of the side force coefficient c_y: $c^* = 0.067$. The triangles correspond to the cases plotted in figure 6.12.

The base pressure distributions corresponding to a minimum and a maximum of the side force are given in figure 6.12. An asymmetric base pressure imprint is admittedly observed but this distribution is not close to the experimental observations. The typical pattern (higher pressure area) associated with the backward jet impinging the base is clearly visible for the two studied ground clearances. In both cases, pressure distributions are mirror one each other ($a-b$ and $c-d$) but do not present the typical patterns related to the symmetry-breaking modes of the wake discussed in chapter 4. There seems to be an impact of the ground on the wake topology but no stabilizing effect can be observed either. These distributions are very different to those obtained with the coarse mesh (not presented in this manuscript) so there might be a non-negligible influence on the mesh. However, the mean pressure levels observed on the base are lower than those associated with the steady simulations, which is consistent with the shorter recirculation bubble observed on the velocity fields of figures 6.10.

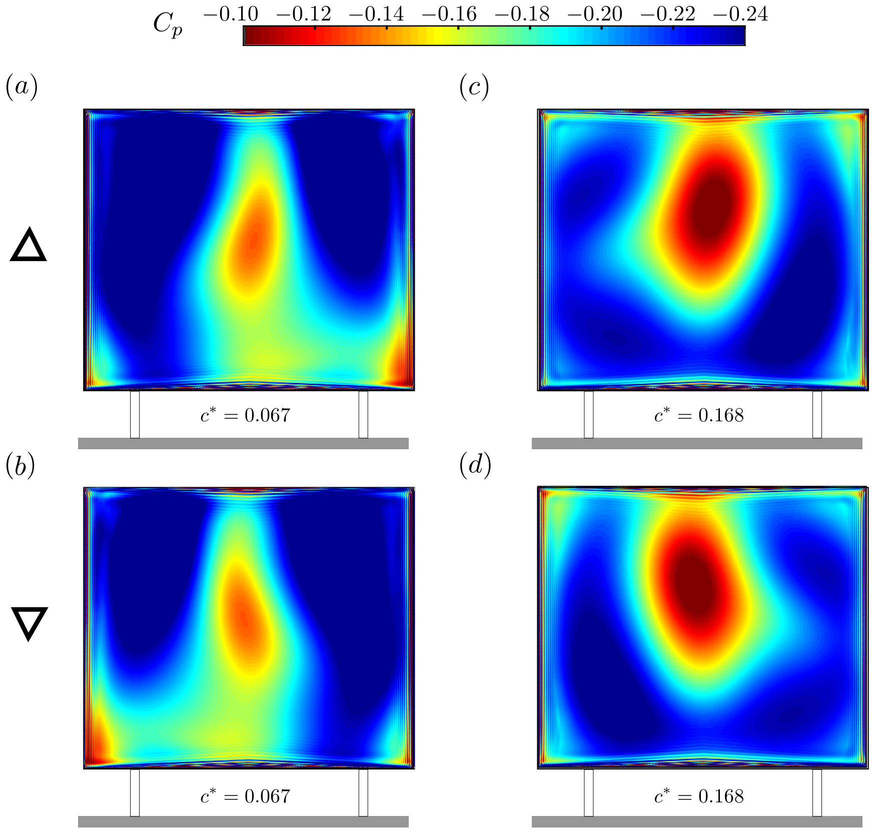

Figure 6.12 – Instantaneous base pressure distributions $c_p(y^*, z^*)$ for squareback Ahmed body ($\alpha = \beta = 0°$) at various ground clearances and corresponding to the triangles in figure 6.11: (a, b) $c^* = 0.067$ (c, d) $c^* = 0.168$. (a) and (c) correspond to negative side force while (b) and (d) to positive. These cases correspond to the triangles in figure 6.11.

6.3.3 Yawing conditions

A brief attempt is made to capture the instability while putting the body under yawing conditions. Only the larger ground clearance $c^* = 0.168$ is considered and both the steady and the unsteady configurations are studied with the fine mesh F. The investigated yaw angle is randomly chosen to be $\beta = -2°$. The results are presented in figure 6.13. The base pressure distribution of the steady simulation (figure 6.13a) is almost similar to that of the aligned configuration; only the location of the backward jet is modified. A similar conclusion can be drawn for that of the unsteady case (figure 6.13b) even if it is closer to that observed experimentally. The wake asymmetry can clearly be observed in figures 6.13(c, d); once again the unsteady case is closer to experimental observations. Nonetheless, this preliminary test is not sufficient to firmly conclude about the presence or the absence of the instability in the simulations.

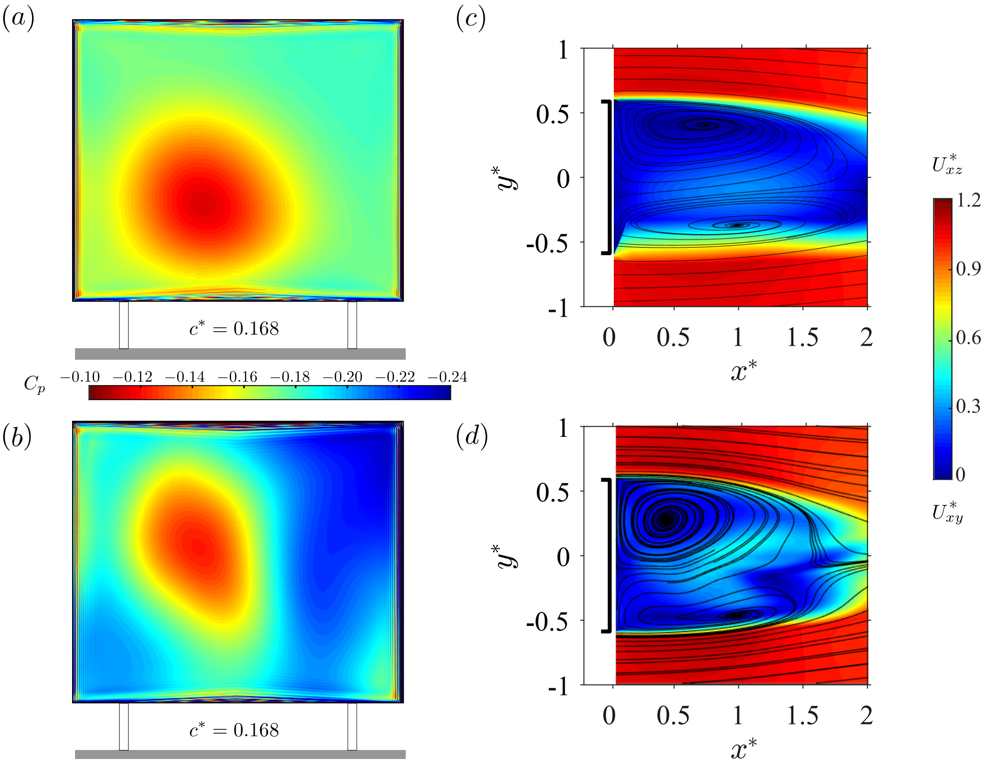

Figure 6.13 – Base pressure distributions $c_p(y^*, z^*)$ for squareback Ahmed body at $c^* = 0.168$ and under yawing conditions ($\beta = -2°$) in the steady (*a*) and unsteady (*b*) simulations. Cross-sections of the mean velocity field at the base the body visualized using streamlines superimposed to the modulus of the velocity in the horizontal plane $z^* = 0$ in the steady (*c*) and unsteady (*d*) simulations for yawing conditions.

6.4 Discussion

6.4.1 Accuracy of steady and unsteady simulations

As stated in the preliminary remark, the aim of this chapter is not to obtain a detailed and high-fidelity simulation of the flow around the Ahmed body in ground vicinity but to implement the simplest possible model – Reynolds Averaged Navier-Stokes simulations – and to conduct a stability analysis on the obtained base flow in order to reveal the wake static asymmetric modes.

As expected, the results of the steady simulations (§ 6.3.1) are quite inaccurate compared to the experimental data presented in chapter 3. The mean flow around the front part of the body is quite accurately simulated, in particular around the rounded leading edge (compare figures 3.2 and 3.3 to figures 6.3 and 6.4) but the wakes are strongly different. However, it turns out that the result could be interpreted as the *basic flow*, *i.e.* the flow without the static wake instability (see chapter 4). As a matter of facts, if one compares the mean wake shown in figure 6.6(b, d) to that obtained experimentally for the squareback body equipped with a base cavity (figure 4.15b, e on page 66), a similar organization but also length of the recirculation bubble is retrieved. We add in figure 6.7 (bottom row) the corresponding mean base pressure distributions obtained experimentally. The pressure imprint is much closer in particular at high ground clearance. However, the mean base suction is bigger in the numerical case because of the additional effect of the base cavity described in Appendix B, which also leads to lower drag (table 6.2).

The results presented for the unsteady Reynolds Averaged Navier-Stokes simulation are inaccurate compared to the physics of the flow. In particular, they are mesh dependent and not sufficiently converged in time. However, they represent promising results, constituting a first milestone in the simulation of the wake instability since the periodic wake mode responsible for vortex-shedding is captured. In our opinion, this does not necessarily mean that the static asymmetry does not exist in the simulation but it unambiguously proves that the simulated time is way too short compared to the wake's dynamics typical time scale to prospectively observe it.

If one were to conduct realistic and accurate simulations of the unstable wake of the squareback Ahmed body, the strategy would be to start with the two kinds of computations considered in this work (RANS and URANS) and then to switch to a Zonal Detached Eddy Simulation. ZDES basically combines a RANS and a Large Eddy Simulation (LES) approach since the model switches to a sub-grid scale formulation in some areas; if this were to be implemented, it would be the case in the wake of the body. The key ideas of this technique can be found for instance in Spalart (1997); a recent paper of Deck (2012) presents an extensive study of this kind of simulations. In the present case, a ZDES formulation based on the $k - \omega$ turbulence model is expected to provide good results on the wake dynamics.

6.4.2 Stability analysis of the wake

Some of the results presented in § 6.3 consequently form, in our opinion, a valuable basis for further analyses. In particular, the RANS analysis indeed provides a satisfactory representation of the *basic flow* described in § 4.4. In agreement with Cadot *et al.* (2015*b*), this symmetric configuration could correspond to a drag optimum. Comparing with mean experimental data, we can clearly see that forcing the bi-stable dynamics does not yield the *basic flow* because of the underlying presence of the instability. This means that, despite the minimum drag observed in bi-stable conditions (§§ 4.3.1, 4.3.2, 4.4.4), better performances could still be obtained. Even if never observed experimentally, we believe that the solution of the RANS problem, since it respects all the symmetries of the problem and therefore does not carry the instability, could be seen as a target for flow control. However, to ensure that, a stability analysis can be performed to ensure that the instability is really absent or determine whether a weakly damped mode representing bistability is indeed present or not. Once an accurate flow is obtained, the aim is to perform a stability analysis on the mean using a frequency domain framework, such as resolvent analysis (Beneddine *et al.*, 2016, 2017).

The shortening of the wake in unsteady simulations could possibly be ascribed either to vortex-shedding either to the static wake instability. Evidences of the presence of vortex-shedding in the turbulent wake of the Ahmed body are reported for instance by Grandemange *et al.* (2014*b*) but, if the observed phenomenon it related to the static wake instability, it should be possible to capture it by means of a stability analysis. Provided a good estimation of the mean flow is obtained, a stability analysis can be conducted. The unanswered question is whether RANS is sufficient to identify the static asymmetric wake modes by means of a stability analysis on the base flow.

In addition, it would be interesting to assess whether the wake asymmetry can persist with this model. We indeed believe that, in order to understand the wake bistability, which is a low frequency phenomenon (see chapter 4 and Grandemange *et al.* (2013*b*, 2014*b*) for preliminary works), it is could be sufficient to perform a – relatively inexpensive – RANS simulation and then a stability analysis on it.

6.5 Concluding remarks

A Reynolds Averaged Navier Stokes simulation of the flow around the squareback Ahmed body considered in the experiments is performed in this chapter both in steady and unsteady conditions. The first one yields the *basic flow* without the instability. There is very little confidence in the results of the unsteady simulations and it was not yet possible to observe the wake asymmetry. However, better results might be obtained with a finer mesh and a longer computation time. The aim of this chapter was not to accurately predict the flow but to establish the bases for an upcoming stability analysis.

Part II

Industrial geometries: real road vehicles

CHAPTER 7

Wake bi-stability created by static instabilities

Real road vehicles with a blunt vertical afterbody and whose wakes will be demonstrated to be subject to static symmetry-breaking modes are investigated in this chapter. After a brief introduction of the setup in § 7.1, the experiments aiming at revealing two possible wake states for identical boundary conditions are conducted. Starting from a baseline configuration representative of daily driving conditions (§ 7.2.1), we first increase the vehicle's ground clearance and obtain a very different wake topology associated with a peculiar base pressure distribution and a strongly modified aerodynamic loading (§ 7.2.2). The pitch angle is however not necessarily sufficient to produce a wake reversal (§ 7.2.3) which, however, can be triggered by side-slip conditions (§ 7.2.4). In a second part, we close the front air-intake to get a configuration closer to that of the Ahmed body (§ 7.2.5) and successfully reproduce the pitch experiment in § 7.2.6 where a bi-stable dynamics is reported for the first time for a vehicle aligned with the incoming flow. The yaw of the vehicle is then found to be able to select the wake state from this dynamics (§ 7.2.7). Finally, control is performed on the vehicle's wake in § 7.2.8 by means of rear tappers or modification of the underbody roughness. In addition, the sensitivity of the wake to external disturbances is investigated. A discussion about the instability of the wake of real vehicles is provided in § 7.3. The main results presented in this chapter are under consideration for publication in Journal of Wind Engineering and Industrial Aerodynamics.

Contents

7.1 Setup 167

7.2 Results 170

7.2.1 Baseline of the vehicles: wake symmetry-breaking 170

7.2.2 Wake reversal operated by the ground clearance 173

7.2.3 Identification of a reversed wake state with the pitch angle α . . . 174

7.2.3.1 Successful identification of a reversed wake state 175

7.2.3.2 Stabilization operated by the cooling flow 177

7.2.4 Wake bistability under yawing conditions 178

7.2.5 Baseline with closed air-intake and wake state selection 183

7.2.6 Wake reversals triggered by the pitch angle α with closed front air-intake 186

7.2.7 Wake state selection operated by the yaw with closed front air-intake 190

7.2.8 Manipulations of the flow around the vehicles 193

7.2.8.1 Effect of rear tappers 193

7.2.8.2 Influence of the underbody roughness 196

7.2.8.3 Wake sensitivity to external disturbances 199

7.3 Discussion 203

7.4 Concluding remarks 205

7.1 Setup

The experiments are conducted in the full-scale wind tunnel of the GIE-S2A presented in § 2.1.1. Realistic driving conditions are reproduced owing to a rolling belt moving at the simulated air-speed and mimicking the road and to rotating wheels. Two different free-stream velocities are used for the tests: $U_\infty = 38.9$ m.s^{-1}, classically used by the car manufacturers as it is close to the maximum allowed speed in most European highways for the Peugeot 5008 and Partner and $U_\infty = 33.3$ m.s^{-1} for the Renault Kangoo and Citroën Berlingo. The corresponding Reynolds numbers based on the vehicles' heights Re_H are given in table 7.1. When the tomographic in-wake measurement system described in § 2.3.1 is in used, it is required not to blow above $U_\infty = 33.3$ m.s^{-1} then chosen as the free-stream velocity for all vehicles. This limitation is imposed by the maximum allowable aerodynamic loading applicable on the mast.

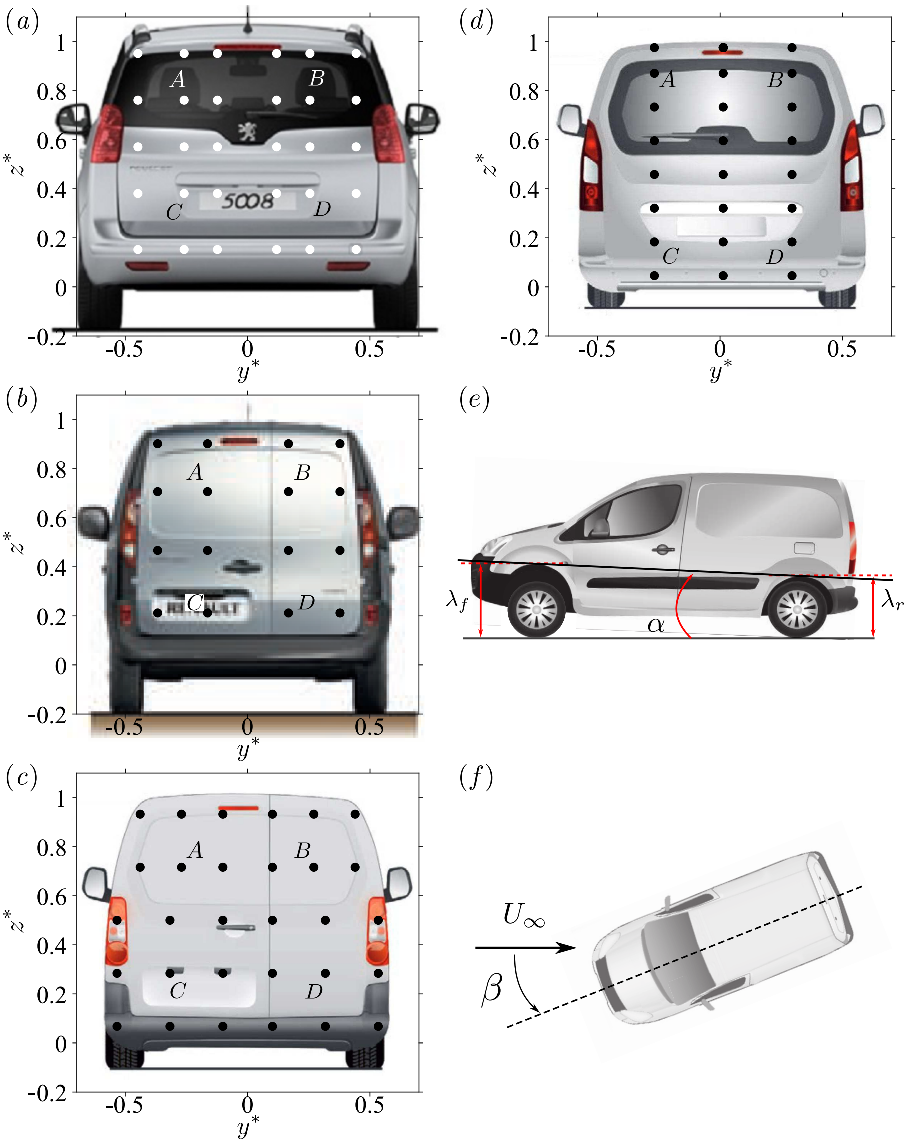

Figure 7.1 – Experimental setup: pressure taps locations for the four vehicles. (*a*) Peugeot 5008 ($N = 30$), (*b*) Renault Kangoo ($N = 16$), (*c*) Peugeot Partner ($N = 30$) and (*d*) Citroën Berlingo ($N = 24$). (*e*) Definition of the distances λ_f and λ_r and of the pitch angle α (not to scale). (*f*) Definition of the yaw angle β.

The vehicle's base pressure distribution is estimated owing to N (indicated in the legend of figure 7.1$a-d$) pressure sensors distributed over the car's base and connected to a Scanivalve ZOC22b pressure scanner operated with the GLE/SmartZOC100 electronics ($f_e = 200$ Hz). Synchronous force measurements are operated at a sampling frequency of $f_b = 10$ Hz. A full description of the pressure acquisition line and of the force balance can be found in §§ 2.2.1 and 2.2.2 respectively. The experiments with the Renault Kangoo were not performed during this thesis and only the results obtained by A. Courbois and already published in Cadot *et al.* (2016) are post-processed. Pressure measurements were obtained with a Scanivalve ZOC33 pressure scanner similar to that of § 2.2.1 but sampling at about $f_e \simeq 10$ Hz only since it is acquired using the same chain as the force balance. As shown in § 2.2.1 (see in particular figure 2.4 on page 24), the actual cut-off frequency of the pressure measurement ranks around 20 Hz due to the attenuation generating by the vinyl tubing. Nonetheless, it is sufficient to capture the long-time dynamics of the wake as shown in Cadot *et al.* (2016) and Bonnavion *et al.* (2017a). The location of the base pressure taps can be found for each of the vehicles in figure 7.1($a-d$).

A base pressure gradient $\hat{g}^*$ is computed from pressure measurements using the taps indicated as A, B, C and D in figure 7.1($a-d$). The procedure is the same for all four vehicles and was already used in previous chapters with the simplified model. The two Cartesian components are computed as:

$$g_y^*(t^*) = \frac{1}{2} \times \left[\frac{c_p(y_A^*, z_A^*, t^*) - c_p(y_B^*, z_B^*, t^*)}{y_A^* - y_B^*} + \frac{c_p(y_C^*, z_C^*, t^*) - c_p(y_D^*, z_D^*, t^*)}{y_C^* - y_D^*} \right] \tag{7.1}$$

and:

$$g_z^*(t^*) = \frac{1}{2} \times \left[\frac{c_p(y_A^*, z_A^*, t^*) - c_p(y_C^*, z_C^*, t^*)}{z_A^* - z_C^*} + \frac{c_p(y_B^*, z_B^*, t^*) - c_p(y_D^*, z_D^*, t^*)}{z_B^* - z_D^*} \right] \tag{7.2}$$

Finally, we combine them to create the complex base pressure gradient $\hat{g}^* = g_y^* + \mathrm{i} g_z^*$. Throughout the chapter, we use both its Cartesian and polar forms respectively denoted (g_y^*, g_z^*), referred to as horizontal and vertical gradients, and (g_r^*, φ), referred to as strength and phase.

For each of the vehicles described in § 7.1, the baseline is chosen as the car geometrically aligned with the incoming flow ($\beta = 0°$). Concerning the pitch and the ground clearance, they are adjusted to represent those of realistic driving conditions with only the driver on-board by means of bags filled with sand placed on the front left seat and of total mass of about $m \simeq 75$ kg. Since it could be rather difficult to measure the actual ground clearance of each of the vehicle's axle, this length is replaced by the distances λ_f between the ground and the top of the wheel-arch for the front axle and λ_r for the rear axle indicated in figure 7.1(e, f). A pitch angle α can be computed from these two measurements and the wheelbase Λ_{fr} such that:

$$\tan \alpha = \frac{\lambda_f - \lambda_r}{\Lambda_{fr}} \tag{7.3}$$

For convenience, this angle is expressed in degrees throughout. From the definition of the pitch angle α in equation (7.3), positive values correspond to nose-up and negative to nose-down. Unlike the Ahmed body, the vehicles may present a *natural* pitch angle α_b in the baseline when $\lambda_f \neq \lambda_r$[1]; in order to avoid confusion, only the difference $\Delta\alpha = \alpha - \alpha_b$

---

[1] In this chapter, this is the case for the Peugeot 5008 (see table 7.1).

will be discussed in this chapter. For simplicity, it will be referred to as the actual pitch angle of the vehicle.

Two test configurations are considered. Either the vehicle is tested in real driving conditions with the front air-intakes dedicated to the engine and breaks cooling system open, or we obstruct them in order to avoid inflow passing through and to obtain a flow closer to that of the Ahmed body. The air-intake condition is described for each of the experiments. In the figures, open air-intakes are indicated with a white rectangle and closed with a black one.

The acquisitions are made during $2-4$ minutes, *i.e.* long enough to capture the long-time dynamics of the wake and explore the different branches of the solution if any but not to ensure statistical convergence of the pressure data. Before each set of experiments, a no-wind acquisition is briefly performed, the averaged value of which is removed to the actual measurements to correct any offset. Practically, we take advantage of the regular breaks imposed by the increasing temperature of the vehicle's tires and of the wheel spinners which must be kept at a reasonable level but increases quickly because of the adherence and the absence of cooling system.

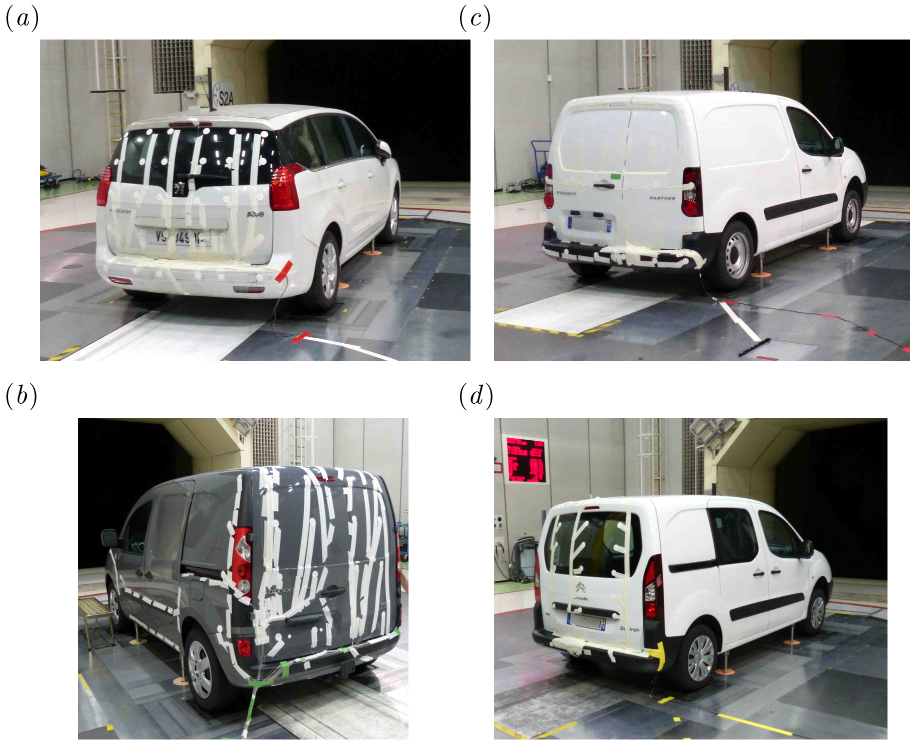

Figure 7.2 – Real vehicles in the full-scale wind-tunnel: (*a*) Peugeot 5008, (*b*) Renault Kangoo, (*c*) Peugeot Partner and (*d*) Citroën Berlingo. The pressure taps, similar to those represented in figure 2.3(*b*), are also visible on the vehicles' bases.

Four blunt based vehicles are used in this chapter: a Renault Kangoo (figure 7.2*a*), a Peugeot 5008 (7.2*b*), a Peugeot Partner (7.2*c*) and a Citroën Berlingo (7.2*d*). These vehicles have been chosen because of the geometry of their afterbody – vertical blunt base – which ensures the presence of wake symmetry-breaking modes (Grandemange, 2013; Cadot *et al.*, 2016) unlike cars having more inclined afterbodies such as the Renault Mégane studied in chapter 8, for which an almost homogeneous base pressure distribution can be observed for the vehicle aligned with the incoming flow (§ 8.2.1). The characteristic dimensions of the vehicles studied in this chapter are provided in table 7.1 in the dimensionless form except for the vehicle's base height H_b chosen as the scaling unit.

Table 7.1 – Dimensions of the vehicles considered in this chapter and height based Reynolds numbers.

Dimension	5008	Kangoo	Partner	Berlingo
Base height H_b:	1.320 m	1.480 m	1.480 m	1.480 m
Base aspect ratio W_b^*:	1.212	1.115	1.121	1.121
Wheelbase Λ_{fr}^*:	2.114	1.822	1.843	1.843
Front wheel-arch height λ_f^*:	0.519	0.488	0.480	0.480
Rear wheel-arch height λ_r^*:	0.539	0.488	0.480	0.480
Natural pitch angle α_b:	$-0.55°$	$0°$	$0°$	$0°$
Frontal surface S^*:	1.578	1.297	1.297	1.297
Vehicle's length L^*:	3.431	2.893	2.959	2.959
Reynolds number Re_H:	5.13×10^6	4.93×10^6	5.76×10^6	5.13×10^6

7.2 Results

Results concerning the Renault Kangoo were already published in Cadot *et al.* (2016) and Bonnavion *et al.* (2017*a*). The results section is organized as follows. We first characterize the baseline flows in § 7.2.1 and perform a first analysis changing the ground clearance (§ 7.2.2). Although a second wake topology may be identified in some cases by imposing a pitch angle to the vehicle (§ 7.2.3.1), the reversal may not occur because of the underbody flow (§ 7.2.3.2). The yaw angle of the vehicles can also be changed as in § 7.2.4 to provoke the reversals. Afterwards, we close the front air-intake system and reproduce the sensitivity analyses (§ 7.2.6). A bi-stable wake dynamics is even identified; it is the first time that such a dynamics is reported for a vehicle aligned with the incoming flow. Starting from the bi-stable behavior, it turns out that a permanent wake state selection can be performed by means of the yaw angle (§ 7.2.7). Finally, we perform flow control trying to select the most efficient wake state in § 7.2.8 in which the wake sensitivity towards external wake perturbations are also considered.

7.2.1 Baseline of the vehicles: wake symmetry-breaking

The vehicles are placed in the test section aligned with the incoming flow ($\beta = 0°$) and in their natural pitch angle with a driver on-board ($\Delta\alpha = 0°$)[1]. The air-intake system is not modified so that air can flow through as required by engine cooling. The mean base pressure distributions $C_p(y^*, z^*)$ are given in figure 7.3. We comment them together since all present the same features. The first obvious comment is that the distributions are almost symmetric in the horizontal direction (left-right symmetry) consistently with the apparent overall symmetry of the vehicles. Negative values of the pressure coefficient c_p indicate the presence of a fully detached flow area (Roshko, 1993). However, all distributions clearly show a pressure gradient in the vertical direction: the pressure levels are significantly lower at the bottom of the bases ($C_p \simeq -0.26$ for the Partner and the Berlingo, $C_p \simeq -0.17$ for the 5008 and the Kangoo) than at the top ($C_p \simeq -0.08$). From these distributions, it is clear that none of the vehicles is subject to a wake static y-instability similarly to the squareback Ahmed body studied in chapter 4. Although the

---

[1] The results presented in this chapter were obtained with rotating wheels and the moving ground. For the Peugeot 5008, the baseline configuration was tested with fixed ground and fixed wheels. It results in an identical base pressure distribution and mean drag value. Only the lift of the vehicle is decreased by about 5% when the road effect is simulated. The ground boundary layer is strongly modified – almost null with the moving ground – but was already very thick upstream of the vehicle since it is controlled by suction (see chapter 2 and in particular § 2.1.1 on page 19).

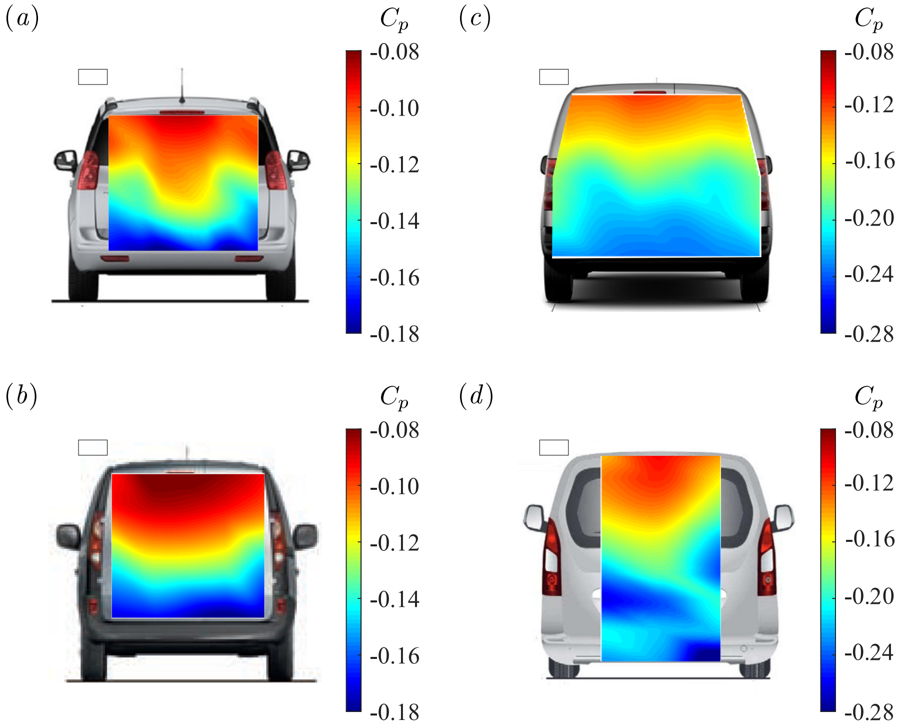

Figure 7.3 – Mean base pressure distributions $C_p(y^*, z^*)$ in the baseline configuration (front air-intake open): (*a*) Peugeot 5008, (*b*) Renault Kangoo, (*c*) Peugeot Partner and (*d*) Citroën Berlingo.

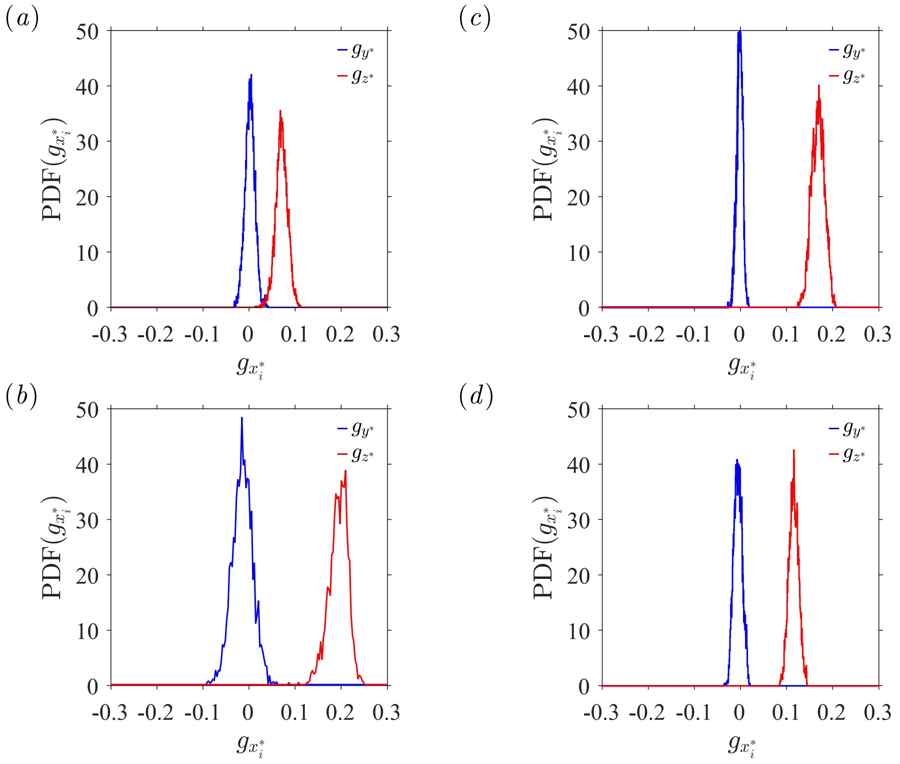

Figure 7.4 – Probability density functions of the Cartesian components of the base pressure gradient in the baseline configuration with open air-intake (blue horizontal gradient g_y^* and red vertical gradient g_z^*): (*a*) Peugeot 5008, (*b*) Renault Kangoo, (*c*) Peugeot Partner and (*d*) Citroën Berlingo.

car bases are wider than high ($W^* > 1$, see table 7.1), their aspect ratios place them in the *interfering region* between the y- and the z-instabilities in the sense of Grandemange *et al.* (2013*a*). Similar apparent inconsistencies were recently reported by Barros *et al.* (2017) or Pavia & Passmore (2018) for simplified geometries – squareback Ahmed and Windsor model equipped with rear wheels respectively – with a base aspect ratio of $W_b^* = W_b/H_b = 1.174$ and $W_b^* = 1.346$ and by Heft *et al.* (2011, 2012*a*,*b*) or more recently by Avadiar *et al.* (2018) for the generic DrivAer estate vehicle, whose mean base pressure distribution in the baseline case is almost identical to the ones provided in figure 7.3. Besides, Grandemange *et al.* (2014*c*) gives an identical distribution for a Renault Trafic. Two explanations are given for the selection of z-instability rather than of the y-instability. The same arguments hold for the four considered vehicles. First, the base's width-to-height aspect ratio is in the interfering zone of Grandemange *et al.* (2013*a*) thus possibly leading to the y- or the z-instability. Consequently, a geometrical symmetry defect is expected to select one or the other. Second, the actual selection can be ascribed to the vehicles' wheels according to the results of Pavia & Passmore (2018). The aim of this chapter is to reveal the mirror wake state if it were to exist and to compare the results with those of the Ahmed body obtained in § 4.3.2.

The hereabove presented distributions are almost steady: no wake reversal can be identified as shown by the single-peak probability density functions of the two Cartesian components of the base pressure gradient $\hat{g}^*$ given in figure 7.4. All show a permanent positive vertical gradient g_z^* only subject to small fluctuations while the Gaussian-like distribution of the horizontal gradient g_y^* is centered on zero. The similarity between figure 7.4(*c*) and figure 7.4(*d*) show an independence towards the Reynolds number in the considered range (see associated values in table 7.1).

The characteristic mean and fluctuating coefficients for the baseline configurations are given in table 7.2. The substantially lower drag of the Peugeot 5008 is the result from a more advanced shape optimization with respect to the other vans. It can also be observed that the mean side force coefficient C_y is never strictly null as a direct consequence of the slight asymmetries of the underbodies, engine compartment... All vehicles are characterized by a positive lift which may reduce their stability at high driving velocities[1]. None of the fluctuating coefficients is higher than 0.01 thus enforcing that none of the baselines is subject to large wake fluctuations.

Table 7.2 – Characteristic mean and fluctuating coefficients for baseline configurations of the four vehicles.

Vehicle	C_b	C'_b	C_x	C'_x	C_y	C'_y	C_z	C'_z
5008	0.128	0.003	0.278	0.009	0.003	0.001	0.010	0.002
Kangoo	0.125	0.003	0.347	0.008	0.004	0.005	0.012	0.005
Partner	0.182	0.005	0.339	0.006	0.003	0.006	0.017	0.004
Berlingo	0.183	0.005	0.336	0.009	0.001	0.005	0.017	0.004

From these configurations, we aim at revealing an hypothetical reversed wake state that would justify the hypothesis of a static z-instability in the minivans' wakes. In § 4.3.2, three methods were successfully tested in that aim for the Ahmed body: changing the ground clearance, the pitch and the yaw angles. In presence of such a symmetry-breaking, the baselines would be associated with state P of the wake characterized by phase lock-in around $\varphi \simeq \pi/2$ or equivalently said $0 < g_z^* \leq 0.1$ and $g_y^* \approx 0$.

---

[1] The lift indeed creates an upward force on each of the vehicle's axle.

7.2.2 Wake reversal operated by the ground clearance

The ground clearance experiment is conducted with the Peugeot 5008 only. By analogy with the Ahmed body (§ 4.3.2.2), we conclude that, starting from the baseline, the ground clearance needs to be increased to switch to state N of the wake and obtain $\varphi \simeq -\pi/2$ as a result of a negative vertical base pressure gradient $g_z^* \leq 0$. We did not perform a full sensitivity analysis but a second ground clearance only is tested. If the car is lifted up by 81 mm on each axle (+6% H) – which consequently results in a similar pitch angle α_b as the baseline –, the wake topology estimated owing to both the base pressure distribution $C_p(y^*, z^*)$ shown in figure 7.5(a) and the base gradient (figures 7.5b and c respectively) changes drastically.

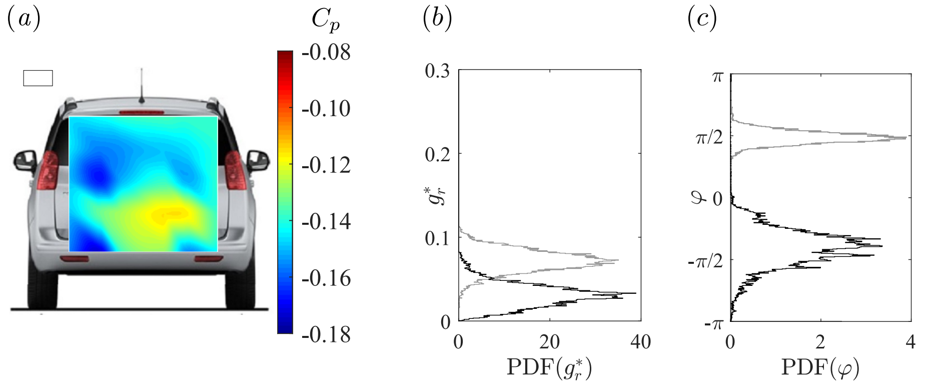

Figure 7.5 – Wake reversal operated by the ground clearance for the Peugeot 5008 ($\lambda_f^* = 0.580$, $\lambda_r^* = 0.600$). Mean base pressure distribution $C_p(y^*, z^*)$ (a). Probability Density Functions for the modulus g_r^* (b) and the phase φ (c) of the complex base pressure gradient $\hat{g}^*$. Reversed wake in black and baseline in grey for comparison.

The mean base pressure distribution $C_p(y^*, z^*)$ is strongly modified with respect to the baseline (figure 7.3a). Although it is not clear whether this configuration actually corresponds to the reversed wake state, there is no doubt that it is strongly different from the wake state P associated with the baseline (figure 7.3a). The vertical pressure gradient indeed becomes negative with a strong pressure drop on the top part of the base. Besides, the highest pressure is now located around the center of the cargo door unlike near the roof in the baseline configuration. The mean pressure is reduced and the base suction coefficient increases accordingly up to $C_b = 0.143$, *i.e.* by +11.72% with respect to the baseline.

The modulus g_r^* of the base pressure gradient (PDF given in figure 7.5b) is reduced while the phase φ appears to be strongly impacted as shown in figure 7.5(c). The most preferred phase ranks now about $\varphi \simeq -\pi/2$ while positive values are not explored anymore unlike the baseline (in grey) for which $\varphi \simeq +\pi/2$. The wake lock-in is not as clear as for the baseline though but the fluctuations are not big enough to let the vertical gradient g_z^* change sign. In other words, the wake state is permanently selected. Unlike the Ahmed body, the very low pressure generated at the rear diffuser (bottom of the base) are not removed when the car is lifted up.

The other differences with respect to the equivalent experiment with the simplified geometry presented in § 4.3.2.2 are that the two base pressure distributions are not mirrors one with respect to each other and cannot therefore be deduced one from the other by the transformation $z^* \to -z^*$. Nonetheless, this might be explained by the strong top-bottom asymmetry of the setup – rough underbody *vs.* streamlined roof, presence of the road and of the wheels (Wang *et al.*, 2018)[1]... Besides, they lead to very different values of the base suction. More importantly, the modulus of the gradient g_r^* is affected by the wake orientation. The latter point will be discussed in § 7.3. In addition, the geometry is modified between the two tested points and may be the cause for the change of the wake topology even without a static z-instability. For these two reasons, doubt sets in concerning the identification of the reversed wake state.

As expected, the mean side force C_y exerted on the vehicle is not affected by the ground clearance modification. However, the mean drag C_x and the mean lift C_z increase respectively by nearly 10.11% and 9.55%. These two variations cannot be ascribed only to the increase of the tires' frontal surface and are also related to the changes in the wake evidenced thanks to the new base pressure distribution. Nonetheless, there is undoubtedly a geometrical effect since the base pressure drop and the drag increase are of the same order while they are rather linked by a factor of two when the geometry is identical as shown for the Ahmed body in Appendix B. The lift increase is also fed by the reduced ground effect since the vehicle is lifted up.

The current – detrimental – geometrical configuration should never be encountered in real driving conditions, except for very limited times and in very specific cases (bumps driven at high speed for instance) but strongly suggests that a second wake state is present. Based on experimental observations with the Ahmed body made in § 4.3.2.4, the easiest way to reveal it seems to be a pitch angle sensitivity analysis. Besides, only two clearances were tested and wake bistability was not found – even if this does not mean that such dynamics does not exist. This makes it harder to conclude about the wake state since the problem's geometry is modified. However, if a similar base pressure distribution is retrieved in the pitch experiment, then we may be able to conclude that wake reversals operated by the ground clearance are also observed for real road vehicles.

7.2.3 Identification of a reversed wake state with the pitch angle α

A pitch angle sensitivity experiment is conducted with the Peugeot 5008 and Partner. Besides, a few operating points are tested with the Citroën Berlingo in order to confirm the results observed with the Partner since the two vehicles are almost identical except for some small details (front face, air-intake, rear panel). For technical reasons regarding for instance the load applied on the masts holding the vehicle and/or on the balance or the maximum travel range of the shock absorbers, it is not always possible to start from the baseline to conduct pitch sensitivity experiments. Nonetheless, in such cases, we ensure that the wake remains in state P shown in figure 7.3 and forces variations are expressed with respect to this new configuration rather than to the baseline. By analogy with the results obtained for the Ahmed body subject to the z-instability in § 4.3.2.4, we rather try to increase positively the pitch angle so that $\Delta\alpha > 0°$ in order to trigger the reversal since we want the vertical gradient to decrease with respect to the baseline so that it eventually becomes negative. Although not reported, nose-down configurations lead to identical base pressure distributions and phase locks-in as the baselines since the wake state P is reinforced by the geometrical constraint. However, it appears in the following that the pitch is not the only ingredient to trigger the reversal.

---

[1] Results enforcing this hypothesis were recently presented by Y. Wang (Institut P' - Michelin), C. Sicot, J. Borée (Institut P') and M. Grandemange (Michelin) at the 2018 annual workshop of the CNRT R2A and at the Aerovehicles 3 conference. They showed that the rear wheels were able to reverse the wake of the ASMO simplified model and to produce similar base pressure distributions as those identified for the 5008, Kangoo, Partner and Berlingo.

7.2.3.1 Successful identification of a reversed wake state

The study is first conducted with the Peugeot 5008 (figure 7.2*a*). Starting from the baseline, the front axle is lifted up, *i.e.* λ_f increases, while λ_r is kept constant to create a pitch angle. The four sensitivity maps are given in figure 7.6.

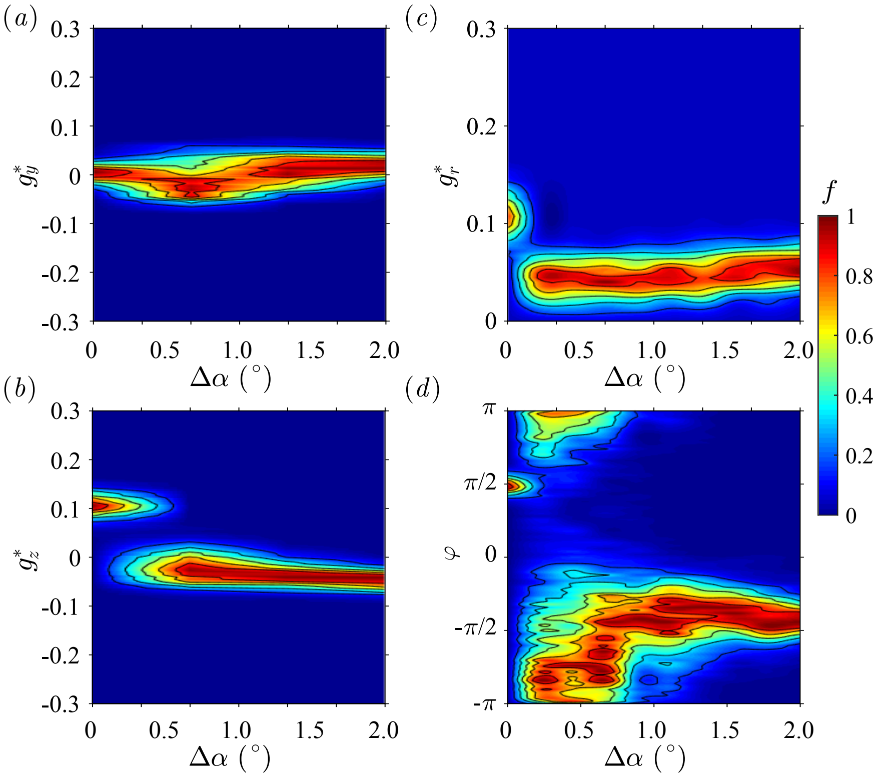

Figure 7.6 – Base pressure gradient response to variations of the pitch angle α for the Peugeot 5008. Sensitivity maps (*a*) $f(\Delta\alpha, g_y^*)$, (*b*) $f(\Delta\alpha, g_z^*)$, (*c*) $f(\Delta\alpha, g_r^*)$ and (*d*) $f(\Delta\alpha, \varphi)$.

The horizontal base pressure gradient g_y^* shown in figure 7.6(*a*) is almost insensitive to the pitch applied to the vehicle except around $0.5° \lesssim \Delta\alpha \lesssim 0.75°$ for which the fluctuations increase slightly. This value corresponds to a discontinuous transition of the vertical base pressure gradient g_z^* (figure 7.6*b*) from a branch around $g_z^* \simeq 0.1$ to negative values ($g_z^* \simeq -0.05$), very similar to the bifurcation operated by the ground clearance (§ 7.2.2). The modulus g_r^* also appears to be divided by nearly two in figure 7.6(*c*). The larger fluctuations of the horizontal gradient directly impact the phase φ which, initially locked around $\varphi \simeq \pi/2$ first totally unlocks with an almost uniform exploration of $\varphi \in [-\pi, 0]$ corresponding to a negative vertical gradient while the horizontal component alternately changes sign. After this fluctuating region, *i.e.* for $1° \lesssim \Delta\alpha$, lock-in around $\varphi \simeq -\pi/2$ is observed (figure 7.6*d*). Because of an inappropriate choice of the pitch angle variation – not enough points were tested around the transition to actually observe it – we were not able to identify a bi-stable behavior and just noticed the discontinuous transition. Nonetheless, we believe that, based on observations for the Ahmed body reported in § 4.3.2 and since the transition is discontinuous, wake bistability exists for the pitch experiment.

The mean base pressure distribution $C_p(y^*, z^*)$ shown in figure 7.7(*a*) obtained after the wake reversal is very similar to that observed after the ground clearance of the model has been increased (figure 7.5*a*) thus suggesting that both indeed correspond to the reversed state N of the wake especially since the modulus g_r^* and the phase φ of the complex base pressure gradient are almost identical for both reversals comparing figure 7.7(b, c) to figure 7.5(b, c). The resulting wake topology is shown in figure 7.7(e) and compared to the baseline given in figure 7.7(d). There is a clear wake reversal between the two configurations whose wakes are nearly symmetric one with respect to the other. The fields shown in the figure are close to that obtained under pitching conditions for the Ahmed body subject to the z-instability (figure 4.28a, b on page 79). In addition, there is an anomaly between the mean lift coefficients C_z before and after the transition which reveals the z-instability: there is a sudden increase while the wake is reversed followed by a linear evolution with the pitch angle α as plotted in figure 7.7(f). The sudden increase is believed to be mainly fed by the wake reversal.

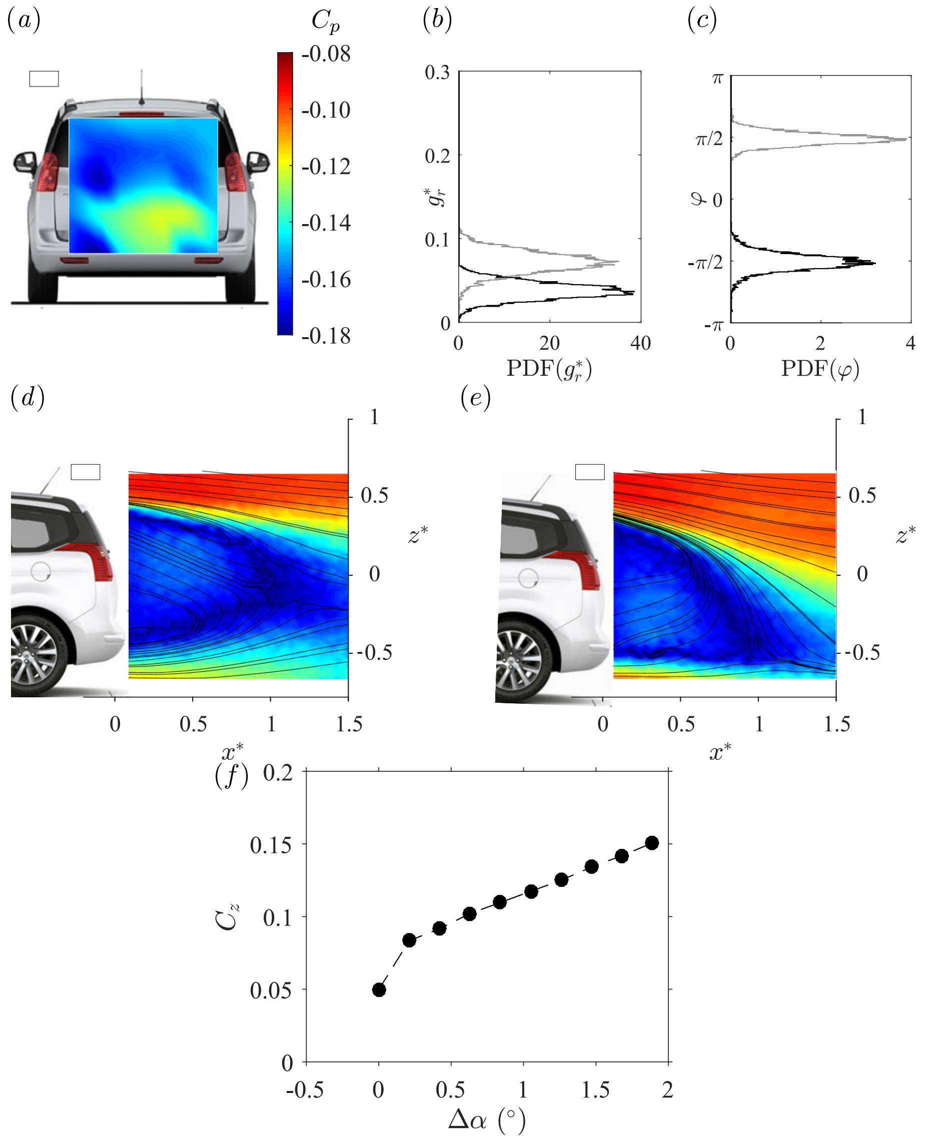

Figure 7.7 – Wake reversal operated by the pitch for the Peugeot 5008 ($\lambda_f^* = 0.580$, $\lambda_r^* = 0.600$). Mean base pressure distribution $C_p(y^*, z^*)$ (a). Probability Density Functions for the modulus g_r^* (b) and the phase φ (c) of the complex base pressure gradient $\hat{g}^*$. Reversed wake in black and baseline in grey for comparison. Results in (a, b, c) are presented for $\Delta\alpha = 2.0°$. Wake topology: cross-sections of the mean velocity magnitude U_{xz}^* superimposed to streamlines in the plane $y^* = 0$ and corresponding mean base pressure in $y^* = 0$. (d) Baseline, (e) reversed wake with $\Delta\alpha = 2.0°$. (f) Mean lift coefficient C_z *vs.* pitch angle variations $\Delta\alpha$.

Although both wake states were not observed simultaneously during a bi-stable dynamics, a global wake reversal is observed for the Peugeot 5008 with open air-intakes in no-yaw and nose-up conditions. Unlike the Ahmed body, the strength of the two wake states is very different which may certainly be ascribed to the much more complex geometry of the cars and to the presence of the wheels. Retrieving twice the same wake topology in two different experiments strongly suggest that the reversed state N is actually observed; to the author's knowledge such wake topology for a vehicle aligned with the incoming stream has not been reported so far.

7.2.3.2 Stabilization operated by the cooling flow

We try to extend the results of § 7.2.3.1 to other vehicles and we now focus on the Peugeot Partner (figure 7.2*c*). The ultimate aim is to obtain the two states at once which would unambiguously attest from their existence and refrain from being questioned about the influence of the car's alignment on the wake topology. As before, the vertical base pressure gradient g_z^* is chosen as the wake topological indicator and negative values indicate a wake reversal. The first experiment is conducted with a front wheel-arch height of $\lambda_f^* = 0.480$, similar to the baseline, while the rear axle is lowered. The mean vertical gradient G_z^* is given as a function of the pitch angle variation $\Delta\alpha$ in figure 7.8(a) with the filled circles. It can be clearly seen that, as the pitch angle is increased, the mean value of the gradient does not become negative but increases instead. In our opinion, this makes the wake state P harder to remove. As a consequence, it seems impossible to reverse the wake in the explored range of pitch angles. Larger nose-up are not permitted by the facility for the present ground clearance. A second try is therefore performed increasing the front axle clearance to $\lambda_f^* = 0.534$ in figure 7.8(b).

We first ensure that the case $\Delta\alpha = 0°$ (not shown) still corresponds to state P. The rear axle is lowered to explore the range $\Delta\alpha \in [1.68°, 2.30°]$ and the results are shown in figure 7.8(b). It turns out that the mean vertical gradient G_z^* is almost insensitive to the pitch angle and remains large ($G_z^* \gtrsim 0.2$) suggesting that our second try will also fail. The same observations are made with the Citroën Berlingo: (figure 7.2*d*) but the results are not reported for the sake of brevity.

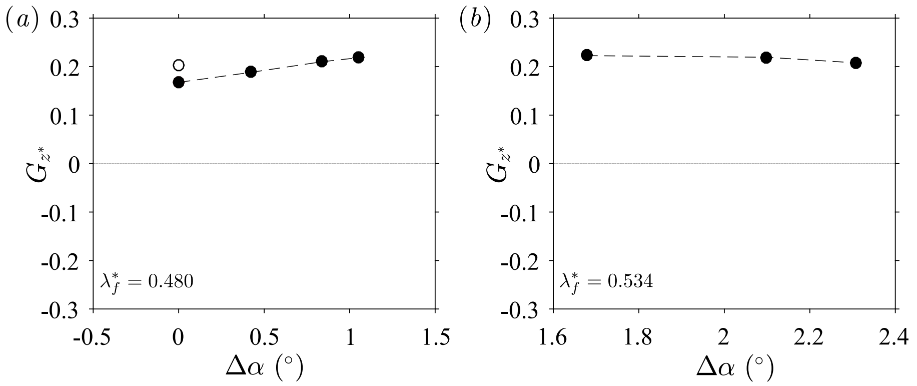

Figure 7.8 – Mean vertical base pressure gradient G_z^* used as a wake's topological indicator *vs.* pitch angle variation $\Delta\alpha$ for the Peugeot Partner with open air-intake and (a) $\lambda_f^* = 0.480$ and (b) $\lambda_f^* = 0.534$. The empty circle in (a) corresponds to the baseline with the front air-intake closed (see § 7.2.5).

From the results presented in this part, it seems impossible to reverse the wake of the Partner / Berlingo in the considered range of pitch angles, unlike the Ahmed body which shows a large sensitivity towards this geometrical parameter or the 5008 for which a reversal is observed as reported in § 7.2.3.1. Comparing the real vehicles to the simplified model, some considerable differences appear. While the Ahmed body has a continuously solid forebody, there is flow streaming through the car's front face air-intake system and aiming at cooling the engine compartment and the breaks of the vehicle. This flow is then driven under the vehicle thus strongly modifying the underbody flow. Recent results (Castelain *et al.*, 2018) show its importance and in particular that of the ratio of the underbody flow velocity with respect to that of the free-stream in state selection. The authors indeed report that either phase lock-in either top-bottom wake bi-stability may be chosen by mean of this ratio called λ in the paper. This is enforced by the successful experiment with the 5008 for which the underbody flow is necessarily different to that of the Partner and may be less disturbed by the cooling stream. In order to reach a configuration closer to the Ahmed body, we close the air-intake systems in § 7.2.5. The second difference lies in the presence of wheels known to strongly influence the wake as shown by the recent results of Pavia & Passmore (2018). However, we aim at testing realistic configurations for which removing the wheels is not an option.

7.2.4 Wake bistability under yawing conditions

Finally, the vehicle's misalignment caused by a yaw angle is considered. It corresponds to the realistic case of cross-wind while driving. The Renault Kangoo (figure 7.2*b*) is used for this analysis. First of all, the rear axle is lowered down to $\lambda_r = 0.464$ thus generating a – nose-up – pitch angle of $\alpha = +0.74°$. We ensure that this angle is not large enough to provoke a wake reversal. As a matter of fact, the mean base pressure distribution is identical to that of the baseline (see figure 7.11*a*) and characterized by a positive vertical base pressure gradient (figure 7.9*b*). The results are grouped in figure 7.9.

The horizontal mean base pressure gradient G_y^* remains almost null whatever the yaw angle (figure 7.9*a*) consistently with the absence of contribution of the z-instability described in § 4.3.2 for the Ahmed body. Its fluctuations (figure 7.9*c*) slightly increase around $|\beta| \simeq 4°$ but not sufficiently to correspond to a crisis. From figure 7.9(*b*), the vertical gradient is almost an even function of the yaw, the discrepancies being ascribed to the small asymmetries of the vehicle. An anomaly showing a high sensitivity of the mean vertical base pressure gradient G_z^* towards the yaw angle β is identified around $|\beta| \simeq 4°$ for which G_z^* is rapidly reduced from a positive value $G_z^* \simeq 0.15$ to almost zero; however, negative mean values are not observed. The fluctuations, reported in figure 7.9(*d*), show two clear crises around $|\beta| = 4.0°$ and a return to the original level for larger angles. The angles $\beta = 4.0°$ and $\beta = -4.0°$ are thus referred to as critical transition angles between two wake orientations indicated by the different gradients.

The aerodynamic loading applied to the Kangoo as a function of the yaw angle β is given in figure 7.10 through its mean and fluctuating coefficients. As expected, all curves present almost even evolutions with the yaw[1]; the symmetry defects are not related to measurements uncertainties but to the flow produced by the asymmetrical parts of the vehicles such as the air intake duct or underbody details. The mean base suction C_b increases with the yaw angle but the same anomaly as that of the gradients is observed with a strong increase for $|\beta| \geq 4°$ (figure 7.10*a*). A striking result is that the mean drag coefficient C_x (figure 7.10*b*) is almost constant in spite of the increase of yaw and of that of the base suction. It even slightly decreases for $|\beta| \geq 4.0°$, *i.e.* during the bi-stable dynamics. A similar observation was made for the z-unstable Ahmed body in figure 4.30(*b*) on page 81. The mean side force coefficient C_y (figure 7.10*c*) shows a linear evolution with respect to

---

[1] Except for the mean side force C_y which obviously cannot; however, it is an odd function so its magnitude verifies this statement

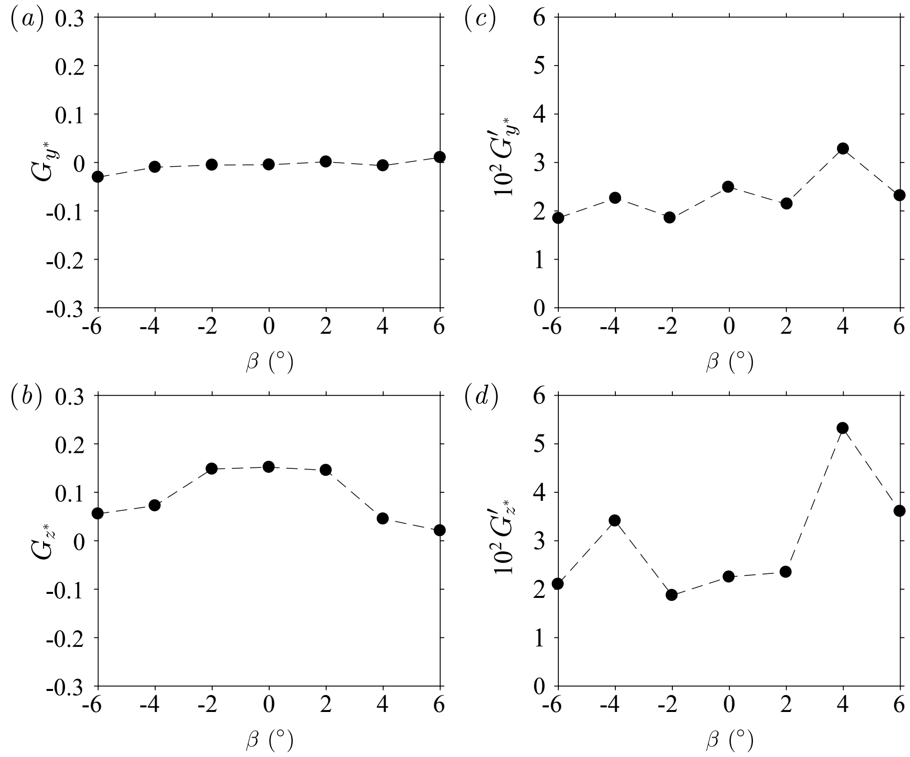

Figure 7.9 – Renault Kangoo at yaw, mean and fluctuating base pressure gradients ($\alpha = 0.74°$): (*a*) G_y^*, (*b*) G_z^*, (*c*) $G_y'^*$, (*d*) $G_z'^*$.

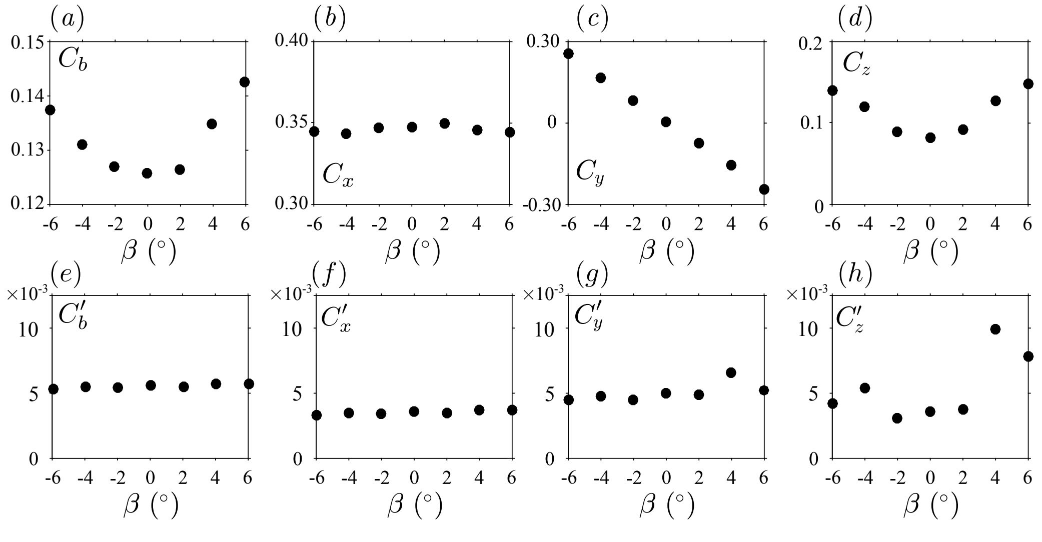

Figure 7.10 – Mean (top row) and fluctuating (bottom row) aerodynamic coefficients *vs.* yaw angle β for the Renault Kangoo ($\alpha = 0.74°$).

yaw in agreement with results on the z-instability for the simplified geometry. The lift coefficient C_z (figure 7.10d) shows a quicker increase for angles such that $|\beta| \approx 4.0°$. Concerning the fluctuations, the sudden lift increase (figure 7.10d) associated with the decrease of the vertical base pressure gradient and increased fluctuations (figure 7.9b, d) at $|\beta| = 4.0°$ corresponds to a crisis for the lift (figure 7.10h) while other components are almost unaffected.

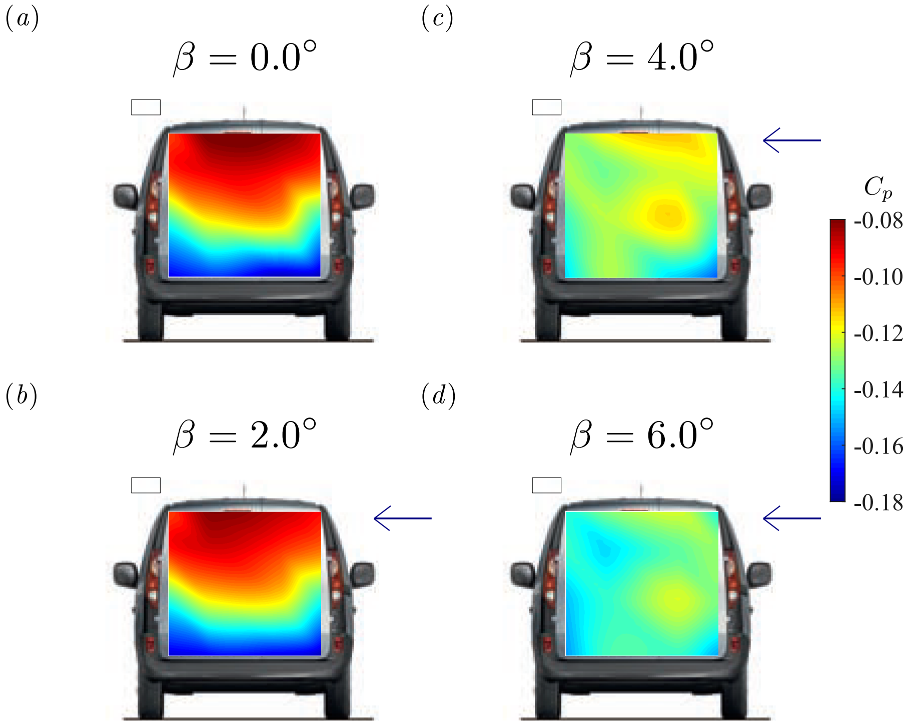

Figure 7.11 – Mean base pressure distributions $C_p(y^*, z^*)$ for the Renault Kangoo at yaw: (a) $\beta = 0°$, (b) $\beta = 2°$, (c) $\beta = 4°$, (d) $\beta = 8°$. The air-intake is open and the vehicle's pitch set to $\alpha = +0.74°$ ($\lambda_r = 0.464$). The arrows correspond to the cross-wind component (not to scale).

The changing wake properties around the critical angles $\beta \approx \pm 4°$ can be related to the mean base pressure distributions $C_p(y^*, z^*)$ plotted for the Renault Kangoo at yaw in figure 7.11. For small yaw angles such that $|\beta| \leq 2°$, the mean base pressure distribution $C_p(y^*, z^*)$ is almost not affected compared to that of the baseline (figure 7.11a and figure 7.11b) with a clearly positive vertical pressure gradient typical of the wake state P of the z-instability. At the critical yaw angles $\beta \approx \pm 4°$, the area of higher pressure located at the top of the base disappears and the pressure distribution becomes more uniform in average (figure 7.11c) explaining thus that the vertical base pressure gradient decreases down to almost zero – again in average. Once the transition is over, *i.e.* for $\beta \approx \pm 6°$, a global pressure drop can be observed in figure 7.11(d) with a complete removal of pressures higher than $c_p \simeq -0.11$. This configuration corresponds to the reversed wake state N.

The transition occurring at $\beta \pm 4°$ corresponds to a switch between two locked wake configurations and, similarly to the Ahmed body studied in § 4.3.2, should be associated with a wake top-bottom bistability. Nonetheless, such dynamics was only identified for $\beta = +4°$; the second bi-stable phase angle is probably slightly shifted because of the small asymmetries of the vehicle. This certainly explains why bistability was not identified in the negative yaw angles since only integer values of the angle were tested. Time-series of the modulus and of the phase of the base pressure gradient are provided in figure 7.12(a, b, d, e)

with the corresponding PDFs. A bi-modal behavior is identified both for the modulus and the phase of the gradient. In fact, state P corresponds to $\varphi \simeq \pi/2$ and $g_r^* \simeq 0.18$ and state N to $\varphi \simeq -\pi/2$ and a half-strength. The time series of the lift coefficient c_z plotted in figure 7.12(c) clearly shows that the lift fluctuates following a random process in the critical case and is bounded by the values taken for the two other configurations (mean value in dashed line). The time-scale is similar to that of the gradient's fluctuations so that it can be stated that, similarly to the Ahmed body, the aerodynamic loading applied on the Kangoo is a direct consequence of the wake orientation. The wake reversals can also be observed on the pressure space-time diagram plotted for $y^* = 0$ in figure 7.12(g). Since the measurements are synchronous, there is a clear correlation between the wake topology and the lift applied on the vehicle. In other words, it means that state N has to be avoided for two reasons as it is not only detrimental to drag but also to the vehicle's stability.

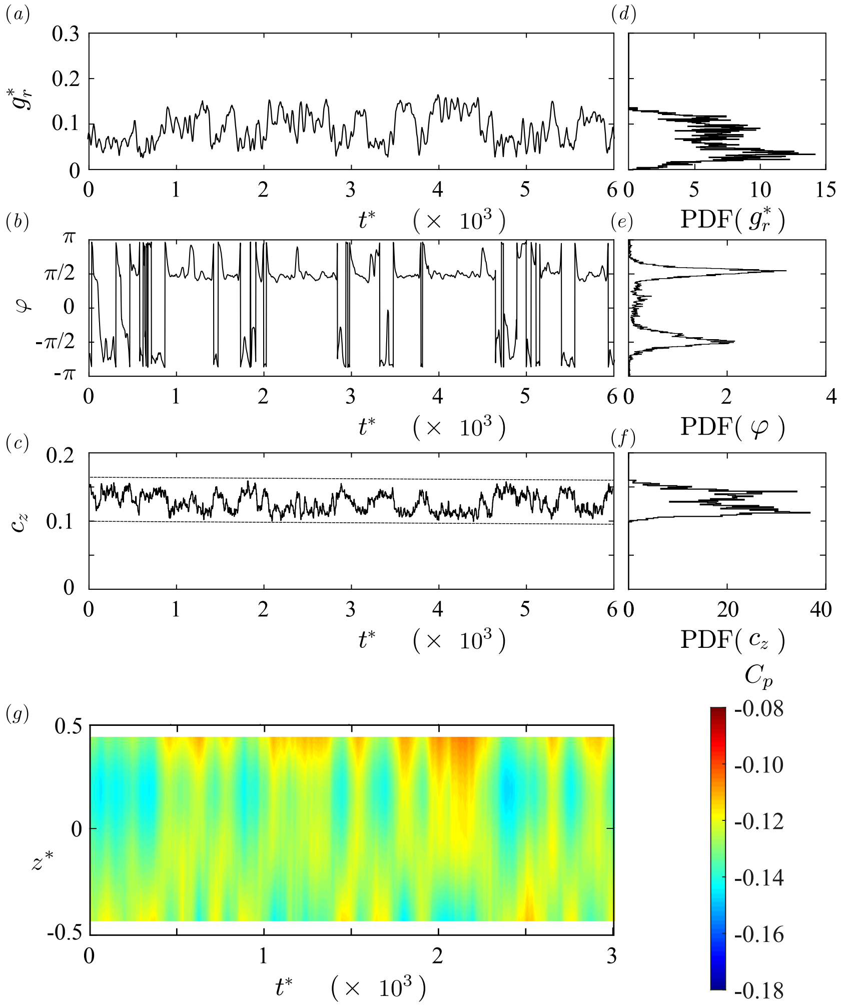

Figure 7.12 – Modulus $g_r^*(t^*)$ (a) and phase $\varphi(t^*)$ (b) time series of the base pressure gradient with corresponding probability density functions (d, e) for the bi-stable configuration of the Kangoo at yaw ($\beta = +4°$). Time-series of the instantaneous lift force c_z given in (c) for $\beta = +4°$ with the corresponding probability density function (f). The dashed lines in (c) correspond to the mean values of the lift coefficient C_z at $\beta = 2°$ and $\beta = 6°$ from bottom to top.(g) Space-time diagram of c_p along the line $y^* = 0$ in the bi-stable case.

The bi-modal probability density function of the phase φ in figure 7.12(e) suggests that conditional averaging can be performed using thresholds at $\varphi = 0$ and $\varphi = \pi$ – which are equivalent to $g_z^* = 0$ – to retrieve the two wake states. The two corresponding mean base pressure distributions $C_p(y*, z^*)$ are given in figure 7.13.

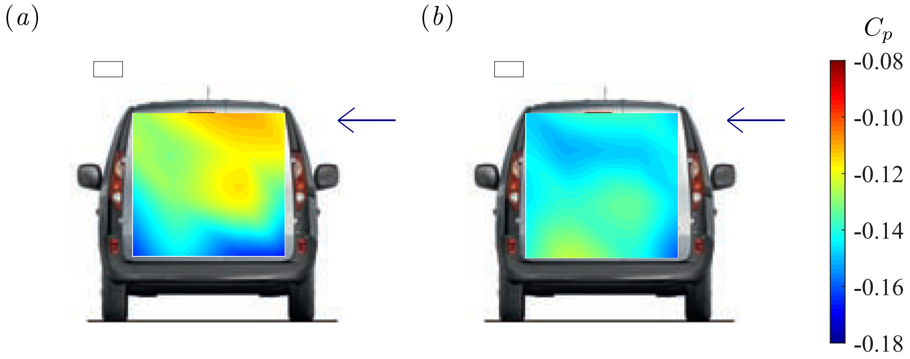

Figure 7.13 – Mean base pressure distributions $C_p(y^*, z^*)$ for states P (a) and N (b) observed at yaw for the Kangoo.

Although close to the baseline's, the mean base pressure distribution of state P shown in figure 7.13(a) is slightly affected by yawing conditions, in particular as the highest pressure is considerably lower. The reversed wake given in figure 7.13(b) does not yield the mirror configuration but is very similar to that observed on the Peugeot 5008. Between the two configurations, base suction increases by 8.0% from $C_{b_T} = 0.125$ up to $C_{b_B} = 0.135$. From the distributions, it is clear that the two peaks of the PDF of the lift force (figure 7.12f) can be associated with state P for $C_z \simeq 0.10$ and state N for $C_z \simeq 0.15$. The fact that bistability corresponds to the transition between the two locked distributions shown in figure 7.12(b, d) is also clearly visible both on the aerodynamic loading and on the base pressure distribution. Unlike the previous case for the 5008, these conditions are likely to be encountered in real driving conditions since it corresponds to a lateral wind of 9 km.h^{-1} while driving in a French highway at 130 km.h^{-1}.

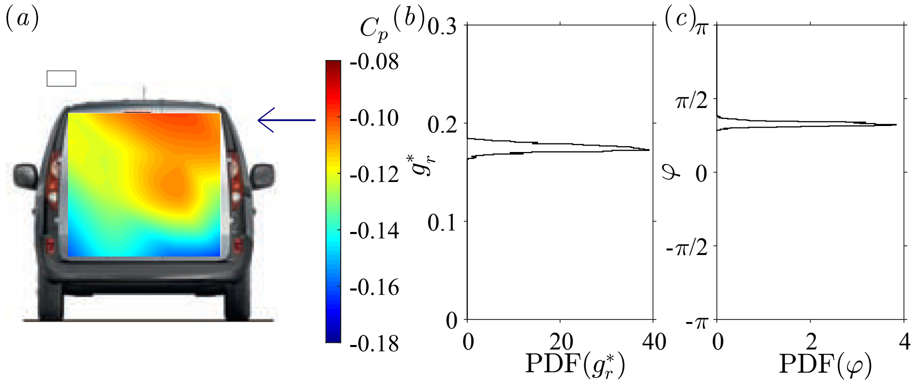

Figure 7.14 – No-pitch yawing conditions for the Kangoo with state P selected for $\beta = 4°$ and $\alpha = 0°$: (a) Mean base pressure distribution $C_p(y^*, z^*)$, probability density functions of the base pressure gradient in the polar form with modulus g_r^* in (b) and phase φ in (c).

Finally, we just would like to highlight the fact that the positive pitch angle is necessary to obtain the wake bi-stable behavior as shown in Bonnavion *et al.* (2017a). The same angle $\beta = 4°$ is reproduced in figure 7.14 for $\alpha = 0°$, *i.e.* $\lambda_f = \lambda_r$. In that case, the mean base pressure distribution (figure 7.14a) is close to the baseline's but slightly rotated because of the yaw angle.It is clear that the distribution has nothing in common with the reversed wake's anyway. As a consequence, the modulus is almost unchanged while the phase ranks around $\varphi \simeq \pi/4$ (figure 7.14b, c). The aerodynamic loading is also strongly modified with lift and drag values close to that of the baseline.

7.2.5 Baseline with closed air-intake and wake state selection

The vehicles' front air-intakes are then closed to prevent from through flow (figure 7.15) and the baseline configuration is reproduced. We do not perform sensitivity analyses for the 5008 and the Kangoo in this configuration but the baselines with closed air-intake are reported.

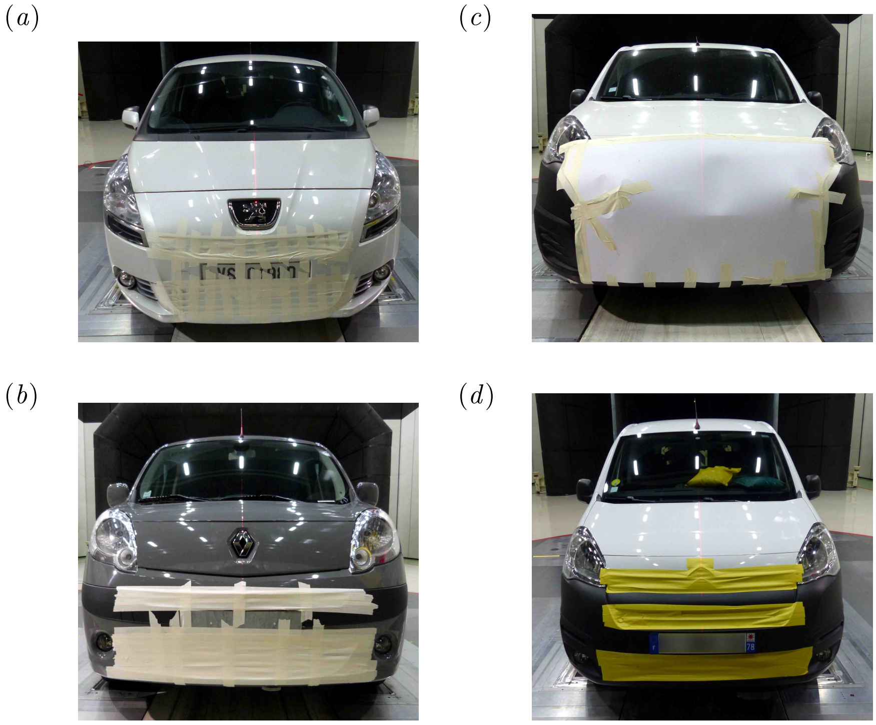

Figure 7.15 – Vehicles with closed front air-intake: (a) Peugeot 5008, (b) Renault Kangoo, (c) Peugeot Partner and (d) Citroën Berlingo.

The mean base pressure distributions are given with the PDFs of the base pressure gradient in the polar form in figure 7.16 and the mean and fluctuating aerodynamic coefficients in table 7.3. The case of the Kangoo is very different and will be discussed next. For now, we focus on the three other vehicles. It can be clearly seen that, regardless of the vehicle, the mean base pressure distribution (left column) is almost not modified with respect to the baseline with open air-intake (figure 7.3). The mean base pressure distributions still present a z-symmetry breaking with a positive vertical base pressure gradient. With respect to the baseline with open air-intake (§ 7.2.1), the strength of the gradient is generally slightly reinforced (see for instance the empty circle in figure 7.8a for the Peugeot Partner) except for the 5008 for which no real sensitivity can be identified. The phase is found to remain permanently locked at $\varphi = \pi/2$ indicating that the wake persists in its state P and thus that the stream through the engine compartment is not the only ingredient for wake state selection.

Nevertheless, its role must not be neglected as demonstrated by the case of the Renault Kangoo in figure 7.16(d). The wake reversal is indeed triggered by this mean while closing the vehicle's front air-intake. Unlike the baseline that exhibits a positive vertical base

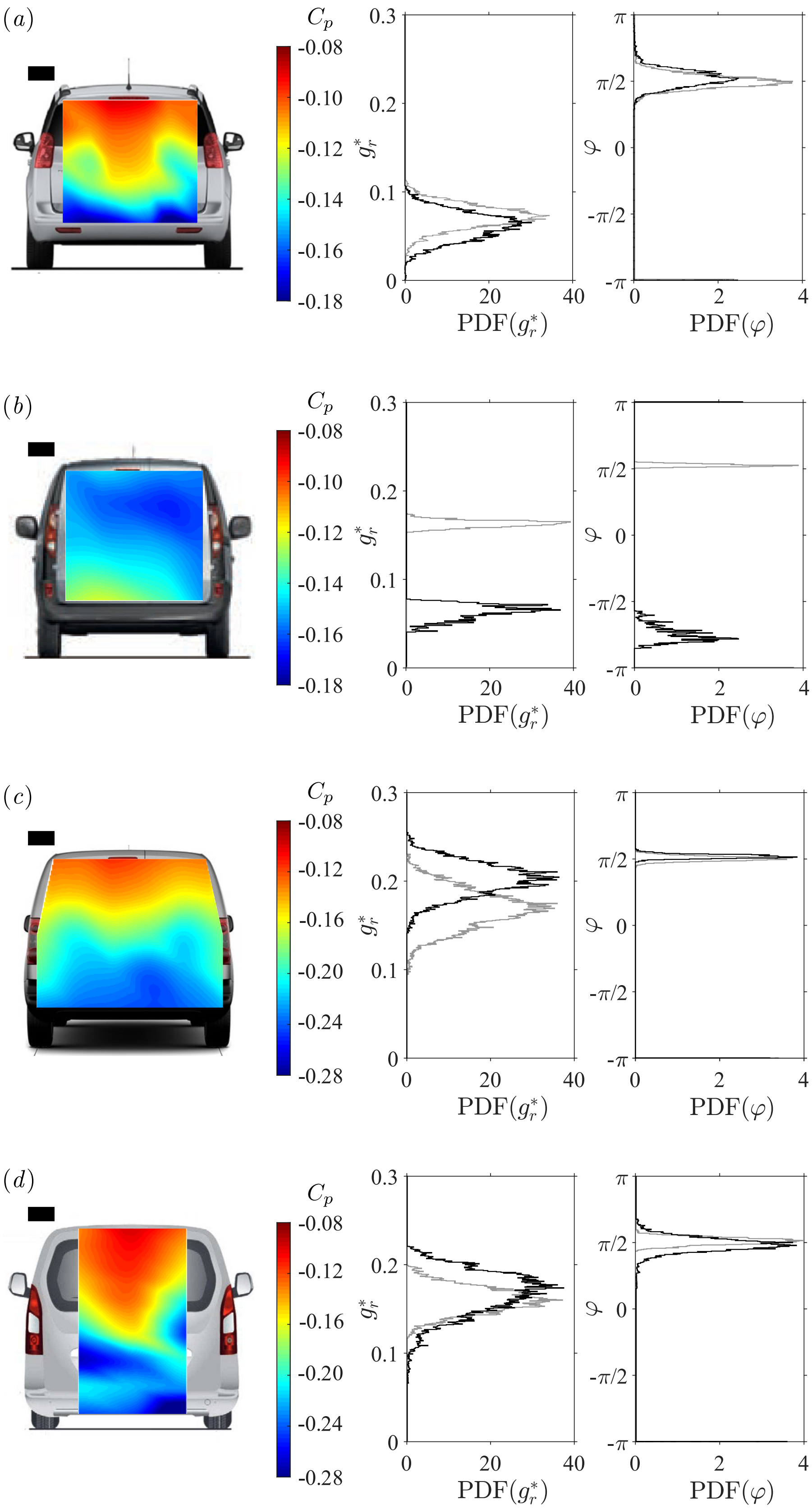

Figure 7.16 – Mean base pressure distributions $C_p(y^*, z^*)$ in the baseline configuration (front air-intake closed) and probability density functions of the base pressure gradient in the polar form: (*a*) Peugeot 5008, (*b*) Renault Kangoo, (*c*) Peugeot Partner and (*d*) Citroën Berlingo. The grey curves are those of the baseline with open air-intake (§ 7.2.1).

pressure gradient with $\varphi \simeq \pi/2$, we obtain a reversed wake with a negative gradient and $\varphi \simeq -3\pi/4$. In addition, the modulus g_r^* of the gradient is strongly attenuated. This configuration corresponds to the wake state N revealed during the yaw experiment (§ 7.2.4) which proves unambiguously that the underbody flow contributes to phase lock-in and unlocking.

Table 7.3 – Characteristic mean and fluctuating aerodynamic coefficients for baseline configurations of the four vehicles with closed air-intake.

Vehicle	C_b	C'_b	C_x	C'_x	C_z	C'_z
5008	0.128	0.003	0.258	0.006	0.015	0.002
Kangoo	0.156	0.003	0.334	0.006	0.029	0.005
Partner	0.173	0.005	0.318	0.002	0.002	0.004
Berlingo	0.172	0.005	0.312	0.005	0.014	0.003

The mean and fluctuating aerodynamic coefficients corresponding to this configuration are given in table 7.3. It appears that closing the front air-intake helps reducing the drag by 3.7 up to 8.9% which is considerable at a vehicle's scale in view of fuel-efficiency and carbon emissions reduction. For the Kangoo, it even overwhelms the detrimental effect on base suction C_b caused by the wake reversal. This gain can be explained by the large hydraulic charge loss as the air-flow goes through the engine compartment. Such values are in agreement with those reported by Hucho (1998*a*).

Since the actual power requested to drive at constant speeds is much smaller than the engine maximum thrust, cooling needs may be lowered thus allowing to decrease the air-flow through the engine compartment. Besides, the development of new reduced-scale heat exchangers and the spreading of electric power engines lead to new forebody designs with smaller intakes and go-through flow rates. Even for fuel-powered vehicles, manufacturers may be tempted to use this method to achieve drag reduction during well-chosen operating cycles. The side force coefficient C_y is not reported since almost identical to the baseline. The mean lift coefficient C_z however can be strongly affected by the closing of the front air-intake. The 5008 and the Berlingo are only slightly affected but the lift decreases largely for the Partner and, on the contrary, bursts for the Kangoo.

The case of the Kangoo illustrates well the importance of wake states control. In that case, closing the air-intake leads to 3.7% drag reduction *only*, *versus* more than 6% for the other vehicles, which means that the wake reversal is responsible for a drag increase by about 3%. In other words, the potential drag reduction is about 3 points larger than the actually realized one if the adequate wake state were selected. It could probably be larger if the z-instability were removed but we only focus on state selection. This additional gain represents nothing less than about 1.5% of the vehicle's fuel consumption or carbon dioxide emissions. This means that wake state control could become a marketing tool – lower consumption – or modify the taxes related to carbon dioxide emissions, for which one gram of CO_2 per kilometer can be the difference between a tax refund and an amount owing. The net gain on drag ranking in $3-7\%$ is interesting compared to active flow control techniques; for instance, on a model-scale lorry trailer, Seifert *et al.* (2008, 2009) achieved $6-7\%$ of drag reduction by means of active flow control.

7.2.6 Wake reversals triggered by the pitch angle α with closed front air-intake

From the baseline described in § 7.2.5, we aim at revealing the reversed wake state N for the two remaining vehicles – Peugeot Partner and Citroën Berlingo – since closing the air-intake is not sufficient to provoke the wake reversal unlike for the Renault Kangoo. Our wish is to identify a bi-stable case which would prove unambiguously that the two wake configurations are related to static modes since the geometrical setup would be identical during the bi-stable dynamics unlike previously reported reversals but the Kangoo at yaw. The pitch sensitivity experiment is reproduced with the closed front air-intake. Only the results obtained with the Berlingo are reported since they are identical for both vehicles. In this set of experiments, the front wheel-arch is placed at $\lambda_f^* = 0.534$ and the rear axle clearance is modified to explore the range of pitch angles $\alpha \in [1.9°, 2.3°]$. We obtain four sensitivity maps of response of the base pressure gradient given in figure 7.17.

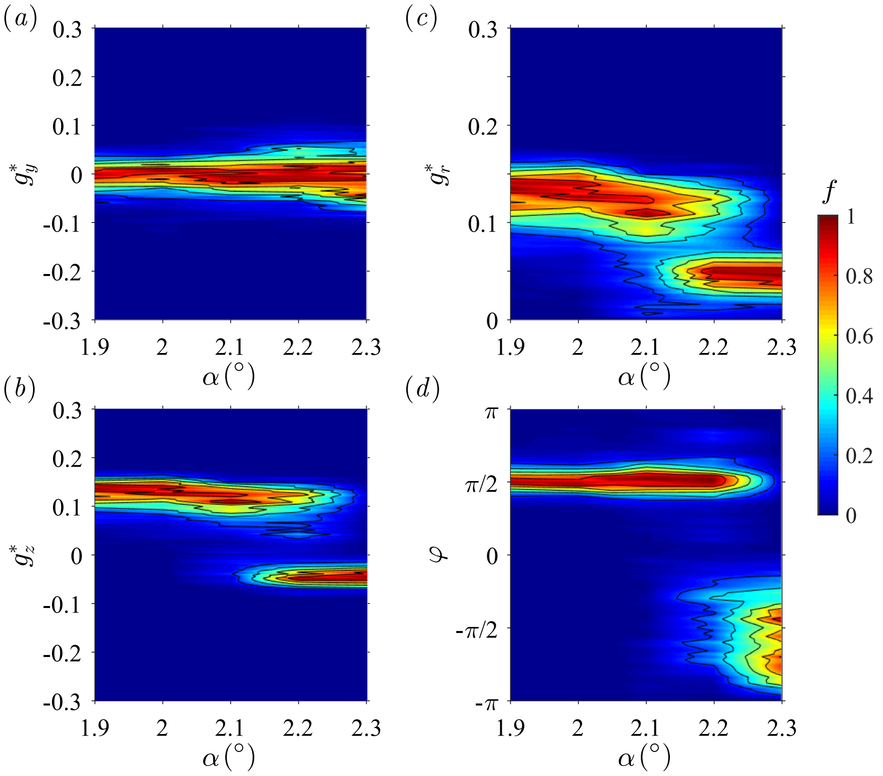

Figure 7.17 – Base pressure gradient response to variations of the pitch angle α for the Citroën Berlingo with closed front air-intake. Sensitivity maps (a) $f(\alpha, g_y^*)$, (b) $f(\alpha, g_z^*)$, (c) $f(\alpha, g_r^*)$ and (d) $f(\alpha, \varphi)$.

It can be observed in figure 7.17(a) that the horizontal component of the gradient g_y^* only shows little sensitivity to the pitch angle. At most, one may notice that the fluctuations increase slightly at large nose-up ($2.25° \lesssim \alpha$). Three regions can be observed on the diagram of the vertical component of the gradient g_z^* (figure 7.17b). For $\alpha \lesssim 2.15°$, the gradient shows small fluctuations about $g_z^* \simeq 0.14$. The same value was already observed for the baseline (figure 7.3) and is associated with state P. For large nose-up configurations ($2.25° \lesssim \alpha$), a wake reversal can be observed as the gradient changes sign and now fluctuates about $g_z^* \simeq -0.08$. Its magnitude is lower than for state P consistently with previously reported results. Nonetheless, this configuration is associated with state N of the wake, the existence of which is unambiguously proved by the overlapping region $2.15° \lesssim \alpha \lesssim 2.25°$ during which a bi-stable behavior is identified, *i.e.* the random succession of both wake states for a given geometrical setup. No similar cases obtained when the vehicle is aligned with the incoming flow in terms of yawing conditions ($\beta = 0°$) were found in the literature. These wake reversals are retrieved for the Peugeot Partner with similar angles although they are not shown here for the sake of brevity.

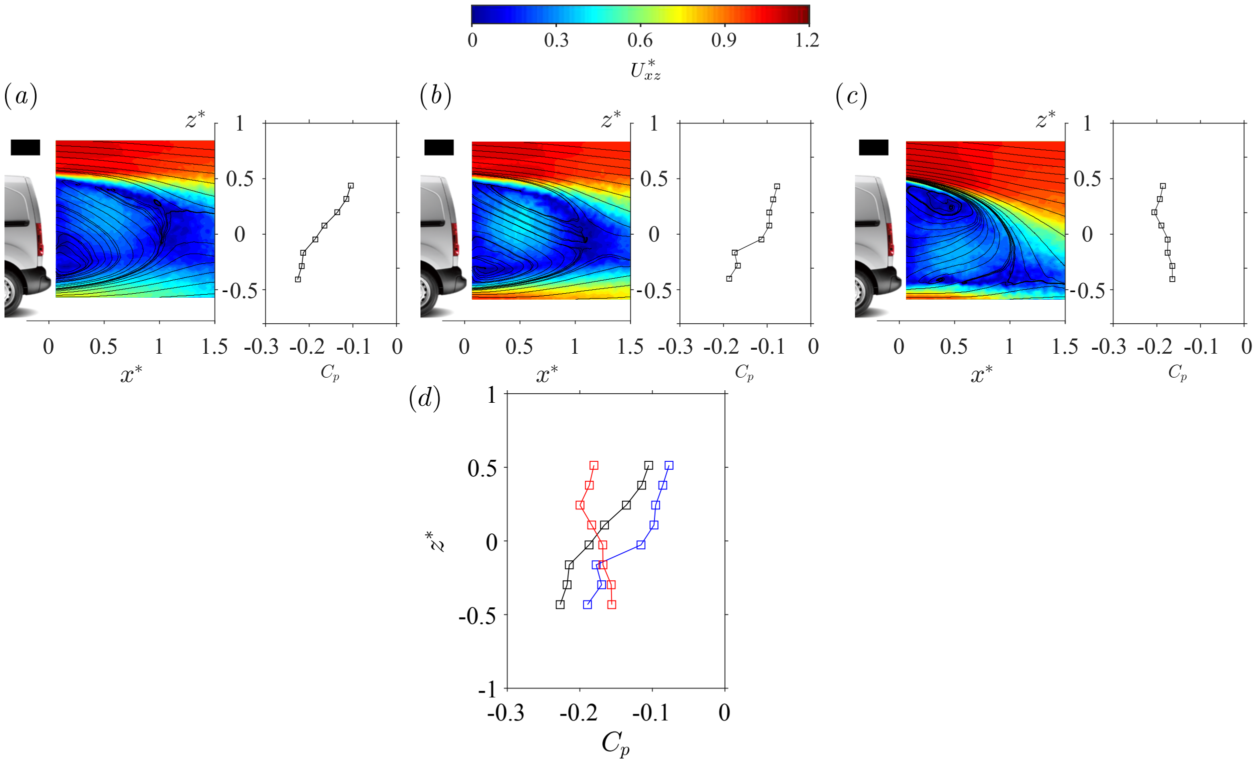

Figure 7.18 – Pitch experiment with the Citroën Berlingo at $\beta = 0°$: cross-sections of the mean velocity magnitude U^*_{xz} superimposed to streamlines in the plane $y^* = 0$ and corresponding mean base pressure in $y^* = 0$. (*a*) Baseline with open air-intake, (*b*) state P with closed air-intake at $\alpha = 1.9°$, (*c*) state N with closed air-intake at $\alpha = 2.3°$. (*d*) Comparison of the three pressure distributions at $y^* = 0$. In black, same curve as in (*a*), in blue same as in (*b*), and in red, same as in (*c*).

Two wake topologies are related to the identified states; they are presented in figure 7.18 showing the streamlines superimposed to the mean velocity magnitude in the mid-track plane $y^* = 0$. The associated mean base pressure distribution along the sensors line located at $y^* = 0$ is also provided. The baseline (figure 7.18*a*) clearly shows a back-flow orientated towards the top side of the base and correspondingly a positive vertical base pressure gradient ($g^*_z \simeq 0.14$). This configuration can be compared to state P of the Ahmed body subject to the z-instability (figure 4.28*b*). Closing the air-intake, this wake state is selected for increasing pitch angles up to $\alpha \simeq +2.15°$. The topology of this case is shown in figure 7.18(*b*) but for an angle of $\alpha = +1.9°$, which is actually the largest before the transition is triggered by the in-wake measurements mast. This point will be discussed later on in § 7.2.8.3. For larger angles, the reversed wake state N is permanently selected. The back-flow becomes orientated towards the bottom of the base and the vertical base pressure gradient changes sign (figure 7.18*c*). This state is similar to state N of the Ahmed body (figure 4.28*b*) except that the strength is about half lower that of state P. The wake reversal is clearly observed in figure 7.18(*d*). In addition, the comparison of figure 7.18(*a*) and figure 7.18(*b*) provides an additional explanation on the different wake flows with open or closed air-intake. As a matter of fact, the flow rate is drastically reduced when the air-intake is open as a result of the cross-flow injection of momentum originating from the stream exiting out of the engine compartment. In our opinion, this explains the slight reinforcement of the wake asymmetry – assessed through g^*_r – between the two baselines

and observed on the modulus PDFs provided in figure 7.16(c, d).
The phase dynamics of the bi-stable configuration is shown in figure 7.19. The modulus and the phase shown respectively in figure 7.19(a) and (b) follow the same bi-stable dynamics. Starting from the baseline's phase $\varphi \simeq \pi/2$ associated with a modulus of about $g_r^* \simeq 0.2$, wake reversal occurs after $500 - 1000$ t^* to state N, characterized by $\varphi \simeq -\pi/2$ and a strength reduced by about two. The transition, almost continuous, can be related to a phase jump since, simultaneously, the modulus becomes very small and around $t^* \sim 6000$ for instance. The typical associated time scale is of a few t^* only. The two plots lead to the bi-modal PDF given in figure 7.19(c) and (d). This behavior is quite similar to that of the Ahmed body subject to bistability at yaw (figure 4.27). No continuous phase drifts can be observed in the provided time series.

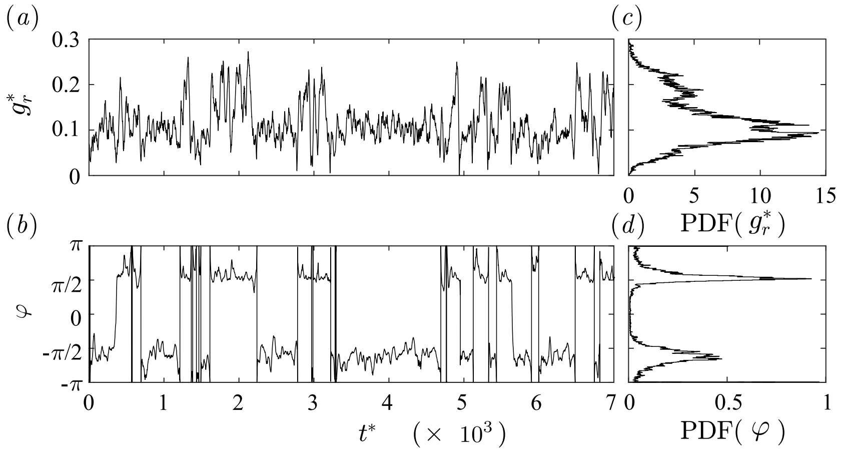

Figure 7.19 – Modulus $g_r^*(t^*)$ (a) and phase $\varphi(t^*)$ (b) time series of the base pressure gradient with corresponding probability density functions (c, d) for the bi-stable configuration of the Berlingo at pitch ($\alpha = +2.25°$).

The consequences of the turbulent wake instability on the aerodynamic loading applied to the vehicle is investigated. Following the general rules derived in § 4.4.3 and in particular in equations (4.28), the instability should be revealed by the present pitch experiment. In particular, for the Partner and the Berlingo, we expect the cross-flow forces to be of the form:

$$c_y(t^*) = C_y^{*B} + \xi {g^*}'_y(t^*) \tag{7.4a}$$

$$c_z(t^*) = C_z^{*B} + \xi g_z^*(t^*) \tag{7.4b}$$

In the system (7.4), the vertical axis of the base is chosen as the *major* one – and thus the horizontal as the *minor* – in the sense of the generalized model of equations (4.26) since the vehicles are subject to the z-instability[1]. The coefficient ξ is found to be equal to $\xi = 1/5.3$ for the Berlingo and $\xi = 1/6.5$ for the Partner, the difference being ascribed to the geometrical discrepancies between the vehicles. As they are quite close in shape, this shows the extremely high sensitivity of the wake towards the vehicle's geometry. The cross-flow coefficients are given in figure 7.20. The contribution of the instability to the force coefficient is similar for both cars; it is about 0.012 for state N, and 0.024 for state

---

[1] We consequently precise that, unlike what was stated in § 4.3.2 for the Ahmed body, *major* and *minor* axes are not geometrically determined but functions of the actual instability. We refer to the (geometrical) base aspect ratio of the wake model and are consistent with the definition of Grandemange *et al.* (2013*a*).

P. As for the simplified geometry it is a substantial contribution to the total aerodynamic force as it represents about 70% and 140% of the baseline lift coefficient.

The cross-flow force coefficients estimated owing to the model (7.4) appear to be quite accurate since the mean side force coefficient C_y measurements give the *basic flow* side force coefficient so that $C_y = C_y^B$ (figure 7.20a). It also appears clearly that the mean lift force coefficient C_z shown in figure 7.20(b) is strongly modified by the instability with respect to that of the basic flow C_z^B plotted with the red line. The two branches for the lift force related respectively to state N – lower branch – and state N of the wake – upper branch – also clearly appear. The lift coefficient of the *basic flow* is assumed to be an affine function of the pitch angle. A fit performed on the experimental data yields:

$$C_z^B(\alpha) = 0.052\alpha - 0.036 \tag{7.5}$$

where α is expressed in degrees. From equations (7.4b) and (7.5), it is possible to accurately reconstruct the mean lift as shown by the blue dashed line in figure 7.20(b) which validates the relationships (7.4) between cross-flow forces and the base pressure gradients. Similarly to the Ahmed body subject to the z-instability (see details in § 4.3.2.6 on page 79), the fluctuations of the cross-flow forces are also well predicted by those of the pressure gradient as shown in figure 7.20(c, d) where the proportionality constant ξ turns out to be the same as for the mean values – similarly to the simplified geometry.

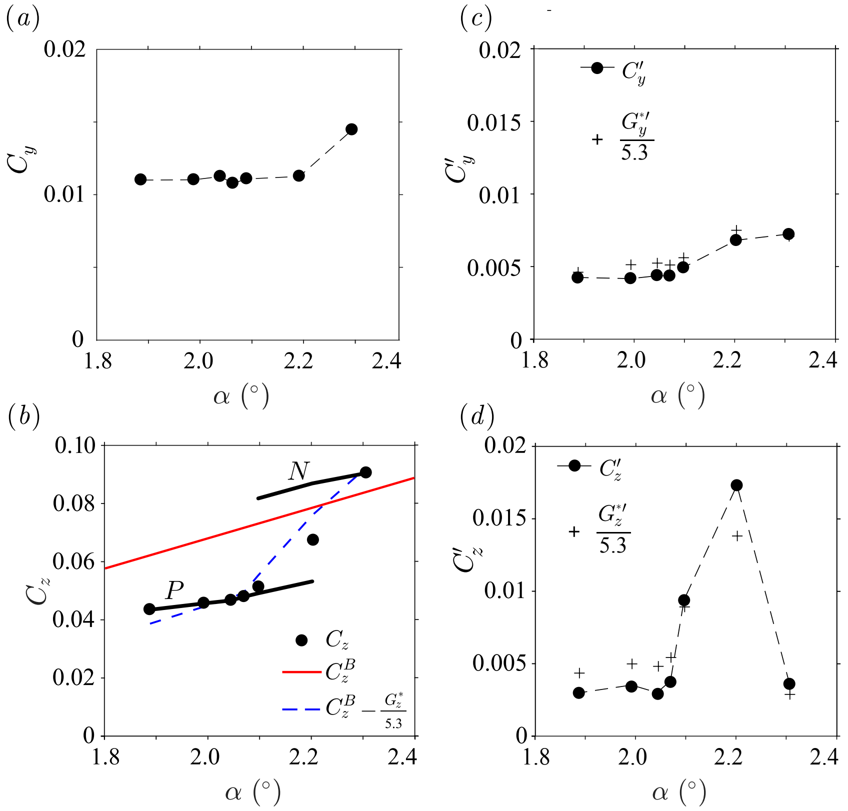

Figure 7.20 – Pitch sensitivity analysis for the Citroën Berlingo: (a) mean side force coefficient C_y, (b) mean (symbols) and most probable lift coefficients c_z (thick black lines), *basic flow* lift coefficient C_z^B (red line) and mean lift computed from equation (7.4b) in blue dashed line. Fluctuations of the force coefficient compared to those of the gradient: (c) side force coefficient and horizontal base pressure gradient, (d) lift coefficient and vertical base pressure gradient.

The comparison between the time series of the lift coefficient c_z and its estimation derived from the measurements of the base pressure gradient following equation (7.4b) is shown for the Berlingo in figure 7.21. As already observed in mean in figure 7.20(b), a clear correlation can be established between the wake orientation and the lift. If one compares figure 7.21 to figure 7.19(b), the time scale indeed appears to be similar. In addition, there is an excellent agreement between the actual and the reconstructed lift force which confirms that during the bi-stable dynamics, the base pressure gradient is responsible for the unsteady aerodynamic cross-flow forces exerted on the vehicle. More generally, by analogy with the flat-backed Ahmed bodies considered in chapter 4, the cross-flow force fluctuations are caused by the wake and can therefore be related to the base pressure gradients which constitute excellent indicators of the instantaneous state. The mean drag coefficient is discussed together with the pitch experiment at the end of § 7.2.7, figure 7.25.

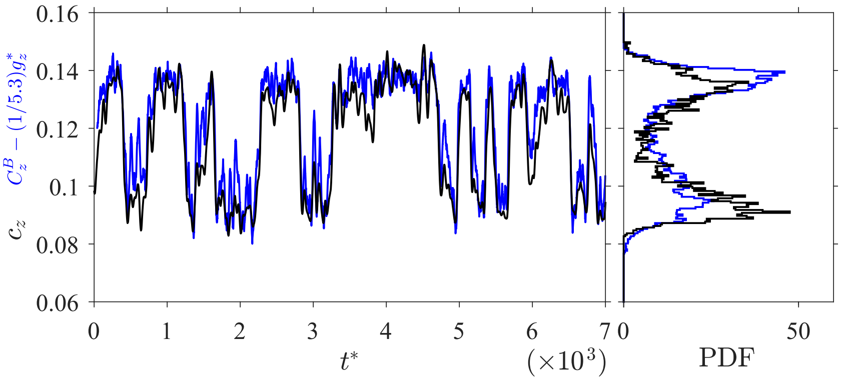

Figure 7.21 – Time series of the lift coefficient $c_z(t^*)$ for the Citroën Berlingo in the bi-stable case under pitching conditions (*left*) with the corresponding probability density function (*right*). The black line is the value measured by the force balance and the blue line is the reconstructed value from equation (7.4b) using $\xi = 1/5.3$.

7.2.7 Wake state selection operated by the yaw with closed front air-intake

A similar experiment to that conducted with the Kangoo with open air-intake in § 7.2.4 is reproduced for the Partner – with closed air-intake – starting from the bi-stable case obtained in pitching conditions. Aligned with the flow, the wake topology is alternately that shown in figure 7.18(b) and in figure 7.18(c). The response of the base pressure gradient is assessed owing to the four sensitivity maps given in figure 7.22. Only positive values of the yaw angle β are considered in view of the quasi-symmetry of the problem similarly to § 7.2.4.

The horizontal pressure gradient g_y^* shown in figure 7.22(a), initially at a slightly negative value, goes to zero as the yaw angle increases without large fluctuations. The same two branches associated with states P and N of the wake can be identified for the vertical base pressure gradient in figure 7.22(b). The two values of the branches are slightly different from the Berlingo though; two explanations are provided. First, the cars are not strictly identical and some details differ such as the cargo door or the front design. Second, the pressure sensors locations are different (figure 7.1c, d). A bi-stable dynamics corresponding to the stochastic exploration of the two branches associated with states P

and N is observed for moderate angles up to $|\beta| \simeq 1.5°$. It is similar to that presented in figure 7.19 for the Berlingo at pitch. The same discontinuity on the modulus g_r^* as that observed for the pitch experiment is identified in figure 7.22(c) for $|\beta| \simeq 1.5°$ as the wake orientation (figure 7.22d) changes from lock-in at $\varphi = -\pi/2$ ($\beta = 0°$) to the permanent selection of state P through the bi-stable case ($\beta \lesssim 0.5°$). Afterwards, the wake orientation becomes independent of the yaw angle applied to the vehicle.

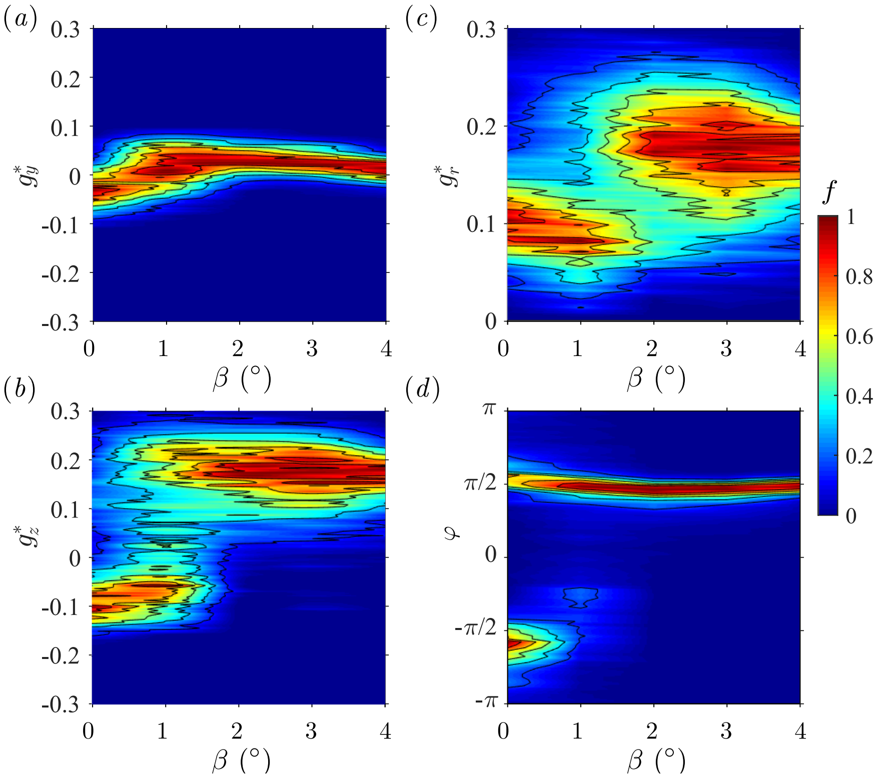

Figure 7.22 – Base pressure gradient response to variations of the yaw angle β for the Peugeot Partner with closed front air-intake. Sensitivity maps (a) $f(\beta, g_y^*)$, (b) $f(\beta, g_z^*)$, (c) $f(\beta, g_r^*)$ and (d) $f(\beta, \varphi)$.

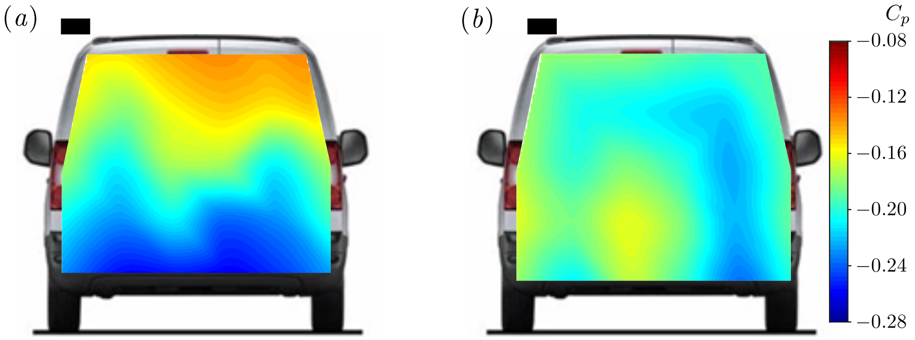

Figure 7.23 – Conditionally averaged mean base pressure distributions $C_p(y^*, z^*)$ for states P (a) and N (b) of the Partner.

The mean base pressure distribution of the Peugeot Partner in the baseline configuration – with closed air-intake – given in figure 7.16(c) is very close to that related to state P and obtained by conditional averaging during the bi-stable dynamics (figure 7.23a), thus justifying the association we made between the baseline and state P of the instability. The most important result is that, similarly to the 5008 and the Kangoo (§§ 7.2.2, 7.2.3.1, 7.2.4), the pressure distribution of state N (figure 7.23b) is not obtained from that of state P by means of a top/bottom mirror symmetry – *i.e.* the transformation $z^* \rightarrow -z^*$

– as it could be the case for the simplified boat-tailed Ahmed body (see § 4.3.2). This discrepancy is likely to be due to the strong non-reflectionnal top-bottom symmetry of the car related to the front design and the large underbody roughness. The distribution shown in figure 7.23(a) is retrieved when lock-in at $\varphi \simeq \pi/2$ is obtained under yawing conditions.

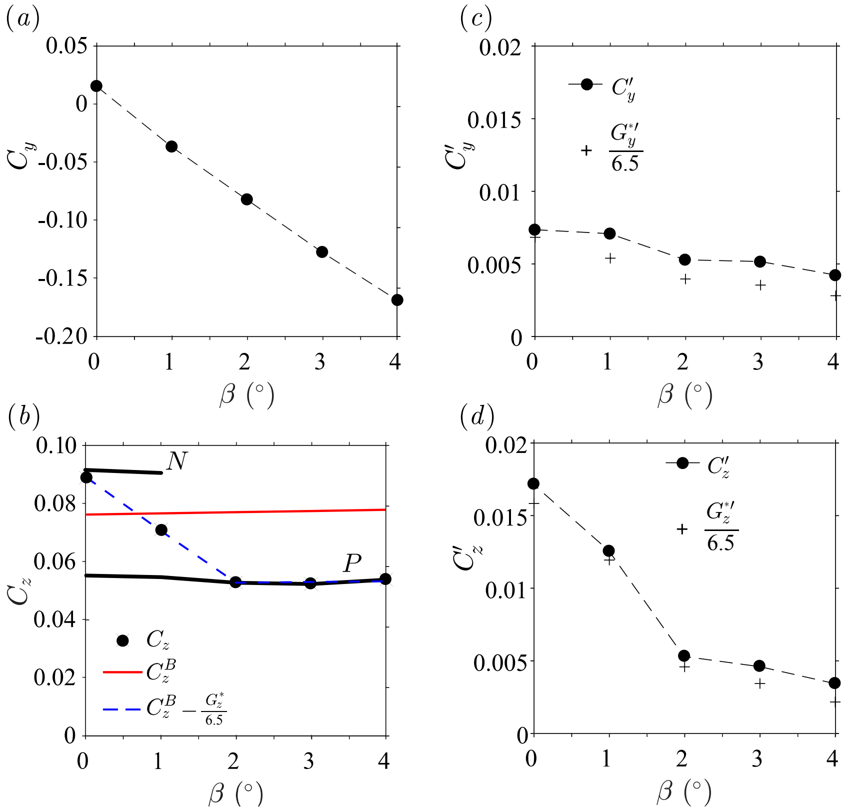

Figure 7.24 – Yaw sensitivity analysis for the Peugeot Partner: (a) mean side force coefficient C_y, (b) mean (symbols) and most probable lift coefficients C_z (thick black lines), *basic flow* lift coefficient C_z^B (red line) and mean lift computed from equation (7.4b) with $\xi = 1/6.5$ in blue dashed line. Fluctuations of the force coefficient compared to those of the gradient: (c) side force coefficient and horizontal base pressure gradient, (d) lift coefficient and vertical base pressure gradient.

The cross-flow forces resulting from the yaw sensitivity analysis are investigated in figure 7.24. Similarly to the pitch experiment in figure 7.20(a), the side force coefficient (figure 7.24a) is that of the *basic flow*, $C_y = C_y^B$, and only the mean lift coefficient (figure 7.24b) reveals the z-instability. A best fit with a quadratic function – chosen because the mean lift coefficient without the instability has to be even with respect to the yaw angle β yields:

$$C_z^B = 4 \times 10^{-4}\beta^2 + 0.078 \tag{7.6}$$

Using the coefficient $\xi = 1/6.5$, the lift is accurately computed from equation (7.4b) as shown by the blue dashed line in figure 7.24(b) in which the P and N branches also are clearly identifiable. Equations (7.4) also provide a satisfactorily estimation of the fluctuations for the Partner as shown in figures 7.24(c, d).

Finally, we consider the mean drag coefficient C_x at once for both experiments. Looking at figure 7.25, it turns out that the bi-stable dynamics at $\alpha \simeq 2.15°$ for the Berlingo and $|\beta| < 1.5°$ for the Partner coincide with the lowest measured drag coefficients. It is worthwhile to mention that the bi-stability observed in yaw conditions at $\beta \simeq \pm 4°$ for a Renault Kangoo is also associated with a drag that is lower than that of the aligned car with $\beta = 0°$ (see figure 7.10*b*). A similar result was previously enlightened in figure 4.29 for the simplified geometry.

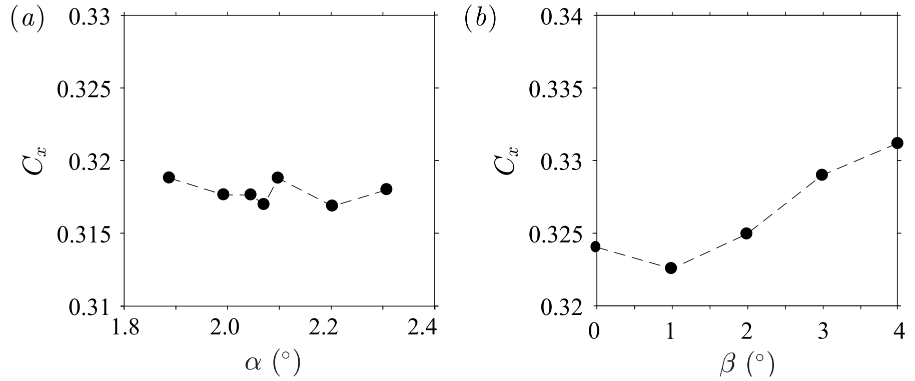

Figure 7.25 – Mean drag coefficient C_x *vs.* pitch angle α for the Citroën Berlingo (*a*) and yaw angle β for the Peugeot Partner (*b*).

7.2.8 Manipulations of the flow around the vehicles

In this section, we perform passive flow control by changing the vehicle's geometry. The case of the front air-intake system, already discussed and shown to be able to select the reversed wake state for the Renault Kangoo, is left apart. However, a global trend was highlighted throughout the chapter: closing the air-intake is an efficient drag reduction technique – applicable in real driving conditions when the need for engine cooling is low – but would generally trigger the reversed state N characterized by both a higher base suction increasing drag and a higher lift reducing the vehicle's stability, especially at high driving speeds. The purpose of this section is to manipulate the wake when in state N in order to retrieve the more efficient state P by simple techniques such as geometrical modifications. The aim is to perform the simplest possible control because the vehicles could not be modified. The z-instability taking place despite the unpropitious base aspect ratio – from experimental observations of Grandemange *et al.* (2013*a*) for a squareback Ahmed body – was said earlier to be possibly ascribed to the underbody roughness. It is modified by means of a smoother underbody. Finally, the wake sensitivity to external disturbances is discussed. The experiments are conducted with the Peugeot Partner (§ 7.2.8.1) and the Citroën Berlingo (§§ 7.2.8.2, 7.2.8.3).

7.2.8.1 Effect of rear tappers

Two passive flow control devices are investigated in this section. The idea is similar to that of Evrard *et al.* (2016) and aims at removing the wake symmetry-breaking modes in order to recover their contribution to drag. It is similar to the base cavity for the Ahmed body used in Appendix B. We consider two vertical plates at the side of the base (similar to the side tapers of Pavia *et al.* (2016) for the Windsor simplified model) and a full base cavity (Evrard *et al.*, 2016; Bonnavion *et al.*, 2017*b*). The devices are respectively shown in figure 7.26(a, b) and 7.26(c, d). The dimensions of the plates are the following: their length is equal to the one of the side of the base they are associated with and their width is $w = 3.0 \times 10^{-1}$ m, *i.e.* $w^* = d/H = 0.203$. The vehicle is placed in pitching conditions so that $\Delta\alpha = 2.3°$. In this section, this pitch angle with open air-intake and no control device installed should be understood as the *baseline*.

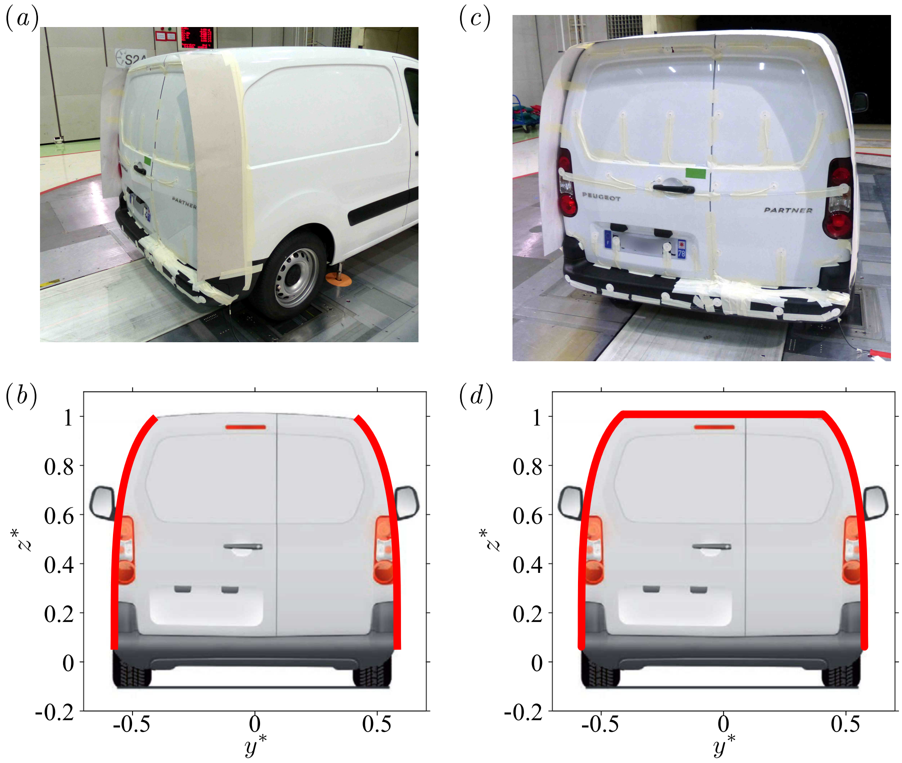

Figure 7.26 – Control devices tested for the Peugeot Partner: (a, b) side plates, (c, d) base cavity. The location of the devices is indicated with the red marks in (b, d).

The two side plates are discussed first. When the air-intake is left open, the associated mean base pressure distribution (figure 7.27a) corresponds to state P of the wake. As shown in the previous sections, when the air-intake is closed, a wake reversal occurs (figure 7.27b). Thanks to the side plates, this reversal is avoided and the mean base pressure distribution shown in figure 7.27(c) is close to that of the wake state P. The mean base suction coefficient C_b drops by nearly 2.08% with respect to the uncontrolled case and gets close to that of the baseline and the drag is further reduced by 1.51%, which represents a total gain of 6.05% with respect to the configuration with the air-intake open. The mean base suction coefficient is indeed 1.09% lower than in the uncontrolled case and the loss of drag efficiency ranks up 2.31% because of the plates. As a result, one can say that the side mixing layers originating from the lateral surfaces of the base strongly influence mode selection since the reversal is suppressed with the side plates. The explanation is that the mixing layers located on the left and on the right of the base of the vehicle are modified and start further downstream from the base. Even if the wake is stabilized and its fluctuations decrease regardless which state was selected before control is applied, this solution appears to be unsatisfactory for several reasons. First, the wake asymmetry is not removed and the z-instability clearly still present. Second, if the air-intake is opened again – which can be considered as the normal driving conditions –, the plates are harmful to drag which increases by nearly 2.31% with respect to the uncontrolled case due to a slightly higher base suction but also to the additional drag generated on the plates.

A second attempt is made with a base cavity which showed excellent results on the squareback Ahmed body (Appendix B, Evrard *et al.* (2016); Bonnavion *et al.* (2017b); Lucas *et al.* (2017)). Our cavity is actually 3-sided (top and sides), the bottom part being constituted by the rear bumper. In this case, all four mixing layers are starting downstream from the rear base. Similarly to the experiment with the side plates described above, the base cavity yields a base pressure distribution $C_p(y_i^*, z_i^*)$ corresponding to that of state P as shown in figure 7.27(e). A larger base pressure recovery is observed than for the side plates (-4.69% for C_b with respect to the uncontrolled case). This allows a larger drag reduction of -3.93% ascribed to the base cavity. With respect to the uncontrolled case with open air-intake, the reduction of drag ranks up 8.36%. The major difference with respect to the simplified model is that the cavity does not remove the symmetry-breaking mode unlike in Evrard *et al.* (2016) for which the suppression occurs for cavity depths below 10% of the base's height. However, contrary to the side plates, a beneficial effect can also be observed as the mean base pressure is increased by 1.63% if the front air-intake is left open while state P is still selected (figure 7.27f). The mean drag coefficient C_x is similar to that of the uncontrolled case, which means that the cavity walls-induced drag is exactly compensated by this base pressure recovery. In one word, we could not identify a detrimental configuration for this pitch angle.

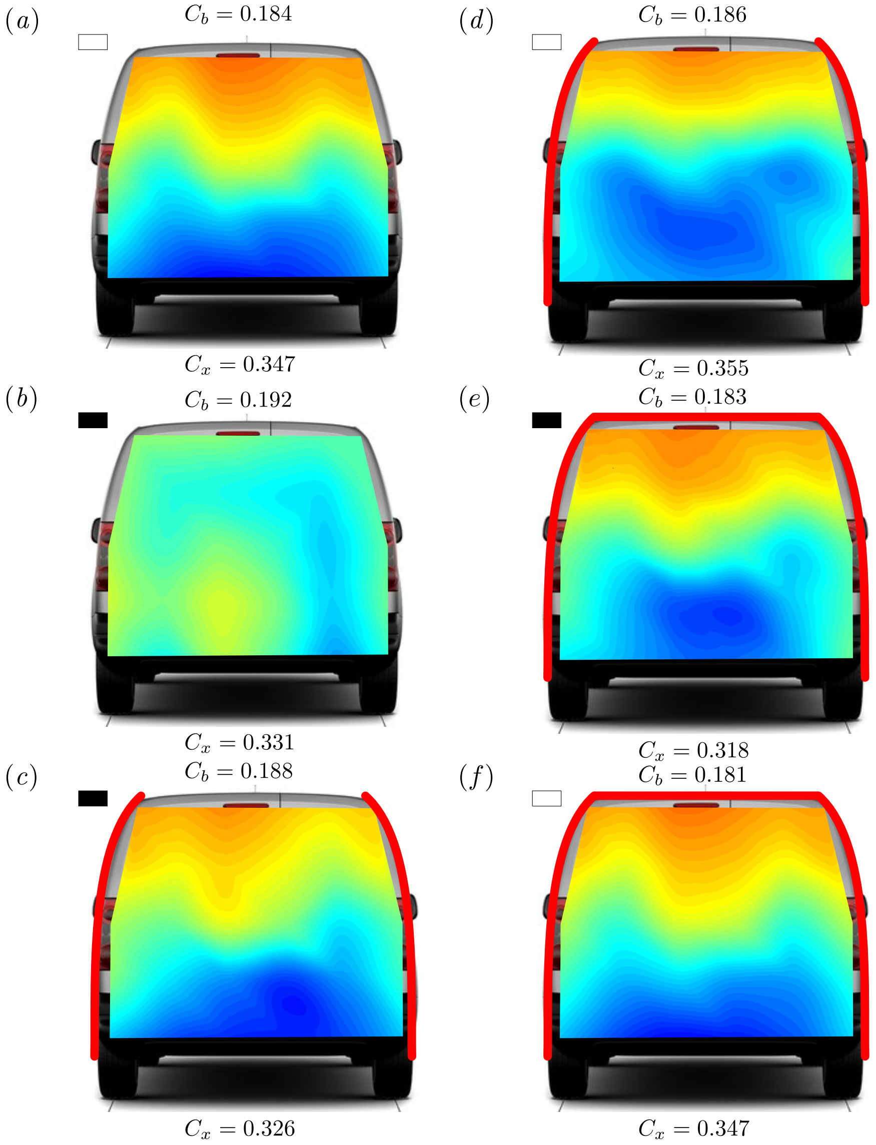

Figure 7.27 – Mean base pressure distribution $C_p(y^*, z^*)$ for the Peugeot Partner at $\Delta\alpha = 2.3°$ and associated mean base suction and drag coefficients C_b and C_x: (a) Open air-intake without control, (b) closed air-intake without control, (c) side plates and closed air-intake, (d) side plates and open air-intake, (e) base cavity and closed air-intake, (f) base cavity and open air-intake. The red lines model the control devices installed on the vehicle.

The difference between the present configuration and that first reported in Evrard *et al.* (2016) and then studied in Lucas *et al.* (2017) and in Appendix B, is that the flow separation is shifted downstream while the vertical part of the base remains at the same location contrary to the other setups where the separation location is fixed in the coordinate system related to the wind-tunnel. However, from the flow, both configurations are identical.

7.2.8.2 Influence of the underbody roughness

In this section, the tests are conducted with a Citroën Berlingo for which a new smooth underbody has been designed and manufactured. It consists in smooth plates of wood installed underneath the vehicle and attached to its chassis. These plates cover the underbody details so that it constitutes a streamline cowl for the vehicle. Some vehicles are equipped with such kind of covering made of plastic plates but not the present one. The aim of this section is to identify the global contribution of the underbody details such as exhaust line, drive shaft, suspension wishbones… to the total vehicle's drag (reported to be around 10% in Hucho (1998*a*)) but also to check whether they can influence the wake dynamics, in particular under pitching conditions.

The Berlingo is tested with closed front air-intake[1]. The aim was initially to trigger the y-wake instability but we obtained quite different results. The test is conducted at $U_\infty = 33.3$ m.s^{-1}. The baseline's results are given in figure 7.28 with the mean base pressure distribution $C_p(y^*, z^*)$ in 7.28(a) and the PDF of the two polar components of the base pressure gradient – modulus g_r^* and phase φ – in 7.28(b).

We can see from the base pressure distribution in figure 7.28(a) that state P of the wake is still selected thanks to the characteristic associated mean base pressure distribution and to the phase locked around $\varphi \simeq \pi/2$ (figure 7.28b). Compared to the case with the rough underbody (see § 7.2.5 and figure 7.16d), the strength of the instability is reduced by about a factor of two since the pressure at the top of the base decreases while the low-pressure at the bottom is almost unchanged. Still, no wake reversal is observed in this configuration. This result shows that the contribution of the underbody roughness to the wake state selection could actually be much less crucial than initially expected.

Table 7.4 – Characteristic mean and fluctuating aerodynamic coefficients for three baselines configurations of the Citroën Berlingo: open or closed Air Intake (AI) and Smooth Underbody (SU).

Baseline	C_b	C_b'	C_x	C_x'	C_z	C_z'
Open AI	0.183	0.005	0.336	0.009	0.017	0.004
Closed AI	0.172	0.005	0.312	0.005	0.014	0.003
Closed AI + SU	0.188	0.005	0.311	0.005	0.004	0.001

The mean and fluctuating aerodynamic loading is given in table 7.4 and compared to the two other baselines for the same vehicle. Closing the air-intake yields a quite low base suction C_b since the pressure at the top of the base increases largely; however, this beneficial effect is canceled by the smooth underbody as shown in figure 7.28(a). The main drag reduction is obtained thanks to the gain related to the charge loss of the flow through the engine compartment; there is – quite surprisingly – almost no contribution of the underbody roughness which might be ascribed to the quite low flow momentum in this area. These results are not consistent with those reported on simplified geometries – Windsor model – by Perry & Passmore (2013) who identified a $9-14\%$ drag increase related to the underbody roughness. The difference can probably be ascribed to the flow which is more complex for industrial geometries and to the moving ground while Perry & Passmore (2013) performed their experiments with a fixed floor. In the light of the analysis made in Hucho (1998*a*), it seems that, due to the quite low flow momentum, the roughness is much less important than the wet surface which consequently explains why both configuration lead to quite similar results. However, there is a clear influence on lift which is drastically reduced and becomes almost null with the smooth underbody. The value reached is close to that of the Partner with closed air-intake. The vehicle's lift becomes almost null, which improves its stability. However, there is no clear impact on the fluctuations. This can be ascribed to an increase of the underbody flow velocity magnitude compared to the series vehicle. This modification is clearly visible on the cross-section of the mean velocity U^*_{xz} in the vertical plane $y^*=0$ (figure 7.28*d*).

---

[1] It is not possible to test the vehicle with open air-intakes because of the through stream which is redirected below the vehicle since the ducts are obstructed by the plates. Opening the air-intake system would create a constraint on the wood plates which could separate from the vehicle or bend.

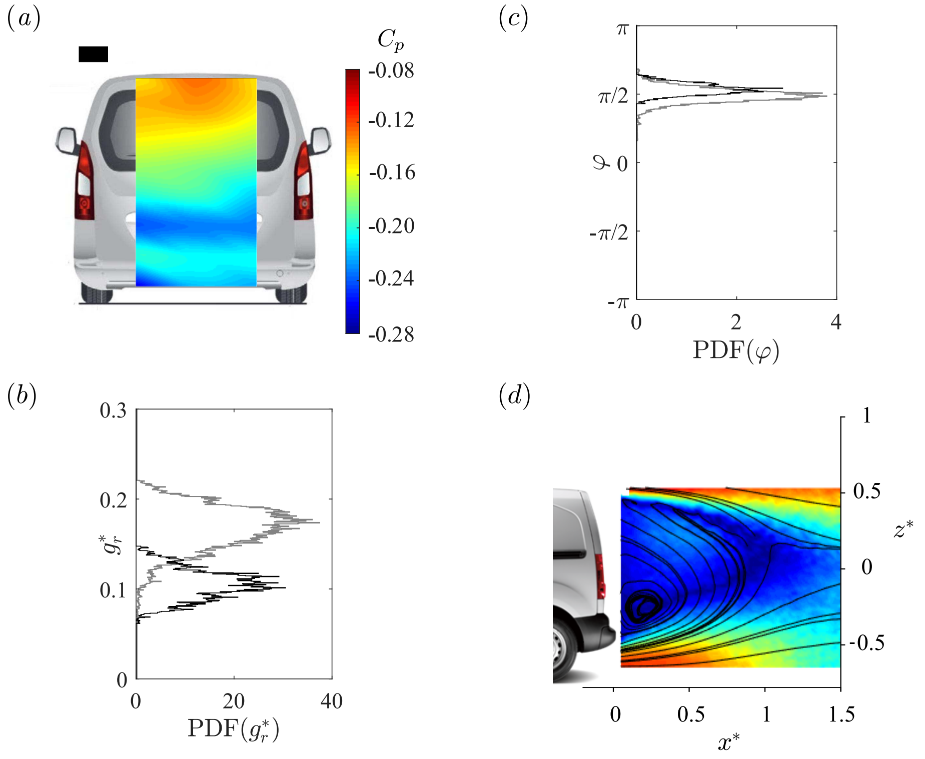

Figure 7.28 – Baseline of the Citroën Berlingo with the smooth underbody: mean base pressure distribution $C_p(y^*,z^*)$ (*a*). Probability Density Functions for the modulus g_r^* (*b*) and the phase φ (*c*) of the complex base pressure gradient $\hat{g}^*$. The baseline with closed air-intake but a rough underbody (see § 7.2.5 and figure 7.16*d*) is given in grey in the PDF. (*d*) Cross-section of the mean velocity U^*_{xz} in the vertical plane $y^*=0$.

Two experiments are made from this configuration in order to obtain a wake reversal: a ground clearance sensitivity and a pitch sensitivity analyses. We first start increasing λ for both axles without modifying the vehicle's pitch. The mean vertical base pressure gradient G^*_z is chosen as a topological indicator to track wake reversals. As it can be observed in figure 7.29(*b*), the mean vertical base pressure gradient remains around $G^*_z \simeq 0.12$ regardless of the investigated ground clearance. Meanwhile, the horizontal gradient G^*_y remains null thus indicating that the wake remains in state P. The base pressure distribution observed at the highest ground clearance ($\lambda^*=0.534$) shown in figure 7.29(*a*) is almost identical to that of the baseline with the smooth underbody (figure 7.28*a*). The wheels consequently do not introduce a significantly different wake behavior and do not trigger a y-instability nor wake reversals. The underlying question is whether the behavior with respect to pitch is modified.

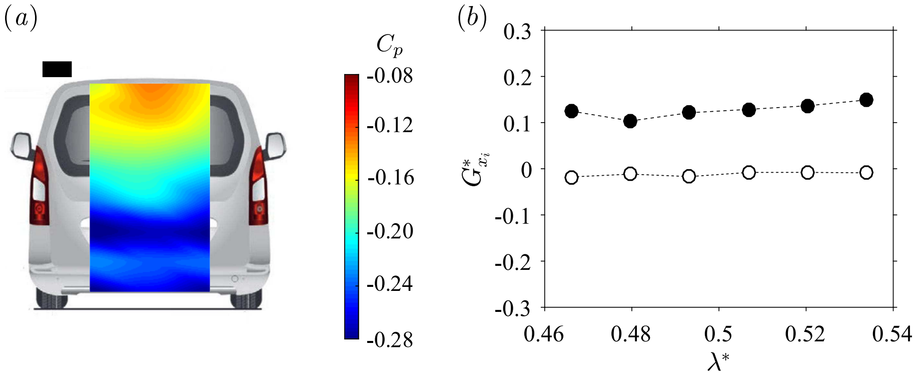

Figure 7.29 – Ground clearance experiment for the Berlingo with the smooth underbody. (a) Mean base pressure distribution $C_p(y^*, z^*)$ for $\lambda^* = 0.534$. (b) Mean base pressure gradients *vs.* distance between the top of the wheelhouse and the ground λ^*; empty symbols: horizontal gradient G^*_y, filled symbols: vertical gradient G^*_z.

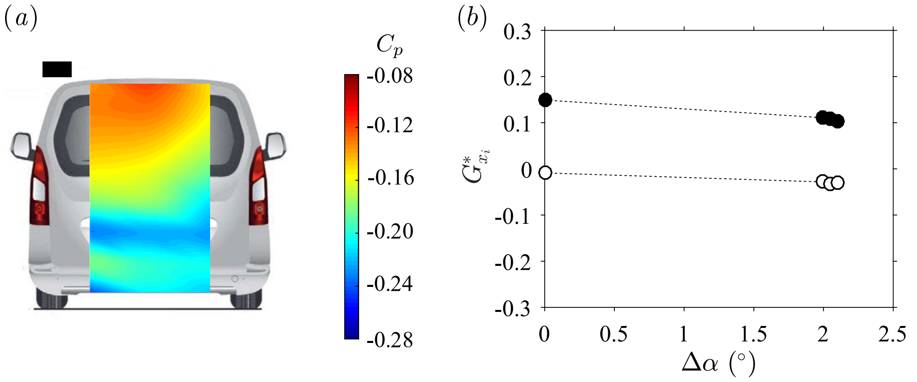

Figure 7.30 – Pitch experiment for the Berlingo with the smooth underbody and $\lambda^*_f = 0.534$. (a) Mean base pressure distribution $C_p(y^*, z^*)$ for $\lambda^* = 0.534$ and $\Delta\alpha = +2.3°$. (b) Mean base pressure gradients *vs.* distance between the top of the wheelhouse and the ground λ^*; empty symbols: horizontal gradient G^*_y, filled symbols: vertical gradient G^*_z.

Afterwards, we perform an experiment varying the pitch angle. Since the same analysis was already performed with the rough underbody, we directly impose $\Delta\alpha > 0°$ and check whether state N is still retrieved for $\Delta\alpha = +2.3°$ or bistability for $\Delta\alpha = +2.1°$ (see § 7.2.6). The front axle is lifted up so that $\lambda^*_f = 0.534$ and the previously cited angles are tested. It turns out from the gradients that the wake remains locked in state P even for the larger angles unlike for the rough underbody for which state N was reached after a bi-stable dynamics. In this case, the vertical gradient remains equal to $G^*_z \simeq 0.12$ and only experiences a slight decrease almost within the measurements uncertainty. The base pressure distribution observed for $\Delta\alpha = +2.3°$ and shown in figure 7.30(a) is similar to the baseline's.

As a conclusion, we can see that the wake reversal is suppressed by the smooth underbody which consequently has a similar effect on the wake as the rear plates or the rear cavity 7.2.8.1 although the implied mechanisms are different. As a matter of facts, while the cavity modifies the wake's streamlines, the smooth underbody modifies the underbody flow which has repeatedly shown its importance in wake state selection as in Pavia & Passmore (2018) or Castelain *et al.* (2018).

7.2.8.3 Wake sensitivity to external disturbances

In this section, we finally discuss the case of external disturbances. The sensitivity of the wake is discussed at two locations: near the vehicle's base and near the recirculation bubble closing and is assessed through three experiments. Investigations are conducted with the Citroën Berlingo with the smooth underbody and closed air-intake. We previously showed in § 7.2.8.2 the wake was permanently locked in state P characterized by a positive vertical base pressure gradient (and thus $\varphi \simeq +\pi/2$) regardless of the investigated ground clearance or pitch angle unlike the case with the rough underbody (§ 7.2.6) for which a wake reversal was identified for $\Delta\alpha = +2.3^\circ$ after a transitional bi-stable dynamics around $\Delta\alpha = +2.1^\circ$.

We first try to provoke a wake reversal following the idea of Barros *et al.* (2017). For this analysis, the vehicle has the front axle lifted up to $\lambda_f^* = 0.534$ and the rear axle adjusted to that $\Delta\alpha = +2.1^\circ$[1]. In § 4.3.2.3, we performed a similar experiment by adding a fifth support to the flat-backed Ahmed body subject to the z-instability. The result was that this additional disturbance would – similarly to the vehicle's wheels – select the P state of the wake. As a consequence, we do not place a disturbance under the Berlingo but on its roof in order to provoke a reversal. We install a cardboard crossbar of triangular section (see figure 7.31a, b) at a distance $x^* = 0.405$ upstream of the vehicle's base. The dimensions of the crossbar are indicated in figure 7.31(b). This setup could be seen as a very simplified model for a roof rack.

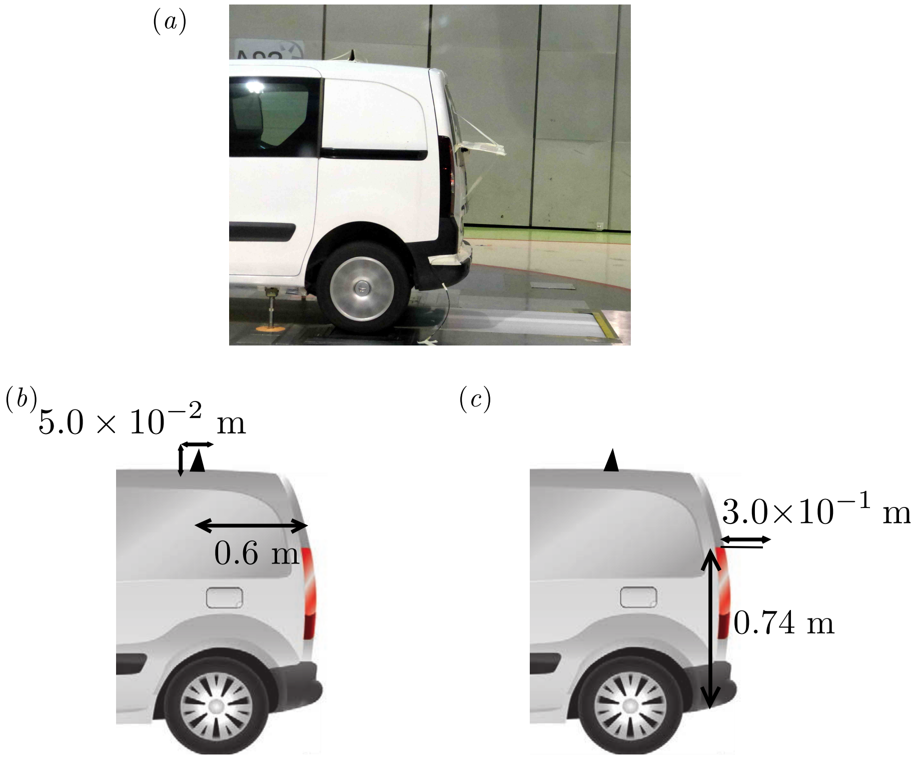

Figure 7.31 – Geometrical modifications of the Citroën Berlingo with the smooth underbody: (a) photograph of the modified vehicle with focus on (b) roof cross bar and (c) horizontal plate fixed at $z^* = 0$ normally to the base.

---

[1] This setup corresponds to that of the bi-stable dynamics with the rough underbody and the front air-intake closed discussed in § 7.2.6.

The results are given in figure 7.32 in terms of mean base pressure distribution $C_p(y^*, z^*)$ in 7.32(a) and of wake orientation with the PDF of the phase φ of the gradient in 7.32(b). It turns out that the expected wake reversal does not occur as proved by the cross-section of the mean velocity U^*_{xz} in the vertical plane $y^* = 0$ given in 7.32(c). Nonetheless, there is a general pressure drop at the rear of the vehicle – notice that the scale in figure 7.32(a) is different to the other pressure distributions.

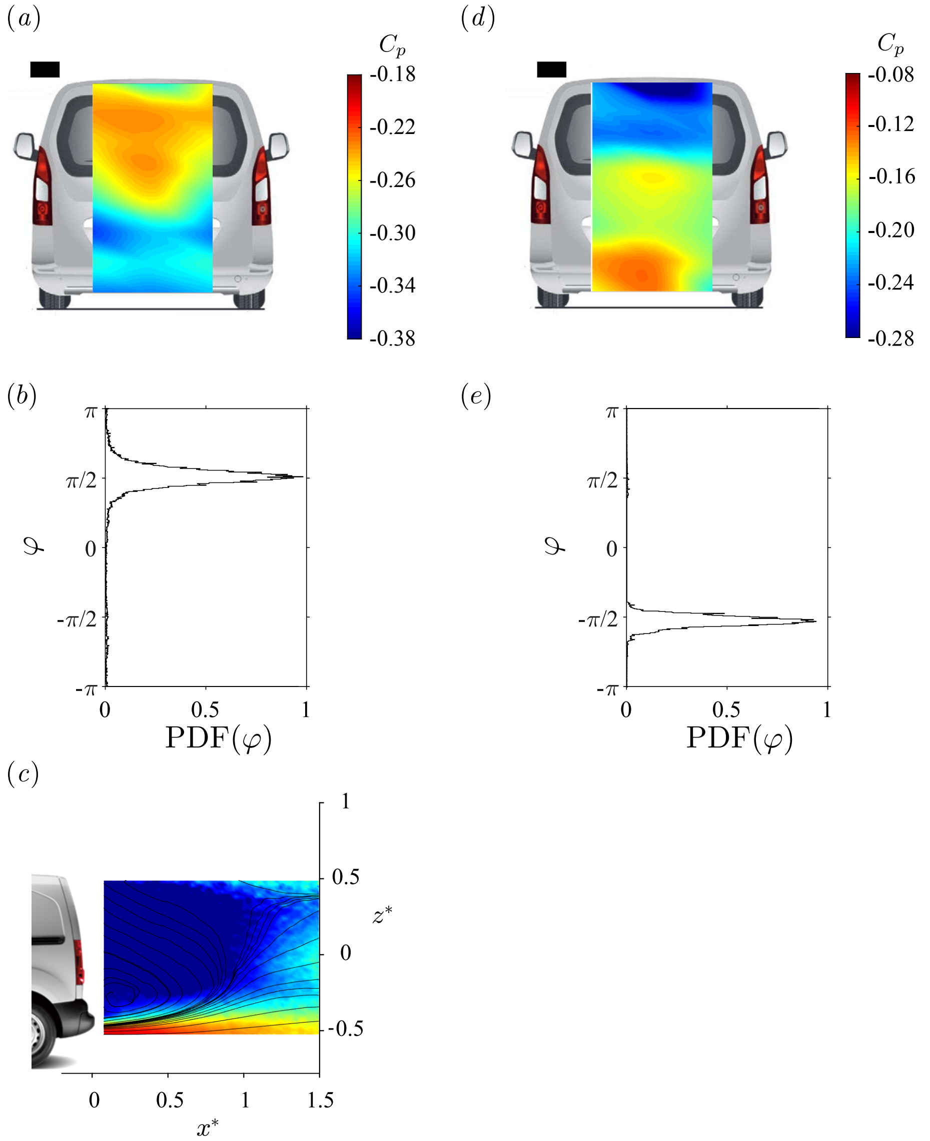

Figure 7.32 – Citroën Berlingo with smooth underbody and roof cross-bar at $\Delta\alpha = +2.1°$: (a) mean base pressure distribution $C_p(y^*, z^*)$, (b) PDF of the phase φ of the gradient and (c) cross-section of the mean velocity U^*_{xz} in the vertical plane $y^* = 0$. Citroën Berlingo with smooth underbody, roof cross-bar and rear spoiler at $\Delta\alpha = +2.1°$: (d) mean base pressure distribution $C_p(y^*, z^*)$, (e) PDF of the phase φ of the gradient.

Besides, if one remembers the fifth support experiment made on the z-unstable Ahmed body (§ 4.3.2.3), it was shown that state P was much longer selected than without the additional support. Besides, the present is consistent with the results of Pavia & Passmore (2018) for the simplified Windsor model. The suppression of the underbody roughness increases the influence of the vehicle's wheels and the z-instability is reinforced (as shown by the grown gradient g^*_r). The y-instability, expected in view of the car's aspect ratio (Grandemange *et al.*, 2013a), could possibly be triggered without the wheels.

Comparing the cross-sections of the mean velocity U_{xz}^* in the vertical plane $y^* = 0$ for the two states P and N of the wake of the Berlingo shown respectively in figures 7.18(a) and 7.18(c) clearly highlights that the main difference between the two states is an oblique jet impinging the top of the vehicle's base when state P is selected. A similar pattern is identified for trailers by Castelain *et al.* (2018). In our opinion, breaking this jet in order to prevent from this back-flow might be sufficient to provoke a wake reversal. We use a plate installed horizontally and placed normal to the vehicle's base in the plane $z^* = 0$ in addition to the crossbar described above. The setup is shown in figure 7.31(a, c).

This setup is sufficient to provoke a wake reversal for the chosen pitch angle of $\Delta\alpha = +2.1°$; the mean base pressure distribution and the PDF of the phase respectively given in figures 7.32(d) and 7.32(e) clearly show that a negative gradient takes place at the base with a large depression on the rear window and higher pressures at the bottom of the base. It is interesting to notice that, despite the similar phase φ and the close strength of the asymmetry – $g_r^* \simeq 0.11$ –, this configuration is quite different to state N of the wake in particular because the base pressure imprints are different (compare figures 7.32d and 7.23b). However, it shows that wake states control can be easily performed with a rear spoiler – which also has the advantage of preventing the spray emitted by the wheels while driving on a wet road to soil the rear window.

Since a wake reversal has been observed, we hint that there might be a bi-stable configuration. It is indeed reached when we set back $\Delta\alpha = 0°$ but keeping $\lambda_f^* = 0.534$[1]. The results are presented in figure 7.33.

Conditional averaging leads to two mirror base pressure distributions shown in figures 7.33(a, b) although the pressure levels are quite different. This results into two very different values of the strength of the gradient g_r^* although they do not appear on the corresponding PDF (figure 7.33c) which is very noisy. However, the two wake orientations are classically captured by the phase φ (figure 7.33d). Its time series plotted in figure 7.33(e) explains the noisiness of the modulus' PDF since very frequent switches – phase jumps – occur. Finally, the cross-section of the mean velocity magnitude U_{xz}^* given in figure 7.33(f) signals the bi-stable dynamics as explained later on. The field is narrower than previous ones since this specific configuration leads to a lot of rejected points by the post-treatment software.

The second wake sensitivity is analyzed with the mast of the tomographic system (see § 2.3.1). From previous results, it turns out that state P of the Berlingo's wake seems very robust, in any case much more than state N since it requires a large pitch angle to be deselected (§ 7.2.6) and since control leads back to it (§§ 7.2.8.1, 7.2.8.2) – similarly to side-slip conditions (§ 7.2.7). The present experiment is conducted both for the smooth and the rough underbodies with the Citroën Berlingo and similar results are obtained.

Unlike near the base, opposite robustness are identified when the wake is disturbed near the closing region of the recirculation bubble. It turns out that state P becomes very hard to stabilize. Several evidences are reported. First, figure 7.18(b) was plotted for $\Delta\alpha = +1.9°$. This angle was the maximum allowable in order to prevent from wake reversals although it is quite far from the transition without the mast. This shows that the vehicle's wake is undoubtedly influenced by the environment and, in driving conditions, possibly modified by other vehicles. In addition, the mast does not simply provoke wake reversals since they depend on its location. As a matter of fact, there are several changeovers between states P and N as the mast is moved throughout the wake. As an evidence, the resulting measured velocity fields present some *fringes* which can be observed in figure 7.33(f). In effect, the downstream motion of the sensors leads to $\varphi = -\pi/2$

---

[1] Unfortunately, the baseline's clearance was not tested with these geometrical modifications.

versus $\varphi = \pi/2$ for the upstream. It becomes much more difficult to observe state P than state N when the perturbation is introduced in the vicinity of the bubble closing. These fringes are in our opinion a reliable indicator of wake reversals or of a setup close to the transition since the mast is sufficient to trigger it (wake lock-in to the mast).

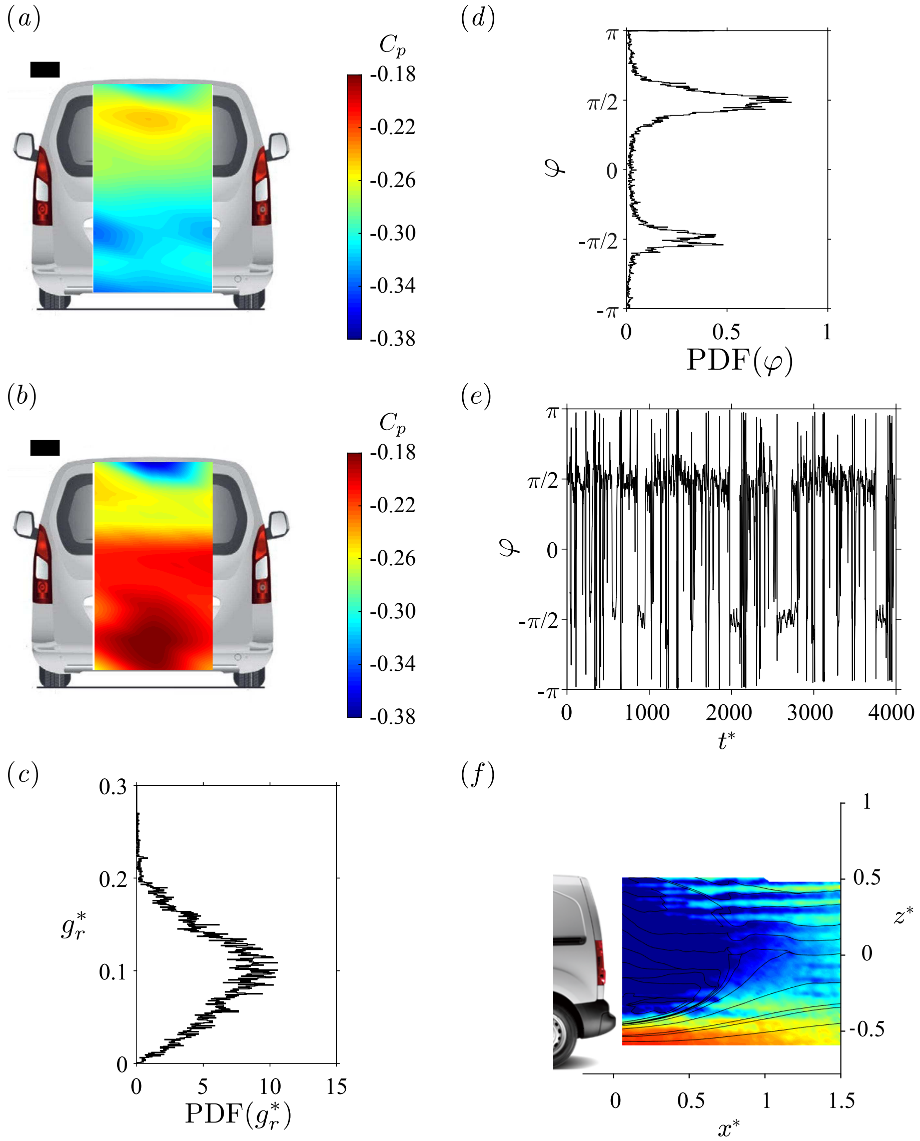

Figure 7.33 – Bi-stable wake dynamics of the Citroën Berlingo with roof crossbar, rear spoiler, smooth underbody and closed front air-intake ($\lambda_f^* = \lambda_r^* = 0.534$): (*a*) conditionally averaged base pressure distribution $C_p(y^*, z^*)|_{g_z^* \geq 0}$ for positive vertical base pressure gradients and (*b*) $C_p(y^*, z^*)|_{g_z^* \leq 0}$ for negative vertical base pressure gradients. PDF of the modulus g_r^* (*c*) and of the phase φ (*d*) of the base pressure gradient $\hat{g}^*$. (*e*) Time series of the phase φ and (*f*) cross-section of the mean velocity magnitude U_{xz}^* superimposed to streamlines in the plane $y^* = 0$.

The two regions identified in this analysis are consistent with those reported in the literature for simplified geometries such as two-dimensional D-shaped bodies (Parezanović & Cadot, 2009; Parezanović & Cadot, 2012), for which selected wake orientations are similar to those presented in this chapter (Parezanović *et al.*, 2015), axisymmetric bluff bodies (Grandemange *et al.*, 2012*b*) or Ahmed bodies (Grandemange *et al.*, 2012*a*, 2014*b*).

7.3 Discussion

Four real blunt based vehicles are investigated in this chapter. The presence of a z-instability of the wake is inferred from base pressure distributions while aligned and confirmed by sensitivity analyses of the vehicle's alignment. Similarly as for the flat-backed Ahmed body subject to the z-instability (§ 4.3.2), a unique wake mode is identified. It is characterized by a strength g_r^* and an orientation, the phase φ.

The experiments conducted on the vehicles confirm the previous observation of bi-stable dynamics at yaw angles presented in § 7.2.4 previously published in Cadot *et al.* (2016) and fully investigated in Bonnavion *et al.* (2017*a*). In this chapter, a bi-stable wake dynamics is identified for the first time for industrial vehicles aligned with the incoming flow in terms of yawing conditions. This dynamics appears to be the transition between a positive and negative base pressure gradients and is selected by an appropriate choice of the pitch angle (§ 7.2.6). The air-intake system may have to be closed to obtain such dynamics.

By analogy with the findings on the flat-backed Ahmed body discussed in § 4.3.2, a straightforward interpretation is that the wakes of the four investigated vehicles (5008, Kangoo, Partner and Berlingo) are permanently subject to a z-instability which appears similar to that of the simplified geometry. The baselines are then associated with state P and the transition towards state N occurs through the bi-stable dynamics. For instance, the transition observed with the Renault Kangoo at yaw (§ 7.2.4, also reported in Cadot *et al.* (2016); Bonnavion *et al.* (2017*a*)) is very similar to that of the boat-tailed Ahmed body subject to the z-instability at $c^* = 0.124$ or $c^* = 0.168$ shown in figure 4.26 on page 77 while the yaw analysis with the Peugeot Partner (§ 7.2.7) clearly reminds us of the yaw sensitivity experiment of the Ahmed body at $c^* = 0.080$ shown on the same figure. As for the pitch, the Citroën Berlingo (§ 7.2.6) presents similar features as the simplified geometry (see figure 4.27 on page 78). Finally, the two topologies reported for the 5008 in the baseline and lifted-up in § 7.2.2 can be compared to the ground clearance sensitivity experiment (see figure 4.22 on page 72).

We believe that, in fact, bistability occurs every time a *symmetry compensation* effect occurs, justifying then the phase selection operated for instance by disturbances. Further details can be found for fundamental geometries such as spheres in Vilaplana *et al.* (2013) or for the squareback Ahmed body in Grandemange *et al.* (2013*a*,*c*, 2014*b*) and more recently in Brackston *et al.* (2016); Barros *et al.* (2017). This selection can also be performed by geometrical changes such the ground clearance, the pitch and yaw angles as for the Ahmed body but additionally the air intake system that can change the momentum of the underbody flow – whose role is enlightened by Castelain *et al.* (2018) with a simplified lorry geometry subject to the z-instability – or the wheels (Pavia & Passmore, 2018). For the minivans, the two branches solution P and N exist and may be explored depending on all the parameters described above – and certainly on others which have not been identified so far... An evidence of the *symmetry compensation* is, in our opinion, brought by the last experiment (§ 7.2.8) with the rear spoiler and the roof crossbar for which, when the wake balance is reached, a bi-stable dynamics takes place.

Despite these similarities, there are some considerable discrepancies between the simplified geometry and industrial models. First, the strength of the gradient characterized by its modulus g_r^* is strongly dependent on the wake orientation. Even though the generalized wake model of equation (4.24) shows that the modulus is phase-dependent, it is a function of $\cos\varphi$ only. As a result, two angles with the same cosine such as $\varphi = \pm\pi/2$ yield the same value of g_r^*, which is not observed throughout this chapter since it is about twice bigger in the P state ($\varphi \simeq \pi/2$) than in the N ($\varphi \simeq -\pi/2$). We ascribe these differences to the large asymmetry of real car models but also to the presence of large flow obstructions generated by the wheels[1]. Second, a common feature of all considered vehicles is that their baselines correspond to a P state unlike a N state for the Ahmed body which may be related to the *apparent* ground clearance[2] related to the underbody flow (Castelain *et al.*, 2018).

As long as the bi-stable dynamics of the wake are not reached within the *driving envelope*[3], they should not represent an issue. From our experiments, the only compatible case would be the yaw triggered fluctuations for the Kangoo (§ 8.2.2). Nonetheless, the sensitivity analyses of the outer wake region show that the presence of a disturbance such as the mast (§ 7.2.8) may force the wake into the N state even though the operating conditions are quite far from the transition. As a result, we believe that the presence of other cars following or overtaking another could trigger a wake reversal and lead to the associated detrimental results in terms of drag and lift on the rear axis.

The wake instability, present in the baseline configurations even though a permanent wake lock-in exists, offers perspective for flow control. From our results, it comes out that it would be useless to target the reversed state N – although targeting state P while in state N yields excellent results as shown in § 7.2.8.1. Nevertheless, there still exists the opportunity of the stabilization towards the symmetric wake – also referred to as *basic flow* throughout – believed to be more fuel efficient. Despite the large modifications of the aerodynamic loading induced by global changes of the wake, we assume that the control would require reasonably small passive or active disturbances in order to pass the safety constraints, be fuel efficient and not considerably modify the vehicle's shape design.

One of the results concerning drag that we found striking for the simplified geometry (§ 4.4.4) is that, based on our experiments, bi-stability is always associated with the lowest mean drag coefficient C_x. A similar explanation as in § 4.4.4 is provided for the lower drag: the permanent asymmetry of the wake is reduced since the unstable state is explored during the state switching. A really interesting question arises: is it possible to conceal the advantages of such operating points in terms of drag and base suction with their large drawbacks, namely large cross-flow fluctuations? They indeed strongly impact the loading applied on the vehicle (§§ 7.2.6, 7.2.7). For the z-instability, the wake reversal is mainly responsible for a strong lift increase which may significantly impact the vehicle's rear axis stability as already mentioned for instance in Cadot *et al.* (2016) or Bonnavion *et al.* (2017*a*).

---

[1] It is quite hard to conclude firmly about the underbody roughness even though there is a large unbalanced asymmetry between the rough under-body structure and the streamlined roof that do not exist for the simplified body. However, the simultaneous observation of the two wake states requires the use of a rear spoiler and of a roof crossbar which change the geometry of the vehicle.

[2] The recent work of Castelain *et al.* (2018) shows that, for a given ground clearance, the wake orientation can be selected by the ratio between the underbody flow and the free-stream velocities. As a result, we mix here both parameters and define and *apparent* ground clearance since the underbody roughness depends on the considered vehicle. This *apparent* clearance corroborates the findings of § 7.2.8.2 with the smooth underbody since the results are modified by its roughness.

[3] Defined by analogy with the flight envelope. This expression, commonly used in aerospace engineering, corresponds to the normal conditions encountered while driving in terms of pitch and ground clearances resulting from payload mass, air free-stream velocity, cooling system condition and so on.

7.4 Concluding remarks

The wake dynamics of four blunt based vehicles is studied in this chapter. The wakes of these vehicles, in the baseline configuration – aligned with the flow at a natural ground clearance – exhibit a strong asymmetry in the vertical direction that is not only related to the shape asymmetry nor to the presence of the road. The cars are indeed found to be subject to a z-instability of the wake in the sense of Grandemange *et al.* (2013a) despite the aspect ratio of their base; Pavia & Passmore (2018) propose that the wheels perform the selection.

Similar wake transitions as those observed with the Ahmed body subject to the z-instability (§ 4.3.2) are identified with these vehicles when the ground clearance, the yaw or the pitch angles are modified. This indicates the relevance of fundamental studies for industrial applications since the implied mechanisms are identical. The impact of these transitions on the aerodynamic loading is also found similar, with a clear correlation between the base pressure gradients and the cross-flow loading not only in mean but also in instantaneous values since the fluctuations of the base pressure distribution directly impact those of the cross-flow loading, with a factor of proportionality which is shape dependent.

Two wake states are identified and characterized by different strength which is ascribed to the strong asymmetries between the top and the bottom of the vehicles; the impact of the wheels wake is visible in the reversed wake state and also contributes to the different strengths. Wake reversals have shown to be not only sensitive to the vehicle's alignment but also to the flow underneath which can be controlled by the air-intake system or underbody roughness. They also show a large sensitivity to external disturbances such as the tomography mast; as a result, another vehicle following or passing-by could also modify the wake topology in real conditions. However, we showed that simple manipulations of the flow such as a rear cavity or a rear spoiler provide easy-to-implement solutions which lead to satisfactory results. Nonetheless, the largest drag reduction should be achieved by removing the instability and stabilizing the flow on the symmetric wake state.

CHAPTER 8

Wake multi-stability created by boundary layer reattachment

This chapter presents a different case of wake transitions for a hatchback vehicle (Renault Mégane). Those transitions are related to another type of multi-stability of real cars' wakes which is not driven by an instability that appeared in the laminar transition regime but still has important consequences on the vehicles' efficiency and stability. This kind of multi-stability is not observed on the squareback Ahmed body because of the sharp geometry of its afterbody. Characterization of the wake is provided owing to unsteady aerodynamic loading and pressure distributions at the car's base. A transition yawing angle of $\beta = \pm 8.6^\circ$ at which a bi-stable behavior occurs is identified. It originates from a massive but intermittent turbulent reattachment occurring simultaneously on the whole slanted rear window, similarly to the well known drag crisis transitions of smooth bluff bodies. The reattachment is suspected to be caused by the increase in curvature of the separated shear layer under side-wind conditions.

Contents

8.1 Setup **209**

8.2 Results **210**

8.2.1 Baseline 211

8.2.2 Influence of the yaw angle 212

8.2.3 Multi-stable case 214

8.3 Discussion **216**

8.3.1 Turbulent flow reattachment versus wake instability caused by symmetry-breaking modes 216

8.3.2 Impact of wake multi-stability on the aerodynamic loading of real vehicles 217

8.4 Concluding remarks **217**

8.1 Setup

The experiments are conducted in the full-scale wind-tunnel of the GIE-S2A described in § 2.1.1. A hatchback car, a 2015-Renault Mégane (type B95), is placed in the test-section. Its characteristic dimensions are given in table 8.1. The ground clearance c^* and the pitch angle α of the vehicle are not modified during this test. For real vehicles, it is easier to define the distances between the ground and the top of the wheel-arch λ_r^* (for the rear axle) and λ_f^* (for the front axle) given in table 8.1. A driver's load of 80 kg is simulated owing to bags filled with sand placed on the front-left seat. The car's rear panel is equipped with $N = 30$ pressure taps distributed over the base as shown in figure 8.1(a, b). In figure 8.1(a), the white rolling belt simulating real driving conditions is clearly visible below the vehicle. A side view of the Renault Mégane with the measurement of the slant angle is made available in figure 8.1(c).

Table 8.1 – Characteristic dimensions of the Renault Mégane. The base height H_b is used as the scaling unit.

H_b(m)	W_b (m)	W_b^*	S (m^2)	S^*	λ_f (m)	λ_f^*	λ_r (m)	λ_r^*
1.000	1.810	1.810	2.210	0.674	0.667	0.667	0.671	0.671

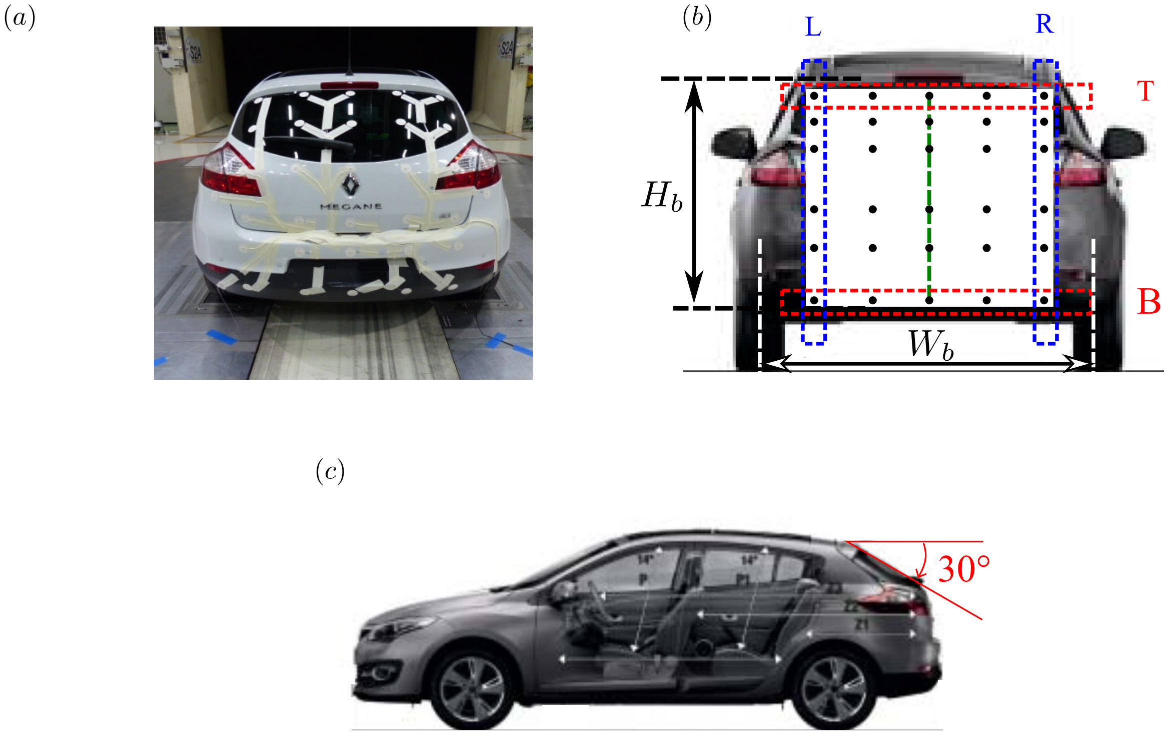

Figure 8.1 – Renault Mégane in the GIE S2A full-scale wind tunnel (a) and location of pressure taps (b). The top T and bottom B (resp. left L and right R) lines are used to compute the vertical (resp. horizontal) base pressure gradient as defined in equation (8.2) (resp. equation (8.3)). The green vertical line is used for space-time diagrams. (c) Side view of the Renault Mégane (flow coming from the left) with rear slant angle.

The acquisition is performed with the ZOC22b pressure scanner (described in § 2.2.1) at a sampling frequency of $f_e = 200$ Hz. Some of the pressure taps indicated in figure 8.1 are used to compute a global base pressure gradient characterized using a Cartesian description in this chapter. It is estimated as follows from the pressure taps located at the contour of the vehicle's base (see figure 8.1*b*) to which a spatial averaging is applied:

$$
\begin{aligned}
c_{p_T}(t^*) &= \frac{1}{n_c}\sum_{i=1}^{n_c} c_p(y_i^*, z_{i,T}^*, t^*) \\
c_{p_B}(t^*) &= \frac{1}{n_c}\sum_{i=1}^{n_c} c_p(y_i^*, z_{i,B}^*, t^*) \\
c_{p_L}(t^*) &= \frac{1}{n_r}\sum_{i=1}^{n_r} c_p(y_{i,L}^*, z_i^*, t^*) \\
c_{p_R}(t^*) &= \frac{1}{n_r}\sum_{i=1}^{n_r} c_p(y_{i,R}^*, z_i^*, t^*)
\end{aligned}
\tag{8.1}
$$

where $n_r = 6$ stands for the number of rows and $n_c = 5$ the number of columns. The *bottom B* pressure coefficient given in equation (8.1) is substracted from the *top T* one and then divided by the distance δ_z between the top and the bottom rows to give a vertical base pressure gradient denoted g_z^*, itself non-dimensionalized by H_b:

$$
g_z^* = H_b \times \frac{c_{p_T}(t^*) - c_{p_B}(t^*)}{\delta_z} \tag{8.2}
$$

Similarly, the horizontal base pressure gradient g_y^* is:

$$
g_y^* = H_b \times \frac{c_{p_R}(t^*) - c_{p_L}(t^*)}{\delta_y} \tag{8.3}
$$

Unlike the previously considered vehicles and simplified models, and as can be seen in figure 8.1(*c*), the Renault Mégane has a 30°-slanted rear window which makes it closer to the original Ahmed body (Ahmed, 1983; Ahmed *et al.*, 1984) also recently investigated by Meile *et al.* (2016) and Rao *et al.* (2018) in the 35°-slanted version.

The aerodynamic loading applied on the vehicle is measured synchronously with the balance described in § 2.2.2 for typical durations of $2-4$ minutes. Following the motivations detailed in § 8.2.1, a parametric study is conducted in terms of the yaw angle β applied to the vehicle, simulating driving in cross-wind conditions. This angle is changed owing to the turn table (see § 2.1.1) and the reference $\beta = 0°$ is taken for the vehicle geometrically aligned with the incoming flow.

The wind tunnel is operated with the boundary layer control system on (see § 2.1.1) and the free-stream velocity is set to $U_\infty = 38.89$ m.s^{-1} (140 km.h^{-1}). At the test temperature of $T_\infty = 293$ K, the corresponding Reynolds number based on the vehicle's height is then $\mathrm{Re}_{H_b} \simeq 2.6 \times 10^6$.

8.2 Results

The results are presented as follows. First, the baseline is characterized in § 8.2.1. Afterwards, the parametric study is conducted in § 8.2.2. Finally, the focus is set on the multi-stable case in § 8.2.3.

8.2.1 Baseline

The baseline is taken as the vehicle aligned with the flow and a ground clearance and a pitch angle corresponding to those of the vehicle with a 80 kg driver on-board as detailed in § 8.1. The mean and mean fluctuating aerodynamic coefficients are given in table 8.2. With respect to the other real vehicles presented in chapter 7, the mean base suction coefficient C_b and mean drag coefficient C_x are low, taking advantage of the more profiled shape of the vehicle with respect to vans. As suggested by the mean side force coefficient C_y, the setup presents a slight asymmetry. In fact, despite the overall symmetry of the car's shape, some details such as the engine compartment or the exhaust gas line for instance present left-right discrepancies which may create a lateral force thus explaining the non-zero mean value of the coefficient c_y. The mean lift coefficient C_z is slightly positive, which is a drawback considering the vehicle's stability, especially at high driving speeds. All standard deviations have an order of magnitude 10^{-3} which shows by analogy with the previous cases that no large fluctuations of the wake can be identified in this configuration.

Table 8.2 – Mean and fluctuating aerodynamic coefficients of the Renault Mégane for the baseline (§ 8.2.1) and state D and A of the wake at $\beta = -8.6°$ (§ 8.2.3).

Configuration	C_b	C'_b	C_x	C'_x	C_y	C'_y	C_z	C'_z
Baseline	0.139	0.002	0.338	0.002	−0.002	0.004	0.099	0.005
State A ($\beta = -8.6°$)	0.194	0.005	0.357	0.002	0.281	0.004	0.128	0.005
State D ($\beta = -8.6°$)	0.214	0.005	0.340	0.002	0.281	0.004	0.250	0.005

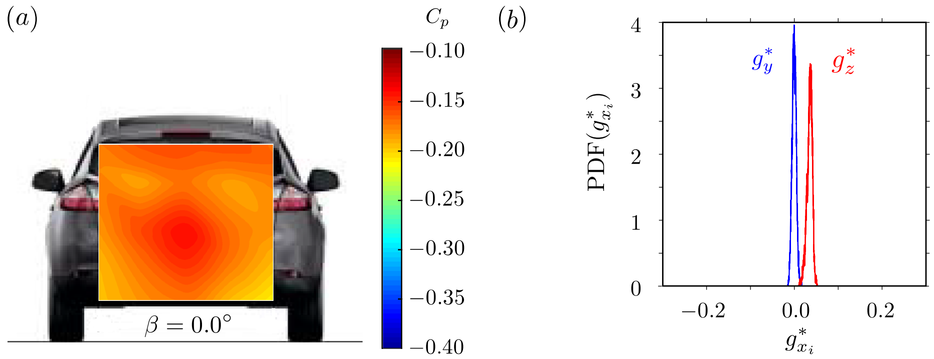

Figure 8.2 – Baseline configuration of the Renault Mégane: (*a*) Mean base pressure distribution $C_p(y^*, z^*)$ and mean base suction coefficient C_b. (*b*) Probability Density Functions of the horizontal base pressure gradient g^*_y (in blue) and of the vertical base pressure gradient g^*_z (in red).

The mean base pressure distribution $C_p(y^*, z^*)$ is shown in figure 8.2(*a*). Its main characteristic is to be nearly symmetrical not only in the horizontal direction (as the other tested real vehicles) but also in the top-bottom orientation. There is no obvious symmetry-breaking in this configuration. The two components of the base pressure gradient are almost steady as proved by the very narrow PDFs plotted in figure 8.2(*b*), respectively in blue for the horizontal gradient g^*_y and in red for the vertical component g^*_z. The absence of strong asymmetry of the wake suggests that no reversal can occur due to static modes which would be triggered changing the pitch, the yaw or even the ground clearance of the vehicle.

8.2.2 Influence of the yaw angle

The mean base pressure gradients G_y^* and G_z^* are plotted against the yaw angle β in figure 8.3(a). The horizontal base pressure gradient does not show any significant dependence on yaw and is much smaller than the corresponding vertical one. An anomaly showing high sensitivity to the yaw angle β can be observed for the vertical base pressure gradients when the absolute value of the yaw angle reaches $|\beta| \sim 8.0°$. Both curves appear to be fairly symmetrical with respect to the considered yaw angle. The mean standard deviations of the base pressure gradients $G_y^{\prime *}$ and $G_z^{\prime *}$ are studied with respect to the yaw angle in figure 8.3(b). The evolution of the standard deviations of both gradients are symmetrical and an increase of about one order of magnitude can be observed for the mean vertical component $G_z^{\prime *}$ for yaw angles such that $8° \leq |\beta| \leq 9°$. Meanwhile, the horizontal fluctuations are not affected. For larger angles (in absolute value), the fluctuations' level drops to that of the baseline suggesting that the wake fluctuations disappear and yield to a more steady flow.

The three force coefficients are given in mean and mean standard deviation values in figure 8.3(c) and figure 8.3(d) respectively. Classically, the mean side force coefficient C_y shows a linear evolution with respect to yaw. A sudden increase of the mean lift coefficient C_z can be observed for yaw angles larger in absolute value than $|\beta| = 8.0°$, *i.e.* the suspected onset of instability (figure 8.3a). Similarly, the mean drag C_x increases faster for such angles. As expected due to the global symmetry of the car's shape and in agreement with the base pressure gradients, all coefficients but the lateral force's are roughly even functions of the yaw angle β. The increase of lift can be correlated with the (negative) growth of G_z^* which suggests a lower pressure level at the top of the base than at its bottom thus creating suction; this might also be the explanation of the larger drag increase for such angles.

The simultaneous anomaly detected on the gradients standard deviations and on the mean force coefficients is also identified on the fluctuations of the aerodynamic loading (figure 8.3d). It appears clearly that the transitions around $|\beta| \sim 8.0°$ are associated with large fluctuations of the drag coefficient $C_x^{\prime}$ and of the lift coefficient $C_z^{\prime}$ while the side force standard deviation $C_y^{\prime}$ is almost unaffected. The maximum fluctuations yield critical angles of $\beta = \pm 8.6°$ for which the transitions of the wake discussed below in § 8.2.3 occur.

Those variations of the mean quantities of the flow can be explained owing to the mean base pressure distributions $C_p(y^*, z^*)$ given in figure 8.4 for six angles from $\beta = 0.0°$, *i.e.* before the transition, in figure 8.4(a) to $\beta = -10.0°$, *i.e.* after the transition, in 8.4(f). In figure 8.4($a - e$) until $\beta = -6.0°$, the mean base pressure distribution is very similar to that of the baseline (figure 8.4a) in its spatial organization although the global pressure level drops with the yaw angle. This change is uniformly distributed though as the pressure gradients are almost not impacted. For $\beta = -8.0°$ (figure 8.4e), *i.e.* just before the transition, the pressure level drops symmetrically on both sides of the rear window. When the angle is further increased (in magnitude) up to $\beta = -10.0°$, figure 8.4(f) shows a very different situation. Although globally unchanged in the lowest part of the base (cargo door), the pressure distribution in the upper part, corresponding to the rear windows, is largely impacted. Despite the quite large yaw angle, the left-right symmetry is preserved but the pressure level is now much smaller since the mean pressure coefficient C_p is almost twice larger in magnitude. This distribution is in total agreement with the aerodynamic loading on the vehicle as the low-pressure area creates a higher suction, whose two components contribute to drag and lift and thus explain their increase.

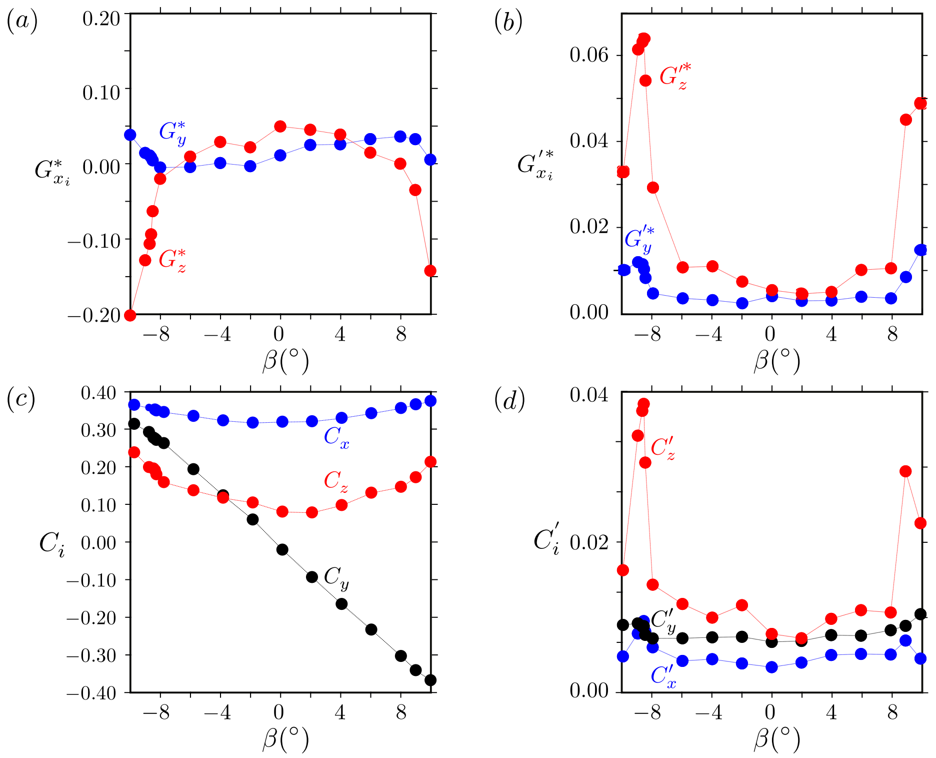

Figure 8.3 – Evolution of the mean and mean fluctuations of global parameters as a function of the yaw angle β: (a) G^*_y (blue) and G^*_z (red), (b) G'^*_y (blue) and G'^*_z (red), (c) C_i, $i \in \{x, y, z\}$, (d) C'_i, $i \in \{x, y, z\}$.

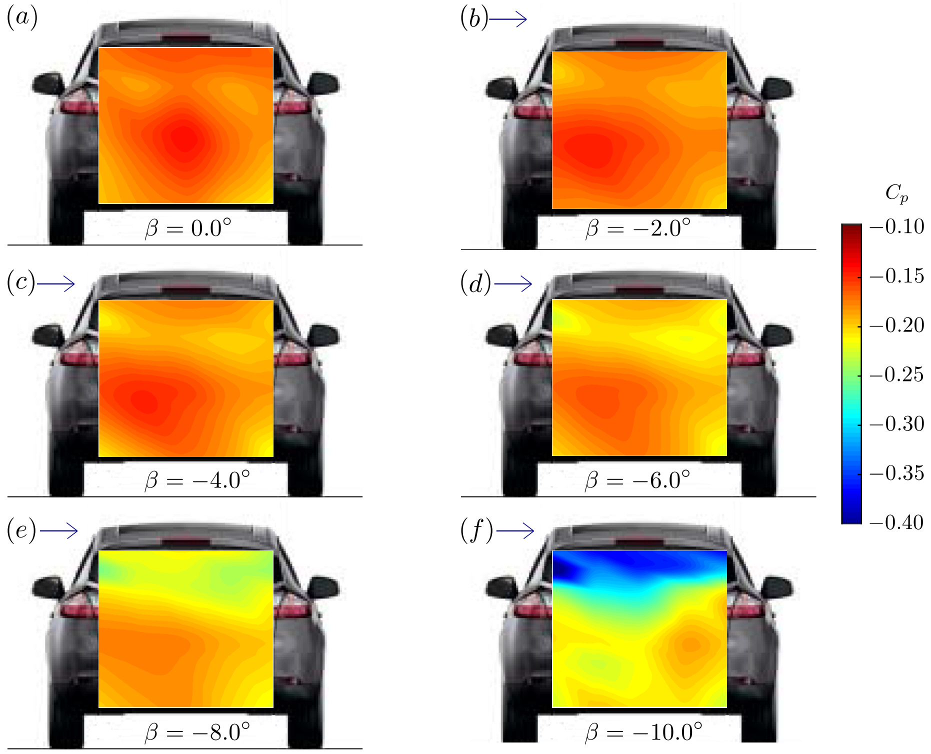

Figure 8.4 – Mean base pressure distributions $C_p(y^*, z^*)$ for the Renault Mégane under yawing conditions: (a) Baseline $\beta = 0.0°$, (b) $\beta = -2.0°$, (c) $\beta = -4.0°$, (d) $\beta = -6.0°$, (e) $\beta = -8.0°$, (f) $\beta = -10.0°$. The horizontal arrow stands for the lateral component of the velocity $U_\infty \sin(\beta)$ of the wind (not to scale).

8.2.3 Multi-stable case

In view of the symmetry of the results, only one of the critical cases identified hereabove in § 8.2.2 is studied in this section. We arbitrarily chose $\beta = -8.6°$. A time series of the lift coefficient c_z is provided in figure 8.5(a). For comparison, those of the two cases before and after the transition ($\beta = -8.0°$ and $\beta = -10.0°$) are also plotted. It is clear that the lift of the critical case experiences low-frequency fluctuations between the values taken for the two angles $\beta = -8.0°$ and $\beta = -10.0°$, with a characteristic time-scale of about $1000 \times t^*$. In addition, all three time series display high-frequency fluctuations of few dozens of t^*. The associated PDF are given in figure 8.5(b) for the lift (in red) and the drag (in blue) coefficients on which the existence of two preferred values of the lift is confirmed by the two peaks of the PDF. These two peaks are indistinguishable for the drag because of the large turbulent fluctuations but could be observed with additional filtering of the signal.

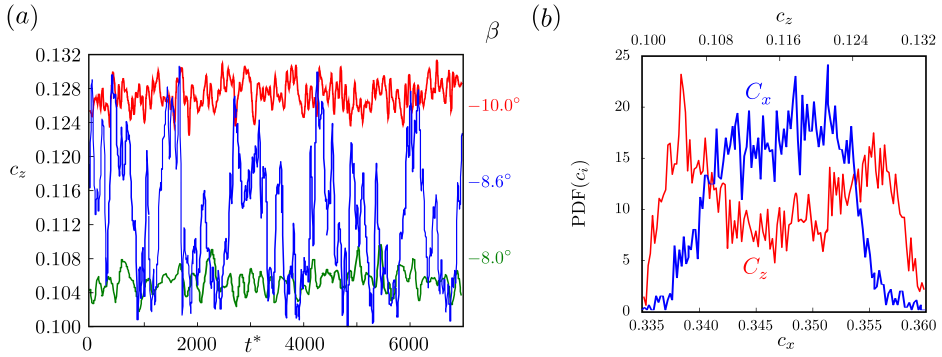

Figure 8.5 – (a) Time series of the lift coefficient c_z for the Renault Mégane at different yaw angles: *red*: $\beta = -10.0°$, *blue*: $\beta = -8.6°$, *green*: $\beta = -8.0°$; (b) PDF of of the lift coefficient c_z (in red) and of the drag coefficient c_x (in blue) for the multi-stable case $\beta = -8.6°$.

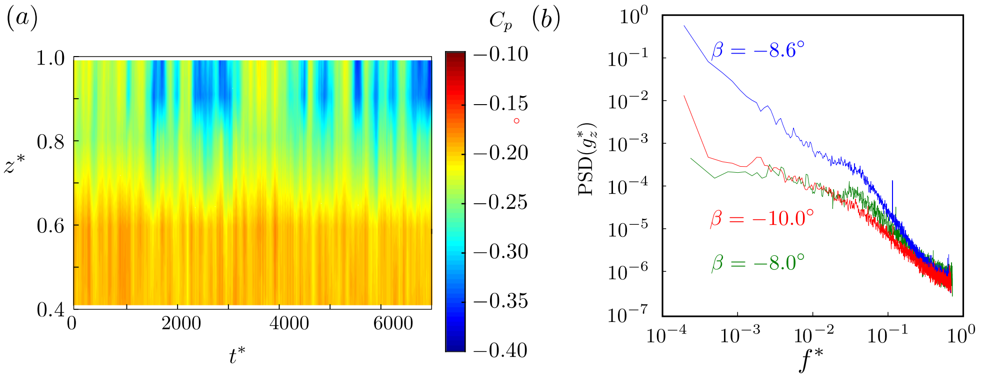

Figure 8.6 – (a) Space-time diagram of $c_p(y^* = 0, z^*, t^*)$ along the line $y^* = 0$ shown in figure 8.1(b) for the Renault Mégane at $\beta = -8.6°$; (b) Spectra of g_z^*: *(green)* Sub-critical case $\beta = -8.0°$, *(blue)* Critical case $\beta = -8.6°$, *(red)* Super-critical case $\beta = -10.0°$

The temporal evolution of the base pressure distribution is a good indicator of the wake dynamics. The space-time diagram in figure 8.6(a) shows the pressure coefficient along the vertical line $y^* = 0$. A low-pressure area intermittently appears and disappears on the vehicle's rear window. The characteristic time of this process is about $1,000$ times longer than the convective time $t_C = H_b/U_\infty$, *i.e.* similar to that identified in figure 8.5(a). No periodicity is associated with this phenomenon as indicated by the absence of peak in the spectral power density of the vertical base pressure gradient given in figure 8.6(b).

Compared to the sub-critical case $\beta = -8.0°$ and to the super-critical case $\beta = -10.0°$, a large range of low frequencies is impacted which corresponds to random events.

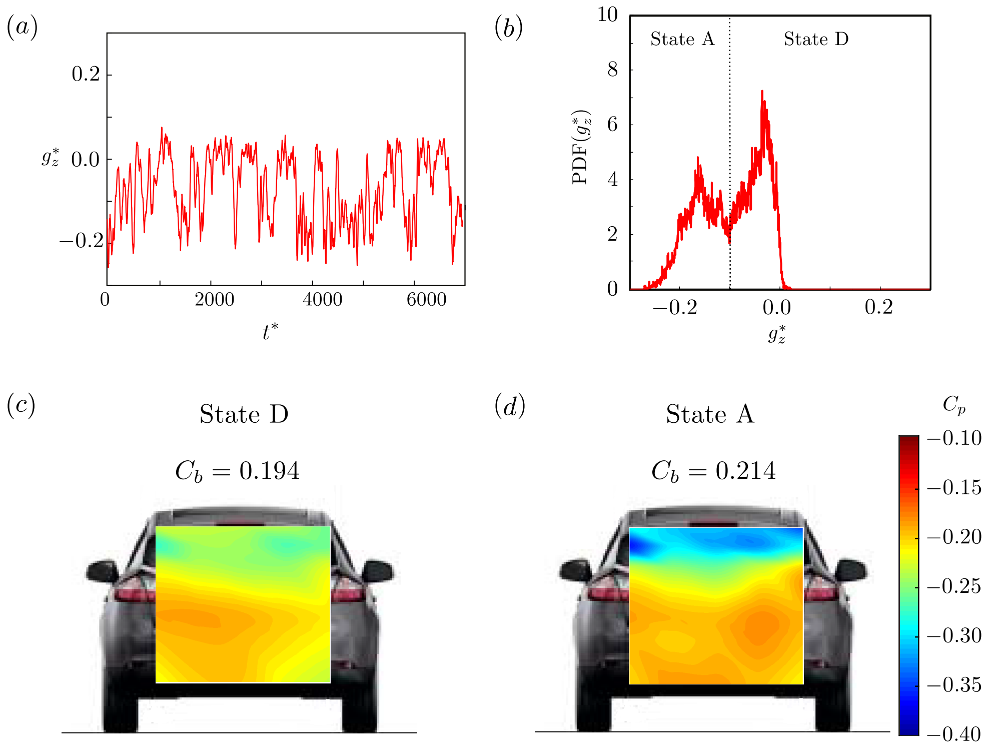

Figure 8.7 – Multi-stable case of the Renault Mégane: (*a*) time series of the vertical base pressure gradient g_z^* at the critical angle probability density function and (*b*) associated PDF; (*c*) base pressure distribution $C_p(y^*, z^*)$ associated with *state D* and (*d*) base pressure distribution $C_p(y^*, z^*)$ associated with *state A*.

The time series and the probability density function of the vertical base pressure gradient at the critical angle are presented in figure 8.7(*a*) and figure 8.7(*b*). As for the lift coefficient in figure 8.5(*b*), two preferred values of the gradient are identified by the presence of two peaks. The natural separation between the two associated states is shown in this plot: *state D*, as Detached, corresponds to $g_z^* \geq -0.1$ while *state A*, as Attached, to $g_z^* < -0.1$ (see later on § 8.3). This criterion is used to perform conditional averaging on the pressure data which yields the two corresponding mean base pressure distributions in figure 8.7(*c*) and figure 8.7(*d*). *State D* appears to be closer to the sub-critical configuration (figure 8.4$a-e$) while *state A* is much more similar to the super-critical topology (figure 8.4f). The multi-stable state is consequently a transition between these limits. Only negative values of the yawing angle are discussed in this section. Nevertheless, due to the general symmetry of the car with respect to the z-axis, similar results are obtained for positive yawing angles as the force coefficients and mean base pressure gradient follow a roughly even behavior with respect to the yaw.

To summarize, a bi-stable behavior is observed for the Renault Mégane during the transition between the flow being massively detached from the base (sub-critical configuration D for $|\beta| \leq 8.0°$) and the global reattachment on the rear window (super-critical configuration A for $|\beta| \geq 10.0°$).

8.3 Discussion

A cause of wake multi-stability not driven by static asymmetric wake modes is identified in § 8.2.3 for the Renault Mégane at yaw. These conditions are very likely to be encountered while driving as it corresponds to a 6.86 m.s^{-1} normal cross-wind while driving at the maximum velocity permitted on French highways of about 36.11 m.s^{-1} (130 km.h^{-1}). This discussion first focuses on the differences between flow reattachment and wake instability in section 8.3.1 and section 8.3.2 details the consequences on the aerodynamic forces.

8.3.1 Turbulent flow reattachment versus wake instability caused by symmetry-breaking modes

The wake bistability observed for $\beta = -8.6°$ corresponds to flow reattachment. The left-right symmetry of the base pressure distribution is conserved even at high yawing angles which, added to the fact that reattachment occurs on the whole rear window as shown in figure 8.7(c), suggests that an explanation can be found at the car's scale. The base suction coefficient C_b increases continuously with the yawing angle in the detached configuration shown in figure 8.4($a - e$) which corresponds to a pressure decrease at the car's base (Roshko, 1993). A simple but meaningful approach based on inviscid detached flows performed in Roshko (1993) indicates that this pressure drop corresponds to larger curvature of the recirculation zone created downstream of the Mégane, similar from a fundamental point of view to a bluff-body. The critical angle at which bi-stability is found corresponds to the situation when the upper shear layer emanating from the roof is close enough from the rear window to trigger reattachment similarly to the drag crisis in simple geometries (Schlichting & Gersten, 2000; Cadot *et al.*, 2015*a*). Furthermore, as the pressure is almost uniform on the rear window in the sub-critical regime, the flow reattaches simultaneously over the whole width of the vehicle. In addition, these two flow configurations were identified years ago by Hucho (1978) and respectively associated with the fastback and the squareback flow regimes, from the vehicle's shape they were taking place with but multi-stability is not reported. In other words, there is no alternate exploration of the two flow regimes for a given vehicle's geometry. The slant angle of 30° of the Renault Mégane places this vehicle right on the edge between the so-called *fastback* (attached) and *squareback* (detached) flow regimes.

A similar phenomenon was observed both experimentally (Meile *et al.*, 2016) and more recently numerically (Rao *et al.*, 2018) for the 35°-slanted Ahmed body modeling a hatchback vehicle. The identified critical angle of $\beta = 12.5°$ is, as the one of the Mégane, much larger than the critical value associated with wake multi-stability caused by static asymmetric modes that are typically smaller than $\beta \sim 5°$ (see chapter 7). As a matter of facts, the 35°-slanted Ahmed body is not subjected to static asymmetric modes in the sense of Grandemange *et al.* (2013*b*). This indicates clearly that such characteristic dynamic could potentially be extended to real cars having a slanted rear window instead of a blunt base similarly to the Renault Mégane. This observation motivates the study conducted in this chapter. Moreover, both the lift and the drag around the critical angle have very similar behaviors to those highlighted in this chapter. From the provided flow visualizations, reattachment also occurs symmetrically on the whole width of the body. Although the multi-stable dynamics is not reported, the two flow topologies can also be observed in Zafer & Haskaraman (2017) for a 35°-slanted Ahmed body, subjected to reattachment under yawing conditions. For a body aligned with the flow, Tunay *et al.* (2014) observe flow separation for slant angles larger than 30°. An efficient active flow control technique to avoid the flow separation on the slant is investigated in Kim *et al.* (2016). The authors use a slant with an adaptable angle in order to control the flow separation and avoid the hereabove discussed detrimental consequences on drag.

8.3.2 Impact of wake multi-stability on the aerodynamic loading of real vehicles

The lift is impacted by the modification of the base pressure distribution and bistability generates lift fluctuations between two limit values corresponding to stable configurations at close yawing angles (figure 8.5*a*). The lift increase observed here is expected because of the formation of a large depression attached to the slanted rear window which obviously will contribute to the total lift through the vertical component of the suction. With respect to the detached state, the lift coefficient increase ranks of about 10%. This peculiar behavior is very detrimental to the vehicle's stability, especially at high driving speeds. As to the mean drag coefficient C_x, the large depression created by the flow reattachment leads to a sensitive increase of about 5%. At the car's scale, this is considerable as it would result in more than 2% of fuel's consumption increase. Besides, the multi-stable dynamics leads to large force fluctuations.

A similar increase of the drag related to base suction is also reported by Tian *et al.* (2017) for a 25°-slanted Ahmed body when the flow is attached *versus* a controlled case leading to flow separation. As regards real cars, Hucho (1978) reports that, for slant angles larger than about 25° as it is the case for the Mégane, the drag of the squareback regime, corresponding to a detached wake, is smaller than that of the fastback attached regime; the gain can rank up 10% with respect to the most detrimental configuration.

Regarding the increase of the drag coefficient after the reattachment, it is large compared to the usual performances of active flow control that could be implemented on a real vehicle. The typical drag reduction on a simplified geometry – squareback Ahmed body – is of the order of $5-10\%$ (Barros *et al.*, 2014; Li *et al.*, 2016). This means that even advanced drag reduction techniques applied to a real vehicle could barely compensate the increase caused by flow reattachment and shows clearly that one would had better avoid it than try to reduce drag afterwards.

8.4 Concluding remarks

The wake flow behind a hatchback vehicle whose Reynolds number is of the order of 10^6 has been characterized with aerodynamic forces and base pressure measurements. The lift and the vertical base pressure gradient were successfully used to detect wake multi-stability, in particular thanks to brutal changes or sudden increases in their fluctuations. Increasing the yawing angle β would eventually lead to the formation of a strong depression attached to a vehicle whose pressure distribution is almost uniform in the absence of yaw as the Renault Mégane. A critical angle at which the wake fluctuates between the detached and the attached configuration resulting in fluctuations of both the lift and the drag is identified.

This chapter highlights the importance of design optimization when massive flow reattachment might occur, *i.e.* for hatchback or fastback vehicles. In particular, the influence of cross-wind conditions has to be taken into account as it is almost always present in real driving and has large consequences on both the drag of the car, thus reducing its fuel efficiency, but also on the lift ergo modifying its stability. The 5% drag increase in such case is considerable with respect to the targeted benefits of optimization as, on fundamental geometries such as the Ahmed body, the use of a base cavity indeed yields a maximum of 8% drag reduction (see appendix B). Nowadays, a commonly implemented solution is the use of lateral spoilers around the rear window which prevent the wake separation point from moving towards the centerline of the vehicle and thus from reattaching on the window with the detrimental consequences identified here.

CHAPTER 9

Conclusion and perspectives

This chapter concludes this manuscript with a general synthesis, where the main results exposed in Parts I and II are presented with a broader view in § 9.1. Afterwards, § 9.2 proposes some possible future works and opens new follow-up perspectives related to the results but also unanswered questions of this thesis.

Contents

9.1 General synthesis **221**
9.2 Perspectives and possible future work **222**

9.1 General synthesis

In this work we examine the dynamics of the turbulent unstable wake of flat-backed Ahmed bodies and highlight the relationships between these dynamics and the aerodynamic loading applied to the model in ground proximity for different base aspect ratios, with boat-tailed afterbodies and varying the model's inclination. We extend the results to real vehicles with blunt afterbodies and whose wakes are also subjected to a static instability. The context of the study is introduced in chapter 1 in which we present some of the specific issues related to full- and to model-scale testing in the framework of automotive industry. A literature review provides the necessary background on the static instabilities of the turbulent wake of flat-backed Ahmed bodies and on their dynamics with a detailed description of their origin in a laminar bifurcation and a highlight on the two kinds of wake asymmetries reported in previous research works. Afterwards, the experimental setup and procedures of the present work are thoughtfully described in chapter 2.
Part I of this manuscript presents our work on flat-backed Ahmed bodies. The main results of each chapter are summarized below.

- The mean flow around the squareback Ahmed body is described in chapter 3. In the test conditions, no significant flow separation or unsteadiness is identified at the forebody. The mean wake and the corresponding base pressure distributions are characterized in the vicinity of the ground.

- The y- and z- wake instabilities identified in Grandemange *et al.* (2013*a*) are extensively studied in chapter 4 varying the body's inclination. The ground stabilizing effect is retrieved for the y-instability with a threshold above which the dynamics is driven by the static asymmetric wake modes; the wake states are then identified with different dynamics depending on the body's inclination. The key result of this chapter is that, regardless of the type of instability and of the considered afterbody, the additional cross-flow force coefficient due to the static instability is estimated to 0.02 compared to that of the equivalent stable flow conditions. This is a substantial contribution since it represents about 7% of the drag coefficient, the major aerodynamic force component. This additional cross-flow loading is directly deduced from the wake dynamics and orientation for which a predictive model is derived depending on the body's alignment.

- The consequences of boat-tailing the afterbody on the wake dynamics and on the aerodynamic loading are investigated in chapter 5. In this chapter, the major contribution regards the ability of the boat-tails geometry to control the global wake dynamics both in terms of orientation and fluctuations. Different main configurations are identified: lock-in, bi-stable y-instability, bi-stable z-instability and periodic mode (vortex shedding) in the z-direction. The drag effectiveness of each geometry is also assessed and we show that the contribution of the periodic wake mode is higher than that of the static instability. Further drag reduction is obtained with a three-dimensional boat-tail for which the contribution of the instability to the aerodynamic loading is reduced by nearly a factor of two although the wake is still subjected to the y-instability.

- Chapter 6 offers perspectives to the first part of the manuscript. We present some preliminary piece of work aiming at conducting stability analyses on the wake of the Ahmed body. One important result is that steady Reynolds Averaged Navier

Stokes simulations might be a candidate for an estimate of the *basic flow* without the instability.

Part II of this manuscript deals with real vehicles and aims at extending the results of Part I to industrial geometries but also to assess a different case of wake multi-stability observed on a real car.

- Chapter 7 focuses on minivans aerodynamics through the extensive study of four vehicles' wakes. The existence of a static wake instability is definitively proved when a bi-stable dynamics is identified under yawing or in pitching conditions. This wake instability is consequently responsible for most of the vertical asymmetry observed in the wake orientation and base pressure distribution in normal driving conditions for all investigated vehicles (Citroën Berlingo, Renault Kangoo, Peugeot Partner and 5008). The most important contribution of this chapter is that the results obtained with the Ahmed body subjected to the z-instability are directly transferable to real vehicles. We find that the contribution of the wake instability to the cross-flow loading is also of the order of 0.02 in terms of force coefficients. Additional parameters such as the air-intake system, the underbody roughness or perturbations have been identified as potential actuators for the wake state selection.

- Finally, chapter 8 presents in the industrial context an alternative to wake multi-stability to the static instability reported in chapter 7. A bi-stable wake behavior is observed during the transition between two wake configurations whose characteristic aerodynamic loadings are strongly different. Unlike previously studied cases, this phenomenon that appears at much larger yaw angles is ascribed to an intermittent turbulent flow reattachment over the vehicle's rear window.

9.2 Perspectives and possible future work

The deeper understanding of the dynamics of bluff bodies' turbulent wakes subjected to a static instability originating in a laminar bifurcation at low Reynolds number proposed in this work opens a broad field for new perspectives, with remaining unanswered questions and new opportunities for flow control aiming at drag reduction, both for fundamental and industrial geometries. This work has a wider impact than just for automotive aerodynamics since the wake asymmetry is a general feature of bluff bodies at high Reynolds numbers. Some specific items that could be addressed following on from this work are provided below.

- *Stability analyses of the wake.*
  This work provides the early steps of a global stability analysis of the turbulent wake of the Ahmed body. If the RANS simulation provides the *basic flow* and could therefore be considered as an objective function of control strategies, it is not yet proved that the unsteady RANS actually contains the instability. Being able to demonstrate so would constitute a breakthrough for numerical studies in particular since URANS cases are much less resource demanding than the corresponding Large Eddy Simulations (LES).

- *Real-time cross-flow aerodynamic loading adaptation.*
  The cross-flow aerodynamic loading can be deduced from the instantaneous base pressure gradient which can offer a strategy of control. As a matter of fact, if the side force might not be considerable since the minivans are subjected to a static z-instability, the lift is directly depending on the instantaneous wake state. Since it impacts the vehicle's stability, especially at high driving speeds, one may imagine that control could be performed *simply* by adjusting the wake state.

- *Favoring low-drag wake states.*
  Even if some aerodynamic appendices are now installed on series cars such as side spoilers next to the rear window, spoilers, diffusers or boat-tailed shapes, there is a possible improvement in favoring the most efficient wake state, either by preventing the other from appearing either by retrieving the "optimal" one if a reversal were to occur. This requires an instantaneous diagnosis of the wake state that could be performed, as shown in this work, by well-chosen base pressure measurements. We showed for the simplified geometry that the bi-stable dynamics actually leads to lower base suction values because the unstable – drag optimal – wake solution is explored during the reversals. Since a similar conclusion can be drawn on some vehicles, favoring the wake equilibrium and thus the bi-stable dynamics could also be a solution to decrease drag, at least for some operating points.

- *Suppression of the static instability: towards a symmetric wake.*
  Despite all our efforts, we were not able to remove the wake static instability except for two cases: the use of a base cavity and the periodic wake mode which is even more detrimental to drag. This constitutes one of the major challenges that the automotive industry will most likely have to face in the upcoming years in view of our results proving that SUVs and minivans wakes are also subjected to a static instability. Removing it might help improving the vehicles' range and efficiency but also might yield a more simple physics to predict the aerodynamics loading with shape optimization.

Part III

Appendices

APPENDIX A

Software for unsteady pressure measurements

This appendix presents the motivations as well as the procedure used for developing a custom LabVIEW software dedicated to unsteady pressure measurements with the Scanivalve ZOC33 scanner used with the GLE/SmartZOC200 electronics described in § 2.2.1. The acquisition procedure is also detailed, in particular as regards the calibration and offset correction procedures. This appendix is based on a National Instrument User Article (Bonnavion et al.*, 2018) co-written with Aurélien* JOLY *(PhD Student, EDF-ENSTA ParisTech) in the framework of our collaboration for testing and improving the test software.*

Contents

A.1 Motivations 228
A.2 Description of the solution 228
A.3 Results, advantages and future developments 229

A.1 Motivations

During the wind-tunnels tests, we aim at being able to acquire but also quickly post-process data in order to adapt instantaneously the test program. A real-time analysis might indeed be needed to adapt the experiment to the observed phenomena but also to check the accuracy of the results. The aim of the developed program is to provide a real-time visualization tool which can be easily tuned depending on the application. In this aim, we developed an effective software for the treatment of unsteady pressure measurements obtained by means of the Scanivalve ZOC33 scanner used with the GLE/SmartZOC200 electronics (details may be found in § 2.2.1 on page 22) during wind tunnel test campaigns.

One of the challenges is to be able to acquired and treat data measured by 32 to 64 pressure sensors at a frequency of $100\text{ Hz} \leq f_e \leq 200\text{ Hz}$. In addition, the program should be adapted for in-house calibration in order to avoid long unavailability periods when pressure scanners have to be send to the manufacturer for calibration.

The software is developed keeping in mind that it will be used in several wind tunnels dedicated to teaching and research but also in industrial facilities (GIE-S2A) by different users, with different scanners and for different applications among which:

- Study of the wake of real or simplified road-vehicles with applications to drag reduction (present work),
- Experimental study of the fluid forces on nuclear plant components,
- Experimental study of the global aerodynamic loading on solar farms.

A similar program dedicated to the GLE/SmartZOC100 electronics was preexisting but the conception of both software is different since the communication with the previous electronics is established using an Ethernet connection – based on a TCP/IP protocol.

A.2 Description of the solution

A software (*Smart-Line Management Suite*) was furnished with the electronics of the scanner by the manufacturer. Although it is able to handle communication, settings and acquisition with the scanner, it does not allow the export of raw measurement data. In fact, data could only be exported in engineers' units such as *psi* or alternately converted into *Pascals*. Data are then exported into an Excel output file generated after each run, which consequently prevents from real-time visualization and processing.

The software must be easily tunable so that it can be used not only with different scanners but also for different applications which may have different needs of visualization (line of sensors *vs.* pressure map, different sensors…) but also of treatment (computation of gradients, filter…). We want to stick on the furnished material (scanner, electronics with USB connection) and to be able to adjust the settings (acquisition frequency, number of enabled channels, data format) directly from the acquisition suite. The communication protocol of the electronics must therefore be respected.

The communication with the electronics is made owing to a native protocol of LabVIEW called VISA which simulates a COM serial port from the USB connection. Note that this method requires the installation of a FTDI driver on the computer so that the electronics is associated with a serial port and not identified as a USB peripheral. The user must send strings formatted according to the communication protocol. They are tipped with the keyboard – in text format so that the user can actually understand them – and then converted into hexadecimal strings. Start and stop orders for the acquisition are send in a similar way but benefit from buttons in the user interface.

During the acquisitions, data is received on the fly. It is then cut in data frames composed of an identifier and of the corresponding pressure data (either formatted in engineering unit, either raw data depending on the settings). The frame length depends on the number of channels of the pressure scanner. They are read one after the other by another VISA instance. Interpretation is then made separately for each of the channels and for the identifier. It depends on the format of the data (2 bytes for the identifier, 4 for each of the channels). To enforce a correct cut and translation of the frames but also to ensure that all data has indeed been received, a several checks are performed. The first one is made on the two starting characters of the received string which must be *sd*. The second one is performed on the frame identifier which must indeed be incremented by one for each frame. In case not, acquisition is stopped and the user is informed.

The frames are cut so that the data can be related to each pressure channel. It is then exported to a text file for post-processing. From § 2.2.1, the pressure is actually a pressure difference. Since the data is exported in raw format, it first needs to be converted in Pascals. In addition, there is an offset as for any acquisition system which must be substracted from the measurements.

The offset is corrected thanks to *No-Wind data* acquired during a certain amount of time – usually around 10 s – without free-stream flow. The average of which is subtracted channel per channel from the actual measurement to correct this offset. This operation is performed in raw data. Afterwards, a multiplicative constant is applied to the obtained value which yields the differential pressure in Pascal. This constant is specific for each channel and was determined during calibration[1].

A.3 Results, advantages and future developments

The implemented solution was tested in our lab. As of now, it has been used for about 40 teaching hours and for more than 150 hours of tests in the model-scale facility of the GIE-S2A. Measurements provided in this work are mostly acquired with this new software – all with the 64 channels sensor ZOC33 are. The software is currently being implemented on a test facility dedicated to the study of the fluid forces on nuclear plant components (PhD thesis of A. Joly). A screenshot of the user interface is given in figure A.1. The user interface was adapted to the needs of this thesis, with direct visualization of the base pressure distribution, of the base pressure gradients and of their histograms.

In addition, raw data allowed the self calibration of the ZOC33 pressure scanner in order to obtain directly the differential pressure in Pascals. Using our software, we set the offset correction to zero and the proportionality factor to one during this procedure by giving a manually written calibration file. Data is post-processed with Matlab to obtain the actual calibration table[2]. The procedure was made at the GIE-S2A for this thesis but a Furness Control device together with the pressure software were used by A. Joly for calibrating his ZOC33 pressure scanner.

During this work, we took the advantage of real time visualization of the data in order to adapt the experimental campaign to the results. The software has reached its final development step during which the potential users must define the tunable parameters – that they can change directly owing to commands – and the ones which should not be modified – and will be coded in hard.

---

[1] Calibration is described briefly in § 2.2.1 on page 22.

[2] Although it cannot replace the certified table obtained by the manufacturer, the results are close enough so that we can use our own calibration.

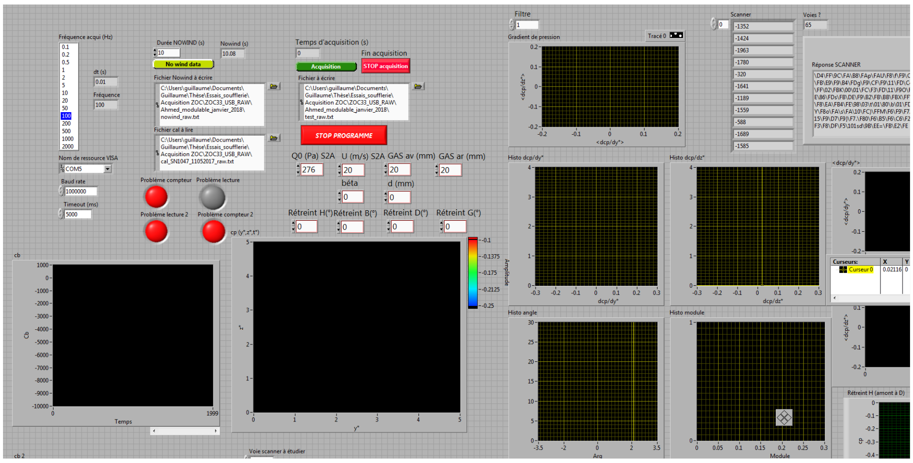

Fréquence acqui (Hz): 0.1, 0.2, 0.5, 1, 2, 5, 10, 20, 50, 100, 200, 500, 1000, 2000
dt (s): 0.01
Fréquence: 100
Nom de ressource VISA: COM5
Baud rate: 1000000
Timeout (ms): 5000
Durée NOWIND (s): 10
Nowind (s): 10.08
Fichier Nowind à écrire: C:\Users\guillaume\Documents\Guillaume\Thèse\Essais_soufflerie\Acquisition ZOC\ZOC33_USB_RAW\Ahmed_modulable_janvier_2018\nowind_raw.txt
Fichier cal à lire: C:\Users\guillaume\Documents\Guillaume\Thèse\Essais_soufflerie\Acquisition ZOC\ZOC33_USB_RAW\cal_SN1047_11052017_raw.txt
Temps d'acquisition (s): 0
Fichier à écrire: C:\Users\guillaume\Documents\Guillaume\Thèse\Essais_soufflerie\Acquisition ZOC\ZOC33_USB_RAW\Ahmed_modulable_janvier_2018\test_raw.txt
Q0 (Pa) S2A: 276
U (m/s) S2A: 20
GAS av (mm): 20
GAS ar (mm): 20
bêta: 0
d (mm): 0
Rétreint H(°): 0
Rétreint B(°): 0
Rétreint D(°): 0
Rétreint G(°): 0
Filtre: 1
Scanner: 0
-1352
-1424
-1963
-1780
-320
-1641
-1189
-1559
-588
-1689
-1585
Voies ?: 65
Réponse SCANNER:
\D4\FF\9C\FA\B8\FAp\FAU\F8\f\F9\C
\FB\E9\F9\B4\FDg\F9\CF\F9\11\FD\C
\FF\02\FBK\00\01\FC\F3\FD\11\F9O\F
E\86\FDs\FB\DE\F9\B2\FB\BB\FBX\FF
\F8\EA\FB4\FE\98\03\t\01\80\b\01\FD
Y\F8o\FA\s\FA\10\FC)\FFM\F6\F9\F7
15\F9\D7\F9}\F7.\F80\F6\B5\F6\C6\F2
F3\F8\DF\F5\101sd\9B\EE=\FB\E2\FE

Curseurs:	X	Y
Curseur 0	0.02116	0

No wind data
Fin acquisition
Acquisition
STOP acquisition
STOP PROGRAMME
Problème compteur
Problème lecture
Problème lecture 2
Problème compteur 2
cb
Cb
Temps
cp (y*,z*,t*)
z*
y*
Amplitude
Gradient de pression
Tracé 0
<dcp/dz*>
<dcp/dy*>
Histo dcp/dy*
dcp/dy*
Histo dcp/dz*
dcp/dz*
Histo angle
Arg
Histo module
Module
Rétreint H (amont à D)
cb 2
Voie scanner à étudier

Figure A.1 – Screenshot of the LabVIEW user interface.

APPENDIX B

Effect of a base cavity on the wake modes of the squareback Ahmed body at various ground clearances and application to drag reduction

This appendix focuses on the cavity effect identified in chapter 4. It aims at extending the results of Evrard et al. *(2016) to all ground clearances in the range* $c^* \in [0.050, 0.180]$ *and provides an explanation for drag reduction. Some of the results of this appendix were presented in Bonnavion* et al. *(2017*b*) and Bonnavion & Cadot (2018).*

Contents

B.1 Brief literature review **232**

B.2 Experimental setup **232**

B.3 Results **233**

B.3.1 Bifurcations of the wake operated by the ground clearance 233

B.3.2 Mechanism for drag reduction 234

B.4 Concluding remarks **236**

B.1 Brief literature review

A significant part of the drag experienced by bluff bodies is ascribed to the full flow separation at their base (Schlichting & Gersten, 2000). Since they are very common in engineering applications, it appears of major interest to investigate the possible drag reductions techniques that can be used without changing the general shape of the vehicles. As a consequence, this appendix is focused on a control technique which does not modify the overall length of the body and therefore the location of flow separation. Roshko (1993) shows that there exists a close relationship between the increase of base pressure and drag reduction. As reported by Viswanath (1996) and more recently by Choi *et al.* (2008, 2014), numerous techniques have been considered over the last decades.

One efficient mean is to use a base cavity as in Howell *et al.* (2012), García de la Cruz *et al.* (2017) or Evrard *et al.* (2016), in which the authors obtained up to 8% drag reduction. This case was recently reproduced numerically by Lucas *et al.* (2017) with a reduction of nearly 9.5%. Similar results are obtained by Morel (1979) or Viswanath (1996) with roughly up to 15% savings for axisymmetric bluff bodies or by Nash *et al.* (1963) for two-dimensional airfoils. Kruiswyk & Dutton (1990), Molezzi & Dutton (1995) and Dutton & Addy (1998) relate the base pressure increase with the remoteness of the recirculating vortex cores responsible for the low pressures in the wake area but also with a reduction of the recirculations' strength (Martín-Alcántara *et al.*, 2014). For axisymmetric bodies, Viswanath (1996) reports that a drag reduction is observed even for steady wakes. The stabilization of the wake by means of the base cavity reported in Evrard *et al.* (2016) is also found in the linear regime for an axisymmetric bluff body by Sanmiguel-Rojas *et al.* (2011); in the last paper, the authors identify a threshold of instability above Re $\sim$ 600 *vs.* less than Re $\sim$ 400 for the blunt based body, in agreement with the results of Grandemange *et al.* (2012*a*). A stabilization of the flow is also reported by Lorite-Díez *et al.* (2017) on an axisymmetric body and interpreted by the authors as an explanation for drag reduction. In addition of the paper by Evrard *et al.* (2016), Dutton & Addy (1998), Irving Brown *et al.* (2010) and Grandemange *et al.* (2015) investigated the cavity effect at the industrial scale with comparable results. Recently, Abikan *et al.* (2018) experimentally obtained 12% drag reduction with a base cavity of half the body's height as depth; however, the authors report only 4% drag reduction for their numerical study.

Regarding the effect of the ground clearance, a review is made in § 4.1 on page 49; the important result is that the wake instability directed by symmetry-breaking modes arises when the ground clearance of the model exceeds about 10% of its height, with a stabilization operated by the ground below this threshold (Grandemange *et al.*, 2013*a*; Cadot *et al.*, 2015*b*).

B.2 Experimental setup

The body considered in this study is the squareback Ahmed body without and with the base cavity ($d^*_{\text{cav}} = 0.285$) used in chapter 4. It is considered aligned with the incoming flow ($\beta = 0°$) and under no-pitch conditions ($c^*_f = c^*_r$, *i.e.* $\alpha = 0°$). The location of the pressure taps is identical and the base pressure gradients computed the same way.

For this appendix, we define the inhomogeneity of the base pressure distribution by means of its spatial standard deviation σ_{c_p}:

$$\sigma_{c_p}(t^*) = \left(< c_p(y^*, z^*, t^*)^2 >_{\text{base}} - c_b(t^*)^2\right)^{1/2} \tag{B.1}$$

where $< \cdot >_{\text{base}}$ denotes spatial averaging over the base. Its temporal mean is Σ_{c_p}. This quantity is used to quantify the overall asymmetry of the base pressure distribution.

B.3 Results

B.3.1 Bifurcations of the wake operated by the ground clearance

Figure 4.3 (on page 56) shows the response of the base pressure gradient to variations of the ground clearance c^* of the Ahmed body. We recall that two different regions were identified: a stable region ($c^* \leq 0.08$) and a region with a fully saturated instability ($c^* \geq c^*_S \sim 0.105$). The first one is characterized by a small modulus of the gradient ($g^*_r \simeq 0.12$) and phase lock-in at $\varphi = \pi/2$ while the unstable region has the typical features of the y-instability (Grandemange *et al.*, 2013*a*) with a larger modulus ($g^*_r \simeq 0.185$) and a stochastic wake dynamics (Rigas *et al.*, 2015; Brackston *et al.*, 2016) between the two preferred phase values of $\varphi = -\pi$ and $\varphi = 0$ corresponding respectively to left and right orientations of the wake (modes N and P).

In the stable regime, the wake is steadily symmetric in the horizontal direction. However, in spite of the symmetry of the body, a vertical pressure gradient is created by the vicinity of the ground with lower pressure levels at the bottom of the base than at its top (figure B.1*a*). When the instability is present and saturated, the typical behavior corresponds to that of the baseline (§ 4.3.1.1 on page 54) with the two mirror mean base pressure distributions $C_p(y^*, z^*)$ associated with the wake modes reproduced in figure B.1(b, c).

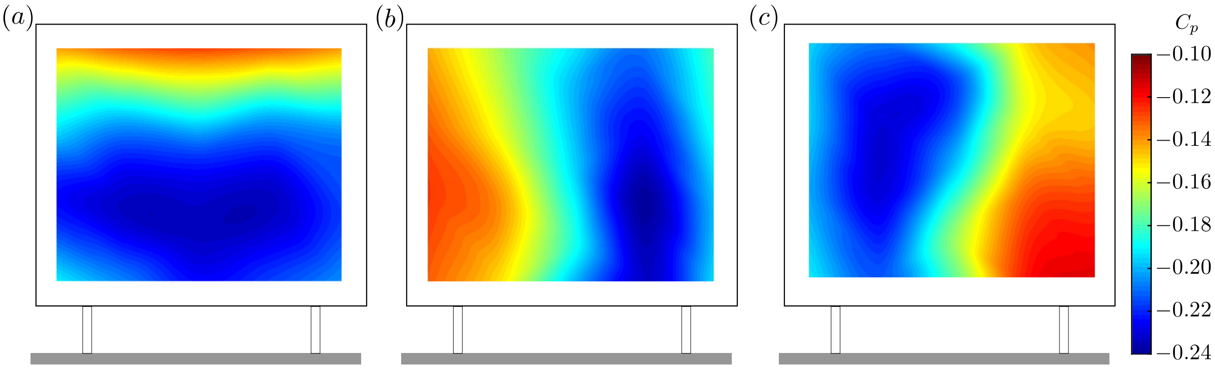

Figure B.1 – Mean base pressure distributions $C_p(y^*, z^*)$ of the squareback Ahmed body ($\alpha = \beta = 0°$). (a) Stable flow ($c^* = 0.060$). Conditionally averaged base pressure distributions $C_p(y^*, z^*)$ for mode N of the wake (b) and for mode P of the wake (c) at $c^* = 0.168$.

The same experiment reproduced with the base cavity at the body's base shows that the bifurcation around $c^* \simeq 0.08$ is suppressed (figure 4.13*a* on page 65). As a consequence, the modulus of the gradient is significantly attenuated over the whole range of ground clearances considered and is almost constant around $g^*_r \approx 0.06$, which represents a reduction by respectively 50% and 65% with respect to the near ground and far ground configurations. Phase lock-in at $\varphi \simeq \pi/2$ is still observed in figure 4.14(d) (on page 65) for very small clearances ($c^* \lesssim 0.07$) but the phase is poorly defined otherwise due to the symmetrization of the flow.

The associated mean base pressure distributions $C_p(y^*, z^*)$ for the near and far ground regions are given in figure B.2. The scale is the same as for the squareback case (figure B.1) and clearly emphasizes a base pressure increase. The vertical base pressure gradient can still be observed for the smallest clearance though. In the latter case, the horizontal asymmetry lies in the imperfections of the setup. A general symmetrization of the wake is obtained as in Evrard *et al.* (2016); Lucas *et al.* (2017), the results of which can consequently be generalized for $c^* \geq 0.075$, *i.e.* for the whole unstable regime. Below this threshold, the phase-locking phenomenon at $\varphi = \pi/2$ resulting from the stabilization of the wake by the ground is conserved; reflectionnal symmetry-breaking modes (RSB) of the wake were not present (Cadot *et al.*, 2015*b*) and the cavity has consequently a geometrical effect only.

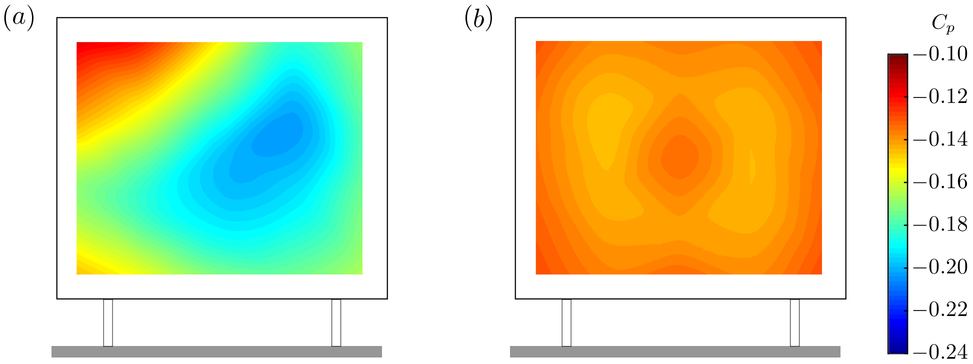

Figure B.2 – Mean base pressure distribution $C_p(y^*, z^*)$ of the flat-backed Ahmed body with a base cavity ($\alpha = \beta = 0°$). (*a*) Near ground regime ($c^* = 0.060$), (*b*) far ground regime ($c^* = 0.168$).

These two new regions will then be compared to the unbifurcated and the bifurcated regions of the squareback geometry in terms of base drag. In a previous work (Evrard *et al.*, 2016), drag reduction by nearly 9% was obtained for $c^* = 0.111$. The authors associated this gain with the removal of the static asymmetric modes of the wake. In this appendix, we suggest an additional plausible explanation for the drag reduction mechanism.

B.3.2 Mechanism for drag reduction

The mean base suction C_b and the mean drag coefficients C_x as a function of the ground clearance can be found in figure B.3(a, b). Both curves show a decrease as the wake stabilization operated by the ground vanishes ($c^* \simeq 0.08$) and then a linear increase that the model's supports are responsible for (linear increase of their frontal area with the ground clearance). The trends are strictly identical without or with the base cavity.

The relative gain with (passive) control is given as a function of the ground clearance in figure B.3(c). It can be observed that the beneficial effect of the base cavity is present regardless of the ground clearance. Above the threshold $c^* = 0.08$ and compared to the squareback geometry, drag reduction by 8% is achieved almost regardless of the ground clearance. The mean base suction coefficient C_b decreases by 23.5% in average, which explains the reduction of the total drag. Below the threshold of instability and despite the stabilized wake, a gain of about $15-20\%$ in terms of base suction is reported corresponding to about $5-7\%$ for the total drag despite the absence of the wake reflectional symmetry-breaking (RSB) modes. With respect to the far ground regime, drag reduction efficiency is reduced though; the vicinity of the ground stabilizes the flow around the body which explains the smaller reduction as the asymmetric wake modes are already removed in the squareback configuration. This indicates clearly that the cavity has an additional effect on the flow. Interestingly, the maximum efficiency of the device for both the drag and the base suction is reached during the transition towards the unstable wake for $c^* \simeq 0.08$.

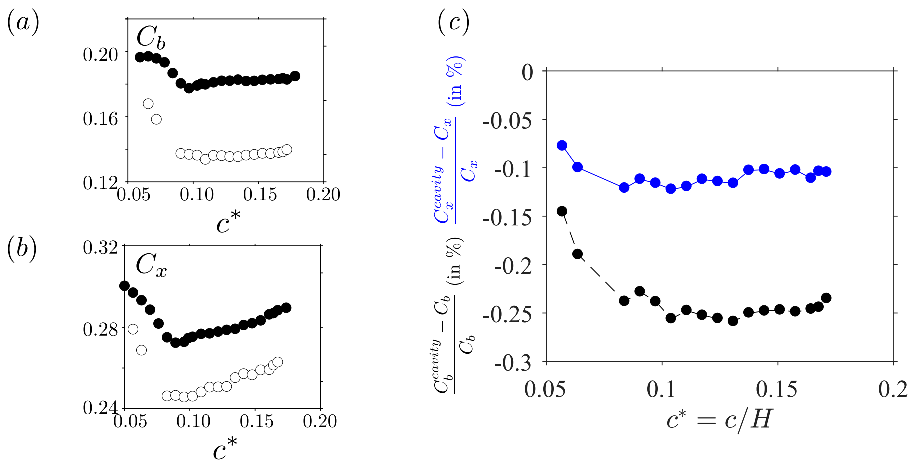

Figure B.3 – Drag reduction and base pressure recovery with the base cavity: (*a*) Mean base suction coefficient C_b of the Ahmed body plotted as a function of the ground clearance c^* for the squareback (filled symbols) and the base cavity (empty symbols) geometries, (*b*) mean drag coefficient C_x. (*c*) Relative reduction for the controlled case *vs.* ground clearance c^*: mean base suction C_b (black dashed line), mean drag C_x (blue continuous line).

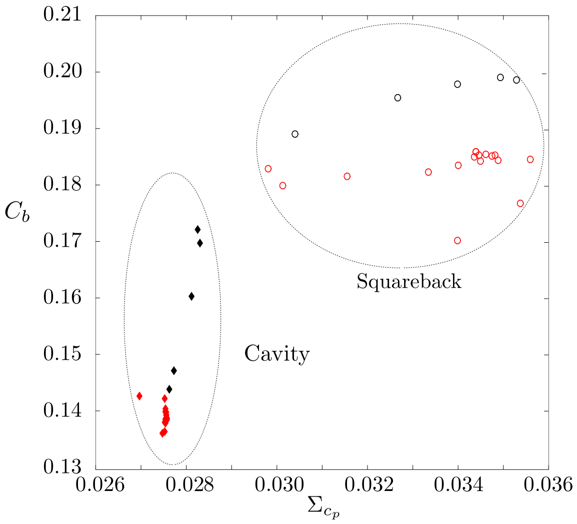

Figure B.4 – Mean spatial standard deviation of the wake of the Ahmed body Σ_{c_p} defined in equation (B.1) plotted as a function of the ground clearance c^* for the squareback (empty circles) and the base cavity (filled diamond shape). Black points are below the threshold at $c^* = 0.080$, red points above.

In order to investigate the relationship between the wake inhomogeneity and the body's drag, the mean spatial standard deviation of the wake Σ_{c_p} defined in equation (B.1) is introduced. The mean base suction coefficient C_b is plotted against Σ_{c_p} in figure B.4 for all considered configurations. It turns out that two groups of points can be clearly identified. Some are associated with both high base suction and high inhomogeneity of the wake: all of them are related to the squareback geometry. The second group has lower base suction; these points correspond to the case with the cavity. The inhomogeneity of the wake is spatially coherent and represents in fact its asymmetry. In short, the larger the asymmetry of the wake, the bigger the base drag. The asymmetry of the wake is reduced by the base cavity, which partly explains drag reduction. Nonetheless, this is not the only implied mechanism as that of the stable case is also lowered.

In addition to the removal of the static asymmetric wake modes assessed by the symmetrization of the wake, the geometrical modifications introduced by the cavity indeed have a beneficial effect on drag. The dead water area (recirculating bubble) is simply elongated[1]. Mean Particle Image Velocimetry fields shown in figure 4.15 (page 66) with the cavity compared to those of figure 4.11 (page 66) for $d^*_{\mathrm{cav}} = 0$ show that the wake closure in the mean flow slightly moves downstream in presence of a base cavity, in agreement with Evrard *et al.* (2016) and Lucas *et al.* (2017). In addition, the streamlines enter the cavity and are therefore elongated in the upstream direction as well. The flow separation points on the body are not affected by the geometry. An additional volume $\mathcal{V}^* = d^*_{\mathrm{cav}} \times (H^*_b - 0.067) \times (W^*_b - 0.067)$ is consequently allocated to the flow as the cavity is created. Since H^*_b and W^*_b are imposed, the associated characteristic dimensions of the recirculating bubble are unchanged. As a consequence of their elongation, the inner streamlines' curvature is reduced. It follows that pressure increases at the base of the model. The base suction is thus lowered and consequently the total drag. The contribution of the cavity walls to drag is negligible since the overall dimensions of the body remain unchanged.

B.4 Concluding remarks

A central rotation of the wake can be observed and phase locking and unlocking phenomena are responsible for the change of the wake topology between the stable and the unstable flow regimes. The effect of a base cavity is generalized to both cases with a minimal gain of about 5% on drag. The base cavity symmetries the flow and therefore reduces the asymmetry-related drag but also elongates the recirculating area at the base of the model which allows for a bigger pressure recovery. This passive flow control device is already used on trucks and could be optimized (size, shape) to achieve a most efficient drag reduction, which in addition depends on the considered cavity depth (Evrard *et al.*, 2016; Lucas *et al.*, 2017).

Furthermore, even if this appendix is focused on the cavity effect at various ground clearances, the same analysis could be performed varying the yaw or the pitch angles from the baseline. One can observe in figure 4.17 (on page 68) that the same benefits resulting from the use of the base cavity in terms of drag reduction also exist for those configurations.

---

[1] The beneficial effect of lengthening the recirculation length is shown in the potential flow simulations presented in chapter 5, § 5.2.3.

APPENDIX C

Sensitivity analyses of the flow around boat-tailed flat-backed Ahmed bodies

This appendix presents sensitivity analyses towards the ground clearance and the body's alignment (yaw and pitch angles) with different boat-tailed afterbodies, similarly to what is done for the squareback geometry in chapter 4. More particularly, it aims at assessing the influence of the boat-tailed afterbody on the wake dynamics and on the base pressure gradient responses to body's misalignment and ground clearance changes through the three typical configurations identified in § 5.4. The result section § C.2 is divided in three parts. A first sensitivity analysis is performed in § C.2.1 for an afterbody subject to the y-instability in order to compare it with the squareback case of chapter 4. Three geometries with the same angles are also compared. Afterwards, the three-dimensional boat-tailed case is considered in § C.2.2. Finally, the same analysis is reproduced for an afterbody subject to z-periodic wake fluctuations in § C.2.3. The mean and fluctuating aerodynamic loading is also investigated during the analyses. A discussion follows in § C.3 about the instability, that is found to be quite similar to that with a squareback afterbody.

Contents

C.1 Setup **239**

C.2 Results **239**

C.2.1 Sensitivity analyses with a y-unstable boat-tailed configuration ($\theta_T = 7.5°$, $\theta_B = 5°$) and three-different geometries 239

C.2.2 Sensitivity analyses with the 3D boat-tailed configuration 251

C.2.3 Sensitivity analyses on a boat-tailed configuration triggering the periodic wake mode 257

C.3 Discussion **260**

C.4 Concluding remarks **264**

C.1 Setup

The flat-backed Ahmed body considered in this appendix and fully described in § 2.4 is equipped with the modifiable afterbody introduced in chapter 5 and described in § 5.3. The experiments are conducted in the model-scale wind-tunnel of the GIE-S2A, details about which are provided in § 2.1.2.

The investigated cases are chosen after the results of chapter 5; in particular, we consider two y-unstable configurations and a periodic wake. From the baseline chosen at $c^* = 0.168$ with the body aligned with the incoming flow (see chapter 5), we change the yaw angle β in $-2° \leq \beta \leq 2°$ and the pitch angle α in $-2° \leq \alpha \leq 2°$[1]. Only small variations are considered to avoid flow separation and for comparison with the squareback geometry investigated in chapter 4 (see in particular § 4.3.1). The three parameters of study are varied one by one. Sensitivity analyses are performed to identify the different branches of the solutions for the base pressure gradient $\hat{g}^*$, described both in Cartesian and in polar forms. The aim of this appendix is to be able to identify the branches and the switch dynamics. The aerodynamic loading is also considered in particular as we want to assess whether the contribution of the instability is similar to the squareback afterbody.

C.2 Results

An afterbody subject to the y-instability is first studied in § C.2.1; its 3D configuration – with side boat-tails – is then considered in § C.2.2. Finally, the same analysis is reproduced for an afterbody subject to a periodic wake mode in § C.2.3.

C.2.1 Sensitivity analyses with a y-unstable boat-tailed configuration ($\theta_T = 7.5°$, $\theta_B = 5°$) and three-different geometries

The first considered configuration is characterized by $\theta_T = 7.5°$ and $\theta_B = 5°$, with long circle-arcs shaped boat-tails ($\ell_B^* = 0.537$) located at the top and at the bottom of the afterbody. Its sides are not modified compared to the squareback. This case was associated with a y-wake instability having a characteristic time scale of about $100 - 500$ t^* (see figure 5.28*a* on page 130).

We first focus on the destabilization of the flow operated by the ground clearance c^* leading to the y-instability. In order to identify the instability onset and saturation clearances, we first perform a sensitivity analysis towards the ground clearance c^* of this boat-tailed model when aligned with the incoming flow ($\alpha = \beta = 0°$). We obtain the four sensitivity maps given in figure C.1($a - d$) representing the base pressure gradient's probability density function f normalized by its maximum. This experiment is similar to that of Grandemange *et al.* (2013*a*) for a squareback body with a width-to-height aspect ratio of $W^* = 1.351$ and to that of § 4.3.1.2 for $W^* = 1.174$.

The Cartesian components of the gradient g_y^* and g_z^* respectively shown in figure C.1(a, b) are very similar to those associated with the squareback geometry subject to the y-instability (see figure 4.3a, b on page 56). Starting from a single-branch solution around $g_y^* \simeq 0$, the pitchfork bifurcation on the y-component (figure C.1a) starts later around $c^* \simeq 0.105$ which means that, with respect to the squareback case, the transition is delayed. Similarly to the squareback, the vertical gradient component g_z^* shown in figure C.1(b) decreases continuously and stabilizes around $g_z^* = 0.05$ when the ground influence is suppressed. The non-zero value is a direct consequence of the two different boat-tail angles (see § 5.4). The full saturation of the instability is observed for $c_S^* \simeq 0.15$ since the modulus g_r^* (figure C.1*c*) stabilizes at a value of about twice that of the stable case. Because of boat-tails, it remains smaller than for the squareback though (figure 4.3*c*). The phase φ (figure C.1*d*) can be interpreted as a direct consequence of the wake matching to the geometrical vertical constraint g_z^* in addition to the imposed strength of the y-instability g_r^*. The two branches are not equally explored for all ground clearances which must be ascribed to a body's misalignment with respect to the incoming stream.

---

[1] The definition of both angles can be found in § 2.4 and in particular in figure 2.5 on page 29.

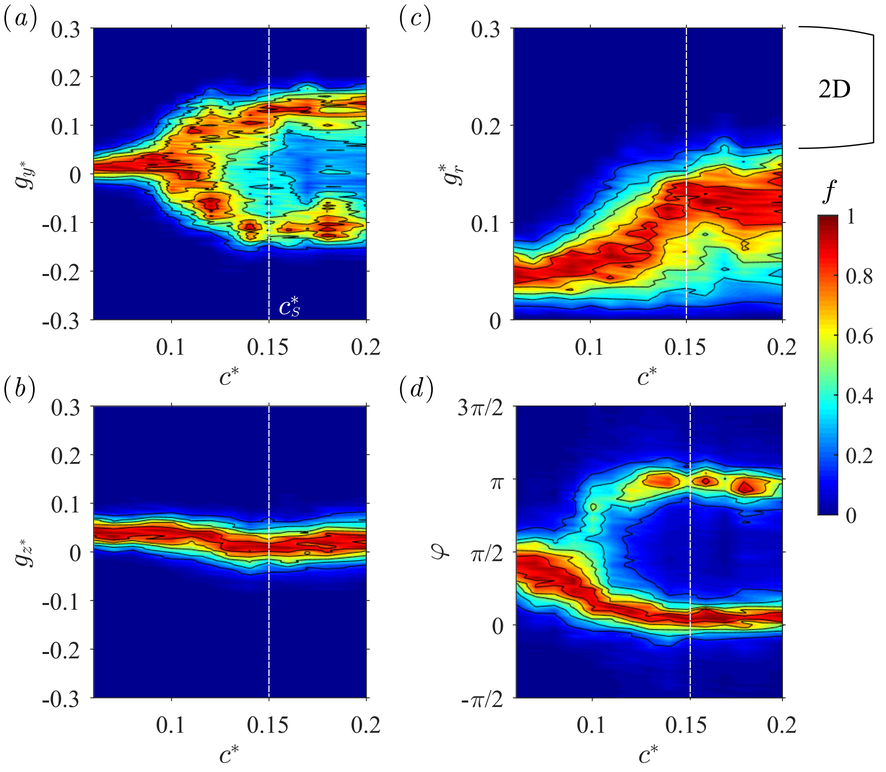

Figure C.1 – Base pressure gradient response to a variation of the ground clearance c^* for a y-unstable boat-tailed afterbody ($\theta_T = 7.5°$, $\theta_B = 5°$). Sensitivity maps: (*a*) $f(c^*, g_y^*)$, (*b*) $f(c^*, g_z^*)$, (*c*) $f(c^*, g_r^*)$ and (*d*) $f(c^*, \varphi)$. The clearance c_S^* (dashed line) is defined as the threshold of the saturated instability.

The dynamics of the bi-stable – and saturated – case at $c^* = 0.168 \geq c_S^*$ is briefly described in figure 5.28(*a*). We reproduce in figure C.2 the time series and associated Probability Density Functions of the modulus g_r^* and of the phase φ of the base pressure gradient $\hat{g}$. The modulus g_r^* (figure C.2*a*) only undergoes high-frequency fluctuations generated by the turbulence, which yields a centered single-peak although quite wide Probability Density Function (figure C.2*a*). The amplitude of the explored values is increased with respect to the squareback afterbody since very small modulus associated with phase jump are more likely to occur. The typical time-scale of the phase dynamics (figure C.2*b*) is modified by the boat-tails and reduced down to $100 - 500\ t^*$. It is mainly made of phase jumps with some phase drifts (continuous rotations of the wake). The quicker dynamics explains the larger imprints in the sensitivity maps as values resulting from phase drift have a higher exploration probability. Two most probable values ($\varphi \simeq 0$ and $\varphi \simeq \pi$) can be identified as confirmed by the two-peaks PDF plotted in figure C.2(*d*). They can be respectively associated with states P and N of the wake following the terminology of Grandemange *et al.* (2013*b*). One may notice that a slight deviation from $\varphi = 0$ and $\varphi = \pi$ can be observed since the two considered boat-tail angles are not equal thus creating a vertical base pressure gradient (figure 5.18).

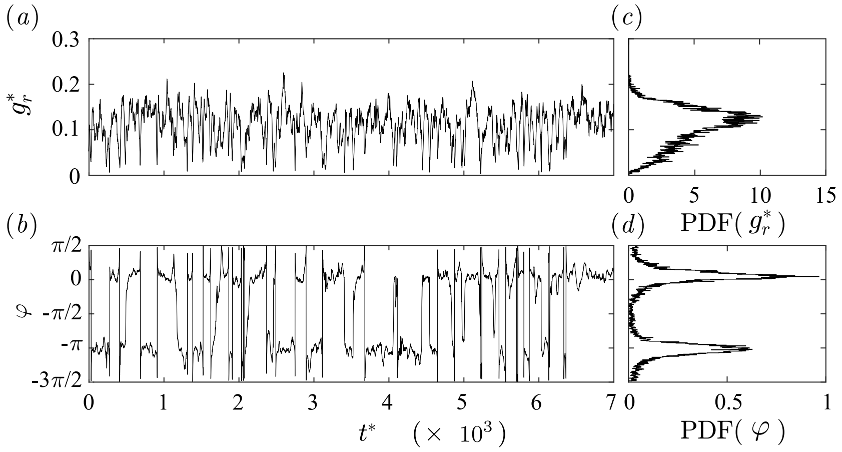

Figure C.2 – Modulus $g_r^*(t^*)$ (a) and phase $\varphi(t^*)$ (b) time series of the base pressure gradient with corresponding probability density functions $(c-d)$ for the baseline of the y-unstable boat-tailed afterbody ($\theta_T = 7.5°$, $\theta_B = 5°$).

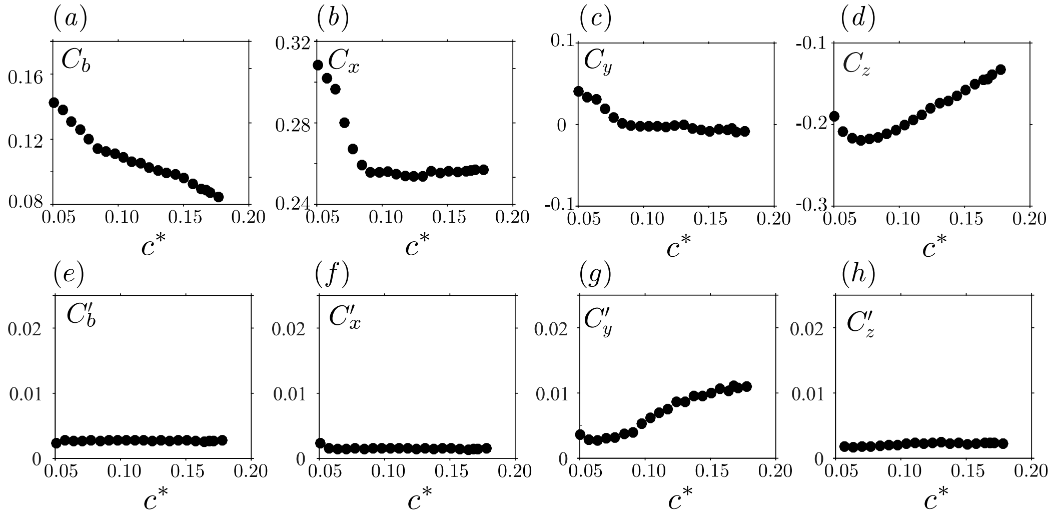

Figure C.3 – Aerodynamic loading applied on the body in the ground clearance sensitivity analysis: mean (top row) and fluctuating (bottom row) base suction (a, e), drag force (b, f), side force (c, g) and lift coefficients (d, h) *vs.* ground clearance for the y-unstable boat-tailed afterbody ($\theta_T = 7.5°$, $\theta_B = 5°$).

The impact on the aerodynamic forces is detailed below. Compared to the squareback case (figure 4.16*a* on page 66), the mean base suction C_b shown in figure C.3(a) decreases continuously. We recall that it is computed on the separated flow area only – vertical base – and does not take the boat-tails into account. As a result, it turns out that the ground vicinity minimizes the boat-tailing beneficial effect on base suction. This variation explains the plateau reached by the mean drag coefficient C_x in the unstable regime (figure C.3*b*) which does not increase despite the continuously larger model's supports frontal surface. The mean side force coefficients C_y is null in average consistently with the symmetry of the setup (figure C.3*c*). The mean lift C_z (figure C.3*d*) increases linearly with the ground clearance except for $c^* \lesssim 0.08$ but this effect might be created by the wires exiting the model and pushing it thus modifying the measured force. The fluctuations given in figure C.3($e-h$) are low for all coefficients except for the fluctuating side force C'_y which increases by one order of magnitude when the instability arises around $c^* \simeq 0.100$ in agreement with the results presented in chapter 4.

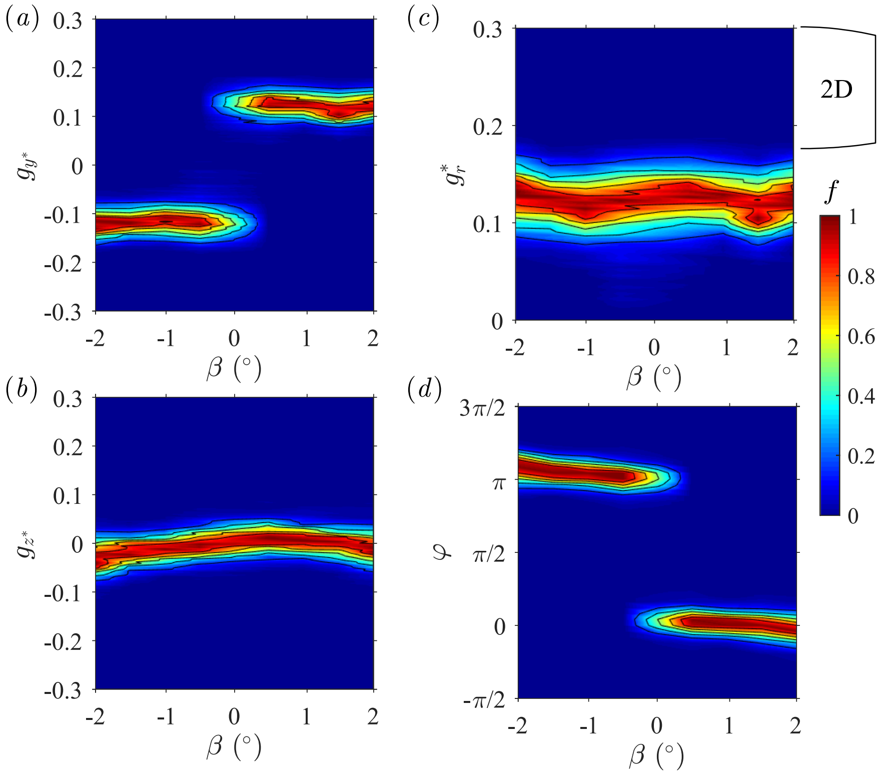

Figure C.4 – Base pressure gradient response to variations of the yaw angle β for a y-unstable boat-tailed afterbody ($\theta_T = 7.5°$, $\theta_B = 5°$). Sensitivity maps (a) $f(\beta, g_y^*)$, (b) $f(\beta, g_z^*)$, (c) $f(\beta, g_r^*)$ and (d) $f(\beta, \varphi)$.

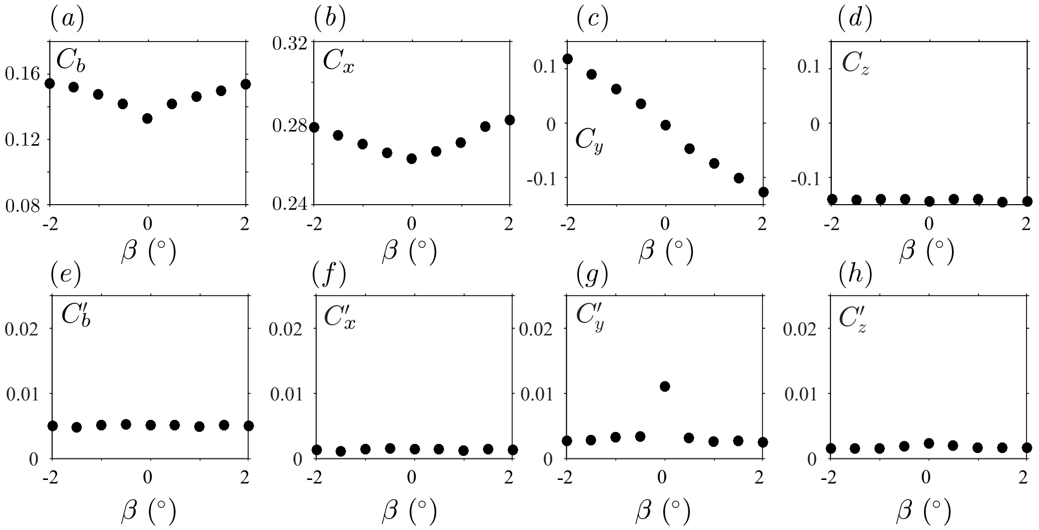

Figure C.5 – Aerodynamic loading applied on the body *vs.* yaw angle β: mean (top row) and fluctuating (bottom row) base suction (a, e), drag force (b, f), side force (c, g) and lift coefficients (d, h) for the y-unstable boat-tailed afterbody ($\theta_T = 7.5°$, $\theta_B = 5°$).

From the baseline described hereabove, the yaw angle β is modified, keeping the pitch to $\alpha = 0°$. The results are presented in the four sensitivity maps for the Cartesian and polar forms of the base pressure gradient $\hat{g}^*$ in figure C.1$(a - d)$. Similarly to the square-back geometry (figure 4.6 on page 58), a g_y^* discontinuous branch selection is operated by the yaw angle as can be observed in figure C.4(a). It consists in a phase jump as indicated in figure C.4(d). Although the horizontal base pressure gradient g_z^* should not be impacted by a change of the yaw angle of the model, figure C.4(b) shows a slight continuous variation which can be ascribed to the setup imperfections, in particular non-symmetric cable passage near the model's supports and free-stream wind deviation. The modulus g_r^* (figure C.4*c*) only undergoes a slight modulation because of these imperfections but is almost constant. Most importantly, it is not affected by the yaw angle thus showing that the wake asymmetry is not either. The phase shown in figure C.4(*d*) also presents the same deviation from the two expected values of $\varphi = 0$ and $\varphi = \pi$ corresponding respectively to states P and N of the unstable wake.

By analogy with the squareback afterbody, we expect the contribution of the y-instability to be only revealed by the mean side force C_y and therefore to observe that the lift C_z is an independent function of the yaw. The mean and fluctuating aerodynamic loading applied to the body is given in figure C.5 as a function of the yaw angle β. Similarly to the previous experiments, the mean base suction C_b (figure C.5*a*) and the mean drag coefficient C_x (figure C.5*b*) have a similar evolution, with a minimum when the body is aligned and an even increase with the pitch angle β. The imprint of the y-instability is clearly visible on the mean side force coefficient C_y plotted in figure C.5(*c*) in which it deviates the mean value from the linear evolution imposed by the geometry, similarly to what has been observed for the squareback afterbody in figure 4.18(*a*) on page 68. The mean lift coefficient C_z shown in figure C.5(*d*) is not affected by the yaw angle. Concerning the fluctuations plotted against the yaw angle in figure C.5($e-h$), the only identified crisis is on the side force coefficient when the body is aligned, corresponding to a bi-stable case.

Finally, the sensitivity of the base pressure gradient towards the pitch angle α of the model is investigated. The body is aligned with the flow ($\beta = 0°$) and no-pitch conditions correspond to the baseline. Figure C.6 gives the four sensitivity maps obtained during the analysis. The two branches of the horizontal base pressure gradient $g_y^* \simeq \pm 0.15$ shown in figure C.6(*a*) for the baseline case $\alpha = 0°$ merge into a single branch $g_y^* \simeq 0$ as the pitch is increased in magnitude ($\alpha \lesssim -1°$) for nose-down configurations. For nose-up cases ($\alpha > 0°$), the two branches persist up to $\alpha \simeq 2°$ from which unlocking starts to be observed. The vertical component of the gradient g_z^* plotted in figure C.6(*b*) shows a linear evolution towards the angle, with saturation for largely negative and largely positive pitches ($\alpha \lesssim -1.5°$ and $1.5° \lesssim \alpha$). The magnitude of the modulus g_r^* corresponds to an unstable case comparing figure C.6(*c*) to figure C.1, with a continuous increase. In fact, it reaches a maximum (around $\alpha \simeq 1.5°$, shifted from $\alpha = 0°$ because of the asymmetric boat-tailing and of the road effect) and decreases when a pitch angle is applied because of the adaptation phenomenon (§ 4.4.2). Nonetheless, no wake stabilization can be observed. The response of the phase φ during this sensitivity analysis given in figure C.6(*d*) shows that, not surprisingly, the two preferred solutions $\varphi = 0$ and $\varphi = \pi$ observed for the baseline continuously merge one towards the other until phase lock-in around $\varphi \simeq \pi/2$ for $\alpha \lesssim -1°$ occurs. For increasing positive pitch angles, *i.e.* nose-up configurations, the phase φ varies linearly and unlocking seems to start at the end of the studied range. The transition is continuous with respect to the pitch angle α.

The similar evolution of the mean base suction and of the mean drag coefficients (figure C.7a, b) shows that a minimum is reached just before lock-in occurs for $\alpha \simeq -0.5°$. The mean side force coefficient remains null regardless of the pitch (figure C.7*c*) while the lift coefficient is not affected by the y-instability (figure C.7*d*) since it is a linear function of the pitch angle α. Only the side force fluctuations C_y' (figure C.7*g*) present a crisis during wake bistability when the pitch angle is small.

To summarize, boat-tailing does not affect the sensitivity of the wake subject to the y-instability towards the yaw angle β compared to the squareback geometry described in § 4.3.1.3 and the response of the base pressure gradient is globally quite similar to the squareback studied in chapter 4.

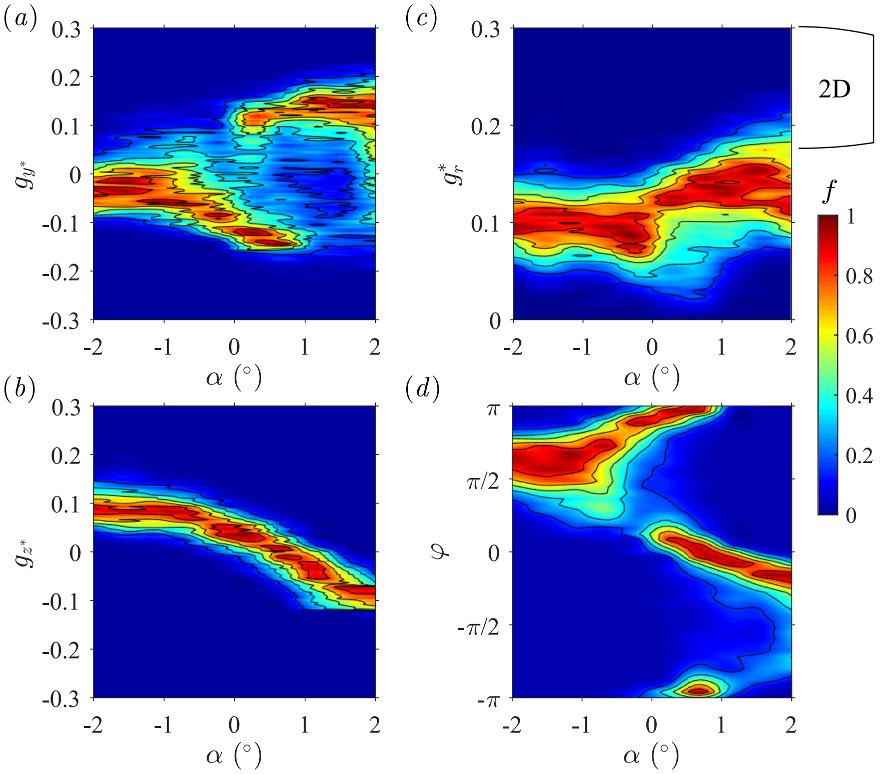

Figure C.6 – Base pressure gradient response to variations of the pitch angle α for a y-unstable boat-tailed afterbody ($\theta_T = 7.5°$, $\theta_B = 5°$). Sensitivity maps (a) $f(\alpha, g_y^*)$, (b) $f(\alpha, g_z^*)$, (c) $f(\alpha, g_r^*)$ and (d) $f(\alpha, \varphi)$.

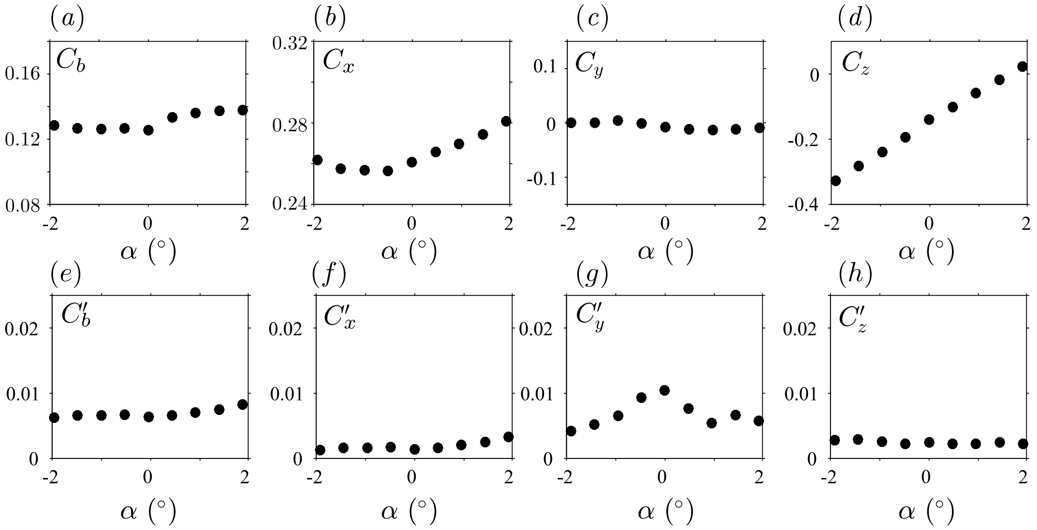

Figure C.7 – Aerodynamic loading applied on the body *vs.* pitch angle α: mean (top row) and fluctuating (bottom row) base suction (a, e), drag force (b, f), side force (c, g) and lift coefficients (d, h) for the y-unstable boat-tailed afterbody ($\theta_T = 7.5°$, $\theta_B = 5°$).

We showed that the only mean component of the cross-flow aerodynamic loading impacted by the instability is the side force coefficient C_y. The drag C_x is excluded from the analysis since, as far as we are concerned, the instability's contribution cannot be extracted directly from the data. The modification of the side loading is clearly identified in the yaw experiment as shown in figure C.8(a). The mean side force coefficient C_y^B for the *basic flow* without the instability is a linear function of the yaw angle β. One can indeed derive the following equation from a linear fit of each of the two branches of the side force coefficient shown in figure C.8(a):

$$C_y^B = -0.055 \times \beta \tag{C.1}$$

where β is expressed in degrees. This equation is strictly identical to equation (4.1) obtained for the squareback case, showing that the *basic flow* only presents few sensitivity to the afterbody's geometry. The coefficient computed from equation (C.1) is displayed as the red solid line in the figure. Similarly to equation (4.2), a relationship between the mean side force coefficient and the mean horizontal base pressure gradient can be derived:

$$C_y(\beta) = C_y^B(\beta) - \frac{G_y^*(\beta)}{6} \tag{C.2}$$

Equation (C.2) presents an excellent agreement with the experimental data as shown by the blue dashed line in figure C.8(a).

The mean additional contribution to the side force $C_y - C_y^B$ is plotted as a function of the yaw angle β in figure C.8(b) and compares well with $-G_y^*/6$. As a direct consequence, the mean side force coefficient C_y can be directly related to the mean horizontal base pressure gradient G_y^* and we write:

$$C_y(\beta) = C_y^B(\beta) - \frac{G_y^*(\beta)}{6} \tag{C.3}$$

The loading without the instability C_y^B does not fluctuate. As a result, we deduce the instantaneous expression of equation (C.3):

$$c_y(t^*) = C_y^B - \frac{g_y^*(t^*)}{6} \tag{C.4}$$

implying that:

$$C_y' = \frac{G_y^{*\prime}}{6} \tag{C.5}$$

Equation (C.5) is confirmed in figure C.8(c) by the correct agreement of the data.

Finally, since the mean lift coefficient C_z is not affected by the y-instability of the wake, the following equation holds regardless of the wake orientation:

$$C_z = C_z^B \tag{C.6}$$

The instantaneous fluctuations are then coming from the vertical base pressure gradient g_z^* and thus:

$$c_z(t^*) = C_z^B + \frac{{g^*}'_z(t^*)}{6} \tag{C.7}$$

implying that:

$${C_z}' = \frac{G_z^{*\prime}}{6} \tag{C.8}$$

A good agreement is found in figure C.8(d) between ${C_z}'$ and $G_z^{*\prime}/6$, justifying equation (C.8). In addition, these relations still hold for the pitch experiment except that we have $C_y(\alpha) = C_y^B(\alpha)$ but the fluctuations are still well predicted by equations (C.5) and (C.8) as shown in figure C.8(e, f).

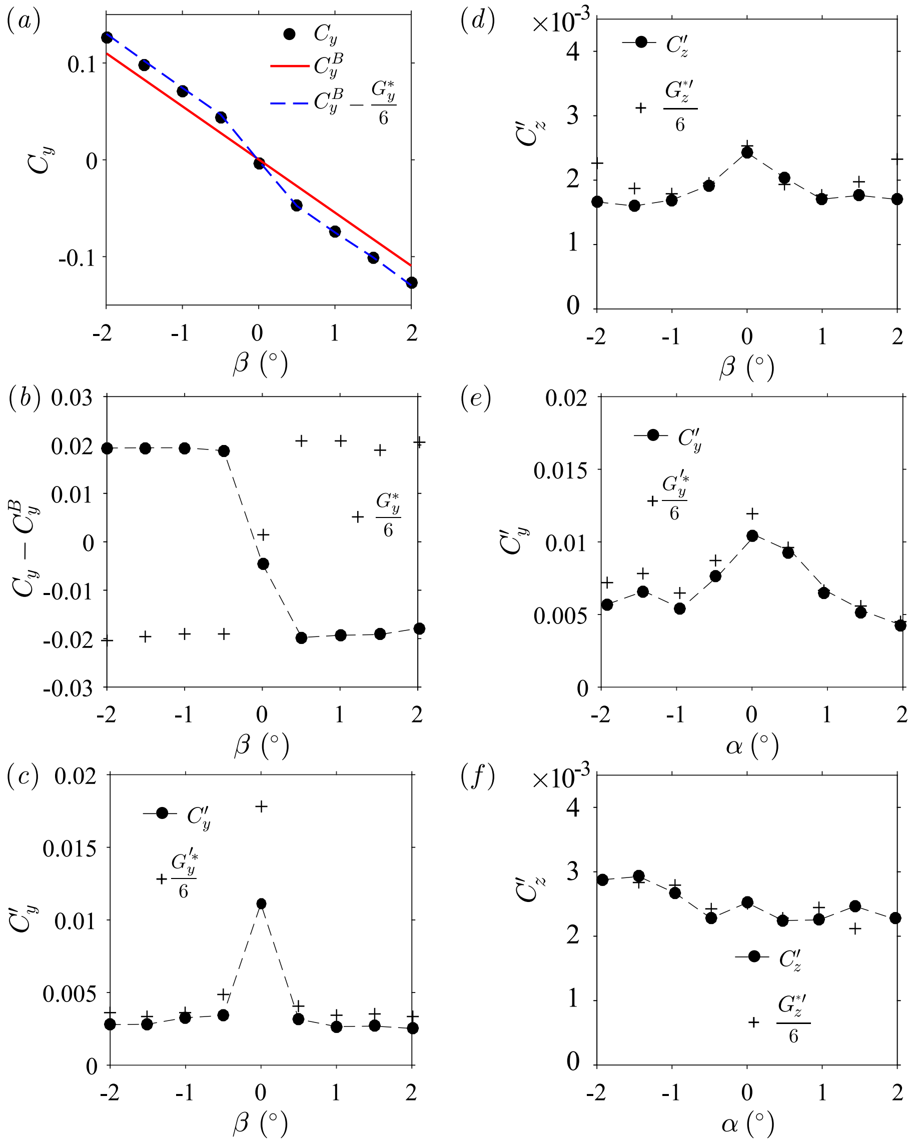

Figure C.8 – Sensitivity alignment experiments for the y-unstable case with boat-tailed body: (a) Measured force coefficient (symbols), *basic flow* coefficient (red line) and coefficient computed from equation (C.2) (blue dashed line, see text). (b) Mean contribution of the instability $C_y - C_y^B$ (filled circles) and mean horizontal base pressure gradient G_y^* (crosses). (c, d) Components of the fluctuating force coefficients C_y' and C_z' (filled circles) compared to the fluctuating base pressure gradients $G_y^{*\prime}$ and $G_z^{*\prime}$ (crosses) *vs.* yaw angle β. (e, f) Components of the fluctuating force coefficients C_y' and C_z' (filled circles) compared to the fluctuating base pressure gradients $G_y^{*\prime}$ and $G_z^{*\prime}$ (crosses) *vs.* pitch angle α.

The two other boat-tail geometries with the same angles of $\theta_T = 7.5°$ and $\theta_B = 5°$ given in table 5.1 are now studied and compared to the long circle-arcs. One consists of two slanted boat-tails of length $\ell_B^* = 0.567$ and the other corresponds to two short circle-arcs with $\ell_B^* = 0.168$. These geometries were previously characterized in § 5.4.6 in which the baseline's wake dynamics is described. We first consider the most probable states explored by the wake through the three sensitivity analyses. Afterwards, the study the mean aerodynamic loading during the yaw sensitivity experiment is made in order to capture the contribution of the instability. The sensitivity analyses are presented at once with the most probable values in figures C.9, C.10, C.11. We let the branches appear only if they are explored more than 10% of the observation time.

The onset of the instability and its saturation can be identified in figure C.9 summarizing the ground clearance sensitivity analysis. The body is pull away from the floor and

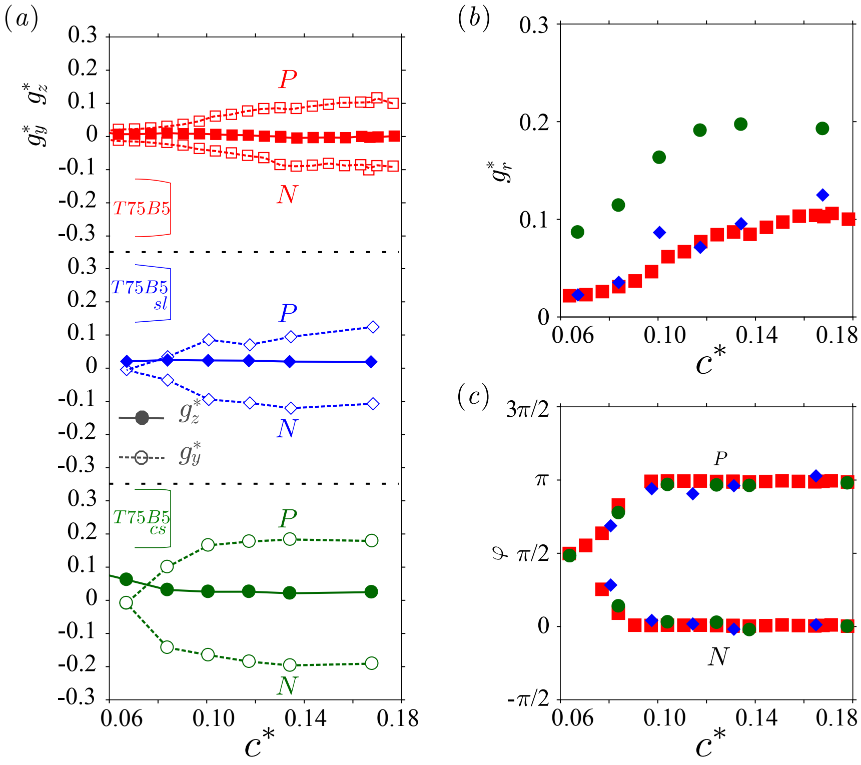

Figure C.9 – Most probable pressure gradients *vs.* ground clearance c^* for different boat-tails geometry with $\theta_T = 7.5°$ and $\theta_B = 5°$ detailed in table 5.1: g_y^* and g_z^* (a), g_r^* (b) and φ (c). The legend of the symbols is given in (a).

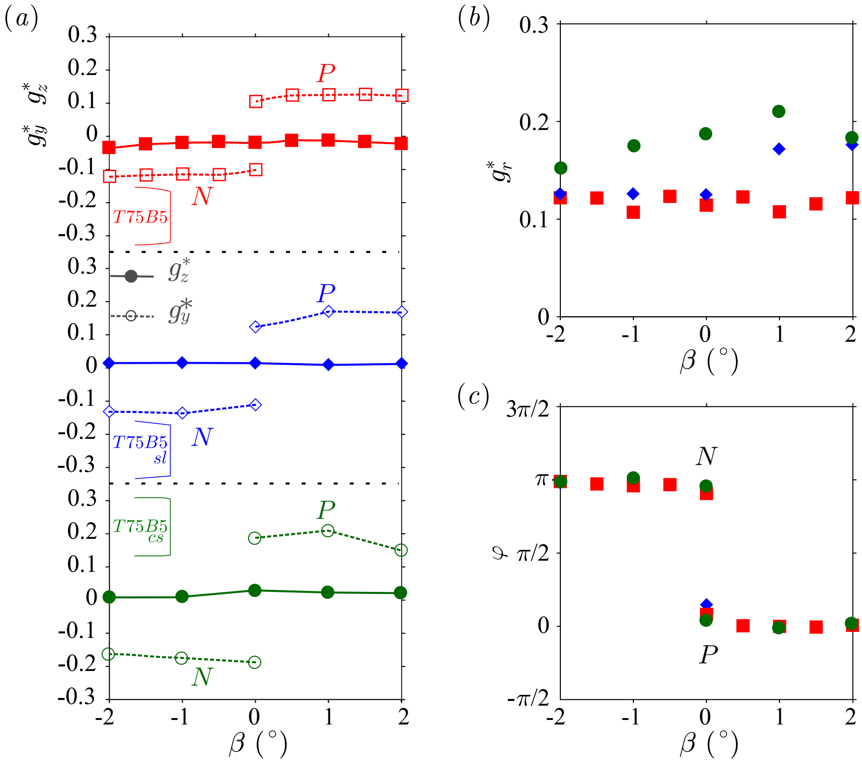

Figure C.10 – Most probable pressure gradients *vs.* yaw angle β for different boat-tails geometry with $\theta_T = 7.5°$ and $\theta_B = 5°$ detailed in table 5.1: g_y^* and g_z^* (a), g_r^* (b) and φ (c). The legend of the symbols is given in (a).

kept aligned with the incoming flow ($\alpha = 0°$, $\beta = 0°$). The same pattern – similar to that of the squareback geometry shown in figure 4.3 on page 56 – can be observed for all three geometries with a pitchfork bifurcation of the horizontal gradient G_y^* into the two branches corresponding to the P and N orientations of the wake while the vertical component G_z^* is almost null and prescribed by the boat-tails. The instability onset and saturation clearances are slightly shifted by the different boat-tails geometries. The two phase branches ($\varphi \simeq 0$ for state P and $\varphi \simeq \pi$ for state N) are clearly visible in figure C.9(d) while the strength attenuation is obviously proportional to the boat-tail length as confirmed by figure C.9(c). For the following, the ground clearance is chosen as $c^* = 0.168$. From figure C.9(c, d), it corresponds to a saturated instability in all cases. The following analyses are conducted starting from this baseline.

As regards the sensitivity towards the body's yaw angle, it can clearly be observed that both Cartesian base pressure gradients have the same evolution regardless of the geometry in figure C.10(a). At most one may notice that the mean horizontal component G_y^* is not symmetric in the modified configurations, which must be ascribed to an asymmetry in the setup since there is no physical explanation for this behavior related to the instability and creates the modulation of G_r^* observed in figure C.10(b). However, it can be observed that the branches corresponding to the N and P wake states collapse remarkably well in figure C.10(c). As a consequence, it can be stated that the wake sensitivity towards the yaw angle β is not dependent on the afterbody's geometry when subject to the y-instability but only on the body's orientation.

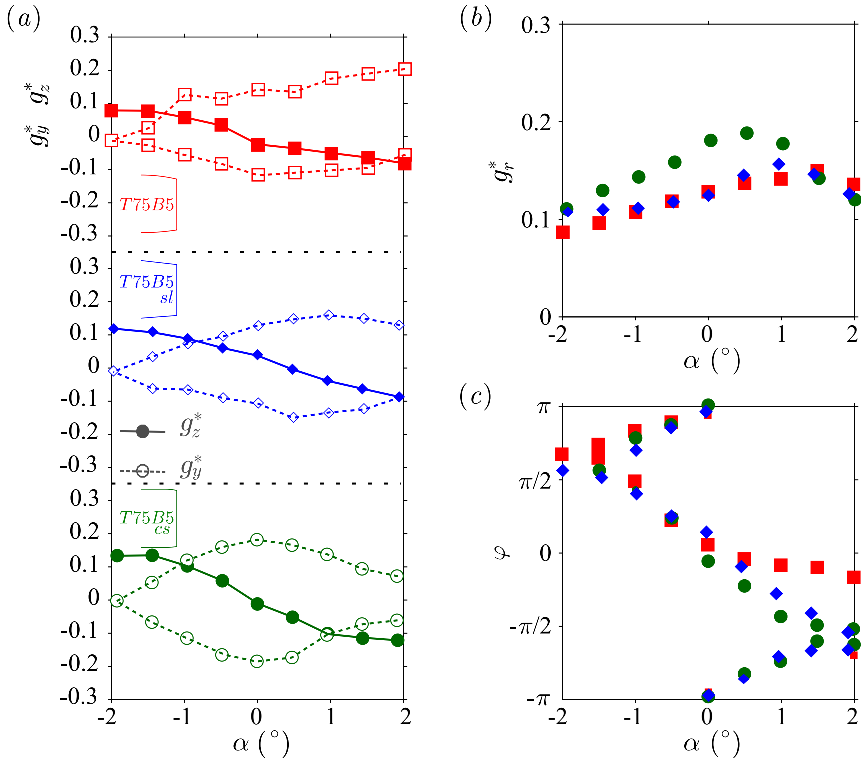

Figure C.11 – Most probable pressure gradients *vs.* pitch angle α for different boat-tails geometry with $\theta_T = 7.5°$ and $\theta_B = 5°$ detailed in table 5.1: g_y^* and g_z^* (a), g_r^* (b) and φ (c). The legend of the symbols is given in (a).

The sensitivity towards the model's pitch angle α is finally investigated for the three geometries in figure C.11. It clearly appears that, once again, the general mechanism described in figure C.6 persists regardless of the geometry, with a convergence of the two branches of solutions towards wake lock-in for nose-down configurations ($\alpha < 0°$)

and global unlocking for nose-up cases ($\alpha > 0°$) – with most probable wake orientations around $\varphi \simeq -\pi/2$ though despite lock-in does not occur since this value is not unique. The main impact of the geometry concerns in fact the saturation threshold for the vertical component of the base pressure gradient G_z^*; nevertheless, it is interesting to notice that the slope of the evolution curve of this component only depends on the body's alignment.

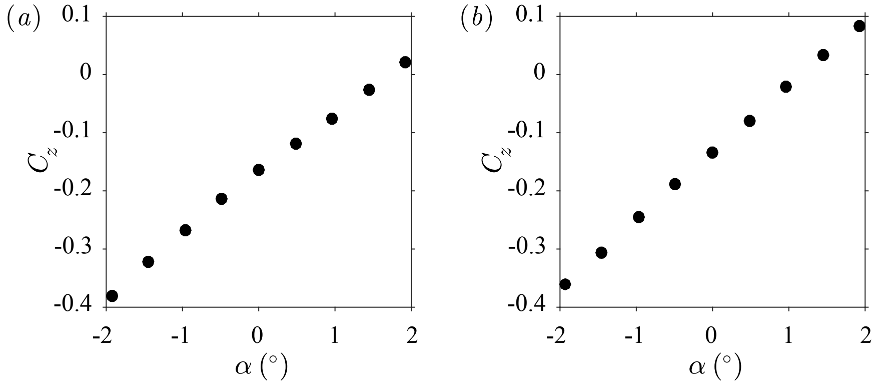

Figure C.12 – Mean lift coefficient C_z *vs.* pitch angle α: (a) *T75B5-sl*, (b) *T75B5-cs*.

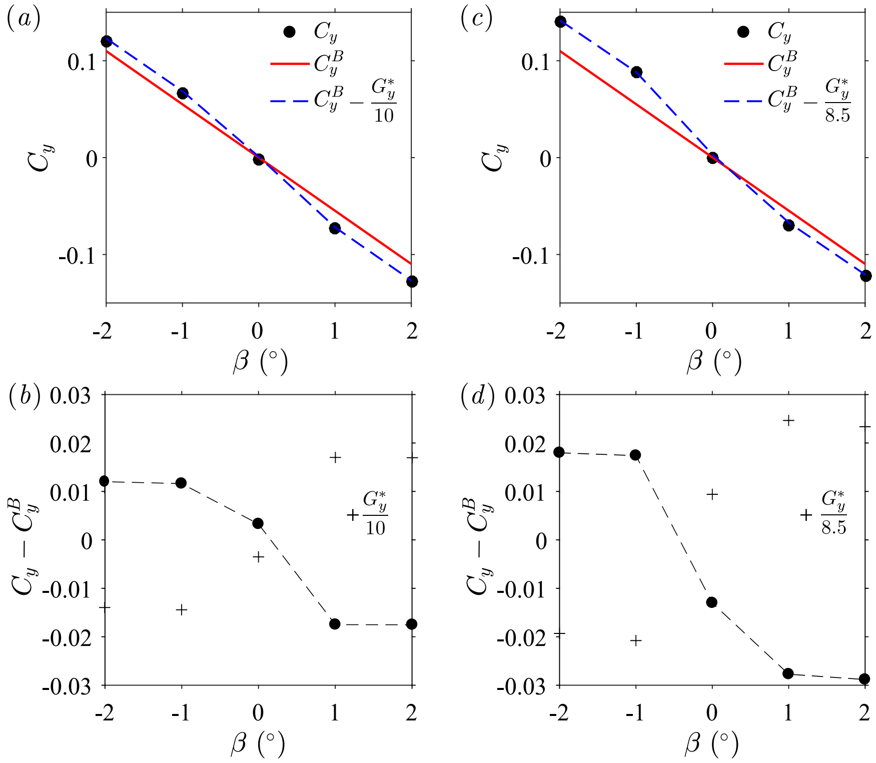

Figure C.13 – Sensitivity alignment experiments for the y-unstable case with boat-tailed body: left column ($a-b$) *T75B5-sl*, right column ($c-d$) *T75B5-cl* (see table 5.1). (a, c) Measured mean side force coefficient C_y (symbols), *basic flow* coefficient C_y^B (red line) and coefficient computed from equation (C.2) (blue dashed line). (b, d) Mean contribution of the instability $C_y - C_y^B$ (filled circles) and mean horizontal base pressure gradient G_y^* (crosses).

We briefly show the evolution of the mean lift coefficient C_z during the pitch sensitivity analysis attesting for the two modified geometries (long slant and short circle-arc) that the y-instability only impacts the side force coefficient and thus that $C_z = C_z^B$ which turns out to be a linear function of α. This result is shown in figure C.12(a) for *T75B5-sl* (see table 5.1 on page 107) and in figure C.12(b) for *T75B5-cs*. These figures clearly show that there is no contribution of the y-instability to this component of the cross-flow aerodynamic loading.

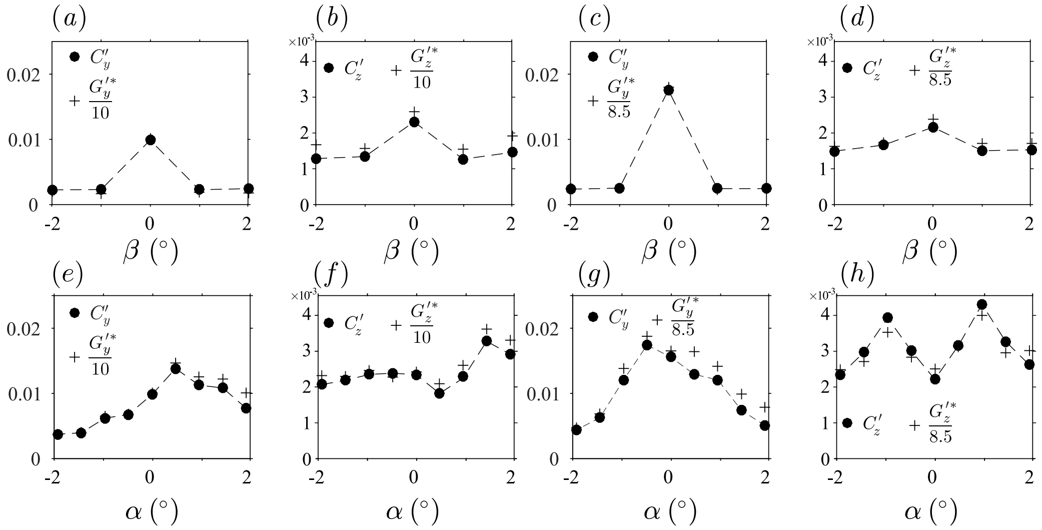

Figure C.14 – Fluctuations of the cross-flow forces and of the base pressure gradient *vs.* body alignment for the slanted *T75B5-sl* (a, b, e, f) and short *T75B5-cs* (c, d, g, h) boat-tails.

Then, the cross-flow forces fluctuations are compared to those of the base pressure gradients in figure C.14. The proportionality coefficients ξ are those indicated in figure C.13(a, c). The difference in the coefficients can be ascribed to geometrical differences between the afterbodies. Fluctuation crises are identified each time wake bistability occurs and correspond to an increase of at least one order of magnitude of the fluctuating coefficient. Comparing the forces (filled circles) and the base gradients (crosses), one may observe the excellent agreement between the two sets of data.

We finally estimate the contribution of the y-instability to the side force loading – similarly to figures C.8$(a - b)$. In view of the involved instability, we only consider the mean side force coefficients C_y *versus* the yaw angle β. Figures C.13(a, c) show the mean side force coefficient C_y^B obtained without the instability which evolves linearly with β. The linearity of the lift coefficient C_z – equal to that of the *basic flow* C_z^B – towards the pitch angle is attested in figure C.12. The contribution of the y-instability to the side force loading is taken as the difference $C_y - C_y^B$ between the actual force and that estimated from the *basic flow* by means of equation (C.1) which still holds for the two other geometries. It is plotted in figures C.13(b, d) and compared to the mean horizontal base pressure gradient G_y^*. Once again, the two quantities are satisfactorily proportional and it follows that a proportionality coefficient ξ of $\xi = 1/10$ for the slanted afterbody and $\xi = 1/8.5$ for that equipped with short boat-tails can be chosen so that equation (C.4) is satisfied for the two modified geometries. As a consequence, the good agreement of equation (C.3) can be seen with the blue dashed line in figures C.13(a, c). Some comments must be done on figures C.13(b, d). First, the overestimation of the horizontal base pressure gradient for $\beta \geq 0°$ ascribed to the setup can clearly be observed. Second, the contribution of the instability to the loading is $|C_y - C_y^B| \simeq 0.02$ for the short boat-tail but reduced down to $|C_y - C_y^B| \simeq 0.12$ by the slants which is, the *3D* geometry apart (see § C.2.2), the only time such a comment can be made. Finally, we satisfactory predict the fluctuations as $C'_y = \xi \times G_y^{*\prime}$ and $C_z{}' = \xi \times G_z^{*\prime}$.

C.2.2 Sensitivity analyses with the 3D boat-tailed configuration

In this section, we perform analyses with the *3D* configuration, whose characteristics are given in table 5.1. We first start by the ground clearance sensitivity analysis to identify the saturated unstable regime. Then, from the baseline, the yaw and finally the pitch angles of the model are modified. The contribution of the y-instability to the cross-flow forces is finally discussed.

We first start by changing the ground clearance c^* of the model aligned with the incoming flow ($\alpha = 0°, \beta = 0°$). The four sensitivity maps of the base pressure gradient's response to a modification of the model's ground clearance c^* are given in figure C.15($a-d$). The base pressure gradient response is very similar to that of the squareback geometry subject to the y-instability shown in figure 4.3 (page 56). The horizontal component of the base pressure gradient g_y^* given in figure C.15(a) bifurcates into two opposite branches $g_y^* \simeq \pm 0.09$ above the ground clearance $c^* \simeq 0.085$ signaling the onset of the instability, quite similar to that observed for the squareback body. The vertical component of the gradient g_z^* remains slightly positive but unchanged over the whole investigated range (figure C.15b). Since the two branches of g_y^* slightly diverge one with respect to the other, the modulus g_r^* of the base pressure gradient continuously increases (figure C.15c) thus suggesting that the full saturation is never reached. The two branches of the phase φ (figure C.15d) are obtained accordingly. The main difference with respect to the squareback case (figure 4.3) is the constant value of the vertical gradient, which originates from the geometry of the afterbody. A characteristic bi-stable dynamics was shown in figure 5.30 which time scale is about 1000 t^* showing that the dynamics is slower than in the squareback configuration; this also suggests that wake control may be easier to perform; since the dynamics is slower, the need of very quick actuators decreases. On the other hand, since the gradient's modulus is reduced, the wake may be more stable. The baseline is chosen when $c^* = 0.168$, far enough from the instability threshold so that one may consider that saturation is (almost) reached. It constitutes the starting point for the two other sensitivity analyses. The two mean base pressure distributions associated with state P ($\varphi \sim 0$) and state N ($\varphi \sim \pi$) are given in figure 5.31 in the previous chapter. The slight deviation from the phase branches at 0 and π can be identified since the distributions are not uniform in the vertical direction.

The mean and fluctuating force coefficients are plotted in figure C.16 against the model's dimensionless ground clearance c^*. Unlike all other bifurcations studied so far, the mean base suction coefficient C_b (figure C.16a) is almost constant regardless of the ground clearance and is not affected by the pitchfork bifurcation. However, the mean drag coefficient C_x reaches a minimum during the onset of the instability and then increases linearly due to the increasing surface of the model's supports (figure C.16b). There is not much to say about the mean side force coefficient C_y shown in figure C.16(c) which remains, as expected, almost null as long as the body is aligned with the incoming flow. The lift coefficient C_z decreases very quickly, reaches a minimum which corresponds to a maximum in magnitude during the onset of the instability and then increases again towards zero (figure C.16d). The only comment that we make on fluctuations is the crises of those of the side force (figure C.16g) associated with the y-instability and the horizontal switches of the wake. The base suction and the lift apart, these curves are quite similar to those of the squareback geometry given in figure 4.16 on page 66.

We then turn to the sensitivity towards the yaw angle β. The four sensitivity maps associated with the yaw experiment are given in figure C.17. A discontinuous transition between the two opposite branches of g_y^* in figure C.17(a) resulting from a phase jump (figure C.17d) between values close to 0 and π can be identified, similarly to the squareback

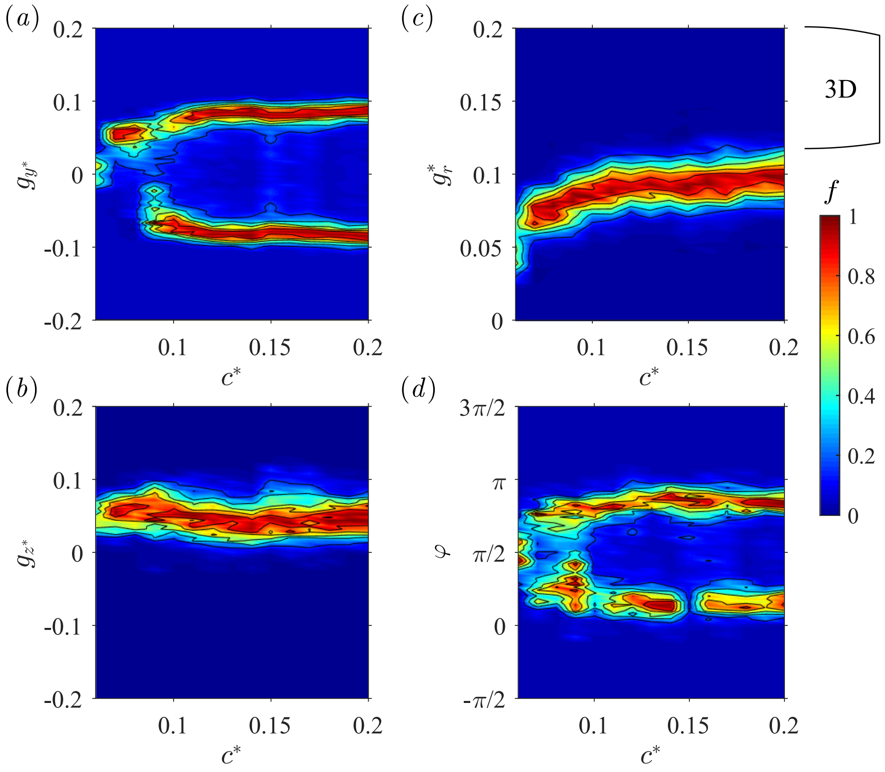

Figure C.15 – Base pressure gradient response to a variation of the ground clearance c^* for the *3D* configuration (see table 5.1). Sensitivity maps (*a*) $f(c^*, g_y^*)$, (*b*) $f(c^*, g_z^*)$, (*c*) $f(c^*, g_r^*)$ and (*d*) $f(c^*, \varphi)$. The clearance $c_S^* \simeq 0.105$ is defined as the threshold from which the instability is saturated.

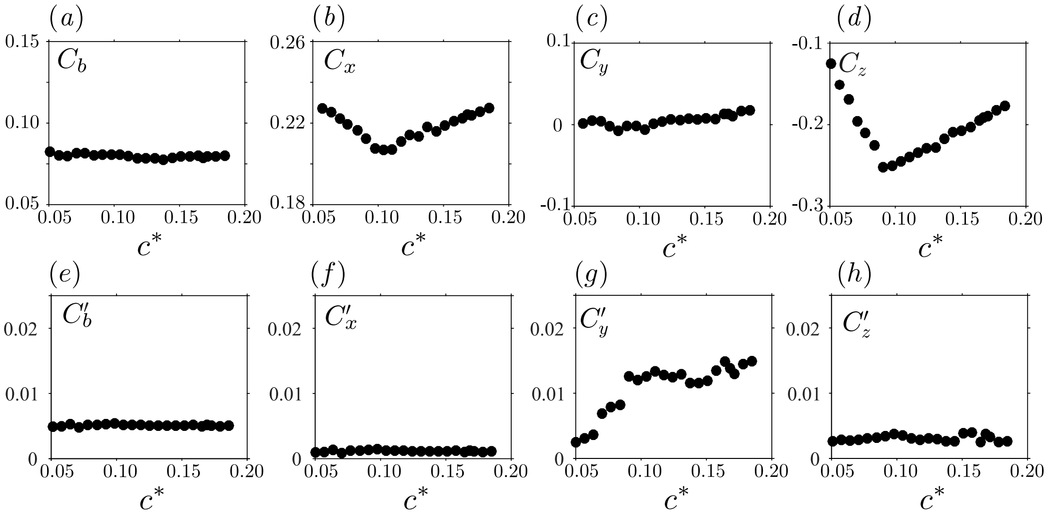

Figure C.16 – Aerodynamic loading applied on the body in the ground clearance sensitivity analysis: mean (top row) and fluctuating (bottom row) base suction (a, e), drag force (b, f), side force (c, g) and lift coefficients (d, h) *vs.* ground clearance for the y-unstable *3D* boat-tailed afterbody.

geometry. The vertical component g_z^* of the base pressure gradient, shown in figure C.17(*b*) is slightly positive with a clear maximum when the body is aligned with the flow ($\beta = 0°$) and a symmetric decrease on both sides. This affects the modulus g_r^* which presents exactly the same evolution (figure C.17*c*) since the horizontal component is constant in magnitude. Due to this slight adaptation, the phase φ (figure C.17*d*) which deviates from $\varphi_0 = 0$ or $\varphi_0 = \pi$. As a conclusion, the yaw drives the phase jumps statistics and, unlike for squareback afterbodies, modifies the gradient's modulus. The side force reveals the instability.

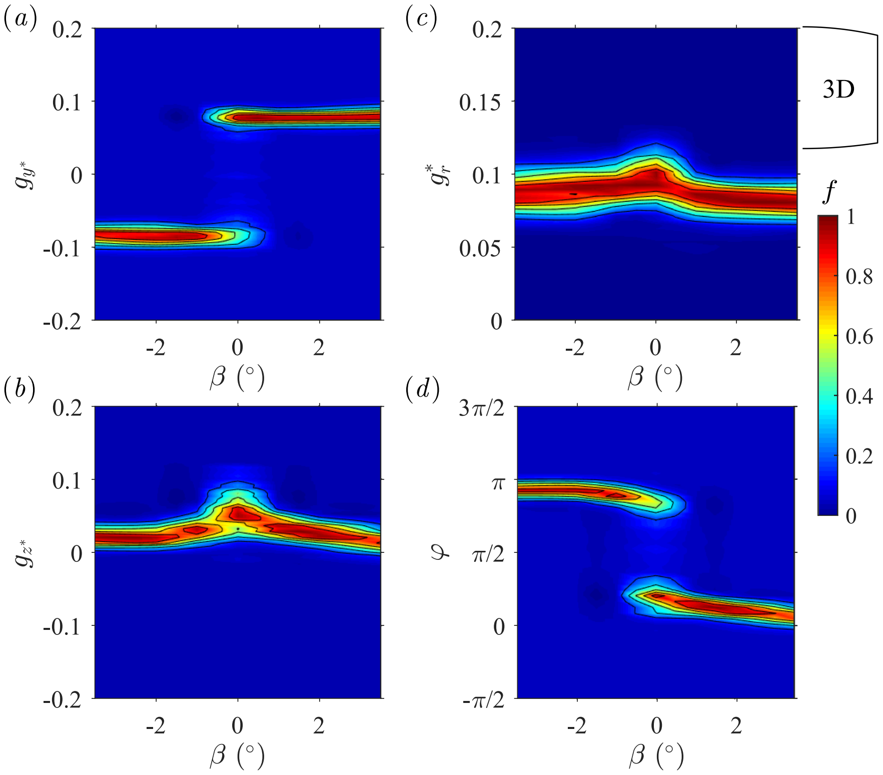

Figure C.17 – Sensitivity maps (a) $f(\beta, g_y^*)$, (b) $f(\beta, g_z^*)$, (c) $f(\beta, g_r^*)$ and (d) $f(\beta, \varphi)$ for the *3D* configuration (see table 5.1).

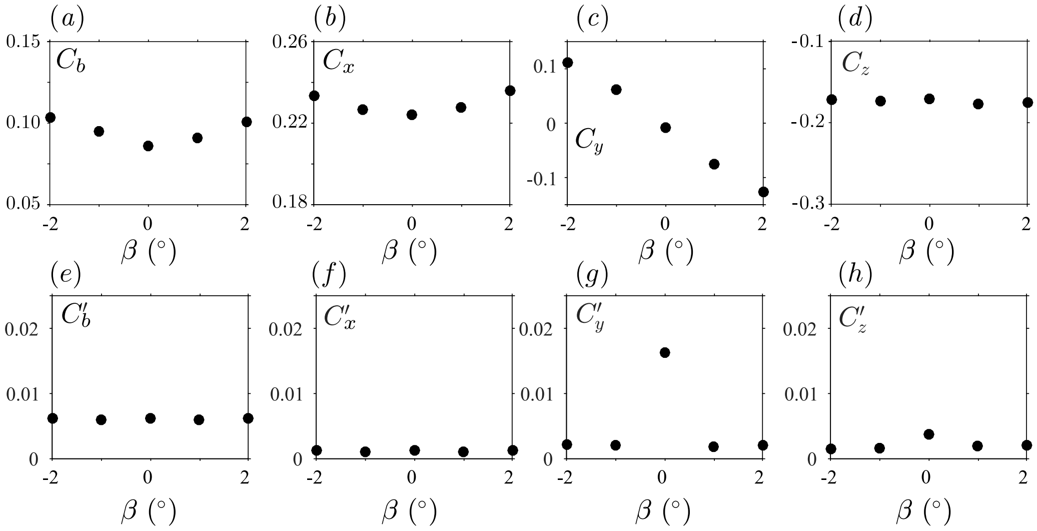

Figure C.18 – Aerodynamic loading applied on the body *vs.* yaw angle β: mean (top row) and fluctuating (bottom row) base suction (a, e), drag force (b, f), side force (c, g) and lift coefficients (d, h) for the y-unstable *3D* boat-tailed afterbody.

The aerodynamic loading is discussed *vs.* the yaw angle β for the mean and fluctuating values given in figure C.18. Both the mean base suction and drag coefficient experience a minimum when the body is aligned with an even increase with the angle (figure C.18a, b). The side force coefficient C_y shown in figure C.18(c) is quite a linear function of the angle except for a shift created by the instability when the wake is reversed. This point is discussed in figure C.21. Similarly to all other bodies subject to the y-instability, the mean lift coefficient C_z shown in figure C.18(d) is insensitive to the yaw angle. The wake is locked except for $\beta = 0°$ as shown by the quite small fluctuations but in the latter case, with a difference of more than one order of magnitude for C_y' (figure C.18*g*). These figures are identical to the squareback's (figure 4.18 on page 68).

Finally, the wake sensitivity towards the pitch angle α is investigated. We start from the baseline and change the pitch angle by adjusting the front and rear ground clearances. We impose $\bar{c}^* = \frac{1}{2}(c_f^* + c_r^*) = 0.168$ in order to recover the baseline when $c_f^* = c_r^*$. The results are presented in figure C.19. As for the squareback afterbody, three main regions can be identified in the sensitivity map of the horizontal base pressure gradient g_y^* provided in figure C.19(a). Largely negative pitch angles $\alpha \lesssim -1°$, associated with nose-down setups, lead to a single-branch solution around $g_y^* \simeq 0$; for smaller angles (in magnitude), it bifurcates into two symmetric branches in the range $-1° \lesssim \alpha \lesssim 1.5°$. Large nose-ups ($1.5° \lesssim \alpha$) impose a quite unexpected configuration compared to the baseline. Rather than a uniform exploration of the range $-0.1 \lesssim g_y^* \lesssim +0.1$, the two branches of the gradient converge into a single-branch solution fluctuating (more than for nose-down lock-in though) around $g_y^* \simeq 0$. As for the horizontal base pressure gradient g_z^*, its behavior in all three regimes is identical to that of the squareback geometry. One can see in figure C.19(c) a linear variation with the pitch angle α in the range $-1° \lesssim \alpha \lesssim 1.5°$ with saturation to a local extremum (of about the same magnitude) on both outer sides of this central range. The modulus g_r^* of the base pressure gradient exhibits in figure C.19(c) a smooth evolution with the pitch with a maximum reached around $\alpha \simeq 0°$. The evolution is almost symmetric for nose-up and nose-down configurations. The phase φ (figure C.19*d*) presents once again the same behavior as the horizontal gradient g_y^*. The single branch at $\varphi = \pi/2$ for $\alpha \lesssim -1°$ corresponding to phase lock-in bifurcates into two branches in the range $-1° \lesssim \alpha \lesssim 1.5°$ in which the slow bi-stable behavior discussed in § 5.4.7 occurs. However, unlike the horizontal gradient, the two branches are not constant but almost linear functions of the pitch angle α due to the constraint created by the vertical gradient g_z^* (see figure C.19*b*). In the last regime, the wake is again locked around $\varphi \simeq -\pi/2$ thus showing that the ground effect is negligible for the considered ground clearances.

Finally, the aerodynamic loading is considered during the pitch sensitivity analysis. The mean base suction and drag coefficients shown respectively in figure C.20(a, b) vary slightly and reach a minimum around $\alpha \simeq -0.5°$, *i.e.* in a nose-down configuration. A similar trend was found for the squareback afterbody in § 4.3.1. The non-zero pitch angle associated with the minimum can be explained by the influence of the road which generates a vertical base pressure gradient. Meanwhile, the mean side force C_y (figure C.20*c*) remains almost null. Since the body is subject to a y-instability, the mean lift coefficient C_z is a linear function of the inclination as shown in figure C.20(d). From figure C.20($e-h$), only the side force C_y' is subject to a large fluctuation crisis for $\alpha \in [0°, 1°]$ corresponding to the range in which wake bistability is observed (figure C.20a, d). However, two (much smaller) increases of the lift fluctuations can be identified in figure C.20(h). They correspond to the start and the end of the bi-stable region, *i.e.* to the transition from wake bistability between states P and N with preferred phase values of $\varphi \simeq 0$ and $\varphi \simeq \pi$ respectively to phase lock-in at $\varphi \simeq \pi/2$ for nose-down and $\varphi \simeq -\pi/2$ for nose-up configurations (figure C.19*d*).

We close this subsection with the contribution of the y-instability to the aerodynamic loading for the three-dimensional boat-tailed afterbody; figure C.21 is discussed. Since the body is subject to the y-instability, the only cross-flow force component that we expect to be modified is the side force C_y whose mean value will reveal the instability during the yaw experiment. For the stable *basic flow*, the constraint would be a linear function of the yaw angle β, plotted as the red line in figure C.21(a). Its equation (where the yaw

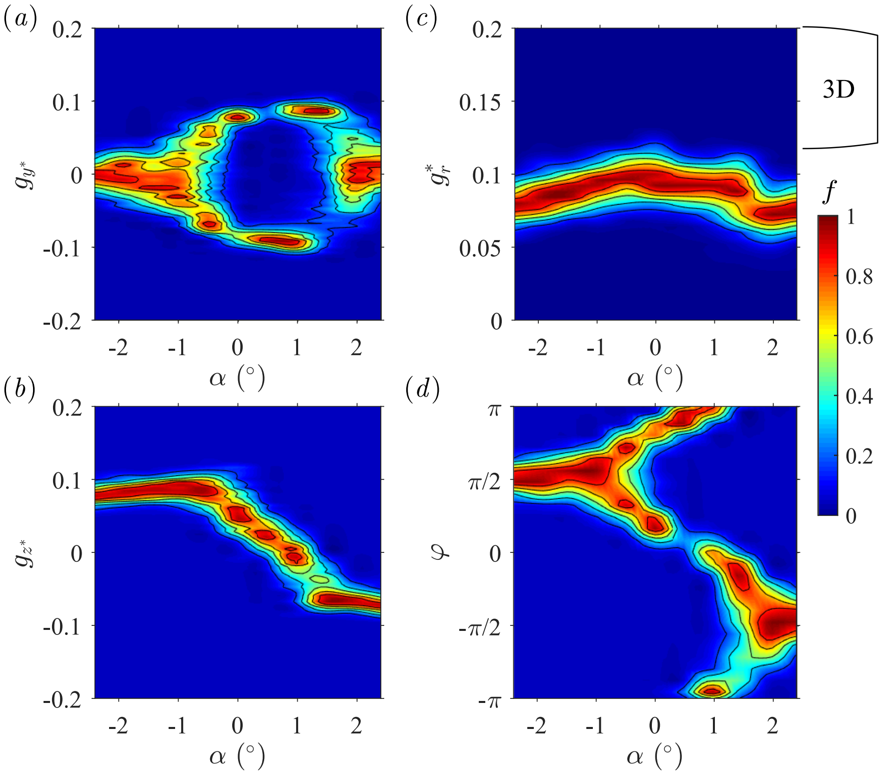

Figure C.19 – Base pressure gradient response to variations of the pitch angle α. Sensitivity maps (a) $f(\alpha, g_y^*)$, (b) $f(\alpha, g_z^*)$, (c) $f(\alpha, g_r^*)$ and (d) $f(\alpha, \varphi)$ for the *3D* configuration (see table 5.1).

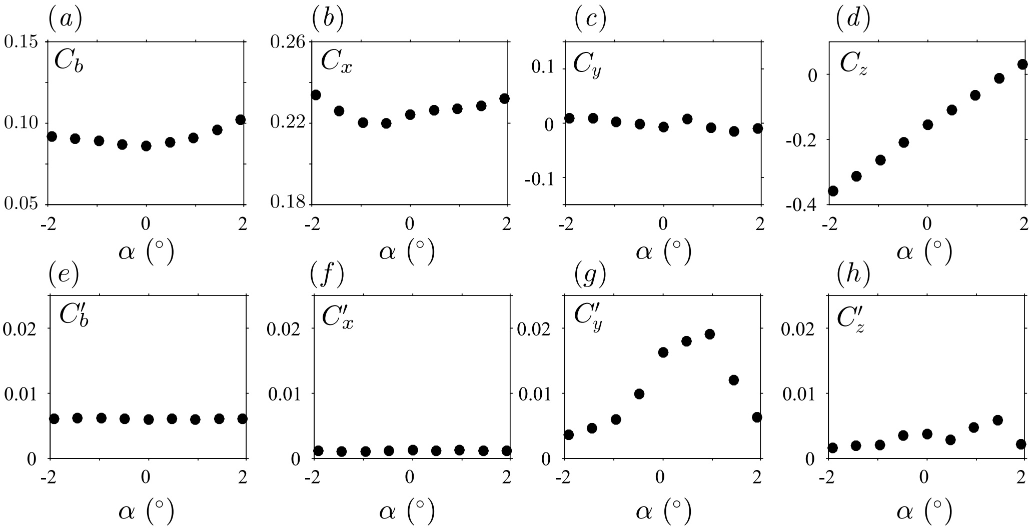

Figure C.20 – Aerodynamic loading applied on the body *vs.* pitch angle α: mean (top row) and fluctuating (bottom row) base suction (a, e), drag force (b, f), side force (c, g) and lift coefficients (d, h) for the y-unstable *3D* boat-tailed afterbody.

angle β is expressed in degrees), obtained from a fit of the two branches of the actual measured force (filled circles), is similar to that of the squareback geometry:

$$C_y^B = -0.055 \times \beta \tag{C.9}$$

The actual contribution of the instability to the side force $C_y - C_y^B$ is found to be constant in magnitude with $|C_y - C_y^B| \simeq 0.12$ in figure C.21(b). The strength is reduced by nearly 40% with respect to the squareback afterbody (figure 4.19b), the *3D* configuration being the only one to provide such a reduction with circular boat-tails[1]. It is found to be proportional to the mean horizontal base pressure gradient G_y^* so that the mean side force coefficient and the mean horizontal base pressure gradient are linked by equation (C.10). The proportionality coefficient ξ (here equal to 1/6) is definitely a function of the afterbody's geometry.

$$C_y(\beta) = C_y^B(\beta) - \frac{G_y^*(\beta)}{6} \tag{C.10}$$

The reconstructed side force from equation (C.10) is plotted as the blue dashed line in figure C.21(*a*). It turns out that the mean experimental data are well predicted. Considering, as done several time throughout the manuscript, that C_y^B is a steady quantity, the horizontal base pressure gradient g_y^* brings the fluctuations as in equation (C.11).

$$c_y(t^*) = C_y^B - \frac{g_y^*(t^*)}{6} \tag{C.11}$$

It follows that the force fluctuations are:

$$C_y' = \frac{G_y^{*\prime}}{6} \tag{C.12}$$

An excellent agreement of equation (C.12) with the experimental data is found both for the yaw and pitch sensitivity experiments in figure C.21(c, e).

The y-instability does not modify the lift exerted on the body and thus $C_z = C_z^B$. Following a similar reasoning as for the side force coefficient, the instantaneous lift can be expressed as a function of the vertical base pressure gradient g_z^* in equation (C.13):

$$c_z(t^*) = C_z^B + \frac{{g^{*\prime}}_z(t^*)}{6} \tag{C.13}$$

from which the mean fluctuating coefficient can be easily deduced:

$$C_z{}' = \frac{G_z^{*\prime}}{6} \tag{C.14}$$

An excellent agreement is found between equation (C.14) and the data obtained experimentally during the yaw analysis as indicated in figure C.21(*d*). However, this method underestimates by almost a factor of 2 the lift mean fluctuations C_z' for the pitch experiment (figure C.21f). This means that a part of the fluctuations of the loading does not originate from the wake in this specific configuration unlike in other experiments reported so far. A global three-dimensional effect at the body's scale may be responsible for these discrepancies.

---

[1] Similar results are indeed obtained with the slants in figure C.13(*b*)

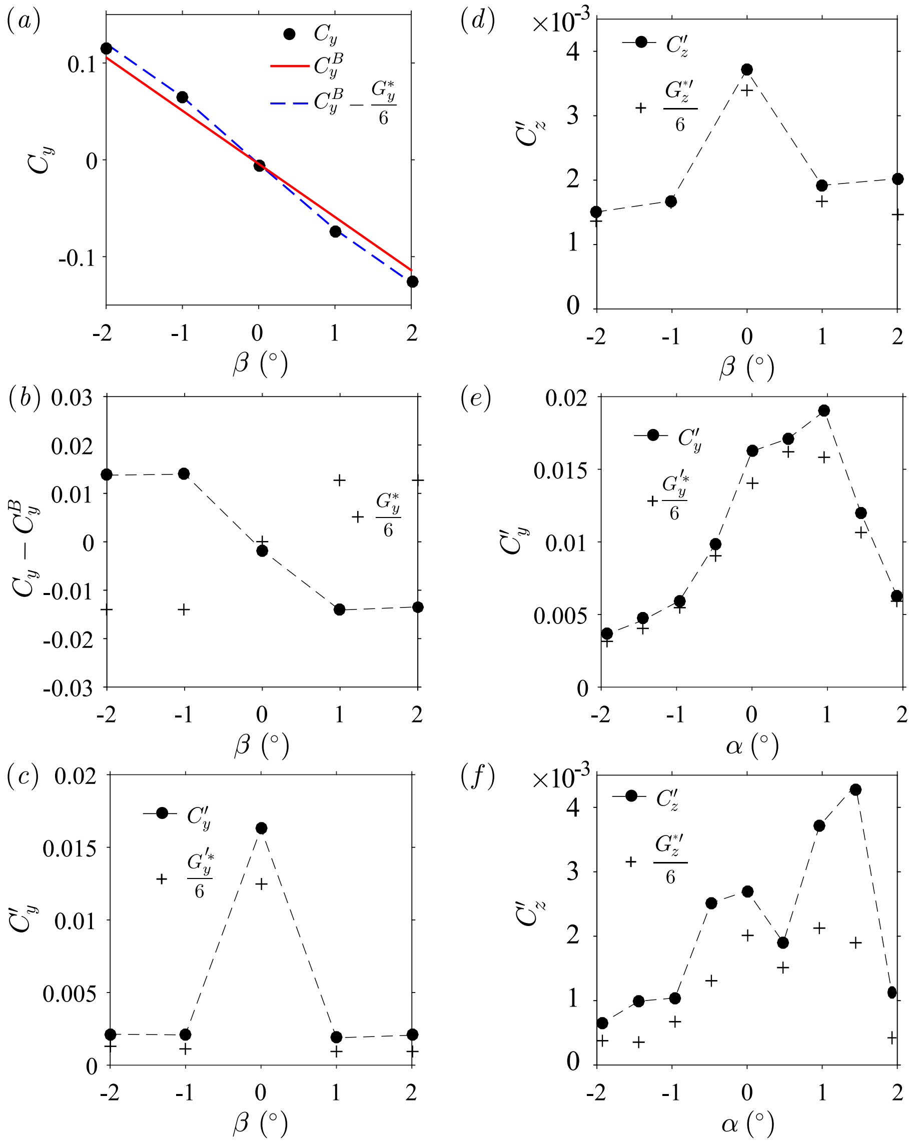

Figure C.21 – Cross-flow forces sensitivity to the body's alignment for the *3D* geometry: (a) Measured force coefficient (symbols), *basic flow* coefficient (red line) and coefficient computed from equation (C.10) (blue dashed line, see text). (b) mean contribution of the instability $C_y - C_y^B$ (filled circles) and mean horizontal base pressure gradient G_y^* (crosses). (c, d) Components of the fluctuating force coefficients C_y' and C_z' (filled circles) compared to the fluctuating base pressure gradients $G_y^{*\prime}$ and $G_z^{*\prime}$ (crosses) *vs.* yaw angle β. (e, f) Components of the fluctuating force coefficients C_y' and C_z' (filled circles) compared to the fluctuating base pressure gradients $G_y^{*\prime}$ and $G_z^{*\prime}$ (crosses) *vs.* pitch angle α.

C.2.3 Sensitivity analyses on a boat-tailed configuration triggering the periodic wake mode ($\theta_T = 12.5°$, $\theta_B = 10°$)

Another typical wake behavior related to boat-tailing identified in chapter 5 is the z-periodic mode investigated in this section through the configuration $\theta_T = 12.5°$, $\theta_B = 10°$. This periodic mode should not be associated with the z-wake instability created by static asymmetric modes described in § 4.3.2 as the two phenomena are completely different. The baseline is chosen as $c^* = 0.168$ with the body aligned with the incoming flow. The ground clearance sensitivity analysis was not done for this configuration but we start our alignment experiments from the periodically bi-stable case identified in § 5.4. The yaw and then the pitch angles are modified starting from the baseline.

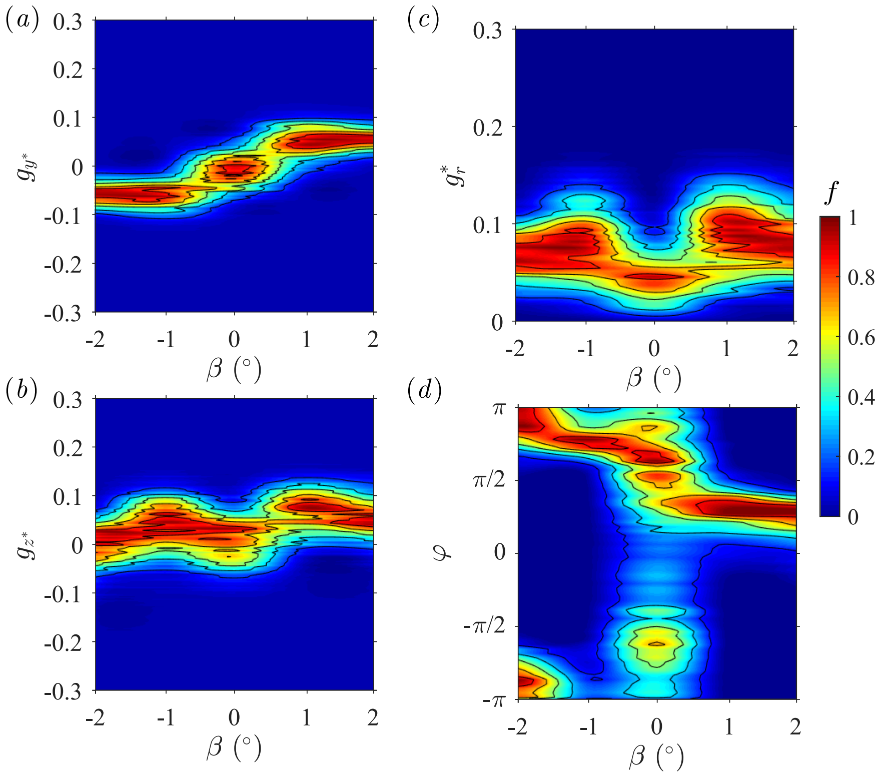

Figure C.22 – Base pressure gradient response to variations of the yaw angle β for the periodic wake mode ($\theta_T = 12.5°$, $\theta_B = 10°$). Sensitivity maps (a) $f(\beta, g_y^*)$, (b) $f(\beta, g_z^*)$, (c) $f(\beta, g_r^*)$ and (d) $f(\beta, \varphi)$.

The sensitivity maps of the base pressure gradient response to variations of the yaw angle β for the periodic wake mode are given in figure C.22. The horizontal base pressure gradient g_y^* shown in figure C.22(a) appears to be an even function of the yaw angle β. For $\beta = 0°$, it only displays small fluctuations around zero and is then shifted almost linearly by the yaw and saturates quickly when $|\beta| \simeq 1°$. It is important to notice that the transition is continuous unlike the discontinuous phase jump observed for the y-instability (see for instance figure C.4a with a boat-tailed afterbody). Meanwhile, the vertical component g_z^* (figure C.22b) remains almost constant in average but fluctuates largely around zero, from negative to positive values. The fluctuations apart, the behavior is quite similar to that obtained for the squareback body with a rear cavity (figure 4.13c on page 65). Unlike the horizontal gradient's component, g_z^* appears to be an even function of the yaw angle. The modulus g_r^* (figure C.22c) is an even function of the yaw angle; it reaches a minimum around $\beta \simeq 0°$ when the horizontal gradient changes sign. This behavior is close to that reported in figure 4.14(c) on page 65 for the squareback afterbody with a base cavity. The phase φ is represented in figure C.22(d). The imprint of the periodic wake bistability is clearly visible when the body is aligned with the flow. There is a preferred phase value around $\varphi \simeq -\pi/2$ versus an almost continuous exploration of the range $\varphi \in [\pi/4, 3\pi/4]$ corresponding to the large fluctuations of g_y^* when aligned with the flow. The sensitivity to the misalignment is large since the lower branch disappears very quickly ($|\beta| \simeq 0.25°$). The continuous solution $\varphi \in [\pi/4, 3\pi/4]$ was in fact a transition between two other branches located respectively at $\varphi \simeq \pi/4$ and $\varphi \simeq 3\pi/4$ that are selected by the yaw depending on the angle's sign. These branches then undergo a linear shift until a sudden wake rotation occurs for $|\beta| = 2°$ when the orientation changes to $\varphi \simeq 0$ or $\varphi \simeq \pi$.

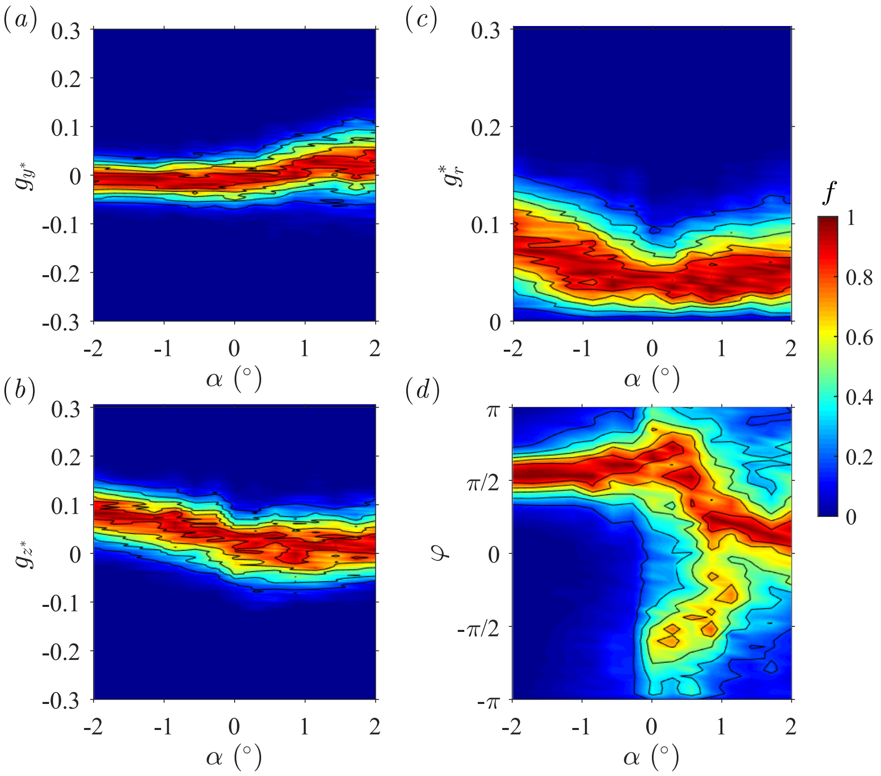

Figure C.23 – Base pressure gradient response to variations of the pitch angle α for the periodic wake mode ($\theta_T = 12.5°$, $\theta_B = 10°$). Sensitivity maps (a) $f(\alpha, g_y^*)$, (b) $f(\alpha, g_z^*)$, (c) $f(\alpha, g_r^*)$ and (d) $f(\alpha, \varphi)$.

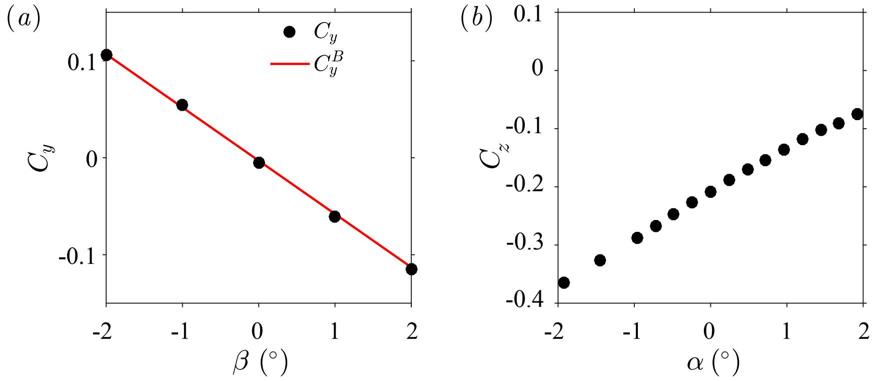

Figure C.24 – Mean cross-flow forces *vs.* body inclination for the configuration *T125B10* (see table 5.1) used to identify the contribution of the instability to the aerodynamic loading. (a) Mean side force coefficient C_y (filled circles) and *basic flow* side force coefficient C_y^B (red line) *vs.* yaw angle β. (b) Mean lift coefficient C_z *vs.* pitch angle α.

Afterwards, pitching conditions are considered. The sensitivity maps of the base pressure gradient response corresponding to the analysis of the periodic wake mode towards the pitch angle α are given in figure C.23. The horizontal base pressure gradient g_y^* remains null for nose-down configurations, *i.e.* $\alpha < 0°$, but increases linearly when the front axle is lifted up until saturation occurs quickly around $\alpha \simeq 1°$ (figure C.23a). The vertical component g_z^* (figure C.23b) has almost a dual evolution: surprisingly unaffected for nose-up cases, it increases linearly up to $g_z^* \simeq 0.1$ when the rear axle is lifted up but the fluctuations remain quite large, more than twice those of the horizontal component. The strength of the wake asymmetry, characterized owing to the gradient's modulus g_r^* in figure C.23 is very similar to that of the squareback afterbody with the cavity (figure 4.14e on page 65). A minimum is identified for $\alpha = 0°$ with an almost even increase on both sides with the pitch angle. The mean value is further reduced with respect to the boat-tailed y-unstable cases. As for the phase φ, figure C.23(d) shows two different behaviors. For negative pitch angles ($\alpha < 0°$), an immediate lock-in around $\varphi \simeq \pi/2$ can be observed since the horizontal base pressure gradient is null. For nose-up configurations however, two regions can be identified. For $\alpha \lesssim 1°$, the wake orientation is poorly defined in average, with almost an equiprobable distribution for all values. The situation is different from the random wake orientation observed for axisymmetric bluff bodies (Rigas *et al.*, 2014; Gentile *et al.*, 2016, 2017) since the static asymmetric wake modes have been removed by the shear layers interaction triggering the periodic wake mode. Nonetheless, as the pitch angle is further increased ($1° \lesssim \alpha$), the (positive) horizontal component of the base pressure gradient g_y^* identified in figure C.23(a) together with the almost zero vertical gradient g_z^* (figure C.23b) yield a phase angle close to $\varphi \simeq 0$, *i.e.* with a permanent wake lock-in. The statistical symmetry of the problem (see chapter 3 for the mean flow) being suppressed in this configuration, we conclude that an imperfection of the setup causes the wake to be shifted. Without it, global unlocking or lock-in around $\varphi = -\pi/2$ would be expected similarly to all other investigated cases. Nonetheless, since the gradient's strength is much reduced ($g_r^* \lesssim 0.05$), the actual wake asymmetry is small.

Earlier in this section, we studied the response of the periodic wake mode to body's misalignment. This mode showed different properties compared to a z-instability investigated in § 4.3.2 although it also leads to vertical fluctuations of the wake. These were found periodic with a frequency close to vortex-shedding ($f^* \sim 0.2$). The aim is now to identify whether the periodic mode has a contribution to the cross-flow aerodynamic loading similarly to a static wake instability. The mean side force coefficient C_y shown with the filled circles in figure C.24(a) is equal to that of the *basic flow* C_y^B proving unambiguously that the y-instability has been completely suppressed while replaced by the periodic mode. The latter one does not influence the mean lift C_z either unlike the z-instability comparing figure C.24(b) to figure 4.31(a). There is indeed no shift from a linear behavior which would be obtained without the instability and consequently we have $C_z = C_z^B$. Nonetheless, its evolution is not completely linear with respect to the pitch angle α, in particular in the range $\alpha > 0°$, *i.e.* for nose-up configurations. This is caused by the absence of wake reversal (figure C.23b, d) despite the loss of horizontal symmetry of the setup: the wake rotates to the right of the base instead. However, the removal of the static wake asymmetry does not yield the *basic flow* in this configuration thus explaining the higher drag (figure 5.13).

C.3 Discussion

The similarities of boat-tailed afterbodies with squareback ones concerning the y-instability and the geometry's impact are discussed first. Afterwards, we undertake the particularities of the 3D afterbody configuration and on the periodic wake mode.

In this chapter, we first compare a two-sided boat-tailed afterbody composed of a top and a bottom circle-arc whose chord angles are respectively $\theta_T = 7.5°$ and $\theta_B = 5°$ leading to a y-instability of the wake to the squareback afterbody. This instability is consistent with the aspect ratio of the base following the criteria of Grandemange *et al.* (2013a) since boat-tailing does not remove the static asymmetric wake states (§ 5.5). Some common characteristics but also some discrepancies between the squareback and the boat-tailed afterbody are identified. First of all, the general wake dynamics appears similar. While the ground has a stabilizing effect removing the instability, yawing and pitching conditions just modify the phase dynamics potentially until a permanent wake lock-in occurs. For large nose-up, the global unlocking is also observed. In fact, due to the geometrical differences, only the thresholds – between the stable and the unstable flows and for phase lock-in/unlocking during the pitch experiment – are modified. Even though the dynamics of the phase becomes slightly slower as shown in figure C.2, the typical features persist (phase jumps and continuous drifts).

The similar phase dynamics confirm that the adaptation phenomenon towards the base minor pressure gradient (g_z^* for the present configuration) described in § 4.4.2 and generalized in § 4.4.3 is not affected by circular boat-tailing since g_z^* still appears to be the driving parameter for wake bistability – in which case it determines the two preferred orientations φ_P and $\pi - \varphi_P$ – but also for lock-in – when $\varphi_P \rightarrow \pi/2$ because of the geometrical constraint – and unlocking. As a direct consequence of the reduction of the strength of the wake asymmetry and of the geometrical modification caused by boat-tailing, unlocking occurs for much larger pitch angles related to the smaller wake sensitivity. The bigger distance between the base and the ground provides a satisfactory explanation for this delay.

It must also be emphasized that the contribution of the y-instability on the cross-flow loading applied to the body is identical not only as regards the mechanism but also in strength since $C_y - C_y^B$ compares well with $\xi \times G_y^*$ (figure C.8*b*) where the proportionality coefficient $\xi = 1/6$ directly depends on the geometry as already highlighted in § 4.4.3. The contribution of the instability to the loading is not only revealed through the mean side force C_y but also through the mean lift fluctuations C_z' proportional to the vertical gradient's fluctuations by the same factor ξ. Similarly to the squareback geometry, this shows clearly the existence of an effective length ℓ (similar to that of § 4.4.2) on which the wake's topology influences the cross-flow aerodynamic loading. In the boat-tailed case, this distance is found to be longer than for the squareback as $\ell = H_b/6$ *vs.* $\ell = H_b/10$. This effect can be explained by the almost similar force contribution while the modulus of the base pressure gradient g_r^* is considerably smaller. Not surprisingly since only top-bottom boat-tails are considered, the *basic flow* mean force coefficient C_y^B is identical to the squareback geometry and thus independent of the boat-tail angles.

In view of drag reduction, several comments can be made on the mean coefficient C_x. First of all, it is found to be the smallest for the body aligned with the flow, *i.e.* in bi-stable cases in agreement with the conclusion drawn in § 4.4.4 that the wake reaches a beneficial equilibrium when two wake states are explored simultaneously. In addition, unlike the squareback afterbody, there is – luckily – a clear independence of the drag towards the ground clearance in the unstable regime thanks to a compensation phenomenon between the increasing frontal surface and the diminishing base suction (see also figure C.3*a*, *b*). This case is particularly interesting since, if similar for real vehicles, it would allow adjusting the ground clearance to improve the stability by reducing the lift without detrimental consequences on drag, provided the balance found in our configuration exists.

For a given geometry – circle-arcs in our case –, the boat-tail length does not modify the mechanisms of the wake response to the body's misalignment comparing results reported in § C.2.1 to those of § 5.4.6 for *T75B5-cs* and the analysis previously made may still be applied to this geometry. The main difference is namely that the angles for which the change of behavior occurs are once again modified. in agreement with previous comments, the proportionality coefficient ξ between the forces' and the gradients' fluctuations is also modified. As a consequence, the effective length ℓ on which the wake's topology influences the cross-flow forces is also identified as a function of the afterbody's shape. The fact that the length of influence of the squareback geometry is retrieved for the slanted afterbody is, in our opinion, a pure coincidence.

However, quite surprisingly, the adaptation mechanism of the wake towards the *minor* base pressure gradient $g_m^* = g_z^*$ and resulting in a shift in the wake orientation φ from the saturated values φ_P and $\pi - \varphi_P$ is not retrieved in the case of slanted boat-tails as observed in figure C.9(d). This means that the adaptation not only results from a *minor* gradient but also from a transfer of curvature from the geometry to the streamlines which does not occur here because of the slant. In other words, resulting from the suppression of the wake adaptation for the body parallel to the floor ($\alpha = 0°$) and aligned with the incoming flow ($\beta = 0°$), the phase dynamics of the slanted afterbody is independent of the ground clearance. As a consequence, it is similar to the dynamics which would be obtained without the ground (infinite clearance). It appears to be quite different from that of the axisymmetric body (Rigas *et al.*, 2014; Gentile *et al.*, 2016, 2017) since the phase is bounded by the four sharp edges of the base and the minor-to-major axes aspect ratio. Nonetheless, the bifurcation diagrams (figures C.9, C.10 and C.11) are quite similar to those of the other boat-tailed configurations the adaptation mechanism apart. In particular, even if not completely reached due to the limited allowed pitch angle in nose-up configuration, unlocking is expected for $\alpha \geq 2°$. As a result, the phase dynamics must still be seen as a key ingredient to understand the wake orientation especially since a strong correlation is observed between the gradients' and the cross-flow forces fluctuations. The other evidence of the role of the flow streamlines' curvature is provided by the contribution to the side force loading of the instability which is reduced with slanted geometries.

Although also subject to the y-instability, the three-dimensional boat-tailed afterbody yields specific results compared to all other investigated geometries. First of all, the instability is so considerably dumped that, from figure C.15(c), the saturated ground clearance is never reached in the range of investigations with an almost linearly growing modulus g_r^*. This means that the ground influence is strongly dependent on the afterbody geometry. In addition, the dynamics of the wake switches of bi-stable cases is almost ten times slower than that of the squareback. The instability's strength increase cannot be related to the adaptation mechanism of the *minor* base pressure gradient $-g_z^*$ for the considered base aspect ratios – since the latter is almost constant (figure C.15b) but through the *major* instead (figure C.15a). Equivalently said, the wake asymmetry becomes a function of the ground clearance. However, since the top and bottom boat-tail angles are different ($\theta_T \neq \theta_B$), the adaptation mechanism is revealed by the yaw sensitivity analysis (figure C.17b).

In addition, this boat-tail configuration is the only one of the few tested for which wake lock-in around $\varphi \simeq -\pi/2$ occurs in nose-up configurations. There is consequently a symmetry between the negative and positive pitch angles (figure C.19a, d) which was not observed for any afterbody so far. The phase unlocking mechanism aims at matching the geometrically imposed base pressure gradient along the *minor* base axis as described in § 4.4.3. It was said in § 4.3.1 to be a consequence of the vicinity of the ground which prevents lock-in around $\varphi \simeq -\pi/2$ corresponding to a reversed wake. However, since the bottom boat-tail angle θ_B, the averaged ground clearance $\bar{c}^* = \frac{1}{2}(c_f^* + c_r^*)$ and the pitch angle α are identical to those of the previous *T75B5* configuration, there is an unsatisfactory contradiction between the two cases. The main discrepancy being the strength of the base pressure gradient g_r^* which appears to be much smaller for the *3D* boat-tailed afterbody, we make the guess that it is also a driving parameter for the selection of the lock-in or unlocking dynamics. In fact, g_r^* becomes smaller than the geometrically imposed $g_z^{*\ B}$ corresponding to the stable *basic flow* and the adaptation mechanism described in § 4.4.3 predicts this lock-in, similarly to nose-down cases ($\alpha < 0°$).

As regards the mean aerodynamic coefficients, it clearly appears that for the first time in our results, the mean base suction becomes independent of the ground clearance (see figure C.16) which constitutes a major draw back in vehicle's design since the drag optimum is then unique and a compromise between drag and lift has to be found. Again, the most fuel-efficient operating point seems to be located around the onset of the instability and bi-stable cases are generally quite adapted to low-drag requirements thus enforcing the idea of Cadot *et al.* (2015*b*) that the – targeted – unstable symmetric wake solution is the key point for drag reduction unlike the unconditional suppression of the bi-stable dynamics – in particular if it leads to wake lock-in…

The contribution of the y-instability to the cross-flow forces is still constant regardless of the flow deviation (figure C.21a, b) although reduced with respect to 2D-boat tailed afterbodies. Interestingly, the length of effectiveness of the wake orientation on the body is identical to that of the *T75B5* configuration with the same angles proving that it is more related to the geometry than to the strength of the gradient g_r^*. The force fluctuations are also well reconstructed from the gradients' except for the lift's C_z' in the pitch experiment which are largely underestimated (figure C.21$c - f$) thus indicating that a global effect occurs. It might be ascribed to the global wake balance which transfers its unsteadiness to the outer flow and then affects the forebody.

The periodic fluctuations of the wake ascribed to a von Kármán-like mode are finally considered in this section. They show some similarities with the vortex-street wakes of cylinders in cross-flow (Bearman, 1967, 1969; Bearman & Trueman, 1972); in particular, a characteristic frequency close to a Strouhal number of $f^* \sim 0.2$[1] is observed for the switches of the wake in figure 5.24. The periodic wake mode is triggered in very specific conditions (§ C.2.3), when the top and bottom boat-tail angles are big enough so that the shear layers observed in figure 6.8(e, f) are close enough to interact. However, drag is increased for the reasons detailed in § 5.5.

The ground clearance sensitivity analysis was not performed for this case so it is impossible to conclude about the critical or the saturation ground clearances. Nonetheless, based on results provided by Mendona Bimbato *et al.* (2013) for a cylinder in a wall vicinity, there should be a considerable effect of the ground on the periodic mode. Provided the behavior of the periodic Ahmed body is similar to that of the cylinder[2], we expect the studied ground clearance of $c^* = 0.168$ to be almost outside the range of the wall influence – limited to a ratio distance-to-diameter of $h/D \leq 0.15$ for the cylinder in Mendona Bimbato *et al.* (2013) –, *i.e.* the instability should be saturated or at least almost saturated so that its strength does not depend on the ground clearance anymore. The yaw experiment shows that the sensitivity of the periodic mode towards the yaw is extremely high since very small angles suppress the wake fluctuations because of destabilization of the two shear layers. It results that a vertical wake orientation is selected but, since the two angles are close one with each other, it mainly results from the presence of the ground and of the model supports rather than from a geometrical constraint. In addition, there is a continuous and almost constant wake adaptation to the horizontal pressure gradient $g_y^{*\ B}$ – identical to that of the *basic flow* – and imposed by the body's misalignment. Unlike with the y-instability, there is no compensation and the phase adapts to match this constraint resulting in a global wake rotation as shown in figure C.22. The pitch experiment clearly shows that the instability is removed since a sudden and discontinuous

---

[1] The Strouhal number is referred to as the *dimensionless frequency* in other chapters. It originates from the seminal work of Strouhal (1878). The standard notation is rather St but we keep f^* for consistency.

[2] At least as regards the behavior of the periodic wake mode, in particular its frequency and the onset of the oscillations…

phase selection is operated by nose-down configurations ($\alpha < 0°$) while the vertical base pressure gradient g_z^* linearly increases without saturation. The case of nose-up ($\alpha > 0°$) is quite surprising since a lateral wake orientation is selected due to asymmetries of the setup but, unlike y-unstable cases, no wake unlocking is observed.
The suppression of the instability is clearly observed in figure C.24(a) since the mean side force coefficient becomes a linear function of the yaw angle β and $C_y = C_y^B$. As a consequence, there is no impact of the periodic vertical wake shifts on the side force loading. By analogy with the z-instability discussed in § 4.3.2, one would expect the mean lift coefficient C_z to reveal the periodic mode during the pitch sensitivity experiment (figure C.24b). However, the lift evolution is linear with the pitch angle at least for $\alpha < 0°$ which shows that, despite the wake rotation, the contribution of the periodic wake mode to the aerodynamic loading is negligible with respect to that of the *basic flow* and that, in first approximation $C_z \approx C_z^B$. Nonetheless, there is a slight deviation from the linear behavior for large nose-up ($1° \lesssim \alpha$). In our opinion, it must not be ascribed to the periodic wake mode but rather to the wake orientation at $\varphi \simeq \pi/4$ which results, as said earlier, from a defect of the setup. This shows that the phase still influences the mean aerodynamic loading because of the wake asymmetry but the contribution of the periodic wake mode is again negligible. Last, even if not extractable from the data, it is likely that the periodic mode contributes to the body's drag coefficient C_x similarly to the cylinder's wake (see for instance Henderson (1995); Fiabane *et al.* (2010); Iungo *et al.* (2012); Mendona Bimbato *et al.* (2013)).

C.4 Concluding remarks

The sensitivity of the wake of flat-backed Ahmed bodies with boat-tailed rear-end geometries towards the ground clearance and the inclination is investigated in this chapter. It turns out that the y-instability is not largely affected by the shape modification with respect to the squareback case presented in § 4.3.1. In particular, the same wake dynamics and similar contributions to the aerodynamic loading are retrieved. Three-dimensional boat-tails do not create major changes though, except for wake lock-in for nose-up pitches which may allow an easier control and at least ensure smaller fluctuations. The periodic wake mode is finally confirmed to replace completely the y-instability of the wake which leads to a different wake dynamics, mainly governed by the geometry, without modifying the aerodynamic loading.

APPENDIX D

Mesh independence of the RANS simulations

This appendix deals with the independence of the RANS solution towards the mesh density (§ D.2.1) but also towards the setup, comparing half-space and full-space simulations in § D.2.2.

Contents

D.1 Numerical setup **266**

D.2 Mesh independence **266**

D.2.1 Independence towards mesh density 266

D.2.2 Independence towards full or symmetrized space 266

D.3 Concluding remarks **268**

D.1 Numerical setup

The numerical setup is identical to that used in chapter 6. We compare two setups. One is the full domain described in § 6.2.1. The second one is a half-space. Considering the symmetry of the setup, we only consider the half-space $y^* < 0$, *i.e.* the left part of the body looking upstream. The plane $y^* = 0$ is replaced by a reflectional symmetry plane. In fact, only this latter case is built and the full-space configuration is obtained using a planar reflectional symmetry of the mesh. The considered simulation is a steady RANS case (§ 6.2.2).

D.2 Mesh independence

D.2.1 Independence towards mesh density

We compare the two meshes C and F described in § 6.2.1. The mesh independence of the solution is estimated owing to the mean aerodynamic loading applied to the body, estimated over the half-space y^* and extended to the whole body. The results are given in table D.1. It turns out that they are almost identical, at least to the requested precision. The coarse mesh C is not necessarily the most compact one but still allows quite quick computations. It means that its spatial resolution is sufficient for the present approach using Reynolds Averaged Navier-Stokes Equations (steady or unsteady) but it might not be the case if a Partially Averaged Navier-Stokes (PANS) or Large Eddy Simulation (LES) approach was chosen with the same geometry.

Table D.1 – Characteristic mean force and base suction coefficients for the squareback Ahmed body with $\alpha = 0°,\ \beta = 0°$ obtained for the two meshes C and F.

Configuration	c^*	C_b	C_x	C_y	C_z
Mesh C	0.067	0.178	0.258	0.000	−0.146
	0.101	0.178	0.254	0.000	−0.150
	0.168	0.181	0.250	0.000	−0.160
Mesh F	0.067	0.179	0.259	0.000	−0.146
	0.101	0.178	0.254	0.000	−0.149
	0.168	0.181	0.250	0.000	−0.160

D.2.2 Independence towards full or symmetrized space

This section aims at comparing results obtained with the full and half-space ($y^* < 0$) RANS simulations. The question treated in this section is legitimate as, unlike unsteady simulations, RANS results are expected to be symmetric; the main concern is then about the imposed symmetry plane at the centerline ($y^* = 0$) which may or not modify the results. One of the motivations for being able to simulate the half-space $y^* < 2$ only is to reduce by almost a factor of two the number of mesh points. As a result, the size of the computational problem is reduced in the same proportion which allows either a smaller allocation on the supercomputer (thus reducing the queuing time) or a shorter computation time for a given number of processors. Calculations are performed on the fine mesh F (see § 6.2.1) for both the half-space and the full-space configurations.

The mean aerodynamic loading and base suction are compared for the two setups. Because the simulation is steady, we do not have access to the fluctuating variables. The corresponding experimental data can be found in chapter 3. The mean base suction and aerodynamic coefficients obtained with the two simulations are given in table D.2. To be comparable, the forces need to be converted into force coefficients. If there is no question about the base suction, which will be identical for both configurations, the force coefficients computed from equation (2.3) are based on a reference surface S, taken as the quantity $H \times W$. For the half-space simulation, we replace this quantity by $2S = 2 \times H \times \frac{W}{2}$ so that the reference surface is identical in both cases. Consistently, the fluxes computed in the simulation have to be doubled. The results are presented using this correction. It can be clearly seen that the two simulations lead to identical quantities. The side force C_y is null by symmetry. In the following, we check whether similar velocity fields are obtained.

Table D.2 – Characteristic mean force and base suction coefficients for the squareback Ahmed body with $\alpha = 0°$, $\beta = 0°$ at various ground clearances obtained with the two computational setups for the fine mesh F.

Configuration	c^*	C_b	C_x	C_y	C_z
1/2-space	0.067	0.179	0.259	0.000	−0.146
	0.101	0.178	0.254	0.000	−0.149
	0.168	0.181	0.250	0.000	−0.160
Full space	0.067	0.179	0.259	0.000	−0.146
	0.101	0.178	0.254	0.000	−0.149
	0.168	0.181	0.250	0.000	−0.160

We compare the mean velocity fields; we focus on the wake in both the vertical and the horizontal planes and on the corresponding base pressure distributions in figure D.1. The flow around the forebody is found to be identical but is not presented in this section. The mean wake is identical for both simulations both in the vertical (figure D.1a, d) and the horizontal planes (figure D.1b, e). The mean base pressure distributions $C_p(y^*, z^*)$ are nearly identical for the full- (figure D.1c) and the half-spaces (figure D.1f) simulations; at most one may notice that the peak of pressure is higher ($C_p \geq -0.10$) for the half-space than for the full-space simulation.

Both the reconstructed velocity fields and base pressure distribution turn out to be identical. Simulating only the half-space $y^* < 0$ therefore yields identical results as the complete problem. This can be an interesting option for RANS simulations of the flow around the Ahmed body as the reduction of the computational problem's size allows shorter computations and/or lighter resources. However, since the goal would be to perform unsteady simulations (URANS), running the whole case was chosen in this work. Since the experimental flow is instantaneously never symmetric, one would expect the unsteady computation to behave similarly; the loss of symmetry of the solution would be prevented by the existence of a plane of reflectionnal symmetry at $y^* = 0$ which constitutes a major drawback of the reduced case.

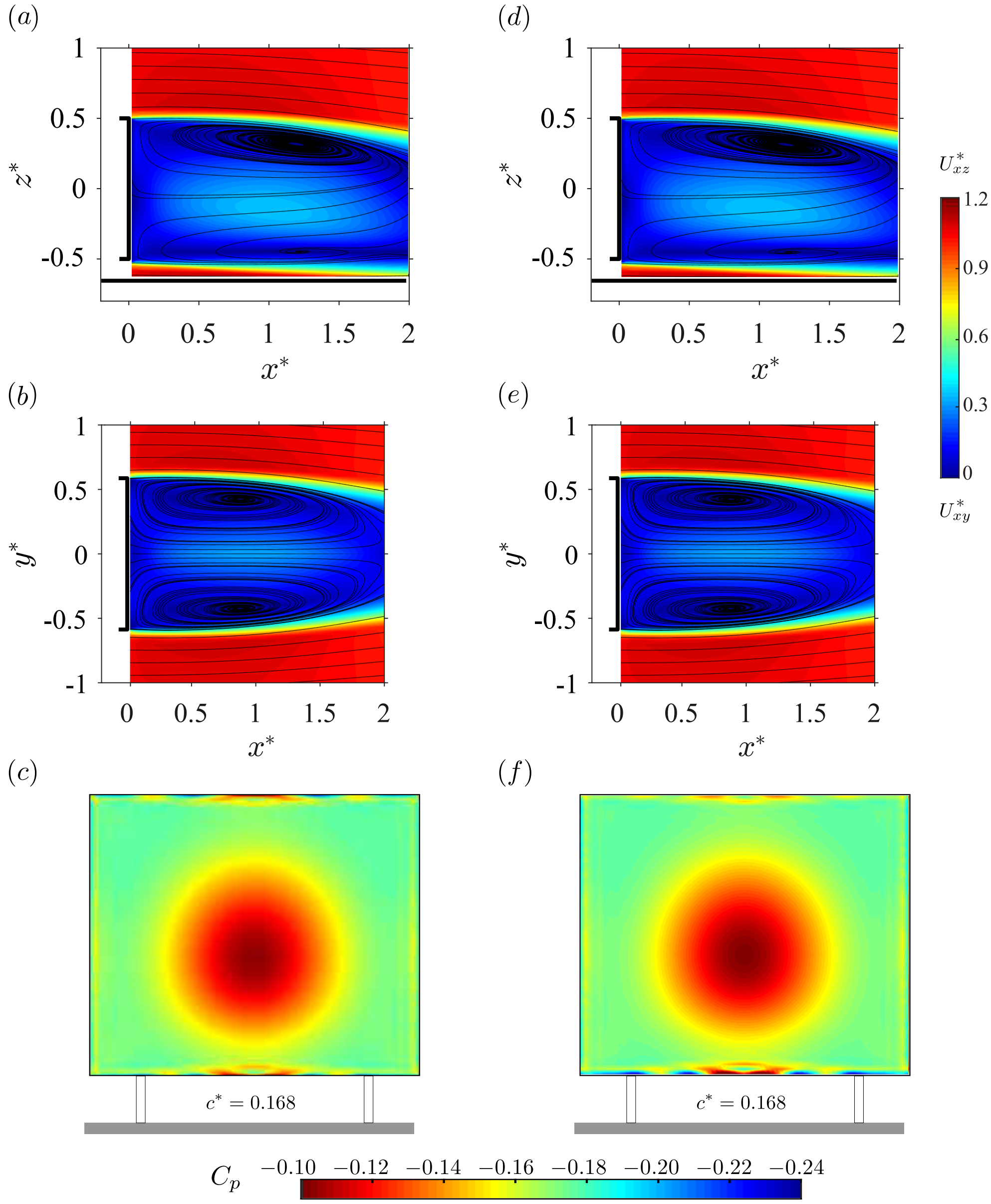

Figure D.1 – Mean wakes in the $y^* = 0$ (a, d) and $z^* = 0$ (b, e) planes for the two computational setups; (c, f) mean base pressure distribution. (a, b, c) Full-space, (c, e, f) half-space $y^* \leq 0$. Results are presented for $c^* = 0.168$. For the half-space simulation, results are symmetrized for easier comparison.

D.3 Concluding remarks

This appendix mainly shows that, once the grid independence in terms of the mesh density is reached – which is required so that the solution does not actually depend on this parameter –, the steady RANS case is identical regardless on the considered computational space. Since the solution is symmetric, simulating only the half space provides an enjoyable economy of computational resources and thus of time. Nevertheless, the use of the whole setup seems unavoidable when dealing with unsteady cases since the aim is to reveal the wake bifurcation.

List of references

2018 European vehicle market statistics, 2017/2018 | International Council on Clean Transportation. [Online]. [Cited on page 2]

Abikan, A., Lu, Y. & Yang, Z. 2018 Numerical study of flow over a bluff body with drag reduction devices. *Proceedings of the World Congress on Mechanical and Mechatronics Engineering* . [Cited on pages 143 and 232]

Ahmed, S.R., Ramm, G. & Faitin, G. 1984 Some salient features of the time-averaged ground vehicle wake. *SAE Technical Paper Series* **840300**. [Cited on pages 6, 7, 27, 30, 37, 39, 45, 50, 51, 54, 71, 95, 96, 150, 156, and 210]

Ahmed, S. R. 1983 Influence of Base Slant on the Wake Structure and Drag of Road Vehicles. *J. Fluids Eng.* **105** (4), 429–434. [Cited on pages 7, 50, 95, 96, 103, 210, and g]

Aljure, D.E., Lehmkuhl, O., Rodrìguez, I. & Oliva, A. 2014 Flow and turbulent structures around simplified car models. *Computers & Fluids* **96**, 122 – 135. [Cited on pages 6, 7, and 45]

Armaly, B.F., Durst, F., Pereira, J.C.F. & Schönung, B. 1983 Experimental and theoretical investigation of backward facing step flow. *Journal of Fluid Mechanics* **127** (473), 20. [Cited on pages 37, 45, and 100]

Atkinson, K.E. 1978 *An introduction to numerical analysis.* Wiley. [Cited on page 149]

Avadiar, T., Thompson, M.C., Sheridan, J. & Burton, D. 2018 Characterisation of the wake of the DrivAer estate vehicle. *Journal of Wind Engineering and Industrial Aerodynamics* **177**, 242 – 259. [Cited on pages 7, 12, and 172]

Baldino, C., Tietge, U., Muncrief, R.l, Bernard, Y. & Mock, P. 2017 Road tested: Comparative overview of real-world versus type-approval NO_x and CO_2 emissions from Diesel cars in Europe . [Cited on page 3]

Barros, D. 2015 *Wake and Drag Manipulation of a Bluff Body Using Fluidic Forcing.* Thèse de doctorat, Chasseneuil-du-Poitou, École nationale supérieure de mécanique et d'aérotechnique (ISAE-ENSMA). [Cited on page 44]

Barros, D., Borée, J., Cadot, O., Spohn, A. & Noack, B. R. 2017 Forcing symmetry exchanges and flow reversals in turbulent wakes. *Journal of Fluid Mechanics* **829**. [Cited on pages 8, 12, 13, 37, 39, 45, 49, 50, 51, 55, 83, 85, 108, 136, 150, 172, 199, 203, and a]

Barros, D., Borée, J., Noack, B. R., Spohn, A. & Ruiz, T. 2016 Bluff body drag manipulation using pulsed jets and Coanda effect. *J. Fluid Mech.* **805**, 422–459. [Cited on pages 8, 12, 151, and a]

Barros, D., Ruiz, T., Borée, J. & Noack, B.R. 2014 Control of three-dimensionnal blunt body wake using low and high frequency pulsed jets. *International Journal of Flow Control* **6** (1), 61–74. [Cited on pages 8, 12, 54, 55, 71, and 217]

Barth, R. 1956 *Einfluß der Form und der Umströmung von Kraftfahrezeugen auf Widerstand, Bodenhaftung und Fahrtrichtungshaltung*. VDI-Zeitschrift. [Cited on page 115]

Baude, M., Dussud, F. X., Ecoiffier, M., Duvernoy, J. & Vailles, C. 2017 Key figures on climate – France, Europe and Worldwide. *Tech. Rep.*. Office of the Commissioner-General for Sustainable Development. [Cited on page 2]

Bearman, P.W. 1967 On vortex street wakes. *Journal of Fluid Mechanics* **28** (4), 625–641. [Cited on page 263]

Bearman, P.W. 1969 On vortex shedding from a circular cylinder in the critical Reynolds number regime. *Journal of Fluid Mechanics* **37** (03), 577–585. [Cited on page 263]

Bearman, P.W. 1984 Some observations on road vehicle wakes. *Tech. Rep.*. SAE Technical Paper. [Cited on page 96]

Bearman, P.W. & Trueman, D.M. 1972 An investigation of the flow around rectangular cylinders. *Aeronautical Quarterly* **23**, 229–237. [Cited on page 263]

Bearman, P. W. 1965 Investigation of the flow behind a two-dimensional model with a blunt trailing edge and fitted with splitter plates. *J. Fluid Mech.* **21** (2), 241–255. [Cited on page 94]

Beaudoin, J.F., Cadot, O., Aider, J.L., Gosse, K., Paranthoën, P., Hamelin, B., Tissier, M., Allano, D., Mutabazi, I., Gonzales, M. *et al.* 2004 Cavitation as a complementary tool for automotive aerodynamics. *Experiments in Fluids* **37** (5), 763–768. [Cited on pages 37 and 44]

Beneddine, S., Sipp, D., Arnault, A., Dandois, J. & Lesshafft, L. 2016 Conditions for validity of mean flow stability analysis. *J. Fluid Mech.* **798**, 485–504. [Cited on pages 144, 161, and k]

Beneddine, S., Yegavian, R., Sipp, D. & Leclaire, B. 2017 Unsteady flow dynamics reconstruction from mean flow and point sensors: an experimental study. *J. Fluid Mech.* **824**, 174–201. [Cited on pages 144, 161, and k]

Bohorquez, P., Sanmiguel-Rojas, E., Sevilla, A., Jiménez-González, JI & Martínez-Bazán, C. 2011 Stability and dynamics of the laminar wake past a slender blunt-based axisymmetric body. *Journal of Fluid Mechanics* **676** (1), 110–144. [Cited on page 8]

Bonnavion, G. & Cadot, O. 2018 Unstable wake dynamics of rectangular flat-backed bluff bodies with inclination and ground proximity. *J. Fluid Mech.* **854**, 196–232. [Cited on pages 47 and 231]

Bonnavion, G., Cadot, O., Évrard, A., Herbert, V., Parpais, S., Vigneron, R. & Délery, J. 2017*a* On multistabilities of real car's wake. *Journal of Wind Engineering and Industrial Aerodynamics* **164**, 22–33. [Cited on pages 14, 51, 74, 79, 90, 168, 170, 182, 203, and 204]

Bonnavion, G., Cadot, O., Herbert, V., Parpais, S., Vigneron, R. & Délery, J. 2017*b* Effect of a base cavity on the wake of the squareback Ahmed body at various ground clearances and application to drag reduction. In *Congrès Français de Mécanique, CFM 2017*. Lille, France. [Cited on pages 12, 50, 193, 194, and 231]

Bonnavion, G., Joly, A., Cadot, O., Herbert, V., Parpais, S., Vigneron, R. & Délery, J. 2018 Visualisation en temps réel de pressions en soufflerie automobile avec LabVIEW. *Tech. Rep.* 17732-17733. Solutions National Instrument. [Cited on pages 23 and 227]

Brackston, R. D., García De La Cruz, J.M., Wynn, A., Rigas, G. & Morrison, J. F. 2016 Stochastic modelling and feedback control of bistability in a turbulent bluff body wake. *Journal of Fluid Mechanics* **802**, 726–749. [Cited on pages 10, 12, 38, 49, 54, 123, 143, 203, 233, and e]

Brackston, R. D., Wynn, A. & Morrison, J. F. 2018 Modelling and feedback control of vortex shedding for drag reduction of a turbulent bluff body wake. *Int. J. Heat Fluid Flow* **71**, 127–136. [Cited on pages 8 and 49]

Brillouin, M. 1910 Les surfaces de glissement d'Helmholtz et la résistance des fluides. *Annales de chimie et de physique* **XXIII** (8), 145–230. [Cited on pages 6, 37, 45, 93, 98, 99, and g]

Bruneau, C.-H., Khadra, K. & Mortazavi, I. 2017 Flow analysis of square-back simplified vehicles in platoon **66**, 43–59. [Cited on page 37]

Buresti, G., Fedeli, R. & Ferraresi, A. 1997 Influence of afterbody rounding on the pressure drag of an axisymmetrical bluff body. *J. Wind Eng. Ind. Aerodyn.* **69-71**, 179–188. [Cited on page 97]

Bury, Y. & Jardin, T. 2012 Transitions to chaos in the wake of an axisymmetric bluff body. *Phys. Lett. A* **376** (45), 3219–3222. [Cited on page 8]

Butcher, J. C. 2016 *Numerical methods for ordinary differential equations*. Wiley Blackwell. [Cited on page 144]

Cabitza, S. 2014 Active control of the wake from a rectangular-sectioned body. PhD thesis, Imperial College London. [Cited on page 50]

Cadot, O. 2016 Stochastic fluid structure interaction of three-dimensional plates facing a uniform flow. *Journal of Fluid Mechanics* **794**. [Cited on pages 5, 12, and a]

Cadot, O., Courbois, A., Ricot, D., Ruiz, T., Harambat, F., Herbert, V., Vigneron, R. & Délery, J. 2016 Characterisations of force and pressure fluctuations of real vehicles. *Int. J. Engineering Systems Modelling and Simulation* **8** (2), 99–105. [Cited on pages 6, 12, 14, 51, 74, 168, 169, 170, 203, 204, and a]

Cadot, O., Desai, A., Mittal, S., Saxena, S. & Chandra, B. 2015*a* Statistics and dynamics of the boundary layer reattachments during the drag crisis transitions of a circular cylinder. *Physics of Fluids* **27** (1), 014101. [Cited on page 216]

Cadot, O., Evrard, A. & Pastur, L. 2015*b* Imperfect supercritical bifurcation in a three-dimensional turbulent wake. *Physical Review E* **91** (6), 063005. [Cited on pages v, vii, 8, 9, 12, 13, 14, 37, 40, 41, 42, 49, 54, 56, 57, 58, 71, 89, 90, 108, 143, 145, 150, 151, 153, 161, 232, 234, 263, a, and e]

Cambier, L., Heib, S. & Plot, S. 2013 The Onera elsA CFD software: input from research and feedback from industry. *Mechanics & Industry* **14** (3), 159–174. [Cited on page 144]

Castelain, T., Michard, M., Szmigiel, M., Chacaton, D. & Juvé, D. 2018 Identification of flow classes in the wake of a simplified truck model depending on the underbody velocity. *Journal of Wind Engineering and Industrial Aerodynamics* **175**, 352–363. [Cited on pages 13, 14, 37, 50, 151, 178, 198, 201, 203, and 204]

Chang, C.-H. & Liou, M.-S. 2003 A new approach to the simulation of compressible multifluid flows with AUSM scheme. *16th AIAA Computational Fluid Dynamics Conference* . [Cited on page 144]

Choi, H., Jeon, W.-P. & Kim, J. 2008 Control of flow over a bluff body. *Annual Review of Fluid Mechanics* **40**, 113–139. [Cited on page 232]

Choi, H., Lee, J. & Park, H. 2014 Aerodynamics of heavy vehicles. *Annual Review of Fluid Mechanics* **46**, 441–468. [Cited on page 232]

Chrust, M., Goujon-Durand, S. & Wesfreid, J.E. 2013 Loss of a fixed plane of symmetry in the wake of a sphere. *Journal of Fluids and Structures* **41**, 51–56. [Cited on page 8]

Cogotti, A. 1998 A parametric study on the ground effect of a simplified car model. *Tech. Rep.*. SAE Technical Paper. [Cited on page 45]

Conan, B., Anthoine, J. & Planquart, P. 2011 Experimental aerodynamic study of a car-type bluff body. *Exp. Fluids* **50** (5), 1273–1284. [Cited on page 37]

Coon, J. D. & Visser, K. D. 2004 Drag reduction of a tractor-trailer using planar boat tail plates. *The Aerodynamics of Heavy Vehicles: Trucks, Buses, and Trains Lecture Notes in Applied and Computational Mechanics* pp. 249–265. [Cited on page 6]

Corallo, M., Sheridan, J. & Thompson, M. C. 2015 Effect of aspect ratio on the near-wake flow structure of an Ahmed body. *Journal of Wind Engineering and Industrial Aerodynamics* **47**, 95 – 103. [Cited on page 156]

Courant, R., Friedrichs, K. & Lewy, H. 1928 Über die partiellen Differenzengleichungen der mathematischen Physik. *Mathematische Annalen* **100** (1), 32–74. [Cited on page 149]

García de la Cruz, J. M., Oxlade, A. R. & Morrison, J. F. 2017 Passive control of base pressure on an axisymmetric blunt body using a perimetric slit. *Phys. Rev. Fluids* **2** (4), 043905. [Cited on page 232]

Dahan, J. A., Morgans, A. S. & Lardeau, S. 2012 Feedback control for form-drag reduction on a bluff body with a blunt trailing edge. *J. Fluid Mech.* **704**, 360–387. [Cited on page 100]

d'Alembert, J. 1752 *Essai d'une nouvelle théorie de la résistance des fluides.* [Cited on page 6]

Dalla Longa, L., Evstafyeva, O. & Morgans, A.S. 2017 Bi-modality in the wakes of simplified road vehicles: simulation and feedback control. In *Proc.52nd 3AF International Conference in Applied Aerodynamics*. 3AF. [Cited on pages 143, 155, and 158]

Deck, S. 2012 Recent improvements in the Zonal Detached Eddy Simulation (ZDES) formulation. *Theor. Comput. Fluid Dyn.* **26** (6), 523–550. [Cited on page 161]

Dekker, R., Bloemhof, J. & Mallidis, I. 2012 Operations Research for green logistics – An overview of aspects, issues, contributions and challenges. *Eur. J. Oper. Res.* **219** (3), 671–679. [Cited on page 2]

Délery, J., Chanetz, B., P., Gilliéron, Gnemmi, P. & Perrier, Ph. 2017 *Aérodynamique expérimentale: souffleries et méthodes de mesure*. Cépadues Editions. [Cited on pages 19 and 25]

Dutton, J.C. & Addy, A.L. 1998 Fluid dynamic mechanisms and interactions within separated flows. *Tech. Rep.*. Illinois University at Urbana. [Cited on pages 50 and 232]

Evrard, A., Cadot, O., Herbert, V., Ricot, D., Vigneron, R. & Délery, J. 2016 Fluid force and symmetry breaking modes of a 3D bluff body with a base cavity. *Journal of Fluids and Structures* **61**, 99–114. [Cited on pages 8, 9, 12, 14, 20, 37, 38, 41, 42, 43, 45, 49, 50, 51, 54, 55, 56, 58, 63, 64, 67, 71, 84, 89, 90, 108, 123, 134, 143, 155, 193, 194, 195, 196, 231, 232, 234, 236, a, and e]

Evrard, A., Cadot, O., Sicot, C., Herbert, V., Ricot, D. & Vigneron, R.i 2017 Comparative effects of vortex generators on Ahmed's squareback and minivan car models. *Proceedings of the Institution of Mechanical Engineers, Part D: Journal of Automobile Engineering* **231** (9), 1287–1293. [Cited on pages 10 and 12]

Evstafyeva, O., Morgans, A. S. & Dalla Longa, L. 2017 Simulation and feedback control of the ahmed body flow exhibiting symmetry breaking behaviour. *Journal of Fluid Mechanics* **817**. [Cited on pages v, vii, 8, 12, 37, 42, 89, 143, and a]

Fabre, D., Auguste, F. & Magnaudet, J. 2008 Bifurcations and symmetry breaking in the wake of axisymmetric bodies. *Physics of Fluids* **20**, 051702. [Cited on page 8]

Fago, B., Lindner, H. & Mahrenholtz, O. 1991 The effect of ground simulation on the flow around vehicles in wind tunnel testing. *Journal of Wind Engineering and Industrial Aerodynamics* **38**, 47–57. [Cited on pages 20 and 66]

Fiabane, L., Gohlke, M. & Cadot, O. 2010 Characterization of flow contributions to drag and lift of a circular cylinder using a volume expression of the fluid force. *European Journal of Mechanics - B/Fluids* **30**, 2011. [Cited on page 264]

Forbes, D., Page, G., Passmore, M. & Gaylard, A. 2017 A study of computational methods for wake structure and base pressure prediction of a generic SUV model with fixed and rotating wheels. *Proceedings of the Institution of Mechanical Engineers, Part D: Journal of Automobile Engineering* **231** (9), 1222–1238. [Cited on page 51]

Franck, G., Nigro, N., Storti, M. & d'Elia, J. 2009 Numerical simulation of the Ahmed vehicle model near-wake. *Latin American Applied Research* **39** (4). [Cited on pages 37 and 44]

Garry, K. P. 1981 Development of container-mounted devices for reducing the aerodynamic drag of commercial vehicles. *J. Wind Eng. Ind. Aerodyn.* **9** (1), 113–124. [Cited on page 94]

Garry, K. P. 1996 Some effects of ground clearance and ground plane boundary layer thickness on the mean base pressure of a bluff vehicle type body. *J. Wind Eng. Ind. Aerodyn.* **62** (1), 1–10. [Cited on page 49]

Gaylard, A. P., Kabanovs, A., Jilesen, J., Kirwan, K. & Lockerby, D. A. 2017 Simulation of rear surface contamination for a simple bluff body. *J. Wind Eng. Ind. Aerodyn.* **165**, 13–22. [Cited on page 49]

Gentile, V., Schrijer, F.F.J., Van Oudheusden, B.W. & Scarano, F. 2016 Low-frequency behavior of the turbulent axisymmetric near-wake. *Physics of Fluids* **28** (6). [Cited on pages 10, 260, and 262]

Gentile, V., Van Oudheusden, B.W., Schrijer, F.F.J. & Scarano, F. 2017 The effect of angular misalignment on low-frequency axisymmetric wake instability. *Journal of Fluid Mechanics* **813**. [Cited on pages 10, 50, 260, and 262]

Gohlke, M., Beaudoin, J.F., Amielh, M. & Anselmet, F. 2007 Experimental analysis of flow structures and forces on a three-dimensional bluff body in constant cross-wind. *Experiments in Fluids* **43** (4), 579–594. [Cited on page 49]

Grandemange, M. 2013 Analysis and control of three-dimensional turbulent wakes : from axisymmetric bodies to real road vehicles. PhD thesis, ENSTA ParisTech. [Cited on pages 5, 12, 37, 41, 44, and 169]

Grandemange, M., Cadot, O., Courbois, A., Herbert, V., Ricot, D., Ruiz, T. & Vigneron, R. 2015 A study of wake effects on the drag of the Ahmed squareback model at the industrial scale. *Journal of Wind Engineering and Industrial Aerodynamics* **145**, 282–291. [Cited on pages 6, 10, 13, 14, 49, 96, 97, 107, 116, 232, and i]

Grandemange, M., Gohlke, M. & Cadot, O. 2012*a* Reflectional symmetry breaking of the separated flow over three-dimensional bluff bodies. *Physical Review E* **86**, 035302. [Cited on pages v, vii, 5, 8, 37, 42, 45, 89, 90, 124, 143, 202, 232, and a]

Grandemange, M., Gohlke, M. & Cadot, O. 2013*a* Bi-stability in the turbulent wake past parallelepiped bodies with various aspect ratios and wall effects. *Physics of Fluids* **25**, 95–103. [Cited on pages 10, 11, 12, 13, 14, 37, 42, 49, 50, 51, 54, 55, 56, 70, 71, 72, 76, 84, 86, 89, 96, 108, 126, 134, 136, 145, 172, 188, 193, 200, 203, 205, 221, 232, 233, 239, 260, a, b, e, and o]

Grandemange, M., Gohlke, M. & Cadot, O. 2013*b* Turbulent wake past a three-dimensional blunt body. Part 1. Global modes and bi-stability. *Journal of Fluid Mechanics* **722**, 51–84. [Cited on pages 8, 9, 10, 12, 29, 38, 42, 44, 49, 50, 54, 57, 62, 85, 108, 124, 136, 143, 144, 155, 161, 216, 240, and a]

Grandemange, M., Gohlke, M. & Cadot, O. 2014*a* Statistical axisymmetry of the turbulent sphere wake. *Experiments in fluids* **55** (11), 1–10. [Cited on page 6]

Grandemange, M., Gohlke, M. & Cadot, O. 2014*b* Turbulent wake past a three-dimensional blunt body. Part 2. Experimental sensitivity analysis. *Journal of Fluid Mechanics* **752**, 439–461. [Cited on pages 8, 10, 12, 38, 49, 50, 83, 89, 143, 158, 161, 202, 203, and a]

Grandemange, M., Mary, A., Gohlke, M. & Cadot, O. 2013*c* Effect on drag of the flow orientation at the base separation of a simplified blunt road vehicle. *Experiments in fluids* **54** (5), 1–10. [Cited on pages 8, 12, 14, 96, 107, 109, 110, 111, 113, 114, 116, 117, 121, 203, a, g, and i]

Grandemange, M., Parezanović, V., Gohlke, M. & Cadot, O. 2012*b* On experimental sensitivity analysis of the turbulent wake from an axisymmetric blunt trailing edge. *Physics of Fluids* **24**, 035106. [Cited on page 202]

Grandemange, M., Ricot, D., Vartanian, C., Ruiz, T. & Cadot, O. 2014*c* Characterization of the flow past real road vehicles with blunt afterbodies. *International Journal of Aerodynamics* **4** (1/2), 24–42. [Cited on page 172]

Guilmineau, E., Chikhaoui, O., Deng, G. & Visonneau, M.l 2013 Cross wind effects on a simplified car model by a DES approach. *Comput. Fluids* **78**, 29–40. [Cited on page 49]

Han, T., Hammond, D.C. & Sagi, C.J. 1992 Optimization of bluff body for minimum drag in ground proximity. *AIAA Journal* **30** (4), 882–889. [Cited on pages 93, 96, 106, 113, 115, 117, 122, 133, 138, and g]

He, W., Yu, P. & Li, . K. B. 2018 Ground effects on the stability of separated flow around a NACA 4415 airfoil at low Reynolds numbers. *Aerosp. Sci. Technol.* **72**, 63–76. [Cited on page 144]

Hecht, F. 2012 New development in FreeFem++. *J. Numer. Math.* **20** (3-4), 251–265. [Cited on page 98]

Heft, A., Indinger, T. & Adams, N. 2011 Investigation of unsteady flow structures in the wake of a realistic generic car model. In *29th AIAA Applied Aerodynamics Conference*, p. 3669. [Cited on pages 6 and 172]

Heft, A., Indinger, T. & Adams, N. 2012*a* Experimental and numerical investigation of the DrivAer model. In *ASME 2012 Fluids Engineering Division Summer Meeting*, pp. 41–51. American Society of Mechanical Engineers. [Cited on pages 6 and 172]

Heft, A., Indinger, T. & Adams, N. 2012*b* Introduction of a new realistic generic car model for aerodynamic investigations. *Tech. Rep.*. SAE Technical Paper. [Cited on pages 6 and 172]

Henderson, R. D. 1995 Details of the drag curve near the onset of vortex shedding. *Physics of Fluids* **7** (9), 2102–2104. [Cited on page 264]

Herry, B.B., Keirsbulck, L. & Paquet, J.B. 2011 Flow bi-stability downstream of three-dimensional double backward facing steps at zero-degree slideslip. *ASME Transactions Journal of Fluids Engineering* **133** (054501), 1–4. [Cited on pages 12 and 49]

Howell, J. 2014 Aerodynamic drag in a windy environment. In *International Vehicle Aerodynamics Conference 2014*, pp. 14–15. [Cited on page 49]

Howell, J. 2015 Aerodynamic drag of passenger cars at yaw. *SAE International Journal of Passenger Cars-Mechanical Systems* **8** (2015-01-1559), 306–316. [Cited on page 49]

Howell, J. & Le Good, G. 2008 The Effect of Backlight Aspect Ratio on Vortex and Base Drag for a Simple Car-Like Shape. *SAE Technical Paper* . [Cited on page 96]

Howell, J., Sims-Williams, D., Sprot, A., Hamlin, F. & Dominy, R. 2012 Bluff body drag reduction with ventilated base cavities. *SAE International journal of passenger cars. Mechanical systems.* **5** (1), 152–160. [Cited on page 232]

Hucho, W.-H. 1978 The Aerodynamic Drag of Cars Current Understanding, Unresolved Problems, and Future Prospects. In *Aerodynamic drag mechanisms of bluff bodies and road vehicles*, pp. 7–44. Springer. [Cited on pages 94, 95, 96, 216, 217, and g]

Hucho, W.-H. 1998*a* *Aerodynamics of road vehicles*. SAE International. [Cited on pages 3, 6, 185, 196, and 197]

Hucho, W.-H. 1998*b* Aerodynamics of road vehicles: From fluid mechanics to vehicle engineering. *SAE International, Warrendale, PA* **177**. [Cited on page 3]

Hunt, J.C.R., Wray, A.A. & Moin, P. 1988 Eddies, streams, and convergence zones in turbulent flows. *Studying Turbulence Using Numerical Simulation Databases-I1* p. 193. [Cited on page 147]

Irving Brown, Y.A., Windsor, S. & Gaylard, A.P. 2010 The effect of base bleed and rear cavities on the drag of an SUV. *SAE Technical Paper Series* **2010-01-0512**. [Cited on page 232]

Iungo, G. V., Pii, L .M. & Buresti, G. 2012 Experimental investigation on the aerodynamic loads and wake flow features of a low aspect-ratio circular cylinder. *Journal of Fluids and Structures* **28**, 279–291. [Cited on page 264]

Jackson, C. P. 1987 A finite-element study of the onset of vortex shedding in flow past variously shaped bodies. *J. Fluid Mech.* **182**, 23–45. [Cited on page 8]

Jiang, B.-N., Hou, L.-J., Lin, T.-L. & Povinelli, L. A. 1995 Least-squares finite element solutions for three-dimensional backward-facing step flow. *International Journal of Computational Fluid Dynamics* **4** (1-2), 1–19. [Cited on page 37]

Johnson, T. A. & Patel, V. C. 1999 Flow past a sphere up to a reynolds number of 300. *Journal of Fluid Mechanics* **378**, 19–70. [Cited on page 8]

Kabanovs, A., Garmory, A., Passmore, M. & Gaylard, A. 2017*a* Computational simulations of unsteady flow field and spray impingement on a simplified automotive geometry. *J. Wind Eng. Ind. Aerodyn.* **171**, 178–195. [Cited on page 51]

Kabanovs, A., Hodgson, G., Garmory, A., Passmore, M. & Gaylard, A. 2017*b* A Parametric Study of Automotive Rear End Geometries on Rear Soiling. *SAE Int. J. Passenger Cars Mech. Syst.* **10** (2), 553–562. [Cited on page 97]

Khalighi, B., Chen, K.H. & Laccarino, G. 2012 Unsteady aerodynamic flow investigation around a simplified squareback road vehicle with drag reduction devices. *Journal of Fluids Engineering* **134** (6). [Cited on pages 143 and 144]

KHALIGHI, B., ZHANG, S., KOROMILAS, C., BALKANYI, S.R., BERNAL, L.P., IACCARINO, G. & MOIN, P. 2001 Experimental and computational study of unsteady wake flow behind a bluff body with a drag reduction device. *SAE Technical Paper Series* **2001-01-1042**. [Cited on pages 143, 153, and k]

KHAN, T. & FREY, H. C. 2018 Comparison of real-world and certification emission rates for light duty gasoline vehicles. *Sci. Total Environ.* **622-623**, 790–800. [Cited on page 3]

KHOURY, G. K. EL, ANDERSSON, H. I. & PETTERSEN, B. 2012 Wakes behind a prolate spheroid in crossflow. *J. Fluid Mech.* **701**, 98–136. [Cited on page 8]

KIM, D., LEE, H., YI, W. & CHOI, H. 2016 A bio-inspired device for drag reduction on a three-dimensional model vehicle. *Bioinspiration Biomimetics* **11** (2), 026004. [Cited on pages 96 and 217]

KIRCHHOFF, G. 1869 Zur Theorie freier Flüssigkeitsstrahlen. *Journal für die reine und angewandte Mathematik* **LXX** (4), 289–298. [Cited on pages 6, 37, 45, 93, 98, and g]

KLOTZ, L., GOUJON-DURAND, S., ROKICKI, J. & WESFREID, J. E. 2014 Experimental investigation of flow behind a cube for moderate reynolds numbers. *Journal of Fluid Mechanics* **750**, 73–98. [Cited on page 8]

KOK, J. C. 2000 Resolving the dependence on freestream values for the $k-\omega$ turbulence model. *AIAA journal* **38** (7), 1292–1295. [Cited on page 147]

KRAJNOVIĆ, S. & DAVIDSON, L. 2002 Large-eddy simulation of the flow around a bluff body. *AIAA journal* **40** (5), 927–936. [Cited on pages 37 and 45]

KRAJNOVIĆ, S. & DAVIDSON, L. 2003 Numerical study of the flow around a bus-shaped body. *Journal of Fluids Engineering* **125**, 500. [Cited on pages 45 and 155]

KRAJNOVIĆ, S. & DAVIDSON, L. 2005*a* Flow around a simplified car, part 1: large eddy simulation. *Journal of Fluids Engineering* **127**, 907. [Cited on page 55]

KRAJNOVIĆ, S. & DAVIDSON, L. 2005*b* Flow around a simplified car. Part 2. Understanding the flow. *Journal of Fluids Engineering* **127**, 919. [Cited on page 55]

KRUISWYK, R. W. & DUTTON, J. C. 1990 Effect of a base cavity on subsonic near-wake flow. *AIAA Journal* **28** (11), 1885–1893. [Cited on page 232]

LA NOTTE, A., TONIN, S. & LUCARONI, G. 2018 Assessing direct and indirect emissions of greenhouse gases in road transportation, taking into account the role of uncertainty in the emissions inventory. *Environ. Impact Assess. Rev.* **69**, 82–93. [Cited on page 2]

LAMBALLAIS, E., SILVESTRINI, J. & LAIZET, S. 2008 Direct numerical simulation of a separation bubble on a rounded finite-width leading edge. *International Journal of Heat and Fluid Flow* **29** (3), 612–625. [Cited on page 37]

LAMBALLAIS, E., SILVESTRINI, J. & LAIZET, S. 2010 Direct numerical simulation of flow separation behind a rounded leading edge: Study of curvature effects. *International Journal of Heat and Fluid Flow* **31** (3), 295–306. [Cited on page 37]

LANDMAN, D., WOOD, R., SEAY, W. & BLEDSOE, J. 2009 Understanding Practical Limits to Heavy Truck Drag Reduction. *SAE Int. J. Commer. Veh.* **2** (2), 183–190. [Cited on page 97]

Langevin, P. 1908 Sur la théorie du mouvement brownien. *Compt. Rendus* **146**, 530–533. [Cited on page 10]

Lanser, W. R., Ross, J. C. & Kaufman, A. E. 1991 Aerodynamic Performance of a Drag Reduction Device on a Full-Scale Tractor/Trailer. [Cited on page 97]

Lay, W. E. 1933 Is 50 Miles Per Gallon Possible With Correct Streamlining? *SAE Trans.* **28**, 177–186. [Cited on page 4]

Le Good, G., Johnson, C., Clough, B. & Lewis, R. 2011 The Aesthetics of Low Drag Vehicles. *SAE Int. J. Engines* **4** (2), 2638–2658. [Cited on page 4]

Le Good, G. M. & Garry, K. P. 2004 On the use of reference models in automotive aerodynamics. *Tech. Rep.*. SAE Technical Paper. [Cited on page 6]

Leuschen, J. & Cooper, K. R. 2006 Full-Scale Wind Tunnel Tests of Production and Prototype, Second-Generation Aerodynamic Drag-Reducing Devices for Tractor-Trailers. [Cited on page 97]

Li, R., Barros, D., Borée, J., Cadot, O., Noack, B. R. & Cordier, L. 2016 Feedback control of bimodal wake dynamics. *Experiments in Fluids* **57** (10), 158. [Cited on pages 8, 12, 37, 49, 55, 89, 217, and a]

Liou, M.-S. 2006 A sequel to AUSM, part II: AUSM-up for all speeds. *Journal of Computational Physics* **214** (1), 137–170. [Cited on page 144]

Liou, M.-S. & Steffen, C. J. 1993 A new flux splitting scheme. *Journal of Computational Physics* **107** (1), 23–39. [Cited on page 144]

Littlewood, R. & Passmore, M. 2010 The optimization of roof trailing edge geometry of a simple squareback. *SAE Technical Paper Series* **2010-01-0510**. [Cited on pages 12, 14, 29, 45, 49, 96, 97, 111, 115, 116, 121, 126, and a]

Littlewood, R. & Passmore, M. 2012 Aerodynamic drag reduction of a simplified squareback vehicle using steady blowing. *Experiments in Fluids* **53** (2), 1–11. [Cited on pages 29, 45, and 49]

Littlewood, R., Passmore, M. & Wood, D. 2011 An investigation into the wake structure of square back vehicles and the effect of structure modification on resultant vehicle forces **4**, 2629–2637. [Cited on pages 29, 45, and 49]

Lorite-Díez, M., Jiménez-González, J. I., Gutiérrez-Montes, C. & Martínez-Bazán, C. 2017 Drag reduction of slender blunt-based bodies using optimized rear cavities. *J. Fluids Struct.* **74**, 158–177. [Cited on page 232]

Lucas, J.-M., Cadot, O., Herbert, V., Parpais, S. & Délery, J. 2017 A numerical investigation of the asymmetric wake mode of a squareback Ahmed body – effect of a base cavity. *Journal of Fluid Mechanics* **831** (1), 675 – 697. [Cited on pages 8, 12, 37, 41, 45, 50, 51, 63, 64, 67, 84, 89, 143, 151, 155, 156, 158, 194, 196, 232, 234, 236, and a]

Mair, W. A. 1969 Reduction of base drag by boat-tailed afterbodies in low-speed flow. *Aeronautical Quarterly* **20** (4), 307–320. [Cited on pages 14, 93, 94, 97, 98, 113, and 128]

Mariotti, A. & Buresti, G. 2013 Experimental investigation on the influence of boundary layer thickness on the base pressure and near-wake flow features of an axisymmetric blunt-based body. *Exp. Fluids* **54** (11), 1612. [Cited on page 50]

Mariotti, A., Buresti, G., Gaggini, G. & Salvetti, M. V. 2017 Separation control and drag reduction for boat-tailed axisymmetric bodies through contoured transverse grooves. *Journal of Fluid Mechanics* **832**, 514–549. [Cited on pages 10, 94, and 138]

Marquet, O. & Larsson, M. 2014 Global wake instabilities of low aspect-ratio flat-plates. *European Journal of Mechanics B/Fluids* **49**, 400–412. [Cited on pages 8, 9, 50, 126, 134, and a]

Martín-Alcántara, A., Sanmiguel-Rojas, E., Gutérrez-Montes, C. & Martínez-Bazán, C. 2014 Drag reduction induced by the addition of a multi-cavity at the base of a bluff body. *J. Fluids Struct.* **48**, 347–361. [Cited on page 232]

Mason, W. T. & Beebe, P. S. 1978 *The Drag Related Flow Field Characteristics of Trucks and Buses*, pp. 45–93. Boston, MA: Springer US. [Cited on page 6]

Maull, D. J. & Hoole, B. J. 1967 The effect of boat-tailing on the flow round a two-dimensional blunt-based aerofoil at zero incidence. *The Journal of the Royal Aeronautical Society* **71** (684), 854–858. [Cited on pages 94 and 98]

McArthur, D., Burton, D., Thompson, M. & Sheridan, J. 2016 On the near wake of a simplified heavy vehicle. *Journal of Fluids and Structures* **66**, 293 – 314. [Cited on pages 6, 37, 41, and 45]

Meile, W., Ladinek, T., Brenn, G., Reppenhagen, A. & Fuchs, A. 2016 Non-symmetric bi-stable flow around the Ahmed body. *International Journal of Heat and Fluid Flow* **57**, 34–47. [Cited on pages 210, 216, and m]

Meliga, P., Chomaz, J. & Sipp, D. 2009 Global mode interaction and pattern selection in the wake of a disk: a weakly nonlinear expansion. *Journal of Fluid Mechanics* **633**, 159–189. [Cited on page 8]

Meliga, P., Pujals, G. & Serre, E. 2012 Sensitivity of two-dimensional turbulent flow past a D-shaped cylinder using global stability. *Physics of Fluids* **24** (6), 061701–061701. [Cited on page 144]

Mendona Bimbato, A., Alcântara Pereira, L.A. & Hiroo Hirata, M. 2013 Suppression of vortex shedding on a bluff body. *Journal of Wind Engineering and Industrial Aerodynamics* **121**, 16 – 28. [Cited on pages 134, 263, and 264]

Menter, F. R. 1993 Zonal two equation $k-\omega$ turbulence models for aerodynamic flows. *23rd Fluid Dynamics, Plasmadynamics, and Lasers Conference* . [Cited on page 147]

Menter, F. R. 1994 Two-equation eddy-viscosity turbulence models for engineering applications. *AIAA Journal* **32** (8), 1598–1605. [Cited on page 147]

Mettot, C., Sipp, D. & Beazrd, H. 2014 Quasi-laminar stability and sensitivity analyses for turbulent flows: Prediction of low-frequency unsteadiness and passive control. *Physics of Fluids* **26** (4), 045112. [Cited on page 144]

Mirzaei, M., Krajnović, S & Basara, B. 2015 Partially-Averaged Navier–Stokes simulations of flows around two different Ahmed bodies. *Computers & Fluids* **117**, 273–286. [Cited on pages 8, 55, and a]

Molezzi, M.J. & Dutton, J.C. 1995 Study of subsonic base cavity flowfield structure using particle image velocimetry. *AIAA Journal* **33** (2), 201 – 209. [Cited on page 232]

Morel, T. 1978 Aerodynamic drag of bluff body shapes characteristic of hatch-back cars. In *SAE Technical Paper*. SAE International. [Cited on page 95]

Morel, T. 1979 Effect of base cavities on the aerodynamic drag of an axisymmetric cylinder. *Aeronautical Quarterly* **30**, 400–412. [Cited on pages 50 and 232]

Mu, X. 2011 *Numerical Simulations of the Flow around a Yawing Truck in Wind Tunnel*. Chalmers University of Technology. [Cited on page 50]

Nash, J.F. 1964 An approximate method for the prediction of the zero lift pressure distribution and drag of symmetrical blunt trailing edge aerofoil sections at subsonic speeds in the absence of a vortex street. *Aero Res Coun R & M* **3436**. [Cited on page 94]

Nash, J. F., Quincey, V.G. & Callinan, J. 1963 *Experiments on two-dimensional base flow at subsonic and transonic speeds*. HM Stationery Office. [Cited on pages 93, 98, and 232]

Natarajan, R. & Acrivos, A. 1993 The instability of the steady flow past spheres and disks. *J. Fluid Mech.* **254**, 323–344. [Cited on page 8]

Ormières, D. & Provansal, M. 1999 Transition to turbulence in the wake of a sphere. *Physical Review Letters* **83** (1), 80–83. [Cited on page 8]

Östh, J., Noack, B.R., Krajnović, S., Barros, D. & Borée, J. 2014 On the need for a nonlinear subscale turbulence term in pod models as exemplified for a high-reynolds-number flow over an ahmed body. *Journal of Fluid Mechanics* **747**, 518–544. [Cited on page 8]

Pagerit, S., Sharer, P. & Rousseau, A. 2006 Fuel economy sensitivity to vehicle mass for advanced vehicle powertrains. *Tech. Rep.*. SAE Technical Paper. [Cited on page 3]

Palmer, A. 2007 *The development of an integrated routing and carbon dioxide emissions model for goods vehicles*. Cranfield University. [Cited on page 2]

Parezanović, V. & Cadot, O. 2009 The impact of a local perturbation on global properties of a turbulent wake. *Physics of Fluids* **21**, 071701. [Cited on pages 50 and 202]

Parezanović, V. & Cadot, O. 2012 Experimental sensitivity analysis of the global properties of a two-dimensional turbulent wake. *Journal of Fluid Mechanics* **693**, 115–149. [Cited on pages 50 and 202]

Parezanović, V., Monchaux, R. & Cadot, O. 2015 Characterization of the turbulent bistable flow regime of a 2D bluff body wake disturbed by a small control cylinder. *Exp. Fluids* **56** (1), 12. [Cited on page 202]

Pasquetti, R. & Peres, N. 2015 A penalty model of synthetic micro-jet actuator with application to the control of wake flows. *Computers & Fluids* **114** (0), 203–217. [Cited on pages 12, 37, 143, 158, and a]

PASSMORE, M., SPENCER, A., WOOD, D., JOWSEY, L. & NEWNHAM, P. 2010 The application of particle image velocimetry in automotive aerodynamics. *Tech. Rep.*. SAE Technical Papers. [Cited on pages 29, 30, 45, and 49]

PAVIA, G. & PASSMORE, M. 2018 Characterisation of Wake Bi-stability for a Square-Back Geometry with Rotating Wheels. In *Progress in Vehicle Aerodynamics and Thermal Management* (ed. J. Wiedemann), pp. 93–109. Springer International Publishing. [Cited on pages 12, 13, 45, 51, 77, 172, 178, 198, 200, 203, 205, and a]

PAVIA, G., PASSMORE, M. & GAYLARD, A. 2016 Influence of short rear end tapers on the unsteady base pressure of a simplified ground vehicle. *SAE Technical Paper Series* . [Cited on pages 7, 12, 14, 29, 45, 49, 97, 111, 126, 134, 193, and a]

PAVIA, G., PASSMORE, M. & SARDU, C. 2018 Evolution of the bi-stable wake of a square-back automotive shape. *Experiments in Fluids* **59** (1), 20. [Cited on pages 12, 45, 49, 134, 143, 158, and a]

PAYNE, P. R., HARTLEY, R. M. & TAYLOR, R. M. 1980 Afterbody drag. volume 1. drag of conical and circular arc afterbodies without jet flow. *Tech. Rep.*. PAYNE INC ANNAPOLIS MD. [Cited on page 95]

PELLERIN, S., PODVIN, B. & PASTUR, L. 2016 Characterization of the near-wake of an ahmed body profile. *World Academy of Science, Engineering and Technology, International Journal of Mechanical, Aerospace, Industrial, Mechatronic and Manufacturing Engineering* **10** (5), 926–931. [Cited on pages 37, 44, and 143]

PERES, N. & PASQUETTI, R. 2013 Numerical study of drag reduction of a car model by active control using mico-jets. In *CFM 2013 - 21ème Congrès Français de Mécanique*. Bordeaux, France. [Cited on pages 37, 44, 143, and 156]

PERRY, A., ALMOND, M., PASSMORE, M. & LITTLEWOOD, R. 2016*a* The study of a bi-stable wake region of a generic squareback vehicle using tomographic PIV. *SAE Int. J. Passeng. Cars - Mech. Syst* **9**, 2. [Cited on pages 12, 45, 49, 97, 107, 111, 112, 134, and a]

PERRY, A.K. & PASSMORE, M. 2013 The impact of underbody roughness on rear wake structure of a squareback vehicle. *Tech. Rep.*. SAE Technical Paper. [Cited on pages 49 and 197]

PERRY, A., PASSMORE, M. A. & FINNEY, A. 2015 Influence of short rear end tapers on the base pressure of a simplified vehicle. *Tech. Rep.*. SAE International. [Cited on pages 12, 14, 49, 96, 110, 121, and a]

PERRY, A., PAVIA, G. & PASSMORE, M. 2016*b* Influence of short rear end tapers on the wake of a simplified square-back vehicle: wake topology and rear drag. *Experiments in Fluids* **57** (11), 169. [Cited on pages 12, 13, 14, 29, 45, 49, 96, 97, 107, 109, 113, 116, 117, 120, 121, 122, 124, 126, 134, a, g, and i]

PETERSON, R. L. 1981 Drag reduction obtained by the addition of a boattail to a box shaped vehicle. *NASA Contractor Report* **163113**. [Cited on pages 14 and 97]

PIER, B. 2008 Local and global instabilities in the wake of a sphere. *Journal of Fluid Mechanics* **603**, 39–61. [Cited on page 8]

PRANDTL, L. & TIETJENS, O.G. 1934 *Fundamentals of hydro-and aerodynamics*. [Cited on page 96]

Prasad, A. K. 2000 Stereoscopic particle image velocimetry. *Exp. Fluids* **29** (2), 103–116. [Cited on page 27]

Provansal, M., Mathis, C. & Boyer, L. 1987 Bénard-von Kármán instability: transient and forced regimes. *J. Fluid Mech.* **182**, 1–22. [Cited on page 8]

van Raemdonck, G. M. R., van Leeuwen, P. & van Tooren, M. J. L. 2016 Comparison of experimental and numerically obtained flow properties of a bluff body. In *The Aerodynamics of Heavy Vehicles III* (ed. A. Dillmann & A. Orellano), pp. 393–411. Springer International Publishing. [Cited on pages 7, 12, 13, 143, and 153]

van Raemdonck, G. M. R. & van Tooren, M. J. L. 2008 Time averaged phenomenological investigation of a wake behind a bluff body. In *Bluff Body Aerodynamics and Application VI Conference, Milan, Italy.* [Cited on pages 50 and k]

Raffel, M., Willert, C. E. & Kompenhans, J. 1998 *Particle Image Velocimetry: a practical guide.* Springer. [Cited on page 27]

Rao, A., Minelli, G., Basara, B. & Krajnovič, S. 2018 On the two flow states in the wake of a hatchback Ahmed body. *Journal of Wind Engineering and Industrial Aerodynamics* **73**, 262 – 278. [Cited on pages 210, 216, and m]

Raul, R., Bernard, P. S. & Buckley, F. T. 1990 An application of the vorticity–vector potential method to laminar cube flow. *Int. J. Numer. Methods Fluids* **10** (8), 875–888. [Cited on page 8]

Reynolds, O. 1895 On the dynamical theory of incompressible viscous fluids and the determination of the criterion. *Philosophical Transactions of the Royal Society of London. A* **186**, 123–164. [Cited on page 148]

Rigas, G., Esclapez, L. & Magri, L. 2016 Symmetry breaking in a 3D bluff-body wake. Center for Turbulence Research, Stanford University. [Cited on pages 8 and 10]

Rigas, G., Morgans, A.S., Brackston, R. D. & Morrison, J.F. 2015 Diffusive dynamics and stochastic models of turbulent axisymmetric wakes. *Journal of Fluid Mechanics* **778**, R2. [Cited on pages 6, 10, 54, 57, 59, 61, 73, 75, 85, 123, 132, and 233]

Rigas, G., Oxlade, A.R., Morgans, A.S. & Morrison, J.F. 2014 Low-dimensional dynamics of a turbulent axisymmetric wake. *Journal of Fluid Mechanics* **755**, 159. [Cited on pages 6, 10, 61, 85, 260, and 262]

Rofail, A. W., Tonin, R. & Hanafi, D. 2004 Sensitivity frequency response to type of tubing. 11th awes workshop, darwin. Windtech Consultants Pty Ltd, Sydney, Australia. [Cited on page 24]

Roshko, A. 1954*a* A new hodograph for free-streamline theory. *NACA Technical Note* **3168**. [Cited on pages 6 and 93]

Roshko, A. 1954*b* On the drag and shedding frequencies of two-dimensional bluff bodies. *NACA Technical Note* **3169**. [Cited on pages 6 and 94]

Roshko, A. 1955 On the wake and drag of bluff bodies. *Journal of the aeronautical sciences* **22** (2), 124–132. [Cited on pages 6 and 94]

Roshko, A. 1993 Perspectives on bluff body aerodynamics. *Journal of Wind Engineering and Industrial Aerodynamics* **49** (1-3), 79–100. [Cited on pages 4, 6, 25, 94, 136, 170, 216, and 232]

Rouméas, M., Gilliéron, P. & Kourta, A. 2009 Analysis and control of the near-wake flow over a squareback geometry. *Computers & Fluids* **38** (1), 60–70. [Cited on page 155]

Ruelle, D. & Takens, F. 1971 On the nature of turbulence. *Commun. Math. Phys.* **20** (3), 167–192. [Cited on page 8]

Saha, A. K. 2004 Three-dimensional numerical simulations of the transition of flow past a cube. *Physics of Fluids* **16** (5), 1630–1646. [Cited on page 8]

Sanmiguel-Rojas, E., Jimenez-Gonzalez, J. I., Bohorquez, P., Pawlak, G. & Martinez-Bazan, C. 2011 Effect of base cavities on the stability of the wake behind slender blunt-based axisymmetric bodies. *Physics of Fluids* **23** (11), 114103. [Cited on page 232]

Sarron, C., Colussi, C., Brasseur, M. F., Druille, B. & Serre, P. 2018 Chiffres clés du transport - Édition 2018. *Tech. Rep.*. Minist'ere de la transition écologique et solidaire, France. [Cited on page 2]

Schlichting, H. & Gersten, K. 2000 *Boundary layer theory*. Springer Verlag. [Cited on pages 216 and 232]

Schmidt, H.-J., Woszidlo, R., Nayeri, C. N. & Paschereit, C. O. 2018 The effect of flow control on the wake dynamics of a rectangular bluff body in ground proximity. *Exp. Fluids* **59** (6), 107. [Cited on pages 12, 37, and 50]

Seifert, A., Stalnov, O., Sperber, D., Arwatz, G., Palei, V., David, S., Dayan, I. & Fono, I. 2008 Large trucks drag reduction using active flow control. In *46th AIAA Aerospace Sciences Meeting and Exhibit*, p. 743. [Cited on page 185]

Seifert, A., Stalnov, O., Sperber, D., Arwatz, G., Palei, V., David, S., Dayan, I. & Fono, I. 2009 Large trucks drag reduction using active flow control. In *The Aerodynamics of Heavy Vehicles II: Trucks, Buses, and Trains*, pp. 115–133. Springer. [Cited on page 185]

Spalart, P. R. 1997 Comments on the feasibility of LES for wings, and on a hybrid RANS/LES approach. In *Proceedings of first AFOSR international conference on DNS/LES*. Greyden Press. [Cited on page 161]

Spalart, P. R. & Allmaras, S. 1992 A one-equation turbulence model for aerodynamic flows. In *30th Aerospace Sciences Meeting and Exhibit*. [Cited on page 147]

Spohn, A. & Gilliéron, P. 2002 Flow separations generated by a simplified geometry of an automotive vehicle. In *Congress IUTAM Symposium on Unsteady Separated Flows*. [Cited on pages 37 and 44]

Sreenivasan, K. R., Strykowski, P. J. & Olinger, D. J. 1987 Hopf bifurcation, Landau equation, and vortex shedding behind circular cylinders. *ASME* pp. 1–13. [Cited on page 8]

Stankiewicz, W., Morz Nski, M., Noack, B. R. & Thiele, F. 2005 Stability properties of 2D flow around Ahmed body. *Mathematical Modelling and Analysis* pp. 5–924. [Cited on page 144]

Strouhal, V. 1878 Über eine besondere Art der Tonerregung. *Annalen der Physik* **241** (10), 216–251. [Cited on pages 10 and 263]

Sychev, V.V. 1982 Asymptotic theory of separation flows. *Fluid Dynamics* **17** (2), 179–188. [Cited on pages 6 and 133]

Szaltys, P., Chrust, M., Przadka, A., Goujon-Durand, S., Tuckerman, L.S. & Wesfreid, J.E. 2012 Nonlinear evolution of instabilities behind spheres and disks. *Journal of Fluids and Structures* **28**, 483–487. [Cited on page 8]

Thompson, M.C., Leweke, T. & Provansal, M. 2001 Kinematics and dynamics of sphere wake transition. *Journal of Fluids and Structures* **15** (3-4), 575–585. [Cited on page 8]

Tian, J., Zhang, Y., Zhu, H. & Xiao, H. 2017 Aerodynamic drag reduction and flow control of ahmed body with flaps. *Advances in Mechanical Engineering* **9** (7), 1–17. [Cited on page 217]

Tomboulides, A. G. & Orszag, S. A. 2000 Numerical investigation of transitional and weak turbulent flow past a sphere. *J. Fluid Mech.* **416**, 45–73. [Cited on page 8]

Toro, E. F. 1999 Approximate-state Riemann solvers. *Riemann Solvers and Numerical Methods for Fluid Dynamics* p. 293–313. [Cited on page 144]

Tunay, T., Sahin, B. & Ozbolat, V.i 2014 Effects of rear slant angles on the flow characteristics of Ahmed body. *Exp. Therm Fluid Sci.* **57**, 165–176. [Cited on page 216]

Van Dyke, M. 1982 *An album of fluid motion*. Parabolic Press. [Cited on page 5]

Varney, M., Passmore, M. & Gaylard, A. 2017 The Effect of Passive Base Ventilation on the Aerodynamic Drag of a Generic SUV Vehicle. *SAE Int. J. Passenger Cars Mech. Syst.* **10** (1), 345–357. [Cited on page 97]

Varon, E., Eulalie, Y., Edwige, S., Gilotte, P. & Aider, J.-L. 2017 Chaotic dynamics of large-scale structures in a turbulent wake. *Physical Review Fluids* **2**. [Cited on pages 8, 10, 49, 143, and a]

Verhoff, A. 2010 Two-dimensional potential flow solutions with separation. *J. Fluid Mech.* **657**, 238–264. [Cited on page 6]

Vilaplana, G., Grandemange, M., Gohlke, M. & Cadot, O. 2013 Experimental sensitivity analysis of the global mode of a sphere turbulent wake using steady disturbances. *Journal of Fluids and Structures* **41**, 119–126. [Cited on pages 50 and 203]

Viswanath, P.R. 1996 Flow management techniques for base and afterbody drag reduction. *Progress in Aerospace Sciences* **32** (2-3), 79–129. [Cited on page 232]

Volpe, R., Devinant, P. & Kourta, A. 2015 Experimental characterization of the unsteady natural wake of the full-scale square back Ahmed body: flow bi-stability and spectral analysis. *Experiments in Fluids* **56** (5). [Cited on pages 8, 12, 14, 38, 49, 54, 58, 71, 108, 143, and a]

Wang, Y., Sicot, C., Borée, J. & Grandemange, M. 2018 Experimental study of wheel-vehicle aerodynamic interactions. In *Third International Conference in numerical and experimental aerodynamics of road vehicles and trains, 3rd Aerovehicles, Milan, Italy*. [Cited on pages 12, 51, and 174]

Waudby-Smith, P., Bender, T. & Vigneron, R. 2004 The GIE S2A full-scale aeroacoustic wind tunnel. *SAE Technical Paper Series* **2004-01-0808**. [Cited on page 19]

Wee, D., Yi, T., Annaswamy, A. & Ghoniem, A. F. 2004 Self-sustained oscillations and vortex shedding in backward-facing step flows: Simulation and linear instability analysis. *Physics of Fluids* **16** (9), 3361–3373. [Cited on page 144]

Welch, P. D. 1967 The Use of Fast Fourier Transform for the Estimation of Power Spectra: A Method Based on Time Averaging Over Short, Modified Periodograms. *IEEE Trans. Audio & Electroacoust., Volume AU-15, p. 70-73* **15**, 70–73. [Cited on page 31]

Wickern, G., Dietz, S. & Luehrmann, L. 2003 Gradient effects on drag due to boundary-layer suction in automotive wind tunnels. *SAE Technical Paper Series* . [Cited on page 20]

Williams, P. T. & Baker, A. J. 1999 Numerical simulations of laminar flow over a 3D backward-facing step. *Int. J. Numer. Methods Fluids* **24** (11), 1159–1183. [Cited on page 37]

Williamson, C.H.K. 1996 Three-dimensional wake transition. *Journal of Fluid Mechanics* **328**, 345–407. [Cited on page 8]

Windsor, S. 2014 Real world drag coefficient–is it wind averaged drag? In *International Vehicle Aerodynamics Conference 2014*, pp. 14–15. [Cited on page 49]

Wong, D.T.-M. & Mair, W.A. 1983 Boat-tailed afterbodies of square section as drag-reduction devices. *Journal of Wind Engineering and Industrial Aerodynamics* **12** (2), 229 – 235. [Cited on pages 94, 95, 103, 122, 133, 138, and g]

Wu, T.Y.T. 1962 A wake model for free-streamline flow theory .1. fully and partially developed wake flows and cavity flows past an oblique flat plate. *Journal of Fluid Mechanics* **13** (2), 161–181. [Cited on page 6]

Yang, J., Liu, M., Wu, G., Zhong, W. & Zhang, X. 2014 Numerical study on instabilities behind a circular disk in a uniform flow. *Int. J. Heat Fluid Flow* **50**, 359–368. [Cited on page 8]

Yoshida, M., Kondo, K. & Suzuki, M. 1992 Fluctuating wind pressure measured with tubing system. *Journal of Wind Engineering and Industrial Aerodynamics* **42** (1-3), 987–998. [Cited on page 24]

Zafer, B. & Haskaraman, F. 2017 Önden ve yanal rüzgar şarti altinda zamana bağli sikiştirilamaz ahmed cisminin sayisal incelenmesi. *Gazi Üniversitesi Mühendislik-Mimarlık Fakültesi Dergisi* **32** (1). [Cited on page 216]

Zdravkovich, M.M. 1997 *Flow around circular cylinders: fundamentals*. Oxford University Press. [Cited on page 8]

Dynamics of the unstable wake modes in automotive aerodynamics: from simplified models to real vehicles

(Dynamique des modes instables de sillage en aérodynamique automobile : des modèles simplifiés aux véhicules réels)

Résumé étendu en Français

Guillaume Bonnavion

Soutenance le 5 octobre 2018 à Palaiseau (91)

ENSTA-ParisTech, Université Paris-Saclay, IMSIA

Introduction

Cette annexe regroupe les principaux résultats du manuscrit et reproduit des figures clés. Chaque section correspond à un chapitre du mémoire et les notations sont celles utilisées précédemment et sont données dans la Nomenclature. Les résultats présentés ici sont détaillés dans le manuscrit, où chaque chapitre s'articule comme suit : une mise en contexte avec éventuellement une courte étude bibliographique, la présentation du dispositif d'étude, les résultats, une discussion puis une courte conclusion.

1 Contexte et revue bibliographique

Le chapitre 1 propose une introduction générale du sujet avec notamment une mise en contexte vis-à-vis des enjeux majeurs auxquels l'aérodynamique automobile doit faire face aujourd'hui alors que le segment des monospaces et plus encore celui des SUV (*Sport Utility Vehicles*) sont en plein essor commercial. Au vu de la complexité des véhicules réels et des difficultés à faire de la recherche fondamentale avec de telles géométries, nous introduisons des modèles simplifiés comme le corps d'Ahmed à culot droit qui est étudié dans cette thèse.

La revue bibliographique est centrée sur le sillage instable du corps. Depuis les travaux précurseurs de Grandemange *et al.* (2013*b*, 2014*b*) sur cette géométrie où une dynamique bi-stable du sillage liée à une instabilité statique de brisure de symétrie est étudiée, de nombreuses études ont considéré cet écoulement à grands nombres de Reynolds ($\mathrm{Re} = 10^4 - 10^5$) et identifié une asymétrie permanente du sillage (Pasquetti & Peres, 2015; Volpe *et al.*, 2015; Cadot *et al.*, 2015*b*; Mirzaei *et al.*, 2015; Barros *et al.*, 2016; Li *et al.*, 2016; Evrard *et al.*, 2016; Barros *et al.*, 2017; Varon *et al.*, 2017; Lucas *et al.*, 2017) . Elle se traduit notamment par l'exploration aléatoire de deux états miroirs du sillage sur des temps caractéristiques de l'ordre de 500 à 1000 fois le temps convectif de l'écoulement. L'origine de cette asymétrie remonte à une bifurcation laminaire (Grandemange *et al.*, 2012*a*; Evstafyeva *et al.*, 2017) que l'on compare à une étude de stabilité sur une plaque plane faisant face à un écoulement (Marquet & Larsson, 2014). Dans le régime turbulent mentionné précédemment, Grandemange *et al.* (2013*a*) ont mis en lumière l'existence de deux instabilités de sillage, dirigées soit horizontalement soit verticalement en fonction du rapport d'aspect du corps, avec une zone d'interférences (figure 1). Ces états asymétriques de sillage ont été régulièrement retrouvés sur des géométries à culots rectangulaires: plaque plane (Cadot, 2016), modèle de Windsor à culot droit (Perry *et al.*, 2016*a*,*b*; Pavia *et al.*, 2018; Pavia & Passmore, 2018). On les retrouve également dans le sillage de certains véhicules réels, associés éventuellement à une dynamique bistable du sillage (Cadot *et al.*, 2016). Ceci ouvre de larges possibilités pour la réduction de traînée, en particulier si l'on supprime l'instabilité (Cadot *et al.*, 2015*b*). Une stratégie consiste à utiliser des rétreints. Pour le corps d'Ahmed, ceci a été brièvement étudié par Grandemange *et al.* (2013*c*) ; des études plus complètes existent pour le corps de Windsor (Littlewood & Passmore, 2010; Perry *et al.*, 2015, 2016*b*; Pavia *et al.*, 2016).

Cette thèse s'attache à étudier l'instabilité de sillage pour différentes configurations d'alignement du corps vis-à-vis de l'écoulement mais aussi de distance par rapport à la route puis lorsque des rétreints d'arrière-corps sont utilisés. On s'intéresse particulièrement aux dynamiques du sillage et à leurs effets sur le chargement aérodynamique appliqué au véhicule qui en résulte. Enfin, les résultats sont transposés aux véhicules réels de type monospace ou utilitaires légers et vérifiés expérimentalement. La

Partie I du manuscrit détaille les travaux effectués sur des géométries simplifiées alors que la Partie II est axée sur les véhicules réels. Des annexes sont fournies en partie III ; elles précisent le propos général ou détaillent certains points mentionnés dans le manuscrit. Elles ne sont pas détaillées dans ce résumé.

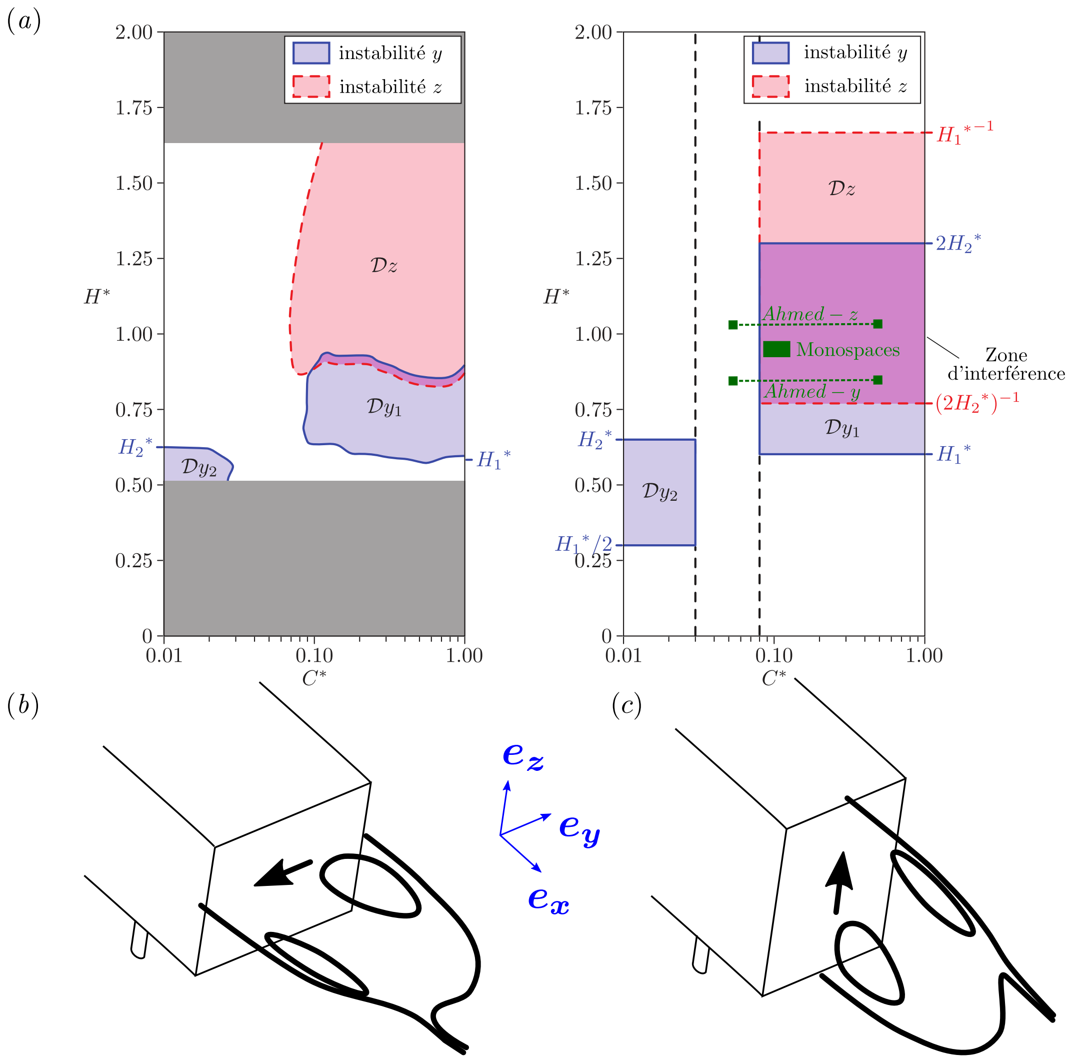

Figure 1 – Domaines de développement des instabilités mesurés expérimentalement (à gauche) et prédits par le modèle de Grandemange *et al.* (2013*a*) (à droite). Figure adaptée de Grandemange *et al.* (2013*a*) où la largeur du corps W est utilisée comme échelle de référence. En vert, rapports d'aspects de culot étudiés : *Ahmed-y*, corps d'Ahmed soumis à l'instabilité y (§ 4.3.1) ; *Ahmed-z*, corps d'Ahmed soumis à l'instabilité z (§ 4.3.2) ; *Monospaces*, Renault Kangoo, Peugeot 5008 et Partner et Citroën Berlingo étudiés dans le chapitre 7. Schémas des zones de recirculation pour les instabilités y (b) et z (c) interprétés à partir des mesures dans le sillage de Grandemange *et al.* (2013*a*). Les flèches correspondent aux gradients de pression au culot.

2 Dispositif expérimental et méthodes

Le chapitre 2 de ce manuscrit décrit le dispositif expérimental utilisé pour les essais. Les souffleries pleine échelle et échelle réduite sont présentées ainsi que les systèmes de mesures de pression instationnaire et d'efforts aérodynamiques. On s'intéresse ensuite aux systèmes de mesure des champs de vitesse puis aux géométries étudiées : corps d'Ahmed à culot droit et véhicules réels. Le chapitre se clot sur la description des procédures

expérimentales et de traitement des données.
Les essais sont réalisés dans les souffleries industrielles du GIE-S2A à Montigny-le-Bretonneux (France). De leurs principales caractéristiques, on retiendra que l'on peut y ajuster le dérapage de la maquette et que la soufflerie pleine échelle possède un sol défilant. Pour la garde au sol et l'angle d'assiette, un système de contrôle a été installé sur la maquette simplifiée. Lors des essais, on réalise des mesures de pression instationnaire au culot des véhicules à l'aide de prises de pressions pariétales reliées à un scanner différentiel mais aussi des mesures d'efforts aérodynamiques avec une balance de force. On les complète par des mesures de vitesse dans le sillage (tomographie ou Imagerie particulaire). Pour les cas étudiés, les nombres de Reynolds typiques (basés sur la hauteur du culot) varient de 4.0×10^5 pour le corps d'Ahmed à environ 3×10^6 pour les véhicules réels. La figure 2 montre le schéma (en vue de dessus) d'une soufflerie, le principe d'installation de la maquette (en *b*), le plénum de la soufflerie pleine échelle (en *c*) et celui de l'installation dédiée aux maquettes (en *d*).

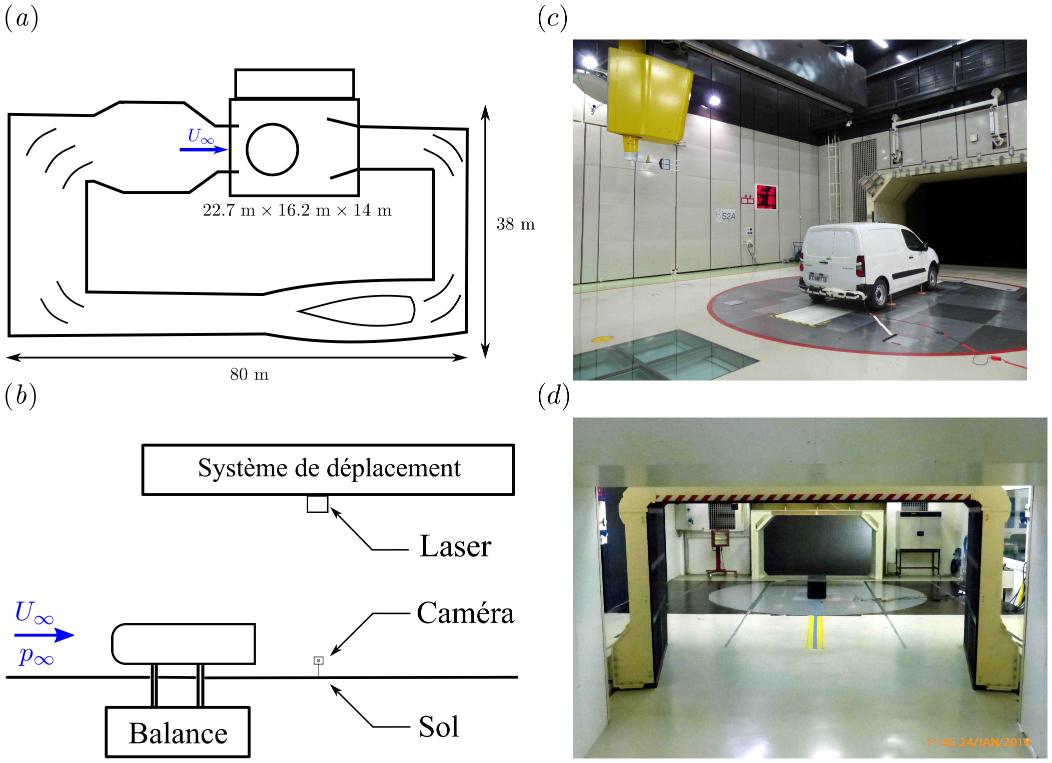

Figure 2 – Souffleries du GIE-S2A. (*a*) Vue schématique de dessus d'une soufflerie boucle fermée avec les dimensions du plénum et de la soufflerie pleine échelle ; (*b*) vue latérale de la section d'essais de la soufflerie maquettes avec un corps d'Ahmed et le dispositif de mesure particulaire par PIV pour les plans verticaux. (*c*) Soufflerie pleine échelle et Peugeot Partner en test, (*d*) soufflerie maquettes et corps d'Ahmed en phase de test.

Les procédures d'acquisition et de traitement des données sont précisées dans ce chapitre. Les moyennes temporelles sont réalisées sur des intervalles suffisamment longs pour avoir une bonne représentativité des phénomènes observés (plusieurs occurrences) même si la convergence statistique est quasi-impossible à atteindre au vu de la dynamique lente par rapport au lâcher tourbillonnaire. Des tares régulières et des recoupements assurent la validité des données présentées. Pour réduire les fluctuations haute fréquence, le signal est filtré avec un passe-bas réalisé à l'aide d'un moyennage par fenêtre glissante ; les séries temporelles des signaux, mais aussi les fonctions densité de probabilité et les coefficients statistiques d'ordre un (moyenne) ou deux (fluctuations) sont étudiés. Les grandeurs caractéristiques du problème sont adimensionnées par la hauteur du culot H_b, par la vitesse de l'écoulement libre U_∞ et par la densité et la viscosité cinématique de l'air notées respectivement ρ et ν.

3 Écoulement moyen autour d'un corps d'Ahmed à culot droit

Dans le chapitre 3, l'écoulement moyen autour du corps d'Ahmed à culot droit est étudié pour trois gardes au sol c (distance entre le sol et le soubassement de la maquette dans la direction normale) : $c^* = c/H_b = 0.067$, $c^* = c/H_b = 0.101$ et $c^* = c/H_b = 0.168$. Grâce à des angles de courbure bien choisis, on n'observe pas de décollement à l'avant du corps pour la vitesse d'écoulement considérée ($U_\infty = 20$ m.s^{-1}), quelle que soit la garde au sol. L'écoulement est quasi-stationnaire et on remarque un point de stagnation à l'avant du corps, situé légèrement au-dessus de la ligne de mi-hauteur dû à la présence du sol. En moyenne, le sillage (figure 3) est symétrique dans les deux directions sauf dans le cas où, à faible garde au sol, l'effet de stabilisation de ce dernier existe. Dans le cas contraire, on observe la trace d'une structure toroïdale grâce à deux recirculations dans chacun des plans. Ce sillage, fortement instationnaire et soumis à une forte asymétrie instantanée, est étudié dans la suite du manuscrit.

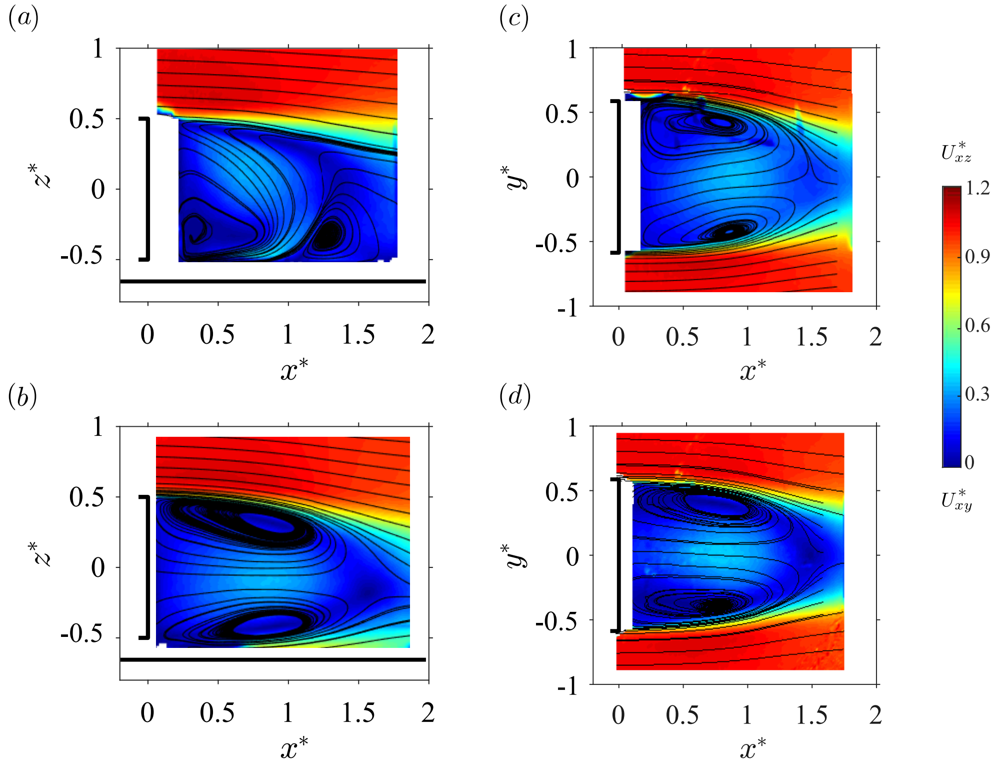

Figure 3 – Champs moyens de vitesse au culot du corps avec les lignes de courant et le module de la vitesse dans les plans $y^* = 0$ (gauche) et $z^* = 0$ (droite). Le corps est aligné avec l'écoulement ($\beta = 0°$), sans angle d'assiette ($\alpha = 0°$). (a, c) $c^* = 0.067$, (b, d) $c^* = 0.168$.

4 Dynamique du sillage instable du corps incliné à proximité du sol

On étudie dans le chapitre 4 les dynamiques du sillage du corps d'Ahmed à proximité du sol en faisant varier trois paramètres géométriques : la garde au sol, l'angle de dérapage et l'angle d'assiette. L'orientation du sillage et l'intensité de l'asymétrie sont étudiées à l'aide du gradient de pression au culot du corps. On retrouve la stabilisation opérée par le sol à faibles gardes au sol (Grandemange *et al.*, 2013*a*) avec une symétrisation du sillage et une réduction de son asymétrie. Au-delà du seuil critique (environ 10% de la hauteur du corps), la dynamique du sillage est contrôlée par l'instabilité et les deux branches de solutions pour le gradient de pression horizontal au culot g_y^* (figure 4*a*) sont explorées alternativement suivant une dynamique aléatoire (Cadot *et al.*, 2015*b*; Evrard *et al.*, 2016; Brackston *et al.*, 2016). À partir du sillage instable saturé (pour $c^* \geq c_S^*$), on impose d'abord un angle de dérapage (rotation autour de l'axe *mineur* du culot). Ceci a pour effet de sélectionner une branche de solutions (figure 4*b*) sans modifier le gradient vertical ni, et c'est plus surprenant, l'intensité de l'asymétrie. Lorsque l'on fait varier l'assiette de la maquette (rotation autour de l'axe *majeur* du culot), on observe trois dynamiques de phase distinctes, comme le montre la figure 4(*c*). Aux petits angles, la dynamique bi-stable est conservée mais le sillage doit s'adapter à la contrainte selon l'axe *mineur* g_z^* qui varie quasi-linéairement avec l'angle d'assiette jusqu'à saturer (figure 4*d*). Aux grands angles, on satisfait cette contrainte soit par un verrouillage de phase (angles à piquer, $\alpha < 0°$) soit par un déblocage total (angles à cabrer, $\alpha > 0°$).

On montre qu'il existe une contribution géométrique au gradient de pression en fonction de l'alignement du corps et qu'un phénomène d'adaptation régit l'instabilité. Les contributions selon le grand axe sélectionnent un état (à intensité constante), tandis que celles selon le petit contraignent l'orientation du sillage et sa dynamique de phase, alors que l'intensité est modulée par une constante égale à environ le rapport d'aspect axe majeur - axe mineur du culot. Ces résultats ont d'abord été obtenus avec un culot plus large que haut ($W_b^* = W_b/H_b = 1.174$) puis retrouvés avec un rapport d'aspect inverse ($W_b^* = W_b/H_b = 0.940$) ; la différence majeure est que l'absence de symétrie du cas aligné (à cause du sol) ne conduit pas à une dynamique bi-stable. En revanche, on retrouve bien la sélection des états du sillage en fonction de l'alignement du corps.

Au niveau du chargement aérodynamique, il est possible d'identifier la contribution de l'instabilité sur les efforts transverses (figure 5). En particulier, elle est clairement visible sur la composante alignée avec l'axe *majeur* de l'instabilité y pour l'expérience en dérapage (figure 5*a* en noir, comparée à l'écoulement sans l'instabilité en rouge) et sur les deux composantes (figures 5b, c) pour l'instabilité z en fonction du désalignement en assiette ou en dérapage. Sa contribution en termes de coefficient de force est toujours de $0,02$ (figure 5*d*) ; nous construisons un modèle (en bleu) qui prédit correctement les efforts transverses à partir du gradient de pression au culot. On observe également que l'on peut déduire les fluctuations du chargement sur les deux composantes connaissant celles du gradient de pression au culot vertical.

Un modèle généralisé pour l'intensité et l'orientation du sillage asymétrique adapté aux deux instabilités y et z est proposé, en fonction des axes *majeur* M et *mineur* m ; on peut ainsi prédire l'intensité du gradient de pression au culot grâce au modèle (1).

$$g_r^*(\varphi_M) = \frac{g_r^*\mathrm{min}}{\sqrt{\left(1-(1-\frac{1}{W^{*2}})\cos^2\varphi_M\right)}} \tag{1}$$

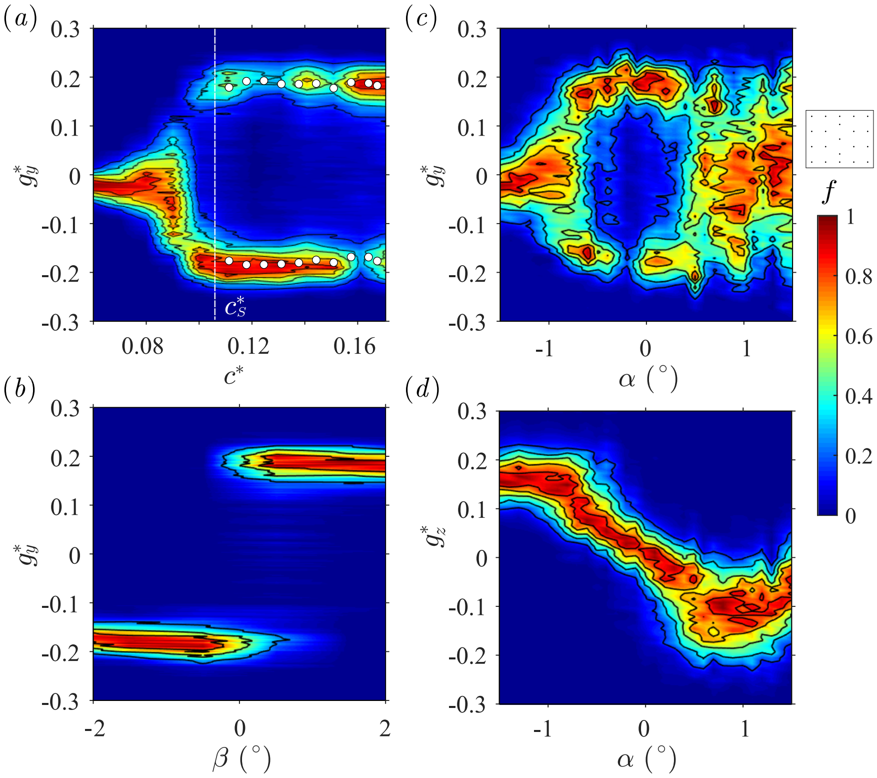

Figure 4 – Diagrammes de réponse du gradient de pression au culot à une variation de l'alignement du corps : (a) composante horizontale g_y^* en fonction de la garde au sol c^*, (b) composante horizontale g_y^* en fonction de l'angle de dérapage β, (c) composante horizontale g_y^* en fonction de l'angle d'assiette α, (d) composante verticale g_z^* en fonction de l'angle d'assiette α.

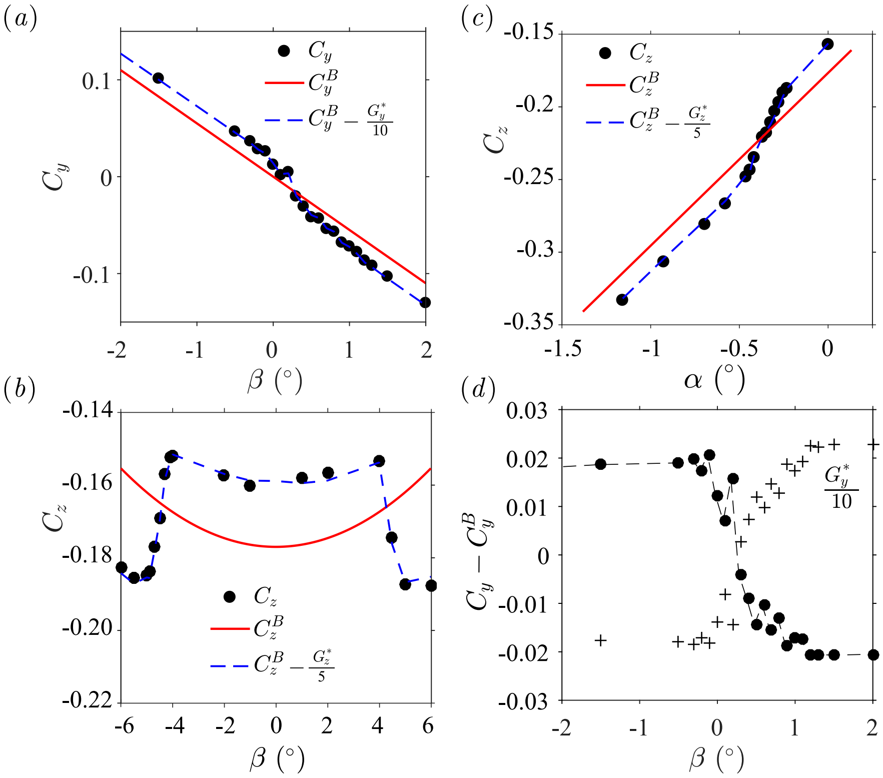

Figure 5 – Coefficient d'effort transverse en fonction de l'angle du corps : (a) effort latéral C_y en fonction de l'angle de dérapage β (instabilité y), (b) effort latéral C_y en fonction de l'angle de dérapage β (instabilité z), (c) coefficient de portance C_z en fonction de l'angle d'assiette α (instabilité z). (d) Contribution de l'instabilité au chargement aérodynamique du cas (a) et gradient de pression au culot. Points noirs : mesures ; ligne continue rouge : chargement de l'*écoulement de base* sans instabilité ; ligne discontinue bleue : modèle des équations (3b) et (3a).

On obtient également les deux composantes G_M^* et G_m^* du gradient de pression au culot (équations 2a and 2b).

$$g_M^*(t) = g_r^*(\varphi_M) \cos \varphi_M \tag{2a}$$
$$g_m^*(t) = g_r^*(\varphi_M) \sin \varphi_M \tag{2b}$$

Enfin, il est aussi possible de déduire le chargement aérodynamique à une constante ξ près connaissant le gradient de pression au culot, estimé par exemple à l'aide des mesures de pression comme le montrent les équations (3a) et (3b). Cette constante ξ dépend de la forme du culot mais est identique pour les deux composantes transverses à géométrie donnée. L'application de ce modèle à des véhicules réels est envisagée en Partie II dans le chapitre 7. Avec le phénomène d'adaptation de l'instabilité à la contrainte appliquée à l'axe *mineur* du culot (alors que l'instabilité s'établit selon l'axe *majeur*) et le modèle de sillage, ces équations constituent un résultat clé du chapitre. On rappelle que l'exposant B correspond à l'*écoulement de base*, sans l'instabilité.

$$c_m(t^*) = {C_m^*}^B + \xi {g^*}'_m(t^*) \tag{3a}$$
$$c_M(t^*) = {C_M^*}^B + \xi g_M^*(t^*) \tag{3b}$$

5 Effet de rétreint sur le sillage instable du corps d'Ahmed

Dans le chapitre 5, l'effet de rétreint d'arrière-corps est étudié. On s'intéresse en particulier aux efforts appliqués sur le corps, notamment la traînée et la portance, mais aussi à leurs fluctuations (ainsi qu'à celles de l'effort latéral) que l'on étudie en parallèle de celles du sillage au vu des résultats du chapitre précédent. Une étude simpliste considérant un écoulement potentiel bidimensionnel avec un sillage modélisé selon la théorie potentielle avec surface libre (Kirchhoff, 1869; Brillouin, 1910) montre que, si la contribution du culot vertical à la traînée est réduite en présence de rétreints – notamment car la pression augmente –, la contribution des rétreints eux-mêmes ne peut et ne doit pas être négligée. Elle s'explique par les bas niveaux de pression observés en raison du transfert de courbure du corps vers les lignes de courant. Néanmoins, on observe une réduction de la traînée globale de l'arrière-corps.

Après cette approche bidimensionnelle, on effectue des essais en soufflerie dans le régime de l'instabilité y caractérisée au chapitre 4. On commence par montrer que les relations quadratiques entre les coefficients de portance et de traînée identifiées par Grandemange *et al.* (2013*c*) puis Perry *et al.* (2016*b*) sont retrouvées. L'existence d'un minimum de traînée s'explique par les effets tri-dimensionnels ; expérimentalement, il est observé pour des angles de rétreint relativement petits.

L'étude de différents angles de rétreint montre qu'il existe un équilibre à atteindre entre petits angles pour lesquels le rétreint contribue peu et grands angles pour lesquels il participe largement, sachant que la traînée générée au niveau du culot vertical diminue lorsque la pression augmente, c'est-à-dire lorsque les angles augmentent. De manière classique, on peut relier directement traînée et pression pariétale, d'où la règle que les trop basses pressions doivent être évitées. Un optimum de traînée est trouvé, parmi les configurations testées, pour $\theta_T = 7.5°$ et $\theta_B = 5°$.

Ce travail porte non seulement sur la traînée, qui a été déjà étudiée de nombreuses fois pour des configurations proches (Wong & Mair, 1983; Ahmed, 1983; Hucho, 1978; Han

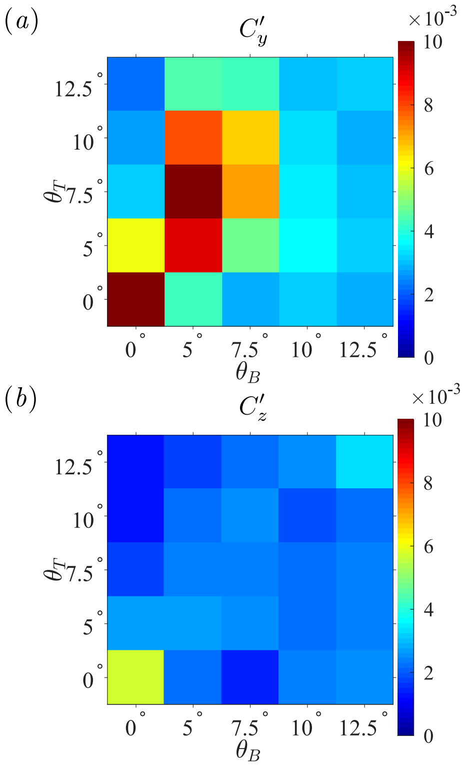

Figure 6 – Fluctuations moyennes en fonction des angles de rétreint θ_T et θ_B : (a) effort latéral, (b) portance, (c) composante horizontale du gradient de pression au culot et (d) composante verticale.

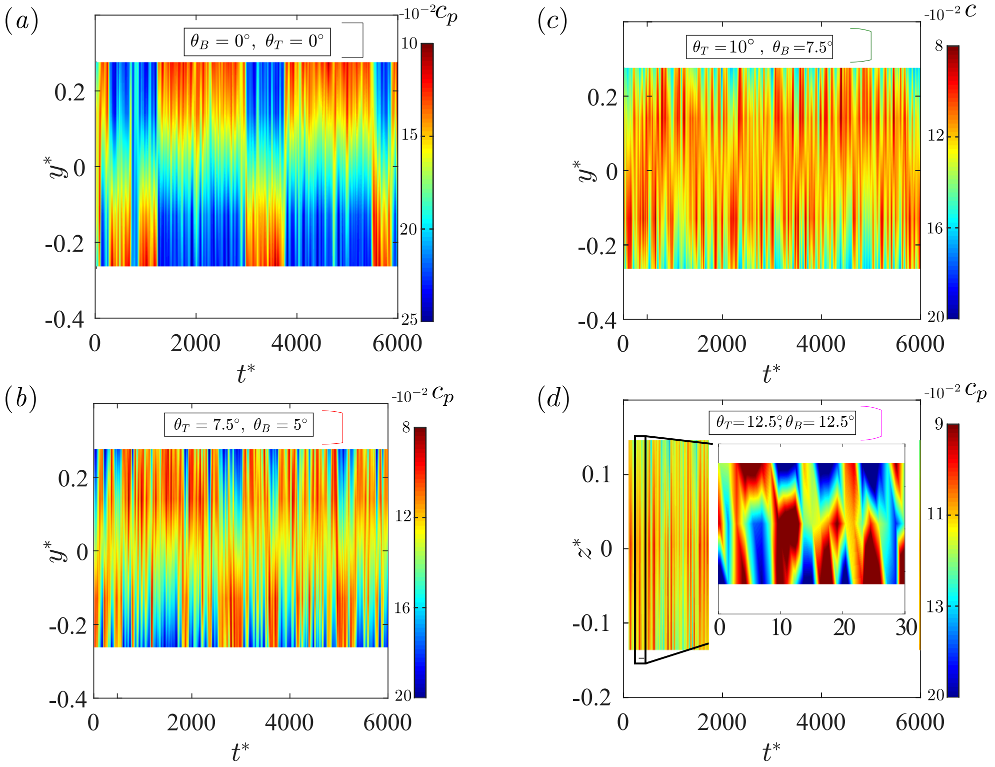

Figure 7 – Diagrammes spatio-temporels du coefficient de pression $c_p(y^*, z^*)$ au culot pour différents arrière-corps : (a) $z^* = 0$ pour la configuration de base ($\theta_T = 0°$, $\theta_B = 0°$), (b) $z^* = 0$ pour la configuration $\theta_T = 7.5°$, $\theta_B = 5°$, (c) $z^* = 0$ pour la configuration $\theta_T = 10°$, $\theta_B = 7.5°$, (d) $z^* = 0$ pour la configuration $\theta_T = 12.5°$, $\theta_B = 12.5°$.

et al., 1992; Grandemange *et al.*, 2013*c*, 2015; Perry *et al.*, 2016*b*), mais aussi sur l'impact du rétreint sur la dynamique du sillage. Trois dynamiques typiques sont identifiées, aussi bien grâce aux efforts transverses que grâce au gradient de pression au culot : bi-stabilité en y, verrouillage de phase et fluctuations en z, comme le montre la figure 6.

Les cas à faibles fluctuations s'expliquent par du verrouillage de phase (soit à $\varphi = \pi/2$ soit à $\varphi = -\pi/2$ en fonction de la contrainte géométrique créée par les rétreints) et correspondent à des configurations très asymétriques en termes d'angles de rétreint haut-bas. Pour des valeurs proches mais modérées, on observe une bi-stabilité y, avec éventuellement une adaptation de phase due à une contrainte géométrique suivant l'axe *mineur* du culot. Aux grands angles, les fluctuations du sillage sont orientées verticalement mais ne sont pas liées au mode asymétrique. Au contraire, on identifie une périodicité et on montre qu'elles sont causées par le lâcher tourbillonnaire (*vortex-shedding*). Comme l'indiquent les diagrammes spatio-temporels de la figure 7, l'instabilité y est affectée par le rétreint qui modifie l'échelle de temps (renversements tous les 500 t^* pour $\theta_T = 7.5°$ et $\theta_B = 5°$ en 7*b*, contre tous les 100 t^* pour $\theta_T = 10°$ et $\theta_B = 7.5°$ en 7*c*) alors que le lâcher tourbillonnaire est beaucoup plus rapide et périodique à St ~ 0.18 (figure 7*d*). On rappelle que la configuration de départ (culot droit) est caractérisée par une échelle de temps de l'ordre de 1000 t^* (figure 7*a*) et une dynamique stochastique. La contribution de l'instabilité apparaît toujours égale à $0,02$ pour les cas où elle existe encore alors que le mode

périodique ne modifie plus le chargement moyen ; en revanche, la traînée augmente beaucoup en raison des grands angles de rétreint.

On s'intéresse finalement à des modifications de géométrie (longueur et forme du rétreint). L'instabilité n'est pas affectée mais la dynamique du sillage est modifiée, notamment au niveau des temps caractéristiques de sélection d'état. Si un petit rétreint est utilisé, l'effet sur la pression au culot est moindre mais les effets de courbure – et donc la traînée – sont augmentés. L'utilisation d'un rétreint droit au lieu d'un arc de cercle produit l'effet inverse, avec une traînée réduite. En revanche, cette géométrie ne supprime pas non plus l'instabilité y ni la dynamique bi-stable du sillage qui en résulte. En conséquence, le niveau de fluctuations du sillage reste identique.

Des analyses de sensibilité en fonction de la garde au sol et des angles de dérapage et d'assiette sont fournies en annexe C. Elles mettent en lumière que le comportement de l'instabilité n'est que peu affecté et permettent de l'identifier clairement par sa contribution à l'effort aérodynamique.

6 Vers une analyse de stabilité du sillage du corps d'Ahmed

Ce chapitre propose une approche préliminaire pouvant mener à une étude de stabilité sur l'écoulement au culot du corps d'Ahmed. Il n'a pas pour but de fournir une simulation précise du sillage du corps en vue de compléter les données expérimentales mais plutôt d'ouvrir de nouvelles perspectives. On utilise les schémas de discrétisation numériques les plus simples possibles avec une moyenne de Reynolds appliquée aux équations de Navier–Stokes (RANS, *Reynolds-averaged Navier–Stokes*). On commence par une simulation moyennée en temps qui permet de modéliser un écoulement proche de celui que l'on obtiendrait sans l'instabilité (*écoulement de base*) ; cet écoulement est caractérisé par un sillage symétrique et une longue bulle de recirculation (figure 8). La garde au sol n'a que peu d'influence sur l'écoulement obtenu et les distributions de pression

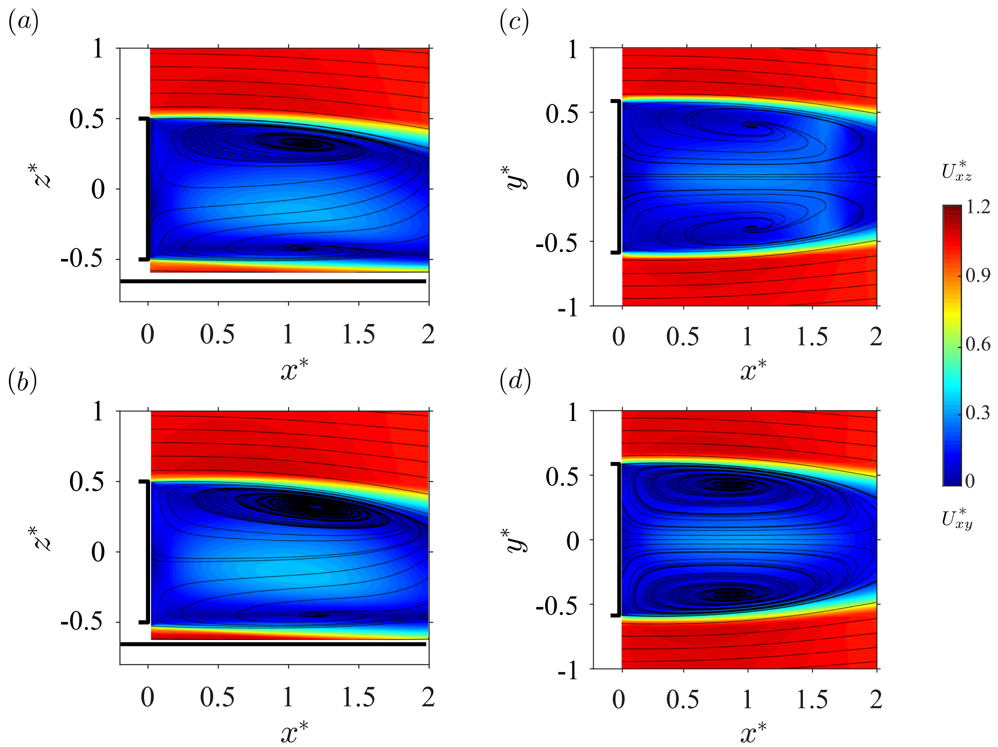

Figure 8 – Champs de vitesse moyens au culot du corps montrant les lignes de courant et le module de la vitesse dans le plan vertical $y^* = 0$ (à gauche) ou horizontal $z^* = 0$ (à droite). Le corps est aligné avec l'écoulement ($\beta = 0°$), sans angle d'assiette ($\alpha = 0°$). (a, c) $c^* = 0.067$, (b, d) $c^* = 0.168$.

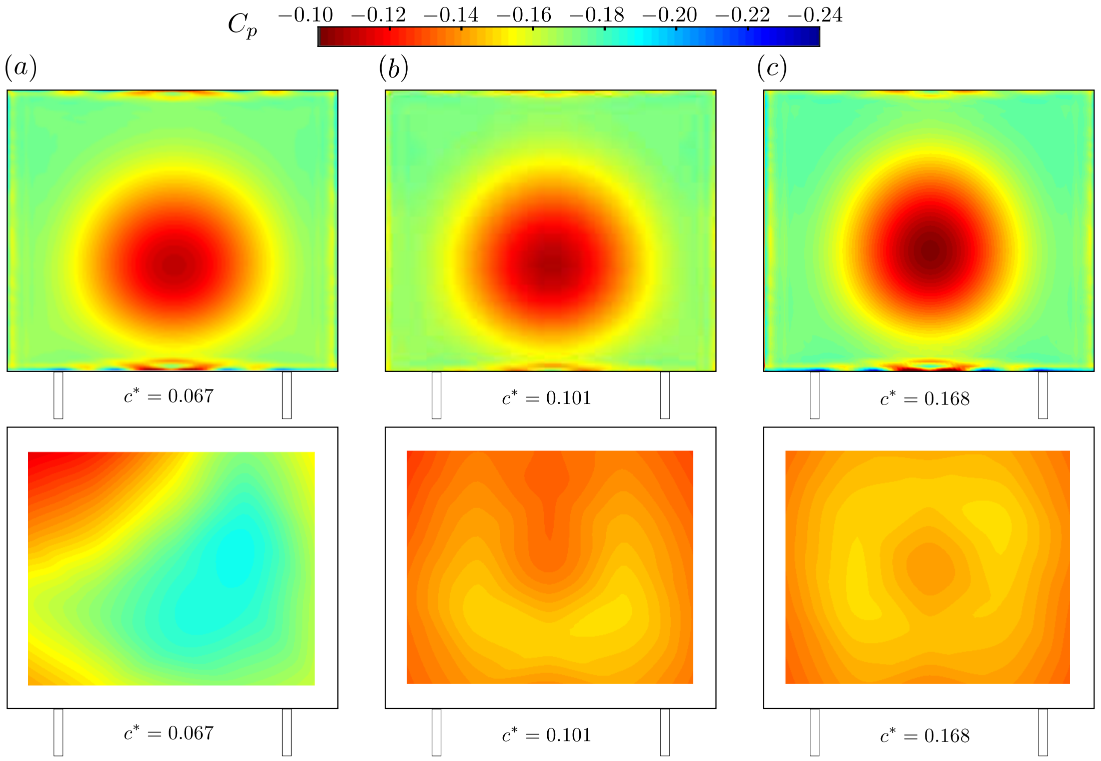

Figure 9 – En haut, distributions de pression moyenne au culot $C_p(y^*, z^*)$ pour le corps d'Ahmed à culot droit ($\alpha = \beta = 0°$) à différentes gardes au sol : (a) $c^* = 0.067$ (b) $c^* = 0.101$ (c) $c^* = 0.168$. En bas, distributions équivalentes pour le cas avec cavité de profondeur $d = 0.285\ H$ observées expérimentalement (voir annexe B).

au culot (figure 9), bien que non observées expérimentalement en raison de la présence de l'instabilité, sont similaires à celles d'autres études RANS (Khalighi *et al.*, 2001; van Raemdonck & van Tooren, 2008). Elles sont en revanche proches de celles observées avec une cavité au culot (voir annexe B) même si l'effet de cavité permet d'obtenir des pressions plus élevées.

Lorsque des calculs instationnaires sont déployés, on observe clairement le lâcher tourbillonnaire et sa contribution à l'effort latéral appliqué au corps. En revanche, la disymétrisation du sillage liée à l'instabilité n'a pas lieu et les résultats obtenus doivent être vus comme une étape préliminaire. L'objectif est de montrer, à l'aide d'une analyse de stabilité, par exemple basée sur le résolvant (Beneddine *et al.*, 2016, 2017), que l'instabilité est bien présente dans les équations URANS.

7 Multi-stabilité de sillage en présence de modes statiques

Dans ce chapitre, on étudie en soufflerie quatre véhicules réels à culot droit (Citroën Berlingo, Renault Kangoo, Peugeot Partner et 5008). Le but est de montrer que l'asymétrie de leur sillage lorsque le véhicule est aligné avec l'écoulement en conditions réelles de conduite (figure 10) est principalement dû à une instabilité statique du même type que celle observée sur le corps simplifié et ne résulte pas uniquement de la présence de la route. La stratégie est de provoquer un renversement pour révéler l'autre état du sillage, voire pour obtenir une dynamique bi-stable qui confirmerait sans ambigüité l'existence de l'instabilité.

Pour cela, on dispose – comme pour le corps d'Ahmed – de plusieurs leviers : la garde au sol du véhicule et ses angles de dérapage et d'assiette. Chacun des véhicules est soumis à une étude de sensibilité. Lorsque la garde au sol du 5008 est augmentée, la distribution de pression est profondément modifiée (figure 11*a*) avec un gradient vertical négatif et une baisse globale des niveaux de pression. Des distributions similaires sont observées pour le Kangoo en dérapage (figure 11*b*). Pour ce dernier véhicule, la sélection entre les deux états peut également être pilotée en fermant les entrées d'air du véhicule. Pour la première fois, de telles transitions sont aussi observées sans modifier la garde au sol et en gardant le dérapage nul. En imposant une assiette à cabrer, on retrouve la même configuration qu'en figure 11(a) pour le 5008. Le Partner et le Berlingo, eux, nécessitent que l'on ferme les entrées d'air pour observer le renversement en assiette (figure 11*c*).

Ces modifications de topologie du sillage ont des conséquences importantes sur le chargement aérodynamique du véhicule (en portance, mais aussi en traînée) comme le montre la série temporelle en figure 11(d). On y observe une succession d'états à faible portance comme ceux de la figure 10 et d'autres à portance plus grande comme ceux de la figure 11. En outre, cette dynamique est identique à celle du gradient ; comme la géométrie est inchangée, cela montre de façon certaine la coexistence de deux états du sillage et donc prouve qu'il est soumis à une instabilité.

L'autre contribution majeure du chapitre est de montrer que les relations gradients-efforts identifiées pour la géométrie simplifiée – voir les équations (3a) et (3b) – sont également applicables pour des véhicules réels pour lesquels on est capable de prédire le chargement instantané comme le prouve la courbe grise sur la figure 11(d).

Contrairement au corps d'Ahmed, les deux états n'ont pas la même intensité en raison des asymétries du véhicule (plancher - toit) et de la présence des roues. Par conséquent, la contribution de l'instabilité au chargement aérodynamique dépend de l'état : elle est de

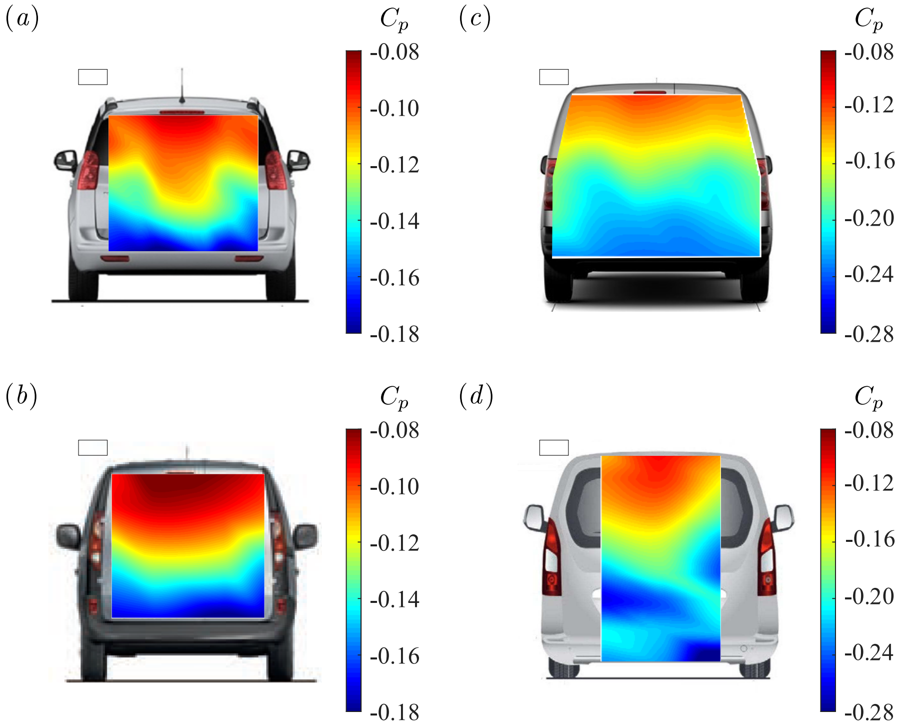

Figure 10 – Distributions de pression moyennes $C_p(y^*, z^*)$ au culot des véhicules alignés avec l'écoulement: (*a*) Peugeot 5008, (*b*) Renault Kangoo, (*c*) Peugeot Partner, (*d*) Citroën Berlingo.

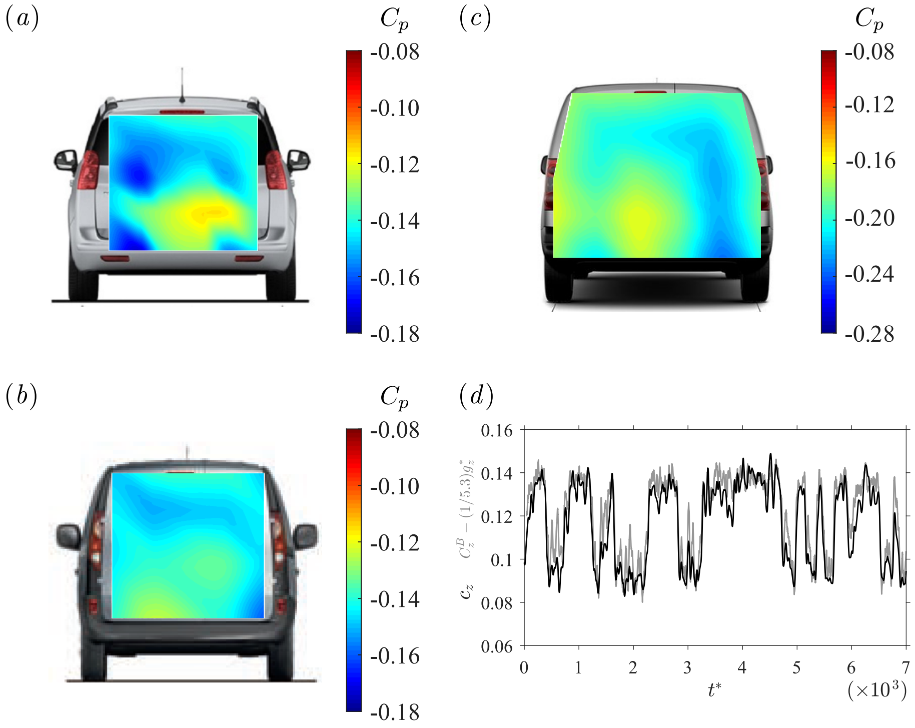

Figure 11 – Distributions de pressions moyennes $C_p(y^*, z^*)$ au culot des véhicules après renversement du sillage (état N): (*a*) Peugeot 5008 à grande garde au sol, (*b*) Renault Kangoo en dérapage, (*c*) Peugeot Partner en assiette avec entrée d'air bouchée. (*d*) Dynamique bi-stable pour le coefficient de portance du Citroën Berlingo.

$0,02$ dans l'état P montré en figure 10 et d'environ moitié moins dans l'état N. L'existence de ces deux états peut s'avérer problématique car l'état N a non seulement une portance mais aussi une traînée plus élevée (de l'ordre de 5%). On déploie des stratégies de contrôle pour tenter de retrouver l'état P à défaut de supprimer l'instabilité. L'utilisation de plaques latérales permet cette manipulation mais s'avère négative lorsque le « bon » état est déjà sélectionné. Une cavité au culot, dont les bénéfices en termes de traînée ont été montrés pour le corps d'Ahmed, permet de retrouver l'état P sans contribuer à la traînée dans ce cas.

On montre aussi que l'instabilité est sensible à la rugosité du soubassement. Dans le cas du Berlingo, un soubassement lisse verrouille le sillage dans l'état P même à grand angle d'assiette. La modification directe de la topologie de l'écoulement à l'aide d'une plaque plane permet de contrôler cette orientation et même de restaurer une dynamique multi-stable.

8 Multi-stabilité de sillage lors d'un recollement de couche limite

Dans le chapitre 8, on étudie finalement un autre cas de multi-stabilité de sillage observé en l'absence de mode à brisure de symétrie pour une Renault Mégane. En considérant les efforts appliqués sur le véhicule et leurs fluctuations (figure 12), on remarque une anomalie entre $\beta = \pm 8°$ et $\beta = \pm 10°$ qui correspond à une crise de fluctuations durant laquelle à la fois la traînée et la portance du véhicule augmentent sensiblement. En étudiant les gradients de pression au culot, on trouve une explication grâce à la composante verticale qui, de quasi-nulle, devient sensiblement négative. Ceci traduit une modification profonde de la topologie du sillage et n'est pas sans rappeler les résultats observés sur des géométries simplifiées à grands angles de dérapage (Meile *et al.*, 2016; Rao *et al.*, 2018).

Lorsque la voiture est alignée avec l'écoulement, le sillage produit une distribution de pression presque uniforme (figure 13a). Contrairement aux véhicules étudiés précédemment, il n'y a ni brisure de symétrie ni donc instabilité statique. Cette distribution typique est conservée jusqu'à la transition, c'est-à-dire pour des angles de dérapage $|\beta| \leq 8°$ (figures 13$a - d$) alors que pour $|\beta| = 10°$ on observe une large dépression sur le vitrage arrière (figure 13f). C'est entre ces deux configurations que s'établit la dynamique bi-stable du sillage qui explique les fluctuations importantes observées sur les grandeurs aérodynamiques.

Le cas industriel apporte une explication satisfaisante aux observations expérimentales et numériques de Meile *et al.* (2016) et Rao *et al.* (2018) avec un corps d'Ahmed : sous l'effet du dérapage, la pression moyenne chute au culot et la bulle de recirculation se raccourcit. Au moment de la transition, elle devient suffisamment proche de la lunette arrière pour qu'un recollement ait lieu. Cependant, celui-ci n'est pas permanent et la séparation de l'écoulement apparaît de façon aléatoire. Pour des angles plus importants, le recollement est permanent ce qui explique la réduction des fluctuations et la topologie du sillage.

Ce phénomène, bien que très différent de la multi-stabilité associée aux modes statiques, pose des problèmes relativement similaires puisque la traînée et la portance du véhicule augmentent drastiquement après la transition. De plus, celle-ci ne nécessite qu'un vent latéral pour se produire sans aucune modification de l'assiette du véhicule. Des modifications géométriques de l'arrière-corps peuvent être envisagées pour fixer le point de décollement aux bords de la lunette et donc éviter le recollement de la couche limite turbulente.

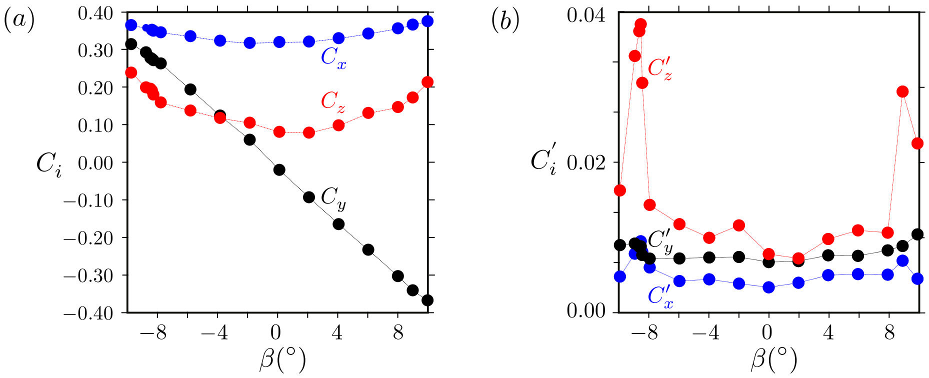

Figure 12 – Coefficients d'efforts en fonction du dérapage pour la Mégane : (*a*) valeurs moyennes, (*b*) fluctuations.

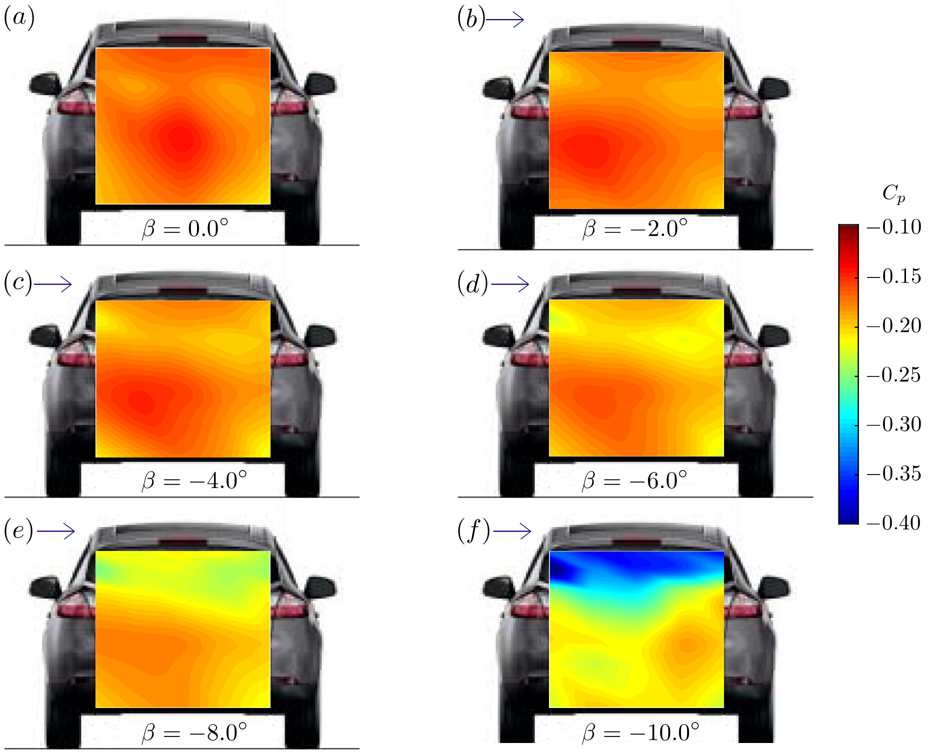

Figure 13 – Distributions moyennes de pression au culot de la Renault Mégane en dérapage : (*a*) cas aligné ($\beta = 0°$), (*b*) $\beta = 2°$, (*c*) $\beta = 4°$, (*d*) $\beta = 6°$, (*e*) $\beta = 8°$, (*f*) $\beta = 10°$. La flèche (pas à l'échelle) représente le vent latéral.

9 Conclusions

Dans cette thèse, la dynamique du sillage turbulent du corps d'Ahmed est étudiée et nous mettons en évidence les relations entre celle-ci et le chargement aérodynamique appliqué au véhicule à proximité du sol et pour différents rapports d'aspects de culot, avec des rétreints d'arrière-corps et pour différentes inclinaisons du corps. Ces résultats sont ensuite appliqués aux véhicules réels à culot vertical dont le sillage est également soumis à une instabilité statique ; les résultats sont en accord avec ceux de la géométrie simplifiée.
Les principales conclusions à retenir de ce travail sont les suivantes :

- L'écoulement est globalement stationnaire autour du corps d'Ahmed, sauf dans le sillage.

- Les instabilités y et z identifiées par Grandemange *et al.* (2013*a*) génèrent une contribution de l'ordre de 0.02 en termes de coefficients de forces aérodynamiques transverses. Ce chargement additionnel se déduit directement de la dynamique du sillage et de son orientation, prédite en fonction de l'alignement du corps par un modèle simple que nous introduisons dans le chapitre 4.

- Les rétreints d'arrière-corps permettent de contrôler la dynamique du sillage, à la fois en termes d'orientation et de fluctuations. L'instabilité n'est jamais supprimée, sauf lorsque l'on déclenche le mode périodique qui contribue encore plus à la traînée. Avec un rétreint tri-dimensionnel, l'instabilité du sillage, bien que toujours présente, contribue moitié moins aux efforts aérodynamiques et la traînée est encore réduite.

- L'existence de modes statiques asymétriques dans le sillage de monospaces et camionnettes est prouvée par l'exploration simultanée des deux états du sillage. Cette instabilité est responsable de l'asymétrie observée (dans la direction verticale) pour les quatre véhicules étudiés (Citroën Berlingo, Renault Kangoo, Peugeot Partner et 5008). La contribution majeure est que les résultats obtenus avec le corps simplifié soumis à l'instabilité z sont directement applicables aux véhicules ; par exemple, la contribution de l'instabilité au chargement aérodynamique est de l'ordre de $0,02$ en termes de coefficients d'efforts.

- L'instabilité statique du sillage n'est pas la seule cause de multi-stabilité. Un autre cas, observé pendant la transition entre deux topologies d'écoulement, est identifié sur une Renault Mégane ; le tenseur aérodynamique est fortement impacté. Le phénomène est associé à un recollement intermittent de la couche limite turbulente et apparaît à des angles de dérapage beaucoup plus importants.

Ce chapitre propose également un certain nombre de perspectives :

- Analyses de stabilité du sillage avec les calculs RANS instationnaires (URANS) pour montrer que l'instabilité est contenue dans les équations.

- Adaptation du chargement aérodynamique transverse en temps réel en contrôlant le sillage. En effet, la portance (sur le train arrière), qui influe fortement sur la stabilité du véhicule, dépend directement de l'état instantané du sillage ce qui offre des possibilités de contrôle.

- Favoriser les états de sillage à basse traînée. L'idée est soit d'empêcher le renversement du sillage, soit de retrouver l'état « optimal » si un renversement s'est produit. Cela nécessite de connaître en temps réel l'état de sillage par exemple, comme cela est fait dans cette thèse, en utilisant des capteurs de pression judicieusement choisis. Comme pour le corps simplifié, on observe que les configurations bi-stables, qui conduisent à l'exploration de l'état symétrique stable, sont associées à un minimum de traînée ; une stratégie pourrait être alors, pour certains cas bien choisis, de forcer cette dynamique.

- Suppression de l'instabilité statique pour symétriser le sillage. Dans ce travail, nous ne sommes pas parvenus à supprimer l'instabilité statique sauf dans deux cas : en créant une cavité au culot du corps et lorsque nous avons déclenché le mode périodique dont la contribution à la traînée est plus importante que l'instabilité. Sa suppression est un objectif majeur en particulier puisque nous avons montré que les monospaces et SUV sont également concernés. Supprimer l'instabilité permet peut-être d'augmenter l'autonomie des véhicules en réduisant leur consommation et leurs émissions polluantes mais aussi d'obtenir une physique plus simple à prédire (orientation du sillage, fluctuations, chargement aérodynamique induit. . .) dans le cadre du processus d'optimisation des arrière-corps.

Titre : Dynamiques des modes instables de sillages en aérodynamique automobile : des modèles simplifiés aux véhicules réels

Mots clés : Sillages, écoulements turbulents, corps non profilés, réduction de traînée, stabilité

Résumé : Depuis la découverte des modes asymétriques dans le sillage d'un corps simplifié d'automobile, réminiscents d'une bifurcation à bas nombre de Reynolds, se posent des questions propres au développement aérodynamique des véhicules terrestres telles que l'influence du vent latéral, de l'assiette et du rétreint d'arrière-corps couramment utilisé en phase d'optimisation. Notre travail s'attache à répondre expérimentalement à ces questions pour des géométries simplifiées mais aussi réelles. Les essais sont réalisés en soufflerie industrielle à l'échelle 2/5 pour le corps académique et en pleine échelle pour les monospaces. Nous montrons que le désalignement du véhicule par rapport à l'écoulement incident n'a pour effet que de modifier l'orientation du mode asymétrique sans en changer l'intensité. Nous construisons un modèle simple prédisant non seulement cette orientation mais aussi les conséquences sur les efforts aérodynamiques transverses. La contribution de l'instabilité sur les coefficients aérodynamiques de portance ou d'effort latéral est de l'ordre de 0,02 indépendamment du vent de travers et de l'assiette du véhicule. Les rétreints d'arrière-corps affectent également la dynamique du sillage et son orientation, mais l'instabilité n'est jamais supprimée. Ces résultats sont retrouvés pour des véhicules réels de type monospace dont le sillage est donc également soumis au même mode asymétrique, révélé sans ambigüité par des expériences de sensibilité en assiette. Nos résultats indiquent que, pour tous les véhicules considérés, le mode asymétrique de sillage est systématiquement présent dans l'enveloppe de conduite. Le contrôle ou la suppression de ce mode devrait offrir de nouvelles perspectives d'optimisation des véhicules à culot droit de type monospaces ou SUV.

Title : Dynamics of the unstable wake modes in automotive aerodynamics: from simplified models to real vehicles

Keywords : Wake flows, turbulent flows, bluff bodies, drag reduction, stability

Abstract : Since the recent discovery of asymmetric modes in the wake of a simplified vehicle geometry, reminiscent from a bifurcation at low Reynolds numbers, some questions related to the aerodynamic development of ground vehicles such as the influence of lateral wind, pitch and afterbody boat-tail classically used during shape optimization remain unanswered. Our work is devoted to assess those questions experimentally for simplified but also real geometries. The tests are conducted in an industrial wind-tunnel, at the 2/5-scale for the academic body and at the full scale for the minivans. We show that the vehicle's misalignment only modifies the asymmetric mode's orientation without affecting its intensity. We build a model predicting not only this orientation but also the consequences on the cross-flow aerodynamic loading. The contribution of the instability to the lift or side force coefficients is of the order of 0,02 independently of lateral wind or of the vehicle's pitch. Afterbody boat-tails also impact the wake dynamics and its orientation but the instability is never suppressed. These results are retrieved for real vehicles such as minivans, whose wake is then subjected to the same asymmetric mode as well, revealed unambiguously with pitch sensitivity experiments. Our results indicate that, for all considered vehicles, the asymmetric wake mode is systematically present in the driving envelope. The control or the suppression of this mode should offer new optimization's perspectives for blunt based vehicles such as minivans or SUVs.